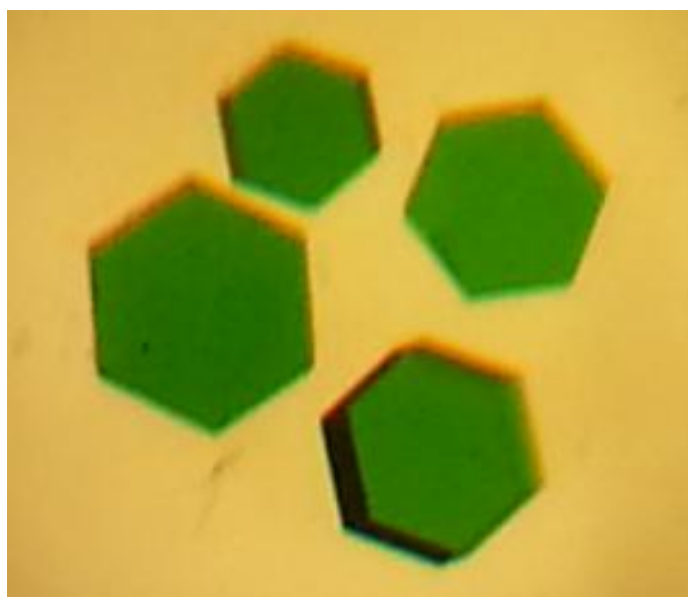
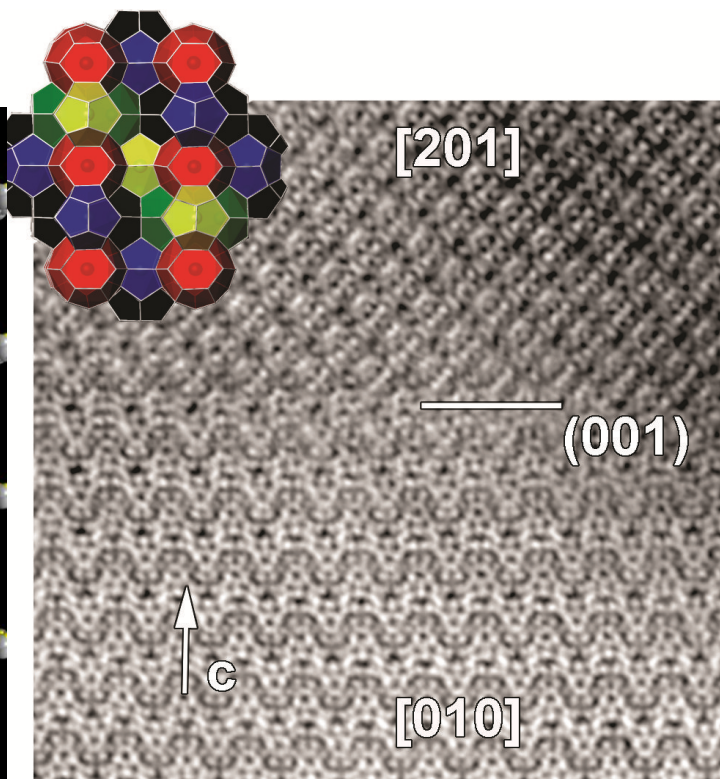
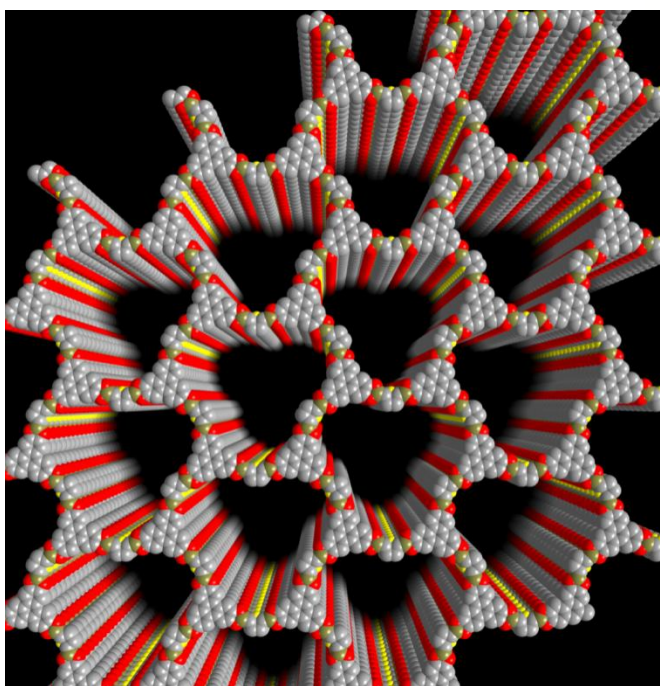


Materials Chemistry Principal Investigators' Meeting—2014

July 14-16, 2014

Hilton Washington DC North Hotel, Gaithersburg, MD



U.S. DEPARTMENT OF
ENERGY

Office of Basic Energy Sciences
Materials Sciences and Engineering Division

On the Cover

Top Left: The image depicts a portion of the ordered structure of a thiophene-based covalent organic framework, with perfect vertical alignment of thiophene units (sulfur atoms in thiophene are yellow)

Courtesy: Dr. Mircea Dincă, Massachusetts Institute of Technology

Top Right: Crystal structure (upper left corner) and one of the numerous twinning interfaces of $\text{Ba}_8\text{Au}_{16}\text{P}_{30}$

Courtesy: Dr. Kirill Kovnir, University of California–Davis

Bottom Left: Crossed polarized optical texture micrograph of a bent-core mesogen.

Courtesy: Dr. Quan Li, Kent State University

Bottom Right: Photographic images of $\text{Na}_4\text{M U}_6\text{F}_{30}$ single crystals

Courtesy: Dr. H.-C. zur Loye, University of South Carolina

This document was produced under contract number DE-AC05-06OR23100 between the U.S. Department of Energy and Oak Ridge Associated Universities.

The research grants and contracts described in this document are supported by the U.S. DOE Office of Science, Office of Basic Energy Sciences, Materials Sciences and Engineering Division.

Foreword

This document is a collection of abstracts of the presentations made at the Principal Investigators' Meeting of the Materials Chemistry program, sponsored by the Materials Sciences and Engineering (MSE) division in the Office of Basic Energy Sciences (BES) of the U. S. Department of Energy (DOE). The meeting was held on July 14–16, 2014, at the Hilton Washington DC North Hotel in Gaithersburg, Maryland, and is one of a series of Principal Investigators' Meetings organized by BES. The purpose of the meeting is to bring together all the Principal Investigators with currently active projects in the Materials Chemistry program for the multiple purposes of raising awareness among PIs of the overall program content and of each other's research, encouraging exchange of ideas, promoting collaboration and stimulating innovation. The meeting also provides an opportunity for the Program Manager and MSE/BES management to get a comprehensive overview of the program on a periodic basis, which provides opportunities to identify program needs and potential new research directions. The meeting agenda is organized in nine sessions around topical areas in materials research that encompass many of the projects in the current Materials Chemistry portfolio. These include: Predictive Materials Discovery; Inorganic Conductors, Semiconductors and Superconductors; Organic and Polymer Assemblies and Networks; Metal and Covalent Organic Frameworks; Materials characterization; Organic and Polymer Assemblies and Networks: *Electronics and photonics*; Nanostructures and Low-dimensional Structures; Electrochemical Interfaces and Energy Storage; and Energy Generation and Conversion.

Recent BES workshops and other reports have identified the concept of “Materials by Design” as a Grand Challenge goal, defined as the ability to design and synthesize new materials with specific properties tailored and optimized for use in next-generation technologies. In support of the Materials by Design objective, the Materials Chemistry program supports basic research in the discovery, design and synthesis of materials with an emphasis on elucidating the complex relationships between a material's functional properties and its composition, atomic and molecular structure and higher-order morphology. Major focus areas of the program include the discovery, synthesis and characterization of new materials and the manipulation of materials' structure across a range of length scales using *chemistry*.

We thank all of the meeting attendees, including the invited speakers, for their active participation and for sharing their ideas and new research results. The assistance of the Meeting Chairs, Jennifer Hollingsworth and Howard Katz, in organizing this meeting is greatly appreciated. Sincere thanks also go to Teresa Crockett in MSE and Tammy Click and her colleagues at the Oak Ridge Institute for Science and Education (ORISE) for their excellent work providing all the logistical support for the meeting.

Michael Sennett
Craig Henderson
Program Managers, Materials Chemistry
Materials Sciences and Engineering Division
Office of Basic Energy Sciences
U.S. Department of Energy

Agenda

Meeting Chairs
Howard Katz and **Jennifer Hollingsworth**
Johns Hopkins University
Los Alamos National Laboratory

Agenda

Monday, July 14, 2014

7:00 – 8:00 am ***** Breakfast*****

8:00 – 8:15 am *Welcome*
Arvind Kini
Team Lead, Materials Discovery Design and Synthesis
Materials Sciences and Engineering Division, Basic Energy Sciences

8:15 – 8:30 am *Introductory Remarks*
Michael Sennett and Craig Henderson
Program Managers, Materials Chemistry
Meeting Chairs: **Howard Katz** and **Jennifer Hollingsworth**
Johns Hopkins University and Los Alamos National Laboratory

Session I **Predictive Materials Discovery**
Chair: **Robert Cava**, Princeton University

8:30 – 9:00 am **Gerbrand Ceder (Invited)**, Massachusetts Institute of Technology
*The Materials Project: Accelerated and Large-Scale Materials Research
through Computation and Data Mining* 291

9:00 – 9:20 am **Andreas Stein**, University of Minnesota
*Computation-Guided Synthetic Strategies for Nanocomposite Electrode
Structures Designed to Probe Critical Size Effects on Charge Storage
and Transport* 241

9:20 – 9:40 am **Karl Freed**, University of Chicago
Towards the Rational Design of Glassy Polymer Materials 127

9:40 – 10:00 am **Arthi Jayaraman**, University of Colorado at Boulder
*Theory and Simulations of Polymer Nanocomposites Linking Molecular
Features of the Polymers and Additives to Composite Morphology for
Organic Photovoltaic Applications* 166

10:00 – 10:20 am ***** Break *****

Session II **Inorganic Conductors, Semiconductors, and Superconductors**
Chair: **Mercouri Kanatzidis**, Argonne National Laboratory/ Northwestern University

10:20 – 10:40 am **Hans-Conrad zur Loye**, University of South Carolina
*A Synthetic Strategy to Prepare New Complex Uranium- and Thorium-
Containing Oxides: Predictive Solid State Synthesis of New Composition
using Radius Ratio Rules and Materials Discovery based on Crystal Growth
from High Temperature Solutions* 285

10:40 – 11:00 am	Svilen Bobev , University of Delaware <i>Novel Pnictides with d- and f-Metals as Prospective Materials for Thermal Energy Conversion</i>	73
11:00 – 11:20 am	Kirill Kovnir , University of California–Davis <i>Unconventional Clathrates Based on Transition Metal Pnictides: A Paradigm-Shifting Approach to Materials with Enhanced Thermoelectric Properties</i>	186
11:20 – 11:40 am	Yi Cui , SLAC National Accelerator Laboratory <i>Two-Dimensional Chalcogenide Nanomaterials</i>	89
11:40 – 1:00 pm	***** Working Lunch***** <i>Informal discussions and poster introductions</i>	
Session III	Organic and Polymer Assemblies and Networks <u>Chair: Ting Xu</u> , Lawrence Berkeley National Lab/ University of California–Berkeley	
1:00 – 1:20 pm	Tomonori Saito , Oak Ridge National Laboratory <i>Polymer-Based Multicomponent Materials</i>	43
1:20 – 1:40 pm	Thomas P. Russell , University of Massachusetts–Amherst <i>Interfacial Behavior of Polymers: Using Interfaces to Manipulate Polymers</i>	233
1:40 – 2:00 pm	Juan de Pablo , Argonne National Laboratory/University of Chicago <i>Solvent-Assisted Nonequilibrium Directed Self-Assembly of Complex Polymeric Materials</i>	93
2:00 – 2:20 pm	Satyendra Kumar , Kent State University <i>Biaxiality in Nematic and Smectic Liquid Crystals</i>	190
2:20 – 2:40 pm	***** Break *****	
Session IV	Metal and Covalent Organic Frameworks <u>Chair: Adam Matzger</u> , University of Michigan	
2:40 – 3:00 pm	Seth Cohen , University of California–San Diego <i>Tuning Sorption Properties of Metal-Organic Frameworks via Postsynthetic Covalent Modification</i>	85
3:00 – 3:20 pm	Hani El-Kaderi , Virginia Commonwealth University <i>Small Gas Storage and Selective Carbon Dioxide Capture by Nanoporous Organic Polymers</i>	111
3:20 – 3:40 pm	Pingyun Feng , University of California–Riverside <i>Pore Space Engineering and Functionalization in Porous Metal-Organic Framework Materials</i>	115
3:40 – 4:00 pm	Mircea Dincă , Massachusetts Institute of Technology <i>Electronic and Ionic Conductors from Ordered Microporous Materials</i>	98
4:00 – 6:00 pm	***** Poster Session 1 *****	
6:00 – 7:30 pm	***** Working Dinner *****	

Tuesday, July 15, 2014

7:00 – 8:00 am ***** Breakfast*****

Session V

Materials Characterization

Chair: **Harald Ade**, North Carolina State University

- 8:00 – 8:30 am **AJ (Timmy) Ramirez-Cuesta (Invited)**, CEMD, Oak Ridge National Laboratory
Neutron Instruments for Chemistry 292
- 8:30 – 8:50 am **May Nyman**, Oregon State University
Fundamental Ion-Association and Acid-Base Behavior of Aqueous Species: Unprecedented Perspective from Anomalous Solubility 213
- 8:50 – 9:10 am **Steve G. Greenbaum**, Hunter College of the City University of New York
NMR Studies of Materials for Electrochemical Energy Storage 143
- 9:10 – 9:30 am **E. M. Levin**, Ames Laboratory
¹²⁵Te NMR and Thermoelectric Properties of Complex Tellurides: The Role of Materials Chemistry 27
- 9:30 – 10:00 am *****Break*****

Session VI

Organic and Polymer Assemblies and Networks: *Electronics and Photonics*

Chair: **Dan Frisbie**, University of Minnesota

- 10:00 – 10:20 am **Robert C. Haddon**, University of California–Riverside
Solid State Electronic Structure and Properties of Neutral Carbon-Based Radicals 147
- 10:20 – 10:40 am **Thomas Gennett**, National Renewable Energy Laboratory
Fundamental Charge Transfer Processes in Stable Free-Radical Organic Polymer Systems 11
- 10:40 – 11:00 am **Thomas G. Gray**, Case Western Reserve University
Cyclometalation Syntheses of Phosphorescent Complexes 139
- 11:00 – 11:20 am **Hong Wang**, Miami University of Ohio
Donor-Acceptor π -Extended Porphyrins for Solar Energy Conversion 269
- 11:20 – 11:40 am **Ryan Hayward**, University of Massachusetts–Amherst
Crystallization-Driven Assembly of Conjugated-Polymer–Based Nanostructures 151
- 11:40 – 1:10 pm ***** Working Lunch*****
Informal discussions and poster introductions
- 1:10 – 1:30 pm **Michael Sennett and Craig Henderson**
BES Presentation on Programmatic Issues

Session VII	Nanostructures and Low-Dimensional Structures <u>Chair:</u> Cherie Kagan , University of Pennsylvania
1:30 – 1:50 pm	Cherie Kagan , University of Pennsylvania, <i>SISGR: Bi-continuous Multi-component Nanocrystal Superlattices for Solar Energy Conversion</i> 178
1:50 – 2:10 pm	Felix Fischer , University of California–Berkeley <i>Atomically Defined Edge Doping of Graphene Nanoribbons for Mesoscale Electronics</i> 119
2:10 – 2:30 pm	Nick Melosh , SLAC National Accelerator Laboratory <i>Diamondoid Science and Applications</i> 202
2:30 – 2:50 pm	Jonathan S. Owen , Columbia University <i>The Dynamic Stoichiometry of Metal Chalcogenide Nanocrystals</i> 217
2:50 – 3:00 pm	*****Break*****

Session VIII	Electrochemical Interfaces and Energy Storage <u>Chair:</u> Nenad Markovic , Argonne National Laboratory
3:00 – 3:20 pm	Sheng Dai , Oak Ridge National Laboratory <i>Materials and Interfacial Chemistry for Next Generation Electrical Energy Storage</i>7
3:20 – 3:40 pm	Xiaowei Teng , University of New Hampshire <i>Transition Metal Oxides Spinel Nanomaterials for Supercapacitor Reactions</i> 249
3:40 – 4:00 pm	Richard L. Brutchey , University of Southern California <i>Mitigating Breakdown in High Energy Density Perovskite Polymer Nanocomposite Capacitors</i> 77
4:00 – 6:00 pm	***** Poster Session 2 *****
6:00 – 7:30 pm	***** Working Dinner *****

Wednesday, July 16, 2014

7:00 – 8:00 am ***** Breakfast *****

Session IX	Energy Generation and Conversion <u>Chairs:</u> Miquel Salmeron and Song Jin , Lawrence Berkeley National Lab/ University of California–Berkeley and University of Wisconsin–Madison
8:00 – 8:30 am	John Rogers , University of Illinois Urbana-Champaign <i>Programming Function in Soft Matter</i> 229
8:30 – 8:50 am	M. A. Baldo , Massachusetts Institute of Technology <i>High Efficiency Biomimetic Organic Solar Cells</i> 69

8:50 – 9:10 am	Samson Jenekhe , University of Washington <i>Molecular and Nanoscale Engineering of High Efficiency Excitonic Solar Cells</i>	170
9:10 – 9:30 am	Thuc-Quyen Nguyen , University of California–Santa Barbara <i>Charge Recombination, Transport Dynamics, and Interfacial Effects in Organic Solar Cells</i>	206
9:30 – 10:00 am	*****Break*****	
10:00 – 10:20 am	Larry Curtiss , Argonne National Laboratory <i>Cluster/Carbon Composite Materials for Energy</i>	3
10:20 – 10:40 am	Philip P. Power , University of California–Davis <i>Activation of Hydrogen under Ambient Conditions by Main Group Molecules</i>	221
10:40 – 11:00 am	Z. Valy Vardeny , University of Utah <i>Novel 'Singlet Fission' in Low-Bandgap Polymers for Enhancing the Efficiency of Organic Photovoltaic Solar Cell</i>	261
11:00 – 12:00 am	Program Managers and Meeting Chairs <i>Wrap-up, debriefing, evaluation</i>	

Poster Session 1: Monday, July 14, 2014 4:00 – 6:00 pm

- 1a. Predictive Materials Discovery
- 1b. Inorganic Conductors, Semiconductors, and Superconductors
- 1c. Organic and Polymer Assemblies and Networks
- 1d. Metal and Covalent Organic Frameworks

Poster Session 2: Tuesday, July 15, 2014 4:00 – 6:00 pm

- 2a. Materials Characterization
- 2b. Organic and Polymer Assemblies and Networks: *Electronics and Photonics*
- 2c. Nanostructures and Low-Dimensional Structures
- 2d. Electrochemical Interfaces and Energy Storage
- 2e. Energy Generation and Conversion

Table of Contents

Table of Contents

Foreword	i
Agenda	v
Table of Contents	xiii
 Laboratory Projects	
<i>Two-Dimensional Chalcogenide Nanomaterials</i>	
Yi Cui and Harold Hwang	3
<i>Cluster/Carbon Composite Materials for Energy</i>	
Larry A. Curtiss, Stefan Vajda, Peter Zapol, and Michael J. Pellin	7
<i>Materials and Interfacial Chemistry for Next-Generation Electrical Energy Storage</i>	
S. Dai, M. P. Paranthaman, C. A. Bridges, X. G. Sun, G. M. Veith, J. B. Goodenough, and A. Manthiram	11
<i>Solvent-Assisted Nonequilibrium Directed Self-Assembly of Complex Polymeric Materials</i>	
Juan J. de Pablo, Paul F. Nealey, and M. Tirrell	15
<i>Fundamental Charge Transfer Processes in Stable Free-Radical Organic Polymer Systems</i>	
Thomas Gennett	20
<i>Linking Ion Solvation and Lithium Battery Electrolyte Properties</i>	
Wesley Henderson	24
<i>“Giant” Nanocrystal Quantum Dots: Controlling Charge Recombination Processes for High-Efficiency Solid-State Lighting</i>	
Jennifer A. Hollingsworth and Han Htoon	28
<i>Rational Synthesis of Superconductors</i>	
Mercouri G. Kanatzidis	32
<i>¹²⁵Te NMR and Thermoelectric Properties of Complex Tellurides: The Role of Materials Chemistry</i>	
E. M. Levin and K. Schmidt-Rohr	36
<i>Energy and Fuels from Multifunctional Electrochemical Interfaces</i>	
Nenad M. Markovic and Vojislav R. Stamenkovic	40
<i>Diamondoid Science and Applications</i>	
Nick Melosh, Z. X. Shen, and Peter Scheiner	44

<i>Nuclear Magnetic Resonance</i> Alexander Pines	48
<i>Hydroxide Conductors for Energy Conversion Devices</i> Matthew Sturgeon, Clay Macomber, Chaiwat Engtrakul, Hai Long, and Bryan Pivovar	52
<i>Polymer-Based Multicomponent Materials</i> Tomonori Saito, Bobby Sumpter, Vera Bocharova, Volker Urban, Alex Kisliuk, Jimmy Mays, Mark Dadmun, Ken Schweizer, Frank Bates, and Alexei Sokolov	56
<i>Structure and Dynamics of Solid-Liquid Interfaces</i> Miquel Salmeron, Gabor Somorjai, and Peidong Yang	60
<i>Directed Energy Interactions with Surfaces</i> Michael Savina, Michael Pellin, and Alexander Zinovev	64
<i>Crystal Growth, Structure, Phase Relationships, and Magnetic Properties of Transition Metal Substituted Mn_{1-x}Bi Compounds</i> Srinivasa Thimmaiah, Qisheng Lin, and Gordon J. Miller	68
<i>Toward Hierarchically Structured Functional Nanocomposites</i> Ting Xu, Miquel Salmeron, Paul Alivisatos, Yi Liu, and Jean Fréchet	72
<i>Understand Organic/Inorganic Interface Toward Electroactive Nanocomposites</i> Ting Xu, Lin-Wang Wang, Miquel Salmeron, Paul Alivisatos, Yi Liu, and Tanja Cuk	76
<i>Physical Chemistry of Inorganic Nanostructures</i> Paul Alivisatos, Stephen Leone, and Peidong Yang	80
University Grant Projects	
<i>Control of Interface- and Mesoscopic Structure in High Performance Organic Solar Cells: Towards a Predictive Device Paradigm</i> Harald Ade	87
<i>High Efficiency Biomimetic Organic Solar Cells</i> M. A. Baldo and T. Van Voorhis	91
<i>Novel Pnictides with d- and f-Metals as Prospective Materials for Thermal Energy Conversion</i> Svilen Bobev	95
<i>Mitigating Breakdown in High Energy Density Perovskite Polymer Nanocomposite Capacitors</i> Richard L. Brutchey	99

<i>New Superconducting Materials</i> Robert J. Cava	103
<i>Tuning Sorption Properties of Metal-Organic Frameworks via Postsynthetic Covalent Modification</i> Seth M. Cohen	107
<i>Electronic and Ionic Conductors from Ordered Microporous Materials</i> Mircea Dincă	111
<i>Rational Design and Nanoscale Integration of Multi-heterostructure Photocatalysts</i> Xiangfeng Duan	116
<i>Molecular Magnets Based on a Modular Approach: Investigation of Coupling, Anisotropy, and Electronic Factors on Bistability</i> Kim R. Dunbar	120
<i>Small Gas Storage and Selective Carbon Dioxide Capture by Nanoporous Organic Polymers</i> Hani M. El-Kaderi	124
<i>Pore Space Engineering and Functionalization in Porous Metal-Organic Framework Materials</i> Pingyun Feng	128
<i>Atomically Defined Edge Doping of Graphene Nanoribbons for Mesoscale Electronics</i> Felix R. Fischer	132
<i>Chemical Frustration: A Design Principle for the Discovery of New Complex Intermetallic and Alloy Phases</i> Daniel C. Fredrickson	136
<i>Towards the Rational Design of Glassy Polymer Materials</i> Karl F. Freed	140
<i>Cathode Catalysis in Hydrogen/Oxygen Fuel Cells: New Catalysts, Mechanism, and Characterization</i> Andrew A. Gewirth, Paul J. A. Kenis, Ralph G. Nuzzo, and Thomas B. Rauchfuss	144
<i>Materials and Interfacial Chemistry for Next-Generation Electrical Energy Storage</i> John B. Goodenough and Arumugam Manthiram	148
<i>Cyclometalation Syntheses of Phosphorescent Complexes</i> Thomas G. Gray	152
<i>NMR Studies of Materials for Electrochemical Energy Storage</i> Steve G. Greenbaum	156

<i>Solid State Electronic Structure and Properties of Neutral Carbon-Based Radicals</i> Robert C. Haddon	160
<i>Crystallization-Driven Assembly of Conjugated-Polymer–Based Nanostructures</i> Ryan C. Hayward	164
<i>Optical Spectroscopy and Scanning Tunneling Microscopy Studies of Molecular Adsorbates and Anisotropic Ultrathin Films</i> John C. Hemminger	167
<i>Relationships between the Chemistry and Physical Interaction Forces (Adhesion, Friction, and Lubrication) between Closely Apposed Surfaces in Liquids</i> Jacob Israelachvili	171
<i>Enhanced Mixed Electronic-Ionic Conductors through Cation Ordering</i> Allan J. Jacobson, Dane Morgan, and Clare Grey	175
<i>Theory and Simulations of Polymer Nanocomposites Linking Molecular Features of the Polymers and Additives to Composite Morphology for Organic Photovoltaic Applications</i> Arthi Jayaraman	179
<i>Molecular and Nanoscale Engineering of High Efficiency Excitonic Solar Cells</i> Samson A. Jenekhe, Guozhong Cao, and David S. Ginger	183
<i>Fundamental Studies of Charge Transfer in Nanoscale Heterostructures of Earth-Abundant Semiconductors for Solar Energy Conversion</i> Song Jin, John C. Wright, and Robert J. Hamers	187
<i>Bi-continuous Multi-component Nanocrystal Superlattices for Solar Energy Conversion</i> Cherie R. Kagan, Christopher B. Murray, James M. Kikkawa, and Nader Engheta	191
<i>Molecularly Designed Localized Static Charging for Energy Efficiency in Organic Electronics</i> Howard E. Katz, Daniel H. Reich, and Nina Markovic	195
<i>Unconventional Clathrates Based on Transition Metal Pnictides: A Paradigm-Shifting Approach to Materials with Enhanced Thermoelectric Properties</i> Kirill Kovnir	199
<i>Biaxiality in Nematic and Smectic Liquid Crystals</i> Satyendra Kumar, Quan Li, D. M. Agra-Kooijman, Alejandro Rey, and M. Srinivasarao	203
<i>Materials Science of Electrodes and Interfaces for High-Performance Organic Photovoltaics</i> Tobin J. Marks, Robert P. H. Chang, Arthur J. Freeman, Thomas O. Mason, and Kenneth R. Poeppelmeier	207

<i>Leveraging Kinetic Control in the Assembly and Sorption Properties of Nanostructured Porous Materials</i> Adam J. Matzger and Antek G. Wong-Foy	211
<i>Charge Recombination, Transport Dynamics, and Interfacial Effects in Organic Solar Cells</i> Alan J. Heeger, Guillermo C. Bazan, Thuc-Quyen Nguyen, and Fred Wudl	215
<i>Programming Function in Soft Matter</i> Ralph G. Nuzzo, John A. Rogers, Jeffrey S. Moore, and K. Jimmy Hsia	219
<i>Fundamental Ion-Association and Acid-Base Behavior of Aqueous Species: Unprecedented Perspective from Anomalous Solubility</i> May Nyman	222
<i>The Dynamic Stoichiometry of Metal Chalcogenide Nanocrystals</i> Jonathan S. Owen	226
<i>Activation of Hydrogen under Ambient Conditions by Main Group Molecules</i> Philip P. Power	230
<i>Molecular Processes Underlying the Structure and Assembly of Thin Films and Nanoparticles at Complex Interfaces</i> Geraldine L. Richmond	234
<i>Programming Function via Soft Materials</i> Paul V. Braun, Randy Ewoldt, Steve Granick, K. Jimmy Hsia, Xiuling Li, Jeffrey S. Moore, Ralph G. Nuzzo, John A. Rogers, and Kenneth S. Schweizer	238
<i>Interfacial Behavior of Polymers: Using Interfaces to Manipulate Polymers</i> Thomas P. Russell	242
<i>Dielectric Ceramics in Nanosheet Form</i> Tina T. Salguero	246
<i>Computation-Guided Synthetic Strategies for Nanocomposite Electrode Structures Designed to Probe Critical Size Effects on Charge Storage and Transport</i> Andreas Stein, Donald G. Truhlar, and William H. Smyrl	250
<i>Electrochemically Smart Bimetallic Materials Featuring Group 11 Metals: In Situ Conductive Network Generation and Its Impact on Cell Capacity</i> Esther S. Takeuchi, Kenneth J. Takeuchi, and Amy C. Marschilok	254
<i>Transition Metal Oxides Spinel Nanomaterials for Supercapacitor Reactions</i> Xiaowei Teng	258

<i>Mesoscale Photophysical Properties of Anisotropic Hybrid Nanostructure Assemblies</i> Vladimir V. Tsukruk and Mostafa El-Sayed	262
<i>Novel 'Singlet Fission' in Low-Bandgap Polymers for Enhancing the Efficiency of Organic Photovoltaic Solar Cells</i> Z. Vally Vardeny	266
<i>Linking Metal Ions via Inorganic Click (iClick) Reactions</i> Adam S. Veige	270
<i>Donor-Acceptor π-Extended Porphyrins for Solar Energy Conversion</i> Hong Wang and Lei Kerr	274
<i>Extracting Hot Carriers from Photoexcited Semiconductor Nanocrystals</i> Xiaoyang Zhu	278
<i>Spectroscopy of Charge Carriers and Traps in Field-Doped Single Crystal Organic Semiconductors</i> Xiaoyang Zhu and C. Daniel Frisbie	281
<i>A Synthetic Strategy to Prepare New Complex Uranium- and Thorium-Containing Oxides: Predictive Solid State Synthesis of New Composition using Radius Ratio Rules and Materials Discovery based on Crystal Growth from High Temperature Solutions</i> Hans-Conrad zur Loye	285
 Invited Talks	
<i>The Materials Project: Accelerated and Large-Scale Materials Research through Computation and Data Mining</i> Gerbrand Ceder and Kristin Persson	291
<i>Neutron Instruments for Chemistry</i> AJ (Timmy) Ramirez-Cuesta	292
 Poster Sessions List	297
Author Index	305
Participant List	307

***LABORATORY
PROJECTS***

Two-Dimensional Chalcogenide Nanomaterials

Prof. Yi Cui (Lead), Prof. Harold Hwang

1. Geballe Laboratory for Advanced Materials, Stanford University

2. Stanford Institute for Materials and Energy Sciences, SLAC National Accelerator Laboratory

Program Scope

Our vision is to build a cutting-edge interdisciplinary program on two-dimensional (2D) chalcogenide (O, S, Se, Te) nanomaterials, with emphasis on their design, growth, and basic electronic, spintronics, electrochemical and catalytic properties. We envision that our research can lead to the rational design and creation of “2D Artificial Materials” with exciting properties. They will form a basis for new materials approaches to charge storage and transfer for advanced batteries and fuel cells, novel electronics/spintronics, catalysis, thermoelectrics, and hybrid functionalities.

Recent Progress

1) Progress on 2D materials synthesis

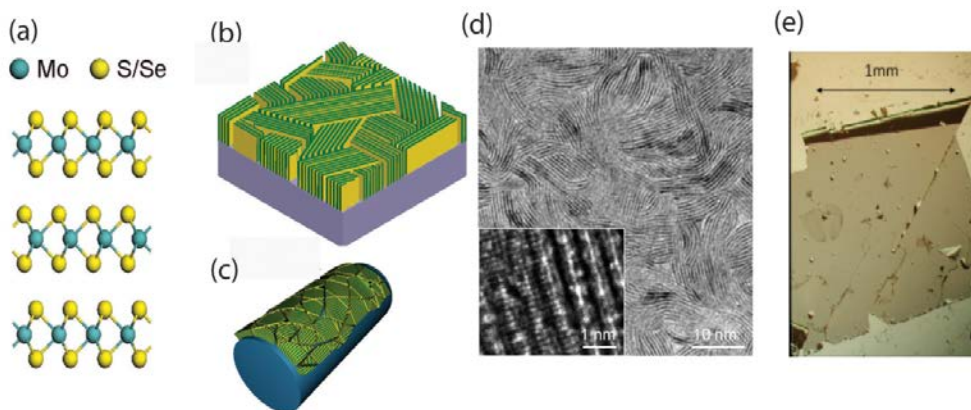


Figure 1: a) Crystal structure of MoS₂ and MoSe₂. Schematic of vertically aligned 2D layered materials on b) flat substrate and c) rough substrate. d) Transmission electron microscopy image of MoS₂ vertical layers. e) Optical microscope image of a Nd_{0.5}Sr_{0.5}MnO₃ free-standing epitaxial film transferred onto a sapphire substrate.

Vertically aligned 2D layered materials: (Fig. 1a to d) Most 2D materials studied in the literature including binary dichalcogenides such as MoS₂ and graphene are inclined to be terminated by the basal planes to reduce the exposed edges due to their inherently high surface energy. However, exposing the edges of 2D materials can provide exciting control opportunities of their electronic and catalytic properties. We have successfully developed the synthesis and structural characterization of a family of 2D-layered metal dichalcogenide nanofilms (MoS₂, MoSe₂, WS₂, WSe₂) whose crystal layers are perpendicular to the substrate surface. The nanofilms were synthesized by the direct reaction of metal films with chalcogen vapor at controlled temperature, pressure and time. We use Raman spectroscopy, transmission electron microscopy and tomography to establish this interesting orientation. We have also demonstrated that vertically

aligned layers can be realized on curved or rough surfaces such as on nanowires. This novel morphology affords unique 2D layered materials for study and utilization of their edge properties.

Free standing perovskite oxide films (Fig. 1e): Many important complex oxides do not have van der Waals interfaces, and thus cannot be exfoliated in 2D nanomaterials form. If we could create such structures, however, this would greatly expand the available properties for incorporation in stacked structures. They would also enable many new experimental techniques (transmission x-ray/electron microscopy/spectroscopy) and devices. Free standing perovskite films have been demonstrated by design and subsequent etching of an epitaxial sacrificial layer. Millimeter-scale films have been released despite a thickness below 100 nm. This first demonstration (using manganite films) can be extended to a wide range of complex oxides, beyond the perovskite structure, providing new component 2D nanomaterials for assembly with other chalcogenide nanomaterials.

2) Progress on electronic property and tuning

Electronic structure of the layered chalcogenide BiTeI: (Fig. 2a, b). We have investigated the electronic structure of the layered chalcogenide BiTeI via quantum oscillation measurements, in addition to ARPES and optical spectroscopy. This material is of interest due to the extremely large spin splitting induced by a bulk Rashba effect, arising from the electric polarity of the crystal structure in the presence of spin-orbit coupling. We showed that Shubnikov-de Haas oscillations are consistent with ARPES measurements of the spin-split inner and outer Fermi surfaces, and demonstrate the bulk nature of the splitting. Furthermore, direct evidence of the Dirac-like band crossing is found from the observed phase shift in magnetotransport and via Landau-level spectroscopy. Given that this semiconductor naturally exfoliates in 2D form, it provides a unique materials component for spin filtering and spin splitting, which would be powerfully combined with superconductors and magnets for novel proximity effect devices.

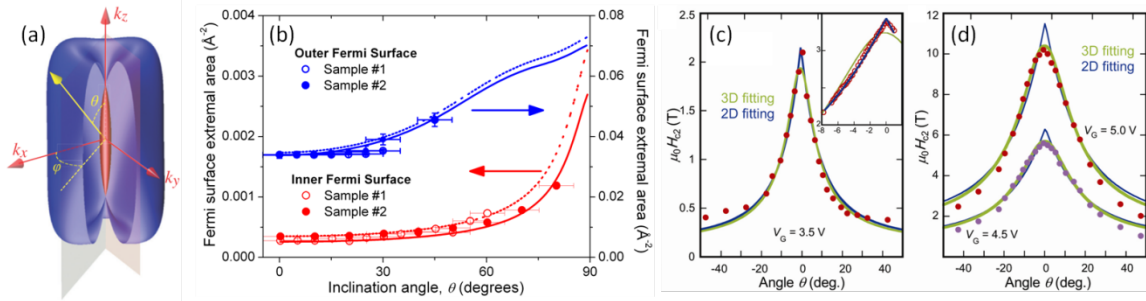


Figure 2. a) Theoretical inner (red) and outer (blue) Rashba-split Fermi surfaces of BiTeI. b) Experimental BiTeI Fermi surface areas for the 2 components extracted from Shubnikov-de Haas quantum oscillations for two samples (open and solid symbols). Solid and dashed lines are theoretical angular dependences for the two slightly different carrier densities. c) 2D angular scaling of the upper critical field (H_{c2}) of a superconducting MoS₂ EDLT at relatively low gate bias V_G . Inset shows the cusp-like character around $\theta = 0^\circ$, confirming the 2D form. d) Fits to $H_{c2}(\theta)$ at higher gate bias suggest anisotropic 3D character.

Superconductivity of MoS₂ nanoflakes by ionic liquid gating: (Fig. 2 c, d) There are several recent efforts in electric field induced phase transitions with liquid gating electric double-layer transistors (EDLTs), aimed at electrical modulation of novel electronic properties and quantum phenomena in oxides and chalcogenides. They hold a great deal of interest in the emergent fields of superconductivity, magnetism and Mott electronics, since the EDLTs exploit the power of

ionic liquid gating to achieve high sheet carrier densities far beyond the maximum attainable range of conventional gate dielectrics. However, even a basic understanding of the dimensionality of the interfacial electronic phase transition and how it is affected by the intrinsically anisotropic electronic structure has so far been elusive. Here by tuning the gate voltage within EDL transistors on flakes of layered MoS₂, we observe an electric field induced quantum insulator-superconductor transition and investigate the nature of the resultant superconducting state. We observe a clear insulator-to-superconductor transition around the pair quantum resistance $R_Q = h/(2e)^2$, and a dimensional crossover of the gate induced superconductivity in MoS₂. The latter feature provides an ideal probe to trace the evolution from electrostatic doping to electrochemical doping at high fields. This has been a central controversy in the microscopic mechanism of EDLT-induced phase transitions, which we can resolve by measuring the dimensionality of the superconducting state.

3) Progress on catalytic properties and tuning

Vertically aligned edge of 2D layered materials for catalysis We demonstrated that MoSe₂ and tungsten diselenide (WSe₂) films with molecular layers perpendicular to the substrate expose the active edge sites in a maximal manner. We show significant improvement of hydrogen evolution reaction (HER) activity of MoSe₂ and WSe₂ on carbon fiber paper, compared with flat (c-axis oriented) films.

Discovery of novel highly effective HER catalysts mimicking hydrogenases: Hydrogenases are efficient hydrogen-producing enzymes in biological systems. The active sites of these enzymes have been identified as the low-spin, low-valence Fe(II). We discovered a class of inorganic mimics of hydrogenases from the first row transition metal dichalcogenides (ME₂, M=Fe, Co, Ni; E= S, Se) for efficient HER catalysis.

Electrochemical tuning of catalysts for improved efficiency: We have invented a completely new approach of lithium electrochemical reaction with catalysts to tune their structure and the oxidation states of active sites. We have discovered that both hydrogen and oxygen evolution can be improved drastically. Our results are preliminary but highly promising.

Future Plans

During the 1st year of seed funded research, we have produced exciting results to lay down the foundation for a vision of “2D Artificial Materials” in the MSD at SLAC. In our future research, our central focus is understanding and utilizing the modification of the physical properties of these materials by their heterogeneous ionic environment. Here the heterogeneous ionic environment is realized through synthesis of heterostructured interfaces, electric double layer gating, electrochemical intercalation and chemical tuning. We outline three thrusts of research to be conducted: Thrust 1. Design and synthesis of novel 2D nanomaterials particularly focusing on interfaces between different chalcogen environments. Thrust 2. Ionic tuning of 2D nanomaterials by electric double layer gating, electrochemical interaction and chemical tuning. Thrust 3. Probe and manipulate the exciting electronic and photonic properties of these novel materials.

References

None.

Publications

1. D. Kong, H. Wang, J. J. Cha, M. Pasta, K. J. Koski, J. Yao, and Y. Cui, "Synthesis of MoS₂ and MoSe₂ Films with Vertically Aligned Layers," *Nano Letters* **13**, 1341 (2013).
2. J. J. Cha, K. J. Koski, C. Y. Huang, K. X. Wang, W. Luo, D. Kong, Z. Yu, S. Fan, M. L. Brongersma, and Y. Cui, "Two dimensional chalcogenidenanoplates as tunable metamaterials via chemical intercalation," *Nano Letters*, **13**, 5913 (2013)
3. H. Wang, D. Kong, P. Johanes, J. J. Cha, G. Zheng, K. Yan, N. Liu, and Y. Cui "MoSe₂ and WSe₂ Nanofilms with Vertically Aligned Molecular Layers on Curved and Rough Surfaces" *Nano Lett.* **13**, 3426 (2013).
4. D. Kong, J. J. Cha, H. Wang, H. R. Lee and Y. Cui, "First-row transition metal dichalcogenide catalysts for hydrogen evolution reaction", *Energy and Environmental Science*, **6**, 3553 (2013).
5. H. Wang, Z. Lu, S. Xu, D. Kong, J. J. Cha, G. Zheng, P.-C. Hsu, K. Yan, D. Bradshaw, F. B. Prinz, and Y. Cui, "Electrochemical tuning of vertically aligned MoS₂ nanofilms and its application in improving hydrogen evolution reaction," *Proceedings of the National Academy of Sciences*, **110**, 19701 (2013).
6. S. S. Hong, Y. Zhang, J. J. Cha, X.-L. Qi, and Y. Cui, "One-Dimensional Helical Transport in Topological Insulator Nanowire Interferometers", *Nano Lett.* **14**, 2815 (2014).
7. H. Wang, Z. Lu, D. Kong, J. Sun, T. M. Hymel, and Y. Cui, "Electrochemical Tuning of MoS₂ Nanoparticles on Three-Dimensional Substrate for Efficient Hydrogen Evolution", *ACS Nano* **8**, 4940 (2014).
8. D. Kong, H. Wang, Z. Lu, and Y. Cui, "CoSe₂ Nanoparticles Grown on Carbon Fiber Paper: An Efficient and Stable Electrocatalyst for Hydrogen Evolution Reaction", *Journal of the American Chemical Society*, **136**, 4897 (2014).
9. J. P. Motter, K. J. Koski, and Y. Cui, "General Strategy for Zero-Valent Intercalation into Two-Dimensional Layered Nanomaterials", *Chemistry of Materials* **26**, 2313 (2014).
10. H. Murakawa, J. G. Checkelsky, M. S. Bahramy, M. Tokunaga, Y. Kohama, C. Bell, Y. Kaneko, N. Nagaosa, H. Y. Hwang, and Y. Tokura, "Detection of Berry's Phase in a Bulk Rashba Semiconductor," *Science*, **342**, 1490 (2013).
11. M. Sakano, M. S. Bahramy, A. Katayama, T. Shimojima, H. Murakawa, Y. Kaneko, W. Malaeb, S. Shin, K. Ono, H. Kumigashira, R. Arita, N. Nagaosa, H. Y. Hwang, Y. Tokura, and K. Ishizaka, "Strongly Spin-Orbit Coupled Two-Dimensional Electron Gas Emerging near the Surface of Polar Semiconductors," *Phys. Rev. Lett.* **110**, 107204 (2013).
12. S. Bordacs, J. G. Checkelsky, H. Murakawa, H. Y. Hwang, and Y. Tokura, "Landau Level Spectroscopy of Dirac Electrons in a Polar Semiconductor with Giant Rashba Spin Splitting", *Phys. Rev. Lett.* **111**, 166403 (2013).
13. C. Bell, M. S. Bahramy, H. Murakawa, J. G. Checkelsky, R. Arita, Y. Kaneko, Y. Onose, M. Tokunaga, Y. Kohama, N. Nagaosa, Y. Tokura, and H. Y. Hwang, "Shubnikov-de Haas Oscillations in the Bulk Rashba Semiconductor BiTeI," *Phys. Rev. B (RC)* **87**, 081109 (2013).
14. Y. Zhang, Y. F. Zhang, Q. Q. Ji, J. Ju, H. T. Yuan, J. P. Shi, T. Gao, D. L. Ma, M. X. Liu, Y. B. Chen, X. J. Song, H. Y. Hwang, Y. Cui, and Z. F. Liu, "Controlled Growth of High-Quality Monolayer WS₂ Layers on Sapphire and Imaging its Grain Boundary", *ACS Nano* **7**, 8963 (2013).

Cluster/Carbon Composite Materials for Energy

Larry A. Curtiss, Stefan Vajda, Peter Zapol, and Michael J. Pellin
Materials Science Division
Argonne National Laboratory
Argonne, IL 60516

Program Scope

In this program we seek a fundamental understanding of a novel class of materials based on supported subnanometer clusters and support materials under electrochemical conditions. We use our unique capabilities to synthesize well-defined small clusters of specific size and composition, which we have demonstrated that on the right type of support they can be stable, highly active, and selective for a variety of catalytic reactions. Materials based on size-specific subnanometer clusters are attractive for catalysis because (1) they have well-defined and identical catalytic sites, (2) the number of sites can be precisely controlled, (3) their activity can provide valuable insights into catalytic mechanisms, and (4) calculations can be done at sufficient accuracy to allow guidance for design of optimal clusters. Two other key parts to this program are the support materials and computational materials design. One of the supports that we are using is a new form of diamond referred to as ultrananocrystalline diamond (UNCD), which has many unique properties due to combining sp^3 diamond grains with sp^2 -like carbon grain boundaries in one material. We also use our capabilities to synthesize metal oxide supports for the clusters. This can open up many more opportunities to tailor the catalytic activity as the choice of support can have dramatic effect on the catalytic properties of subnanometer clusters. Another key part of this program is the use of characterization and computational capabilities to both understand the properties of the new cluster/nanocarbon composites as well as to perform screening to find optimal candidate clusters to be used on the supports.

Recent Progress

Grazing-incidence small angle X-ray scattering (GISAXS) measurements at the Advanced Photon (APS) source has been used in several studies to demonstrate that subnanometer Co and Pd clusters deposited on UNCD and other supports can withstand elevated temperatures in various reactive environments, as well as harsh electrochemical conditions without aggregation or being lifted off. Grazing-incidence X-ray absorbance near edge structure (GIXANES) at the APS has been used to determine the oxidation states of supported clusters such as Co, Pd, and Ag. For example, the GIXANES spectra of UNCD and alumina supported cobalt tetramer clusters in combination with computational studies have indicated that the clusters have a 1:1 Co:O composition.

Water oxidation is a key catalytic step for electrical fuels generation. We have studied water oxidation in alkaline conditions using size-selected clusters of Pd to probe the relationship between cluster size and the water oxidation reaction.¹ We find that Pd₄ shows no reaction, while

Pd₆ and Pd₁₇ deposited clusters are among the most active (in terms of turnover rate per Pd atom) catalysts known. Theoretical calculations suggest that this striking difference may be a demonstration that bridging Pd-Pd sites (which are only present in three-dimensional clusters) are active for the Oxygen Evolution Reaction (OER) in Pd₆O₆. The system (soft-landed Pd₄, Pd₆, or Pd₁₇ clusters on an UNCD Si coated electrode) shows stable electrochemical potentials over several cycles, and synchrotron studies of the electrodes show no evidence for evolution or dissolution of either the electrode material or the clusters.

The Li-O₂ battery has the potential for the very high energy densities needed for long range electric vehicles, but the charge and discharge chemistries are complex and not well understood. The active sites on cathode surfaces and their role in the electrochemical reactions in aprotic Li-O₂ cells are difficult to ascertain because the exact nature of the sites are unknown. Deposition of subnanometer Ag clusters of exact size and number on a carbon surface with an alumina coating that passivates carbon defects is used to study the discharge process in Li-O₂ cells. The results reveal dramatically different morphologies of the electrochemically grown lithium peroxide dependent on the size of the clusters.² This dependence is found to be due to the influence of the cluster size on the formation mechanism, which also affects the charge process. The results of this study suggest that precise control of subnanometer surface structure on cathodes can be used as a means to improve the performance of Li-O₂ cells.

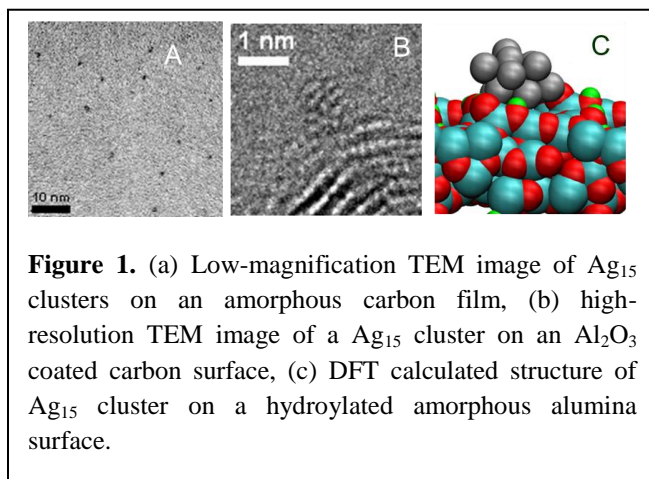


Figure 1. (a) Low-magnification TEM image of Ag₁₅ clusters on an amorphous carbon film, (b) high-resolution TEM image of a Ag₁₅ cluster on an Al₂O₃ coated carbon surface, (c) DFT calculated structure of Ag₁₅ cluster on a hydroxylated amorphous alumina surface.

Future Plans

Our plans for fundamental studies for design and discovery of novel materials based on supported size-specific clusters will focus on new strategies for materials synthesis including (1) extending our capabilities in generating size- and composition- specific clusters to a larger range of clusters, (2) metal alloy clusters, and (3) new concepts in metal oxide supports for controlling stability, activity, and introduction of bifunctionality. In addition we will carry out first principles for materials design and understanding of the cluster-based materials for three key catalytic reactions in this program: water oxidation, lithium-oxidation, and CO₂ reduction.

References

1. Size dependent Subnanometer Pd Cluster (Pd₄, Pd₆ and Pd₁₇) Water Oxidation Electrocatalysis, G. Kwon, E. C. Tyo, C. Yin, G. A. Ferguson, J. DeBartolo, S. Seifert, R. E. Winans, A. J. Kropf, C. J. Heard, R. L. Johnston, J. P. Greeley, L. A. Curtiss, M. J. Pellin, and S. Vajda, ACS Nano, ACS Nano, 7, 5808 (2013).

2. Effect of the Size-selective Silver Clusters on Li_2O_2 Morphology in Lithium-Oxygen Batteries, J. Lu, L. Cheng, K. C. Lau, E. Tyo, X. Luo, J. Wen, D. Miller, R. Assary, H.-H. Wang, P. C. Redfern, H. Wu, J.-B. Park, Y.-K. Sun, S. Vajda, K. Amine, L. A. Curtiss, Nature Communications, submitted

Publications

3. "Theoretical Studies of UNCD Properties" S. Adiga, P. Zapol, and L. A. Curtiss, Invited Chapter for Book on Ultrananocrystalline Diamond, Edited by O. Shenderova and D. Gruen, pp 85-102, Elsevier (2012).
4. "Controlling the Particle Size of ZrO_2 Nanoparticles in Hydrothermally Stable $\text{ZrO}_2/\text{MWCNT}$ Composites", C. Liu, S. Lee, Dong Su, B. Lee, S. Lee, R. E. Winans, C. Yin, S. Vajda, L. Pfefferle, G. L. Haller, Langmuir 28, p. 17159–17167 (December, 2012)
5. "Stable Subnanometer Cobalt Oxide Clusters on Ultrananocrystalline Diamond and Alumina Supports: Oxidation State and the Origin of Sintering-Resistance", G. A. Ferguson, C. Yin, G. Kwon, S. Lee, J. P. Greeley, P. Zapol, B. Lee, S. Seifert, R. E. Winans, and S. Vajda, and L. A. Curtiss, J. Phys. Chem. C 116, p. 24027–24034 (2012).
6. "Oxidative Dehydrogenation of Cyclohexane on Cobalt Oxide (Co_3O_4) Nanoparticles: The Effect of Particle Size on Activity and Selectivity", by E. C. Tyo, C. Yin, M. Di Vece, Q. Qian, S. Lee, B. Lee, S. Seifert, R. E. Winans, R. Si, B. Ricks, S. Goergen, M. Rutter, B. Zugic, M. Flytzani-Stephanopoulos, Z. Wang, R. E. Palmer, M. Neurock, and S. Vajda, ACS Catal. 2, p. 2409–2423 (2012) invited paper
7. "CO Oxidation by Subnanometer $\text{Ag}_x\text{Au}_{3-x}$ Supported Clusters via DFT Simulations", F. R. Negreiros, L. Sementa, G. Barcaro, S. Vajda, E. Aprà, and A. Fortunelli, ACS Catal. 2, 1860–1864 (2012)
8. "Structure Sensitivity of Oxidative Dehydrogenation of Cyclohexane over FeO_x and $\text{Au}/\text{Fe}_3\text{O}_4$ Nanocrystals", S. Goergen, C. Yin, M. Yang, B. Lee, S. Lee, C. Wang, P. Wu, M. B. Boucher, G. Kwon, S. Seifert, R. E. Winans, S. Vajda, and M. Flytzani-Stephanopoulos, ACS Catal. 3, p. 529-539 (2013)
9. "Atomic Layer Deposition of a Submonolayer Catalyst for the Enhanced Photoelectrochemical Performance of Water Oxidation with Hematite, S.C. Riha, B. M. Klahr, E. C. Tyo, S. Seifert, S. Vajda, M. J. Pellin, T. W. Hamann, and A. B. F. Martinson, ACS Nano 7, 2396-2405 (2013).
10. "Physical Fabrication of Nanostructured Heterogeneous Catalysts", C. Yin, E. Tyo and S. Vajda, Chapter 3 in "Heterogeneous Catalysis at the Nanoscale for Energy Applications", Eds. F. Tao, W. Schneider, and P. Kamat, Wiley-VCH, ISBN 9780470952603.
11. Size dependent Subnanometer Pd Cluster (Pd_4 , Pd_6 and Pd_{17}) Water Oxidation Electrocatalysis, G. Kwon, E. C. Tyo, C. Yin, G. A. Ferguson, J. DeBartolo, S. Seifert, R. E. Winans, A. J. Kropf, C. J. Heard, R. L. Johnston, J. P. Greeley, L. A. Curtiss, M. J. Pellin, and S. Vajda, ACS Nano, ACS Nano, 7, 5808 (2013).

12. "The Electronic Structure of Lithium Peroxide Clusters and Relevance to Lithium-Air Batteries," Kah Chun Lau, Rajeev S. Assary, Paul C. Redfern, Jeffrey P. Greeley, and Larry A Curtiss *Journal of Physical Chemistry C* **116**, 23890 (2012).
13. "Oxidation and Reduction of Size-Selected Subnanometer Pd Clusters on Al₂O₃ Surface", B. H. Mao, R. Chang, S. Lee, S. Axnanda, E. Crumlin, S. D. Wang, S. Vajda, Z. Liu, J. Chem. Phys, **138**, 214304 (2013).
14. "Interactions of Dimethoxy Ethane with Li₂O₂ Clusters and Likely Decomposition Mechanisms for Li-O₂ Batteries," R. S. Assary, K. C. Lau, K. Amine, Y. K. Sun, L. A. Curtiss, *J. Phys. Chem. C* **117**, 8041-8049 (2013) DOI: 10.1021/jp400229n
15. Regioselective Oxidation of Strained Graphene for Controllable Synthesis of Nanoribbons Graphene", X. Tan and P. Zapol, *J. Phys. Chem*, **117**, 19160–19166 (2013). Journal Cover
16. Structure-activity relationships for propane oxidative dehydrogenation by anatase-supported vanadium oxide monomers and dimers," L. Cheng, G. A. Ferguson, S. A. Zygmunt, L. A. Curtiss, *J. Catalysis* **302**, 31-36 (2013).
17. Evidence for lithium superoxide-like species in the discharge product of a Li-O₂ battery, Y. B/ Yang, D. Y Zhai, H. H. Wang, K. C. Lau, J. A. Schlueter, P. Du, D. J. Myers, Y. K. Sun, L. A. Curtiss, K. Amine, *Physical Chemistry Chemical Physics*, **15**, 3764-3771 (2013).
18. "Oxidation of Cyclohexane by Size-Selected Palladium Clusters Pinned in Graphite: Cluster Stability and Identification of the Catalytic Active Site", V. Habibpour, C. Yin, G. Kwon, Z. Wang, S. Vajda and R. E. Palmer, *J. Nanoscale Res.*, **8**, 993-1003 (2013)
19. "Reaction Mechanism for Direct Propylene Epoxidation by Alumina-Supported Silver Aggregates: The Role of the Particle/Support Interface" L. Cheng, C. Yin, F. Mehmood, B. Liu, J. Greeley, S. Lee, B. Lee, S. Seifert, R. E. Winan, D. Teschner, R. Schlög, S. Vajda, L. A. Curtiss, *ACS Catal.* **4**, 32–39 (2014) doi.org/10.1021/cs4009368
20. Computational Studies of Structure and Catalytic Activity of Vanadia for Propane Oxidative Dehydrogenation," L. Cheng and L. A. Curtiss, *Novel Materials for Catalysis and Fuels Processing*, Book Series: ACS Symposium Series Volume: 1132 Pages: 71-82 (2013).
21. "Ultrafast Dynamics & Control: From Electronic State Population Control to Selective Bond Breaking" S. Vajda, and L. Wöste in *The Dekker Encyclopedia of Nanoscience and Nanotechnology Third Edition*, Ed.: S.E. Lyshevski, *Third Edition*. CRC Press: New York, 2014, pp. 4560–4574.
22. "Support and Oxidation Effects on Subnanometer Palladium Nanoparticles" C. J. Heard, S. Vajda, R. L. Johnston *J Phys. Chem C* **118**, 3581-3589 (2014)
23. "Atomically Precise (Catalytic) Particles Synthesized by a Novel Cluster Deposition Instrument" C. Yin, E. Tyo, K. Kuchta, B. von Issendorff, and S. Vajda, *J Chem. Phys* **140**, 174201-1-7 (2014)
24. "Ambient pressure XPS study of silver clusters on Al₂O₃ and TiO₂ ultrathin film supports", B. H. Mao, R. Chang, L. Shi, Q. Q. Zhuo, S. Rani, X. S. Liu, E. C. Tyo, S. Vajda, S. D. Wang, and Z. Liu *Phys. Chem. Chem. Phys.*, *submitted*.

Materials and Interfacial Chemistry for Next Generation Electrical Energy Storage

S. Dai, M. P. Paranthaman, C. A. Bridges, X. G. Sun, G. M. Veith
Oak Ridge National Laboratory, Oak Ridge, TN 37831

J. B. Goodenough, A. Manthiram – The University of Texas at Austin, Austin, TX 78712

Program Scope

The overarching goal is to *investigate fundamental principles governing energy storage through integrated synthesis and advanced characterization*. Our current research is focused on fundamental investigation of electrolytes based on ionic liquids and rational synthesis of novel electrode architectures through Fermi level engineering of anode and cathode redox levels by employing porous structures and surface modifications as well as advanced operando characterization techniques including neutron diffraction and scattering. The key scientific question concerns the relationship between chemical structures and their energy-storage efficacies.

Recent Progress

Electrolyte Chemistry

Ionic liquids have many advantages such as non-volatility, high thermal stability, non-flammability, and wide electrochemical window (>5.0V). Their exceptional flexibility in structural design allows extensive tuning of their (electro)chemical properties. Our primary goal is first to understand the basic relationship between structure and properties of ionic liquids, better enabling targeted design of new ionic liquids with improved compatibility with high capacity anodes (e.g., graphite) for application in intercalation batteries. We have found that manipulating the stereochemical structure of the imidazolium cation can profoundly influence the electrochemical properties of the corresponding ionic liquids. In particular, an imidazolium ionic liquid with a bicyclic architecture has been developed and found to be compatible to graphite anodes. Secondly, a new orthocheletated salt, lithium bis(monofluoro malonato)borate (LiBFMB), has been synthesized and purified for tailoring SEIs in lithium ion batteries. The presence of fluorine in the borate anion of LiBFMB increases its oxidation potential and also facilitates ion dissociation. Initial results also indicate that using high dielectric constant solvent PC alters the surface chemistry, reduces the interfacial impedance, and enhances the performance of the LiBFMB-based 5.0V cell. In addition, LiBFMB has been used to synthesize a task-specific ionic liquid, 1-butyl-1,2-dimethylimidazolium bis(monofluoro malonato) borate (BDMI_m.BFMB), which can be used as an additive in 1 M LiPF₆/PC electrolyte to suppress graphite exfoliation and improve cycling performance (Fig.1).

Understanding the Chemistry of Main Group Anodes for Sodium Ion Batteries

In order to develop an understanding of the structure/property correlations within Li-ion batteries the team has focused on a similar electrochemical system based on sodium. Through this work we have revealed that the larger Na-ion diffuses almost an order of magnitude faster than a Li-ion in the same Sb electrode matrix. Furthermore, these experiments have revealed the mechanisms of some insertion anodes differ significantly between Li and Na. For example, FeSb₂ reacts with Na to form superparamagnetic Fe particles with cycling whereas Li forms a unique range of Li-Fe-Sb₂ phases. Similarly, the reaction between Na and Sn proceeds through a number of previously unidentified Na-Sn compounds. The structure of these new phases have not yet been identified but through understanding the structures we believe we will have the ability to design new anodes with

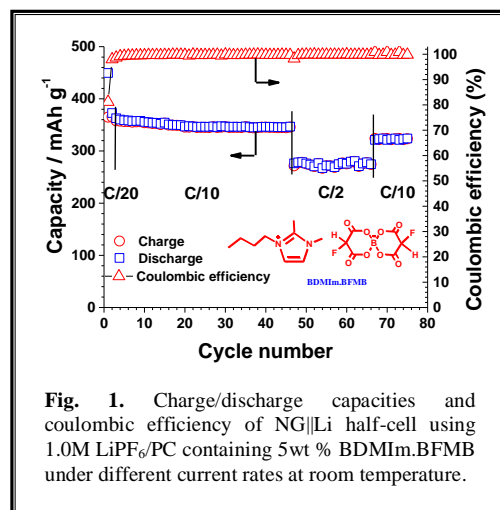


Fig. 1. Charge/discharge capacities and coulombic efficiency of NG||Li half-cell using 1.0M LiPF₆/PC containing 5wt % BDMI_m.BFMB under different current rates at room temperature.

selective inert dopants which will enable rapid ion transport while minimizing volume changes revolutionizing energy storage methodologies.

In Situ Investigations of Electrode and Interfacial Reactions with Neutron Scattering

Our novel approach to investigate electrochemical processes in situ with small angle neutron scattering (SANS) has been continued, and additional work using neutron reflectometry (NR) has shown great promise. Changes in neutron scattering intensity, associated with contrast between ordered mesopores in carbon and the carbon framework, show the processes of SEI formation and sodium intercalation have been investigated (see Fig. 2). Changes in pore-pore spacing with time clearly indicate that the sodium has intercalated, and suggest that the relaxation of the framework is slow upon deintercalation. A separate experiment focused on electrochemical processes in ionic liquid electrolyte with a lithium salt (LiPF_6) show an extensive period of change in the mesoporous framework associated with intercalation. The team has performed *in situ* NR experiments to probe the surface chemistry of battery cathode and anode materials as a function of charge. These studies have revealed the formation of a number of condensed surface layers on the surface of electrode materials at various states of charge. For example, on Si anode materials we have strong evidence for the formation of 8 nm thick well defined layer. Based on the scattering length density this layer is hydrogen rich due to the selective segregation of dimethyl carbonate at the electrode surface in solution. This layer represents the earliest stages of SEI formation. By understanding this chemistry we will predict new electrolyte chemistries (e.g. ionic liquids) to optimize interfacial reactions.

Future Plans

- Further understand the structure-property relationship of ionic liquids and design new ionic liquids with good SEI formation ability to be compatibility with graphite and high voltage cathodes.
- Understanding the limiting factors in rate performance of anode and cathode materials and design novel electrode materials with enhanced rate capability.
- Further explore the understanding gained from small angle neutron scattering (SANS) on the electrochemical processes occurring at the surface and in the bulk of both anode and cathode electrode materials
- Continue to work with UT-Austin to develop a more comprehensive picture of next-generation electrode and electrolyte materials being investigated as a part of this project
- Experiment on model systems to better understand the effects of surface modification on surface chemistry and cycle stability in high voltage electrode materials
- Explore the synthesis of Na-intercalation batteries and understand how the surface reactivity of these materials changes in comparison with their Li analogs.
- Probe ion segregation on electrodes via neutron reflectometry as a function of charge

Publications

1. Y. C. Lu, E. J. Crumlin, G. M. Veith, J. R. Harding, E. Mutoro, L. Baggetto, N. J. Dudney, Z. Liu, and Y. Shao-Horn, "In situ ambient pressure X-ray photoelectron spectroscopy studies of lithium-oxygen redox reactions," *Nature Scientific Reports* 2, 715 (2012).

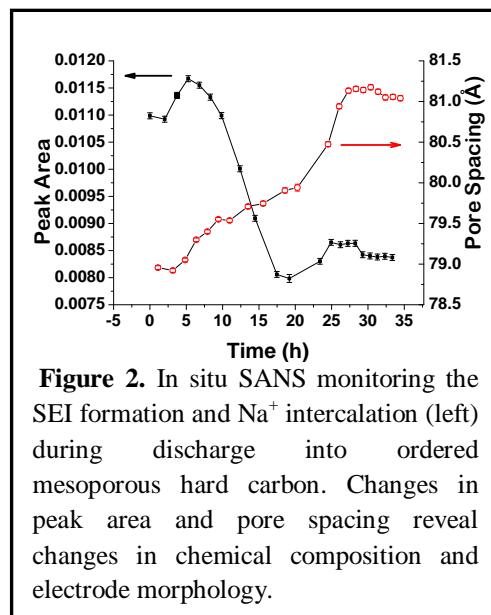


Figure 2. In situ SANS monitoring the SEI formation and Na^+ intercalation (left) during discharge into ordered mesoporous hard carbon. Changes in peak area and pore spacing reveal changes in chemical composition and electrode morphology.

2. S. D. Wook, C. A. Bridges, A. Huq, M. P. Paranthaman, and A. Manthiram, "Role of cation ordering and surface segregation in high-voltage spinel $\text{LiMn}_{1.5}\text{Ni}_{0.5-x}\text{M}_x\text{O}_4$ ($\text{M} = \text{Cr, Fe, and Ga}$) cathodes for lithium-ion batteries," *Chem. Mater.* 24(19), 3720–3731, 2012.
3. K. L. Harrison, C. Bridges, M. P. Paranthaman, C. U. Segre, J. Katsoudas, V. A. Maroni, J. Carlos Idrobo, J. B. Goodenough, and A. Manthiram, "Temperature dependence of aliovalent-vanadium doping in LiFePO_4 cathodes," *Chem. Mater.* 25, 768–781 (2013).
4. C. Liao, X.-G. Sun, and S. Dai, "Crosslinked gel polymer electrolytes based on polyethylene glycol methacrylate and ionic liquid for lithium ion battery applications," *Electrochim. Acta* 87, 889–894 (2013).
5. X. G. Sun, X. Q. Wang, R. T. Mayes, S. Dai, Lithium-Sulfur Batteries Based on Nitrogen-Doped Carbon and an Ionic-Liquid Electrolyte, *ChemSusChem*, 2079–2085(2012).
6. A. B. Papandrew, C. Chisolm, S. Zecevic, G. M. Veith, and T. Zawodzinski "Activity and evolution of vapor deposited Pt-Pd oxygen reduction catalysts for solid acid fuel cells," *J. Electrochem. Soc.* 160(2), F175–F182, 2013.
7. L. Baggetto, P. Ganesh, R. P. Meisner, R. R. Unocic, J.-C. Jumas, C. A. Bridges, and G. M. Veith, "Characterization of sodium ion electrochemical reaction with tin anodes: experiment and theory," *J. Power Sources* 234(1), 48–59, 2013.
8. L. Baggetto, E. Allcorn, A. Manthiram, and G. M. Veith "Cu₂Sb thin films as anode for Na-ion batteries," *Electrochem. Commun.* 27(1), 168–171, 2013.
9. B. Cao, G. M. Veith, R. E. Diaz, J. Liu, E. A. Stach, R. R. Adzic, and P. G. Khalifah, "Cobalt molybdenum oxynitrides: synthesis, structural, characterization, and catalytic activity for the oxygen reduction reaction," *Angew. Chem. Int. Ed.* 52(41), 10753–10757 (2013).
10. C. A. Bridges, K. Harrison, R. R. Unocic, J. C. Idrobo, M. P. Paranthaman, and A. Manthiram, "Defect chemistry of phospho-olivine nanoparticles synthesized by a microwave-assisted solvothermal process," *J. Solid State Chem.* 205, 197–204 (2013).
11. B. Guo, X.-G. Sun, G. M. Veith, Z. Bi, S. M. Mahurin, C. Liao, C. Bridges, M. P. Paranthaman, and S. Dai, "Nitrogen-enriched carbons from alkali salts with high coulombic efficiency for energy storage applications," *Adv. Energy Mater.* 3, 708–712 (2013).
12. J. C. Li, L. Baggetto, S. K. Martha, G. M. Veith, J. Nanda, C. D. Liang, and N. J. Dudney, "An artificial solid electrolyte interphase enables the use of $\text{LiNi}_{0.5}\text{Mn}_{1.5}\text{O}_4$ 5 V cathode with conventional electrolytes," *Adv. Energy Mater.* 3, 1275 (2013).
13. Z. Bi, M. P. Paranthaman, P. A. Menchhofer, R. R. Dehoff, C. A. Bridges, M. Chi, B. Guo, X.-G. Sun, and S. Dai, "Self-organized amorphous TiO_2 nanotube arrays on porous Ti foam for rechargeable lithium and sodium ion batteries," *J. Power Sources* 222, 461–466 (2013).
14. C.-N. Sun, K. L. More, G. M. Veith, and T. A. Zawodzinski, "Composition dependence of the pore structure and water transport of composite catalyst layers for polymer electrolyte fuel cells," *J. Electrochem. Soc.* 160(9), F1000–F1005 (2013).
15. H. Jeon, Z. Bi, W. S. Choi, M. F. Chisholm, C. A. Bridges, M. P. Paranthaman, and H. N. Lee, "Orienting oxygen vacancies for fast catalytic reaction," *Adv. Mater.* 25, 6459 (2013).
16. L. Baggetto, J.-C. Jumas, J. Gorka, C. A. Bridges, and G. M. Veith, "Predictions of particle size and lattice diffusion pathway requirements for sodium-ion anodes using $\eta\text{-Cu}_6\text{Sn}_5$ thin films as a model system," *Phys. Chem. Chem. Phys.* 15(26), 10855–10894 (2013).
17. K. L. Browning, L. Baggetto, R. R. Unocic, N. J. Dudney, and G. M. Veith, "Gas evolution from cathode materials: a pathway to solvent decomposition concomitant to SEI formation," *J. Power Sources* 239(1), 341–346 (2013).
18. X.-G. Sun, C. Liao, N. Shao, J. R. Bell, H. Luo, D. Jiang, and S. Dai, "Bicyclic imidazolium ionic liquids as potential electrolytes for rechargeable lithium ion batteries," *J. Power Sources* 237, 5–12 (2013).
19. L. Baggetto, J. K. Keum, J. F. Browning, and G. M. Veith, "Germanium as negative electrode material for sodium-ion batteries," *Electrochem. Commun.* 34(1), 41–44 (2013).
20. L. Baggetto, R. R. Unocic, E. Allcorn, A. Manthiram, and G. M. Veith, "Mo₃Sb₇ as a very fast anode material for lithium-ion and sodium-ion batteries," *J. Mater. Chem. A* 1(37), 11163–11169 (2013).
21. L. Baggetto, P. Ganesh, C.-N. Sun, R. A. Meisner, T. A. Zawodzinski, and G. M. Veith, "Intrinsic thermodynamic and kinetic properties of Sb electrodes for Li-ion and Na-ion batteries: experiment and theory," *J. Mater. Chem. A* 1(27), pg 7985–7994 (2013).
22. H. Zhou, J. Nanda, S. K. Martha, J. Adcock, J. C. Idrobo, L. Baggetto, G. M. Veith, S. Dai, S. Pannala, and N. J. Dudney, "Formation of iron oxyfluoride phase on the surface of nano- Fe_3O_4 conversion compound for electrochemical energy storage," *J. Phys. Chem. Lett.* 4(20), 3798–3805 (2013).

23. L. Baggetto, M. Marszewski, J. Gorka, M. Jaroniec, and G. M. Veith, "AlSb thin films as negative electrodes for Li-ion and Na-ion batteries," *J. Power Sources* 243(1), 699–705 (2013).
24. B. Guo, T. Ben, Z. Bi, G. M. Veith, X.-G. Sun, S. Qiu, and S. Dai, "Highly dispersed sulfur in porous aromatic framework as cathode for lithium-sulfur batteries," *Chem. Commun.* 49(43), 4905 (2013).
25. C. Do, P. Lunkenheimer, D. Diddens, M. Götz, M. Weiß, A. Loidl, X.-G. Sun, J. Allgaier, D. Richter, and M. Ohl, "Li⁺ transport in poly(ethylene oxide) based electrolytes: neutron scattering, dielectric spectroscopy, and molecular dynamics simulations," *Phys. Rev. Lett.* 111(1), 018301/1–018301/5 (2013).
26. P. F. Fulvio, P. C. Hillesheim, Y. Oyola, S. M. Mahurin, G. M. Veith, and S. Dai, "A new family of fluidic precursors for the self-templated synthesis of hierarchical nanoporous carbons," *Chem. Commun.* 49(66), 7289–7291 (2013).
27. P. F. Fulvio, G. M. Veith, J. L. Adcock, S. S. Brown, R. T. Mayes, X. Wang, S. M. Mahurin, B. Guo, X.-G. Sun, A. A. Puzek, C. M. Rouleau, D. B. Geohegan, and S. Dai, "Fluorination of "brick and mortar" soft-templated graphitic ordered mesoporous carbons for high power lithium-ion battery," *J. Mater. Chem. A* 1(33), 9414–9417 (2013).
28. Y.-C. Lu, E. Crumlin, T. Carney, L. Baggetto, G. M. Veith, N. J. Dudney, Z. Liu, and Y. Shao-Horn, "The influence of hydrocarbon and CO₂ on the reversibility of Li₂O₂ chemistry using in situ ambient pressure X-ray photoelectron spectroscopy," *J. Phys. Chem. C* 117(49), 25948–25954 (2013).
29. B. Cao, G. M. Veith, J. Neufeind, R. Adzic, and P. Khalifah, "Mixed close packed cobalt molybdenum nitrides as non-noble metal electrocatalysts for the hydrogen evolution reaction," *J. Am. Chem. Soc.* 135(51), 19186–19192 (2013).
30. Z. Bi, M. P. Paranthaman, B. Guo, R. R. Unocic, H. M. Meyer III, C. A. Bridges, X.-G. Sun, and S. Dai, "High performance Cr, N-codoped mesoporous TiO₂ microspheres for lithium-ion batteries," *J. Mater. Chem. A* 2 [6], 1818–1824 (2014).
31. S. A. Hawks, L. Baggetto, C. A. Bridges, and G. M. Veith, "The electrochemical reactions of pure Indium with Li and Na: anomalous electrolyte decomposition, benefits of FEC additive, phase transitions and electrode performance," *J. Power Sources* 248 [1], 1105–1117 (2014).
32. M. P. Paranthaman, T. Aytug, L. Stan, Q. X. Jia, C. Cantoni, and S. H. Wee, "Chemical solution derived planarization layers for highly aligned IBAD-MgO templates," *Supercond. Sci. Tech.* 27, 022002 (2014). (Article featured on cover)
33. Y. Q. Cheng, Z. Bi, A. Huq, M. Feyngenson, C. A. Bridges, M. P. Paranthaman, and B. G. Sumpter, "An integrated approach for structural characterization of complex solid state electrolytes: the case of lithium lanthanum titanate," *J. Mater. Chem. A* 2, 2418 (2014).
34. C. Liao, B. Guo, D. Jiang, R. Custelcean, S. M. Mahurin, X.-G. Sun, and S. Dai, "Highly soluble alkoxide magnesium salts for rechargeable magnesium batteries," *J. Mater. Chem. A* 2 [3], 581–584 (2014).
35. G. M. Veith, L. Baggetto, R. L. Sacci, R. R. Unocic, W. E. Tenhaeff, and J. F. Browning, "Direct measurement of the chemical reactivity of silicon electrodes with LiPF₆-based battery electrolytes," *Chem. Commun.* 50 [23], 3081–3084 (2014).
36. R. L. Sacci, L. A. Adameczyk, G. M. Veith, and N. J. Dudney, "Dry synthesis of lithium intercalated graphite powder and fiber," *J. Electrochem. Soc.* 161 [4], A614–A619 (2014).
37. C.-N. Sun, F. M. Delnick, L. Baggetto, G. M. Veith, and T. A. Zawodzinski Jr., "Hydrogen evolution at the negative electrode of the all-vanadium redox flow batteries" *J. Power Sources* 248 [1], 560–564 (2014).
38. Z. Zhang, G. M. Veith, G. M. Brown, P. F. Fulvio, P. C. Hillesheim, S. Dai, and S. H. Overbury, "Ionic liquid derived carbons as high efficient oxygen reduction catalysts: first elucidation of pore size distribution dependent kinetics," *Chem. Commun.* 50 [12], 1469–1471 (2014).
39. H. Xing, C. Liao, Q. Yang, G. M. Veith, B. Guo, X.-G. Sun, Q. Ren, Y.-S. Hu, and S. Dai, "Ambient lithium-SO₂ batteries with ionic liquids as electrolytes," *Angew. Chem. Int. Ed.* 53 [8], 2099–2103 (2014).
40. X.-G. Sun, C. Liao, L. Baggetto, B. K. Guo, R. R. Unocic, G. M. Veith, S. Dai, Bis(fluoromalonato)borate (BFMB) anion based ionic liquid as an additive for lithium-ion battery electrolytes, *J. Mater. Chem. A*, 2(20), 7606–7614 (2014).
41. C. Liao, K. S. Han, L. Baggetto, D. A. Hillesheim, R. Custelcean, E.-S. Lee, B. K. Guo, Z. H. Bi, D. E. Jiang, G. M. Veith, E. W. Hagaman, G. M. Brown, C. Bridges, M. P. Paranthaman, A. Manthiram, S. Dai, X.-G. Sun, Synthesis and Characterization of Lithium Bis(fluoromalonato)borate for Lithium-Ion Battery Applications, *Adv. Energy Mater.*, 4(6), 1301368/1-1301368/12 (2014).

Solvent-Assisted Non-Equilibrium Directed Self-Assembly of Complex Polymeric Materials

Juan J. de Pablo – Paul F. Nealey – M. Tirrell

Institute for Molecular Engineering
Argonne National Laboratory
University of Chicago

Program Scope

The aim of this program is to direct the assembly of block polymers by relying on chemically patterned substrates. While past efforts in this area have considered assembly of relatively simple materials, this project seeks to increase the complexity of the polymers considered for assembly, as well as that of the dynamic processes followed to achieve that assembly. The specific goals are to (1) generate a fundamental understanding of directed assembly of multi-block polymers, under non-equilibrium conditions, in the presence of solvents; (2) to understand the role of charges and liquid crystallinity in directed assembly and (3) to apply that understanding to develop processes leading to defect-free three dimensional assembly of polymeric systems with target structures. The project includes elements of synthesis, whereby polymeric systems of controlled structure and functionality will be prepared, characterization, where advanced scattering techniques will be developed to provide structural information at unprecedented levels of detail, and theory and simulation, where molecular models of the materials of interest will serve to guide design of materials and to interpret experimental data.

Recent Progress

Solvent-assisted morphology formation: In the context of block polymer directed assembly, the term “solvent annealing” generally refers to a process in which a solvent atmosphere is used to improve the assembly of a block polymer film by removal of defects. From a fundamental point of view, solvent annealing represents a relatively complex, non-equilibrium process; multiple effects, including swelling, shrinkage, and morphological transitions, act in concert to yield an ordered or disordered structure. In order to design processes that involve solvent annealing for creation of desirable structures it is therefore necessary to develop a computational formalism capable of capturing all such effects. By relying on a theoretically informed coarse grain model

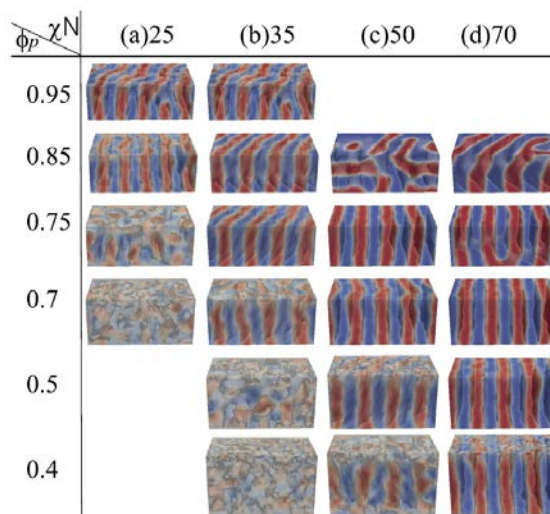


Figure 1 – Representative morphology of diblock copolymer films during solvent annealing as a function of χN and solvent fraction ϕ_p . Higher solvent fractions lead to swelling and a disorder transition. Gradual removal of the solvent leads to elimination of defects.

of block polymers, we have presented a conceptual framework that permits prediction or rationalization of experimentally observed behaviors. Through proper selection of several process considerations, we have shown that a narrow window of solvent pressures exists over which one can direct a block polymer material to form well-ordered, defect-free structures.

Manipulation of interfacial energy for self-assembly: The morphology of a block copolymer thin film is particularly sensitive to its boundary conditions. Lithographic applications of block polymers in the microelectronics and memory device industries require formation of morphologies with perpendicularly oriented domains. Current fabrication targets envisage the creation of dense arrays of structures with domain sizes in the sub-10 nm regime. Such length scales can be reached by resorting to block polymers with highly incompatible blocks (and a large Flory–Huggins parameter, χ). High χ values, however, generally lead to large differences in the surface energies of the corresponding blocks, thereby interfering with formation of the sought-after perpendicularly oriented domains. In this project, a coarse grain model has been used to develop a topcoat strategy that enables control of the orientation of block copolymer domains in highly incompatible block polymer materials. We carried out a systematic study of a wide range of polymeric material combinations, and the conditions leading to optimal assembly of perpendicular morphologies were clearly identified. We considered the effect of molecular weight, block

polymer film thickness and architecture, and degree of incompatibility.

We produced a wide range of generic phase diagrams that now serve as a guide for experimental

deployment of the topcoat strategy conceived in this work.

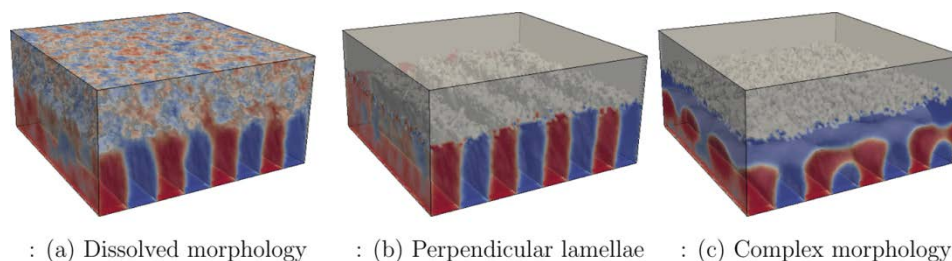


Figure 2. Representative three-dimensional compositional profiles of morphologies obtained from Monte Carlo simulations. The color map shows the scalar field $\psi(\mathbf{r}) = \langle [\phi_A(\mathbf{r}) - \phi_B(\mathbf{r})] / [\phi_A(\mathbf{r}) + \phi_B(\mathbf{r})] \rangle$. Red represents A-rich domains, blue is used for B-rich domains, gray shows the topcoat polymers, and the surface indicates the interface between these two domains.

Tunable polyelectrolyte complexes by coacervation: In order to develop a better understanding of the role of charges in the self-assembly of polymeric molecules, we have started by investigating complex formation in the bulk. Specifically, we achieved complex coacervation by combining poly(allylamine) (PAH) or branched poly(ethylenimine) (PEI) with poly(acrylic acid) (PAA) and poly(N,N-dimethylaminoethyl methacrylate) (PDMAEMA). We systematically investigated the effects of stoichiometry, salt concentration, and pH. Ternary coacervates formed over a broader range of stoichiometries compared to the base PAA/PDMAEMA system. An enhanced resistance to salt, that is, resistance to dissolution of the complex with added salt, was observed for ternary coacervates. PEI-containing systems showed a considerable difference in salt resistance at pH

6–8 due to the dramatic change in charge density. This change was interpreted in the context of a theoretical treatment that relies on the Voorn–Overbeek model for the free energy. Coacervate stability and viscoelastic behavior were affected by stoichiometry, salt, and pH. Ternary coacervates maintain the characteristics and tunability of typical binary coacervates, but the choice of the third component is important, as it significantly affects the response and material properties.

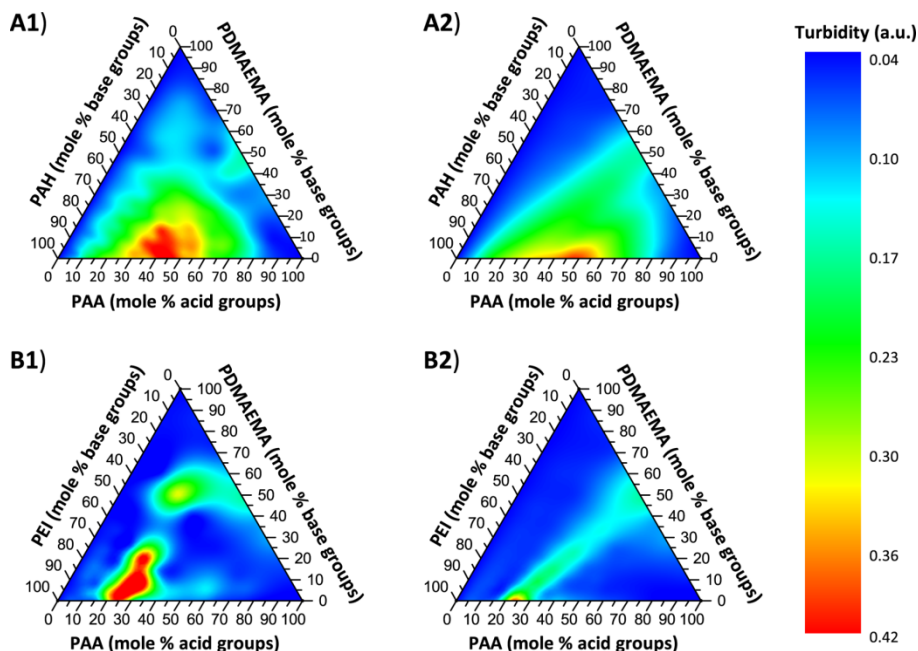


Figure 3. Plots of turbidity as a function of composition for (A) PAA/PDMAEMA/PAH and (B) PAA/PDMAEMA/PEI mixtures as a function of acid/base groups (mol %). Samples were prepared with a total polymer concentration of 0.1 wt %, pH 7.0, and no added salt. Experimental data are shown in (A1) and (B1). (A2) and (B2) show predicted turbidity diagrams calculated by linear interpolation of the individual binary turbidity data.

Interfacial energy in coacervates: One of the key properties of coacervates that will have to be controlled in order to direct the assembly of charged block polymers will be the interfacial energy. Coacervates are unique in that they exhibit an extremely small surface tension – many of their applications in fact derive from that low surface tension. Theoretical models for the interfacial energy of coacervates were not available; in order to derive one, we started by considering bulk polyelectrolyte solutions which, under suitable conditions, phase separate into a liquid-like coacervate phase and a coexisting supernatant phase. By combining a Debye–Hückel treatment for electrostatic interactions with the Cahn–Hilliard theory, we arrived at explicit expressions for the interfacial tension. In the absence of added

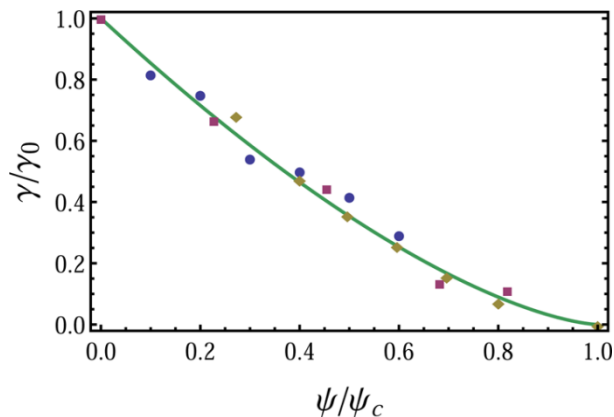


Figure 4. Test of 3/2 scaling for the interfacial tension near the critical salt concentration. The solid line shows the theoretical prediction: $\gamma/\gamma_0 = (1 - \psi/\psi_c)^{3/2}$. Symbols correspond to experimental data and results from simulations; γ_0 and ψ_c are fitting parameters. (Circles: Piftus et al., Langmuir, 2012; $\gamma_0 = 1.2$ mJ/m² and $\psi_c = 1000$ mM. Diamonds: Spruijt et al., Soft Matter, 2010; $\gamma_0 = 0.6$ mJ/m² and $\psi_c = 1250$ mM. Squares: Riggleman et al., J.Chem.Phys., 2012; $\gamma_0 = 1.2$ and $\psi_c = 110$ (both quantities are non-dimensionalized in the original figure; γ in k_BT/Rg² and ψ_c in 1/Rg³).

salts, we showed that the interfacial tension scales as $N^{-3/2}(\eta/\eta_c-1)^{3/2}$ near the critical point of the demixing transition, and that it scales as $\eta^{1/2}$ far away from it, where N is the molecular weight and η measures the electrostatic interaction strength as a function of temperature, dielectric constant, and charge density of the polyelectrolytes. For the case with added salts, we showed that the interfacial tension scales with the salt concentration ψ as $N^{-1/4}(1-\psi/\psi_c)^{3/2}$ near the critical salt concentration ψ_c . Our predictions were shown to be in quantitative agreement with experiments and our models provide a means to design new materials based on polyelectrolyte complexation for specific applications.

Effect of chemical sequence on coacervate structure: More recently we started to investigate the effect of chirality on the solid or liquid character of polyelectrolyte complexes formed from oppositely-charged polypeptides. One of the goals of this work is that by adopting chemical structures or motifs found in nature, it will be possible to replicate in the laboratory some of the assembly strategies that nature relies on to create complex organisms. We have demonstrated that the physical state of the resultant complex is determined by the combination of electrostatic and polar interactions present. Thus, the formation of dynamic, liquid complexes requires at least one racemic partner to disrupt backbone hydrogen bonding networks. Conversely, homochiral polypeptides enable the collapse of complexes into compact, fibrillar solids with a β -sheet structure. Similar trends are observed in analogous polyelectrolyte complex micelles, where microphase separation is stabilized by conjugation of the polyelectrolyte domain to a neutral, water-soluble polymer. These systems represent an intriguing class of materials in which associative charged and polar forces may be juxtaposed for morphological control without otherwise altering the chemical composition, and could have significant implications for the tailoring of material properties, for example in the formulation of delivery systems with controlled water content.

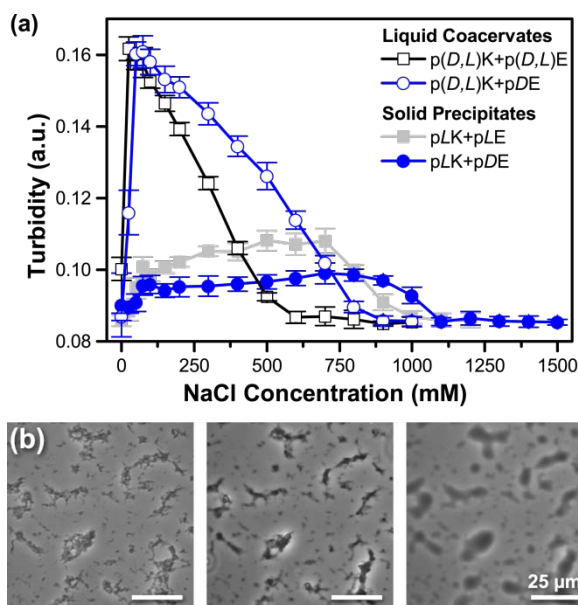


Figure 5. (a) Turbidity as a function of NaCl concentration for various liquid coacervates (open symbols) and solid precipitates (solid symbols) prepared at 1 mM total residue concentration and pH = 7.0. (b) Optical micrographs showing the transition from solid precipitate to liquid coacervate for pLK+pLE complexes with increasing urea concentration. Scale bars are 25 μ m.

Directed assembly of supramolecular (liquid crystalline) systems: A supramolecular system, polystyrene-block-poly(4-vinylpyridine) (PS-b-P4VP/PDP) blended with 3-pentadecylphenol (PDP), was directed to assemble on lithographically-defined chemically nanopatterned surfaces. PDP hydrogen bonds with the 4-vinylpyridine segments of the block copolymer to create

lamellae-within-lamellae nanostructure. Perfect and registered assembly was achieved using solvent annealing and by adjusting the period of the supramolecular material by controlling the volume fraction of PDP to match the period (or a multiple of the period) of the chemical pattern. Furthermore, the PDP molecules can be selectively removed from the supramolecular assemblies to fabricate nanoporous structures, or subsequently decorated with nanoparticles for functionality (see Figure 6).

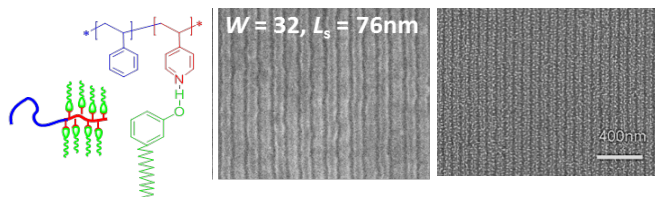


Figure 6. (a) PS(33000)-b-P4VP(8000)/PDP_{2.0} materials system, (b) directed assembly, (c) functionalized assembly with Au particles.

Future Plans

Moving forward, our immediate plans are focused on the following three issues:

- (1) Understanding the pathways through which defects are eliminated in directed assembly and the role of solvents in altering those pathways through the use of solvents.
- (2) Understanding the role of sequence and chirality in coacervation and precipitation
- (3) Understanding the role of specific or supramolecular interactions in directed self-assembly

Publications

- (1) Interfacial Tension of Polyelectrolyte Complex Coacervate Phases, J. Qin, D. Priftis, R. Farina, S.L. Perry, L. Leon, J. Whitmer, K. Hoffmann, M. Tirrell, and Juan J. de Pablo, † *MacroLetters*, 3, 565 (2014).
- (2) Ternary, Tunable Polyelectrolyte Complex Fluids Driven by Complex Coacervation, D. Priftis, X. Xia, K.O. Margossian, S.L. Perry, L. Leon, J. Qin, J. J. de Pablo, and Matthew Tirrell, *Macromol.*, 47, 3076 (2014).
- (3) Control of Directed Self-Assembly in Block Polymers by Polymeric Topcoats, A. Ramírez-Hernández, H. S. Suh, P. F. Nealey, and Juan J. de Pablo, *Macromol.*, in press (2014).
- (4) Solvent Annihilation in Copolymer Thin Films by Solvent Annealing, S. Hur, D. Khaira, A. Ramirez-Hernandez, M. Mueller, P.F. Neale and Juan J. de Pablo, submitted for publication (2014).
- (5) Chirality selected phase transitions in ionic polypeptide complexes, S. L. Perry, L. Leon, K. Q. Hoffmann, M.J. Kade, D. Priftis, K.A. Black, D. Wong, R. A. Klein, C. F. Pierce, K. O. Margossian, J.K. Whitmer, J. Qin, Juan J. de Pablo and Matthew Tirrell, submitted for publication (2014).

Fundamental Charge Transfer Processes in Stable Free-Radical Organic Polymer Systems

Principal Investigator: Thomas Gennett, Principle Scientist
National Renewable Energy Laboratory (NREL)
15013 Denver West Parkway, Golden, CO 80401-3305
thomas.gennett@nrel.gov

Program Scope:

Polymers with stable pendant radical groups are a unique class of redox-active materials emerging as potentially the next generation energy storage breakthrough. These polymers facilitate apparently remarkably rapid, efficient and reversible multi-step charge-transfer processes. The focus of this project is to advance the fundamental understanding of the structure-property relationships associated with the mechanism(s) of electron transfer and ion transport, along with associated interfacial mass-transfer processes that impact the charge-transfer processes of a unique class of organic free-radical polymeric redox active materials.

The project involves an integrated approach of chemical synthesis, electrochemistry, spectroscopy and theoretical modeling of a series of stable organic radical materials. Initially, we have focused on the 2,2,6,6-tetramethylpiperidine-N-oxyl (TEMPO) organic radical moiety incorporated into a complex materials set of poly(4-methacryloyloxy-2,2,6,6-tetramethylpiperidine-N-oxyl) (PTMA).

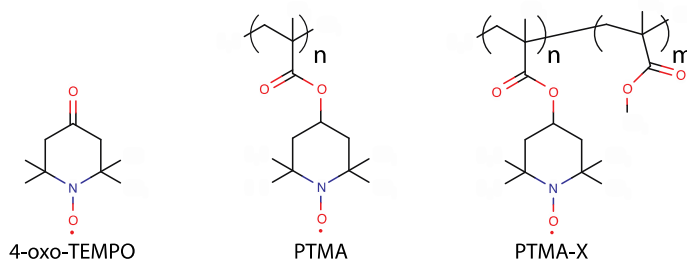


Figure 1. Model compound (4-oxo-TEMPO) and polymer structures (PTMA and PTMA-X) investigated

We focused our work to probe, and establish, the charge-transfer mechanisms of a series of the TEMPO-containing macromolecules with varying chain lengths and side-chain compositions. As shown in Figure 1, we have investigated the model compound, 4-oxo-2,2,6,6-tetramethylpiperidine-N-oxyl (4-oxo-TEMPO), and compared the results to those for non-cross-linked and cross-linked PTMA oligomers and polymers with: (i) various oligomer chain-lengths; and (ii) controlled densities of the TEMPO radical moieties along the chain (i.e. with some TEMPO-methacrylate units replaced by methyl methacrylate).

Recent Progress

Since the beginning of our project in September 2012, we have made significant progress in the advancement of the controlled-synthesis of various PTMA materials. These efforts have allowed for a detailed series of electrochemical and spectro-electrochemical (Electron Paramagnetic Resonance, Photoluminescence, Raman and UV-Vis spectroscopies) characterizations of the various materials in various redox states. Furthermore, through theoretical modeling, the possible effects of packing on electron-transport mechanisms of the PTMA materials were predicted. The first-generation theoretical packing morphologies were modeled using classical molecular dynamics simulations and the electronic coupling matrix element between each radical site was then calculated. The following summarizes some of our recent efforts with a more detailed explanation of results to be presented at the BES Materials Chemistry Principal Investigators' meeting.

Our initial synthetic efforts focused on developing strategies to alter the fundamental charge transport phenomena in the nitroxide radical polymers through structure control. For example we systematically changed the radical density within the polymers by introducing “blanks”, or

monomers not bearing any nitroxide radical, Figure 1. Several series of copolymers and oligomers bearing 20, 40, 60, 80, and 100 mol % of the radical moiety were synthesized. The electrochemical and EPR analysis and theoretical models then coalesced on a unique property of the 20 mol % where the change in electron-transfer rates, ionic mobility and observed overpotentials correlated to some of the changes in predicted molecular packing.

Figure 2, shows the room temperature X-band EPR data for the nitroxyl radical containing compounds TEMPO-100, TEMPO-60, TEMPO-20 and model compound 4-oxo-TEMPO. The 4-oxo-TEMPO model spectrum (Fig 2d) exhibits the classic isotropic hyperfine triplet structure normally encountered for TEMPO radicals in solution. In Figs 2 a–c, a general trend for these compounds emerges: as the percentage of TEMPO radicals within the polymer backbone decreases, the EPR spectra exhibit more resolved resonances. These spectra share a common zero-field crossing with the TEMPO model compound indicating that the isotropic g -value does not shift appreciably when the radical is attached to the polymer. Overall, the EPR spectra of any TEMPO-polymer compound should replicate the TEMPO model of Fig. 2d when the TEMPO radicals are sufficiently isolated. In the case of TEMPO-100, each available side-chain contains a TEMPO radical, hence the possible intrapolymer exchange is maximal. This could contribute to the coalescence of the triplet structure into one broad resonance observed in Fig 2a, but additional broadening may be present if the inter-polymer exchange contributes significantly. The low temperature experiments (77K) which freeze out the rotational motion to reveal the hyperfine anisotropy, are completed, and the results will be presented. It is interesting to note that the first generation radial distribution functions as calculated by theory, Figure 3, show that the intermolecular distance between radicals is predicted to be similar for the entire TEMPO series, however, the number of neighbors for a TEMPO moiety is proportional to the *number density* of TEMPO rings *times* the radial distribution function, so there should be roughly one fifth as many close TEMPO-TEMPO interactions in TEMPO-20 than in PTMA. The EPR spectra do indicate that the population of these in-

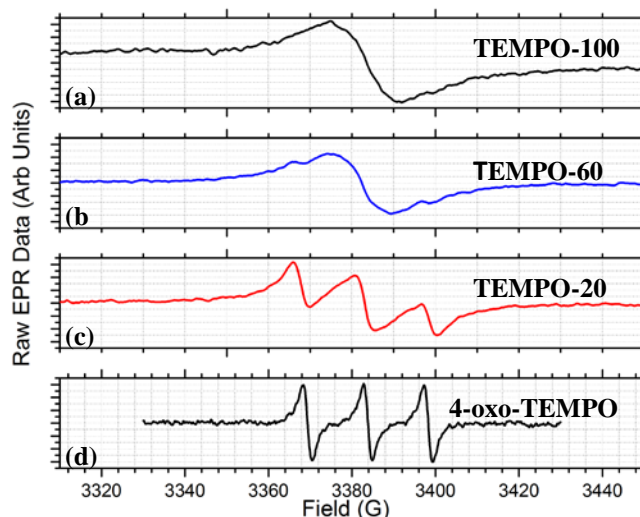


Figure 2: Room temperature, X band EPR spectra of the nitroxyl radical-polymer structures: (a) TEMPO-100; (b) TEMPO-60; (c) TEMPO-20; and (d) the model 4-oxo-TEMPO model compound.

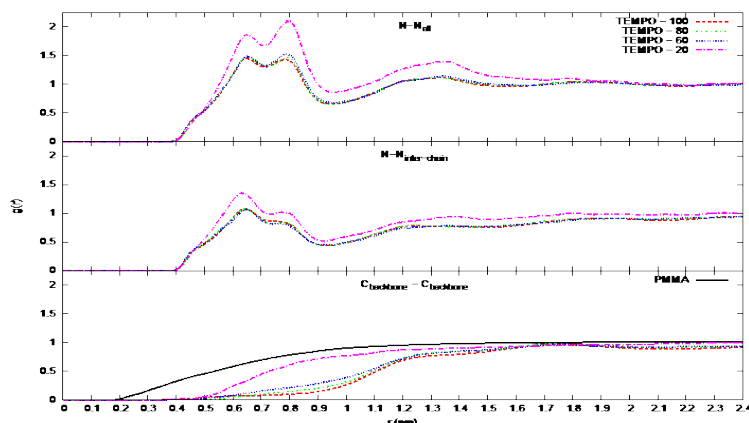


Figure 3: Radial distribution functions, RDFs, as calculated for the TEMPO 20, 60, 80 and 100 mole percent materials.

interactions is drastically reduced for the TEMPO-20, which correlated well to the electron-transfer rate decrease and the 100 mV overpotential observed. In addition, the simulated radial distribution functions between chain backbone carbons shown in Figure 3 predicts that the polymer backbones can be much closer together than for the rest of the TEMPO-X/PTMA structures and it is anticipated that the resulting structure will hinder ion motion significantly. Hence, we are currently investigating the rate of ion-migration at the interfacial polymer-electrolyte interface to determine the effect of reduced redox active group concentration on the driving force for anion mass transfer for the polymeric materials.

We have used atomistic molecular dynamics simulations of the structure and morphology of polymer films to examine the interplay between intermolecular packing and charge transport in PTMA films in great detail. Our predictions indicated that the radical electron was found to primarily occupy the oxygen-nitrogen bond of the TEMPO ring of PTMA. The simulated thin-film structures revealed three primary packing motifs associated with the inter TEMPO radical position, consisting of close contact of the TEMPO oxygen atoms in a head on arrangement, oxygen-nitrogen bond stacking and TEMPO ring stacking. When the electronic-coupling between TEMPO rings was calculated, it was found that the strongest inter-TEMPO ring coupling was between rings on different chains, with inter-chain rings able to arrange with the head-on and oxygen-nitrogen bond stacking. By forming and analyzing a novel electron-coupling-weighted radial distribution function, two primary distances were found to contribute to the effective electron transfer length of 5:5 Å, with a majority of the electron transfer, nearly 85 %, predicted to occur between radical sites on different polymer chains.

As we worked towards the evaluation of fundamental charge transport phenomena using time-resolved photoluminescence (PL) spectroscopy, we found an absence of strong spectral signatures for the redox species derived from nitroxyl radical. Since our goal is to use polymer-brush materials of specific lengths and radical density, the lack of spectral signatures necessitated an indirect method to be developed to measure the redox induced charge transfer. Since radical species are known fluorescence quenchers, the organic dye perylene was used as the indirect sensor of electron transfer. However, we first needed to establish the quenching dynamics between perylene and the various nitroxyl radicals in our materials set. Our objective was to establish the quenching distance, static or dynamic properties of the mechanism, the rate of reaction and finally how polymer morphology affects quenching properties. We examined a series of oligomers of different chain length and radical content. The perylene quenching occurs by a process that requires the radical to be within ~ 2.2 nm (a relatively large sphere of interaction) of the perylene, when each component is allowed to freely diffuse through solution, i.e., the case for the model compound, 4-oxo-TEMPO. The dynamics of this interaction are changed significantly once the quencher is poly-

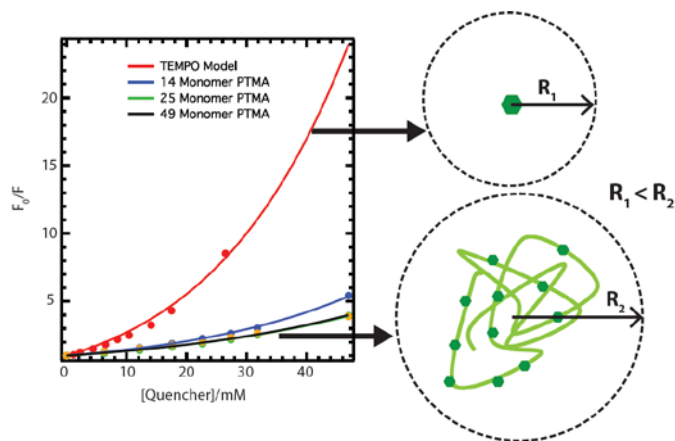


Figure 4: Stern-Volmer plot of the steady-state luminescence versus quencher concentration for TEMPO-containing oligomers of various lengths. A length-dependent sphere of interaction is evident.

mer-bound. The mechanism of quenching transitions from the diffusion limited process to a predominantly static quenching process indicating that as the polymer becomes larger and mass transfer effects dominate, the fluorophores are being effectively trapped adjacent to TEMPO moieties resulting in immediate quenching. This behavior, coupled with the EPR experiments have provided valuable experimental insight as we proceed to look at the specifics of the inter- and intra- molecular electron hopping mechanisms within the TEMPO polymer.

Future Plans

A synthetic route to tethered polymer brushes with 100% nitroxide radical functionality is being pursued since the current controlled radical polymerization (CRP) technique has limitations. The new synthetic technique utilizes a nitroxide radical monomer protected with a thermally labile functional group that spontaneously dissociates to generate the nitroxide radical at elevated temperatures. This allows us to grow the brushes with the powerful CRP technique, yet circumvent the problem of needing an oxidizing agent to diffuse into a dense brush.

In the coming fiscal year a full functional ENDOR Q-Band and X-Band system with electrochemical resonant cavities will go on-line at NREL. Our plan is to perform a series of both static and dynamic experiments with the various materials sets already characterized, to establish definitively the molecular environment around the radical with the materials matrix.

We are also exploring the preliminary solution-phase spectro-electrochemical measurements of the TEMPO radical. Currently a custom absorbance spectrometer is being assembled to allow for triggered-potential modulation experiments, which will enable us to determine rates of electron transfer on our polymer-brush samples.

Building on our theoretical work with pure PTMA we will continue to incrementally add complexity to the system and calculate transport relevant quantities, which can be compared to experiment using classical molecular dynamics (MD) simulations. The first addition to the pure system we are addressing is solvent effects on electron transport. Based on these results a range of solvent concentrations around the experimental value will be simulated and the effects of solvent and crosslinking on the electronic-coupling-weighted radial distribution function will be evaluated. Subsequently the incorporation of anions into systems at various charge states will be examined in a similar manner.

References

(1) H. Nishide, et. al., , *Organic Radical Battery: Nitroxide Polymers as a Cathode-Active Material*. *Electrochimica Acta* 2004, 50, 827-831. (2) N. R. Baker et.al., *An Evaluation of the Potential Triggers of Photoinactivation of Photosystem II in the Context of a Stern-Volmer Model for Downregulation and the Reversible Radical Pair Equilibrium Model*. *Phil. Trans. R. Soc. Lond. B* 2000, 355, 10. (3) H. A. López-Peña et. al., *Electrochemical and spectroelectrochemical properties of nitroxyl radical species in PTMA, an organic radical polymer. Influence of the microstructure* *Electrochem. Comm.* 2009 (11) 1369–1372. (4) M.K. Hung, et.al., *Synthesis and Electrochemical Behaviour of Nitroxide Polymer Brush Thin-Film Electrodes for Organic Radical Batteries* *J. Mater. Chem.* 2012, 22, 1570. (5) A. Liemant, *A Drift Diffusion Equation for Charge Transport in Inhomogeneous Materials*; Citeseer, 1997.

Publications: “*Relationship between Molecular Structure and Electron-Transfer in a Polymeric Nitroxyl-Radical Energy Storage Material*”, T. Kemper, R. Larsen, T. Gennett *J. Phys Chem C*. accepted pending revisions. “*Quenching of the Perylene Fluorophore by Stable Nitroxide Radical-Containing Macromolecules*”, B. Hughes, A. Ferguson, T. Gennett, submitted to *J. Phys. Chem. B*.

Linking Ion Solvation and Lithium Battery Electrolyte Properties

Wesley Henderson, PI

(former) **Department of Chemical & Biomolecular Engineering, North Carolina State University**

(current) **Electrochemical Materials & Systems Group, Energy & Environmental Directorate, Pacific Northwest National Laboratory (PNNL)**

Program Scope

The research objective of this proposal was to provide a detailed analysis of how solvent and anion structure govern the solvation state of Li^+ cations in solvent-LiX mixtures and how this, in turn, dictates the electrolyte physicochemical and electrochemical properties which govern (in part) battery performance. Lithium battery electrolytes remain a poorly understood and hardly studied topic relative to the research devoted to battery electrodes. This is due to the fact that it is the electrodes which determine the energy (capacity) of the battery. The electrolyte, however, plays a crucial role in the practical energy density, power, low and/or high temperature performance, lifetime, safety, etc. which is achievable. The development within this project of a "looking glass" into the molecular interactions (i.e., solution structure) in bulk electrolytes through a synergistic experimental approach involving three research thrusts complements work by other researchers to optimize multi-solvent electrolytes and efforts to understand/control the electrode-electrolyte interfaces, thereby enabling the rational design of electrolytes for a wide variety of battery chemistries and applications (electrolytes-on-demand). The three research thrusts pursued include:

- (1) conduction of an in-depth analysis of the thermal phase behavior of diverse solvent-LiX mixtures,
- (2) exploration of the ionic association/solvate formation behavior of select LiX salts with a wide variety of solvents, and
- (3) linking structure to properties—determination of electrolyte physicochemical and electrochemical properties for comparison with the ionic association and phase behavior.

Thrust I involved the creation of a library of binary solvent-LiX phase diagrams. These are highly informative when combined with the ionic association information provided by Thrust II. Solvate crystal structures were determined to provide insight into the manner of solvent... Li^+ and anion... Li^+ coordination and these served as models for the Raman spectroscopic analyses used in Thrust II to determine the degree of ionic association.

Thrust II began the development of a " Li^+ Solvation Scale for Solvents" by directly examining anion... Li^+ interactions within a wide variety of solvents to determine which types of solvates exist in solution (thus proving that commonly used solvent polarization parameters such as donor number and dielectric constant are poor determinants for solvation interactions for Li^+ cations).

Thrust III involved the extensive determination of solvent-LiX electrolyte properties over broad temperature and

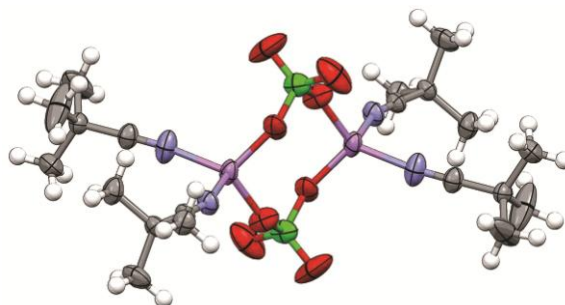


Fig. 1. Example of solvent and ion coordination within a crystalline solvate structure: $(\text{TMAN})_2:\text{LiClO}_4$ (Li-purple, N-blue, O-red, Cl-dark green).

concentration ranges including conductivity, viscosity and density. These detailed data, in combination with the information from Thrusts I and II, resulted in a comprehensive understanding of the electrolyte/battery composition-property-performance relationships which are essential for utilizing this fundamental information for improved electrolyte selection (formulation) for new battery chemistries. Information has been shared throughout the project with a collaborator who has utilized the data to aid in the optimization of molecular dynamics (MD) simulations of electrolytes which have provided further insight unobtainable directly from the experimental data. This work clearly delineates which solvent and anion structural features are critical for determining electrolyte bulk properties and how these properties are interrelated.

Recent Progress

A diverse collection of solid-liquid binary phase diagrams have been prepared for nitrile, carbonate and ester solvents with varying lithium salts and the crystal structures for numerous crystalline solvate phases (e.g., $(\text{TMAN})_2:\text{LiClO}_4$ —Fig. 1) have been determined to complement the phase diagrams. Using Raman spectroscopic evaluations of the known solvate structures, 'tools' (data sets) were then created to unambiguously assign Raman band positions to specific modes of anion... Li^+ coordination for LiBF_4 , $\text{LiN}(\text{SO}_2\text{CF}_3)_2$ (i.e., LiTFSI), LiClO_4 and LiCF_3SO_3 . This has enabled a greatly improved characterization of the solvation (solvent... Li^+) and ionic association (anion... Li^+) interactions within liquid electrolytes which has subsequently been used to provide mechanistic explanations for electrolyte property variations (e.g., Fig. 2).

In addition to delineating extensive information about the solution structure of the electrolytes, this project has demonstrated that much of the conventional wisdom/methods associated with electrolyte characterization and optimization is/are fallacious or flawed. Examples include the demonstration that conductivity and viscosity—as well as salt solubility and solvation—are not

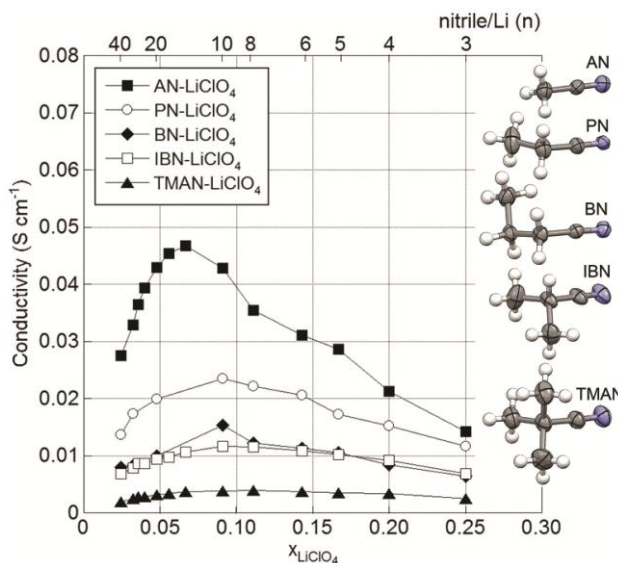


Fig. 2. Isothermal conductivity (60°C) as a function of salt concentration (bottom - mole fraction of salt; top - solvent/Li mole ratio) for varying nitrile solvents.

Table 1. Solvent polarization parameter values (dielectric constant and donor number).

Solvent	ϵ	DN
diglyme (G2)	7.2	24
monoglyme (1,2-DME or G1)	7.1	20
tetrahydrofuran (THF)	7.4	20
2-methyltetrahydrofuran (2-MeTHF)	7.0	18
diethyl ether (Et_2O)	4.2	19

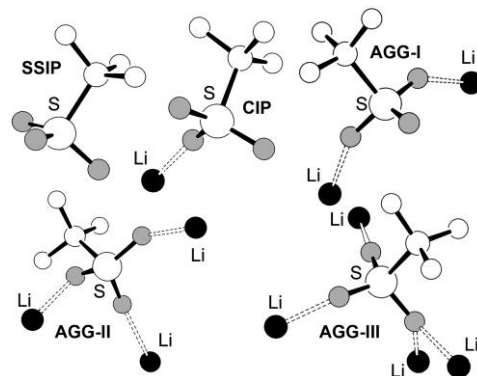


Fig. 3. Varying modes of $\text{CF}_3\text{SO}_3^- \dots \text{Li}^+$ coordination: (a) SSIP, (b) CIP, (c) AGG-I, (d) AGG-II and (e) AGG-III.

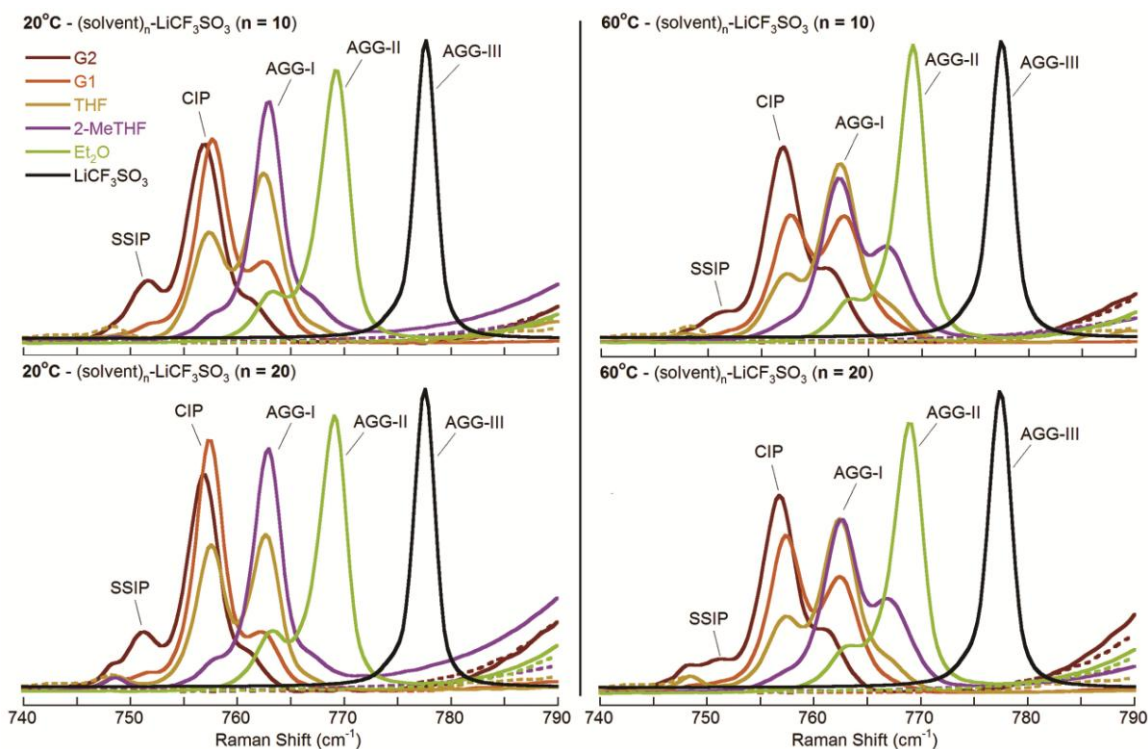


Fig. 4. Raman spectra of the CF_3SO_3^- anion vibrational bands for $(\text{solvent})_n\text{-LiCF}_3\text{SO}_3$ mixtures with ether solvents. The spectra for the pure salt (black) and pure solvents (dashed) are shown for comparison.

directly correlated with one another, as is commonly assumed. The work has also demonstrated that widely used solvent polarizability parameters (Table 1) are poor indicators of ionic association (Figs. 3 and 4)—and thus solvation—interactions for lithium salts dissolved in aprotic solvents. Correcting misinformation about electrolytes and thus aligning the intuition of battery researchers much more closely with the actual characteristics of electrolytes at the molecular- and mesoscale-level is one of the key accomplishments of this project.

Future Plans

Funding for this project has ended.

References

None

Publications

- Seo DM, Borodin O, Han S-D, Ly Q, Boyle PD, Henderson WA. *J. Electrochem. Soc.* **2012**, 159, A553. Electrolyte Solvation and Ionic Association. I. Acetonitrile-Lithium Salt Mixtures: Intermediate and Highly Associated Salts.
- Seo DM, Borodin O, Han S-D, Ly Q, Boyle PD, Henderson WA. *J. Electrochem. Soc.* **2012**, 159, A1489. Electrolyte Solvation and Ionic Association. II. Acetonitrile-Lithium Salt Mixtures: Highly Dissociated Salts.
- Seo DM, Boyle PD, Borodin O, Henderson WA. *RSC Adv.* **2012**, 2, 8014. Li^+ Cation Coordination by Acetonitrile—Insights from Crystallography.

- Seo DM, Borodin O, Balogh D, O'Connell M, Ly Q, Han S-D, Passerini S, Henderson WA. *J. Electrochem. Soc.* **2013**, *160*, A1061. Electrolyte Solvation and Ionic Association. III. Acetonitrile-Lithium Salt Mixtures—Transport Properties.
- Seo DM, Afroz T, Han S-D, Allen JL, Boyle PD, Henderson WA. *Energy Environ. Sci.* **2014**, under review. Delving Within Lithium Salt Solvates.
- Seo DM, Borodin O, McOwen DW, Han S-D, Sommer RD, Henderson WA. *Energy Environ. Sci.* **2014**, under review. Disjoining Electrolyte Salt Solubility, Solvation and Ionic Association Interactions.
- Seo DM, Boyle PD, Allen JL, Han S-D, Jónsson E, Johansson P, Henderson WA. *J. Phys. Chem. C*, **2014**, under review. Solvate Structures and Computational/Spectroscopic Characterization of LiBF₄ Electrolytes.
- Seo DM, Boyle PD, Sommer RD, Daubert JS, Borodin O, Henderson WA. *J. Phys. Chem. B*, **2014**, under review. Solvate Structures and Spectroscopic Characterization of LiTFSI Electrolytes.
- Borodin O, Han S-D, Daubert JS, Seo DM, Yun S-H, Henderson WA. *J. Electrochem. Soc.* **2014**, under review. Electrolyte Solvation and Ionic Association. VI. Acetonitrile-Lithium Salt Mixtures: Highly Associated Salts Revisited.
- Henderson WA. Ch. 1 Nonaqueous Electrolytes: Advances in Lithium Salts in *Electrolytes for Lithium and Lithium-Ion Batteries*—Modern Aspects of Electrochemistry Series No. 58 (Eds. Jow TR, Xu K, Borodin O, Ue M), Springer, New York 2014.
- Yun S-H, Han S-D, Seo DM, Afroz T, Borodin O, Keller M, Passerini S, Sommer RD, Henderson WA. *J. Phys. Chem. C*, **2014**, in-preparation. Solvate Structures and Spectroscopic Characterization of LiCF₃SO₃ Electrolytes.
- Daubert JS, Afroz T, Seo DM, Boyle PD, Henderson WA. *J. Phys. Chem. C*, **2014**, in-preparation. Solvate Structures and Spectroscopic Characterization of LiClO₄ Electrolytes.
- Seo DM, Daubert JS, Borodin O, Balogh D, O'Connell M, McOwen DW, Henderson WA. *J. Electrochem. Soc.* **2014**, in-preparation. Electrolyte Solvation and Ionic Association. VII. Propionitrile and Butyronitrile-Lithium Salt Mixtures: Dissociated Salts.
- Seo DM, Daubert JS, Borodin O, McOwen DW, Balogh D, Henderson WA. *J. Electrochem. Soc.* **2014**, in-preparation. Electrolyte Solvation and Ionic Association. VIII. Propionitrile and Butyronitrile-Lithium Salt Mixtures: Associated Salts and Transport Properties.
- Han, S-D, Lloyd A, Yun S-H, Henderson WA. *J. Electrochem. Soc.* **2014**, in-preparation. Electrolyte Solvation and Ionic Association. IX. Isobutyronitrile and Trimethylacetonitrile-Lithium Salt Mixtures: Linking Solvent Structure to Solvation and Transport Properties.
- Seo DM, Allen JL, Daubert JS, O'Connell M, Borodin O, Henderson WA. *J. Electrochem. Soc.* **2014**, in-preparation. Electrolyte Solvation and Ionic Association. X. Cyclic Carbonate and Ester-Lithium Salt Mixtures.
- Daubert JS, Afroz T, Han S-D, Balzer A, Allen JL, Borodin O, Henderson WA. *J. Electrochem. Soc.* **2014**, in-preparation. Electrolyte Solvation and Ionic Association. XI. Acyclic Carbonate-Lithium Salt Mixtures.
- Daubert JS, Afroz T, Han S-D, Balzer A, Allen JL, Borodin O, Henderson WA. *J. Electrochem. Soc.* **2014**, in-preparation. Electrolyte Solvation and Ionic Association. XII. Acyclic Ester-Lithium Salt Mixtures.
- Henderson WA, Han S-D, Yun S-H, Seo DM, Allen JL, McOwen DW, Borodin O. *Nat. Chem.* **2014**, in-preparation. Reassessing Polarization Parameters and Li⁺ Cation Solvation.

“Giant” Nanocrystal Quantum Dots: Controlling Charge Recombination Processes for High-Efficiency Solid-State Lighting

**Dr. Jennifer A. Hollingsworth and Dr. Han Htoon, Materials Physics & Applications
Division: Center for Integrated Nanotechnologies, Los Alamos National Laboratory, Los Alamos, NM**

Program Scope

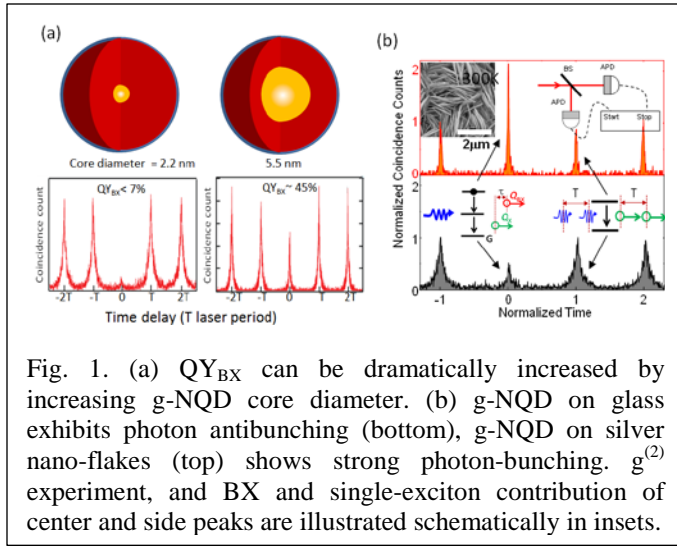
Solid-state lighting (SSL) has the potential to replace less efficient and robust lighting technologies, such as incandescent and fluorescent lamps. Significant inroads into the commercial and residential general-lighting markets have been made in recent years as light-emitting diodes (LEDs) find consumer acceptance. That said, science challenges remain as underpinning drivers of fundamental research required for *disruptive advances* in SSL. Existing technologies (nitride and organic-LEDs) suffer from some combination of flaws: non-optimal efficiencies and/or manufacturing/materials costs, insufficient access to a full-spectrum ‘color palette,’ inadequate longevity, etc. A fundamental understanding of the processes that impact the conversion of electricity into light is still needed. As recently observed (DOE/EERE 2011 Joint Roundtable), nanostructures can serve as *platforms for understanding* such fundamental processes, but also as *solutions* to realizing control over exciton→photon conversion pathways. In our work, we study and develop a new class of optical nanomaterial – the “giant” nanocrystal quantum dot (g-NQD). g-NQDs are thick-shell core/shell NQDs that exhibit unique photo-physical/chemical behavior (non-blinking, non-photobleaching, suppressed non-radiative Auger recombination, large Stokes shift, surface-independent emission) resulting from effects of a thick shell, a relatively large per-particle volume, at least partial spatial separation of the excited-state electron-hole pair, and/or possibly compositional alloying at the core/shell interface. By judicious nanoscale-heterostructuring, we are able to influence these parameters and, thereby, to alter the interplay between radiative/nonradiative carrier-recombination processes. Through three Research Goals, we aim to establish g-NQDs as functional “building blocks” for SSL with combined attributes of high-efficiency, robustness, low-cost, and color tunability: (1) Establish quantitative g-NQD “structure-function” relationships for fully predictable/consistent performance and new g-NQD development, (2) Understand/control exciton (*and multi-exciton*)→photon conversion pathways via strategic manipulation of intrinsic and extrinsic g-NQD properties, and (3) Demonstrate performance-benchmarking in light-emitting devices.

Recent Progress

Research Goal 1

Through a systematic investigation of the reaction parameters controlling the Successive Ionic

Layer Adsorption and Reaction (SILAR) synthesis of thick-shell CdSe/CdS core/shell NQDs, we previously realized a *complete suppression of g-NQD blinking*, as well as a clear structure:function correlation showing a common volume threshold for realizing non-blinking behavior *over long observation times of 1 hour* ($\sim 750 \text{ nm}^3$).¹ To more fully explore the impact of g-NQD volume and/or core-size on blinking behavior and Auger recombination (AR), we subsequently investigated single-dot photoluminescence (PL) intensity and biexciton (BX) quantum yields (QY_{BX}) as a function of these parameters in CdSe/CdS g-NQDs. We showed that g-NQD *core size* significantly affects QY_{BX} and can be utilized as an effective tuning parameter towards higher QY_{BX} while keeping the total volume of the g-NQD constant.² Moreover, our study confirmed that long shell anneal times plays a critical role in achieving high QY_{BXs} .



Research Goal 2

Intrinsic control: nanoscale-architecture engineering. Extending the property of stable, non-blinking emission and AR suppression to other regimes of the electromagnetic spectrum is an essential step in realizing the potential of the g-NQD approach for a variety of technological applications. To this end, we recently synthesized a novel InP/CdS g-NQD characterized by a type II band alignment, where electrons and holes are confined separately in the CdS shell and InP core, respectively. With these g-

NQDs, non-blinking excitonic emission and a strong suppression of AR were achieved for the first time in the near-infrared (800-1300 nm).³ More recently, we investigated the precise blinking mechanism – AR/charging mediated (A-type) vs. hot-carrier trapping (B-type).⁴ We observed that while A and B type blinking compete in defining the blinking behavior for NQDs with thin shells, the role of hot-carrier trapping dominates for NQDs with thick shells. Our studies further revealed that higher laser pump fluences result in the creation of additional hot-carrier traps, while higher repetition rates cause a saturation in hot-carrier traps, thus activating AR related PL fluctuations. Furthermore, we showed that AR of negatively charged excitons is suppressed more strongly than that for positively charged excitons due to asymmetry in electron-hole confinement in type II NQDs. Thus, our study provides *new understanding of how both NQD structure (shell thickness and carrier-separation characteristics) and excitation conditions can be used to tune PL stability*, with important implications for room-T single-photon generation. Specifically, ours is the first non-blinking NQD capable of single-photon emission in the near-infrared spectral regime.

Extrinsic control: hybrid systems. In the past decade, a tremendous amount of research has been directed at the study of metal nanoparticle (MN)-semiconductor emitter interactions in

attempts to *extrinsically* control electron-hole recombination pathways of nanoemitters. Most of these studies have been conducted in the context of MNs interacting with single excitons. In contrast, we ventured into the realm of multi-exciton-MN interactions by performing systematic photon-correlation spectroscopy studies on individual CdSe/CdS g-NQDs.⁵ We revealed for the first time that the statistics of photons emitted by an individual g-NQD can be transformed from sub-Poissonian (photon antibunching) to strong super-Poissonian (photon-bunching) when the NQD is coupled to a nano-roughened silver surface, with implications for important applications involving multiexcitons, such as optical amplification and carrier multiplication. In addition, we have reported the first low-T single NQD PL-spectroscopy study of plasmon-multiexciton interactions.⁶ Through a careful analysis of the PL saturation behavior of single-exciton emission, we were able to decouple plasmonic enhancements of absorption and emission. We revealed: (1) multi-exciton emissions in MN/g-NQD coupled systems are enhanced by both absorption and radiative recombination enhancement; (2) strong multiexciton enhancement can occur in the absence of absorption enhancements; and (3) multiexciton emission enhancement becomes stronger as the multiexciton order increases. These findings indicate that this coupled excitonic/ plasmonic system holds tremendous potential for lasing and photon-pair source applications, which require efficient multi-exciton emission.

Research Goal 3

Down-conversion and direct-charge-injection g-NQD light-emitting diodes (LEDs). Previously, we demonstrated novel g-NQD advantages in both down-conversion and direct-injection LEDs benchmarked against conventional core/shell NQDs.^{7,8} Currently in the context of down-conversion, we are developing new concepts for coupling g-NQDs with high-power LED sources, addressing the issue of temperature stability through chemical modification of the g-NQDs and using novel ultra-thin spacers to thermally isolate the g-NQD emitters from the LED source. To date, we have achieved high-power down-conversion efficiencies up to 75% of the g-NQD QY, reflecting both minimal thermal and self-reabsorption losses. In the area of direct-injection devices, we are also exploring the possibility for new device designs. For example, because charge/energy-transfer processes between emitters and an electrode and/or charge transport layers are critical for optimal performance, we have investigated the interactions between g-NQDs and a novel transparent conductive electrode material – *graphene*. We show that PL quenching by Förster energy transfer (ET) to the graphene layer is significantly reduced in the case of g-NQDs compared to conventional core/shell NQDs (only 3 times vs. 80-fold). We previously showed that suppressed ET dramatically reduces deleterious dot-to-dot ‘energy funneling’ to non-radiative, lowest-energy states in close-packed g-NQD films (yielding excellent solid-state performance).⁸ Now, we show that g-NQDs are compatible with electrode materials that would otherwise quench conventional NQD emitters. Perhaps of even greater significance, we reveal that g-NQD QY_{BXs} on graphene are enhanced by an order-of-magnitude compared to that on glass and are made possible by the ability of graphene to modify the radiative rates of the single- and bi-exciton states. This surprising result is only possible if the nano-semiconductor – in a charged state – is able to induce a graphene plasmonic response in the

visible spectral region, i.e., to overlap with the g-NQD emission. Again, we propose significant potential for such novel hybrid systems in a range of applications requiring highly efficient multi-exciton emission, e.g., light amplification, lasing and entangled photon-pair generation.

Future Plans

Research Goal 1: Free-flow electrophoresis will be used to separate g-NQDs based on size and charge (influenced by shape), allowing us to precisely correlate these properties with g-NQD ensemble and single-dot function, providing critical feedback to growth, which will be facilitated by novel capability for automated synthesis. We will continue to work with internal and external collaborators to definitively characterize the g-NQD core/shell interface at the atomic scale. *Research Goal 2:* We will extend our exploration of core/shell electronic structure paired with core/shell architecture to define a “road map” for g-NQD behavior, while pursuing excitonic-plasmonic hybrids and mesoscale supercrystal assemblies as key approaches to extrinsic properties manipulation and emergent, collective behavior. *Research Goal 3:* We will apply fundamental experimental observations in g-NQD/graphene system to devices and achieve thermal stability with down-conversion efficiencies >50%.

References

1. Ghosh, Y. et al. *J. Am. Chem. Soc.* 2012, *134*, 9634–9643.
2. Mangum, B. D., Sampat, S., Ghosh, Y., Hollingsworth, J. A., Htoon, H. & Malko, A. V. *Nanoscale* **6**, 3712-3720 (2014).
3. Dennis, A., Mangum, B. D., Piryatinski, A., Park, Y.-S., Hannah, D., Casson, J. L., Williams, D. J., Schaller, R., Htoon, H. & Hollingsworth, J. A. *Nano Lett.* **12**, 5545-5551 (2012).
4. Mangum, B. D., Wang, F., Dennis, A., Hollingsworth, J. A. & Htoon, H. *Small*, DOI SMLL201202896 (2013).
5. Park, Y.-S., Ghosh, Y., Chen, Y., Piryatinski, A., Xu, P., Mack, N. H., Wang, H.-L., Klimov, V. I., Hollingsworth, J. A. & Htoon, H. *Phys. Rev. Lett.* **110**, 117401 (2013).
6. Park, Y.-S., Ghosh, Y., Xu, P., Mack, N. H., Wang, H.-L., Hollingsworth, J. A. & Htoon, H. *J. Phys. Chem. Letts.* **4**, 1465-1470 (2013).
7. Kundu, J. et al. *Nano Lett.*, **2012**, *12*, 3031-3037.
8. Pal, B.N. et al. *Nano Lett.* **2012**, *12*, 331.

Publications

References **2, 3, 4, 5, 6, above** and

1. Mangum, B. D., Ghosh, Y., Hollingsworth, J. A. & Htoon, H. *Optics Express* **21**, 4713 (2013).
2. Mangum, B. D., Park, Y.-S., Ghosh, Y., Hollingsworth, J. A. & Htoon, H. in *SPIE Defense, Security, and Sensing*. 87270S-87270S-87214 Internat'l Soc. for Optics & Photonics (2013).
3. Hollingsworth, J. A. *Chem. Mater. (Invited Review Article)* **25**, 1318–1331 (2013).
4. Hollingsworth, J. A. *Coordin. Chem. Rev. (Invited Review Article)* **263-64**, 197-216 (2014).

Rational Synthesis of Superconductors
Mercouri G Kanatzidis
Materials Science Division, Argonne National Laboratory
Department of Chemistry, Northwestern University

Program Scope

This program emphasizes the synthesis of novel electronic materials and fuels new synergies with several condensed matter physics groups at MSD. This collaborative research generate: a) a rational concept for new material design aiming at emerging superconductivity, b) new insights in controlling structural/electronic instabilities in complex materials, c) new synthesis and crystal growth techniques for advanced electronic materials, and d) Fermi surface tuning accompanied by judicious doping which may drive the phase from a normal state to a superconducting state. Our long-term vision is to develop a more complete picture of how materials with superconducting properties can be predicted and prepared. We target specific two-dimensional lattices as structural motifs with charge or spin density waves. These can signify that a material is on the verge of an electronic instability, which if properly disrupted, may permit the emergence of superconductivity. Narrow-gap semiconductors, not traditionally associated with superconductivity, now appear to be a promising area to investigate for superconducting materials. Modifying the density of states in the electronic band structure of this class of materials may induce superconductivity, although the mechanism has yet to be fully defined.

Recent Progress

The current project enables MSD to expand its synthesis activities to important new classes of materials, particularly low-dimensional compounds involving chalcogenides, pnictides and intermetallics that exhibit electronic instabilities. We are guided by several design hypotheses that can yield new charge and spin-density wave compounds and narrow band-gap compounds involving transition metal, main group and rare earth pnictides and chalcogenides, whose interactions can be tuned to yield strongly competing interactions and superconductivity.

The Superconductive Phase in KFe_xSe_y . For alkali metal-intercalated iron selenides, even the structure of the superconducting phase is a subject of debate, in part because the onset of superconductivity is affected much more strongly by stoichiometry and preparation than in cuprate or pnictide superconductors. If the intertwined physics and complicated chemistry are to be explained, high-quality, pure, superconducting intercalated iron selenides need to be made. To that end, we developed a new experimental route to prepare pure $K_2Fe_4Se_5$ and a number of non-superconducting $K_xFe_{2-y}Se_2$ phases with different x and y values as well as the $K_xFe_{2-y}Se_2$ phase exhibiting superconductivity and found four distinct phases: semiconducting $K_2Fe_4Se_5$, a metallic superconducting phase $K_xFe_2Se_2$ with x ranging from 0.38 to 0.58, the phase $KFe_{1.6}Se_2$ with full K occupancy and no Fe vacancy ordering, and a oxidized phase $K_{0.51(5)}Fe_{0.70(2)}Se$ that forms the PbFCl structure upon exposure to moisture. Confirming the nature of the superconducting phase to be $K_xFe_2Se_2$ stabilized by a matrix of essentially $K_2Fe_4Se_5$ is a significant contribution to the understanding of this complex multi-phase system.

New Superconductors. We have published on two new superconductors. The first is a superconductor with exceptionally high upper critical field (H_{c2}) discovered by doping the

narrow gap semiconductor CsBi_4Te_6 . CsBi_4Te_6 crystallizes as highly anisotropic needles in the monoclinic space group $C2/m$ and has a layered structure composed of $[\text{Bi}_4\text{Te}_6]$ anionic layers and Cs^+ ions residing between the layers, Fig. 1(a, b). Only upon doping of CsBi_4Te_6 either by changing the Bi/Te ratio (p-type $\text{CsBi}_{4.1}\text{Te}_{5.9}$) or creating Cs vacancies (p-type $\text{Cs}_{0.96}\text{Bi}_4\text{Te}_6$) do the samples exhibit superconductivity at 4.4 K, Fig. 1(c). Field dependent Hall resistivity measurements at 5 K on the superconducting samples verified the doping character with carrier density of $0.9 \times 10^{19} \text{ cm}^{-3}$ for $\text{Cs}_{0.96}\text{Bi}_4\text{Te}_6$ and $1.2 \times 10^{19} \text{ cm}^{-3}$ for $\text{CsBi}_{4.1}\text{Te}_{5.9}$. Field dependent resistivity measurements revealed that the upper critical field of the CsBi_4Te_6 family is remarkably high and above 10 T, Fig. 1(d, e). The second bulk superconductor is $\text{LaPd}_{1-x}\text{Bi}_2$. It features Bi-square nets and PbO-type PdBi layers with significant partial Pd occupancy. A small residual resistance ratio indicates a strong scattering effect presumably induced by the Pd vacancies, which implies an s-wave pairing symmetry in $\text{LaPd}_{1-x}\text{Bi}_2$. Hall effect measurements reveal dominantly electron-like charge carriers and single-band transport behavior in $\text{LaPd}_{1-x}\text{Bi}_2$. Band structure calculations reveal the possibility of Fermi surface nesting near the fully stoichiometric case in $\text{LaPd}_{1-x}\text{Bi}_2$. By creating Pd vacancies the Fermi surface nesting is avoided which suppresses any potential CDW on the Bi net, apparently allowing the emergence of superconductivity.

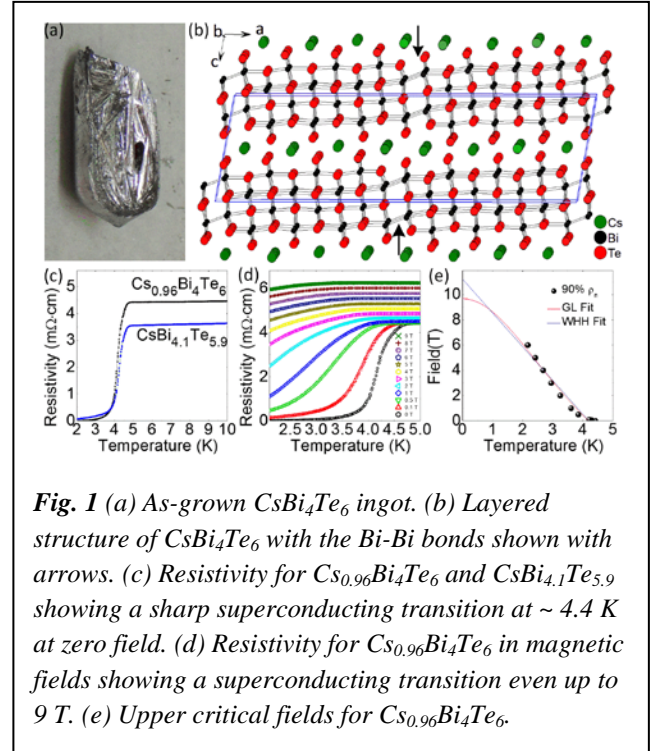


Fig. 1 (a) As-grown CsBi_4Te_6 ingot. (b) Layered structure of CsBi_4Te_6 with the Bi-Bi bonds shown with arrows. (c) Resistivity for $\text{Cs}_{0.96}\text{Bi}_4\text{Te}_6$ and $\text{CsBi}_{4.1}\text{Te}_{5.9}$ showing a sharp superconducting transition at ~ 4.4 K at zero field. (d) Resistivity for $\text{Cs}_{0.96}\text{Bi}_4\text{Te}_6$ in magnetic fields showing a superconducting transition even up to 9 T. (e) Upper critical fields for $\text{Cs}_{0.96}\text{Bi}_4\text{Te}_6$.

CDW structure of 2H-NbSe₂. Superconductivity and density waves are competing orders and therefore the understanding of electronic instabilities in low-dimensional correlated electron systems is of fundamental importance. Because 2H-NbSe₂ is a canonical CDW layered material yet structural details of its CDW were lacking, we solved the structure for the first time using a (3 + 2)-dimensional crystallographic approach on single-crystal X-ray diffraction data collected at 15 K. The detailed structure of the CDW in NbSe₂ provides critical information on the exact nature of the CDW instability in this system. It is the Nb network that defines the CDW instability whereas the Se atoms act as spectators. These insights open a path for more informed theoretical treatments and better data interpretation as well as new lines of experimentation and deeper understanding.

Re-entrant Magnetic Order in an Iron Pnictide Superconductor. With collaboration with neutron scattering group at MSD (Rosenkranz and Osborn), we have for the first time observed re-entrant magnetic order coincident with superconductivity at low temperatures in the $\text{Ba}_{1-x}\text{Na}_x\text{Fe}_2\text{As}_2$ series. The conventional thinking was that the parent compound, BaFe_2As_2 , undergoes an antiferromagnetic, spin-density wave transition at ~ 140 K that is accompanied by a lowering in crystallographic symmetry from tetragonal (C_4) to orthorhombic (C_2). Increasing the doping concentration of Na on the Ba site gradually lowers the temperature at which this transition occurs, and also induces superconductivity at a transition temperature (T_c) below

which there is no magnetic ordering. Through a careful investigation of this system via high-resolution neutron diffraction, we have determined that for a very narrow Na composition range ($0.24 \leq x \leq 0.28$), the orthorhombic C_2 superconducting phase is accompanied by a re-entrant tetragonal C_4 antiferromagnetic phase, Fig. 2. This finding is a crucial step toward the understanding of the mechanism of superconductivity in the iron pnictides (and perhaps by extension, all high-temperature superconductors in general). These results provide strong evidence for the validity of an itinerant model of nematic order in the iron-based superconductors, in which the orbital reconstruction of the iron 3d states is a consequence of SDW interactions induced by Fermi surface nesting. Whether nematic order, or at least strong nematic fluctuations, is a prerequisite for superconductivity is another challenge to address in the future. The observation of the re-entrant magnetic order and the studies of the $\text{Ba}_{1-x}\text{Na}_x\text{Fe}_2\text{As}_2$ and $\text{Ba}_{1-x}\text{K}_x\text{Fe}_2\text{As}_2$ phase diagrams would not have been possible in the absence of extremely homogeneous samples of finely tuned composition.

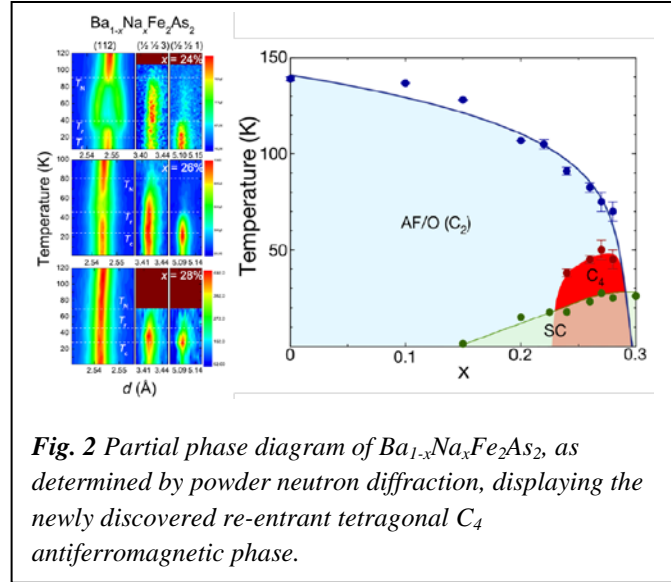


Fig. 2 Partial phase diagram of $\text{Ba}_{1-x}\text{Na}_x\text{Fe}_2\text{As}_2$, as determined by powder neutron diffraction, displaying the newly discovered re-entrant tetragonal C_4 antiferromagnetic phase.

Future Plans

We will target specific two-dimensional (2D) square lattices as a type of structural motif which oftentimes manifests as charge or spin density waves (CDW or SDW), and 2D narrow gap semiconductors. For example, low-dimensional systems are more likely to exhibit enhanced fluctuations and amplify the appearance of competing states. The CDW/SDW can signify that a material is on the verge of an electronic instability, which if properly disrupted, may permit the emergence of superconductivity. The iron-based superconductors are examples of totally unexpected emergent behavior from low-dimensional materials with complex composition. The materials are anisotropic and, remarkably, can tolerate extensive chemical modification such as substitution on all crystallographic sites. Because of the clearly unconventional superconducting mechanism (likely spin-fluctuation-mediated pairing), higher transition temperatures are likely.³ The classes of interest include REMX_2 , REMX_3 , RETe_2 , and RETe_3 (RE = rare-earth element, M = transition or main-group metal, $X = \text{P, As, Sb, Bi}$). Chemical tuning of properties is accomplished on the RE , M , X/Te sites with alkaline-earth, other transition metals, and main group elements (Ga, Sn, Se), respectively. Novel compounds may also be derived from the series $A(\text{AM}_4\text{Te}_{3+x})_n(\text{RETe}_2)_m(\text{RETe}_3)_k$ (A = alkali metal) as two examples of metallic systems and $\text{Cs}_4[\text{Bi}_{2n+4}\text{Te}_{3n+6}]$, $\text{AM}_{3+m}\text{Te}_{5+m}$, and $(\text{MSe})_n(\text{Bi}_2\text{Se}_3)_m$, as examples of semiconducting systems. There are a number of homologous series of these compounds which lower order members are known, but much of the higher order phase space remains to be explored. Even if superconductivity does not emerge, these provide fundamental insights into a wealth of physical phenomena such as charge and spin density waves, phase transitions, magnetic interactions in

low-dimensional systems, as well as thermodynamics, kinetics and stability limits of hierarchical structures.

References

1. Johnston, D. C. *Adv. Phys.* 2010, 59 (6), 803.

Publications supported by BES

1. Mihai S., Fei H., Christos D. M., D. Y. Chung, H. Claus, M. G. Kanatzidis, **2014**, *Phys. Rev. B* **2014**, 89, 054512.
2. Knox, K. R.; Bozin, E. S.; Malliakas, C. D.; Kanatzidis, M. G.; Billinge, S. J. L. *Phys. Rev. B* **2014**, 89, 014102.
3. Han, F.; Malliakas, C. D.; Stoumpos, C. C.; Sturza, M.; Claus, H.; Chung, D. Y.; Kanatzidis, M. G. *Phys. Rev. B* **2013**, 88, 144511.
4. Malliakas, C. D.; Chung, D. Y.; Claus, H.; Kanatzidis, M. G. *J. Am. Chem. Soc.* **2013**, 135, 14540.
5. Shoemaker, D. P.; Chasapis, T. C.; Do, D.; Francisco, M. C.; Chung, D. Y.; Mahanti, S. D.; Llobet, A.; Kanatzidis, M. G. *Phys. Rev. B* **2013**, 87, 094201.
6. Avci, S.; Chmaissem, O.; Allred, J.; Rosenkranz, S.; Eremin, I.; Chubukov, A.; Bugaris, D.; Chung, D. Y.; Kanatzidis, M.; Castellán, J.-P.; Schlueter, J.; Claus, H.; Khalyavin, D.; Manuel, P.; Daoud-Aladine, A.; Osborn, R. *Nature Comm.*, **2014**, 4845.
7. Malliakas, C.D.; Kanatzidis, M.G. *J. Am. Chem. Soc.* **2013**, 135, 1719.
8. Manuel, P.; Chapon, L. C.; Trimarchi, G.; Todorov, I. S.; Chung, D. Y.; Ouladdiaf, B.; Gutmann, M. J.; Freeman, A. J.; Kanatzidis, M. G. *Phys. Rev. B* **2013**, 88, 104414.
9. Romanowich, M.; Lee, M.-S.; Chung, D.-Y.; Mahanti, S. D.; Kanatzidis, M. G.; Tessmer, S. H. *Phys. Rev. B* **2013**, 87, 085310.
10. Sturza, M.; Han, F.; Shoemaker, D. P.; Malliakas, C. D.; Chung, D. Y.; Jin, H.; Freeman, A. J.; Kanatzidis, M. G. *Inorg. Chem.* **2013**, 52, 7210-7217.
11. Bud'ko, S. L.; Chung, D. Y.; Bugaris, D.; Claus, H.; Kanatzidis, M. G.; Canfield, P. C. *Phys. Rev. B* **2014**, 89, 014510.
12. Bud'ko, S. L.; Sturza, M.; Chung, D. Y.; Kanatzidis, M. G.; Canfield, P. C. *Phys. Rev. B* **2013**, 87, 100509.
13. Avci, S.; Allred, J. M.; Chmaissem, O.; Chung, D. Y.; Rosenkranz, S.; Schlueter, J. A.; Claus, H.; Daoud-Aladine, A.; Khalyavin, D. D.; Manuel, P.; Llobet, A.; Suchomel, M. R.; Kanatzidis, M. G.; Osborn, R. *Phys. Rev. B* **2013**, 88, 094510.
14. Peter, S. C.; Malliakas, C. D.; Kanatzidis, M. G. *Inorg. Chem.* **2013**, 52, 4909-4915.
15. Peter, S. C.; Sarker, S.; Kanatzidis, M. G. *Inorg. Chem.* **2012**, 51, 10793-10799.
16. Avci, S.; Chmaissem, O.; Chung, D. Y.; Rosenkranz, S.; Goremychkin, E. A.; Castellán, J. P.; Todorov, I. S.; Schlueter, J. A.; Claus, H.; Daoud-Aladine, A.; Khalyavin, D. D.; Kanatzidis, M. G.; Osborn, R. *Phys. Rev. B* **2012**, 85, 184507.
17. Shoemaker, D. P.; Chung, D. Y.; Claus, H.; Francisco, M. C.; Avci, S.; Llobet, A.; Kanatzidis, M. G. *Phys. Rev. B* **2012**, 86, 184511.
18. Peter, S. C.; Malliakas, C. D.; Nakotte, H.; Kothapilli, K.; Rayaprol, S.; Schultz, A. J.; Kanatzidis, M. G. *J. Solid State Chem.* **2012**, 187, 200-207.

¹²⁵Te NMR and Thermoelectric Properties of Complex Tellurides:

The Role of Materials Chemistry

E.M. Levin^{1,2} and K. Schmidt-Rohr^{1,3}

¹ – Division of Materials Sciences and Engineering, Ames Laboratory US DOE, ² – Department of Physics and Astronomy, ³ – Department of Chemistry, Iowa State University, Ames, IA 50011

Project Scope

Thermoelectric materials [1a] can be used to transform heat to electricity (the Seebeck effect) in thermoelectric generators, or they achieve electricity to heat removal (the Peltier effect) for refrigeration. A large number of novel complex solids were studied during the last decade, but complex tellurides still exhibit the highest thermoelectric efficiency. However, the nature of thermoelectric effects is still not deeply understood; this requires the use of advanced experimental methods, e.g., nuclear magnetic resonance (NMR). Our goals are (i) to better understand the role of materials chemistry in formation of thermoelectric properties, and (ii) to establish relations between the composition and structural parameters of materials vs. the Seebeck effect, using complex tellurides as model systems.

Recent Progress

Since the last PI meeting in Materials Chemistry (2012), we have studied several complex tellurides [1b-8b] and other materials, including ferrimagnetic oxides [9b] and diamagnetic silicides [10b]. Firstly, we have confirmed that ¹²⁵Te NMR is a unique probe of the local structure of multi-component thermoelectric telluride materials, and, secondly, we have obtained novel fundamental results in the area of thermoelectric materials [8b]. Note that the combination of common experimental methods (measuring the Seebeck coefficient, electrical resistivity, thermal conductivity, and SEM) and advanced techniques (¹²⁵Te NMR, and temperature dependent XRD) makes our research unique world-wide.

We have chosen Ag_xSb_xGe_{50-2x}Te₅₀ alloys (well-known TAGS-*m* series) [1a,3a-5a] as a model system. Doping of TAGS-85 (Ag_{6.52}Sb_{6.52}Ge_{36.94}Te₅₀) with the rare earth Dy (TAGS+Dy) allows us to understand the effects from atoms with large size and localized magnetic moment on the Seebeck coefficient and thermoelectric efficiency [1b]. We have shown that a small amount of Dy (1-2 at.%) increases the efficiency by ~15%, which is explained by energy filtering. Our result was selected as a BES “Science Highlight” <http://science.energy.gov/bes/highlights/2012/bes-2012-10-d/>, and was presented by Dr. Harriet Kung as one of eight highlights in her overview at the BESAC meeting in 2013.

In addition, we have studied Ag₂Sb₂Ge_{46-x}Dy_xTe₅₀ (TAGS-96+Dy) [2b], which contains a smaller amount of [Ag+Sb], ~4 at.%, compared to TAGS-85+Dy, ~13 at.%. The [Ag+Sb] and Dy in this system also enhances the Seebeck coefficient while the carrier concentration deduced from ¹²⁵Te NMR spin-lattice relaxation time increases. We have also found that the power factor of Ag₂Sb₂Ge₄₅Dy₁Te₅₀ at ~720 K is one of the highest among tellurides, 40 μWcm⁻¹K⁻² [2b].

Detailed studies of GeTe [3b] have allowed us to recognize the differences between GeTe and PbTe and the effects of the replacement of Ge by various atoms [1b,2b]. ¹²⁵Te NMR enabled us to study the distribution of the carrier concentration in binary compounds, *p*-type GeTe and *p*- or *n*-type PbTe. Using ¹²⁵Te NMR spin-lattice relaxation measurements (Fig. 1), we have shown that GeTe is electronically homogeneous, while both *p*- and *n*-type PbTe is inhomogeneous. This fact was

explained by chemical inhomogeneity, i.e., the Pb/Te ratio as well as the charge carrier concentration produced by Pb or Te vacancies varies across the material [3b].

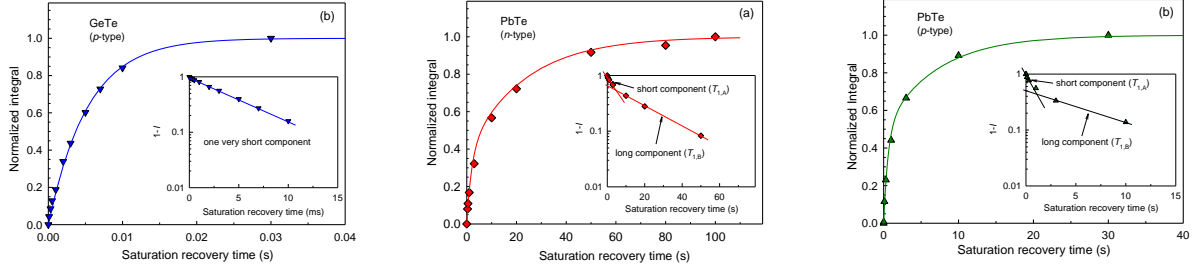


Fig. 1. (a) ^{125}Te NMR spin-lattice relaxation in (a) p -type GeTe, (b) n -type PbTe, and (c) p -type PbTe. Our data demonstrate that GeTe is electronically homogeneous, while both samples of PbTe are electronically inhomogeneous (see also Fig. 2).

Our data have a significant impact because the Seebeck coefficient strongly depends on the carrier concentration, and electronic inhomogeneity may result in incorrect conclusions regarding thermoelectric properties. We also have expanded our diagram (Fig. 2) that enables conversion of the spin-lattice relaxation time, T_1 , to the carrier concentration [3b].

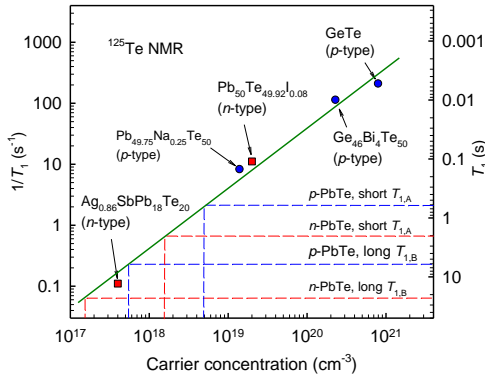


Fig. 2. ^{125}Te NMR spin-lattice relaxation time, T_1 , and rate, $1/T_1$, vs. carrier concentration in n - and p -type tellurides. The relation was plotted on the basis of ^{125}Te NMR spin-lattice relaxation times and carrier concentrations obtained from Hall and Seebeck effects for n -type $\text{Ag}_{0.86}\text{SbTe}_{18}\text{Te}_{20}$ and $\text{Pb}_{50}\text{Te}_{49.92}\text{I}_{0.08}$, and p -type $\text{Pb}_{49.75}\text{Na}_{0.25}\text{Te}_{50}$, $\text{Ge}_{46}\text{Bi}_4\text{Te}_{50}$, and GeTe; all these samples exhibit nearly single-exponential T_1 relaxation. ^{125}Te NMR short, $T_{1,A}$, and long, $T_{1,B}$, components were determined for n - and p -type PbTe samples (horizontal dashed lines) and converted to carrier concentration (vertical dashed lines), demonstrating to what extent both PbTe samples are electronically inhomogeneous [4b].

Figure 3 shows the dependence of the experimental ^{125}Te NMR resonance frequency, and the calculated Knight and chemical shifts in a series of $\text{Ag}_x\text{Sb}_x\text{Ge}_{50-2x}\text{Te}_{50}$ alloys. The experimental T_1 values allow us to calculate the Knight shift and then estimate the average chemical shift for each alloy studied. The figure demonstrates that both the Knight and average chemical shifts depend on $[\text{Ag}+\text{Sb}]$ content. Thus, the change of the ^{125}Te NMR resonance frequency is a result of the interplay between contributions from Knight (positive) and chemical (negative) shifts. The chemical shift behavior shows that replacement of Ge by $[\text{Ag}+\text{Sb}]$ affects the electronic environment around Te, i.e., NMR confirms XRD data that $[\text{Ag}+\text{Sb}]$ atoms mostly are present in the lattice. The change of the chemical shift to the direction of more negative values (diamagnetic shift) with $[\text{Ag}+\text{Sb}]$ content can be attributed to the reduction in the electron density on the Te nucleus. We have shown that ^{125}Te NMR chemical shifts exhibit a linear trend with the number of Pb neighbors in $\text{Pb}_{1-x}\text{Ge}_x\text{Te}$ and $\text{Pb}_{1-x}\text{Sn}_x\text{Te}$ systems [5b].

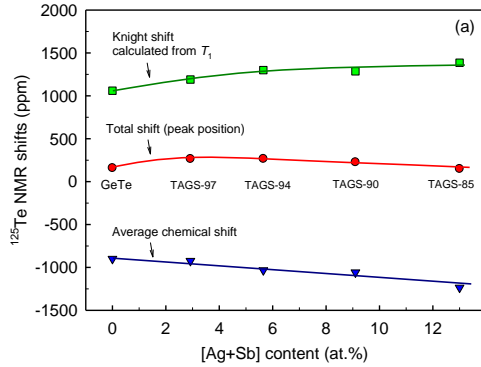


Fig. 3. ^{125}Te NMR resonance frequency, the Knight shift calculated from spin-lattice relaxation time, and the chemical shift for $\text{Ag}_x\text{Sb}_x\text{Ge}_{50-2x}\text{Te}_{50}$ alloys (TAGS- m).

One of our most significant findings is the unusual inverse dependence of the Seebeck effect vs. the carrier concentration in TAGS- m materials obtained by ^{125}Te NMR (see Fig. 4 containing our and literature data [2a-5a]). Such a relation cannot be explained within the common theory for the Seebeck coefficient in metals and degenerate semiconductors where charge-carrier scattering is energy independent [1a], even within a non-parabolic band model [6a], and demonstrates the presence of an additional strong mechanism. We believe that energy filtering (low-energy carriers are significantly scattered while high-energy carriers are not) [7a,8a] due to potential barriers formed by [Ag+Sb] pairs is the origin of such a relation and results in the high thermoelectric efficiency of TAGS- m materials.

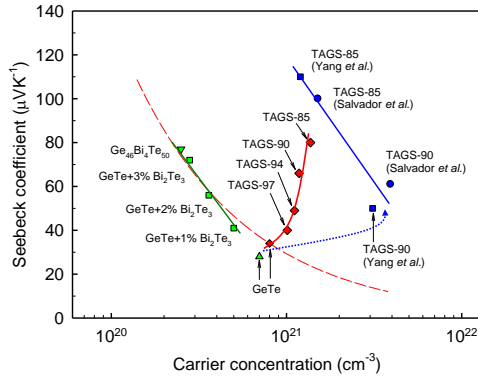


Fig. 4. Absolute Seebeck coefficient vs. carrier concentration for GeTe-based materials measured at 300 K. Data for TAGS- m were obtained by ^{125}Te NMR T_1 measurements (red diamonds, our data). Carrier concentrations for GeTe- Bi_2Te_3 [2a] (green squares), TAGS-90 and TAGS-85 (blue squares [3a] and blue circles [4a]), our data [3b] (green diamond) and literature data [5a] (green triangle) for GeTe are derived from Hall effect, and for $\text{Ge}_{46}\text{Bi}_4\text{Te}_{50}$ derived from ^{125}Te NMR T_1 [4b] (inverted green triangle). The red dashed line interpolates the Seebeck coefficient vs. Hall-effect derived carrier concentration from GeTe to TAGS-90 with a nonlinear change that is difficult to explain. The red dashed line shows the Seebeck coefficient vs. carrier concentration [1a] calculated by us using GeTe as a reference material.

Hence, it is likely that pairs of particular atoms may significantly enhance the Seebeck coefficient; this exemplifies the important role of materials chemistry and opens a new pathway to design better thermoelectric materials. Our finding also demonstrates that the Seebeck effect still holds surprises, and innovative research in the area of materials chemistry may help to better understand and utilize thermoelectric phenomena via exploring the effects on the Seebeck coefficient from both the carrier concentration and energy filtering.

Future Plans

- Synthesize complex tellurides with various compositions in order to understand the effects of materials chemistry on thermoelectric properties; use ^{125}Te NMR to obtain the carrier concentration, study chemical and electronic inhomogeneities along with measurements of the Seebeck coefficient, electrical resistivity, Hall effect, thermal conductivity, XRD, SEM, and other relevant properties.
- Analyze the structural parameters of complex GeTe-based tellurides, including the lattice parameters and local lattice distortion, establish relations between materials chemistry and thermoelectric properties.
- Study relations between structural parameters, ^{125}Te NMR spin-lattice relaxation, carrier concentration and mobility, in order to understand energy filtering at the atomic level as a mechanism for enhancement of thermoelectric efficiency in complex tellurides.

References

- [1a] G.J. Snyder and E. S. Toberer. *Nature Mater.* **7**, 105 (2008).
- [2a] M.S. Lubell and R. Mazelsky. *J. Electrochem. Soc.* **110**, 520 (1963).
- [3a] S.H. Yang *et al.* *Nanotechnology* **19**, 245707 (2008).
- [4a] J.R. Salvador *et al.* *J. Solid State Chem.* **182**, 2088 (2009).
- [5a] Y. Gelbstein *et al.* *J. Electron. Mater.* **39**, 2049 (2010).
- [6a] X. Chen, D. Parker, and D.J. Singh. *Scientific Reports* **3**: 3168 (2013).
- [7a] S.V. Faleev and F. Leonard. *Phys. Rev. B* **77**, 214304 (2008).
- [8a] G. Benenti and G. Casati. *Phil. Trans. R. Soc. A* **369**, 466 (2011).

Our Publications

- [1b] E.M. Levin, S.L. Bud'ko, and K. Schmidt-Rohr. *Advanced Functional Materials* **22**, 2766 (2012).
- [2b] E.M. Levin, R. Hanus, M. Hanson, W.E. Straszheim, and K. Schmidt-Rohr. *Physica Status Solidi A* **210**, 2628 (2013).
- [3b] E.M. Levin, M.F. Besser, and R. Hanus. *J. Applied Physics* **114**, 083713 (2013).
- [4b] E.M. Levin, J.P. Heremans, M.G. Kanatzidis, and K. Schmidt-Rohr. *Physical Review B* **88**, 115211 (2013).
- [5b] B. Njelic, E.M. Levin, and K. Schmidt-Rohr. *Solid State Nuclear Magnetic Resonance* **55-56**, 79 (2013).
- [6b] S.N. Girard, K. Schmidt-Rohr, T.C. Chasapis, E. Hatzikranniotis, B. Njelic, E.M. Levin, A. Rawal, K.M. Paraskevopoulos, and M.G. Kanatzidis. *Advanced Functional Materials* **23**, 747 (2013).
- [7b] E.M. Levin, M.J. Kramer, and K. Schmidt-Rohr. *Journal of Physics and Chemistry of Solids*. (Accepted, June 2014).
- [8b] E.M. Levin and K. Schmidt-Rohr. (Submitted to *Physical Review Letters*).
- [9b] I.C. Nlebedim, E.M. Levin, R. Prozorov, K.W. Dennis, R.W. McCallum, and D.C. Jiles. *IEEE Transactions on Magnetism* **49**, 4269 (2013).
- [10b] E.M. Levin, R. Hanus, J. Cui, Q. Xing, T. Riedermann, T. Lograsso, and K. Schmidt-Rohr. (In preparation).

Energy and Fuels from Multifunctional Electrochemical Interfaces

Nenad M. Markovic and Vojislav Stamenkovic, Argonne National Laboratory

Program Scope

Program is an interdisciplinary, atomic/molecular level approach, integrating both experimental- and- computational-based methodologies to design, synthesize, and characterize EC interfaces with tailored properties. Two fold strategies is used: (i) first is based on *materials-by-design strategy*, involving transferring the knowledge gained from the single crystalline materials and thin metal films to nanoscale materials; and (ii) the second relies on the *double-layer-by-design strategy*, bearing precise organization of multiple functionalities of the electrolyte components at the sub-nano-scale regime that is operating in the double layer. These two strategies form a closed-loop material/electrolyte design approach wherein the knowledge gained from the model systems is used to tailor the more complex, real-world systems.

Recent Progress

The most active catalysts for the water splitting reaction and production of hydrogen:

Improving the sluggish kinetics for the electrochemical reduction of water to molecular hydrogen in alkaline environments is the key to reducing energy losses in water-alkali and chloro-alkali electrolyzers. We found that a controlled and well-characterized arrangement of nanometer-scale $\text{Ni}(\text{OH})_2$ clusters on Pt single crystal surfaces, as well as cation-induced destabilization of the HO-O bond (AC^+ in Figure 1), results in a 10-fold activity increase in catalyzing the hydrogen production relative to state-of-the-art metal and metal-oxide catalysts[1]. Significantly, the observed enhancement on single crystal surfaces is also observed on Pt, Ni, Ag and Cu nanoparticles modified by $\text{Ni}(\text{OH})_2$ clusters; demonstrating how fundamental understanding can lead to the development of real-world materials [1]. This work was highlighted by the Office of Science as a significant contribution to the field of electrocatalysis

Thin films with tunable structure and composition: Instead of building the crystal lattice from a seed or epitaxially by underlying crystalline substrate our research team managed to merge individual randomly oriented nanoscale grains of sputtered thin film to form large highly-ordered surface facets with unique mesostructured morphology. This fundamental breakthrough reflects the feasibility of controlling surface ordering of thin films of various

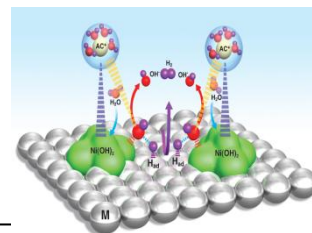


Figure 1. Water dissociation: formation of H_{ad} , and subsequent recombination of two H_{ad} to form H_2 .

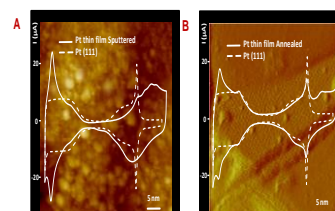


Figure 1. Tuning catalytic properties of the thin film

materials deposited over a non-crystalline substrate without use of templates for epitaxial growth. Mesostuctured thin films with adjustable structure and composition represent a novel class of materials, which will be tailored to emulate single crystalline properties in electrochemical devices such as fuel cells, electrolyzers and batteries[2].

Activity trends on well-characterized 3d-oxide catalysts: Design and synthesis of oxide materials for efficient oxygen production is of great importance to reducing energy losses in water-alkali electrolyzers. By developing a new approach for studying electrocatalytic trends on well-ordered 3d hydroxyoxides (M=Ni, Co, Fe and Mn), we were able to find a unifying descriptor that can explain the reaction mechanism and activity trend (Figure 3). These trends have provided the foundation for the rational design of practical alkaline OER electrocatalysts and defined the new directions in the proposed work summarized below [3].

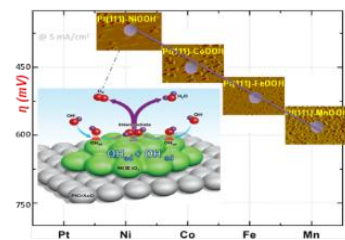


Figure 3. Activity trends for oxygen evolution

Future Plans

We propose a science-based approach to develop highly conductive, stable, selective and active electrochemical interfaces that can solve the challenging problems of clean energy production, conversion and storage. The range of materials and electrolytes that will be explored by these two strategies is broad, involving metals, metal/metal-oxides, pure oxides, sulfur-based and carbon-based materials as well as aqueous electrolytes with a wide pH range and organic solvents that are traditionally used in the battery systems. The methods for unraveling complexities that is controlling interfacial properties is diverse, ranging from ex situ and in situ optical methods to microscopy-based structural probes to synchrotron-based techniques and classical electrochemical methods. Advancing in fundamental understanding of the reaction mechanisms and kinetics involved on well-characterized metal, oxide, and metal/metal-oxide materials in both aqueous-based and organic-based environments will be critical in our quest to learn how to design efficient, stable and selective electrochemical systems that are needed by our society.

References

1. R. Subbaraman, D. Tripkovic, D. Strmcnik, K-C. Chang, M. Uchimura, A. P. Paulikas, V. Stamenkovic, N. M. Markovic; “Enhancing Hydrogen Evolution Activity in Water Splitting by Tailoring Li^+ -Ni(OH)₂-Pt Interfaces”; *Science*, **334** (2011) 1256-1260.
2. D. van derVliet, C. Wang, D. Tripkovic, D. Strmcnik, X.F. Zhang, M.K. Debe. R.T. Atanasoski, N.M. Markovic, V.R. Stamenkovic; “Mesostuctured Thin Films as Electrocatalysts with Tunable Composition and Surface Morphology”; *Nature Materials*, **11**(2012)550-557.
3. R. Subbaraman, D. Tripkovic, K-C. Chang, D. Strmcnik, A. P. Paulikas, H.P. Hurinsit, M. Chan, J. Greeley, V. Stamenkovic, N. M. Markovic; “Trends in

Activity for the Water Electrolyzer Reactions on 3d-M(Ni,Co,Fe,Mn)-Hydr(oxy)oxide Catalysts”; *Nature Materials*, **11**(2012)550-557.

Publications

1. J. Snyder, N. Danilovic, P. A. Paulikas, D. Tripkovic, D. Strmcnik, N. M. Markovic, V. R. Stamenkovic; “Thin Film Approach to Single Crystalline Electrochemistry”; *Journal of Physical Chemistry C*, **117**(45), (2013)23790-23796.
2. N. M. Markovic; “Interfacing Electrochemistry”; *Nature Materials*; **12**(2013)101-102
3. D. Strmcnik, M. Uchimura, C. Wang, R. Subbaraman, N. Danilovic, D. van der Vliet, A. P. Paulikas, V.R. Stamenkovic, N.M. Markovic; “ Improving the Hydrogen Oxidation Reaction Rate by Promotion of Hydroxyl Adsorption”; *Nature Chemistry*; **5**(2013)300-306.
4. N. Danilovic, R. Subbaraman, D. Strmcnik, K-C. Chang, A. P. Paulikas, V.R. Stamenkovic, N.M. Markovic; “Enhancing the Alkaline Hydrogen Evolution Reaction Activity through the Bifunctionality of Ni(OH)₂/Metal Catalysts”; *Angewandte Chemie Int.Ed.*, **51**(2012)12495-12498.
5. N. Danilovic, R. Subbaraman, D. Strmcnik, A. P. Paulikas, D. Myers, V.R. Stamenkovic, N.M. Markovic; “The Effect of Noncovalent Interactions on the HOR, ORR, and HER on Ru, Ir, and Ru_{0.5}Ir_{0.5} Metal Surfaces in Alkaline Environments ”; *Electrocatalysis*, **3**(2012)221-229.
6. J. Greeley and N.M. Markovic; “The Road from Animal Electricity to Green Energy: Combining Experiment and Theory in Electrocatalysis”; *Energy & Environmental Science*, **115**(2012)9246-9256.
7. D. van derVliet, C. Wang, D. Tripkovic, D. Strmcnik, X.F. Zhang, M.K. Debe. R.T. Atanasoski, N.M. Markovic, V.R. Stamenkovic; “Mesostructured Thin Films as Electrocatalysts with Tunable Composition and Surface Morphology”; *Nature Materials*, **11**(2012)550-557.
8. R. Subbaraman, N. Danilovic, P.P. Lopes, D. Tripkovic, D. Strmcnik, V.R. Stamenkovic, N.M. Markovic; “Origin of Anomalous Activities for Electrocatalysts in Alkaline Electrolytes”; *Journal of Physical Chemistry C*, **116**(2012)22231-22237
9. R. Subbaraman, D. Tripkovic, K-C. Chang, D. Strmcnik, A. P. Paulikas, H.P. Hurinsit, M. Chan, J. Greeley, V. Stamenkovic, N. M. Markovic; “Trends in Activity for the Water Electrolyzer Reactions on 3d-M(Ni,Co,Fe,Mn)-Hydr(oxy)oxide Catalysts”; *Nature Materials*, **11**(2012)550-557.
10. D. van der Vliet, C. Wang, D. Li, A. P. Paulikas. J. Greeley, R B. Rankin, D. Strmcnik, D. Tripkovic, N. M. Markovic, V. R. Stamenkovic; “Unique Electrochemical Adsorption Properties of Pt-Skin Surfaces”; *Angewandte Chemie Int.Ed.*, **51**(2012)3139-3142.
11. R. Subbaraman, D. Tripkovic, D. Strmcnik, K-C. Chang, M. Uchimura, A. P. Paulikas, V. Stamenkovic, N. M. Markovic; “Enhancing Hydrogen Evolution Activity in Water Splitting by Tailoring Li⁺-Ni(OH)₂-Pt Interfaces”; *Science*, **334** (2011) 1256-1260.
12. D. Strmcnik, D. van der Vliet, K-C. Chang , V. Komanicky, K. Kodama, H.You, V. R. Stamenkovic, N.M. Markovic ; “Effects of Li⁺, K⁺, and Ba²⁺, Cations on the ORR at Model and High Surface Area Pt and Au Surfaces in Alkaline Solutions”; *Journal of Physical Chemistry Letters*, **2** (2011) 2733-2736.

13. C. A. Lucas, P. Thompson, Y. Gründer, N. M. Markovic; “The Structure of the Electrochemical double layer: Ag(111) in Alkaline Electrolyte”; *Electrochemistry Communications*, **13** (2011) 1205-1208.
14. M. Escudero-Escribano, Z. Michoff, E.P. Leiva, N.M. Marković, N. M., C. Gutiérrez, A. Cuesta; “Quantitative Study of Non-Covalent Interactions at the Electrode–Electrolyte Interface Using Cyanide-Modified Pt(111) Electrodes”; *ChemPhysChem*, **12** (2011) 2230–2234
15. B. Genorio, R. Subbaraman, D. Strmcnik, D.Tripkovic, V.R. Stamenkovic, N.M. Markovic; “Tailoring the Selectivity and Stability of Chemically Modified Platinum Nanocatalysts To Design Highly Durable Anodes for PEM Fuel Cells”; *Angewandte Chemie Int. Ed.*, **123** (2011) 5582–5586.

Diamondoid Science and Applications

PIs: Nick Melosh, SIMES, SLAC

ZX Shen, SIMES, SLAC

Peter Scheiner, Dept of Chemistry, University of Giessen

Program Scope

Diamondoids are unique new carbon-based nanomaterials consisting of 1-2 nanometer, fully hydrogen-terminated diamond particles (Fig 1). Unlike their conjugated counterparts, graphene or carbon nanotubes, the carbon atoms in diamondoids are sp^3 hybridized, leading to unique electronic and mechanical properties. Diamondoids behave much like small molecules, with atomic-level uniformity, flexible chemical functionalization, and systematic series of sizes, shapes and chiralities. At the same time diamondoids offer more mechanical and chemical stability than other small molecules, and vastly superior size and shape control compared to inorganic nanoparticles.

This program explores and develops diamondoids as a new class of functional nanomaterials based upon their unique electronic, mechanical, and structural properties. This includes diamondoid isolation from petroleum, chemical functionalization, and molecular assembly, as well as electronic, optical and theoretical characterization. We have currently focused on three areas of research: synthesis, direct self-assembly, and thin film growth

Recent Progress

We have emphasized unconventional materials growth guided by diamondoid molecules, particularly for forming novel low-dimensional chalcogenides. We have named this new class of low-dimensional materials as steric-directed chalcogenides (SDCs). Using a self-assembly approach, we were able to synthesize a large variety of molecular-scale metal chalcogenides wires that are surrounded by bulky side groups such as diamondoids and their analogues. Using single-crystalline x-ray diffraction (SC-XRD) we were able to determine the atomic structure of several representative SDCs with different metal cations such as Ag(I) and Cu(I), as well as side groups such as adamantane, diamantane and *m*-carborane. The bulky side groups with tunable intermolecular interactions serve as self-assembly templates that guide the formation of

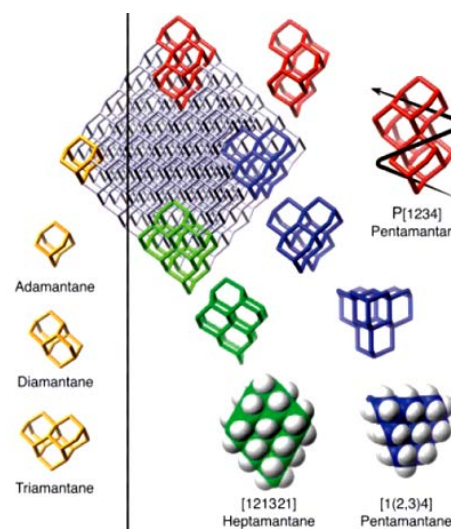


Fig 1. Molecular structures of diamondoids

distinctive structures at several length scales. Interestingly, the intra-chain bonding chemistry can be altered by tuning the van der Waals interaction between the side groups, as illustrated by the case of Cu(I) adamantyl- and diamantyl-sulfides. The steric-controlled Cu-S bond configuration modulates their electronic structures, as revealed by their ultraviolet-visible (UV-Vis) absorption and photoluminescence (PL) spectra. Moreover, the inter-chain interaction can be controlled by tuning the dipole momentum of the side group, as demonstrated in the case of Ag(I) adamantyl sulfide and Ag(I) *m*-carborane sulfide. The dipole-dipole interaction between carborane side groups favors a pseudo-two-dimensional crystal growth, leading to the plate-like morphology of the Ag(I) carborane sulfide crystals. Lastly, we showed that a large variety of low-dimensional metal chalcogenides can be synthesized via this steric-modulated self-assembly approach.

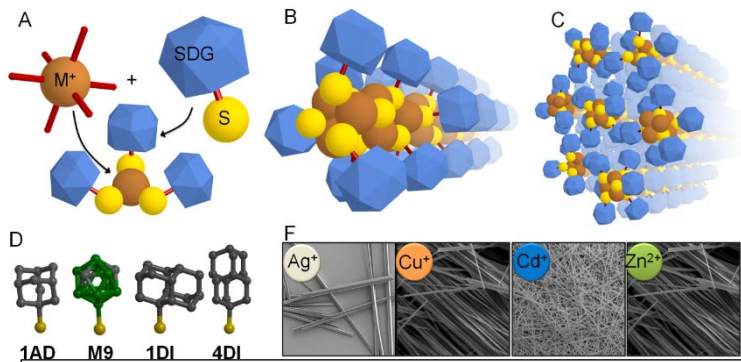


Fig 2. (a). Diamondoids serve as structure directing agents during assembly of chalcogenide materials. (b,c) Solved single crystal structure of adamantine CuS shows multi-atom nanowires surrounded by a diamondoid shell. (d) a number of diamondoid and related cage structures provide unique directing agents. (f) Depending on process conditions, either thin nanowires or large single crystals can be produced.

In addition to diamondoid organization, diamondoids can serve as the seed particles for CVD growth of crystalline diamond. Unlike previous processes, we were able to precisely control the particle size down to <3 nm diameter, with seeding densities of greater than 5×10^{12} seeds/cm², among the highest ever reported. These crystalline diamond nanoparticles are particularly interesting since they do not contain nitrogen impurities present from detonation diamond seeds, and are smaller. Using argon and methane growth conditions we were able to nearly eliminate graphitic impurities, giving considerable promise for these particles to host nitrogen-vacancy (NV) centers with limited life-time degrading impurities. Interestingly, it is currently unknown what the minimum diamond nanoparticle diameter is that can support a stable NV center. Theoretical models estimate the minimum size is ~5nm, yet this limit has not been tested. Part of next year's efforts will be to experimentally validate determine this limit using the diamondoid-seeded particles.

For new diamondoid synthetic targets, we have prepared several of the initially proposed functional diamondoid derivatives such as the next member of diamondoid dimers with the longest alkane C–C bonds reported. The metal-induced coupling of tertiary diamondoid bromides gave highly sterically congested hydrocarbon (hetero)dimers with exceptionally long central C–C bonds of up to 1.71 Å in 2-(1-diamantyl)[121]tetramantane. These dimers are thermally very stable even at temperatures above 200 °C, which is not in line with common C–C bond length versus bond strengths correlations. The extraordinary stabilization arises from

numerous intramolecular van-der-Waals attractions between the neighboring H-terminated diamond-like surfaces.¹ The C–C bond rotational dynamics of 1-(1-adamantyl)diamantane, 1-(1-diamantyl)diamantane, 2-(1-adamantyl)triamantane, 2-(1-diamantyl)triamantane, and 2-(1-diamantyl)[121]tetramantane were studied through variable-temperature ¹H- and ¹³C-NMR spectroscopies. The shapes of the inward (*endo*) CH surfaces determine the dynamic behavior, changing the central C–C bond rotation barriers from 7 to 33 kcal mol⁻¹. Using density functional theory (DFT) approaches with 6-31G(d,p) and cc-pVDZ basis sets, only functionals accounting for dispersion are able to reproduce the experimental geometries, while most DFT functionals are able to reproduce the experimental rotational barriers due to error cancellations. Computations on larger diamondoids reveal that the interplay between the shapes and the sizes of the CH surfaces may even allow the preparation of open-shell alkyl radical dimers (and possibly polymers) that are strongly held together exclusively by dispersion forces. This work challenges common views on the “chemical bond” and has triggered broad discussions on the role of London dispersion interactions in molecular chemistry.

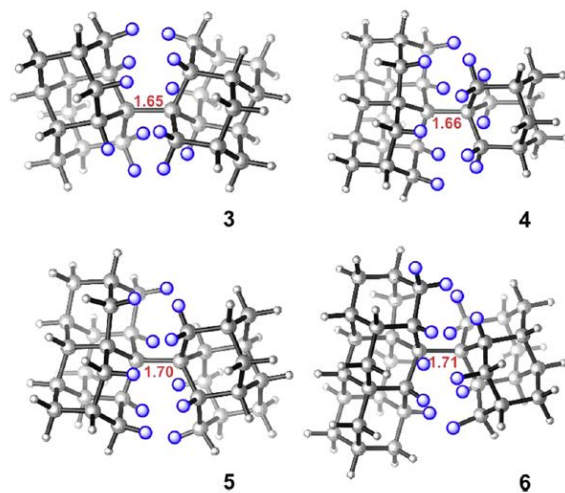


Fig 3. Large vdW interactions between diamondoids supplants some of the ordinary covalent bonds, producing stable, ultra-long bond distances. Dispersion interactions around the central bonds are marked in blue.

Future Plans

We are focusing on three main thrust directions based on our previous results: new metal-oxide framework diamondoid synthetic constructs, high-density; small diamond nanoparticles for NV center hosts; and new synthetic diamondoids that take advantage of the unusual dispersion interactions. The rigid structure of the diamondoids may allow for rational design of new classes of MOFs based on their steric packing and the large vdW forces observed. These structures could have unique properties such as confined optical absorption quantum effects, superconductivity, or energy storage capacity. Bulk diamond synthesis based on a diamondoid seed layer is a highly promising way to achieve very high diamond seeding density, thin diamond films, and NV-centers in diamond nanoparticles. We have shown growth of small diamond particles from seed diamondoid monolayers, and will extend these efforts to create even smaller nanoparticles (<5 nm) that are highly coveted for NV magnetic detectors.

References

1. Schreiner, PR et al, “Overcoming lability of extremely long alkane carbon-carbon bonds through dispersion forces”, *Nature*, **2011**, 308-311.

Publications

1. Zhang J. et al. “Synthesis and transformation of linear adamantane assemblies inside carbon nanotubes.” *ACS Nano* **2012**, 6, 8674-83.
2. Bostedt, C., Landt L., Moller T., Dahl J.E. and Carlson R.M.K Diamondoids. *In Nature’s Nanostructures*. Barnard A.S. and Guo H. (eds.) Pan Stanford Publ. Ltd., **2012**, p169-195.
3. Ishiwata H., et al, “Diamondoid coating enables disruptive approach for chemical and magnetic imaging with 10nm spatial resolution.” *Applied Phys. Letters* **2012**, 101, 163105.
4. Fokina N.A. et al., “Synthesis of diamondoid carboxylic acids.” *Synthesis* **2012**, 2, 259-264.
5. Fokin A. et al., Stable alkanes containing very long carbon-carbon bonds. *J. Amer. Chem. Soc.* **2012**, 134, 13641-50.
6. Clay W.A. et al. “Photocathode device using diamondoid and cesium bromide films.” *Applied Phys. Letters* **2012**, 241605-11.
7. Fokina N.A. et al, “Synthesis of diamondoid carboxylic acids” *Synthesis* **2012**, 44, 259-264.
8. Zhang et al., “Evidence of Diamond Nanowires Formed inside Carbon Nanotubes from Diamantane Dicarboxylic Acid”, *Angew. Chem. Int. Ed.* **2013**, 52, 3717–3721.
9. Fokin et al., “Preparative Synthesis of Vinyl Diamondoids. Functionalized Nanodiamonds”, *Synth. Commun.* **2013**, 43, 1772–1777.
10. Rander et al, “Electronic structure tuning of diamondoids through functionalization. Functionalized Nanodiamonds” *J. Chem. Phys.* **2013**, 135, 024310 (1–7).
11. Wang, F., Melosh, N.A. “Power-independent wavelength determination by hot carrier collection in metal-insulator-metal devices.” *Nature Communications* **2013**, 4, 1711-1715.
12. Li, F.H. et al. Covalent Attachment of Diamondoid Phosphonic Acid Dichlorides to Tungsten Oxide Surfaces. *Langmuir* **2013**, 29, p9790-9797.
13. Fokin et al., “Diamondoids: Functionalization and subsequent applications of perfectly defined molecular cage hydrocarbons. Functionalized Nanodiamonds”, *New. J. Chem.* **2014**, 38, 28–41.
14. Kahl, P, et al., “Efficient preparation of apically substituted diamondoid derivatives. Functionalized Nanodiamonds”, *Synthesis* **2014**, 787–798.

Nuclear Magnetic Resonance

Alexander Pines
Materials Sciences Division
Lawrence Berkeley National Laboratory

Program Scope

Nuclear Magnetic Resonance (NMR) techniques yield chemical and structural information of unparalleled specificity through experiments that do not perturb the natural state of the object under study. When NMR is combined with magnetic field gradients, this rich spectral information can be resolved as a function of space and time. The resulting Magnetic Resonance Imaging (MRI) experiment is a kind of “chemical microscope” which peers into opaque objects to elucidate the structure and dynamics within. The NMR Program, under Alexander Pines’ leadership, pursues transformational theoretical, methodological, and technological advances in magnetic resonance. Our historical contributions include a set of NMR methods and technologies now critical to the application of magnetic resonance in solid materials ranging from proteins to battery electrodes; more recent contributions include the combination of microfluidic technologies with NMR for portable NMR applications; zero field and low field NMR and MRI; techniques for enhancing the sensitivity of NMR through combination of optical methods and magnetic resonance; and, finally, xenon-based molecular sensing.

Recent Progress

The optically pumped nitrogen-vacancy (NV-) defect center in diamond, with almost complete electron spin polarization at room temperature, suggests promising applications for the polarization of nuclear spins both inside and outside the diamond. Such polarization may be achieved independently of the use of high magnetic field, cryogenic temperature, and application of strong high frequency microwaves. We have recently demonstrated the use of the ground-state level anti-crossing conditions (GSLAC) to unlock an efficient, internal polarization transfer mechanism for strongly coupled nuclei in which NV centers are used both as a polarizer and nuclear polarization sensor.

We have adapted microfabrication techniques used to create microchip-scale atomic clocks and magnetometers for the purpose of producing hyperpolarized ^{129}Xe at the volume scales required for compatibility with integrated chemical analysis platforms. Recently we completed and characterized a prototype of our design for the production and optical remote detection of hyperpolarized ^{129}Xe gas at ultra-low magnetic fields. We have worked to overcome the long acquisition times inherent to remote detection by implementing compressive sensing. We have also developed a method of spatially encoding MRI information on flow devices using thin film permanent magnets coupled with frequency-selective RF pulses in place of current-driven magnetic field gradients. This method allows for small, compact instrumentation requiring no large electronic amplifiers and may be implemented as an NMR “bar code” for labeling flow path and history in microfluidics devices.

We demonstrate the use of a vapor-cell magnetometer for chemically sensitive measurements of relaxation and diffusion properties of water and hydrocarbons. Current NMR logging tools are based on conventional high-field NMR techniques, using permanent magnets to increase the magnetic field penetrating into the formation surrounding the borehole and inductive coils for detection. However, there are distinct advantages to instead performing these measurements in the ambient Earth's field, using an atomic magnetometer for detection at the relatively low proton NMR frequency of about 2 kHz. Contrast between the spin relaxation properties of materials is enhanced at very low fields, allowing for oil to be more easily distinguished from other fluids, such as water.

Despite the use of atomic magnetometers, low-field NMR using samples thermally prepolarized in a permanent magnet typically suffers from low signal-to-noise ratio compared with inductively detected high-field NMR. This is partly due to the low polarization available from thermalization in a permanent magnet. To avoid this difficulty, we have demonstrated large nuclear-spin polarization in zero-field NMR by employing the technique of parahydrogen-induced polarization (PHIP), whereby order from the nuclear spin singlet state of parahydrogen is transferred to a molecule of interest, either by hydrogenation or through reversible chemical exchange. We have also published theoretical work using symmetry arguments and simple model systems to describe the conversion of the singlet state of parahydrogen into observable oscillating magnetization at zero-field. We have measured the zero-field spectra of a number of small molecules representing spin topologies relevant to organic chemistry and we have developed an analytical theory to describe the signals.

Future Plans

Future work will focus on the transfer of spin polarization from NV- centers to ^{13}C nuclei in diamond and subsequent transfer to target nuclear spins outside the diamond. Thereby enabling higher sensitivity, faster magnetic resonance imaging and spectroscopy. This will involve the production of ^{13}C -enriched, structured diamonds to maximize spin diffusion transfer of polarization to the diamond surface.

NV- centers in diamond also provide an effective small-scale magnetometer. We will harness this technique to detect nuclear magnetic resonance in microfluidic devices. In combination with nuclear spin hyperpolarization and remote detection techniques under development, this affords the possibility of sensitivity enhanced NMR spectroscopy on a chip.

We will develop chemical shift agents using xenon based molecular sensors coupled to lanthanide metals for use in remote detection and oriented media. By varying the binding mechanism for both the metal center and the target analyte we can maximize the anisotropy of the sensor upon binding which will enhance the affect of orientation. These sensors will give us increased sensitivity and allow us to better distinguish different binding events with higher resolution.

Publications

1. Emondts, M., Ledbetter, M. P., Pustelny, S., Theis, T., Patton, B., Blanchard, J. W., Butler, M. C., Budker, D., Pines, A. (2014). Long-lived Heteronuclear Spin-Singlet States in Liquids at a Zero Magnetic Field. *Physical Review Letters*, 112(7).
2. Ganssle P.J, Shin H.D, Seltzer S.J, Bajaj V.S., Ledbetter M.P, Budker D., Knappe S., Kitching J., & Pines A. (2014). Ultra-Low_Field NMR Relaxation and Diffusion Measurements Using an Optical Magnetometer. *Angewandte Chemie*, In Press. (Cover).
3. Jiménez-Martínez, R., Kennedy, D.J., Rosenbluh, M., Donley, E.A., Knappe, S., Seltzer, S.J., Ring, H.L., Bajaj, V.S., & Kitching, J. (2014). Optical hyperpolarization and NMR detection of ^{129}Xe on a microfluidic chip. *Nature Communications*. 5:3809. doi:10.1038/ncomms4908.
4. Palaniappan, K. K., Francis, M. B., Pines, A., & Wemmer, D.E. (2014). Molecular Sensing Using Hyperpolarized Xenon NMR Spectroscopy. *Israel Journal of Chemistry*, 54, 104-112. doi: 10.1002/ijch.201300128
5. Shin, C.S., Butler, M.C., Wang, H.J., Avalos, C.E., Seltzer, S.J., Liu, R.B., Pines, A., & Bajaj, V.S. (2014). Optically detected nuclear quadrupolar interaction of ^{14}N in nitrogen-vacancy centers in diamond. *Physical Review B*. 89(20), 205202-1 - 205202-6. Doi: 10.1103/PhysRevB.89.205202
6. Shapiro, M.G., Ramirez, M.R., Sperling, L.J., Sun, G., Sun, J., Pines, A., Schaffer, D.V., & Bajaj, V.S. (2014). Genetically encoded reporters for hyperpolarized xenon MRI. *Nature Chemistry*. doi:10.1038/nchem.1934
7. Wang H.J., Shin C.S., Seltzer S.J., Avalos C.E., Pines A., & Bajaj V.S. (2014). Optically detected cross-relaxation spectroscopy of electron spins in diamonds. *Nature Communication*. In Press
8. Butler, Mark C., Ledbetter, Micah P., Theis, Thomas, Blanchard, John W., Budker, Dmitry, & Pines, Alexander. (2013). Multiplets at zero magnetic field: The geometry of zero-field NMR. *The Journal of Chemical Physics*, 138(18), 184202-184215.
9. Garimella, Praveena D., Meldrum, Tyler, Witus, Leah Suzanne, Smith, Monica, Bajaj, Vikram Singh, Wemmer, David E., Francis, Matthew, B., & Pines, Alexander. (2013). Hyperpolarized xenon-based molecular sensors for label-free detection of analytes. *Journal of the American Chemical Society*. doi: 10.1021/ja406760r
10. Shin, Chang S., Avalos, Claudia E., Butler, Mark C., Wang, Hai-Jing, Seltzer, Scott J., Liu, Ren-Bao, Pines, Alexander, & Bajaj, Vikram S. (2013). Suppression of electron spin decoherence of the diamond NV center by a transverse magnetic field. *Physical Review B*, 88(16), 161412. (selected as an Editor's Suggestion)
11. Stevens, T. K., Ramirez, R. M., & Pines, A. (2013). Nanoemulsion contrast agents with sub-picomolar sensitivity for xenon NMR. *Journal of the American Chemical Society*. doi: 10.1021/ja402885q
12. Wang, H. J., Shin, C. S., Avalos, C. E., Seltzer, S. J., Budker, D., Pines, A., & Bajaj, V. S. (2013). Sensitive magnetic control of ensemble nuclear spin hyperpolarization in diamond. *Nat Commun*, 4, 1940. doi: 10.1038/ncomms2930

13. Blanchard, J. W., Ledbetter, M. P., Theis, T., Butler, M. C., Budker, D., & Pines, A. (2013). High-Resolution Zero-Field NMR J-Spectroscopy of Aromatic Compounds. *Journal of the American Chemical Society*, *135*(9), 3607-3612. doi: Doi 10.1021/Ja312239v
14. Butler, Mark C., Kervern, Gwendal, Theis, Thomas, Ledbetter, Micah P., Ganssle, Paul J., Blanchard, John W., Budker, Dmitry and Pines, Alexander. (2013). Parahydrogen-induced polarization at zero magnetic field. *The Journal of Chemical Physics*, *138*(23), 234201. doi: <http://dx.doi.org/10.1063/1.4805062>
15. Colell, J., Turschmann, P., Glogglar, S., Schleker, P., Theis, T., Ledbetter, M., Budker, D., Pines, A., Blumich, B., & Appelt, S. (2013). Fundamental Aspects of Parahydrogen Enhanced Low-Field Nuclear Magnetic Resonance. *Physical Review Letters*, *110*(13). doi: Artn 137602. Doi 10.1103/Physrevlett.110.137602
16. Palaniappan, K. K. , Ramirez, R.M. , Bajaj, V.S. , Wemmer, D.E. , Pines, A., & Francis, M.B. (2013). Molecular imaging of cancer cells using a bacteriophage-based (¹²⁹Xe) NMR biosensor. *Angewandte Chemie-International Edition*, *52*(18), 4849-4853. doi: 10.1002/anie.201300170
17. Stevens, T.K. , Palaniappan, K.K. , Ramirez, M.R. , Francis, M.B. , Wemmer, D.E., & Pines, A. (2013). HyperCEST detection of a ¹²⁹Xe-based contrast agent composed of cryptophane-A molecular cages on a bacteriophage scaffold. *Magnetic Resonance in Medicine*, *69*(5), 1245-1252.
18. Theis, Thomas, Blanchard, John W., Butler, Mark C., Ledbetter, Micah P., Budker, Dmitry, & Pines, Alexander. (2013). Chemical analysis using J-coupling multiplets in zero-field NMR. *Chemical Physics Letters*. doi: <http://dx.doi.org/10.1016/j.cplett.2013.06.042>

Hydroxide Conductors for Energy Conversion Devices

Matthew Sturgeon, Clay Macomber, Chaiwat Engtrakul, Hai Long and Bryan Pivovar (PI)
National Renewable Energy Laboratory, Chemical and Materials Science Center

Program Scope

This project is focused on fundamental investigation of hydroxide conductors for their ability to be used in energy conversion devices. The stability of cations in hydroxide has been a major concern and a central focus of this work and has been investigated using combined experimental and computational techniques. The aim of the computational subtask is to determine the degradation pathways and relative rates of different cations in order to identify potential candidates with higher stability. The most recent experimental work has focused on quantifying degradation rates of the benzyltrimethylammonium (BTMA) cation in order to address inconsistencies in the literature and observations of degradation rates obtained within the project.

Recent Progress

Benzyltrimethyl ammonium (BTMA) is the standard cation that has historically been used in anion exchange membranes (AEMs)/AMFCs. BTMA degradation has been a topic of past studies; however, methodologies of degradation were not standardized and reported values of stability were widely varied. In fact, in our efforts on the topic we had become perplexed by the variability of results between tests (see Table 1), and by the dependence of our observations on experimental conditions.

Table 1. Variability of methodologies employed to investigate BTMA hydroxide stabilities.

Ref	Experimental conditions	Analytical Methods	BTMA degradation
Bauer ¹	160 °C, 0.01N BTMA 2N KOH	“Spectroscopic”	29.1 min ½ life
Einsla (Pivovar) ²	80 °C: 1M BTMA in 1, 2, 3M NaOH (in D ₂ O) 120 °C: 10 – 30 wt% BTMA (diluted from 40 wt% with D ₂ O)	NMR	80 °C: 90% remaining after 29 days 120 °C: 10wt% (0.55M) ½ life = 35 h 20wt% (1.1M) ½ life <5h 30wt% (1.65M) ½ life <2h
Deavin (Varcoe) ³	60 °C, 1 M BTMA and OH ⁻ , glass vial – formed unexplained white ppt	FT-Raman	No significant degradation
Noonan (Coates) ⁴	80 °C 0.1 M BTMA Br ⁻ in 1M NaOD (CD ₃ OD), fluoropolymer vessel	NMR, GC-MS	66% degraded after 20 days
Nunez (Hickner) ⁵	3:1 CD ₃ OD:D ₂ O 20 eq of KOD Used paramethylBTMCl ⁻	NMR w/ in situ heating	½ life = 2887 h 99.5 ±0.6 remaining after 779 min (~13h)
Price (Beyer) ⁶	80 °C 4-vinylBTMCl ⁻ 1M NaOD in D ₂ O	NMR	½ life longer than limit of detection for experiment (>400h)

The variability in reported values of BTMA stability highlight the difficulty encountered when performing high temperature, high pH testing to determine stability. The results of experiments when tested under these conditions can be highly impacted by reaction variables, including: reaction vessel, heating method, and internal standards. Glass reaction vessels should be avoided in these caustic reactions as they not only introduce a competing reaction pathway for hydroxide ions, the resulting precipitates that form can complicate sample analysis.³ Standards which are exposed to reaction conditions (elevated temps in caustic environments) can be subject to degradation; thus giving an artificial increase in concentration.

We have found additional factors also impact observed degradation rates. In recent work, we

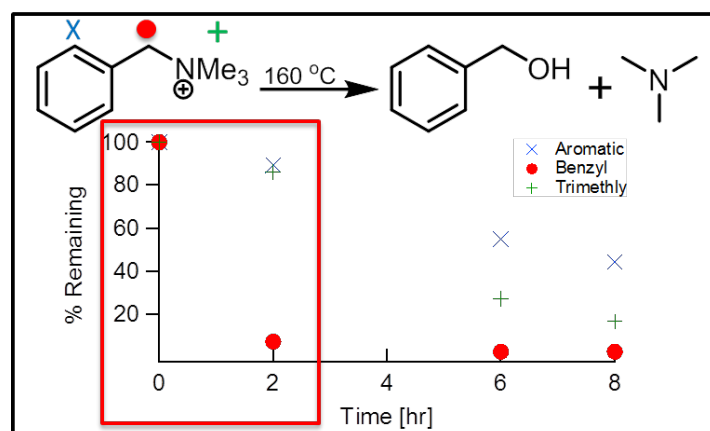


Figure 1. Different rates of BTMA degradation based on integration of: aromatic (blue X), methyl (green +), and benzyl protons (red •).

observed that degradation rates of BTMA OH⁻ solutions >0.5M were higher than those of lower concentration studies due to formation of an organic phase composed of degradation products. The presence of this organic phase resulted in accelerated degradation rates.

Degradation experiments using

deuterated solvents are known to involve H/D exchange.^{2-4,6} This exchange can result in decreasing NMR peak intensity which has been used to assess stability.

When investigating hydroxide stability of BTMA in deuterated solvents one must carefully utilize all peaks in NMR analysis as the rate of H/D exchange differs from one type of proton to another. We have recently shown (Figure 1) that previously reported degradation routes^{1,7} were not specifically due to cation degradation, rather they were an artifact of isotopic exchange.

We have optimized reaction procedures to obtain relevant and reproducible mechanistic data. We have employed Teflon lined Parr reactors, low concentration cations (in 2 M KOH), avoided the use of deuterated water, and performed NMR analysis employing an external standard sealed in a capillary tube that is never exposed to reaction conditions. This experimental setup resulted in slower, more reproducible rates being observed for the degradation of BTMA, showing that the BTMA cation is several times more stable than previously reported.¹⁻⁶ Because BTMA is a relatively compact, easily synthesized, and potentially low cost cation, any other cations being pursued for use in AEMs should offer substantial advantages over BTMA. Also, accurate kinetic and mechanistic data are required for computational model validation, and currently the data available in the literature for different systems is too often in conflict with each other and experimental variable are often not reported in detail, leaving one to question the validity of the any previously reported results.

We have extended our previous computational modeling research⁸⁻¹⁰ to investigate the influence of different substitution groups on the benzene ring of BTMA (Fig 2). We have used Gaussian 09 to optimize the reactants and the transition state (TS) structures by the B3LYP method, 6-311++G(2d,p) basis set and PCM solvations. The reaction free energy barrier ΔG^\ddagger was then obtained by comparing the total free energies of the ground states of reactants (cation + OH⁻) with the free energy of the TS state. For the substituted cations,

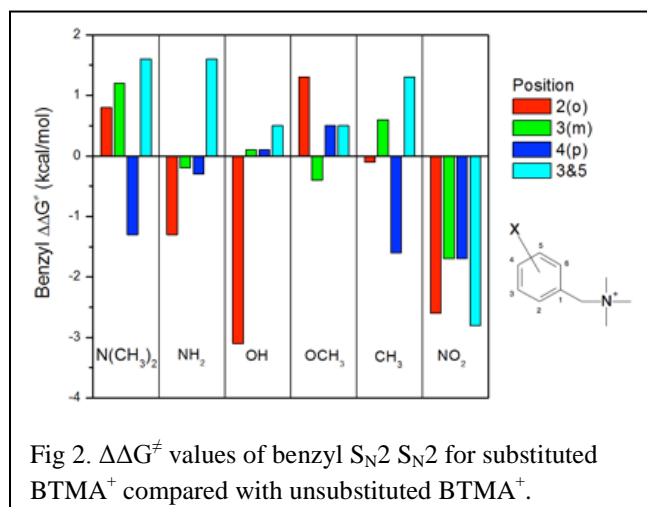
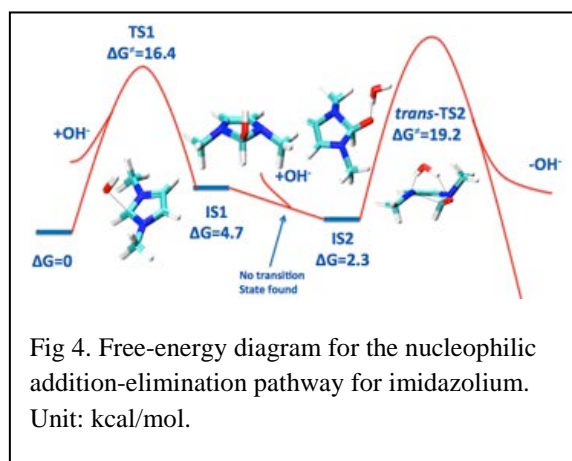
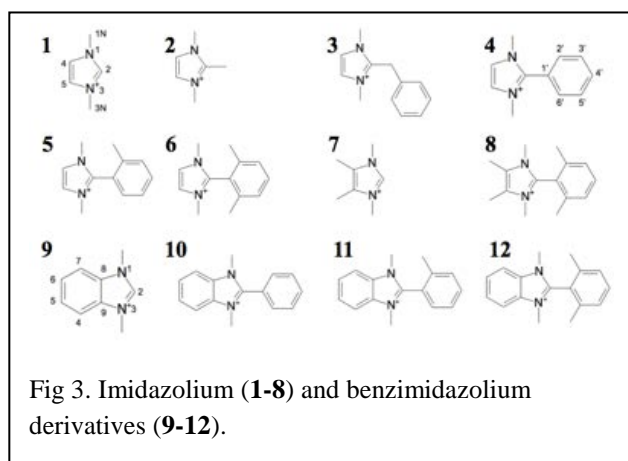


Fig 2. $\Delta\Delta G^\ddagger$ values of benzyl S_N2 S_N2 for substituted BTMA⁺ compared with unsubstituted BTMA⁺.



the benzyl S_N2 pathway was still the dominant pathway. The largest improvement on benzyl S_N2 ΔG^\ddagger found in our calculations was from the double-meta $-N(CH_3)_2$ substitution, with a $\Delta\Delta G^\ddagger$ of only 1.6 kcal/mol. This will result in less than an order of magnitude increase in stability, and suggests that further increases in stability requires investigation of other types of cations.

We have studied in reasonable depth, imidazolium and benzimidazolium cations (Fig 3), as alternative cations to BTMA, using DFT calculations to investigate degradation pathways and energy barriers of these cations. It was found that for the cations with sp^2 hybridized nitrogen atoms, M06 method with SMD solvation could provide better results than the B3LYP/PCM method used for substituted BTMA⁺ cations, where the nitrogen atom was sp^3 hybridized. We found that the nucleophilic addition-elimination pathway is the dominant degradation pathway for imidazolium and benzimidazolium derivatives. The OH⁻ will not only attack the ring of imidazolium first, but also catalyze the following ring-open reaction. The overall reaction mechanisms were presented in Fig 4, involving two intermediate states (ISs) and two transition states. The results of these computational studies resulted in a wide range of degradation energy barriers for different imidazolium cations.¹¹ Through steric hindrance and electronic effects an

imidazolium cation (species 8 in Figure 3) was determined to have 7 orders of magnitude higher stability compared to dimethyl imidazolium (species 1 in Figure 3). This and other results suggest that cations with significantly enhanced hydroxide stability may exist and might be key components in enabling energy conversion devices based on hydroxide conduction.

Future Plans

We have already begun expanding our experimental studies using our improved methodology to different families and classes of cations. We will use these studies to validate the computational results presented here for substituted BTMA and imidazolium cations. Some of the DMIm⁺ derivatives such as cation **8** have very high stability as predicted by our computational study and we will investigate them experimentally.

We will continue our computational investigations to include the degradation pathways of advanced cations ($X^+[N(CH_3)_2]_n$, X=C, S, S=O and n=3; X=P and n=4). These cations also have sp^2 hybridization nitrogen atoms and will also take the nucleophilic addition-elimination pathway when attacked by OH⁻. For the TMA⁺ derivatives, we will explore the cations with cyclic alkyls, which will introduce steric interferences and results in enhancement of reaction barriers. We will also investigate the degradation of organometallic cations such as cobaltocenium.

References

- (1) Bauer, B.; Strathmann, H.; Effenberger, F. *Desalination* **1990**, *79*, 125.
- (2) Einsla, B. R.; Chempath, S.; Pratt, L.; Boncella, J.; Rau, J.; Macomber, C.; Pivovar, B. *ECS Transactions* **2007**, *11*, 1173.
- (3) Deavin, O. I.; Murphy, S.; Ong, A. L.; Poynton, S. D.; Zeng, R.; Herman, H.; Varcoe, J. R. *Energy & Environmental Science* **2012**, *5*, 8584.
- (4) Noonan, K. J. T.; Hugar, K. M.; Kostalik, H. A.; Lobkovsky, E. B.; Abruña, H. D.; Coates, G. W. *Journal of the American Chemical Society* **2012**, *134*, 18161.
- (5) Nunez, S. A.; Hickner, M. A. *Acs Macro Letters* **2013**, *2*, 49.
- (6) Price, S. C.; Williams, K. S.; Beyer, F. L. *Acs Macro Letters* **2014**, *3*, 160.
- (7) A. Herring and B. Pivovar, Anion Exchange Membranes for Fuel Cells, http://energy.gov/sites/prod/files/2014/03/f11/amfc_110811_herring.pdf.
- (8) S. Chempath, B. Einsla, L. Pratt, C. Macomber, J. Boncella, J. Rau and B. Pivovar, *J. Phys. Chem. C*, 2008, v112, pp3179-3182.
- (9) S. Chempath, J. Boncella, L. Pratt, N. Henson and B. Pivovar, *J. Phys. Chem. C*, 2010, v114, pp11977-11983.
- (10) H. Long, K. Kim, and Pivovar, *J. Phys. Chem. C*, 2012, v116, pp9419-9426.
- (11) H. Long and B. Pivovar, *J. Phys. Chem. C*, 2014, v116, pp9880-9888.

Publications

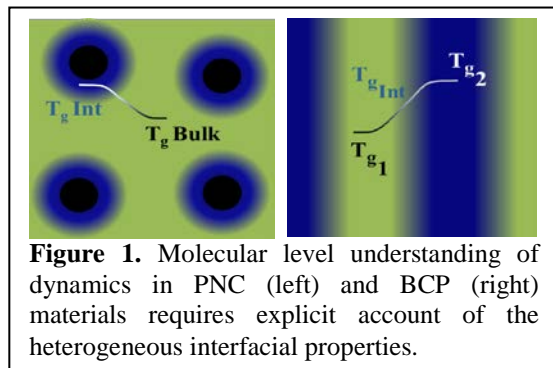
- H. Long, K. Kim, B. Pivovar, *J. Phys. Chem. C*, 2012, v116, pp9419-9426.
- H. Long and B. Pivovar, *J. Phys. Chem. C*, 2014, v116, pp9880-9888.

Polymer-Based Multicomponent Materials

Tomonori Saito¹, Bobby Sumpter¹, Vera Bocharova¹, Volker Urban¹, Alex Kisliuk¹, Jimmy Mays², Mark Dadmun², Ken Schweizer³, Frank Bates⁴, Alexei Sokolov¹ ¹Oak Ridge National Laboratory, ²University of Tennessee, ³University of Illinois, ⁴University of Minnesota

Program Scope

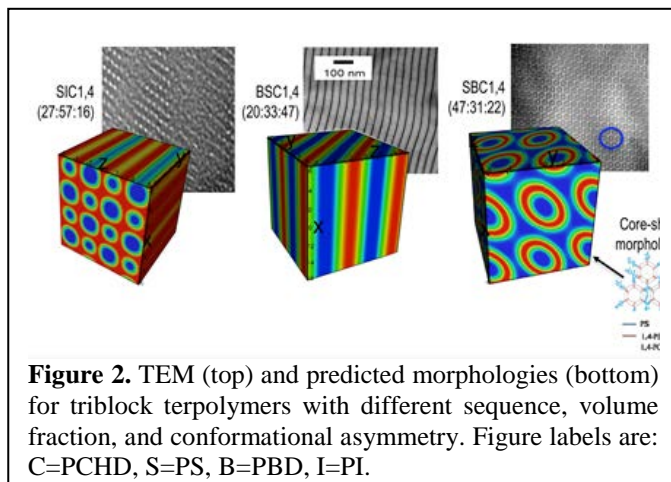
Polymers are a class of materials that are increasingly utilized in energy generation and conversion, energy storage and lightweight materials, chemical separations and gas purification. Yet fundamental understanding of the interactions that control macroscopic properties in these materials remains limited, especially in multicomponent systems including polymer nanocomposites (PNC) and block copolymers (BCP). The overarching goal of this project is to develop a fundamental understanding of how interfacial properties and interactions affect structure, morphology, dynamics, and macroscopic properties of multicomponent polymeric systems, in both the liquid and solid states. The pervasive presence of interfaces between different phases or species in multicomponent systems (**Fig. 1**), and their effect on bulk properties, is the unifying aspect of our research. We address the following fundamental issues: How do the nanoparticle polymer interactions and polymer rigidity affect the structure and dynamics in the interfacial region? How do confinement and interactions affect polymer and nanoparticles diffusion? How are viscoelastic properties of composites affected by nanoparticle size, softness and surface fluctuations? How do molecular architecture and morphology of segregated block copolymers affect structure and dynamics of the interfacial region and macroscopic viscoelastic properties of these materials? We pursue a comprehensive interdisciplinary approach led by advanced theory and simulations, precise synthesis and state-of-the-art characterization. The fundamental knowledge developed in this program will contribute to the scientific foundation for the rational design of multicomponent polymer based materials with superior properties and function that can address many DOE challenges.



Recent Progress

Our primary focus has been on fundamental understanding how interfacial interactions affect structure, morphology and dynamics of nanocomposite and multiblock polymeric systems. We have made significant progress over the last two years in studies that integrate experimental, theoretical and computational efforts and that resulted in 47 peer-reviewed publications. A few of the major achievements are summarized below.

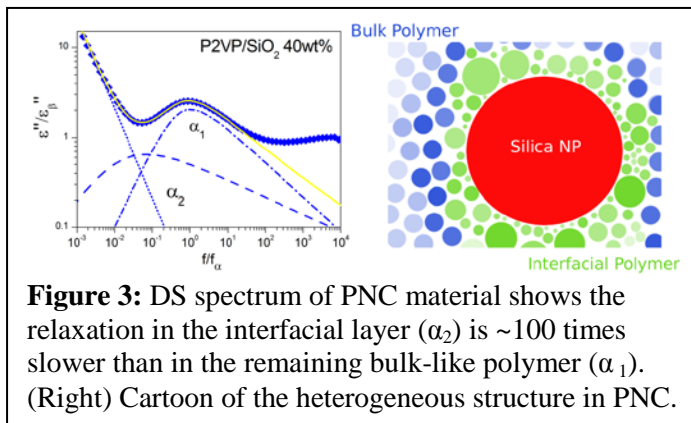
Structure and Morphology: *Tuning Macromolecular Architecture, Chain Stiffness, and Electrostatics of Block Copolymers:* Understanding the effects of conformational asymmetry and chain rigidity in multiblock copolymer materials involves a parameter space far larger than for symmetric block copolymers. We are addressing this problem via an integrated theory, simulation, precise synthesis and detailed characterization approach (**Fig. 2**) using diblock and triblock copolymers



based on the unique polymer poly(1,3-cyclohexadiene) (PCHD)¹⁻⁴ as the semi-flexible block, and polystyrene (PS), polyisoprene (PI), and polybutadiene (PBD) as flexible blocks.³ The microstructure of the PCHD block (1,2 vs 1,4) was controlled to tune conformational asymmetry. Triblock terpolymer melts containing high 1,2-PCHD are disordered at 110 °C for all samples, independent of block composition or sequence. Triblock melts containing high 1,4-PCHD formed various morphologies ranging from core-shell (**Fig. 2**, right frame) to lamellar (**Fig. 2**, middle frame), but with an additional novel morphology (**Fig. 2**, left frame). Also the studies have led to the development of self-consistent field theory (SCFT) calculations that can account for the enhancement of the χ parameter with an increase in conformational asymmetry, with excellent agreement between theory and experiment. Architectural asymmetry was also studied using linear PS-PI diblock copolymers and miktoarm stars (PS₂PI, PSPI₂, and PS₂PI₂) of *fixed* molecular weights and volume fractions.^{1,5} We demonstrated that tethering two polymer chains at a junction point led to chain crowding and enhanced excluded volume effects which drive morphological changes. All these results provide guidance of how architectural and conformational asymmetry can be used to predictably tune BCP morphologies. The impact of electrostatics on BCP microphase separation was also studied, by examining BCPs with charged and neutral blocks.⁶ The synthesis of well-defined poly(acrylic acid) (PAA)-PI block copolymers was developed, which demonstrate that triblock copolymers of PS-b-PI-b-PAA form unique “flower-like” multicomponent micelles due to competition between local and global self-assembly in aqueous media.⁷ The construction of multigeometry nanoparticles, disk-sphere and disk-cylinder was achieved with binary mixtures of BCPs and control of kinetic assembly pathways.⁸

Dynamics: *Structure and Dynamics of Interfacial Layer in Nanocomposites:* We used dielectric spectroscopy (DS), differential scanning calorimetry (DSC) and small angle x-ray scattering (SAXS) to unravel the role of nanoparticles on the structure and dynamics of polymer nanocomposites.⁹ A thin interfacial polymer layer that has very different density and dynamics than the bulk polymer was deduced. The thickness of the interfacial layer of poly (2-vinyl pyridine) (P2VP) on SiO₂ nanoparticles is ~5 nm in both static (SAXS) and dynamic (DS and

DSC) measurements. The layer is not “dead” or “glassy”, but its dynamics are slowed by ~ 100 times relative to the bulk polymer (**Fig. 3**). These results explain many controversies in the PNC field,¹⁰ provide new insight into the structurally and dynamically heterogeneous nature of PNCs, and demonstrate the need to explicitly consider the interfacial layer to construct predictive models.



Theory and Simulation of Nanoparticle Diffusion in Polymer Melts: A predictive theory of intermediate-time anomalous transport and long-time diffusion of a single nanoparticle in polymer melts has been created.¹¹ The influence of multiple nanoparticle-to-polymer length-scale ratios and degree of entanglement on particle dynamics has been predicted, and the physics that underlies Stokes-Einstein (SE) violation behavior elucidated. For entangled melts, nanoparticle motion exhibits four distinct dynamical regimes associated with a rich and variable coupling of particle mobility to the entanglement network. The predicted diffusion coefficients are in good agreement with recent experiments^{12, 13} and simulations¹⁴. This theory is instrumental in addressing nanoparticle diffusion in dense polymers and will be thoroughly tested in the proposed research.

Future Plans

Our prior studies of equilibrium phenomena in PNC and BCP materials provide a solid foundation for the proposed research on dynamics. *The overarching goal of our future research is to develop a fundamental and predictive understanding of dynamics in multi-component polymeric materials, and establish how interfacial structure, properties, and interactions, combined with mesoscale confinement, affect molecular motions and macroscopic properties in these intrinsically heterogeneous materials.* This is pivotal for designing new materials for energy applications (e.g., photovoltaic, energy storage and conversion) by developing the knowledge that connects molecular structure and interactions to macroscopic properties necessary to achieve the vision of Materials by Design.

References

1. Dyer, C.; Driva, P.; Sides, S. W.; Sumpter, B. G.; Mays, J. W.; Chen, J.; Kumar, R.; Goswami, M.; Dadmun, M. D., *Macromolecules* 2013, 46 (5), 2023-2031.
2. Kumar, R.; Sides, S. W.; Goswami, M.; Sumpter, B. G.; Hong, K. L.; Wu, X. D.; Russell, T. P.; Gido, S. P.; Misichronis, K.; Rangou, S.; Avgeropoulos, A.; Tsoukatos, T.; Hadjichristidis, N.; Beyer, F. L.; Mays, J. W., *Langmuir* 2013, 29 (6), 1995-2006.

3. Mays, J. W.; Kumar, R.; Sides, S. W.; Goswami, M.; Sumpter, B. G.; Hong, K. L.; Wu, X. D.; Russell, T. P.; Gido, S. P.; Avgeropoulos, A.; Tsoukatos, T.; Hadjichristidis, N.; Beyer, F. L., *Polymer* 2012, 53 (22), 5155-5162.
4. Misichronis, K.; Rangou, S.; Ashcraft, E.; Kumar, R.; Dadmun, M.; Sumpter, B. G.; Zafeiropoulos, N. E.; Mays, J. W.; Avgeropoulos, A., *Polymer* 2013, 54 (5), 1480-1489.
5. Kumar, R.; Li, Y. G.; Sides, S. W.; Mays, J. W.; Sumpter, B. G., *J. Phys.: Conf. Ser.* 2012, 402, 012042.
6. Wang, X.; Goswami, M.; Kumar, R.; Sumpter, B.; Mays, J., *Soft Matter* 2012, 8, 3036-3052.
7. Wang, X. J.; Chen, J. H.; Hong, K. L.; Mays, J. W., *ACS Macro Lett.* 2012, 1 (6), 743-747.
8. Zhu, J. H.; Zhang, S. Y.; Zhang, K.; Wang, X. J.; Mays, J. W.; Wooley, K. L.; Pochan, D. J., *Nat. Commun.* 2013, 4, 2297.
9. Holt, A. P.; Griffin, P. J.; Bocharova, V.; Agapov, A. L.; Imel, A. E.; Dadmun, M. D.; Sangoro, J. R.; Sokolov, A. P., *Macromolecules* 2014, 47 (5), 1837-1843.
10. Holt, A. P.; Sangoro, J. R.; Wang, Y.; Agapov, A. L.; Sokolov, A. P., *Macromolecules* 2013, 46 (10), 4168-4173.
11. Yamamoto, U.; Schweizer, K. S., *Soft Matter* 2014, submitted.
12. Grabowski, C. A.; Adhikary, B.; Mukhopadhyay, A., *Appl. Phys. Lett.* 2009, 94, 021903.
13. Tuteja, A.; Mackay, M. E.; Narayanan, S.; Asokan, S.; Wong, M. S., *Nano Lett.* 2007, 7 (5), 1276-1281.
14. Kalathi, J. T.; Yamamoto, U.; Schweizer, K. S.; Grest, G. S.; Kumar, S. K., *Phys. Rev. Lett.* 2014, 112 (10), 108301.

Publications (past two years, 21 publications *solely* supported by this FWP)

1. J. Zhang, S. Sides, F.S. Bates, *Macromolecules* 45, 256-265 (2012).
2. J. Zhang, F.S. Bates, *J. Am. Chem. Soc.* 134, 7636-7639 (2012).
3. M. Mutz, D.W. Holley, D. Baskaran, J.W. Mays, M.D. Dadmun, *Polymer*, 53, 5087-5096 (2012).
4. V. S. Urban. "Small-Angle Neutron Scattering." in *Characterization of Materials 2nd Edition*, Editor: Elton N. Kaufmann (Editor), by John Wiley and Sons.
5. R. Kumar, M. Goswami, B.G. Sumpter, V. N. Novikov, A. P. Sokolov, *Phys. Chem. Chem. Phys.* 15, 4604-4609 (2013).
6. V.N. Novikov, K.S. Schweizer, A.P. Sokolov, *J. Chem. Phys.* 138, 164508 (2013).
7. D. Banerjee, M.D. Dadmun, B. Sumpter, K. Schweizer, *Macromolecules*, 46, 8732-8743 (2013).
8. S.Mirigian and K.S.Schweizer, *J.Phys.Chem.Lett.* 4, 3648 (2013).
9. D.W. Holley, M. Ruppel. J.W. Mays, V.S. Urban, D. Baskaran, *Polymer* 55, 58-65 (2014).
10. J.G. Kennemur, L Yao, F.S. Bates, M.A. Hillmyer, *Macromolecules* 47, 1411-1418 (2014).
11. S. Mirigian and K.S. Schweizer, *J. Chem. Phys.* (2014 in print)
12. S.Mirigian and K.S.Schweizer, *J.Chem. Phys.*, (2014, in print).
- 13-21. 1-7, 9, 10 in References

Structure and dynamics of solid-liquid interfaces

Miquel B. Salmeron^{1,2}, Gabor Somorjai^{1,3}, Peidong Yang^{1,3}

¹Materials Sciences Division, Lawrence Berkeley National Laboratory

²Materials Science and Engineering Dept. U.C. Berkeley

³Chemical Science Dept. U.C. Berkeley

A subtask of the “Chemical and Mechanical Properties of Surfaces, Interfaces and Nanostructures” program FWP KC3101

Program-subtask Scope

This project-subtask aims at developing the fundamental science of solid-liquid interfaces and the role of electric fields in determining molecular structure and dynamics. It encompasses a broad range and phenomena of atoms and molecules at the interface. Focus topics are: structure of the Helmholtz layer, solvation/de-solvation phenomena, reactions, ion intercalation and charge transfer dynamics. We aim at determining electronic level alignments of adsorbed molecules when solvated and when de-solvated as they determine chemical and photochemical reactions. This subtask is a natural extension of the main program, building on the team expertise in the development of new experimental techniques, by bringing microscopy (STM, AFM), and spectroscopy techniques (XPS, XAS, SFG), to solve fundamental problems in solid-liquid interface research [1].

Recent Progress

Fig. 1 illustrates how the chemical state of a Cu electrode (a 300 nm film evaporated on the back side of a SiN membrane) was determined *in situ* using XAS in the fluorescence detection mode during oxidation and reduction cycles [2]. The spectra shown on the right were obtained at the voltages indicated. A crucial aspect of this work is the strong connection with theory because interpretation of the XAS spectra necessitates the application of advanced methods to calculate x-ray induced core to valence transitions electrons [3,4]. In collaboration with D. Prendergast of the Molecular Foundry we showed that the measured O1s spectra correspond to that expected from the Cu^{+1} and Cu^{+2} oxides.

While fluorescence yield detection works well for thin electrodes, it is not adequate for studies of the Helmholtz layer, due to the penetration depth of soft x-ray photons, which is of the order of a micrometer. To make XAS surface sensitive we used the electron emission current arising from the de-excitation of the core holes created by x-ray absorption, in the total electron yield mode (TEY). The current is collected at the sample electrode. Since the effective attenuation length of electrons with of energies of a few hundred eV is estimated between 5-10 Å, the TEY signal originates from species located in the first few layers next

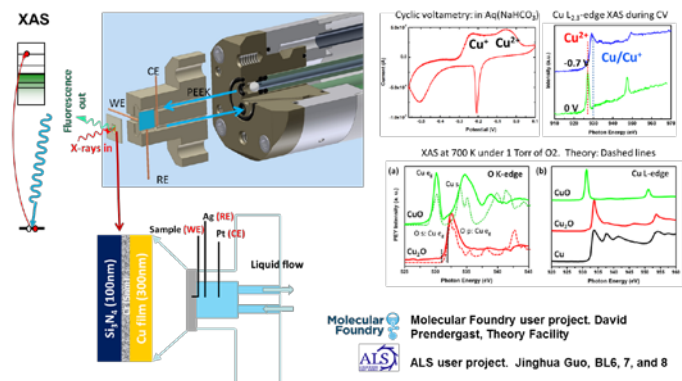


Figure 1. Left: Schematic of the electrochemical cell for *in situ* spectroscopic studies of electrode surfaces under potentiostatic control. Right: oxidation and reduction of a thin Cu film deposited on the back side of a SiN membrane in a 2mM NaHCO₃ solution. Top: Cyclic voltammogram and fluorescence mode XAS of the Cu L_{2,3} edges at two particular voltages. Bottom: measured and calculated XAS spectra of the O 1s edge for CuO and Cu₂O.

to the collecting electrode. This opens the way to studies of the structure of the electrical double layer.

The technique was demonstrated in a recent study of the structure of water near a gold electrode, in the form of a thin (20 nm) film on the back on the SiN membrane. As shown in Fig. 2, the fluorescence mode XAS spectrum (top) of water in a 10 μ M mol NaCl solution is very similar to that of liquid water. The simultaneously acquired TEY XAS (middle) is however different. Peak A, at 535 eV, characteristic of water molecules with dangling H-bonds (about 25% in water), is strongly suppressed. There are also differences in peaks B and C that indicate changes in the backbonding orbitals of water. These results indicate that the water molecules close to the gold electrode are highly structured.

In another experiment the gold surface was coated with a monolayer of hexadecanethiol. The TEY XAS in this case shows that the peak at position A is that of normal liquid water (bottom curve), demonstrating that the structuring of water occurs only near the metallic Au electrode. A detailed interpretation of these results is currently under way by theoretical modeling in collaboration with the Prendergast group at the Molecular Foundry [5].

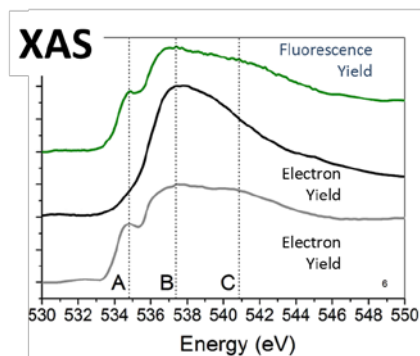


Figure 2. XAS O K-edge spectra of water near a gold electrode in a 10 μ M mol NaCl solution. Top: total fluorescence yield (TFY). Middle: total electron yield (TFY). Bottom: TEY after covering the Au surface with a hexadecanethiol monolayer.

Vibrational spectroscopies provide excellent information on the vibrational structure of surface species and are particularly appropriate for studies of solid-liquid interfaces. Sum Frequency Generation (SFG) is highly sensitive to the first interfacial layer, by virtue of the selection rules for second order processes. As an example of its capabilities we show in Fig. 3 the spectra in the C-H stretch region of isopropanol during its oxidation to acetone on Pt nanoparticles of controlled size (2 to 8 nm), in both the liquid and gas phases. The reaction at the solid/liquid interface is two orders of magnitude slower than that at the solid/gas interface, while catalytic activity increases with the size of platinum nanoparticles for both the liquid-phase and gas-phase reactions. The activation energy of the gas-phase reaction decreases with the platinum nanoparticle size and is in general much higher than that of the liquid-phase reaction which is largely insensitive to the size of catalyst nanoparticles. Water substantially promotes isopropanol oxidation in the liquid phase. However it inhibits the reaction in the gas phase. The kinetic results suggest different mechanisms between the liquid-phase and gas-phase reactions, correlating well with different orientations of adsorbed species at the solid/liquid and solid/gas interfaces, as probed by SFG under reaction conditions and simulated by computational calculations. [6]

Future Plans

We plan to apply the *in situ* XAS and SFG techniques to study

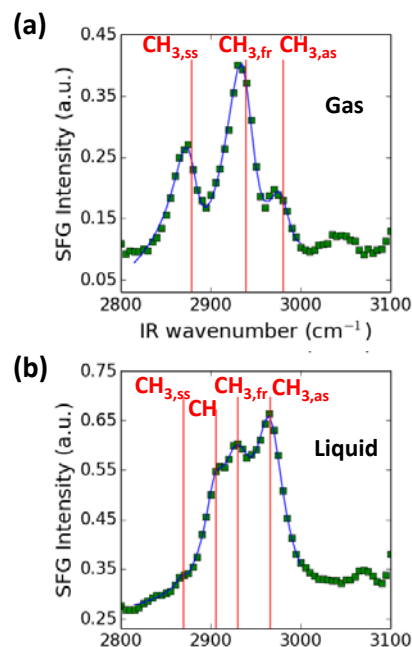


Fig. 3. SFG spectroscopy of isopropanol under reaction conditions on 4 nm Pt nanoparticles. (a) SFG spectra under gas-phase conditions. (b) SFG spectra under liquid-phase reaction conditions.

the chemical nature and the orientation of molecules, including water, carbonates (used in Li battery electrolytes) that play an important role in photocatalysis and in electrical storage applications.

We plan to rebuild our electrochemical STM used successfully in the past for the study of de-alloying of Au-Cu crystals [7]. Planned experiments include underpotential deposition of Cu and other metals which will also be studied by STM and will serve as calibration and test of the capabilities of combining both techniques. Other planned experiments to be carried in parallel with STM, XAS and SFG include the study of Si and the effects of ion (Li, Na, Mg) intercalation.

References

- [1] M. Salmeron, and R. Schlögl. *Surf. Sci. Rep.* 63, 169 (2008).
- [2] P. Jiang, et al.. *Electrochem. Com.* 12, 820 (2010)
- [3] P. Jiang, D. Prendergast, et al. *J. Chem. Phys.* 138, 024704 (2013).
- [4] T. Pascal, M. Salmeron, N. Balsara, D. Prendergast, et al. *J. Phys. Chem. Letters.* 5, 1547 (2014).
- [5] J.-J. Velasco, et al. Submitted (2014).
- [6] H. Wang, Lin-Wang Wang, G.A. Somorjai, et al. *JACS.* Submitted (2014).
- [7] S. J. Chen, M. Salmeron, et al. *Surf. Sci.* 292, 289 (1993).

Publications (2012-2014)

- [1] S. Maier, M. Salmeron, et al. “Adsorbed water-molecule hexagons with unexpected rotations in islands on Ru(0001) and Pd(111)”. *Phys. Rev. B.* 85, 155434 (2012).
- [2] Z. Zhu, M. Salmeron, G. A. Somorjai, et al. “Reversible Formation of Nanometer-sized Surface Platinum Oxide Clusters on a Stepped Pt(557) Single Crystal Surface Induced by Oxygen: A High-pressure STM and Ambient Pressure XPS Study”. *Nano Letters.* 12, 1491 (2012).
- [3] X. Feng, S. Maier, M. Salmeron. “Water splits epitaxial graphene and intercalates.” *J. Am. Chem. Soc.* 134, 5662 (2012)
- [4] S. Maier, I. Stass, J. I. Cerda, and M. Salmeron. “Bonding of ammonia and its dehydrogenated fragments on Ru(0001)”. *J. Phys. Chem. C.* 116, 25395 (2012).
- [5] F. Besenbacher, P. Thstrup, and M. Salmeron. “The structure and reactivity of surfaces revealed by scanning tunneling microscopy”. *MRS Bulletin.* 37, 677 (2012).
- [6] Y. Borodko, G. A. Somorjai, et al. “From Single Pt Atoms to Pt Nanocrystals: Photoreduction of Pt²⁺ inside of a PAMAM Dendrimer.” *J. Phys. Chem. Lett.* 3, 236 (2012).
- [7] F. Zheng, S. Alayoglu, G.A. Somorjai, et al. “In-situ Study of Oxidation States and Structure of 4 nm CoPt Bimetallic Nanoparticles during CO Oxidation using X-ray Spectroscopies in Comparison with Reaction Turnover Frequency.” *Catalysis Today* 182 54 (2012).
- [8] J.Y. Park, G.A. Somorjai, et al. “Size Effect of RhPt Bimetallic Nanoparticles in Catalytic Activity of CO Oxidation: Role of Surface Segregation.” *Cat. Today* 181 133 (2012).
- [9] Z. Zhu, M. Salmeron, G. A. Somorjai, et al. “Formation of Nanometer-sized Surface Platinum Oxide Clusters on a Stepped Pt(557) Single Crystal Surface Induced by Oxygen: A High-Pressure STM and Ambient-pressure XPS Study.” *Nano Letters* 21, 1491(2012).
- [10] R. M. Onorato, A.P. Yoon, J. T. Lin and G. A. Somorjai. “Adsorption of Amino Acids and Dipeptides to the Hydrophobic Polystyrene Interface Studied by SFG and QCM: The Special Case of Phenylalanine.” *J. Phys. Chem. C* 116, 9947 (2012).
- [11] V. Iablokov, G.A. Somorjai, et al. “Size Controlled Co Nanoparticle Catalysts for CO₂ Hydrogenation: Synthesis, characterization and Catalytic Reactions”. *NanoLetters* 12, 3091 (2012).

- [12] J. M. Krier, W. D. Michalak, L. R. Baker, K. An, K. Komvopoulos and G. A. Somorjai. "Sum Frequency Generation Vibrational Spectroscopy of Colloidal Platinum Nanoparticle Catalysts: Disordering Versus Removal of Organic Capping." *J. Phys. Chem. C* 116, 17540 (2012).
- [13] S. J. Kweskin, P. Yang, G. A. Somorjai, et al. "High-Pressure Adsorption of Ethylene on Cubic Pt Nanoparticles and Pt(100) Single Crystals Probed by In-Situ Sum Frequency Generation Vibrational Spectroscopy." *ACS Catalysis* 2, 2377 (2012).
- [14] L. R. Baker, G.A. Somorjai, et al. "The Role of an Organic Cap in Nanoparticle Catalysis: Reversible Restructuring of Carbonaceous Material Controls Catalytic Activity of Platinum Nanoparticles for Ethylene Hydrogenation and Methanol Oxidation". *Cat. Lett.* 142, 1286 (2012).
- [15] K. Qadir, et al. "Intrinsic Relation between Catalytic Activity of CO Oxidation on Ru Nanoparticles and Ru Oxides Uncovered with AP-XPS." *NanoLetters* 12, 5761 (2012).
- [16] H. Wang, G. A. Somorjai, et al. "The Influence of Size Induced Oxidation State of Platinum Nanoparticles on Selectivity and Activity in Catalytic Methanol Oxidation in the Gas Phase." *Nano Letters* 13, 2976 (2013).
- [17] D.R. Butcher, M. Salmeron and G.A. Somorjai, et al. "Mobility on the Reconstructed Pt(100)-hex Surface under Ethylene and its Mixture with H₂ and CO. *Chem. Commun.* 49, 6903 (2013).
- [18] S. Alayoglu, G. A. Somorjai, et al. "Surface Composition of Stable Bimetallic CoCu Nanoparticles Supported on Silica under Redox Atmospheres and During Reaction Between CO₂ and H₂: In situ X-ray Spectroscopic Characterization." *J. Phys. Chem. C*. Accepted (2013).
- [19] K. An, G. A. Somorjai, et al. "Dramatic Enhancement of CO Oxidation Rates at the Interface of Mesoporous Oxides and Pt Nanoparticles." *J. Am. Chem. Soc.* (2013). Accepted.
- [20] S. K. Beaumont, G.A. Somorjai, et al. "Exploring Surface Science and Restructuring in Reactive Atmospheres of Colloidally Prepared Bimetallic CuNi and CuCo Nanoparticles on SiO₂ in situ Using Ambient Pressure XPS". *Faraday Discussions*. DOI: 10.1039/c2fd20145c
- [21] P. Jiang, D. Prendergast, M. Salmeron, et al. "Experimental and theoretical investigation of the electronic structure of Cu₂O and CuO thin films on Cu(110) using XPS and XAS". *J. Chem. Phys.* 138, 024704 (2013).
- [22] C. Escudero, M. Salmeron. "A reaction cell with sample laser heating for in situ soft X-ray Absorption Spectroscopy under environmental conditions". *J. Synchrotron Rad.* 20, 504 (2013).
- [23] C. Escudero and M. Salmeron. "From solid-vacuum to solid-gas and solid-liquid interfaces: in situ studies of structure and dynamics under relevant conditions". *Surf. Sci.* 607, 2 (2013).
- [24] Xiaofeng Feng, Sangku Kwon, Jeong Young Park, and Miquel Salmeron. "Superlubric Sliding of Graphene Nanoflakes on Graphene". *ACS Nano*. 7, 1718 (2013).
- [25] Xiaofeng Feng and Miquel Salmeron. "Electronic screening in graphene flakes revealed by scanning tunneling microscopy" *Applied Phys Letters*. 102, 053116 (2013).
- [26] Z. Zhu, M. Salmeron, G.A. Somorjai, et al. "In Situ Scanning Tunneling Microscopy and X-ray Photoelectron Spectroscopy Studies of Ethylene-Induced Structural Changes on the Pt(100)-hex Surface". *J. Phys. Chem. C*. 117, 2799 (2013).
- [27] D.R. Butcher, M. Salmeron and G.A. Somorjai, et al. "Mobility on the Reconstructed Pt(100)-hex Surface under Ethylene and its Mixture with H₂ and CO". *Chem. Comm.* 49, 6903 (2013).
- [28] J.J. Velasco-Velez, M. Salmeron, et al. "In-situ XAS investigation of the electrochemical reactions of graphene in aqueous electrolyte". *J. Electrochem. Soc.* 160, C445 (2013).
- [29] S. Maier, I. Stass, J.I. Cerda, M. Salmeron. "Unveiling the mechanism of water partial dissociation on Ru(0001) via variable temperature scanning tunneling microscopy and density functional theory". *Phys. Rev. Letters*. 112, 126101 (2014)

Directed Energy Interactions With Surfaces

Michael Savina, Michael Pellin, Alexander Zinovev

Materials Science Division, Argonne National Laboratory

Program Scope

The Directed Energy Interactions with Surfaces program focuses on fundamental studies of the interaction of directed energy sources such as energetic ions with materials, which provides the basis for characterizing and modifying materials. Fundamental understanding of energy-material interactions drives the development of world-class instruments and methods for materials characterization, which in turn enables us to answer questions about new or previously unobservable phenomena and develop new materials. The long-term goal is to understand the interaction of directed energy sources with materials, both in model systems in which basic interactions can be studied in great detail, and in complex systems relevant to DOE missions in which multiple interactions occur and evolve over varying length and time scales.

Recent Progress

Ion sputtering as a means of generating clusters of various compositions remains one of the least understood phenomena in particle-solid interactions. During sputtering, three distinct processes, *i.e.* cluster formation, ionization, and fragmentation, occur quasi-simultaneously; the challenge is to distinguish between them and learn basic laws driving the cluster formation process. Secondary Neutral Mass Spectrometry (SNMS) with Single Photon Ionization (SPI) minimizes fragmentation while separating cluster formation and ionization. We have applied this technique to study clusters sputtered from pure metals and metal alloys [1-6]. The sputter yield of clusters containing n atoms (Y_n) was found to scale as $n^{-\delta}$, where the exponent δ is inversely proportional to the total sputtering yield of the element [2, 7].

Recently we studied cluster emission from the ternary alloy $\text{Au}_7\text{Cu}_5\text{Al}_4$, with a focus on the effect of surface modification via ion irradiation. The metal was irradiated with doses of $\sim 1.5 \times 10^{17}$ Ar^+ ions/cm² (~ 100 incident ions per surface atom) prior to sputtering with vanishing small doses of 5 keV Ar^+ ions for analysis. Fig. 1 shows the Au_2Al_2 yield after pretreatment with Ar^+ ions at two different pretreatment energies, and shows a large energy-dependent change in sputter yield. Fig. 1 also shows the effect of pretreatment energy on the yield of all clusters, and shows that high-energy pretreatment significantly enhances Al-containing clusters, while low-energy pretreatment significantly enhances Au-containing clusters. The effect is strongest at the lowest energies, *i. e.* below about 300 eV.

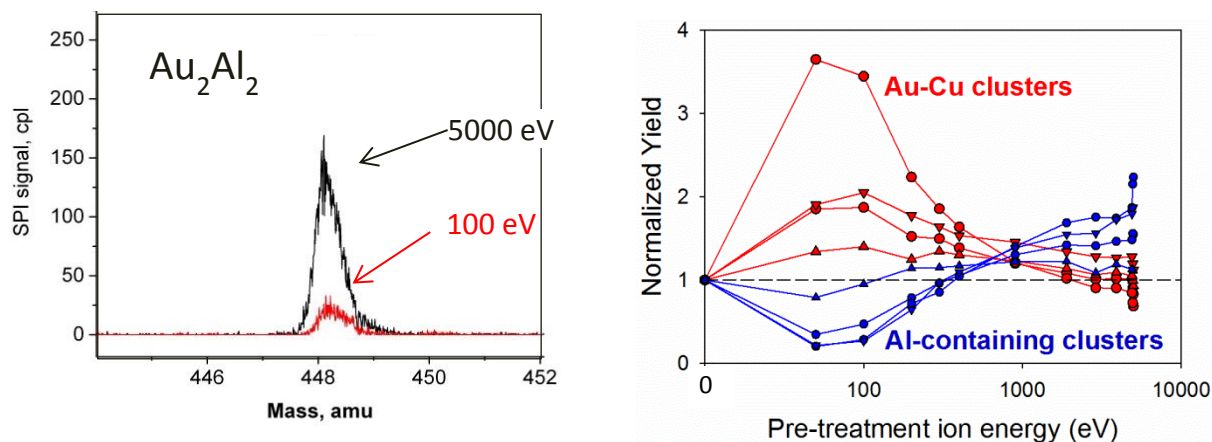


Figure 1. Left: The effect of pretreatment ion energy on the yield of neutral Au_2Al_2 clusters sputtered from $\text{Au}_7\text{Cu}_5\text{Al}_4$, showing a decreased yield after treatment with 100 eV Ar^+ ions compared to 500 eV ions. Right: Yields of all clusters as a function of pretreatment ion energy.

We have previously shown that the cluster yield depends strongly on the first layer composition of the alloy, but that the effect vanishes as the cluster size increases [8]. Preferential sputtering (i.e. depletion of the surface layer in one or more components) is well known for alloys and could account for changes in the relative cluster yields for low ion doses, but this is not the case here; even at the lowest dosing energy the system has come to equilibrium and should have a surface composition close to the bulk composition. Furthermore, the effect persists for large clusters, which are relatively insensitive to the surface composition. Preferential sputtering is governed by differences in mass and binding energies of the components of a mixture and should not depend on ion energy [9].

The Ar^+ penetration depth decreases with ion energy as shown by SRIM (Stopping Range of Ions in Matter [10]) calculations. At energies below 1 keV, the stopping range of Ar^+ ions has a maximum in the first 2-5 monolayers, so that damage done by the dosing beam is concentrated in the near-surface region. Preliminary XPS measurements on the freshly dosed materials indicate that some Ar is implanted, though significant numbers of Ar atoms are not expected to remain at such shallow depths. This must be quantified since the presence of implanted Ar atoms near the surface would have an effect on sputtering yields. Cluster compositions and yields are clearly affected by chemical and morphological changes due to irradiation, and represent a sensitive measure of the surface state, one that gives different and perhaps richer information than simply surface concentration.

Understanding the effects of low-energy ion irradiation is important in materials characterization. Fig. 2 shows a high-resolution depth profile of a multilayer metal sulfide composite synthesized by Atomic Layer Deposition (ALD). Profiles were determined by milling the material with low-energy Ar^+ (250 eV) prior to analysis at 5 keV [11]. This method has a depth resolution of ~ 0.4 nm [12]. Ultrathin $\text{ZnS}/\text{SnS}_2/\text{Cu}_2\text{S}$ multilayers were studied because of the relevance of this material as a precursor for the photovoltaic alloy $\text{Cu}_2\text{ZnSnS}_4$ (CZTS). We characterized interfacial sharpness to determine the diffusion distance of atoms during synthesis.

In contrast to metal oxides grown by ALD, sulfide interfaces were initially diffuse. Annealing at 275 °C showed that the alloy reaction proceeds in a quasi- two-step process, with Cu_2SnS_3 forming first. Annealing at 425 °C fully mixes the layers, albeit with significant diffusion into the Si substrate. Diffusion during synthesis plays a critical role in determining the composition profile of multilayer films. For metal sulfides, the diffusion length of cations is on the order of the layer thickness, and so diffuse interfaces will form. This is distinct from metal oxides, for which sharp interfaces are observed and the diffusion length is much shorter than the layer thickness, even for much thinner (~5.5 nm) layers [12].

Future Plans

The energy dependence of the cluster composition observed in Fig. 1 is not explained by sputtering models, in which the partial sputtering yield depends on concentration, mass, and surface binding energy, but not on the energy of the irradiating ion. To first order, the data suggests changes in the surface binding energies of the various components. While binding energies generally vary linearly with concentration [9, 13], the presence of implanted species or vacancies near the surface can cause changes unrelated to concentration. Further, since clusters form vibrationally hot, their fragmentation probability is affected by the binding energies of the sputtered components. Thus ion irradiation affects both sputtering yield and energy distribution and therefore the ability to form stable clusters. This provides a means of determining the effect of ion irradiation on solids via studying the sputtering yields of various components after irradiation, since the energy distributions of each component of the sputtered flux can be measured independently, and related to the binding energy. Because the sputtering and ionization processes are decoupled, we can determine absolute yields via saturation spectroscopy, which we previously applied to UO_x molecular sputtering [14]. Finally, XPS will help to resolve the question of energy-dependent sputtering under low energy bombardment and its effect on surface composition. The thickness and composition of ion disturbed/reformed layers in irradiated material will be determined with angle-resolved X-ray photoelectron spectroscopy (ARXPS) to determine composition at various depths without ion sputtering.

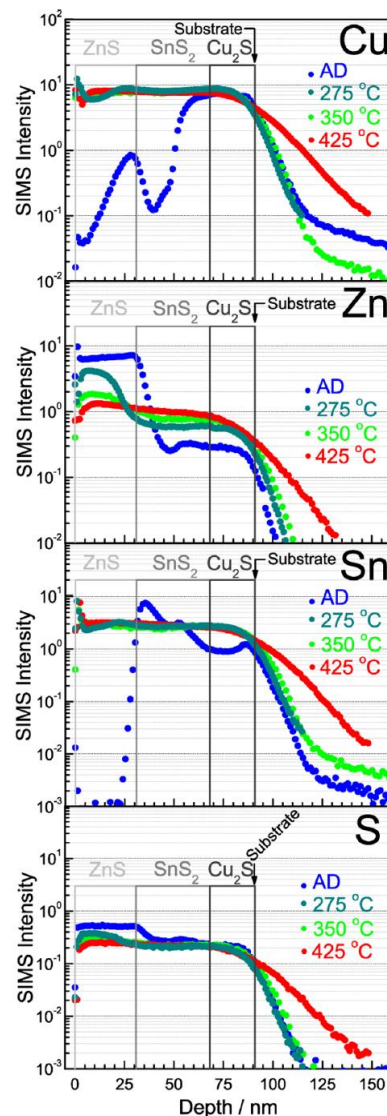


Figure 2. Composition profiles for Cu, Zn, Sn, and S measured by high resolution TOF SIMS from a ZnS/SnS₂/Cu₂S composite on Si, for the as-deposited (AD) material, as well as annealed in Ar at various temperatures.

References

1. King, B.V., et al., *Appl. Surf. Sci.*, 2006. **252**(19): p. 6426-6428.
2. King, B.V., et al., *Nucl. Instrum. Methods B*, 2013. **317**: p. 115-120.
3. King, B.V., et al., *Appl. Surf. Sci.*, 2009. **256**(4): p. 991-994.
4. King, B.V., et al., *Nucl. Instrum. Methods B*, 2009. **267**(16): p. 2757-2760.
5. King, B.V., et al., *Appl. Surf. Sci.*, 2003. **203**: p. 244-247.
6. Pellin, M.J., et al., *J. Vac. Sci. Tech. B*, 1987. **5**(5): p. 1477-1481.
7. King, B., et al., *Surf. Sci.*, 2009. **603**(5): p. 819-825.
8. Lill, T.B., et al., *Phys. Rev. Lett.*, 1994. **73**(12): p. 1719-1722.
9. Gnaser, H., *Low-energy ion irradiation of solid surfaces*. 1999: Springer-Verlag.
10. Ziegler, J.F., M.D. Ziegler, and J.P. Biersack, *Nucl. Instrum. Methods B*, 2010. **268**(11): p. 1818-1823.
11. Thimsen, E., et al., *Chem. Mater.*, 2013. **25**(3): p. 313-319.
12. Baryshev, S.V., et al., *Rapid Comm. Mass Spectrom.*, 2012. **26**(19): p. 2224-2230.
13. Gades, H. and H.M. Urbassek, *Nucl. Instrum. Methods B*, 1994. **88**(3): p. 218-228.
14. Willingham, D., et al., *J. Radioanal. Nucl. Chem.*, 2013. **296**(1): p. 407-412.

Publications

“Dual-beam versus Single-beam Depth Profiling: Same Sample in Same Instrument”, S. V. Baryshev, N. G. Becker, A. V. Zinovev, C. E. Tripa, and I. V. Veryovkin, *Rapid Comm. Mass Spectrom.*, **27**(24), 2828–2832 (2013)

“High sensitivity sputter neutral mass spectrometry – Sputtering of neutral mixed clusters from gold–aluminum alloys”, B. V. King, J. F. Moore, I. V. Veryovkin, M. J. Pellin, *Nucl. Instrum. Methods B*, **317**(15), 115–120 (2013)

“Interfaces and Composition Profiles in Metal–Sulfide Nanolayers Synthesized by Atomic Layer Deposition”, E. Thimsen, S. V. Baryshev, A. B. F. Martinson, J. W. Elam, I. V. Veryovkin, M. J. Pellin, *Chem. Mater.*, **25**(3), 313–319 (2013)

“Measuring the roughness of buried interfaces by sputter depth profiling”, S. V. Baryshev, J. A. Klug, A. V. Zinovev, C. E. Tripa, Q. Peng, J. W. Elam and I. V. Veryovkin, *Nanotechnology*, **24**, 015708 (2013)

“Characterization of surface modifications by white light interferometry: applications in ion sputtering, laser ablation, and tribology experiments”, S. V. Baryshev, R. A. Erck, J. F. Moore, A. V. Zinovev, C. E. Tripa, I. V. Veryovkin, *J. Visualized Experiments: JoVE* **72**:e50260 (2013)

High-resolution secondary ion mass spectrometry depth profiling of nanolayers”, S. V. Baryshev, A. V. Zinovev, C. E. Tripa, M. J. Pellin, Q. Peng, J. W. Elam, I. V. Veryovkin, *Rapid Comm. Mass Spectrom.*, **26**(19), 2224–2230 (2012)

“White light interferometry for quantitative surface characterization in ion sputtering experiments”, S. V. Baryshev, A. V. Zinovev, C. E. Tripa, R. A. Erck, and I. V. Veryovkin, *Appl. Surf. Sci.*, **258**, 6963-6968 (2012)

"RIMS analysis of ion induced fragmentation of molecules sputtered from an enriched U₃O₈ matrix," D. Willingham, M. R. Savina, K. B. Knight, M. J. Pellin and I. D. Hutcheon, *J. Radioanal. Nucl. Chem.* **296** 407-412 (2013)

Crystal Growth, Structure, Phase Relationships, and Magnetic Properties of Transition Metal Substituted $Mn_{1-x}Bi$ Compounds

Srinivasa Thimmaiah, Qisheng Lin, and Gordon J. Miller
Ames Laboratory and Iowa State University, Ames, Iowa 50011

Program Scope:

The main objectives of this program are to design and develop new methodologies to understand structure-bonding-property relations among complex intermetallics through exploratory synthesis, structure determination, and electronic structure calculations. The chemical bonding in metal-rich phases generally does not follow classical valence rules. Across the periodic table, metals and semimetals that have different sizes, electronegativities, and valence orbitals can be combined to produce intermetallics that display a wide range of distinct physical and chemical properties, e.g. metallic conductors, semiconductors, superconductors, itinerant magnets, thermoelectrics, magnetocaloric materials, strongly correlated electron materials, catalysts, and hydrogen storage materials. Our present appreciation and expectations of what is important in the stability, structure, and bonding of intermetallic phases evolves from synthetic explorations ranging from Zintl (valence) compounds between the active metals and the *p*-elements to Hume-Rothery (nearly free electron-like) intermetallics constituted from late *d*-elements.

Recent Progress

We recently started exploring possible substitutional effects of late transition metals (TM = Fe, Co, Ni, Zn, Rh, between 2 to 10 at.%) for Mn in the low-temperature MnBi phase (LT-MnBi) for synthesizing new materials with useful magnetic properties like high Curie temperature and saturation magnetization. This study is designed to enhance our understanding of structure-property relationships within such transition metal substituted MnBi phases. LT-MnBi is ferromagnetic with a Curie temperature (T_c) of 623 K with high uniaxial magnetocrystalline anisotropy. Additionally, its large coercivity at high temperatures is comparable to $Nd_2Fe_{14}B$. Therefore, LT-MnBi and possible derivatives have enormous potential as a rare-earth-free permanent magnetic material for high temperature applications. LT-MnBi crystallizes in the hexagonal NiAs structure type (*B8*-type) in which Bi atoms form a hexagonal close packed arrangement and Mn atoms occupy all octahedral interstitial sites. All trigonal bipyramidal (*tbp*) sites in the Bi substructure are completely empty. LT-MnBi undergoes peritectic decomposition at 628 K to yield the high-temperature phase, $Mn_{1.08}Bi$ (HT-MnBi), with 24 % lower saturation magnetization compared to LT-MnBi. The enrichment of Mn in HT-MnBi may be due to the partial filling of *tbp* sites. So, one goal of this effort is examine partial filling of the vacant *tbp* sites in LT-MnBi with different transition metals so as to study issues of phase stability and

effects on magnetic behavior. Moreover, such substitutions could result in unprecedented superstructures related to NiAs-type structures.

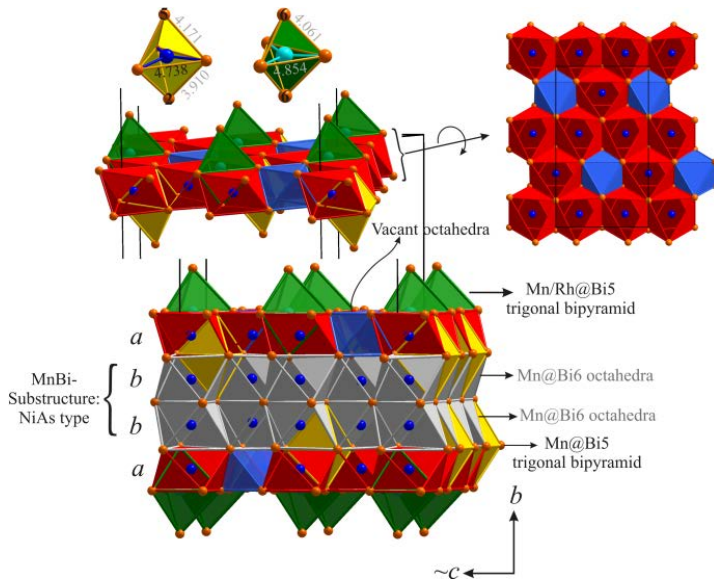


Figure 1: Crystal structure of Rh-doped MnBi phase. The structure is an intergrowth of NiAs and Ni₂In sub-units. Mn, Mn/Rh and Bi atoms are shown as blue, cyane and orange, respectively.

Single crystals of TM-doped Mn_{1+x}Bi phases were grown using Bi as a self-flux. During this exploratory synthesis effort, we have able to grow a single crystal of HT-MnBi. Single crystal structure refinement revealed that HT-MnBi crystallizes in the trigonal space group $P3_212$, and adopts a new structure type, whose composition is Mn₅₁Bi₄₈ per unit cell (Mn_{1.063}Bi). We also confirmed the slight enrichment of Mn compared to LT-MnBi, an effect which is due to (i) partial substitution of Mn atoms in certain *tbp* sites (located in planes of Bi atoms) in an ordered manner; and (ii) consequent formation of ordered vacancies at certain octahedral holes (Mn site) in the structure. We

discovered similar behavior for Rh-doped Mn_{1+x}Bi, see Figure 1 and text below. HT-MnBi adopts a $2a \times 2a \times 6c$ superstructure of LT-MnBi and belongs to the NiAs/Ni₂In family of structures. Preliminary magnetic measurements indicate that the Curie temperature is well above room temperature, and the coercive field of an unaligned sample is ~ 150 Oe at room temperature.

Another new member of the NiAs/Ni₂In family was observed when MnBi was doped with Rh. The Rh-doped Mn_{1+x}Bi compound crystallizes in the orthorhombic crystal system, with a refined composition of Mn_{66.4}Rh_{1.6}Bi₆₄ per unit cell (Mn_{1.038}Rh_{0.025}Bi). Its lattice parameters are related to those of LT-MnBi (a_h and c_h) as follows: $a_o \approx 2a_h$, $b_o \approx 4c_h$ and $c_o \approx 2\sqrt{3}a_h$. The deviation from stoichiometric 1:1 composition arises due to partial substitution of Mn and Rh atoms on the *tbp* sites and ordered Mn octahedral vacancies, similar to HT-MnBi discussed above. Rh substitution was confirmed by Wavelength-Dispersive X-Ray Spectroscopic (WDS) analysis and found to be 4 at.%. According to preliminary magnetic measurements Mn_{1.038}Rh_{0.025}Bi has a T_c of 425 K, but its magnetization (emu/g) dropped by 25% compared to LT-MnBi.

Fibers with multi-scale morphologies and a completely different crystal structure were observed for Co-doped MnBi. The needle-shaped crystals adopt a new orthorhombic crystal structure with characteristic one-dimensional MnBi columns $\frac{1}{\infty} \{ \text{Mn/Co@Mn}_5\text{@Bi}_5 \}$ exhibiting

pseudo-fivefold rotational symmetry. Atomic arrangements in the structure mimic double-walled nanotubes. The inner shell is composed of Mn/Co centered Mn pentagonal antiprisms, which are surrounded by a second larger shell of Bi pentagonal antiprisms. Structure refinement indicates that Co atoms are statistically mixed with Mn atoms at the center of the antiprisms. However, further analyses are required to confirm the exact position of Co atoms. The WDS analysis confirms the presence of Co in the structure, which was found to be 5-7 at.%. Electronic structure calculations were performed using “Mn₆Bi₅” as a model structure. These calculations showed an anisotropic band structure indicating one-dimensional metallic behavior.

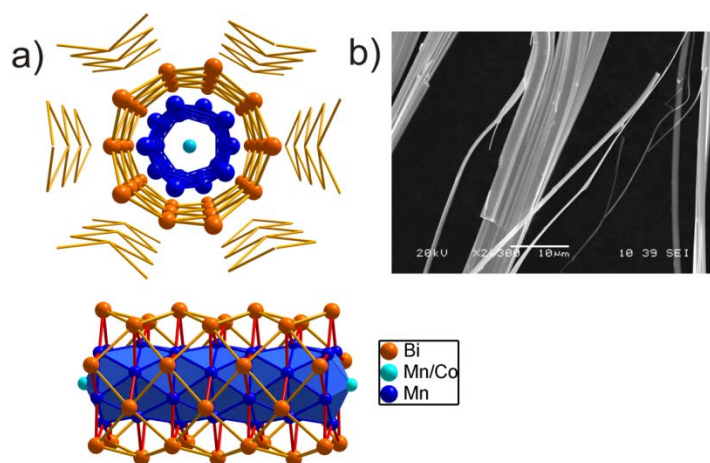


Figure 2: (a) crystal structure of Co-doped MnBi, double-walled nanotube arrangement of Mn and Bi atoms (b) SEM micrograph showing fibrous morphology.

Future Plans

We shall continue our exploratory syntheses of other transition metal substituted MnBi phases and their subsequent structural characterization to identify new members of NiAs/Ni₂In family of compounds. We shall also extend the exploration to main-group elements substituting for Mn as well. Future studies will address the impact of crystal structure on the magnetic properties of recently uncovered transition metal doped Mn_{1+x}Bi compounds. We will also focus on growing larger single crystals with the

aid of different low melting fluxes for physical property measurements. Additionally, electronic structure calculations will be performed to understand the site preference of the substituents, chemical bonding throughout the crystal structure, and overall structural stability with respect to competing phases.

Crystal growth and magnetic property measurements are part of a collaborative effort with Prof. M.J. Kramer and Prof. Canfield, Ames Laboratory.

References

1. J.D. Corbett, “Exploratory Synthesis: The Fascinating and Diverse Chemistry of Polar Intermetallic Phases,” *Inorganic Chemistry*, **49**, 13 (2010).
2. G.J. Miller, “Metal-Rich Chemistry of the *d*-Metals,” *Comprehensive Inorganic Chemistry*, **2**, 311 (2013).
3. S. Lidin, Superstructure Ordering of Intermetallics: B8 Structures in the Pseudo-Cubic Regime, *Acta Cryst.* **B54**, 97, (1998).

4. T. Chen and W.E. Stutius, "The phase transformation and physical properties of the MnBi and Mn_{1.08}Bi compounds," *IEEE Trans. Magn.*, **MAG-10**, 581 (1974).
5. J. Cui *et.al.*, Thermal stability of MnBi magnetic materials, *J. Phys.: Condens. Matter*, **26**, 064212 (2014).

Selected Publications (2012-2014)

V. Smetana, Q. Lin, D.K. Pratt, A. Kreyssig, M. Mehmet, J.D. Corbett, A.I. Goldman, G.J. Miller, "A Sodium-Containing Quasicrystal: Using Gold To Enhance Sodium's Covalency in Intermetallic Compounds", *Angew. Chem. Int. Ed.*, **51**, 12699 (2012)

Q. Lin, V. Smetana, G.J. Miller, J.D. Corbett, "Conventional and stuffed Bergman-type phases in the Na-Au-T (T = Ga, Ge, Sn) systems: syntheses, structures, coloring of cluster centers, and Fermi sphere-brillouin zone interactions", *Inorg. Chem.*, **51**, 8882 (2012)

S. Thimmaiah and G.J. Miller, "Rhombohedrally Distorted γ -Au_{5-x}Zn_{8+y} Phases in the Au-Zn System," *Inorg. Chem.*, **52**, 1328 (2013).

V. Smetana, G.J. Miller, J.D. Corbett, Polyclusters and Substitution Effects in the Na-Au-Ga System: Remarkable Sodium Bonding Characteristics in Polar Intermetallics, *Inorg. Chem.*, **52**, 12502 (2013).

W. Xie, S. Thimmaiah, J. Lamsal, J. Liu, T.W. Heitmann, D. Quirinale, A.I. Goldman, V. Pecharsky, G.J. Miller, β -Mn-Type Co_{8+x}Zn_{12-x} as a Defect Cubic Laves Phase: Site Preferences, Magnetism, and Electronic Structure," *Inorg. Chem.*, **52**, 9399 (2013).

Q. Lin, T. Mishra, J.D. Corbett, "Hexagonal-Diamond-like Gold Lattices, Ba and (Au,T)₃ Interstitials, and Delocalized Bonding in a Family of Intermetallic Phases Ba₂Au₆(Au,T)₃ (T = Zn, Cd, Ga, In, or Sn)", *J. Am. Chem. Soc.*, **135**, 11023 (2013).

S.L. Samal, A. Pandey, D.C. Johnston, J.D. Corbett, "Y₃MnAu₅: Three Distinctive *d*-Metal Functions in an Intergrown Cluster Phase" *J. Am. Chem. Soc.*, **135**, 910 (2013).

W. Xie, G.J. Miller, New Co-Pd-Zn γ -Brasses with Dilute Ferrimagnetism and Co₂Zn₁₁ Revisited: Establishing the Synergism between Theory and Experiment, *Chem. Mater.*, **26**, 2624 (2014)

A. Provino, P. Manfrinetti, K. A. Gschneidner Jr., S.K. Dhar, D.L. Schlagel, T.A. Lograsso, G.J. Miller, S. Thimmaiah, H. Wang, A.M. Russell, A. Becker. Y. Mudryk, Self-assembled nano- to micron-size fibers from molten R₁₁Ni₄In₉ intermetallics, *Acta Materialia* **73**, 27 (2014).

S.L. Samal, A. Pandey, D.C. Johnston, J.D. Corbett, G.J. Miller, "Taking Advantage of Gold's Electronegativity in R₄Mn_{3-x}Au_{10+x}(R = Gd or Y; 0.2 ≤ x ≤ 1)" *Chem. Mater.*, **26**, 3209 (2014)

J A. Jesche, R.W. McCallum, S. Thimmaiah, J.L. Jacobs, V. Taufour, A. Kreyssig, R.S. Houk, S.L. Bud'ko, P.C. Canfield, "Giant magnetic anisotropy and tunnelling of the magnetization in Li₂(Li_{1-x}Fe_x)N", *Nature Comm.* **5**, 4333/1 (2014)

Toward Hierarchically Structured Functional Nanocomposites

Ting Xu^{1,2,3}, Miquel Salmeron^{1,2}, Paul Alivisatos^{1,2,3}, Yi Liu^{1,4}, Jean Fréchet^{1,3}

¹ Materials Sciences Division, Lawrence Berkeley National Laboratory,

² Department of Materials Sciences & Engineering, UC Berkeley,

³ Department of Chemistry, UC Berkeley,

⁴ Molecular Foundry, Lawrence Berkeley National Laboratory

Program Scope

Nanoparticles (NPs) with controlled size, shape, and chemical composition can be readily synthesized and have demonstrated various new phenomena due to quantum confinement¹. Hierarchical assemblies of nanoparticles with different composition and sizes lead to new functionalities due to coupling effects². As a new family of functional materials, they provide great opportunities to address several grand challenges in energy applications, such as precise control over atoms, electrons and photons, and new materials with tailored properties. Our long-term goal is to generate hierarchically structured, functional nanocomposites with tunable optical and electronic properties for energy applications. To this end, current and future research will be focused on the following aspects: 1) 3-D hierarchical assemblies of large, plasmonically active NPs, 2) complex NP assemblies via external confinement, and 3) structure-property correlations in NP assemblies.

Recent Progress

Directed nanoparticle assembly with long-range order or tailored geometry over large areas is requisite to effectively harness the collective properties of NP arrays. Recently, we show that by using saw-toothed faceted or lithographically patterned substrates, thin films of supramolecular nanocomposites containing 3-D NP arrays with long-range order can be readily obtained⁴. NP arrays, aligned normal to the ridge direction of the saw-toothed substrate with orientation parameters of up to 0.92, are fabricated in films with thicknesses, t , < 200 nm on saw-toothed sapphire substrate with an average pitch size \sim 5 times of the periodicity of the supramolecular nanocomposite (Fig. 1). The 3-D nanostructure of the supramolecular nanocomposite on the faceted substrate is similar to that on a flat surface where 1-D NP chains form a distorted hexagonal lattice with a distortion factor of \sim 0.75 (Fig. 1). Substrates containing lithographically patterned trenches are also employed to impose lateral

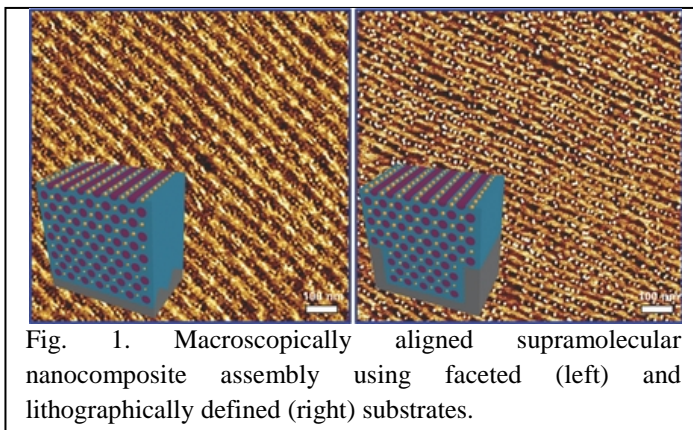


Fig. 1. Macroscopically aligned supramolecular nanocomposite assembly using faceted (left) and lithographically defined (right) substrates.

confinement on the supramolecular nanocomposite. Highly aligned 3-D NP arrays with orientation parameters > 0.86 can be achieved in films with $t < 350$ nm on a trench pattern that is 50 nm in depth and 125 nm in width. As the ratio of the trench width to the lateral periodicity of the nanocomposite increases above 11, the long-range order of the NP arrays deteriorates. The trench pattern also affects the spatial organization of the 3-D NP arrays normal to the surface and the distortion factor of the hexagonal lattice is 0.87 as opposed to 0.75 observed in the same films on a saw-toothed surface or a flat substrate. Our studies show that either faceted or lithographically patterned surfaces are effective in guiding NP assemblies parallel and normal to the substrate surface and can lead to hierarchically structured nanocomposite thin films with tunable directional properties over macroscopic distances to meet material needs for a wide range of NP-based devices.

In addition to substrate guided assembly, we have also recently demonstrated that geometric confinement of the supramolecular nanocomposite induce polymer chain frustration and symmetry breaking, which result in a wide range of nanostructures that are unique from bulk and thin film nanocomposite morphologies. Specifically, by subjecting the composites to 2-D cylindrical confinement with anodic

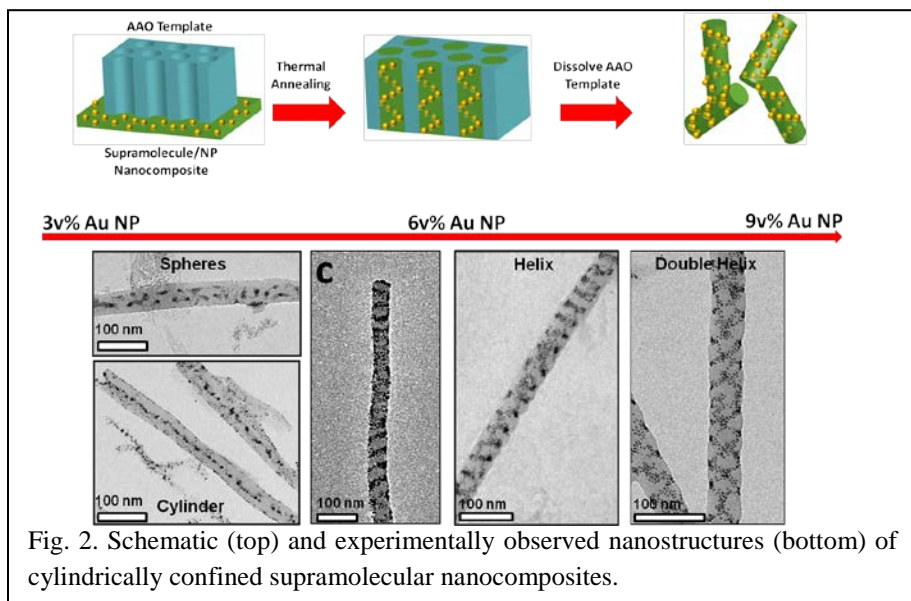


Fig. 2. Schematic (top) and experimentally observed nanostructures (bottom) of cylindrically confined supramolecular nanocomposites.

aluminum oxide membranes, a range of new NP assemblies such as stacked rings, and single and double helices can be readily obtained with precisely defined morphology by simply varying the NP loading (Fig. 2). These recent studies provide simple yet versatile routes to obtain hierarchical NP assemblies with tunable 3-D structures for the investigation of structure-property relationships in this new family of functional materials.

For cylindrically confined supramolecular nanocomposites, we recently developed a dark field scattering microscopy technique for property characterization in close collaboration with the metamaterial program at MSD. The circular dichroism (CD) signal of a single Au NP helix can be recorded using an inverted optical microscope equipped with a dark-field objective. The white light from a halogen lamp passes through a polarizer followed by a quarter waveplate which converts linear polarization to circular polarization. By rotating the fast axis of the quarter wave-plate set to -45° and 45° with respect to the axis of the polarizer, left-handed and right-

handed circular polarization can be generated respectively and coupled into a dark-field reflector and objective to excite the structure. Then the CD spectrum can be recorded by subtracting the spectrum for right-handed circular polarization from that taken with left-handed circular polarization. Initial measurement results are in good agreement with numerical simulation of the structure (Fig. 3).

Future Plans

For future studies, we aim to establish design principles to control the 3-D assembly of NPs of different sizes in supramolecular thin films to obtain hierarchically structured nanocomposites with tunable optoelectronic properties. We aim to conduct further studies on the thermodynamics and commensurability effects of the self-assembly process of supramolecular nanocomposites in thin films. When appropriate, we will seek collaborations with theoreticians to develop systematic understanding of phase behavior of supramolecular nanocomposite thin films under external confinement. We will also characterize coupling of plasmons and excitons within ordered arrays of nanoparticles. The structural control demonstrated here will be applied to optimize the inter-particle transfer and fabricate assemblies of heterogeneous nanoparticles to funnel the transport along an engineered path. Their optoelectronic properties will be investigated using state of the art nanooptics recently developed in the Weber-Bargioni and Salmeron groups.⁵ Together, these studies will lay the foundation for the design and development of next generation optoelectronically active materials.

References

- (1) Murray, C. B.; Norris, D. J.; Bawendi, M. G. *Journal of the American Chemical Society* 1993, *115*, 8706-8715.
- (2) Talapin, D. V.; Murray, C. B. *Science* 2005, *310*, 86-89.
- (3) Kao, J.; Bai, P.; Lucas, J. M.; Alivisatos, A. P.; Xu, T. *Journal of the American Chemical Society* 2013, *135*, 1680-1683.
- (4) Kao, J.; Jeong, S.-J.; Jiang, Z.; Lee, D. H.; Aissou, K.; Ross, C. A.; Russell, T. P.; Xu, T. *Advanced materials* 2014, *26*, 2777-81.

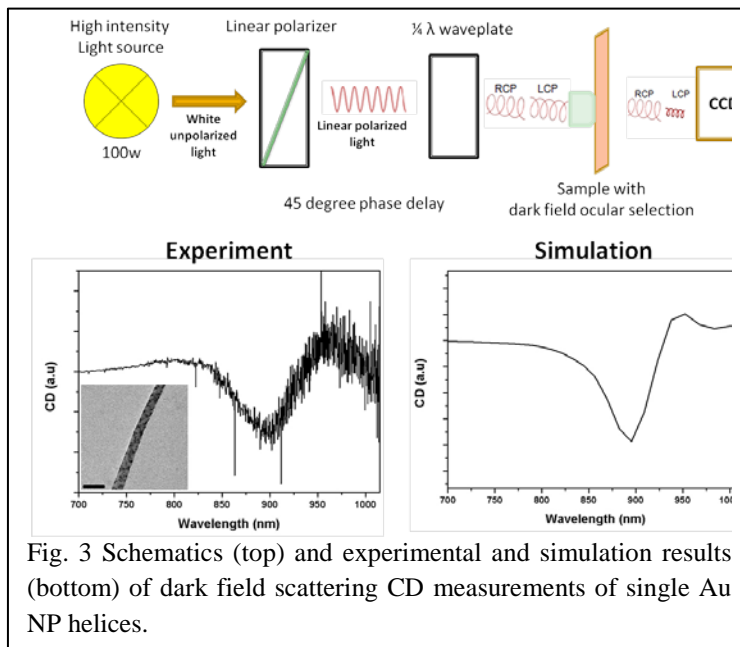


Fig. 3 Schematics (top) and experimental and simulation results (bottom) of dark field scattering CD measurements of single Au NP helices.

(5) Bao, W.; Melli, M.; Caselli, N.; Riboli, F.; Wiersma, D. S.; Staffaroni, M.; Choo, H.; Ogletree, D. F.; Aloni, S.; Bokor, J.; Cabrini, S.; Intonti, F.; Salmeron, M. B.; Yablonovitch, E.; Schuck, P. J.; Weber-Bargioni, A. *Science* 2012, 7, 1317-1321.

Publications

- [1] J. Kao, K. Thorkelsson, P. Bai, Z. Zhang, C. Sun and T. Xu. Rapid Fabrication of Hierarchically Structured Supramolecular Nanocomposite Thin Films in One Minute, *Nature Communications*, **2014**, ASAP.
- [2] J. Kao, S. J. Jeong, Z. Jiang, D. H. Lee, K. Aissou, C. A. Ross, T. P. Russell, and T. Xu. Direct 3-D Nanoparticle Assemblies in Thin Films via Topographically Patterned Surfaces, *Advanced Materials*, **2014**, 26 (18), 2777-2781
- [3] K. Thorkelsson, J. H. Nelson, A. P. Alivisatos, and T. Xu. End-to-End Alignment of Nanorods in Thin Films, *Nano Letters*, **2013**, 13 (10), 4908-4913
- [4] J. Kao, P. Bai, J. M. Lucas, A. P. Alivisatos, and T. Xu, Size-Dependent Assemblies of Nanoparticle Mixtures in Thin Films, *Journal of the American Chemical Society*, **2013**, 135 (5), 1680-1683.
- [5] B. J. Rancatore, C. E. Mauldin, J. M. J. Fréchet, and T. Xu, Small Molecule-Guided Thermoresponsive Supramolecular Assemblies, *Macromolecules*, **2012**, 45 (20), 8292-8299.
- [6] J. Kao, P. Bai, V. P. Chuang, Z. Jiang, P. Ercius, and T. Xu, Nanoparticle Assemblies in Thin Films of Supramolecular Nanocomposites, *Nano Letters*, **2012**, 12 (5), 2610-2618.
- [7] K. Thorkelsson, A. Mastroianni, P. Ercius, T. Xu, Direct Nanorod Assembly Using Block Copolymer-based Supramolecules, *Nano Letters*, **2012**, 12, 498.

Understand Organic/Inorganic Interface Toward Electroactive Nanocomposites

Ting Xu^{1,2,3}, Lin-Wang Wang¹, Miquel Salmeron^{1,2}, Paul Alivisatos^{1,2,3}, Yi Liu^{1,4}, Tanja Cuk^{1,3}

¹ Materials Sciences Division, Lawrence Berkeley National Laboratory,

² Department of Materials Sciences & Engineering,

³ Department of Chemistry, UC Berkeley,

⁴ Molecular Foundry, Lawrence Berkeley National Laboratory

Program Scope

The organic/inorganic interface governs the nanocomposite properties since the surface area increases substantially as the nanoparticle size is reduced. The nanoparticle surface passivation, i.e. the structure and energetic alignment of the organic and inorganic components, is a key to modulate the charge separation and transfer and the macroscopic optoelectronic properties. Current progress towards addressing the tasks includes fundamental understanding of the nanoparticle/organic semiconductor interface [1], optimization of optoelectronic properties with high level of tenability [2], investigation of trap states that influence optoelectronic properties of surfaces and films [3].

Recent Progress

Controlling the structure of colloidal nanocrystals (NCs) and nanocrystal/organic molecules interface is a key to the generation of their complex functionality. This requires an understanding of the NC surface at the atomic level. The structure of colloidal PbS-NC passivated with oleic acid has been studied theoretically and experimentally. We started from the consideration on the reaction steps involved in the typical synthetic process of metal chalcogenides NCs [4]

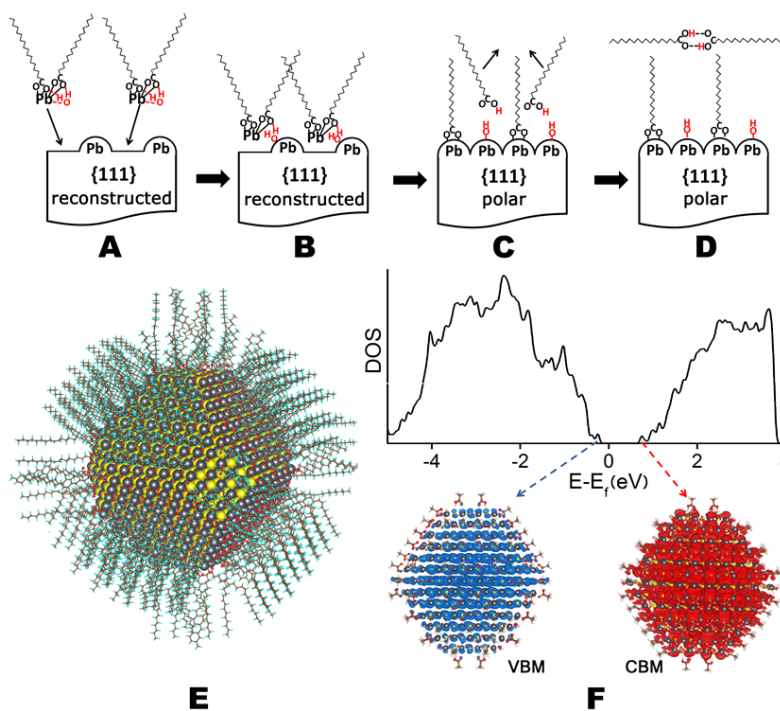


Fig. 1. Model of PbS-NC in colloidal solution. (A-D) Multistep process for building up the (111) facets of PbS-NC: (A) Pb(OA)₂·H₂O precursors approach the nonpolar and stoichiometric (111) facets. (B) Pb ions bind to surface vacancies. (C) One of the two OA⁻ in each Pb(OA)₂·H₂O complex is removed due to steric effects, and the water molecule dissociates to provide an OH⁻ group to the surface, and H⁺ for desorbing OA⁻. (D) The desorbed OAH molecules dimerize in the solvent. (E) Calculated atomic structure of a 5nm diameter NC passivated with OA⁻ and OH⁻ ligands. (F) Electron density of states, showing the valence band maximum (VBM) and conduction band minimum (CBM) levels, of a NC passivated with truncated oleic acid alkyl chains.

on example of PbS-NCs and performed *ab initio* electronic structure calculations on relevant sub-systems. The colloidal PbS-NCs are synthesized by dissolving PbO in hot oleic acid. One of the by-products of the reaction is water, which was proposed to remain as free molecules in the solution [5, 6]. Our calculations however show and FTIR measurements confirm that it is energetically more favorable for water to bind to the Pb-precursor. Thus, the first reaction step can be written as: $PbO + 2OAH \rightarrow Pb(OA)_2 \cdot \cdot H_2O$ where OAH denotes oleic acid. Metal chalcogenide nanocrystals typically contain an excess of metal ions that should be passivated by anionic ligands to satisfy the charge neutrality condition. However, it is impossible to passivate every excess metal ion with the sterically demanding organic ligands. We showed that water molecules from the precursors play important role in the NC synthesis process. Water provides small OH⁻ groups that passivate the NC surface together with big organic ligands (Fig.1A-D). X-ray photoelectron spectroscopy confirms that OH⁻ groups present on the PbS-NC surface. Using this knowledge, we constructed complete atomic structure of the passivated colloidal PbS-NC (Fig.1E). The constructed model is in agreement with all available spectroscopic and chemical experiments. Furthermore, the long oleyl chains were replaced with shorter ethyl groups, which is the same as the acetic acid ligand exchange. This exchange allows direct *ab initio* calculations of PbS-NC electronic structure (Fig.1F). Our model, along with the existing observations of NC surface termination and passivation by ligands, helps to explain and predict the properties of NCs and their assemblies.

Starting with ordered, self-assembled films of PbS nanocrystals (NC) capped with oleate and hydroxyl, we perform a ligand exchange with tetrathiafulvalenetetracarboxylate (TTFTA) to fabricate thin films of PbS-TTFTA core-shell semiconductor nanoparticles. We fabricate a field-effect transistor (Fig.2a-c) from the covalently functionalized colloidal PbS nanoparticles. Following experimental results from cyclic voltammetry and ambient pressure X-ray photoelectron spectroscopy, we postulate a near-resonant alignment of the PbS-NC 1Sh

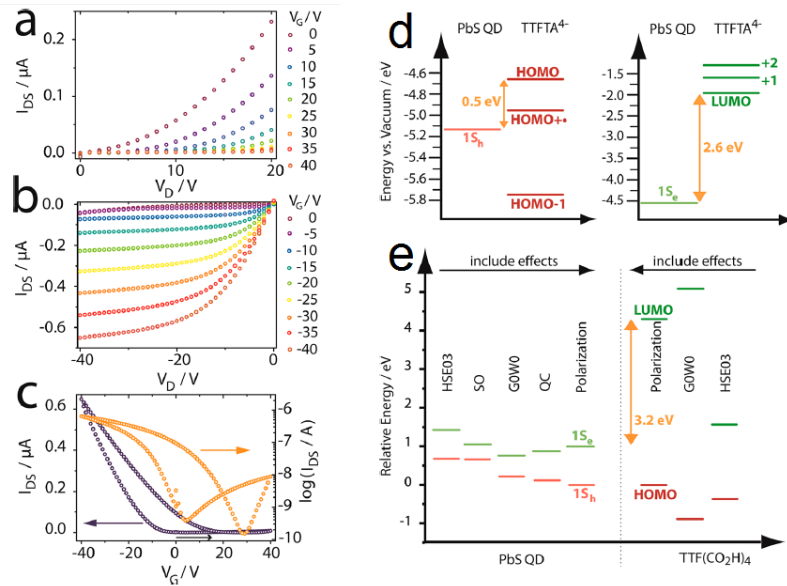


Fig. 2. Field-effect transistor characteristics of thin films of 9.8 nm PbS-TTFTA. (a, b) Positive and negative source-drain sweeps, with the applied gate voltages for an individual sweep denoted next to each color. (c) Transconductance under a constant bias of 5 V. Left and right axes are linear and logarithmic plots of the same measurement, respectively. The black arrow indicates the beginning and direction of the closed loop scan. (d) Comparison of energy levels for PbS nanoparticles and free TTFTA⁺ derived by experiment. The left graph displays the region near the 1Sh state, whereas the right side represents the 1Se region. (e) Calculated energy levels of a 9.8 nm PbS nanoparticle (left) and a covalently bound TTF(CO₂H)₄ molecule (right). The final results are the offsets next to the dashed line, which are obtained by starting with a basic Heyd-Scuseria-Ernzerhof functional (HSE03) and consecutively taking into account spin-orbit (SO) effects, the GW approximation (G0W0), quantum confinement (QC), and polarization effects wherever applicable.

state and HOMO level of the TTFTA (Fig.2d), which is confirmed by atomistic calculations (Fig.2e). Considering the large width of interparticle spacing, we observe an abnormally high field-effect hole mobility, which we attribute to the postulated resonance. In contrast to nanoparticle devices coupled through common short-chained ligands, our system maintains a large degree of macroscopic order as revealed by X-ray scattering. This provides a different approach to the design of hybrid organic-inorganic nanomaterials, circumvents the problem of phase segregation, and holds for versatile ways to design ordered, coupled nanoparticle thin films.

Using Kelvin probe force microscopy (KPFM) we studied the local charge trapping states at the SiO_2 – oligothiophene interface in a field effect transistor (FET), where SiO_2 is the gate dielectric (Fig. 1). KPFM reveals surface potential inhomogeneities within the oligothiophene monolayer, which correlate with its structure. A large peak of trap states with energies in the oligothiophene’s bandgap due to hydroxyl groups is present at the oxide surface. We show that these states are successfully eliminated by pre-adsorption of a layer of (3-Aminopropyl) triethoxysilane (APTES). Time resolved surface potential transient measurements further show that the charge carrier injection in the non-passivated FET contains two exponential transients, due to the charge trapping on the oxide surface and in the bulk oxide, while the APTES passivated FET only has a single exponential transient due to the bulk oxide. The results demonstrate that APTES is a good SiO_2 surface passivation layer to reduce trap states while maintaining a hydrophilic surface, pointing out the importance of dielectric surface passivation to bridge the gap between soft materials and electronic devices.

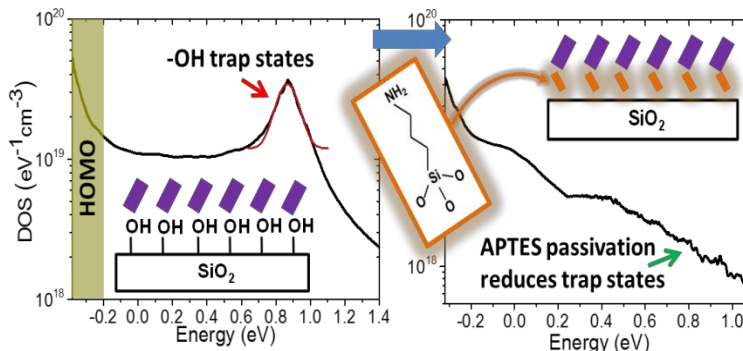


Fig. 3. The presence of trap states due to $-\text{OH}$ groups on the surface of SiO_2 . After passivation with the APTES monolayer, these trap states are removed.

hydroxyl groups is present at the oxide surface. We show that these states are successfully eliminated by pre-adsorption of a layer of (3-Aminopropyl) triethoxysilane (APTES). Time resolved surface potential transient measurements further show that the charge carrier injection in the non-passivated FET contains two exponential transients, due to the charge trapping on the oxide surface and in the bulk oxide, while the APTES passivated FET only has a single exponential transient due to the bulk oxide. The results demonstrate that APTES is a good SiO_2 surface passivation layer to reduce trap states while maintaining a hydrophilic surface, pointing out the importance of dielectric surface passivation to bridge the gap between soft materials and electronic devices.

Future Plans

In the future, we are going to investigate trap states in thin films of quantum dots. It is also important to understand an influence of colloidal intrinsic defects in NC on their optoelectronic properties. One of the most important goals is to investigate and understand functional small molecules, such as organic semiconductors that can be used for functionalization of NC. The small molecules can be readily used to construct supramolecules to introduce properties complementary to those of the nanoparticles and to modulate the local environment of nanoparticles.

Reference

- [1] Zherebetskyy D., Scheele M., Zhang Y., Bronstein N, Thompson C., Britt D., Salmeron M., Alivisatos P., Wang L.-W., “Hydroxylation of the Surface of PbS Nanocrystals Passivated with Oleic Acid“, *Science*, 2014, 10.1126/science.1252727.
- [2] Scheele M., Hanifi D., Zherebetskyy D., Chourou S. T., Axnanda S., Rancatore B. J., Thorkelsson K., Xu T., Liu Z., Wang L.-W., Liu Y., Alivisatos P. „PbS Nanoparticles Capped with Tetrathiafulvalenetetracarboxylate: Utilizing Energy Level Alignment for Efficient Carrier Transport“ *ACS Nano* 2014, 8, 2532-2540.
- [3] Zhang Y., Ziegler D., Salmeron M. “Charge Trapping States at the SiO₂-Oligothiophene Monolayer Interface in Field Effect Transistors Studied by Kelvin Probe Force Microscopy” *ACS Nano* 2014, 7, 8258-8265.
- [4] Murray B., Sun S., Gaschler W., Doyle H., Betley T. A., Kagan C. R., “Colloidal synthesis of nanocrystals and nanocrystal superlattices” *IBM J. Res. Develop.* 2001, 45, 47–56.
- [5] Steckel J. S., Yen B. K., Oertel D. C., Bawendi M. G., “On the mechanism of lead chalcogenide nanocrystal formation” *J. Am. Chem. Soc.* 2006, 128, 13032–13033.
- [6] Liu H., Owen J. S., Alivisatos A. P., “Mechanistic study of precursor evolution in colloidal group II-VI semiconductor nanocrystal synthesis” *J. Am. Chem. Soc.* 2007, 129, 305–312.

Publications

1. Zherebetskyy D., Scheele M., Zhang Y., Bronstein N, Thompson C., Britt D., Salmeron M., Alivisatos P., Wang L.-W., “Hydroxylation of the Surface of PbS Nanocrystals Passivated with Oleic Acid“, *Science*, **2014**, 10.1126/science.1252727.
2. Scheele M., Hanifi D., Zherebetskyy D., Chourou S. T., Axnanda S., Rancatore B. J., Thorkelsson K., Xu T., Liu Z., Wang L.-W., Liu Y., Alivisatos P. „PbS Nanoparticles Capped with Tetrathiafulvalenetetracarboxylate: Utilizing Energy Level Alignment for Efficient Carrier Transport“ *ACS Nano* **2014**, 8, 2532-2540.
3. Zhang Y., Ziegler D., Salmeron M. “Charge Trapping States at the SiO₂-Oligothiophene Monolayer Interface in Field Effect Transistors Studied by Kelvin Probe Force Microscopy” *ACS Nano* **2014**, 7, 8258-8265.
4. Scheele, M.; Engel, J. H.; Ferry, V. E.; Hanifi, D.; Liu, Y.; Alivisatos, A. P., Nonmonotonic Size Dependence in the Hole Mobility of Methoxide-Stabilized PbSe Quantum Dot Solids. *Acs Nano* **2013**, 7, 6774-6781.
5. Zhu, Y.; Kuang, H.; Xu, L.; Ma, W.; Peng, C.; Hua, Y.; Wang, L.; Xu, C., Gold nanorod assembly based approach to toxin detection by SERS. *Journal of Materials Chemistry* **2012**, 22, 2387.
6. Rancatore, B. J.; Mauldin, C. E.; Fréchet, J. M. J.; Xu, T., Small Molecule-Guided Thermoresponsive Supramolecular Assemblies. *Macromolecules* **2012**, 45, 8292-8299.
7. Bao, W.; Melli, M.; Caselli, N.; Riboli, F.; Wiersma, D. S.; Staffaroni, M.; Choo, H.; Ogletree, D. F.; Aloni, S.; Bokor, J.; Cabrini, S.; Intonti, F.; Salmeron, M. B.; Yablonovitch, E.; Schuck, P. J.; Weber-Bargioni, A., Mapping local charge recombination heterogeneity by multidimensional nanospectroscopic imaging. *Science* **2012**, 338, 1317-1321.
8. Zhang, Y.; Hanifi, D.; Lim, E.; Chourou, S.; Alvarez, S.; Pun, A.; Hexemer, A.; Ma, B.; Liu, Y. “Enhancing the Performance of Solution-Processed n-Type Organic Field-Effect Transistors by Blending with Molecular ‘Aligner’”, *Adv. Mater.* **2014**, 26, 1223-1228.
9. Geyer, F. L.; Pun, A.; Hanifi, D.; Bunz, U. H. F.; Liu, Y. “Growth of Rylene Diimide Crystalline Layers on Aminoalkyltriethoxysilane-Monolayers for Organic Field Effect Transistor Applications”, *J. Mater. Chem. C.* **2013**, 1, 6661-6666.

Physical Chemistry of Inorganic Nanostructures

Paul Alivisatos, Laboratory Director Materials Sciences Division Lawrence Berkeley National Laboratory Berkeley (LBNL)

Stephen Leone, Senior Faculty Scientist, LBNL

Peidong Yang, Senior Faculty Scientist, LBNL

Program Scope

Nanoscience offers unprecedented opportunities to study novel materials and tailor their properties for applications such as solar energy conversion. Highly efficient energy conversion devices require an integrated system of nanomaterials, each of which is designed to perform a specialized function. A fundamental understanding of how light absorption, charge transfer and chemical reactions occur in the individual and in between components is crucial to design efficient integrated systems. Emphasizing the synthesis and integration of these inorganic nanomaterial components and the subsequent characterization of their physical properties, this program has several goals: 1) advancement in the synthetic control of nanocrystals and nanowires for their use in integrated energy conversion systems; 2) establishment of measurement techniques and technology measure charge generation and transport 3) measurement and interpretation of the electronic and chemical interactions of nanostructured materials at interfaces. To achieve these goals, physical measurements such as x-ray transient absorption spectroscopy and single-particle fluorescence will be applied to synthetically controlled systems. Insight gained from these studies will be used to develop fully integrated nanoscale devices for energy conversion applications. The combined expertise in synthesis, characterization, and device applications allows continuous feedback between materials development, fundamental insight, and device performance, providing rapid progress to be made toward more efficient devices for energy conversion applications.

Recent Progress

Cation exchange reactions are reactions in which cations ligated within a nanocrystal host lattice are substituted with those in solution. This is a powerful tool for obtaining acute control over composition and phase in nanocrystal synthesis and for making epitaxial semiconductor heterostructures often infeasible to obtain via traditional methods. The heterostructures include such axial superlattice nanorods and core-shell nanocrystals and nanowires¹. We are currently working towards understanding the mechanism of cation exchange in nanodots, nanorods, and nanowires. To this end, we

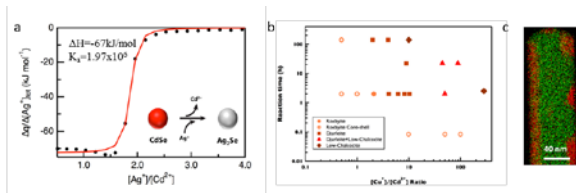


Figure 1. a. Isothermal calorimetry titration data for the exchange from CdSe QD to Ag₂Se QD. b. Cu_xS crystal structure as a function of time and cation ratios. c. partially converted Cu₂S/CdS nanowire

have used isothermal titration calorimetry to probe the thermodynamics of CdSe quantum dots (QD) exchanged with Ag, which shows a single phase transition and allows for the quantification of enthalpy and equilibrium constant of the reaction. Furthermore, we also conducted a study on the cation exchange in CdS nanowires to form Cu₂S nanowires. Interestingly, the crystal phase of the resulting Cu₂S can be controlled through time and Cu²⁺ concentration as shown in

figure 1b. Cation exchange Figure 1c illustrates our finding that Cu₂S to CdS nanowires was found to occur through island formation and coalescence.

In-situ liquid-cell TEM provides a unique and powerful tool to probe and visualize dynamic processes with nanometer resolution in a liquid environment, and represents one of the newly developed technologies under this program. Used initially to examine the electron beam-induced growth of Pt nanoparticles², the method has recently been extended to image the dynamics of soft materials, namely double stranded DNA connecting Au nanocrystals³.

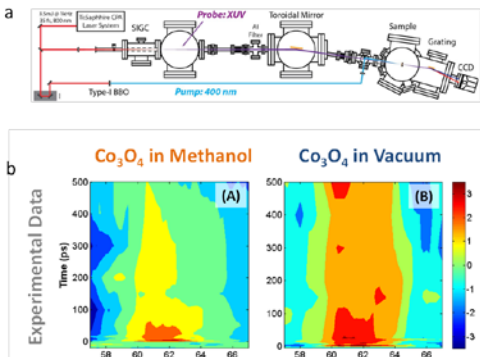


Figure 2. a. Transient X-Ray absorption setup . b. Transient cobalt M-edge absorption in methanol and in vacuum

the charge transfer dynamics of this material at a catalyst-liquid interface⁵. In the presence of liquid methanol, the photoexcited M_{2,3}-edge of Co₃O₄ thin film returns to ground state with a time constant of 597 ± 37 ps, which is more than 3 times faster than the 1.95 ± 0.33 ns observed in vacuum, suggesting a hole transfer from O 2p orbital of Co₃O₄ to the adsorbed methanol layer.

Charge transfer at the semiconductor-ligand interface of quantum dots was investigated via ensemble and single particle fluorescence lifetime measurements to understand the charge transfer of quantum dots. A study of individual CdSe/CdS QDs and a new class of chalcogenidometalate (ChaM) ligands, specifically Sn₂S₆⁴⁻ or In₂Se₄²⁻, revealed an increased density of charge-trapping sites and an increased stabilization of surface-trapped charges for the ChaM-capped QDs as compared to the traditional Soleyamine-capped QDs⁶. Next, ensemble studies of the quantum yield and luminescence lifetime of CdSe/CdS QDs as a function of the coverage of a hole accepting ligand ferrocene were investigated. The driving force and coupling parameters in the Marcus charge transfer model were tuned by changing the redox potential of the hole acceptor and modulating the thickness of the CdS energy Results agree well with predicted models.

Future Plans

To probe the dynamics of cation-exchange reactions, the conversion of CdSe nanocrystals into Ag₂Se will be investigated using the graphene liquid cell TEM technique. The Z-contrast difference between Ag₂Se and CdSe will differentiate the reactant and product species. A multichannel flow cell will enable several reactants to be introduced into the viewing area during imaging, enabling observation of the reaction's

onset. We will also study how the effect of growth directions of CdS nanowires affects the cation exchange mechanism by conducting in situ solid state cation exchange within the TEM on CdS nanowires. The graphene liquid cell will allow for the imaging of the same wire before, during and after the cation exchange reaction. PL lifetime measurements will then be performed on devices processed using cation exchange chemistry to probe the dynamics of charge generation and transfer at the Cu₂S/CdS interface.

Transient X-ray absorption will be applied to probe real-time charge transfer across a semiconductor-semiconductor heterojunction such as TiO₂-Si and a semiconductor-catalyst heterojunction such as TiO₂-Co₃O₄. In the former system, electron-hole pairs will be generated in both semiconductors. It is anticipated that electrons will rapidly transfer from the n- TiO₂ to the p-Si as a result of the p-n junction's built-in potential. In the TiO₂-Co₃O₄ heterojunction, the electron/hole occupation levels on the Ti and Co atoms and their oxidation states can be measured simultaneously by following the M-edge absorption of Co and Ti.

Single particle fluorescence lifetime measurements will further elucidate the heterogeneity in fluorescence lifetimes of CdSe/CdS-ferrocene hole donor-acceptor system. Further studies on the effect of driving force will be investigated by examining the hole transfer rate from the quantum dot to a library of ferrocene ligands that span a range of redox potentials. From this systematic series of measurements, we hope to produce a Marcus parabola for charge transfer in colloidal semiconductor nanocrystals.

References

1. J. B. Rivest and P. K. Jain, "Cation Exchange on the Nanoscale: an Emerging Technique for New Material Synthesis, Device Fabrication, and Chemical Sensing," *Chem Soc Rev*, 42, 89-96 (2013).
2. J. M. Yuk, J. Park, P. Ercius, K. Kim, D.J. Hellebusch, M.F. Crommie, J.Y. Lee, A. Zettl, A.P. Alivisatos, "High-Resolution EM of Colloidal Nanocrystal Growth Using Graphene Liquid Cells," *Science*, 336, 6077, 61-4 (2012).
3. Q. Chen, J. M. Smith, J. Park, K. Kim, D. Ho, H. I. Rasool, A. Zettl, and A. P. Alivisatos. "3D Motion of DNA-Au Nanoconjugates in Graphene Liquid Cell Electron Microscopy," *Nano Lett*, 13, 9, 4556-4561 (2013)
4. C.-M. Jiang, L. R. Baker, J. M. Lucas, J. Vura-Weis, A. P. Alivisatos, and S. R. Leone, "Characterization of Photo-induced Charge Transfer and Hot Carrier Relaxation Pathways in Spinel Cobalt Oxide (Co₃O₄)," *in preparation*.
5. L. R. Baker, C.-M. Jiang, S. T. Kelly, J. M. Lucas, J. Vura-Weis, M. K. Gilles, A. P. Alivisatos, and S. R. Leone, "Charge Carrier Dynamics of Photoexcited Co₃O₄ in methanol: Extending High Harmonics Generation Transient Absorption Spectroscopy to Liquid Environments," *in preparation*
6. Cordones, A. A., Scheele, M., Alivisatos, A. P. & Leone, S. R. Probing the Interaction of Single Nanocrystals with Inorganic Capping Ligands: Time-Resolved Fluorescence from CdSe-CdS Quantum Dots Capped with Chalcogenidometalates. *J. Am. Chem. Soc.* 134, 18366-18373 (2012)

Publications

1. D. K. Britt, Y. Yoon, P. Ercius, T. Ewers, A. P. Alivisatos, "Hexameric Octahedral Clusters of PbSe Nanocrystals, Grown from Amorphous Lead(II) Carboxylate Nanoparticles," *Chemistry of Materials*, 25, 2544-2548 (6/2013).
2. Cordones, K. L. Knappenberger, Jr., and S. R. Leone, "Linking On-State Memory and Distributed Kinetics in Single Nanocrystal Blinking," *J. Phys. Chem. B: Paul F. Barbara Memorial*, 117, 4241 (2013).
3. A. Cordones and S. R. Leone, "Mechanisms for Charge Trapping in Single Semiconductor Nanocrystals Probed by Fluorescence Blinking," *Chem. Soc. Rev.*, 42, 3209 (2013).
4. H. Gao, A. Fu, S. C. Andrews, P. Yang, "Cleaved-Coupled Nanowire Lasers", *Proc. Natl. Acad. Sci. USA*, 110, 865 (2013).
5. C. Hahn, A. A. Cordones, S. C. Andrews, H. Gao, A. Fu, S. R. Leone, and P. Yang, "Effect of Thermal Annealing in Ammonia on the Properties of InGaN Nanowires with Different Indium Concentrations," *J. Phys. Chem. C.*, 117, 3627 (2013).
6. B Liu, H. M. Chen, C. Liu, S. C. Andrews, C. Hahn, P. Yang, "Large Scale Synthesis of Transition-metal Doped TiO₂ Nanowires with Low Overpotential," *J. Am. Chem. Soc.*, 135 (27), 9995–9998 (2013). DOI: 10.1021/ja403761s.
7. C.Liu, J. Tang, H. Chen, B. Liu, P. Yang "A Fully Integrated Nanosystem of Semiconductor Nanowires for Direct Solar Water Splitting", *Nano. Lett.*, 13, 6, 2989– 2992 (2013). DOI: 10.1021/nl401615t.
8. M.J. Polking, P. K. Jain, Y. Bekenstein, U. Banin, O. Milio, R. Ramesh and A. P. Alivisatos "Controlling Localized Surface Plasmon Resonances in GeTe Nanoparticles Using an Amorphous-to-Crystalline Phase Transition," *Physical Review Letters*, 111, 3 (7/2013).
9. B. J. Beberwyck & A.P. Alivisatos, "Ion Exchange Synthesis of III-V Nanocrystals," *JACS*, 134 (49), 19977-19980 (2012). DOI:10.1021/ja309416c.
10. T. J. Bixby, A. A. Cordones, and S. R. Leone, "CdSe/ZnS Quantum Dot Intermittency in the Semiconducting Polymer N,N'-diphenyl-N,N'-bis(3-methylphenyl)-(1,1'-biphenyl)-4,4'-diamine (TPD)," *Chem. Phys. Lett.*, 521, 7 (2012).
11. A. Cordones, M. Scheele, A. P. Alivisatos, S. R. Leone, "Probing the Interaction of Single Nanocrystals with Inorganic Capping Ligands: Time-Resolved Fluorescence from CdSe-CdS Quantum Dots Capped with Chalcogenidometalates," *J. Am. Chem. Soc.*, 134, 44, 18366-18373 (2012).
12. Y. J. Hwang, C. Hahn, B. Liu, P. Yang, "Photoelectrochemical Properties of TiO₂ Nanowire Arrays: A Study on the Dependence of Length and Atomic Layer Deposition Coating," *ACS Nano*, 6, 5060 (2012).
13. Y. J. Hwang, C. H. Wu, C. Hahn, H. E. Jeong, P. Yang, "Si/InGaN Core/Shell Hierarchical Nanowire Arrays and their Photoelectrochemical Properties," *Nano Lett.*, 12, 1678, 2012.
14. P. K. Jain, D. Ghosh, R. Baer, E. Rabani, A.P. Alivisatos, "Near-Field Manipulation of Spectroscopic Selection Rules on the Nanoscale," *Proceedings of the National Academy of Sciences*, 109, 21, 8016-19 (2012).

15. C. Liu, J. Sun, J. Tang, P. Yang, "Zn-Doped P-Type Gallium Phosphide Nanowire Photocathodes From A Surfactant-Free Solution Synthesis," *Nano. Lett.*, 12, 5407 (2012).
16. H. Schlicke, D. Ghosh, L-K. Fong, H. L. Xin, H. Zheng and A. P. Alivisatos, "Selective Placement of Faceted Metal Tips on Semiconductor Nanorods," *Angew. Chem.*, Pub.online Nov. 28, 2012. DOI: 10.1002/ange.201205958.

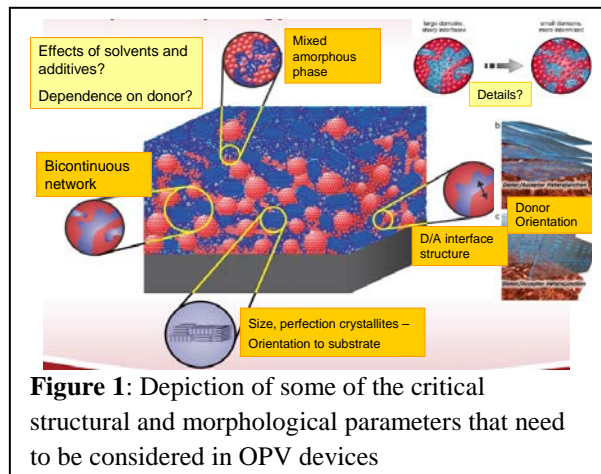
***UNIVERSITY GRANT
PROJECTS***

Control of Interface- and Mesoscopic Structure in High Performance Organic Solar Cells: Towards a Predictive Device Paradigm

Harald Ade, Dept. of Physics, NCSU, Raleigh, NC 27695

Program Scope

Tremendous effort is currently focused on the development of high performance OPV cells, since they have numerous attractive technological characteristics including low manufacturing cost, mechanical flexibility, and low weight.¹ While significant progress has been made in the synthesis and processing of organic semiconductors for solar cell applications, progress has been largely by “trial and error” and there is a pressing need for comprehensive *understanding* of the devices.



Over the last few years, the morphology paradigm has become vastly more complex. While still evolving, it now includes: 1) considerations of *hierarchies*, 2) possibility of *multiple phases*, 3) impact of *average purity* of domains in relation to *size*,²⁻⁷ 4) wetting layers, 5) orientation of polymer crystallites with respect to the electrode interface, and 6) *molecular orientation relative to the D/A interface*.^{8,9} Fig. 1 is capturing some of this complexity.

The Ade group has pioneered polarized Resonant Soft X-ray Scattering (R-SoXS/P-SoXS) in combination with grazing incidence wide angle x-ray scattering (GIWAXS), atomic force microscopy (AFM), and light intensity device characterization on a number of systems.^{4,5,8,10,11} We exhaustively investigate some of the highest performing systems as well as some suitable lesser performing model systems to devise generalized optimization strategies based on data and knowledge. We seek a detailed understanding of the performance *bottlenecks* as well as elucidation of the controlling materials aspects to help facilitate a transition from a “*trial and error*” approach in a OPV field to a *constructionist* approach to device design and fabrication.

Recent Progress

A recent breakthrough by us has shown that preferential polymer orientation (*edge-on* versus *face-on*) relative to the discrete or dominant D/A interface can be determined in complex bulk-heterojunction devices and can be critical to performance. (*Nature Photonics*).¹² A summary of the results is depicted in Figure 2.

Furthermore, preliminary transient absorption spectroscopy (TAS) experiments in a collaboration between the Ade and Gundogdu groups have revealed differences in charge dynamics and energetics for samples with different molecular orientation. Photo-induced absorption (PIA) features near 1.6-1.7 eV (Fig. 3), which are due to polaron pair/charge transfer

state formation, are more intense in the “face-on” sample than the “edge-on” sample, clearly indicating that charge dynamics proceeds faster in the “face-on” sample. Furthermore, the dominant PIA feature is at different energies, indicating that the CT states are different and that coupling across the interface matters.

Furthermore, soft x-ray scattering can be used to measure the relative composition variations in domains, i.e. *purity/molecular mixing*, a critical parameter that impacts bimolecular recombination and thus the fill factor (FF) as well as the short circuit current (J_{sc}) of devices. We have demonstrated for the first time that the crystalline coherence length observed with GIWAXS can set the size scale of the compositional variations in the devices.¹³ These studies also reveal that the hierarchical structure observed is not beneficial for device performance in this particular case. Rather, the composition variations observed at the two different lengthscales are anti-correlated and the less pure fraction is limiting the FF and thus device performance.

Future Plans

We essentially plan to execute the research as initially proposed, with an emphasis on:

1. Investigating how miscibility and solubility/solvent characteristics determine device morphology and thus device performance,
2. elucidating the special nature of FTAZ, a unique material that has exhibited excellent performance with FF above 54% for films as thick as 1,000 nm, and
3. establishing processing rules for solution-cast small molecule devices

Regarding 1), we hypothesize based on a limited, initial data set that fullerene miscibility in the donor polymer that is either very low or near the percolation threshold leads to best devices. We will acquire systematic data in order to further develop a model.

Regarding 2), we are working with Profs. You (UNC - Chapel Hill) and Neher (Potsdam) to systematically study a set of copolymers that include the FTAZ moiety. This initial study is almost complete. It will be complemented with a series of devices with well controlled

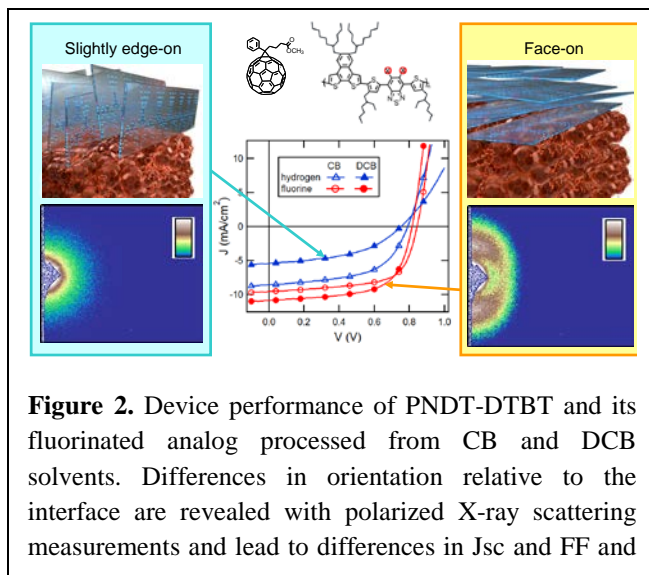


Figure 2. Device performance of PNDT-DTBT and its fluorinated analog processed from CB and DCB solvents. Differences in orientation relative to the interface are revealed with polarized X-ray scattering measurements and lead to differences in J_{sc} and FF and

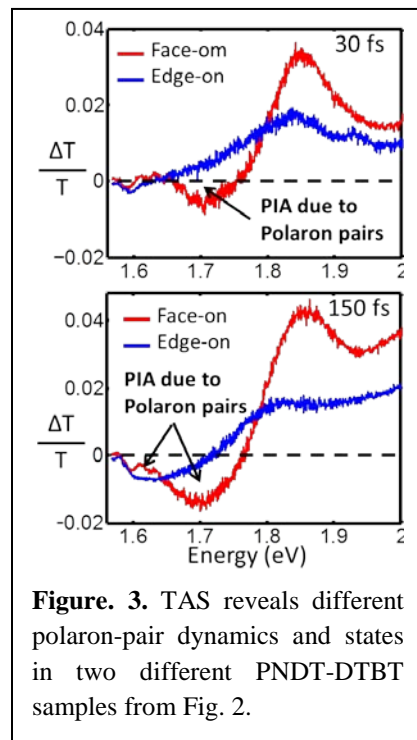


Figure 3. TAS reveals different polaron-pair dynamics and states in two different PNDT-DTBT samples from Fig. 2.

morphology and variable thickness. Both these studies follow work that systematically investigated the molecular weight dependence.

Regarding 3), we are collaborating with Profs. Bazan and Nguyen from UCSB to study a number of highly promising small molecule materials.

References

- (1) Graetzel, M.; Janssen, R. A. J.; Mitzi, D. B.; Sargent, E. H. *Nature* **2012**, *488*, 304-312.
- (2) Ye, L.; Zhang, S.; Ma, W.; Fan, B.; Guo, X.; Huang, Y.; Ade, H.; Hou, J. *Adv. Mater.* **2012**, *24*, 6335–6341.
- (3) Yang, L.; Tumbleston, J. R.; Zhou, H.; Ade, H.; You, W. *Energy Environ. Sci.* **2012**, DOI: 10.1039/C2EE23235A.
- (4) Yan, H.; Collins, B. A.; Gann, E.; Wang, C.; Ade, H.; McNeill, C. R. *ACS Nano* **2012**, *6*, 677-688.
- (5) Collins, B. A.; Li, Z.; Tumbleston, J. R.; Gann, E.; McNeill, C. R.; Ade, H. *Advanced Energy Materials* **2013**, *3*, 65-74.
- (6) Bartelt, J. A.; Beiley, Z. M.; Hoke, E. T.; Mateker, W. R.; Douglas, J. D.; Collins, B. A.; Tumbleston, J. R.; Graham, K. R.; Amassian, A.; Ade, H.; Fréchet, J. M. J.; Toney, M. F.; McGehee, M. D. *Adv. Energy Mater.* **2012**, DOI: 10.1002/aenm.201200637.
- (7) Lyons, B. P.; Clarke, N.; Groves, C. *Energy Environ. Sci.* **2012**, *5*, 7657-7663.
- (8) Ma, W.; Tumbleston, J. R.; Wang, M.; Gann, E.; Huang, F.; Ade, H. *Adv. Energy Mater.* **2013**, *3*, 864–872.
- (9) Collins, B. A.; Cochran, J. E.; Yan, H.; Gann, E.; Hub, C.; Fink, R.; Wang, C.; Schuettfort, T.; McNeill, C. R.; Chabiny, M. L.; Ade, H. *Nat. Mater.* **2012**, *11*, 536–543.
- (10) Tumbleston, J. R.; Stuart, A. C.; Gann, E.; Yan, H.; Collins, B. A.; You, W.; Ade, H. *Adv. Funct. Mater.* **2013**, DOI: 10.1002/adfm.201300093.
- (11) Stuart, A. C.; Tumbleston, J. R.; Zhou, H.; Li, W.; Liu, S.; Ade, H.; You, W. *J. Am. Chem. Soc.* **2013**, *135*, 1806–1815.
- (12) Tumbleston, J. R.; Collins, B. A.; Yang, L.; Stuart, A. C.; Gann, E.; Ma, W.; You, W.; Ade, H. *Nat Photon* **2014**, *8*, 385-391.
- (13) Ma, W.; Tumbleston, J. R.; Ye, L.; Wang, C.; Hou, J.; Ade, H. *Advanced Materials* **2014**, n/a-n/a.

Publications (since 2013 only)

1. J. R. Tumbleston, B. A. Collins, L. Yang, A. C. Stuart, E. Gann, W. Ma, W. You, and H. Ade, *Nat Photon* **8**, 385-391 (2014). (Front Cover 4/26/2014)
2. S. Albrecht, J. R. Tumbleston, S. Janietz, I. Dumsch, S. Allard, U. Scherf, H. Ade, and D. Neher, *Physical Chemistry Letters* **5**, 1131-1138 (2014).
3. Y. Huang, W. Wen, S. Mukherjee, H. Ade, E. J. Kramer, and G. C. Bazan, *Advanced Materials*, 10.1002/adma.201400497 (2014)
4. R. Steyrleuthner, R. Di Pietro, B. A. Collins, F. Polzer, S. Himmelberger, M. Schubert, Z. Chen, S. Zhang, A. Salleo, H. Ade, A. Facchetti, and D. Neher, *Journal of the American Chemical Society* **136**, 4245-4256 (2014).
5. M. Schubert, B. A. Collins, H. Mangold, I. A. Howard, W. Schindler, K. Vandewal, S. Roland, J. Behrends, F. Kraffert, R. Steyrleuthner, Z. Chen, K. Fostiropoulos, R. Bittl, A.

- Salleo, A. Facchetti, F. Laquai, H. W. Ade, and D. Neher, *Advanced Functional Materials*, 10.1002/adfm.201304216 (2014).
6. W. Ma, J. R. Tumbleston, L. Ye, C. Wang, J. Hou, and H. Ade, *Advanced Materials*, 10.1002/adma.201400216 (2014)
 7. F. Liu, W. Zhao, J. R. Tumbleston, C. Wang, Y. Gu, D. Wang, A. L. Briseno, H. Ade, and T. P. Russell, *Advanced Energy Materials* **4**, 10.1002/aenm.201301377 (2014)
 8. W. Li, L. Yang, J. R. Tumbleston, L. Yan, H. Ade, and W. You, *Advanced Materials*, 10.1002/adma.201305251 (2014)
 9. X. He, S. Mukherjee, S. E. Watkins, M. Chen, T. Qin, L. Thomsen, H. W. Ade, and C. R. McNeill, *The Journal of Physical Chemistry C*, 10.1021/jp501222w (2014)
 10. X. Guo, M. Zhang, W. Ma, L. Ye, S. Zhang, S. Liu, H. Ade, F. Huang, and J. Hou, *Advanced Materials*, 10.1002/adma.201400411 (2014)
 11. E. Buchaca-Domingo, A. J. Ferguson, F. C. Jamieson, T. McCarthy-Ward, S. Shoaee, J. R. Tumbleston, O. G. Reid, L. Yu, M. B. Madec, M. Pfannmoller, F. Hermerschmidt, R. R. Schroder, S. E. Watkins, N. Kopidakis, G. Portale, A. Amassian, M. Heeney, H. Ade, G. Rumbles, J. R. Durrant, and N. Stingelin, *Materials Horizons* **1**, 270-279 (2014)
 12. S. Albrecht, K. Vandewal, J. R. Tumbleston, F. S. U. Fischer, J. D. Douglas, J. M. J. Fréchet, S. Ludwigs, H. Ade, A. Salleo, and D. Neher, *Advanced Materials* **26**, 2533-2539 (2014).
 13. M. Zhang, X. Guo, W. Ma, S. Shaoqing Zhang, L. Huo, H. Ade, J. Hou, *Advanced Materials*, 2089-2095 (2014)
 14. P. Westacott, J. R. Tumbleston, S. Shoai, S. Fearn, J. Bannock, J. Gilchrist, S. Heutz, J. deMello, M. Heeney, H. Ade, J. Durrant, D. S. McPhaila, and N. Stingelin, *Energy Environ. Sci.* **6**, 2756-2764 (2013)
 15. J.R. Tumbleston, A. Gadisa, Y. Liu, B.A. Collins, E. Samulski, R. Lopez, and H. Ade. *ACS Applied Materials & Interfaces.* **5**, 8225-8230 (2013)
 16. Y. Wu, Z. Li, W. Ma, Y. Huang, L. Huo, X. Guo, M. Zhang, H. Ade, and J. Hou, *Advanced Materials* **25**, 3449–3455 (2013)
 17. W. Ma, L. Ye, S. Zhang, J. Hou, and H. Ade, *J. Mat. Chem. C* **1**, 5023-5030 (2013)
 18. D. Qian, W. Ma, Z. Li, X. Guo, S. Zhang, L. Ye, H. Ade, Z. A. Tan, and J. Hou, *J. Am. Chem. Soc.* **135**, 8464-8467 (2013)
 19. H. Yan, C. Wang, A. R. McCarn, and H. Ade, *Phys. Rev. Lett.* **110**, 177401 (2013)
 20. W. Ma, J. Tumbleston, M. Wang, F. Huang, and H. Ade, *Adv. Energy Mater.* **3**, 864-872 (2013). (Inside Cover)
 21. J. R. Tumbleston, A. C. Stuart, E. Gann, H. Yan, B. A. Collins, W. You, and H. Ade, *Adv. Funct. Mater.* **23**, 3463-3470 (2013)
 22. J. A. Bartelt, Z. M. Beiley, E. T. Hoke, W. R. Mateker, J. D. Douglas, B. A. Collins, J. R. Tumbleston, K. R. Graham, A. Amassian, H. Ade, J. M. J. Fréchet, M. F. Toney, and M. D. McGehee, *Adv. Energy Mater.* **3**, 364-337 (2013)
 23. A. C. Stuart, J. R. Tumbleston, H. Zhou, W. Li, S. Liu, H. Ade, and W. You, *J. Am. Chem. Soc.* **135**, 1806-1815 (2013)
 24. L. Yang, J. R. Tumbleston, H. Zhou, H. Ade, and W. You, *Energy Environ. Sci.* **6**, 316-326 (2013)
 25. C. R. McNeill and H. Ade, *J. Mater. Chem. C* **1**, 187-201 (2013)
 26. B. A. Collins, Z. Li, J. R. Tumbleston, E. Gann, C. R. McNeill, and H. Ade, *Adv. Energy Mater.* **3**, 65-74 (2013). (Front Cover)

High Efficiency Biomimetic Organic Solar Cells

M.A. Baldo, *Dept. of Electrical Engineering and Computer Science, MIT*

T. Van Voorhis, *Dept. of Chemistry, MIT*

Program Scope

Charge transfer (CT) states govern both charge generation and recombination losses in organic solar cells.^{1,2} Consisting of bound electron-hole pairs located on separate molecules, CT states are formed at donor-acceptor interfaces after the dissociation of excitons or from the recombination of charge.

CT states are also the basis of the latest generation of organic light emitting devices (OLEDs).³ Because they are not as tightly bound as typical molecular excitons, CT states behave more like inorganic quantum dots. They exhibit small splitting between their bright and dark spin states, such that thermal activation can allow ~100% of CT excitations to emit light. No heavy metal is required. Consequently, CT state emitters are promising for low cost, high efficiency lighting.

Our focus is studying the optimum size of CT states and understanding the spin mixing processes that contribute to light emission. These two phenomena are crucial to the rational design of CT states in solar cells and light emitting devices.

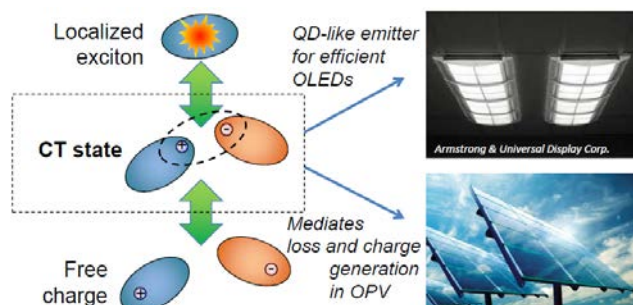


Fig. 1. CT states mediate the conversion between charge and localized excitons. They are crucial to the operation of solar cells and the latest generation of organic light emitting devices.

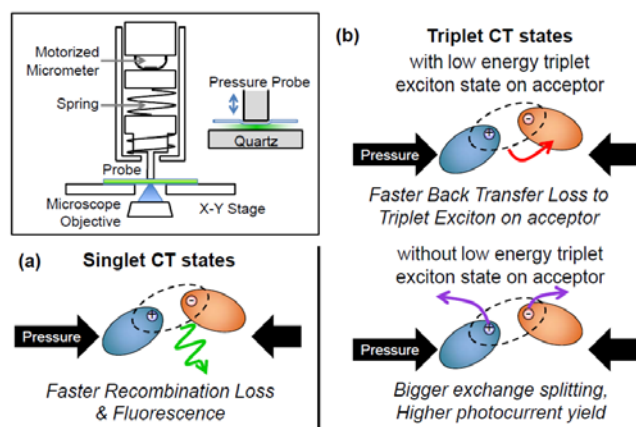


Fig. 2. (a-b) Schematic of expected changes in singlet and triplet CT states as a function of their size. The possible triplet dynamics are dependent on the presence of a triplet exciton quenching state on the donor or the acceptor. **(inset)** The measurement apparatus used to apply pressure to the films.

can be summarized as follows: singlet CT states can intersystem cross to the triplet CT state, dissociate

Recent Progress: Rational Design of CT states for solar cells.

We directly vary electron-hole spacing using external pressure and take particular note of the impact on CT spin dynamics; see Fig. 2. Spin dependence is a unique aspect of organic solar cells that arises due to electronic localization in organic materials, where exchange interactions define distinct spin 0 singlet and spin 1 triplet CT states. Indeed, spin controls all the crucial processes involving CT states. For example, it is possible to use spin engineering to turn off recombination losses through the triplet CT state. The spin dependent CT processes can be

into charge, or recombine because the ground state is typically also a singlet. The triplet CT state can dissociate into charge or reverse intersystem cross to the singlet state, but direct recombination of the triplet CT state to ground state is spin forbidden. However, triplet CT states can play a significant role in one potential major loss process, triplet back transfer, in which the triplet CT state relaxes to a lower energy excitonic triplet state on either the donor or the acceptor. This loss may be mitigated if the excitonic triplet has a higher energy. Both singlet and triplet channels are coupled by spin mixing processes, which vary according to the exchange splitting and the spin mixing element(s) of the Hamiltonian.

Key CT state recombination dynamics are shown in Fig. 3 as a function of CT state size. We study two donor-acceptor systems: m-MTDATA:t-Bu-PBD, which has a low energy triplet exciton acceptor state on t-Bu-PBD, and m-MTDATA:3TPYMB, which has no available triplet acceptor state. In general, the t-Bu-PBD system may provide a more accurate representation of a traditional organic solar cell system that is designed with maximum power output and minimal energetic separation between the optical absorption edge, defined by the singlet exciton, and the open circuit voltage, defined by the CT state.

To study recombination of the triplet CT state, we measure the lifetime and intensity of delayed fluorescence from the CT states. The delayed dynamics show significant deviation between the two material systems; see Figs 3(a) and (b).

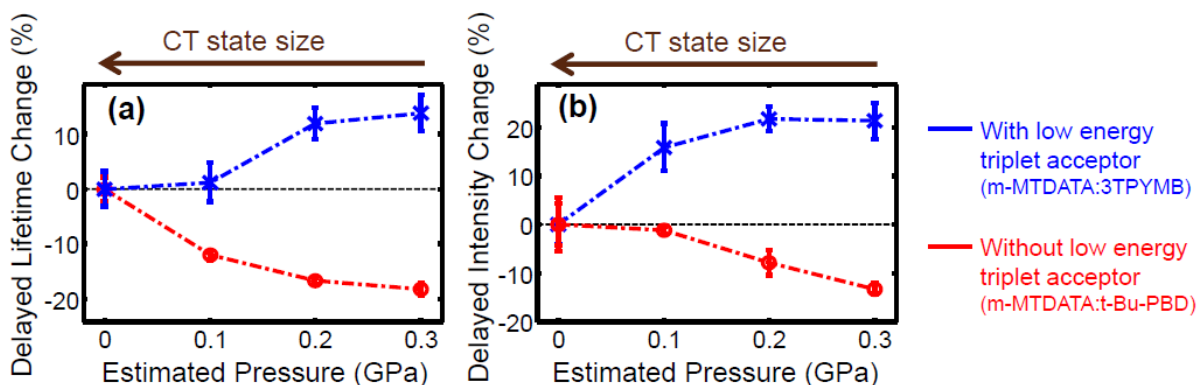


Fig. 3. Integrated (a) delayed lifetime and (b) intensity changes with applied pressure for the two exciplex systems. Blue data points are from the m-MTDATA:3TPYMB system; red are from the m-MTDATA:t-Bu-PBD. The delayed fluorescence quenching in m-MTDATA:t-Bu-PBD clearly indicates triplet back transfer.

In systems with low energy triplet acceptors, increasing the pressure significantly decreases the delayed lifetime and intensity. We attribute this to an increase in triplet back transfer loss: the CT states are drained through this loss channel due to better coupling with the localized t-Bu-PBD triplet (reflected in the decreased lifetime).

Next, we probe the CT state dynamics while under photovoltaic operation by monitoring the fluorescence and applying a magnetic field to the device. The magnetic field slows forward and reverse intersystem crossing rates by decreasing the number of triplet states involved in the singlet-triplet coupling.

We expect that slowing the intersystem crossing rate should increase the singlet CT state population and decrease the rate of ISC relative to fluorescence and thus increase the PL

quantum yield. Indeed, an increase in fluorescence under magnetic field (green dots) was observed in both material systems in Fig. 4(a) and (b). A striking difference occurs, however, when we examine the simultaneously extracted photocurrent for both of these materials. In the presence of a low energy triplet acceptor in the t-Bu-PBD system, the magnetic field effect on the photocurrent is also positive, *i.e.*, as the singlet CT population increases with applied field, the photocurrent simultaneously increases. This signifies that the photocurrent is more efficiently generated from the singlet CT state, confirming our observation of significant back transfer loss processes for the triplet CT states in this material system.

The photocurrent from the m-MTDATA:3TPYMB system shows the opposite effect, decreasing with applied magnetic field. As the singlet CT population increases under external magnetic field, triplet CT population decreases. Because the change in the photocurrent is negative with increasing applied field, we conclude that photocurrent is more effectively collected through the triplet CT state in the m-MTDATA:3TPYMB system. Indeed, photocurrent generation in m-MTDATA:3TPYMB is spin protected in the triplet state. There are no major loss processes since recombination to the ground state is spin-forbidden, and recombination to a triplet exciton is energetically unfavorable.

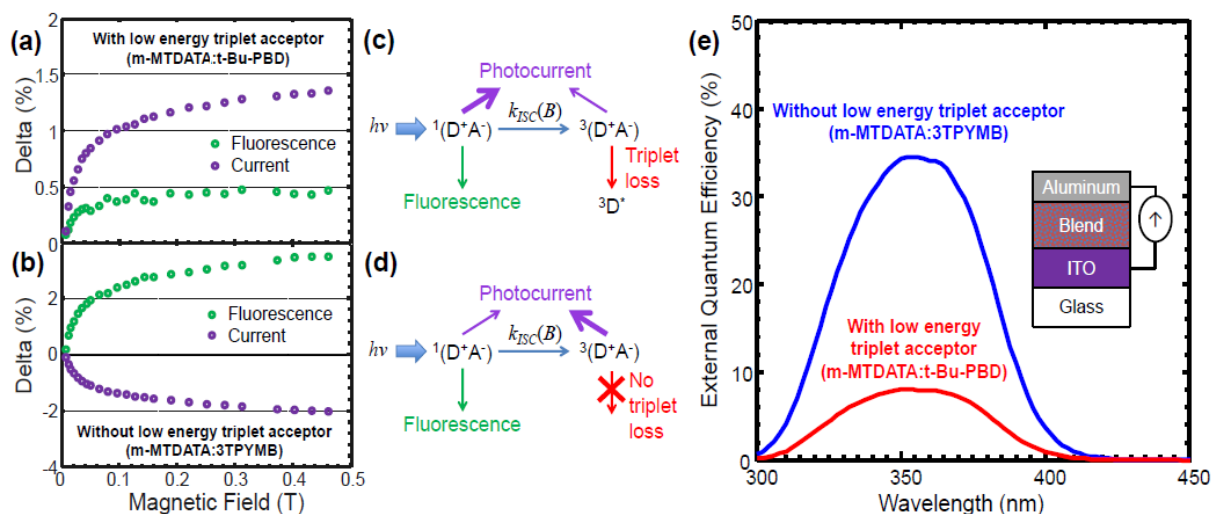


Fig. 4 (a) Magnetic field effect on fluorescence (green) and current (purple) for m-MTDATA:t-Bu-PBD. (b) Magnetic field effect on fluorescence (green) and current (purple) for m-MTDATA:3TPYMB. The negative current magnetic field effect indicates that photocurrent is more efficiently collected from the triplet state in this system. (c) The photocurrent collection process for m-MTDATA:t-Bu-PBD. The triplet back transfer (red) drains the triplet state and reduces collection efficiency from the triplet. (d) The photocurrent collection process for the m-MTDATA:3TPYMB. Without a triplet drain, photocurrent can be more efficiently collected from the triplet CT state than from the singlet CT state. (e) External quantum efficiencies of m-MTDATA:3TPYMB (blue) and m-MTDATA:t-Bu-PBD blends (red). The removal of triplet back transfer is associated with higher device performance in the 3TPYMB system.

Finally, we examine the effects on actual device performance in Fig. 4e. Drastic performance reductions due to the triplet back transfer are readily apparent in m-MTDATA:t-Bu-PBD. Allowing the triplets to generate photocurrent in the m-MTDATA:3TPYMB system is associated with a factor of four increase in the peak external quantum efficiency as compared to t-Bu-PBD, unequivocally demonstrating the necessity of minimizing triplet back transfer in future photovoltaic material designs.

In conclusion, open circuit voltage maximization requires that CT states must be as high in energy as possible - higher, in fact, than the triplet exciton. Thus, unless we find donor and acceptor materials with minimal splitting between singlet and triplet exciton states, the design of OPVs must confront energetically available excitonic triplets. Our work here demonstrates the ability to reduce CT state recombination and back transfer losses by maximizing the electron-hole spacing at the interface. By designing materials with physically large, delocalized CT states, both fluorescence and electron back transfer can be minimized.

Future plans

Thermally activated delayed fluorescence (TADF) materials are based on charge transfer states. They offer the potential for highly efficient, bright OLEDs without the expense of traditional phosphorescent materials. To achieve high efficiency devices, the distance between the electron and hole plays a significant role: decreasing the distance between the two increases the overall radiative rate, but the singlet-triplet exchange splitting increases, reducing the ability to extract energy from the triplet. We have directly monitored this effect by modulating the intermolecular spacing in a donor-acceptor exciplex system under applied pressure and demonstrate increased photoluminescence. To understand the mechanism of the triplet-singlet interconversion, we have also measured magnetic field effects on photoluminescence in both exciplex and single molecule TADF systems. To model the magnetic field effect, we assume that the singlet-triplet transitions are due to interactions with the magnetic nuclei and take place only after dissociation of the CT state into separated pairs of charges, which later recombine with their geminate partners. The simulation uses a semiclassical approach, which treats the coherent singlet-triplet oscillations on a quantum mechanical level and the incoherent hopping and relaxation transitions with standard stochastic rate constants based on physical intuition. We plan to complete the modeling of this system, to determine paths to faster spin mixing in TADF.

References

1. Lee, J. *et al.* Charge transfer state versus hot exciton dissociation in polymer-fullerene blended solar cells. *J. Am. Chem. Soc.* **132**, 11878–80 (2010).
2. Rao, A. *et al.* The role of spin in the kinetic control of recombination in organic photovoltaics. *Nature* **500**, 435–9 (2013).
3. Goushi, K., Yoshida, K., Sato, K. & Adachi, C. Organic light-emitting diodes employing efficient reverse intersystem crossing for triplet-to-singlet state conversion. *Nat. Photonics* **6**, (2012).

Publications supported under this program

1. S. R. Yost and T. Van Voorhis, “Electrostatic effects at organic semiconductor interfaces: A mechanism for “cold” exciton breakup”, *J. Phys. Chem C* **117**, 5617-5625 (2013).

Novel Pnictides with *d*- and *f*-Metals as Prospective Materials for Thermal Energy Conversion

P.I. Prof. Svilen Bobev, Department of Chemistry and Biochemistry, University of Delaware, Newark DE 19716

Program Scope

Our work under the auspices of DOE aims at gaining new knowledge through designed synthesis and thorough characterization (structure and properties) of NOVEL compounds with NOVEL properties. This work is motivated by two of the greatest challenges of our time – energy beyond fossil fuels and environment. Thermoelectric materials, which allow for the direct inter-conversion of electricity and heat and can be used in power generators or conversely, in solid-state refrigerators [1], can help reduce carbon emissions and utilize thermal energy, otherwise wasted, e.g. exhaust heat. The technology based on thermoelectricity is environmentally benign and has the potential for widespread applications; however, it is not yet part of the everyday life because of the low efficiencies. This limitation is a result of the unsatisfactory properties of almost all currently available materials.

The project we present herein focuses on synthetically very challenging intermetallic compounds the pnictogen elements phosphorous, arsenic, antimony and bismuth. These compounds are typically narrow-gap semiconductors and exhibit intermediate properties between those of typical insulators and typical metals [1,2]. Such structural characteristics provide unique combination of charge/heat transfer properties [1].

The motivation and the underlying principles for conducting these studies are based upon the formal electronic structure and can be described in terms of the Zintl concept. Zintl compounds are at the borderline between the valence compounds (typical insulators) and the intermetallic compounds (typical metals) and often exhibit intermediate properties. We seek new materials, which will be available through bulk processing, and which potentially will have high power factors ($S^2\sigma$) in desirable temperature ranges (subject to further optimization and materials engineering). If this can be accomplished while keeping good overall thermopower and low thermal conductivity, the thermoelectric efficiency of those materials may be brought closer to practically useful ranges.

From a more fundamental point of view, the established structural relationships can provide some logical and reasonable predictions for possible new compounds in the targeted systems, their likely structures and potential properties. Thus, our studies will help open an emergent field with great opportunities for groundbreaking discoveries and new knowledge.

Recent Progress

We have recently (simultaneous to other ongoing activities) embarked on studies of the $RE-Li-Pn$ systems ($RE = La - Nd, Y$; $Pn = P, As, Sb, Bi$), which have been partially investigated by Schuster and coworkers in the 1970s and 1980s [3]. They initially reported the existence of ternary phases with composition $RELi_2Pn_2$ (trigonal, $P\bar{3}m1$) [3], adopting the

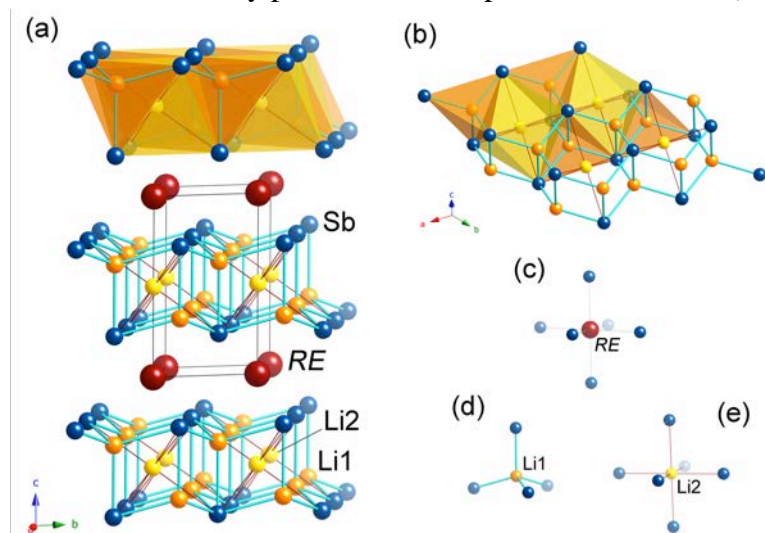


Figure 1. (a) Schematic representation of the trigonal crystal structure of $RELi_3Sb_2$. The $\{Li_3Sb_2\}^{3-}$ slabs are drawn in a way emphasizing the similarity to the $CaAl_2Si_2$ structure type, i.e., the “filler” Li2 atoms are connected to their neighbors with hair-lines, while the Li1–Sb interactions are represented with cylinders. Close-up projections of the $\{Li_3Sb_2\}^{3-}$ slab (b), and the coordination of the rare-earth metal (c), Li1 (d) and Li(2) atoms.

$CaAl_2Si_2$ structure type, and they are still categorized as such in the Pearson’s Handbook [4]. In our study, we carefully remapped this section of the corresponding $RE-Li-Sb$ diagrams and confirmed the crystal structures of the $RELi_3Sb_2$ ($RE = Ce - Nd, Sm, Gd - Ho$) compounds using single-crystal X-ray diffraction data. Interestingly, the structural data gathered using a state-of-the-art CCD-based diffractometer not only allowed for the location of both Li sites in the structure (Figure 1), but also for the refinement of the very light Li atoms with anisotropic displacement parameters, which apparently was impossible 30-40 years ago with film methods

and/or point detectors. Schuster *et al.* also identified $RELi_2Sb_2$ ($RE = Ce, Pr, Nd$) [3] with the tetragonal $CaBe_2Ge_2$ structure type [4], which this study found no evidence for. Our explorations also confirm the earlier observation that among the lanthanides, the trigonal $RELi_3Sb_2$ structure extends only until Ho, which appears to be the “break-point” for this series.

As seen from the schematic representation of the structure in Figure 1, and it best described as a Li-filled derivative of the imaginary $RELi_2Sb_2$ with the $CaAl_2Si_2$ structure (space group $P\bar{3}m1$; Pearson code $hP5$) [4]. The lattice parameters decrease from $a = 4.6065(3)$ Å and $c = 7.3769(10)$ Å for $CeLi_3Sb_2$ ($c/a = 1.601$) to $a = 4.5186(4)$ Å and $c = 7.1202(15)$ Å for $HoLi_3Sb_2$ ($c/a = 1.576$) as expected from the lanthanide contraction. The Sb atoms in the structure have a hexagonal closed packed arrangement, in which the (Li1) atoms are occupying half of the tetrahedral holes, and the RE -atoms fill half of the octahedral holes located at the origin (0, 0, 0). The “filled” Li (Li2) resides in the other half of the octahedral voids on (0, 0, 1/2). Another way to describe the structure is to consider $\{Li_2Sb_2\}^{4-}$ layers that are based on slightly distorted $[Li(1)Sb_4]$ tetrahedra, linked via edge-sharing to three neighboring $[Li(1)Sb_4]$

tetrahedra. The three Li(1)–Sb bonds within the *ab*-planes measure from 2.761(3) Å for CeLi₃Sb₂ to 2.717(3) Å for HoLi₃Sb₂, decreasing in order following the lanthanide contraction. The fourth bond within the [Li(1)Sb₄] tetrahedra (commonly referred to as a “handle”), which is collinear with the direction of the *c*-axis is longer, does not appear to follow the same trend. Li(1)–Sb measure from 2.865(4) Å for the Ce-compound to 2.87(1) Å for the Ho phase. The Li(2) atoms (the “fillers” of the {Li₂Sb₂}⁴⁻ sub-structure) are located at the centers of [Sb₆] octahedra with Li(2)–Sb varying from 3.2141(3) Å for CeLi₃Sb₂ to 3.1790(4) Å for HoLi₃Sb₂, respectively. Flat layers of RE³⁺ cations (also octahedrally coordinated by Sb) separate the {Li₃Sb₂}³⁻ slabs with distances ranging from d_{Ce-Sb} = 3.2591(3) Å to d_{Ho-Sb} = 3.1434(3) Å.

As discussed already, both Li(1) and Li(2) atoms in the RELi₃Sb₂ structure are mandatory to fulfill the electron preciseness for these compounds, which given the lack of Sb–Sb bonding, can be readily rationalized as [RE³⁺][Li(1)⁺]₂[Li(2)⁺][Sb³⁻]₂, i.e., as Zintl phases [37], where the La and Li atoms donate their electrons to the Sb atoms and all atoms fill their valence shell orbitals. Not surprisingly, the electronic structure of LaLi₃Sb₂ displays typical features of Zintl compounds—the Fermi level is indeed located between the top of the valence and the bottom of the conduction band. The band gap is very small, ca. 0.25 eV. The s bands and p bands in Sb and Li have substantial overlapping throughout the entire energy range. Accordingly, the bonding interactions within the {Li₃Sb₂}³⁻ polyanionic framework are mainly s-, and p- in character. This is commonly seen in many “classic” Zintl phases. Such conjecture also supports the discussion on the crystal chemistry of the title compounds that the corresponding Li–Sb bond lengths are close to the sum of the Pauling radii of Li (1.225 Å) and Sb (1.391 Å).

Future Plans

Currently, our efforts are focused on the syntheses and characterization of the series RELi₃Bi₂, where preliminary data show improved stability in air and more facile conditions for crystal growth. More exploratory work on is worthy of pursuing since property measurements have confirmed these materials to be semiconductor/semimetals. Their bonding characteristics offer many possibilities for property-tuning, which could prove very useful for the generation of new ideas and concepts in modern thermoelectrics development.

References

- [1] “CRC Handbook of Thermoelectrics”, Rowe, D. M. (Ed.), CRC Press, 1995.
- [2] ”Recent Trends in Thermoelectric Materials: Semiconductor and Semimetals”, Tritt, T. (Ed.) Vol. 69, 70, 71, Academic Press, **2001**, and the references therein.
- [3] H.-U. Schuster, H.-O. Fischer, Z. Naturforsch. 34b (1979) 1169.
- [4] P. Villars, L. D. Calvert (Eds.), Pearson’s Handbook of Crystallographic Data for Intermetallic Compounds, 2nd Ed., American Society for Metals, Materials Park, OH, USA 1991.

Publications

(in reverse order; the names of the contributing undergraduate researchers are underlined)

"Novel Lithium-containing Pnictides with 1-D Infinite Chains of Supertetrahedral Clusters. Synthesis, Crystal and Electronic Structure of $Ba_4Li_2Cd_3Pn_6$ ($Pn = P, As$ and Sb)"

Makongo, J. P. A.; You, T.-S.; He, H.; Suen, N.-T.; Bobev, S. *Eur. J. Inorg. Chem.* **2014** – submitted 05/15/2014.

"New Type-I and Type-II Clathrates in the Systems $Cs-Na-Ga-Si$, $Rb-Na-Ga-Si$, and $Rb-Na-Zn-Si$ "

Schäfer, M. C.; Bobev, S. *Inorganics* **2014**, 2, 79.

"On the Possibility for Rb- and Eu-cation Ordering in Type-I Clathrates. Synthesis and Homogeneity Range of the Novel Compounds $Rb_{8-x}Eu_x(In,Ge)_{46}$ ($0.6 \leq x \leq 1.8$)"

Schäfer, M. C.; Bobev, S. *Acta Cryst.* **2013**, C69, 1457.

"The Layered Antimonides $RELi_3Sb_2$ ($RE = Ce-Nd, Sm, Gd-Ho$). Filled Derivatives of the $CaAl_2Si_2$ Structure Type"

Schäfer, M. C.; Suen, N.-T.; Raglione, M.; Bobev, S. *J. Solid State Chem.* **2014**, 210, 89.

"Copper and Zinc Substitutions in Clathrates of Tin. Synthesis, Structural Characterization, and Physical Properties of $A_8Cu_{2.67}Sn_{43.33}$ and $A_8Zn_4Sn_{42}$ ($A = K, Rb, Cs$) with the Type-I Structure"

Schäfer, M. C.; Bobev, S. *Chem. Mater.* **2013**, 25, 3737.

"New Ternary Phosphides and Arsenides. Syntheses, Crystal structures, Physical Properties of Eu_2ZnP_2 , $Eu_2Zn_2P_3$ and $Eu_2Cd_2As_3$ "

Wang, J.; Xia, S.-Q.; Tao, X.-T.; Schäfer, M. C.; Bobev, S. *J. Solid State Chem.* **2013**, 205, 116.

"Ternary $K_2Zn_5As_4$ -type Pnictides $Rb_2Cd_5As_4$, $Rb_2Zn_5Sb_4$, and the Solid Solution $Rb_2Cd_5(As,Sb)_4$ "

He, H.; Stoyko, S.; Mar, A.; Bobev, S. *Acta Cryst.* **2013**, C69, 455.

"K and Ba Distribution in the Structures of the Clathrate Compounds $K_xBa_{16-x}(Ga,Sn)_{136}$ ($x = 0.8, 4.4, \text{ and } 12.9$) and $K_xBa_{8-x}(Ga,Sn)_{46}$ ($x = 0.3$)"

Schäfer, M. C.; **Bobev, S.** *Acta Cryst.* **2013**, C69, 319.

"Synthesis, Crystal Structure, and Electronic Structure of the New Zintl Compounds $Ba_3Ga_3P_5$ and $Ba_3Al_3Pn_5$ ($Pn = P, As$)"

He, H.; Tyson, C.; Saito, M.; Bobev, S. *Inorg. Chem.* **2013**, 52, 499.

"Tin Clathrates with the Type-II Structure"

Schäfer, M. C.; Bobev, S. *J. Am. Chem. Soc.* **2013**, 135, 1696.

Mitigating Breakdown in High Energy Density Perovskite Polymer Nanocomposite Capacitors

Richard L. Brutchey

Department of Chemistry, University of Southern California, Los Angeles, CA 90089 USA

Program Scope

Current electrical energy storage technologies do not meet the demands of transportation applications in terms of energy density. For example, the conversion from gasoline-powered vehicles to all-electric vehicles requires higher energy density pulsed power sources. Such applications require a new generation of robust dielectric capacitors that have (1) high electrical energy density (D , where $D = 0.5\epsilon'\epsilon_0 E_{bd}^2$), (2) low dielectric loss, (3) high field endurance, and (4) increased temperature stability. One of the most promising solutions to this challenge is to utilize polymer nanocomposites, whereby high permittivity inorganic nanocrystals are integrated into a polymer matrix. The fundamental challenges for these composites include: (1) the synthesis of small, solution processible nanocrystal fillers with high dielectric constants, and (2) the aggregation of the inorganic filler at the percolation threshold, which leads to a precipitous drop in breakdown voltage. To solve these challenges, and maximize the energy density of the resulting nanocomposites, our objectives are two-fold:

- (1) Develop a low temperature solution-phase synthesis of small perovskite oxide nanocrystals with tunable dielectric properties. An exquisite level of control over such nanocrystal properties will be accomplished by a thorough understanding of the nanocrystal structure and ability to tune nanocrystal composition.
- (2) Control filler size and surface chemistry such that reductions in breakdown strength may be mitigated.

Good progress on both objectives has been achieved during the previous two years (August 1, 2012 – May 1, 2014). See publications 2, 3, 5, 8 and 9 relevant to objective #1 and publications 1 and 7 relevant to objective #2. The following section will summarize our recent progress towards addressing local structure–composition relationships in perovskite nanocrystals.

Recent Progress

1. Local structure–composition relationships in isovalently substituted perovskite oxide nanocrystals. The research challenge that we address in the synthesis of complex oxide nanocrystals is establishing the physical properties that determine their functionality at the nanoscale, and in turn maximizing that functionality for energy needs (such as maximizing relative permittivity for dielectric capacitors). Bulk $Ba_{1-x}Sr_xTiO_3$ and $BaTi_{1-y}Zr_yO_3$ are known to possess a broad range of compositionally dependent phenomena that result from off-centering of the Ti^{4+} cation (leading to polar, non-centrosymmetric structures, ferroelectricity, and high dielectric constants at room temperature),¹ which make them useful functional materials for dielectric capacitors. For example, the room temperature crystal structure of $Ba_{1-x}Sr_xTiO_3$ changes from tetragonal to cubic upon substitution of ~30–50% of Sr^{2+} for Ba^{2+} .² This is accompanied by a decrease in the temperature of the ferroelectric-to-paraelectric transition along with an enhancement of the room temperature dielectric permittivity. In the case of $BaTi_{1-y}Zr_yO_3$, a multiphase point in which the rhombohedral, orthorhombic, tetragonal, and cubic phases coexist near room-temperature is observed upon substitution of ~10–20% of Zr^{4+} for Ti^{4+} ; an enhancement of the room temperature dielectric permittivity also occurs in this substitution range.³ Although composition–structure relationships are well established for $Ba_{1-x}Sr_xTiO_3$ and

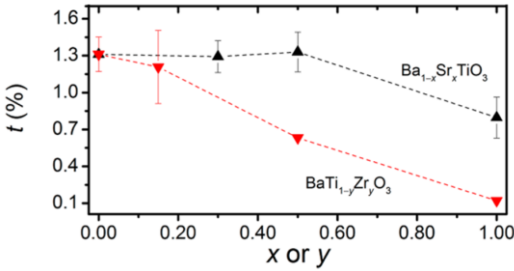


Fig. 1 Degree of tetragonality ($t = (c/a - 1) \times 100\%$) of the perovskite unit cell extracted from the fit of the $P4mm$ space group to the experimental PDFs of $\text{Ba}_{1-x}\text{Sr}_x\text{TiO}_3$ and $\text{BaTi}_{1-y}\text{Zr}_y\text{O}_3$ nanocrystals in the 1.5-20 Å range. A reduction of the magnitude of the titanium off-centering was observed upon replacing 50% of Ba^{2+} with Sr^{2+} in $\text{Ba}_{1-x}\text{Sr}_x\text{TiO}_3$, but the coherence length remained unchanged. In contrast, a noticeable reduction in the coherence length was observed upon replacing 15% of the ferroelectrically active Ti^{4+} with Zr^{4+} in $\text{BaTi}_{1-y}\text{Zr}_y\text{O}_3$ nanocrystals. The same dependence of t on composition is observed in the bulk materials.

(publication 5). Interestingly, these results revealed that evolution of the room temperature local crystal structure with chemical composition in these nanocrystals mirrors that of bulk ceramics (**Fig. 1**); that is, the most polar local structures (and the highest room temperature dielectric constants) for the $\text{Ba}_{1-x}\text{Sr}_x\text{TiO}_3$ and $\text{BaTi}_{1-y}\text{Zr}_y\text{O}_3$ nanocrystals were observed at the same compositions as the corresponding bulk ceramics. This demonstrates that compositional control over cooperative properties such as ferroelectricity in these perovskites is possible even for nanocrystals as small as 10 nm, which is important for utilizing these nanomaterials in dielectric capacitors.

2. Local structure of aliovalently doped BaTiO_3 nanocrystals. Similar to isovalent chemical substitution, aliovalent chemical substitution with lanthanides can be employed to alter the crystal structure and dielectric properties of BaTiO_3 .⁵ From this perspective, understanding the defect chemistry of lanthanide-doped BaTiO_3 is critical to gain compositional control of structure–function relationships. Elucidating the distribution of the lanthanide ion in the BaTiO_3 lattice involves determining whether it substitutes at a single site (Ba or Ti) or multiple sites (Ba and Ti), the solubility limit in each site, and how this distribution changes with the lanthanide concentration.

We have investigated the local structure of Eu^{3+} -doped BaTiO_3 nanocrystals to elucidate the distribution of the lanthanide dopant in the perovskite lattice (**Fig. 2**). PDF analysis, steady-state photoluminescence, and XANES and EXAFS spectroscopies suggest that at low dopant concentrations (≤ 1 mol%), Eu^{3+} substitutes for Ba^{2+} ions via creation of a Ti^{4+} vacancy next to the lanthanide ion, according to the nominal formula $\text{Ba}_{1-x}\text{Eu}_x\text{Ti}_{1-x/4}\text{O}_3$ (publication 3). The size and charge mismatch between the lanthanide and the alkaline earth, along with the simultaneous creation of a titanium vacancy, induces significant structural relaxations of the perovskite lattice around the lanthanide ion, consistent with published computational predictions.⁶ Invoking substitution of Eu^{3+} for Ba^{2+} ions via creation of a Ti^{4+} vacancy in $\text{Eu}^{3+}:\text{BaTiO}_3$ nanocrystals simultaneously explains the following experimental results: (1) the decrease in the volume of the unit cell observed in the 0–1 mol% range measured by X-ray total scattering, (2) the highly

$\text{BaTi}_{1-y}\text{Zr}_y\text{O}_3$ single crystals and bulk ceramics, free-standing nanocrystals of similar compositions have not been the subject of a systematic structural investigation.

We have previously measured average room temperature dielectric constants as high as $\epsilon' = 240$ (at 1 MHz) for $\text{Ba}_{0.69}\text{Sr}_{0.31}\text{TiO}_3$ nanocrystals prepared by our benign vapor diffusion sol-gel

route as compared to $\epsilon' = 80$ for BaTiO_3 nanocrystals of the same size prepared in an identical way.⁴ This demonstrates that compositional control can be used to tune the dielectric properties of the nanocrystals. We employed X-ray absorption and PDF analysis of X-ray total scattering (20-BM-B and 11-ID-B beam lines of the Advanced Photon Source) to gain fundamental insight into the dependence of polar nanoregions in such

$\text{Ba}_{1-x}\text{Sr}_x\text{TiO}_3$ and $\text{BaTi}_{1-y}\text{Zr}_y\text{O}_3$ nanocrystals

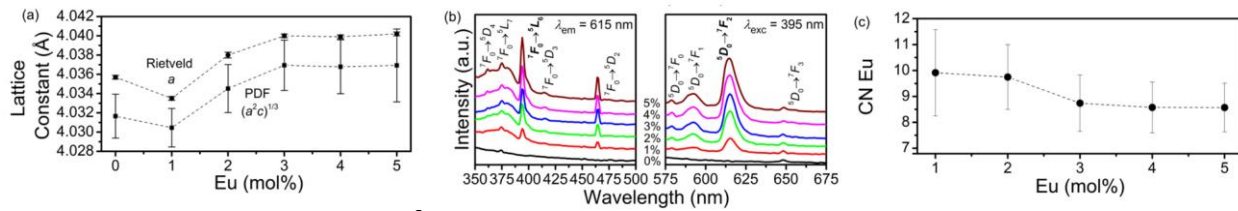


Fig. 2 Structural characterization of $\text{Eu}^{3+}:\text{BaTiO}_3$ nanocrystals. (a) Evolution of the perovskite lattice constants with the europium concentration. These were extracted by probing the local (tetragonal) and average (cubic) crystal structures using Rietveld and PDF analysis, respectively. (b) Steady-state excitation and emission photoluminescence spectra of $\text{Eu}^{3+}:\text{BaTiO}_3$ nanocrystals. Europium concentrations (mol%) are indicated. (c) Evolution of the average europium coordination number (CN_{Eu}) with the europium concentration according to Eu L_3 EXAFS spectroscopy.

distorted, non-centrosymmetric coordination environment of the Eu^{3+} ion observed by steady-state photoluminescence, and (3) the approximate 9-fold europium coordination extracted from X-ray absorption analysis. The structural distortions that we observe caused by aliovalent substitution are an excellent impetus to study the resulting dielectric properties of these nanocrystals. Indeed, the vapor diffusion sol-gel method has been extended to other lanthanide-doped perovskite nanocrystals (publication 2); results demonstrate that the enhanced dielectric properties of the nanocrystals can be correlated to local structural distortions. This therefore reinforces our objective of using compositional control to tune the dielectric properties of the nanocrystals coupled with using high-level structural characterization to understand how the composition affects their local structure (and dielectric properties).

Future Plans

- (1) Leverage our vapor diffusion sol-gel method to synthesize more compositionally complex oxide nanocrystals. Focus will be placed on research to efficiently expand the library of complex oxide nanocrystals that are available using our unique synthesis method, in order to tune nanocrystal properties through synthetic compositional control.
- (2) Perform high-level structural characterization of the resulting complex oxide nanocrystals to establish structure-property relationships at the nanoscale. Using a combination of synchrotron X-ray diffraction, pair distribution function (PDF) analysis, and X-ray absorption (EXAFS, XANES), we will create a comprehensive structural picture of the resulting complex oxide nanocrystals to understand how their structure and functional properties change as a function of size and/or composition. This will allow us to correlate local structural distortions induced by chemical substitution with the dielectric properties of the nanocrystals.
- (3) Assess the functionality of the resulting complex oxide nanocrystals. The basic dielectric properties of the perovskite nanocrystals will be tested and subsequently applied toward polymer nanocomposites for dielectric capacitors. Focus will be placed on minimizing the permittivity gradient across the interface between the inorganic filler and polymer.

References

1. Lemanov, V. V. *Ferroelectrics* **2007**, *354*, 69.
2. Lemanov, V. V.; Smirnova, E. P.; Syrnikov, P. P.; Tarakanov, E. A. *Phys. Rev. B* **1996**, *54*, 3151.
3. Dobal, P. S.; Dixit, A.; Katiyar, R. S.; Yu, Z.; Guo, R.; Bhalla, A. S. *J. Appl. Phys.* **2001**, *89*, 8085.
4. Beier, C. W.; Cuevas, M. A.; Brutchey, R. L. *J. Mater. Chem.* **2010**, *20*, 5074-5079.
5. Moulson, A. J.; Herbert, J. M. *Electroceramics*, Chapman and Hall, London, 1990.
6. Freeman, C. L.; Dawson, J. A.; Harding, J. H.; Ben, L.-B.; Sinclair, D. C. *Adv. Funct. Mater.* **2012**, *23*, 491.

Publications

1. Culver, S. P.; Beier, C. W.; Rafson, J. P.; Brutchey, R. L. Surface Modification of BaTiO₃ Inclusions in Polydicyclopentadiene Nanocomposites for Energy Storage. *Journal of Applied Polymer Science* **2014**, *131*, 40290.
2. Culver, S. P.; Stepanov, V.; Mecklenburg, M.; Takahashi, S.; Brutchey, R. L. Low Temperature Synthesis and Characterization of Lanthanide-Doped BaTiO₃ Nanocrystals. *Chemical Communications* **2014**, *50*, 3480-3483.
3. Rabuffetti, F. A.; Culver, S. P.; Lee, J. S.; Brutchey, R. L. Local Structural Investigation of Eu³⁺-Doped BaTiO₃ Nanocrystals. *Nanoscale* **2014**, *6*, 2909-2914.
4. Rabuffetti, F. A.; Culver, S. P.; Suescun, L.; Brutchey, R. L. Structural Disorder in AMoO₄ (A = Ca, Sr, Ba) Scheelite Nanocrystals. *Inorganic Chemistry* **2014**, *53*, 1056-1061.
5. Rabuffetti, F. A.; Brutchey, R. L. Local Structure of Ba_{1-x}Sr_xTiO₃ and BaTi_{1-y}ZryO₃ Nanocrystals Probed by X-ray Absorption and X-ray Total Scattering. *ACS Nano* **2013**, *7*, 11435-11444.
6. Culver, S. P.; Rabuffetti, F. A.; Zhou, S.; Mecklenburg, M.; Song, Y.; Melot, B. C.; Brutchey, R. L. Low Temperature Synthesis of AMoO₄ (A = Ca, Sr, Ba) Scheelite Nanocrystals. *Chemistry of Materials* **2013**, *25*, 4129-4135.
7. Beier, C. W.; Sanders, J. M.; Brutchey, R. L. Improved Breakdown Strength and Energy Density in Thin Film Polyimide Nanocomposites with Small Barium Strontium Titanate Nanocrystal Fillers. *Journal of Physical Chemistry C* **2013**, *117*, 6958-6965.
8. Rabuffetti, F. A.; Lee, J. S.; Brutchey, R. L. Low Temperature Synthesis of Complex Ba_{1-x}Sr_xTi_{1-y}ZryO₃ Perovskite Nanocrystals. *Chemistry of Materials* **2012**, *24*, 3114-3116.
9. Rabuffetti, F. A.; Brutchey, R. L. Structural Evolution of BaTiO₃ Nanocrystals Synthesized at Room Temperature. *Journal of the American Chemical Society* **2012**, *134*, 9475-9487.

New Superconducting Materials

Robert J. Cava, Department of Chemistry, Princeton University 08540

Program Scope

The objectives of this program are to discover new superconducting materials, to use the tools of solid state chemistry to establish the relationships between crystal structure, chemical bonding, and the electronic properties of superconducting materials and related compounds, and to collaborate with researchers in the materials physics community through providing the highest possible quality materials, carefully chemically and structurally characterized, for them to perform state-of-the-art characterization of the properties of superconductors.

Recent Progress

Several areas of research in the solid state chemistry of new superconducting materials are being pursued by the PI. One of those areas – the tungsten oxide bronzes – is described briefly here; information on other systems is found in the DOE-supported publications at the end of this document. The tungsten oxide bronzes were among the first oxide superconductors discovered. They are unusual because they display superconductivity in non-perovskite oxide crystal structures with very low electron counts, with the electrons in orbitals that are derived from tungsten $5d$ states, which are therefore expected to be broad in energy and relatively

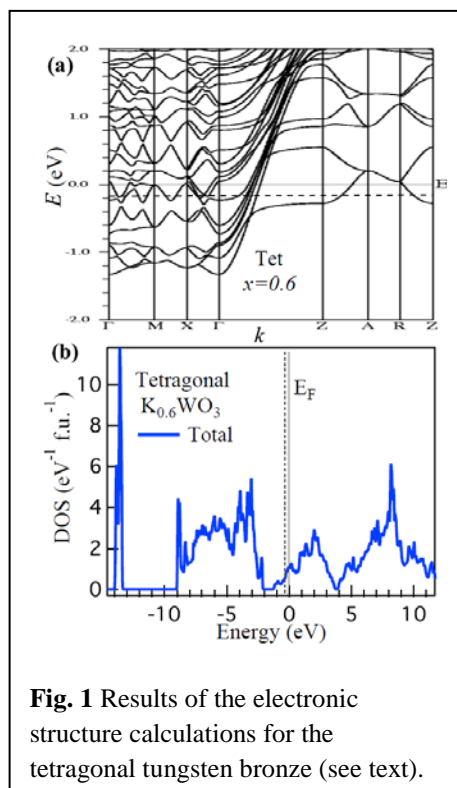


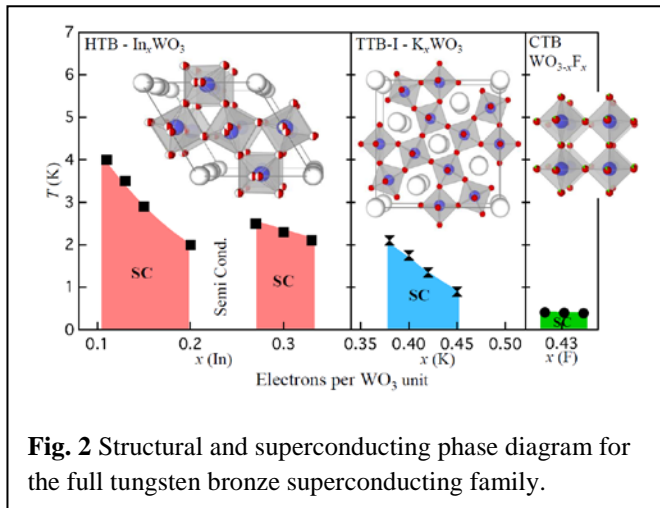
Fig. 1 Results of the electronic structure calculations for the tetragonal tungsten bronze (see text).

uninteresting from an electronic perspective. The PI has developed an understanding of these potential superconductors over the course of recent studies indicating that O-W-O bonding with angles other than 180 degrees in their crystal structures can lead to sharper than expected features in their electronic density of states and therefore greater potential for superconductivity. Work in the past two years has concentrated in particular on independently varying the crystal structure and the electronic doping in these superconductors through the establishment of the structure-electron-count-superconducting behavior.

The $M_x\text{WO}_3$ tungsten bronzes, where M is an ion that donates electrons to the WO_3 framework, show several distinct crystal structures. Many studies have been performed on the superconductivity in this family since its initial discovery [1]. Tungsten bronzes share features with other oxide superconducting systems, such as having a relatively low density of electronic states at the Fermi Energy and Tc's that are highest close to a structural phase boundary. The superconducting $M_x\text{WO}_3$ tungsten bronzes are non-stoichiometric compounds that can have

hexagonal bronze (i.e. “HTB”), tetragonal bronze (“TTB-I”), or perovskite-derived tetragonal (TTB-II) and cubic (CTB) structures [1-22]. Although the superconducting HTBs in particular have been well studied, a detailed investigation of the superconducting properties of the TTB-I compound [2,5,13] was lacking until our recent work. In that work, we performed a detailed study on the superconducting K_xWO_3 tetragonal tungsten bronze TTB-I phase, made possible through the careful chemical treatment and handling of the highly water-sensitive samples. The experimental characterization was supplemented by electronic structure calculations. Finally, we presented the first structural and electronic phase diagram across the full HTB, TTB-I, and CTB tungsten bronze family.

K_xWO_3 was prepared by a solid state reaction method starting from pre-made K_2WO_4 purified WO_2 and WO_3 in a stoichiometric reaction. Pellets were pressed inside an Ar-filled glove box, transferred into alumina crucibles and sealed inside evacuated quartz glass tubes that were heated at 650 C and 800 C. The reacted samples were kept inside the glove box. This handling was required to avoid the decomposition that resulted in the observation of semiconducting behavior by some previous researchers [23]. The purity and cell parameters of the samples were evaluated by powder X-ray diffraction on a Bruker D8 FOCUS diffractometer. Elemental analysis performed using EDS showed that the potassium contents were very close to the nominal values. The electrical resistivity was measured using a standard four-probe dc-technique from 0.4 K to 300 K in zero-field and also in magnetic fields up to 1 T using a Quantum Design Physical Property Measurement System (PPMS). The electronic structure calculations were performed by density functional theory using the WIEN2K code with a full-potential linearized augmented plane-wave and local orbitals together with the PBE parameterization of the GGA, including spin orbit coupling [24].



Figs. 1a and b show the calculation of the electronic density of states (DOS) for the potassium doped tetragonal tungsten bronze. 1(a) shows the band structure in the vicinity of E_F , and (b) shows the total DOS of $K_{0.6}WO_3$ as a function of energy. The dotted lines in Fig. 1 represent E_F for the $x=0.4$ doping level. The band structure calculation clearly shows that at $x=0.35$ E_F transitions through a van Hove singularity (vHs). This anomalous electronic structure is found close to the change from hexagonal to tetragonal structural phases in the K_xWO_3 . Although it is generally expected that a

vHs has a significant influence only on superconductivity in 2D electronic systems, the highest T_c observed at $x=0.38$ in the doped TTB-I phase appears to be well correlated with the vHs present in the band structure. Fig. 1(b) shows the potassium doping effect, i.e. of increased electron concentration, on insulating WO_3 . E_F is shifted upward into the bottom of conduction band. This leads to the metallic behavior of the K_xWO_3 TTB-I phase up to the highest possible K doping level $x=0.6$.

With this characterization of the TTB-I superconductor, it is now possible to present a complete superconducting phase diagram for the tungsten bronze family (Fig. 2). The diagram

shows that the superconducting T_c s generally decrease with increasing electron doping of the WO_3 framework within a single crystal structure. Also, the superconducting transition temperatures are highest at the lowest doping levels for both the HTB and TTB systems. Finally, it is clear that at comparable doping levels, the perovskite-based CTB is a significantly worse superconductor than the TTB-I bronze phase. This is one of the few systems known where a direct comparison of perovskite-based and non-perovskite-based structure superconductors is possible at the same electron count; in this case the perovskite is the worse superconductor.

Future Plans

Three topic areas are of interest. As a result of DOE-sponsored research, the PI has been able to determine a variety of unusual structure-property relationships that arise in ThCr_2Si_2 -structure phases due to the presence of a pnictogen dimer in their crystal structures – in effect, a molecule imbedded inside a metal. Future plans are to these relationships deeper in other superconducting ThCr_2Si_2 -type compounds. Secondly, superconducting materials based on the tungsten oxygen structural networks are of interest as, based on a $5d$ element at the beginning of the transition metal series, they may not be expected to display the kind of electron-lattice coupling that leads to a high superconducting transition temperatures, but that is not so obviously the case on more detailed consideration. Future plans are to study more structure-chemistry-property relations in this family. Finally, the half-Heusler crystal structure hosts relatively few superconductors but the ones that do form are very interesting from an electronic perspective. The PI plans a future set of studies to determine how common superconductivity is in compounds with this crystal structure, and the primary chemical requirements for the superconductivity when it does occur.

References

1. Ch. J. Raub, et. al., Phys. Lett. **13**, 746 (1964).
2. A. R. Sweedler, Ch. J. Raub and B. T. Matthias, Phys. Letters, **15**, 108 (1965).
3. P. J. Wiseman and P. G. Dickens, J. of Solid State Chemistry **6**, 374 (1973).
4. L. H. Cadwell, R. C. Morris and W. G. Moulton, Phy. Rev. B **23**, 546 (1989).
5. A. R. Sweedler, J. K. Hulm, B. T. Matthias and T. H. Geballe, Physics Letters **19**, 82 (1965).
6. A. W. Sleight, J. L. Gillson, P. E. Bierstedt, Solid State Comm. **17**, 27 (1975).
7. J. E. Ostenson, H. R. Shanks and D. K. Finnemore, J. of Less-Com. Met., **62**, 149 (1978).
8. Juan Guo, Cheng Dong, Lihong Yang and Hong Chen, Mat. Res. Bull. **43**, 779 (2008).
9. C. Kasl and M. J. R. Hoch, J. Mater Sci **48**, 3003 (2013).
10. E. Banks and A. Goldstein, Inorganic Chemistry **7**, 966 (1968).
11. J. P. Remeika, et. al. , Phys. Lett. **24A**, 565 (1967).
12. R. Brusetti, P. Bordet, and J. Bossy, Phy. Rev. B **76**, 174511 (2007).
13. Howard R. Shanks, Solid State Comm. **15**, 753756 (1974).
14. J. D. Bocarsly et. al., Euro. Phys. Lett. **103**, 17001 (2013).
15. D. Hirai, E. Climent-Pascual and R. J. Cava, Phy. Rev. B **84**, 174519 (2011).
16. I. R. Shein and A. L. Ivanovskii, JETP Lett. **95**, 66 (2011).
17. K. S. Lee, D. K. Seo and M. H. Whangbo, J. Am. Chem. Soc **110**, 4043 (1997).
18. D. M. Sagar, et. al., Phys. Rev. B **81** 045124 (2010).
19. B. Ingham, S. C. Hendy, S. V. Chong and J. L. Tallon, Phy. Rev. B **72**, 075109 (2005).
20. L. C. Ting, et. al. J. Sup. and Novel Mag. **20**, 249 (2007).

21. M. R. Skokan, W. G. Moulton and R. C. Morris, *Phy. Rev. B* **20**, 3670 (1979).
22. R. K. Stanley, R. C. Morris and W. G. Moulton, *Phy. Rev. B* **20**, 1903 (1979).
- 23 R. Fan, et. al, *J. Phys. Chem. Sol.* **61**, 2029 (2000).
24. P. Blaha, K. Schwarz, G. Madsen, D. Kvasnicka and J. Luitz, , Technische Universitat Wien, Austria, (2001).

Publications of RJ Cava Supported by DOE Materials Chemistry Program 2012-2014

1. “p-Type CuRhO₂ as a Self-Healing Photoelectrode for Water Reduction under Visible Light”, J. Gu, Y. Yan, J.W. Krizan, Q.D. Gibson, Z.M. Detweiler, R.J. Cava, and A.B. Bocarsly, *J. Am. Chem. Soc.* **136** 830 (2014).
2. “Pressure-induced structural phase transition in the half-Heusler compound CaAuBi”, L.L.S. Xie, L.M. Schoop, S.A. Medvedev, C. Felser, and R.J. Cava, *Solid State Sciences* **30** 6 (2014).
3. “Superconducting properties of the K_xWO₃ tetragonal tungsten bronze and the superconducting phase diagram of the tungsten bronze family”, N. Haldolaarachchige, Q. Gibson, J. Krizan, and R.J. Cava, *Phys. Rev. B* **89** 104520 (2014).
4. “beta-HfCuGe-A new polymorph of HfCuGe with a novel structure type”, L.M. Schoop, J.M. Allred, N. Ni, D. Hirai, J. Krez, M. Schwall, H.W. Ji, M.N. Ali, R.J. Cava, *J. Sol. St. Chem.* **199** 66 (2013).
5. “Superconductivity in the Cu(Ir_{1-x}Pt_x)₂Se₄ spinel”, H.X. Luo, T. Klimczuk, L. Muchler, L. Schoop, D. Hirai, M.K. Fuccillo, C. Felser, and R.J. Cava, *Phys. Rev. B* **87** 214510 (2013).
6. “Mg-Doped CuFeO₂ Photocathodes for Photoelectrochemical Reduction of Carbon Dioxide”, J. Gu, A. Wuttig, J.W. Krizan, Y.A. Hu, Z.M. Detweiler, R.J. Cava, and A.B. Bocarsly, *J. Phys. Chem. C* **117** 12415 (2013).
7. “Superconductivity in HfCuGe₂: A non-magnetic analog of the 1111 iron pnictides”, L. Schoop, D. Hirai, C. Felser and R.J. Cava, *Europhys. Lett.* **6** 67001 (2013).
8. “Lone Pair Effect, Structural Distortions, and Potential for Superconductivity in TI Perovskites”, Leslie M. Schoop, Lukas Muchler, Claudia Felser, and R. J. Cava, *Inorganic Chemistry* **52** 5479 (2013).
9. “Spontaneous Formation of Zigzag Chains at the Metal-Insulator Transition in the beta-Pyrochlore CsW₂O₆” D. Hirai, M. Bremholm, J.M. Allred, J. Krizan, L.M. Schoop, Q. Huang, J. Tao, and R.J. Cava, *Phys. Rev. Lett.* **110** 166402 (2013).
10. “Superconductivity in the Heusler family of intermetallics”, T Klimczuk, C.H. Wang, K. Gofryk, F. Ronning, J. Winterlik, G.H. Fecher, J.C. Griveau, E. Colineau, C. Felser, J.D. Thompson, D.J. Safarik, and R.J. Cava, *Phys. Rev. B* **85** 174505 (2012).
11. “Negative thermal expansion and antiferromagnetism in the actinide oxypnictide NpFeAsO”, T. Klimczuk, H.C. Walker, R. Springell, A.B. Shick, A.H. Hill, P. Gaczynski, K Gofryk, S.A.J. Kimber, C. Ritter, E. Colineau, J.C. Griveau, D. Bouexiere, R. Eloirdi, .R.J. Cava, R. Caciuffo, *Phys. Rev. B* **85** 174506 (2012)
12. “Emergence of superconductivity in BaNi₂(Ge_{1-x}P_x)₂ at a structural instability”, D. Hirai, F. von Rohr, R.J. Cava, *Phys. Rev. B* **86** 100505 (2012).
13. “Ordered CoSn-type ternary phases in Co₃Sn_{3-x}Ge_x”, JM Allred, S Jia, M Bremholm, BC Chan, RJ Cava, *J. Alloys and Compounds* **539** 137 (2012).
14. “Effect of pressure on superconductivity in NaAlSi”, L. Schoop, L. Muechler, J. Schmitt, V. Ksenofontov, S. Medvedev, J. Nuss, F. Casper, M. Jansen, R.J. Cava, and C. Felser, *Phys. Rev. B* **86** 174522 (2012).

Tuning Sorption Properties of Metal-Organic Frameworks via Postsynthetic Covalent Modification

Seth M. Cohen, Professor and Chair, Department of Chemistry and Biochemistry,
University of California, San Diego, 9500 Gilman Drive, La Jolla, California 92093-0358

Program Scope

Metal-organic frameworks (MOFs) are porous, crystalline materials that display great promise for use in separation, sensor, gas sorption, and nanotechnology applications.^{1,2} The specific objective of this research program is to utilize heterogeneous chemical reactions to alter the organic components (ligands) of MOFs. This approach, termed postsynthetic modification (PSM, see Figure),³ has proven to be a very powerful method for the introduction of functional groups into MOFs that are incompatible with traditional MOF synthetic methods (see

Figure, which generally involve solvothermal procedures that often utilize high temperature and pressure). Our ongoing investigations will continue to explore fundamental approaches for the covalent PSM of MOFs, with a special emphasis on tuning the gas sorption and other physical properties of MOFs.

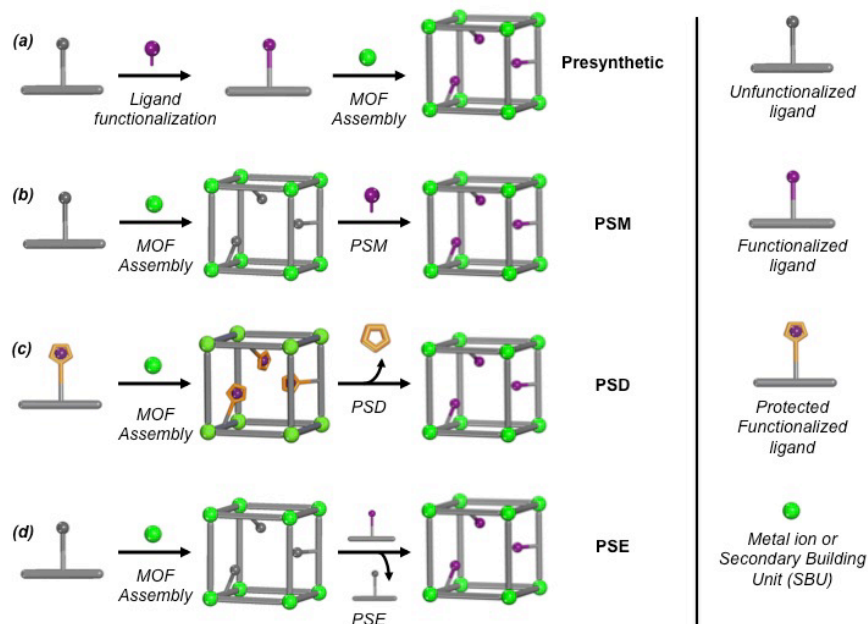


Figure. Approaches to Functionalized MOFs. (a) In the conventional presynthetic approach, a ligand is functionalized and then suitable conditions to assemble the desired MOF are identified. (b) In postsynthetic modification (PSM), the desired MOF lattice is first prepared and then the ligand is modified in a heterogeneous fashion. (c) In postsynthetic deprotection (PSD), a ligand with a protected functional group is employed to produce a MOF from which a protecting group can be liberated giving a functionalized material. (d) In postsynthetic exchange (PSE), an unfunctionalized MOF is exposed to a functionalized ligand, resulting in ligand metathesis resulting in a functionalized mixed-ligand MOF.

Recent Progress

Our work on the modification and functionalization of MOFs in order to tune gas sorption and other physical properties of these materials has been very productive in the prior 2-year period. On average, we have published more than one DOE-supported paper every-other month since the beginning of this grant (18 publications in the 28 months of funding to date). Many of these publications have been highlighted as ‘hot articles’ or ‘top downloaded’ articles by the journals or other scientific media sources. This DOE grant has supported the work of at least 8 junior scientists, including several women and underrepresented minority students. Several of the junior scientists on this project have gone on to successful positions in academia and the government, including DOE national laboratories.

As shown in the Figure above, during the course of the last 28 months we have greatly expanded our studies beyond just PSM. We have developed and utilized other related postsynthetic methods, including postsynthetic deprotection (PSD),⁴ and postsynthetic exchange (PSE, also known as solvent-assisted ligand exchange, SALE).⁵⁻⁷ These methods have proved to be powerful techniques for the introduction of sophisticated functional groups into MOFs that are related to a number of energy-relevant applications, including hydrogen storage and production,⁸ as well as the development of new, crosslinked MOFs.⁹

Future Plans

The specific objective of this program is to utilize highly innovative ligand design and state-of-the-art synthetic methodologies to modify the organic components of MOFs and hence the MOF properties. Our prior work in this area has shown that we can tune the properties of MOFs, primarily via postsynthetic approaches, that have been widely adopted by the research community. Through our development of new synthetic approaches and strategies, we have enabled our group and others to advance MOFs well beyond what was initially achieved by basic solvothermal synthetic methods. Our ongoing studies will continue to explore fundamental approaches for the functionalization of MOFs, with a special emphasis in two areas: (a) MOFs relevant to H₂ production and storage, and (b) new classes of functionalized materials based on crosslinked, oligomeric, and polymeric ligands.

References

- (1) Long, J. R.; Yaghi, O. M. *Chem. Soc. Rev.* **2009**, *38*, 1213-1214.
- (2) Tranchemontagne, D. J.; Mendoza-Cortes, J. L.; O’Keeffe, M.; Yaghi, O. M. *Chem. Soc. Rev.* **2009**, *38*, 1257-1283.
- (3) Cohen, S. M. *Chem. Rev.* **2012**, *112*, 970-1000.

- (4) Tanabe, K. K.; Allen, C. A.; Cohen, S. M. *Angew. Chem. Int. Ed.* **2010**, *49*, 9730-9733.
- (5) Karagiari, O.; Bury, W.; Tylianakis, E.; Sarjeant, A. A.; Hupp, J. T.; Farha, O. K. *Chem. Mater.* **2013**, *25*, 3499-3503.
- (6) Kim, M.; Cahill, J. F.; Su, Y.; Prather, K. A.; Cohen, S. M. *Chem. Sci.* **2012**, *3*, 126-130.
- (7) Kim, M.; Cohen, S. M. *CrystEngComm* **2012**, *14*, 4096-4104.
- (8) Wang, Z.; Tanabe, K. K.; Cohen, S. M. *Chem. Eur. J.* **2010**, *16*, 212-217.
- (9) Allen, C. A.; Boissonault, J. A.; Cirera, J.; Gulland, R.; Paesani, F.; Cohen, S. M. *Chem. Commun.* **2013**, *49*, 3200-3202.

Publications

1. Phuong V. Dau and Seth M. Cohen, "The influence of nitro groups on the topology and gas sorption property of extended Zn(II)-paddlewheel MOFs" *CrystEngComm* **2013**, *15*, 9304-9307. DOI: 10.1039/c3ce41124a
2. Sang Ho Lim and Seth M. Cohen, "Self-Assembled Supramolecular Clusters Based on Phosphines and Coinage Metals: Tetrahedra, Helicates, and Mesocates" *Inorg. Chem.* **2013**, *52*, 7862-7872. DOI: 10.1021/ic302840x
3. Honghan Fei, John F. Cahill, Kimberly A. Prather, and Seth M. Cohen, "Tandem Postsynthetic Metal Ion and Ligand Exchange in Zeolitic Imidazolate Frameworks" *Inorg. Chem.* **2013**, *52*, 4011-4016. DOI: 10.1021/ic400048g
4. Corinne A. Allen, Jake A. Boissonault, Jordi Cirera, Ryan Gulland, Francesco Paesani and Seth M. Cohen, "Chemically crosslinked isorecticular metal-organic frameworks" *Chem. Commun.* **2013**, *42*, 3200-3202. DOI: 10.1039/c3cc40635k
5. Phuong V. Dau, Luis R. Polanco, and Seth M. Cohen, "Dioxole functionalized metal-organic frameworks" *Dalton Trans.* **2013**, *42*, 4013-4018. DOI: 10.1039/c3dt32588a
6. Marco Taddei, Ferdinando Costantino, Andrea Ienco, Angiolina Comotti, Phuong V. Dau, and Seth M. Cohen, "Synthesis, breathing, and gas sorption study of the first isorecticular mixed-linker phosphonate based metal-organic frameworks" *Chem. Commun.* **2013**, *49*, 1315-1317. DOI: 10.1039/c2cc38092g

7. Gregory E. Cmarik, Min Kim, Seth M. Cohen, and Krista S. Walton, "Tuning the Adsorption Properties of UiO-66 via Ligand Functionalization" *Langmuir* **2012**, *28*, 15606-15613. DOI: 10.1021/la3035352
8. Min Kim, John F. Cahill, Honghan Fei, Kimberly A. Prather, and Seth M. Cohen, "Postsynthetic Ligand and Cation Exchange in Robust Metal–Organic Frameworks" *J. Am. Chem. Soc.* **2012**, *134*, 18082-18088. DOI: 10.1021/ja3079219
9. Sang Ho Lim, Yongxuan Su, and Seth M. Cohen, "Supramolecular Tetrahedra of Phosphines and Coinage Metals" *Angew. Chem. Int. Ed.* **2012**, *51*, 5106-5109
10. Min Kim, John F. Cahill, Yongxuan Su, Kimberly A. Prather, and Seth M. Cohen, "Postsynthetic Ligand Exchange as a Route to Functionalization of 'Inert' Metal-Organic Frameworks" *Chem. Sci.* **2012**, *3*, 126-130. DOI: 10.1039/c1sc00394a
11. Chao Chen, Corinne A. Allen, and Seth M. Cohen, "Tandem Postsynthetic Modification of Metal-Organic Frameworks Using an Inverse-Electron-Demand Diels-Alder Reaction" *Inorg. Chem.* **2011**, *50*, 10534-10536. DOI: 10.1021/ic2017598
12. Min Kim, John F. Cahill, Kimberly A. Prather, and Seth M. Cohen, "Postsynthetic Modification at Orthogonal Reactive Sites on Mixed, Bifunctional Metal-Organic Frameworks" *Chem. Commun.* **2011**, *47*, 7629-7631. DOI: 10.1039/c1cc12101d
13. Phuong V. Dau, Min Kim, and Seth M. Cohen, "Site-selective cyclometalation of a metal-organic framework" *Chem. Sci.* **2013**, *4*, 601-605. DOI: 10.1039/c2sc21289g
14. Seth M. Cohen, "Postsynthetic Methods for the Functionalization of Metal-Organic Frameworks" *Chem. Rev.* **2012**, *112*, 970-1000. DOI: dx.doi.org/10.1021/cr200179u
15. Phuong V. Dau, Min Kim, Sergio J. Garibay, Frédéric L. Münch, Curtis E. Moore, and Seth M. Cohen, "Single-Atom Ligand Changes Affect Breathing in an Extended Metal-Organic Framework" *Inorg. Chem.* **2012**, *51*, 5671-5676. DOI: dx.doi.org/10.1021/ic202683s
16. Min Kim and Seth M. Cohen, "Discovery, development, and functionalization of Zr(IV)-based metal-organic frameworks" *CrystEngComm* **2012**, *14*, 4096-4104. DOI: 10.1039/c2ce06491j
17. Min Kim, Jake A. Boissonault, Corinne A. Allen, Phuong V. Dau and Seth M. Cohen, "Functional tolerance in an isoreticular series of highly porous metal-organic frameworks" *Dalton Trans.* **2012**, *41*, 6277-6282. DOI: 10.1039/c2dt30120b

Electronic and Ionic Conductors from Ordered Microporous Materials

Mircea Dincă, Massachusetts Institute of Technology, Cambridge, MA

Program Scope

High surface area conducting materials are poised to transform the energy landscape in the near future. Microporous conducting ceramics and activated carbons are used in high temperature fuel cells and supercapacitors, while porous chalcogenide semiconductors and conductive polymers are attractive targets for applications in electrocatalysis, separation, and sensing technologies. One class of materials that could have an important impact in these areas are MOFs. Although these materials have high intrinsic porosity that has led to applications in gas separation and storage among others, they typically exhibit very low electrical conductivity. This is not surprising: MOFs are usually made from hard metal ions connected by redox-inactive organic ligands; this combination does not provide a good conjugation pathway for charge transport. Our project aims to synthesize new microporous metal-organic frameworks that show good charge mobility and conductivity. Our design of electrically conductive MOFs is guided by the three fundamental formalisms for charge transport in molecular materials: A) “through-space” transport involving π -stacking interactions between electroactive moieties, B) “through-bond” transport, where charge transfer through the covalently-bonded building blocks requires appropriate symmetry and energy overlap, and C) hopping (Marcus-like) transport, as observed in metalloenzymes, for instance. Using these principles, we have synthesized materials that have the highest electrical conductivity among microporous solids.

Recent Progress

Through-space charge transport: microporous MOFs with high charge mobility

MOFs with high charge carrier mobility. Molecular conductors involving bands formed by π -stacked molecules are most famously exemplified by charge transfer salts such as TTF-TCNQ (tetrathiafulvalene-tetracyano-quinodimethane), which exhibits metallic conductivity and even superconductivity.¹ We showed that the propensity of TTF to π -stack balances the stronger driving force of the metal-ligand bond formation and made the first microporous MOF that exhibited high charge mobility. Reaction of TTF tetrabenzoate (H_4 TTFTB) with Mn^{2+} , Co^{2+} , Zn^{2+} , and Cd^{2+} salts formed isostructural materials with infinite one-dimensional hexagonal pores and surface areas of ~ 600 m²/g (Figure 1A).² The pores are lined with infinite columns of π -stacked TTF moieties with S...S separations of only 3.8 Å, sufficiently small for good intermolecular orbital overlap. Using flash-photolysis time-resolved microwave conductivity (FP-TRMC) measurements, we measured an outstanding intrinsic charge mobility, $\mu_{TRMC} = 0.2$ cm²V⁻¹s⁻¹, for $Zn_2(TTFTB)$. This exceeded the mobility values of even some of the best organic semiconductors (e.g. $\mu_{polythiophene (TRMC)} < 0.075$ cm²V⁻¹s⁻¹). $Zn_2(TTFTB)$ was the first example of a permanently porous MOF with high charge mobility.

Through-bond charge transport: conductive molecular chains

Promoting charge transfer through a covalent construct may seem more challenging than doing so through π -stacking because in addition to proper *symmetry* overlap, good *energy* overlap must also exist between the neighboring inorganic and organic building blocks.³ Synthetically, however, the through-

bond charge transport formalism is more tractable because the directionality of the metal-ligand bond can be controlled, which reduces the serendipity involved with engineering weak π -stacking interactions within otherwise covalent frameworks such as MOFs. In order to prove that better energy overlap between the organic ligands and the inorganic nodes is beneficial for charge transport, we identified materials that exhibited infinite metal-oxygen chains, $(-M-O-)_\infty$, and sought to isomorphically replace the oxygen atoms by sulfur. We surmised that the resulting $(-M-S-)_\infty$ chains would exhibit better transport properties. One iconic class of materials that fit this description was $M_2(\text{DOBDC})$ (MOF-74, $H_4\text{DOBDC} = 2,5$ -dihydroxybenzene-1,4-dicarboxylic acid). These frameworks contain $(-M-O-)_\infty$ chains where each pair of metal atoms is bridged by one phenolate group. We replaced the phenol groups by thiophenol and showed that 2,5-disulphydrylbenzene-1,4-dicarboxylic acid ($H_4\text{DSBDC}$) generates $Mn_2(\text{DSBDC})$, a new material with permanent porosity and a high intrinsic charge mobility, $\mu_{\text{TRMC}} = 0.02 \text{ cm}^2\text{V}^{-1}\text{s}^{-1}$ (Figure 1B).⁴ This material continues to hold the record for the most porous MOF ($S_{\text{BET}} = 978 \text{ m}^2/\text{g}$) among those that show intrinsic charge delocalization or conductivity.

Two-dimensional microporous conductors: towards tunable metal-organic graphene analogs

One-dimensional conductors are excellent platforms for investigating the fundamentals of charge transport in open-framework materials, but are of limited use in polycrystalline films, where anisotropic transport and grain boundaries lead to poor bulk conductivity. To address this challenge, we have complemented our studies on one-dimensional transport with efforts to increase the charge delocalization to two dimensions.

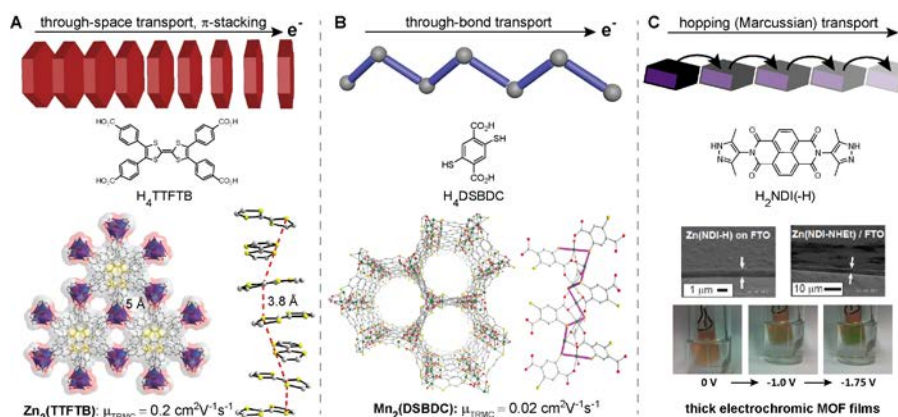


Figure 2. A) Through-space, and B) through-bond formalisms for charge transport led to the synthesis of the first MOFs with high charge mobility made from infinite TTF stacks and $(-M-S-)_\infty$ chains, respectively. Presumed electron transport pathways are shown in pink. C) charge hopping transport with electroactive naphthalenediimide ligands enabled the isolation of the first electrochromic

Mindful of the importance of good charge delocalization across the metal-ligand bond, we focused on metal bis(diiminobenzosemiquinonato) complexes (e.g. $\text{Ni}(\text{isq})_2$, see Figure 2A) as potential nodes in our 2-D materials. These are landmark molecules whose electronic structure has stoked a prominent debate over the last century and was finally shown to involve a singlet biradical ground state with full spin delocalization over the Ni atom and the aromatic rings (Figure 2A).⁵ We showed that the extent of charge delocalization is maintained when $\text{Ni}(\text{isq})_2$ is extended in two dimensions: reaction of 2,3,6,7,10,11-hexaaminotriphenylene with NiCl_2 in the

presence of NH_3 and O_2 produced a crystalline black powder of $\text{Ni}_3(2,3,6,7,10,11\text{-hexaiiminotriphenylene})_2$ ($\text{Ni}_3(\text{HITP})_2$) (Figure 2B). Electrical measurements of bulk polycrystalline pellets and thin films of $\text{Ni}_3(\text{HITP})_2$ yielded remarkable conductivity values of $200 \Omega^{-1}\cdot\text{m}^{-1}$ and $4,000 \Omega^{-1}\cdot\text{m}^{-1}$.⁶ These values are two orders of magnitude higher than for any other MOF and are the best for any microporous metal-organic hybrid material.

Future Plans

Our early result with TTF MOFs opened several avenues for further exploration. We have since observed that the Mn^{2+} and Co^{2+} analogues display charge mobility values of $0.02 \text{ cm}^2\text{V}^{-1}\text{s}^{-1}$, one order of magnitude lower than that $\text{Zn}_2(\text{TTFTB})$. We postulated that a charge transfer event may trap the photogenerated charge carriers, thereby limiting their mobility. We are currently investigating this hypothesis. Future extensions of our conductive chain approach are even more general: because the isomorphous sulfur-for-oxygen replacement strategy is amenable to many other MOFs containing similar $(-\text{M}-\text{O}-)_\infty$ chains, our report of $\text{Mn}_2(\text{DSBDC})$ may provide a universal blueprint for the formation of other porous crystalline materials with high charge mobility.

Our discovery of $\text{Ni}_3(\text{HITP})_2$ also provided several exciting avenues of future studies in our group. Most importantly, temperature-dependent conductivity studies showed an increase of conductivity with temperature (Figure 2C), characteristic of semiconducting behavior. This suggests that a single sheet of $\text{Ni}_3(\text{HITP})_2$ may be regarded as an analog of graphene with a non-zero, potentially tunable band gap, an important feature that is not readily available with other two-dimensional electronic materials. Efforts to synthesize and characterize devices made from

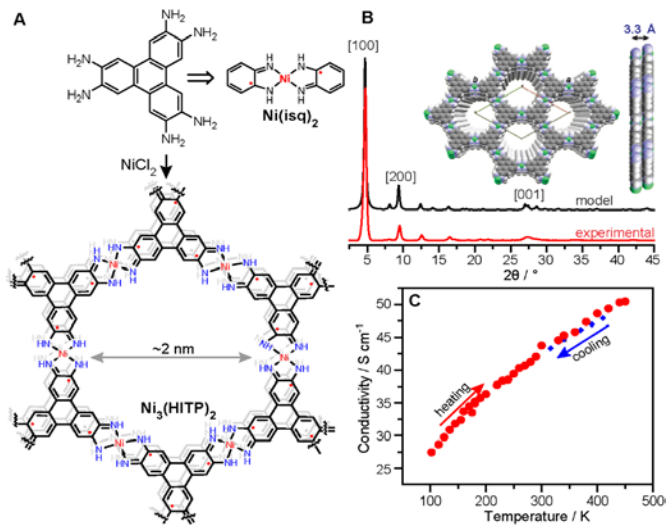


Figure 2. **A**) Structure of $\text{Ni}_3(\text{HITP})_2$ highlighting its radical character based on its $\text{Ni}(\text{isq})_2$ components. **B**) Powder X-ray diffraction pattern and **C**) variable temperature film conductivity of $\text{Ni}_3(\text{HITP})_2$.

single sheets of Ni₃(HITP)₂ are currently underway, as are additional experiments to understand the unusual linear dependence of the bulk conductivity with temperature and its magnetic properties. Furthermore, owing to its modular structure, Ni₃(HITP)₂ is clearly amenable to further synthetic manipulations. To this end, we are exploring different combinations of metals and organic cores, all centered around the essential M(isq)₂ node.

References

- (1) Ferraris, J.; Cowan, D. O.; Walatka, V.; Perlstein, J. H. *J. Am. Chem. Soc.* **1973**, *95*, 948.
- (2) Narayan, T. C.; Miyakai, T.; Seki, S.; Dincă, M. *J. Am. Chem. Soc.* **2012**, *134*, 12932.
- (3) Hoffmann, R. *Acc. Chem. Res.* **1971**, *4*, 1–9.
- (4) Sun, L.; Miyakai, T.; Seki, S.; Dincă, M. *J. Am. Chem. Soc.* **2013**, *135*, 8185–8188.
- (5) Stiefel, E. I.; Waters, J. H.; Billig, E.; Gray, H. B. *J. Am. Chem. Soc.* **1965**, *87*, 3016.
- (6) Sheberla, D.; Sun, L.; Blood-Forsythe, M. A.; Er, S.; Wade, C. R.; Brozek, C. K.; Aspuru-Guzik, A.; Dincă, M. *J. Am. Chem. Soc.* **2014**, *136*.

Publications 2012-2014

- (1) Narayan, T. C., Miyakai, T., Seki, S. & Dincă, M. High Charge Mobility in a Tetrathiafulvalene-Based Microporous Metal-Organic Framework. *J. Am. Chem. Soc.* **134**, 12932–12935 (2012).
- (2) Bertrand, G. H. V, Michaelis, V. K., Ong, T.-C., Griffin, R. G. & Dincă, M. Thiophene-based covalent organic frameworks. *Proc. Nat. Acad. Sci. USA* **110**, 4923–4928 (2013).
- (3) Sun, L., Miyakai, T., Seki, S. & Dincă, M. Mn₂(2,5-disulfhydrylbenzene-1,4-dicarboxylate): a Microporous MOF with Infinite (–Mn–S–)_∞ Chains and High Intrinsic Charge Mobility. *J. Am. Chem. Soc.* **135**, 8185–8188 (2013).
- (4) Wade, C. R., Li, M. & Dincă, M. Facile deposition of multicolored electrochromic metal-organic framework thin films. *Angew. Chem. Int. Ed.* **52**, 13377–81 (2013).
- (5) Sheberla, D., Sun, L., Blood-Forsythe, M. A., Er, S., Wade, C. R., Brozek, C. K., Aspuru-Guzik, A. & Dincă, M. High Electrical Conductivity in Ni₃(2,3,6,7,10,11-hexamino-triphenylene)₂, a Semiconducting Metal–Organic Graphene Analogue. *J. Am. Chem. Soc.* **136**, in press (2014). DOI: 10.1021/ja502765n.
- (6) Brozek, C. K. & Dincă, M. Lattice-imposed geometry in metal–organic frameworks: lacunary Zn₄O clusters in MOF-5 serve as tripodal chelating ligands for Ni²⁺. *Chem. Sci.* **3**, 2110–2113 (2012).
- (7) Brozek, C. K., Cozzolino, A. F., Teat, S. J., Chen, Y. & Dincă, M. Quantification of Site-Specific Cation Exchange in Metal–Organic Frameworks Using Multi-Wavelength Anomalous X-ray Dispersion. *Chem. Mater.* **25**, 2998–3002 (2013).
- (8) Brozek, C. K., Bellarosa, L., Soejima, T., Clark, T. V., López, N. & Dincă, M. Solvent-Dependent Cation Exchange in Metal–Organic Frameworks. *Chem.-Eur. J.* in press (2014).
- (9) Brozek, C. K. & Dincă, M. Ti³⁺-, V^{2+/3+}-, Cr^{2+/3+}-, Mn²⁺-, and Fe²⁺-Substituted MOF-5 and Redox Reactivity in Cr- and Fe-MOF-5. *J. Am. Chem. Soc.* **135**, 12886–12891 (2013).
- (10) Brozek, C. K. & Dincă, M. Cation exchange at the secondary building units of metal–organic frameworks. *Chem. Soc. Rev.* (2014), in press. DOI: 10.1039/C4CS00002A.
- (11) Cozzolino, A. F., Brozek, C. K., Palmer, R. D., Yano, J., Li, M. & Dincă, M. Ligand Redox Non-innocence in the Stoichiometric Oxidation of Mn₂(2,5-dioxidoterephthalate) (Mn-MOF-74). *J. Am. Chem. Soc.* **136**, 3334–3337 (2014).

(12) Li, M. & Dincă, M. Selective formation of biphasic thin films of metal–organic frameworks by potential-controlled cathodic electrodeposition. *Chem. Sci.* **5**, 107 (2014).

Rational Design and Nanoscale Integration of Multi-Heterostructure Photocatalysts

Xiangfeng Duan, University of California, Los Angeles

Program Scope

This research program aims to design and synthesize multi-heterostructures that integrate a nanoscale light harvesting antenna with two distinct redox nanocatalysts, probe the charge generation, separation and transport in such heterostructures, and investigate their potential as efficient and robust photocatalysts in the visible range.

Recent Progress

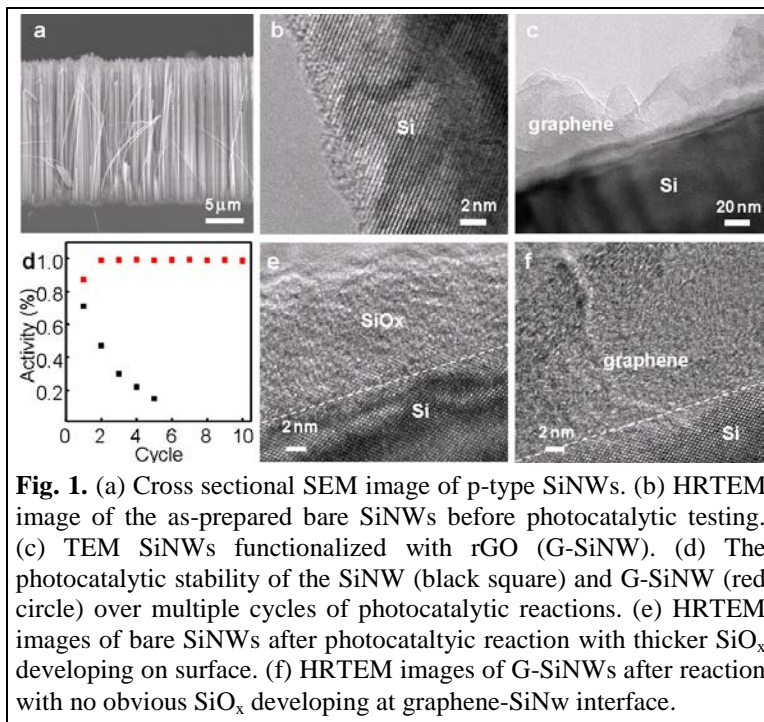
Most photocatalysts available today are limited by relatively poor photocatalytic activity under visible light and/or insufficient photoelectrochemical stability. Semiconductor materials have been broadly used for light harvesting due to their ability to absorb broad solar spectrum. However, most traditional semiconductors (*e.g.* Si, CdS) exhibit poor photoelectrochemical stability in the harsh photocatalytic environment. Oxide semiconductors (*e.g.* TiO₂) are generally more stable and more commonly used for photocatalytic purposes, but typically with too large a band gap to efficiently absorb visible solar energy. Aiming to develop stable photocatalyst in the visible range, we are exploring two parallel strategies: (1) by introducing a protective layer onto the surface of traditional semiconductors (*e.g.* Si) to promote charge separation and utilization for the desired photocatalytic reaction and the same time minimize undesired semiconductor degradation side reaction; and (2) to modify the photoelectrochemically stable oxide semiconductor (*e.g.* TiO₂) for improved visible absorption and photocatalytic activity.

1. Highly active and stable graphene-silicon nanowire (G-SiNW) heterostructure photocatalysts

To harness the light-harvesting capability of the traditional semiconductors (*e.g.* Si) for photocatalytic applications, it is essential to improve their photoelectrochemical stability. Photoelectrochemical instability is usually caused by the accumulation of photo-generated electrons or holes on the semiconductor surface, which are either highly reductive or highly oxidative and can induce severe electrochemical degradation of the semiconductor materials themselves. Therefore, to improve the photocatalyst stability, it is essential to introduce a protective layer that can chemically insulate the semiconductor from the harsh environment while maintaining an effective charge separation and transport pathway for efficient utilization of the photo-generated electrons and holes for the desired photochemical reactions. The rapid and efficient utilization of the excited photo-carriers can prevent piling up highly reactive free charges on the semiconductor surface, and prevent undesired side reactions.

Silicon nanowires (SiNWs) have been explored as light harvesting antenna in photocatalysts due to their ability to absorb broad solar spectrum, but typically exhibit rather poor photoelectrochemical stability. To this challenge, we have created graphene-SiNW (G-

SiNW) heterostructures (Fig. 1a-c) and investigated their photocatalytic characteristics. Here graphene (or reduced graphene oxide, RGO) flakes are conjugated on the SiNW surface, to function as a physical protection layer to insulate the SiNWs from the harsh electrochemical environment, and as a charge mediator to facilitate the charge separation and transport processes. Furthermore, the reduced graphene oxide may also function as effective redox catalysts to ensure efficient utilization of photo-carriers for the desired reactions. Importantly, our photocatalytic studies show the G-SiNW photocatalysts exhibit stable photocatalytic activity over multiple cycles of photocatalytic reactions, while the SiNWs show a much lower and rapidly degrading photocatalytic activity (Fig. 1d). TEM studies show that bare SiNWs exhibit a relatively clean surface with little SiO_x before the photocatalytic reactions (Fig 1b), but develop a thick SiO_x layer (>10 nm) after photocatalytic reactions (Fig. 1e), which could retard the charge transport for continued photocatalytic reactions. In contrast, the G-SiNWs exhibit a relatively clean interface with no obvious oxide development at G-SiNW interface before or after the reaction (Fig. 1c,f), consistent with the sustained photochemical stability.



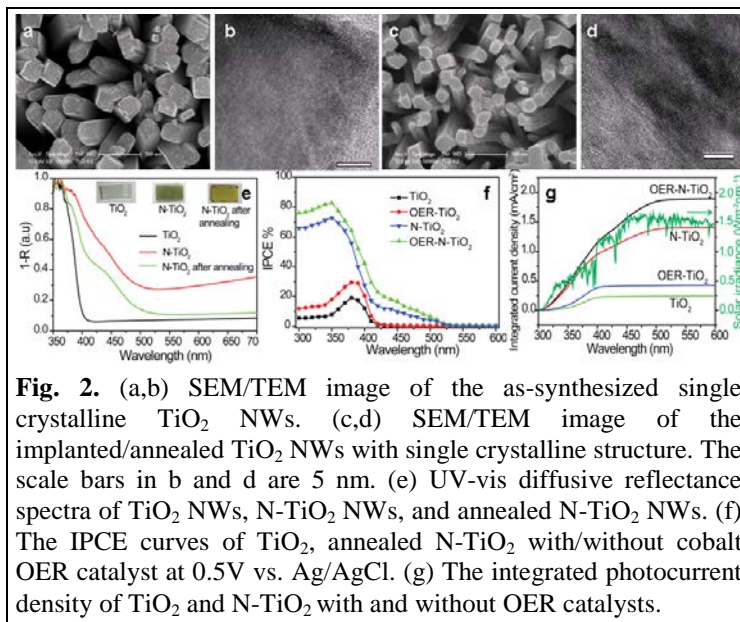
G-SiNW photocatalysts exhibit stable photocatalytic activity over multiple cycles of photocatalytic reactions, while the SiNWs show a much lower and rapidly degrading photocatalytic activity (Fig. 1d). TEM studies show that bare SiNWs exhibit a relatively clean surface with little SiO_x before the photocatalytic reactions (Fig 1b), but develop a thick SiO_x layer (>10 nm) after photocatalytic reactions (Fig. 1e), which could retard the charge transport for continued photocatalytic reactions. In contrast, the G-SiNWs exhibit a relatively clean interface with no obvious oxide development at G-SiNW interface before or after the reaction (Fig. 1c,f), consistent with the sustained photochemical stability.

To further probe the charge separation and transport at the SiNW-graphene interface and their impact on photocatalytic properties, we have conducted systematic electrochemical and photoelectrochemical studies. The cyclic voltammogram studies demonstrates that G-SiNWs exhibit obvious oxygen reduction activity, in contrast to bare SiNWs, suggesting that graphene could facilitate oxygen reduction during the photocatalytic process and thus improve the photocatalytic activity of G-SiNW heterostructures. Furthermore, electrochemical impedance studies show that the presence of graphene can greatly reduce charge transfer resistance, and photoelectrochemical studies show that G-SiNWs exhibit enhanced photocurrent in both the positive and negative potential regime when compared with the bare SiNWs, suggesting that graphene could facilitate the charge transport process for both the electrons and holes. Together, we have shown that graphene (or RGO) can protect SiNWs from harsh electrochemical environment, facilitate charge separation and improve the charge transport to ensure efficient utilization of the photocarriers for desired reactions, to greatly enhance the photocatalytic activity and stability.

2. Probing the role of nitrogen-doping in TiO₂ for visible light photocatalysts

TiO₂ has been extensively investigated as a photoanode for photoelectrochemical water splitting due to its excellent photochemical stability, suitable band edge positions, low cost and environmental friendliness. However, TiO₂ typically show little photocatalytic activity in the visible range because its large band-gap (rutile 3.0 eV; anatase 3.2 eV). To this end, impurity doping has been explored to modify the optical and electronic properties of TiO₂ for improved optical absorption in the visible range. In particular, nitrogen doped TiO₂ has been shown to exhibit visible light absorption and but still with rather limited photocatalytic activity in the visible range. Most doping strategies involve amine functional chemicals during synthesis or post thermal annealing in ammonia. These chemical doping processes are usually hard to control because they usually involve many other elements that could induce unintentional doping (e.g. by hydrogen or carbon). Alternatively, an ion implantation approach has been reported for introducing N-doping in TiO₂, yet with limited improvement in visible photo-activity (e.g. IPCE <3% at 450 nm)¹. With a polycrystalline/amorphous structure, this system is plagued with extensive defects and/or trapping states that prevent a fundamental understanding of the exact role of the nitrogen doping for further improvement.

Comparing with other doping approaches, the ion implantation process does not involve any elements other than element of interest, and could offer a cleaner and more reliable method for introducing selected impurities into a solid material. It is also a general approach that can allow introducing different and/or multiple impurity elements for systematic studies. The presence of nitrogen in TiO₂ has a profound effect on the photocatalysis, but the exact mechanism for the enhancement remains illusive. To probe the fundamental role of N-doping in TiO₂, we have synthesized single crystalline rutile TiO₂ NW arrays (Fig. 2a,b) and implanted them with nitrogen by using variable implantation dosage and acceleration voltage (Fig. 2c,d). The resulted doped NW arrays were then used as photoanodes in photoelectrochemical cells (PEC) for water splitting reaction. TEM studies show that the single crystalline structure of the TiO₂ NWs is well maintained after N-implantation/thermal annealing processes (Fig. 2b,d). The single crystalline structure is essential for minimizing the trapping states and undesired recombination centers that could degrade the photocurrent and complicate the understanding of the system. Optical diffusive reflectance



studies show that the N-implanted TiO₂ NW arrays exhibit significant absorption in the visible range (Fig. 2e). X-ray photoelectron studies show that the as-implanted nitrogen atoms mainly occupy the interstitial sites and a proper anneal can restore the crystallinity to convert the interstitial nitrogen atoms into substitutional ones. PEC studies show that the as-implanted TiO₂ show no obvious improvement while the annealed sample exhibits a dramatic improvement of the photoresponse in the visible range (Fig. 2e). Significantly, the incident photon to current conversion efficiency (IPCE) can reach ~23% at 420nm and ~18% at 450 nm (Fig. 2f), which represents the highest IPCE ever achieved in TiO₂ in the visible range (in comparison, the IPCE <3% at 450 nm and <5% at 420 nm in previous studies of N-implanted polycrystalline TiO₂ nanotubes)¹. Integrating the IPCE curves using standard air mass 1.5G solar spectrum, we can obtain a photocurrent density as high as 1.9 mA/cm² (Fig. 2g), which represents the highest value reported for the TiO₂ based photoanode to date. With few defects and trapping states, the single crystalline N-TiO₂ NWs provide an excellent system for probing the fundamental role of N-doping. To this end, we have determined the charge separation efficiency, charge injection efficiency, and well as the electrochemical impedance properties NWs before and after N-implantation. These studies demonstrate that the N-doping can improve the charge transport properties as well as charge separation and injection efficiency in TiO₂ NWs. Therefore, the enhanced photoactivity of N-implanted TiO₂ can be attributed to the increased visible light absorption and suppression of charge recombination in the TiO₂ NWs. Furthermore, it also possible to further improve the charge injection efficiency and overall IPCE by integrating oxygen evolution reaction (OER) catalysts on the surface of TiO₂ NWs (Fig. 2f,g).

Future Plans

We will continue to probe the molecular mechanism governing the electron and hole extraction process in the graphene-SiNW heterostructures; further investigate the role of nitrogen-doping in TiO₂ NWs and use the single crystalline TiO₂ NWs as a platform to investigate effect of doping or co-doping by different elements; and eventually integrate of the doped TiO₂ with redox catalysts for highly active photocatalysts in the visible range.

References

1. A. Ghicov, J. Macak, H. Tsuchiya, J. Kunze , V. Haeublein, L. Frey, P. Schmuki, Ion implantation and annealing for an efficient N-doping of TiO₂ nanotubes, *Nano Lett.*, 6, 1080-1082, 2006

Publications

1. Y. Qu and X. Duan, Progress, challenge and perspective of heterogeneous photocatalysts, *Chem. Soc. Rev.* 42, 2568-2580 (2013).
2. H. Zhang, X. Zhong, J. C. Shaw, L. Liu, Y. Huang and X. Duan, Very high energy density silicide-air primary batteries, *Energy Environ. Sci.* 6, 2621-2625 (2013).

Molecular Magnets Based on a Modular Approach: Investigation of Coupling, Anisotropy and Electronic Factors on Bistability

Kim R. Dunbar, Department of Chemistry, Texas A&M University, College Station, TX

Program Scope

Molecular magnets are materials assembled from discrete molecular building blocks under mild conditions, typically at ambient temperatures and pressures using solution techniques. Through the implementation of a modular approach, chemists can exert considerable control over connectivity, architecture and properties of molecule-based magnets by arranging appropriate pre-organized building blocks with specific geometries into zero-, one-, two- or three-dimensional architectures. The obvious importance of conventional magnetic solids in current technologies notwithstanding, molecular magnets offer several key advantages including optical transparency, solubility, and “softness” of the crystalline network that renders them susceptible to chemical modifications and multifunctionality.²⁻⁶

Molecular magnets can be obtained through chemical assembly of organic radicals (unpaired electrons localized on p orbitals) or paramagnetic metal ions (unpaired electrons in d or f orbitals) connected by bridging units in such a way that exchange interactions between spins occur through intervening overlapping orbitals of diamagnetic bridges (superexchange) or direct exchange. In addition to paramagnetic building blocks, there are many other molecules bearing various additional functionalities that can be incorporated into the framework of molecule-based magnets. Appropriate combinations and arrangements of the “functional” units in a molecular or extended architecture can lead to multifunctional molecular magnetic solids, which, apart from interesting magnetic properties, may also exhibit additional physico-chemical properties in response to external stimuli including light, pressure, electric field, and guest molecules/solvent vapors.⁷⁻⁹ Clearly, the fascinating, interdisciplinary field of molecular magnetism research that incorporates basic concepts of chemistry, physics, and materials science has much to offer to the future of materials science and the elaboration of new types of devices at the nanoscale. The scope of this project is to design new magnetic molecules based on early 3d transition metals and heavier transition metal ions of the second and third row transition elements that exhibit strong single-ion anisotropy. Owing to strong spin-orbit coupling and the effect of significant zero-field splitting effects as well as the symmetry of the molecule, paramagnetic compounds based on anisotropic metal ions can behave as single molecule magnets (SMMs). In particular, anisotropy stemming from specific combinations of metal ions in the M-CN-M' linkages lead to anisotropic exchange interactions and extraordinarily strong coupling as evidenced by our recent results. We are using experimental and theoretical studies in tandem to test how the symmetry and strength of the ligand field of the metal affect the zero-field splitting parameter that leads to Ising (or easy axis) anisotropy. Detailed analyses of key complexes are being conducted using magnetometry, inelastic neutron scattering and High Field, High Frequency EPR methods. In addition we have

established collaborations with theorists who are providing aid in *ab initio* theory and DFT calculations to support the experimental results.

Recent Progress

Our success in preparing a mixed Mo_2V_3 molecule with a record exchange coupling through the cyanide ligand and an SMM with a record barrier and hysteresis for a cyanide compound based on Mn_2Mo (Figure 1) constitute important evidence that we are headed in the right direction by using early 3d/4d metal ion combinations. Another major result in the past six months is our synthesis of the first example

of the 5d heptacyanotungstate anion (Figure 2), a finding that presages a future of exciting new studies for 5d metal ion cyanide magnetism. We have also isolated a number of new Single

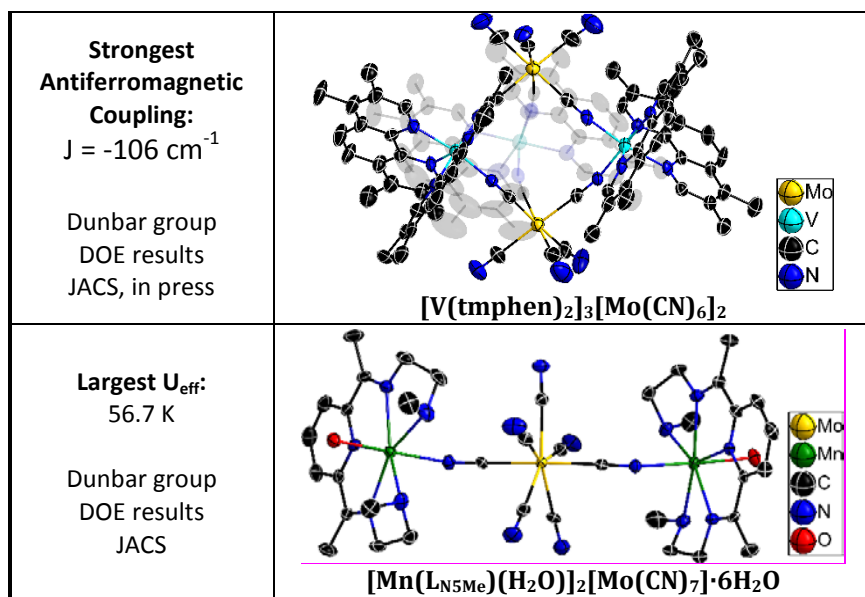


Figure 1. Records for Magnetism of Cyanide Compounds from DOE funded research.

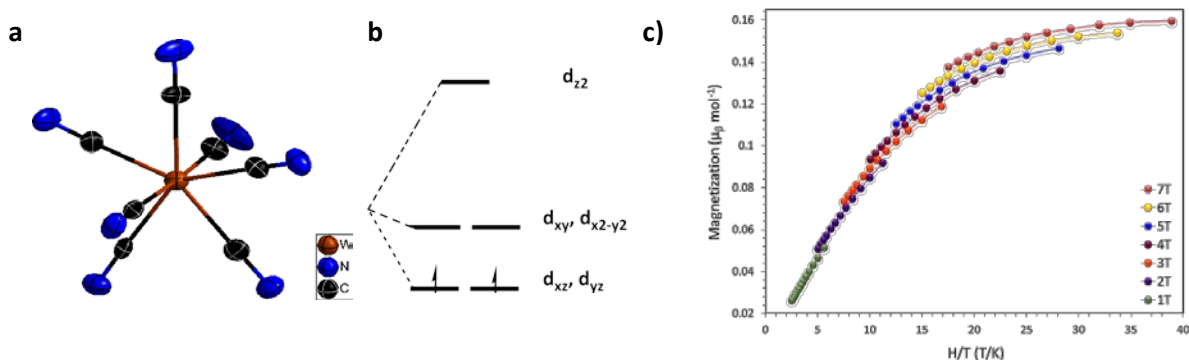


Figure 2. (a) Crystal structure of $[\text{W}^{\text{IV}}(\text{CN})_7]^{3-}$. Ellipsoids drawn at the 50% probability, (b) Pentagonal bipyramidal splitting diagram and (c) reduced magnetization data for $(\text{Bu}_4\text{N})_3[\text{W}^{\text{IV}}(\text{CN})_7]$.

Molecule Magnets. For example trigonal monopyramidal Schrock-type complexes with bulky triamidoamine-type ligands were prepared and the Co^{II} derivative (Figure 3) exhibits field-induced slow paramagnetic relaxation characteristic of SMMs with a relatively high energy barrier for the magnetization reversal of $U_{\text{eff}}/k_{\text{B}} = 27.8 \text{ K}$. More importantly these compounds possess an open axial coordination site that can be used to form a cyanide bridge to a second metal spin center which is the next phase of this research.

Another recent promising result is the isolation of $[\text{Co}(\text{TPMA})(\text{CH}_3\text{CN})][\text{BF}_4]_2 \cdot \text{CH}_3\text{CN}$ (TPMA = tris(2-pyridinemethyl)amine) in which the Co^{II} center is in a slightly distorted trigonal bipyramidal environment. The coordinated CH_3CN ligand should be easily replaced by a cyanide ligand which makes it an ideal synthon for the synthesis of trinuclear complexes in reactions with hexa-, hepta-, or octa-cyanometallates. This molecule displays slow relaxation of the magnetization under a 1000 Oe applied DC field and adds to the growing number of mononuclear SMMs based on Co^{II} in non-traditional coordination environments.

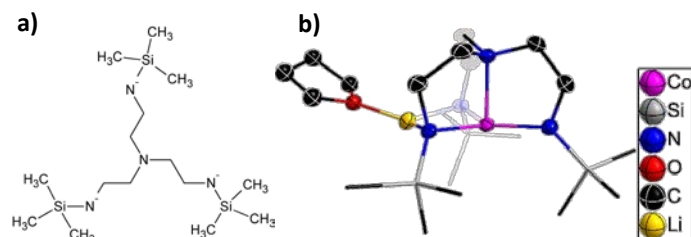


Figure 3. (a) Tris-(2-aminoethyl)-amine-based ligand, $[\text{N}_3\text{N}]^{3-}$. (b) X-ray structure of $[\text{Co}^{\text{II}}(\text{N}_3\text{N})\text{Li}(\text{THF})]$.

Future Plans

In addition to continuing to probe the role of strong first-order spin-orbit coupling and anisotropic exchange interactions on the magnetic properties

of paramagnetic molecules and assemblies that contain cyanide or reduced organocyanide bridging ligands, we plan to prepare new lanthanide and transition metal mononuclear SMMs. The modular approach to designing homologous series of compounds has led to structurally related molecules with the same geometrical arrangement of spin centers. Armed with the successful elaboration of record magnetic coupling and blocking temperatures for cyanide-based SMMs, we are poised to advance fundamental knowledge about how single-ion anisotropy manifests itself in terms of magnetic bistability. We will also target families of mononuclear compounds of transition metal and lanthanide ions that display SMM behavior in spite of the few number of spins that they possess.

References

1. Qian, K.; Huang, X.-C.; Zhou, C.; You, X.-Z.; Wang, X.-Y.; Dunbar, K. R., *J. Am. Chem. Soc.* **2013**, *135* (36), 13302-13305.
2. *Magnetism: Molecules to Materials (I-V)*. Wiley-VCH: Weinheim, 2002-2005.
3. Thompson, L. K., Ed., *Coord. Chem. Rev.* **2005**, (249), 2549-2730.
4. Coronado, E., Dunbar, K. R., *Inorg. Chem.* **2009**, (48), 3293-3896.
5. Brechin, E. K., *Dalton Trans.* **2010**, (39), 4671-5038.
6. Miller, J. S., Gatteschi, D., Eds., *Chem. Soc. Rev.* **2011**, (40), 3053-3368.
7. Ohkoshi, S.-i.; Tokoro, H., *Acc. Chem. Res.* **2012**, *45* (10), 1749-1758.
8. Sato, O.; Tao, J.; Zhang, Y. Z., *Angew. Chem., Int. Ed.* **2007**, *46* (13), 2152-2187.
9. Shimomura, S.; Matsuda, R.; Tsujino, T.; Kawamura, T.; Kitagawa, S., *J. Am. Chem. Soc.* **2006**, *128* (51), 16416-16417.

DOE Publications (2012-2014)

1. A Mn(III) Chain Derived from Mn_{12} -Acetate that Exhibits Both Glauber Dynamics and Antiferromagnetic Ordering Regimes. Andrey Prosvirin, Hanhua Zhao and Kim R. Dunbar, *Inorg. Chim. Acta., (Jon Zubieta special issue)*, **2012**, *389*, 118-121.
2. Crystal-to-Crystal Transformation of Magnets Based on $[\text{Mo}(\text{CN})_7]^{4-}$ with Dramatic Changes in Coordination Mode and Ordering Temperature. Qing-Lun Wang, Heather

- Southerland, Jian-Rong Li, Andrey V. Prosvirin, Hanhua Zhao, and Kim R. Dunbar, *Angew. Chem. Int. Ed.*, **2012**, *51*, 932-934.
3. A Porous Sm(III) Coordination Nanotube with Hydrophobic and Hydrophilic Channels, Nazario Lopez, Hanhua Zhao, Dan Zhao, Hong-Cai Zhou, Joseph P. Riebenspies and Kim R. Dunbar, *Dalton Trans.*, **2013**, *42*, 54-57.
 4. Spin-Crossover Materials: Properties and Applications in “*Charge Transfer-Induced Spin Transitions in Cyanometallate Materials*”, Chapter 6. “Malcolm Halcrow, Editor. Wiley-Blackwell. Kim R. Dunbar, Michael Shatruk, Catalina Achim, **2013**, 171-202.
 5. Reversible Switching from Antiferro- to Ferromagnetic Behavior by Solvent-Mediated, Thermally-Induced Phase Transitions in a Trimorphic MOF-based Magnetic Sponge System Mario Wriedt, Andrey A. Yakovenko, Gregory J. Halder, Andrey Prosvirin, Kim R. Dunbar and Hong-Cai Zhou, *J. Am. Chem. Soc.*, **2013**, *135*, 4040-4050.
 6. An unprecedented double layered Fe₃₆ phosphonate cage. Christine M. Beavers, Tina Tezgerevska, Andrey V. Prosvirin, John D. Cashion, Brendan F. Abrahams, Carmel Abrahams, Kim R. Dunbar, and Anne F. Richards, *Inorg. Chem.*, **2013**, *52*, 1670-1672.
 7. A tetranuclear oxofluorovanadium(IV) cluster encapsulating a Na(H₂O)_n⁺ subunit. Tiffany M. Smith, Nika Mahne, Andrey Prosvirin, Kim R. Dunbar, and Jon Zubieta, *Inorg. Chem. Commun.*, **2013**, *33*, 1-5.
 8. One-Dimensional Square- and Ladder-Type Architectures Incorporating Octacyanometallates of Molybdenum(V) and Tungsten(V), Hanhua Zhao, Andrew J. Brown, Andrey V. Prosvirin, Kim R. Dunbar, *George Christou Special Issue, Polyhedron*, **2013**, *12*, 321–327.
 9. A Single-Molecule Magnet Based on [Mo^{III}(CN)₇]⁴⁻ with the Highest Energy Barrier for a Cyanide Compound Xin-Yi Wang, Kun Qian, Xing-Cai Huang, Chun Zhou, Xiao-Zeng You, and Kim R. Dunbar, *J. Am. Chem. Soc.*, **2013**, *135*, 13302-13305.
 10. A Neutral Fe(III) Compound Exhibiting A Two-Step Spin Transition and Dielectric Anomalies. Zhao-Yang Li, Jing-Wei Dai, Kevin J. Gagnon, Hong-Ling Cai, Takashi Yamamoto, Yasuaki Einaga, Han-Hua Zhao, Shinji Kanegawa, Osamu Sato, Kim R. Dunbar, and Ren-Gen Xiong, *Dalton Trans.*, **2013**, *42*, 14685-14688.
 11. Squaring the cube: A Family of Octametallate Lanthanide Complexes Including a Dy₈ Single-Molecule Magnet Ming Fang, Hanhua Zhao, Andrey V. Prosvirin, Dawid Pinkowicz, Kim R. Dunbar, Bin Zhao, Wei Shi, Peng Cheng, Wolfgang Wernsdorfer and Euan K. Brechin, *Dalton Trans.*, **2013**, *42*, 14693-14701. (Cover art article).
 12. Trigonal bipyramidal 5d-4f Single Molecule Magnets. Mohamed R. Saber and Kim R. Dunbar, *Chem. Commun.*, **2014**, *50*, 2177-2179.
 13. Variations in Topology and Magnetic Properties of Hepta- and Octacyanometallates of Molybdenum with Manganese (II). Qing-Lun Wang, Yuan-Zhu Zhang, Heather Southerland, Andrey V. Prosvirin, Hanhua Zhao and Kim R. Dunbar, *Dalton. Trans.*, **2014**, *43*, 6802-6810.
 14. Record antiferromagnetic coupling for a 3d/4d cyanide bridged compound, Dawid Pinkowicz, Heather Southerland, Xin-Yi, Wang and Kim R. Dunbar, **2014**, *J. Am. Chem. Soc.*, in press.
 15. Ligand effects on the magnetic anisotropy of tetrahedral cobalt complexes, Mohamed Saber and Kim R. Dunbar, **2014**, submitted to *Angew. Chem. Int. Ed.*

Small Gas Storage and Selective Carbon Dioxide Capture by Nanoporous Organic Polymers

Hani M. El-Kaderi, Department of Chemistry, Virginia Commonwealth University

Program Scope

Our research targets the synthesis of porous organic polymers that have adjustable pore size, surface area, and chemical composition for use in gas separation and storage applications. Among the promising materials for CO₂ capture from flue gas and methane-rich gases are nitrogen-functionalized porous materials such as organic polymers, organic-inorganic hybrid materials, and porous carbons.¹⁻⁴ Recent studies by Wilmer *et al.* identified the chemical and structural properties of porous materials relevant to CO₂ separation under vacuum and pressure swing methods.² These processes were selected over temperature swing because the latter is less applicable as it consumes considerable energy.

Recent Progress

Benzimidazole-linked polymers: We have demonstrated the use of pyrene-derived benzimidazole-linked polymers (BILPs, Figure 1) in CO₂ removal from flue and methane-rich gases. The implication of different physical properties (pore size and surface area) on selective CO₂ uptake or separation from N₂ and CH₄ under pressure swing adsorption (PSA) and vacuum swing adsorption (VSA) were investigated. The Ideal Adsorbed Solutions Theory (IAST) data show that BILPs exhibit high CO₂/N₂ selectivity values (32-56 at 298 K, Figure 2). Furthermore, the optimal porosity and CO₂ enthalpy of adsorption render BILP-12 very efficient in landfill and natural gas separation by PSA. On the other hand, the moderate porosities and higher CO₂ binding affinities of BILP-11 and BILP-13 make them better fit for flue gas separation by VSA. Interestingly, the diverse physical properties of BILPs and their N-rich pores place them among the top performing materials for landfill gas and flue gas separation by VSA and PSA. Tailoring such properties within one class of materials has been a challenge especially while also maintaining chemical stability. We used a synergistic experimental and theoretical study (DFT) to highlight

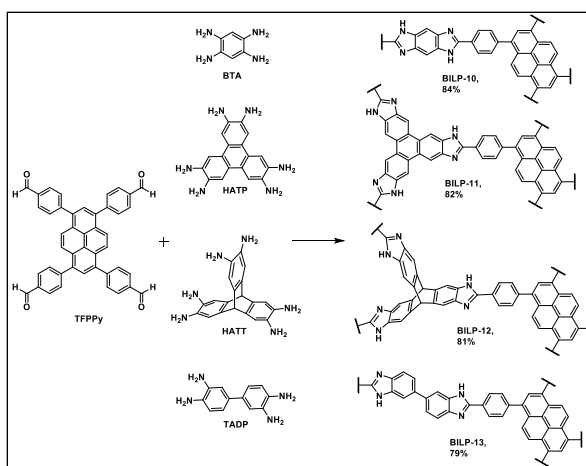


Figure 1. Synthesis of BILPs: (i) DMF, -30 °C, 3 hr, (ii) DMF, RT, 6 hr under N₂, (iii) DMF, 130 °C, 72 hr under O₂.

the impact of material design at the molecular and electronic levels on the binding affinity and interaction sites of CO₂ with BILPs. DFT calculations indicate that CO₂ is stabilized by benzimidazole units through Lewis acid-base (N \cdots CO₂) and aryl C-H \cdots O=C=O interactions. It is notable that DFT calculations of the CO₂ binding affinity were in good agreement with experimental data collected from pure CO₂ isotherms (32-35 kJ mol⁻¹).

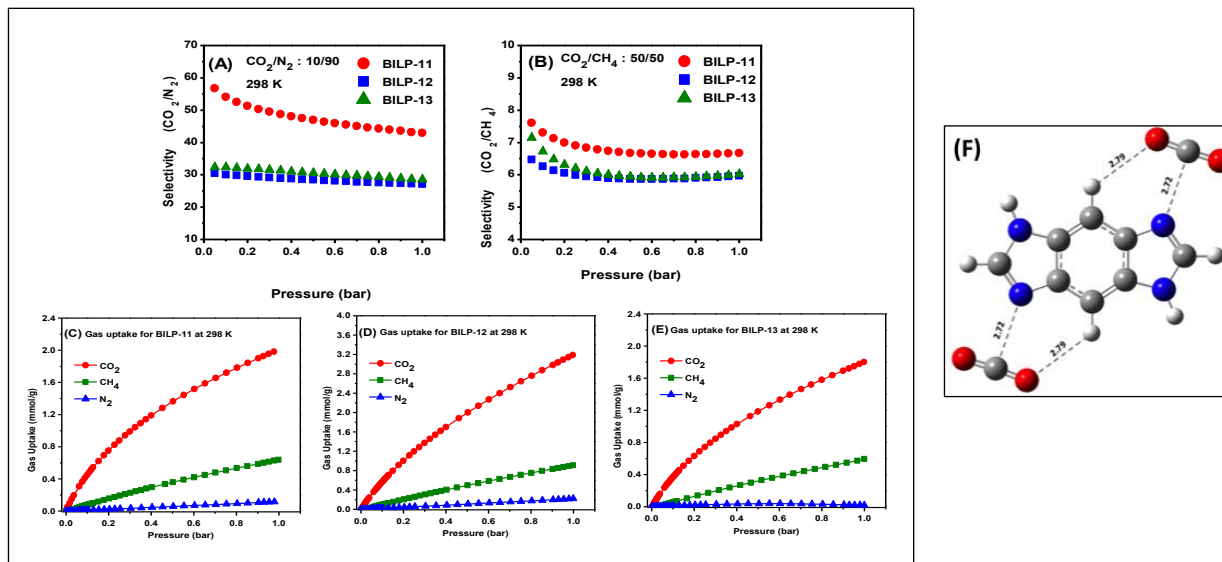


Figure 2. IAST selectivity of BILPs at 298 K: (A) CO₂/N₂ (10/90) and (B) CO₂/CH₄ (50/50). Gas uptake for BILPs at 298 K; CO₂ (red circle), CH₄ (olive square), and N₂ (blue triangle). (F) Fully optimized geometries of selected BILPs-CO₂ interactions calculated at M06/6-311+G* level of theory. The bond lengths are in Å.

Azo-linked polymers: We reported the synthesis of azo-linked polymers (ALPs) that have high surface area and high CO₂ uptake at room temperature (Figure 3). Azo-linkage formation (-N=N-) was catalyzed by Cu(I) to link triptycene and other 3D organic building units to construct highly porous organic polymers having high N-functionality. We have shown that ALPs not only have exceptionally high CO₂ uptake at ambient pressure but also have the desired chemical and thermal stability to withstand the harsh conditions under which CO₂ is captured and separated from flue and natural gases (acidic and humid conditions). In addition to their high CO₂ uptake, ALPs display very good selectivity toward CO₂ over CH₄ and N₂. However, their selectivity levels remain below those of BILPs. Accordingly, we used IAST to predict binary gas mixture behavior at 273 K and 298 K, with gas mixture compositions similar to those of flue gas (CO₂/N₂: 15/85) and natural gas (CO₂/CH₄: 5/95), as depicted in Figure 4 and summarized in Table 1. The IAST CO₂/N₂ selectivity of ALPs at 273 K and 1 bar was found to be 34-44. The impact of temperature on the CO₂/N₂ selectivity can be seen in Table 1, which clearly indicates a decrease in the selectivity of all ALPs with increasing temperature. The IAST CO₂/N₂ selectivities at 298 K and 1 bar were found to be 26-35, which are lower than those at 273 K. At 273 K, ALP-3 has the highest CO₂/N₂ selectivity, which starts at 54 at low coverage and then drops slightly with increased pressure to reach 44 at 1 bar. Other ALPs have similar CO₂/N₂

selectivities that remain almost constant with pressure. The CO₂/CH₄ selectivity of ALPs at 273 K is very similar reaching ~8 at 1 bar. Increasing the temperature to 298 K reduces the CO₂/CH₄ selectivity of ALPs to 5-6, which again is in line with our results from initial slope calculations. The CO₂/CH₄ selectivity of ALPs is considerably lower than that of CO₂/N₂ since CH₄ has much higher adsorption potential than N₂ because of the higher polarizability of CH₄ ($26 \times 10^{-25} \text{ cm}^3$) compared to that of N₂ ($17.6 \times 10^{-25} \text{ cm}^3$). Our study indicated that the use of azo-linkage in porous organic polymers could provide physicochemically stable materials for gas separation applications. In addition to their use in gas separation, azo-linked materials are light responsive (cis/trans conformation) which could trigger gas release upon exposure to light.

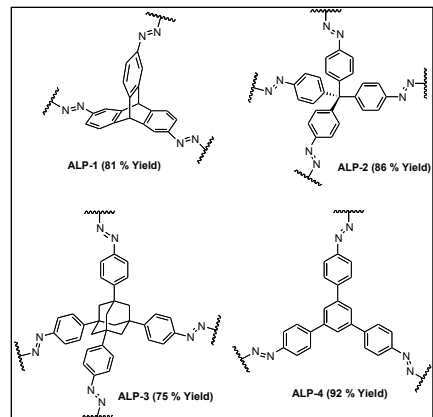


Figure 3. 2D and 3D ALPs.

Polymer	Selectivity [Initial Slope] ^a		Selectivity [IAST] ^b	
	CO ₂ /N ₂	CO ₂ /CH ₄	CO ₂ /N ₂	CO ₂ /CH ₄
ALP-1	35 (27)	6 (5)	40 (28)	8(6)
ALP-2	29 (27)	7 (5)	34 (26)	8(5)
ALP-3	43 (35)	8 (6)	44 (35)	8(6)
ALP-4	30 (28)	7 (5)	35 (26)	8(5)

^aSelectivity (mol mol⁻¹) was calculated by initial slope method at 273 K and (298 K). ^bSelectivity (mol mol⁻¹, 1 bar) was calculated by IAST method at mole ratio of 15:85 for CO₂/N₂ and mole ratio of 5:95 for CO₂/CH₄ at 273 K and (298 K).

Table 1. CO₂/N₂ and CO₂/CH₄ selectivity of ALPs.

Future Plans

Our future plans focus on the use of pore-functionalized organic frameworks for improved gas separation properties. Specifically, we will target alkoxy-functionalized pores (-OR: R = alkyl) to alter the chemical nature of the pores (hydrophilicity) as well as their size. In addition to gas selectivity studies from pure gas isotherms, the use of binary gas mixtures under dynamic flow will be studied (gas breakthrough studies). The new polymers will be processed with liquid and supercritical carbon dioxide to improve porosity and micropore accessibility.

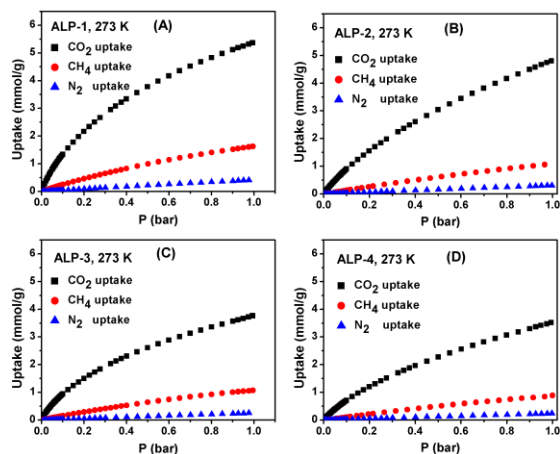


Figure 4. CO₂, CH₄, and N₂ adsorption isotherms of ALPs at 273 K.

References

1. Dawson, R.; Cooper, A. I.; Adams, D. J. *Polym. Int.* **2013**, *62*, 345-352.
2. Wilmer, C. E.; Farha, O. K.; Bae, Y. S.; Hupp, J. T.; Snurr, R. Q. *Energ. Environ. Sci.*, **2012**, *5*, 9849-9856.
3. Sumida, K.; Rogow, D. L.; Mason, J. A.; McDonald, T. M.; Bloch, E. D.; Herm, Z. R.; Bae, T.-H.; Long, J. R. *Chem. Rev.* **2011**, *112*, 724-781.
4. Li, P. Z.; Y. Zhao, L. *Chem-Asian J*, **2013**, *8*, 1680-1691.

Publications

1. Sekizkardes, A. K.; Islamoglu, T.; Kahveci, Z.; El-Kaderi, H. M.* “Application of pyrene-derived benzimidazole-linked polymers to CO₂ separation under pressure and vacuum swing adsorption settings,” *J. Mater. Chem. A.*, **2014** (DOI: 10.1039/C4TA01281J).
2. Altarawneh, S.; Behera, S.; Jena, P.; El-Kaderi, H. M.* “New insights into carbon dioxide interactions with benzimidazole-linked polymers,” *Chem. Commun.*, **2014**, *50*, 3571-3574. (Invited paper for a thematic issue on CO₂ capture, separation, and reuse)
3. Arab, P.; Rabbani, M. G.; Sekizkardes, A. K.; Islamoglu, T.; El-Kaderi, H. M.* “Copper(I)-Catalyzed Synthesis of Nanoporous Azo-Linked Polymers: Impact of Textural Properties on Gas Storage and Selective Carbon Dioxide Capture,” *Mater. Chem.* **2014**, *26*, 1385–1392 (featured on the cover of *Chemistry of Materials*, Issue 3)
4. Islamoglu, T.; Rabbani, M. G.; El-Kaderi, H. M.* “Impact of post-synthesis modification of nanoporous organic frameworks on small gas uptake and selective CO₂ capture,” *J. Mater. Chem. A*, **2013**, *1*, 10259-10266.
5. Rabbani, M. G.; Sekizkardes, A. K.; Kahveci, Z.; Reich, T. E.; Ding, R.; El-Kaderi, H. M.* “A Highly Porous Pyrene-Derived 2D Imine-Linked Covalent Organic Framework for Enhanced Gas Storage Applications,” *Chem. Eur. J.* **2013**, *19*, 3324–3328.
6. Kahveci, Z.; Islamoglu, T.; Shar, G. A.; Ding, R.; El-Kaderi, H. M.* “Targeted Synthesis of A Mesoporous Triptycene-Derived Covalent Organic Framework” *CrystEngComm.* **2013**, *15*, 1524-1527. (Invited paper for a thematic issue on Covalent Organic Frameworks)
7. Reich, T. E.; El-Kaderi, H. M.* “Impact of Tailored Chemical and Textural Properties on The Performance of Nanoporous Borazine-Linked Polymers in Small Gas Uptake and Selective Binding”. *J. Nanopart. Res.* **2013**, *15*,1368.
8. Rabbani, M. G, Sekizkardes, A. K.; El-Kadri, O. E.; Kaaffarani, B. R.; El-Kaderi, H. M.* “Pyrene-Directed Growth of Nanoporous Benzimidazole-Linked Nanofibers and their Application to Selective CO₂ Capture and Separation”. *J. Mater. Chem.* **2012**, *22*, 25409-25417.

Pore Space Engineering and Functionalization in Porous Metal-Organic Framework Materials

Pingyun Feng, University of California at Riverside, Riverside, CA 92521

Program Scope

The current program aims to develop innovative synthetic methods and paradigms to create new crystalline porous materials with intricate and exotic architectural design and chemical features for energy related applications. Chemical and solvothermal synthesis together with topological analysis and prediction are being used to design new materials with advanced properties. Crystal structures, thermal and chemical stability of newly designed materials are fully characterized. Sorption properties of various gases, ionic conductivity, and ion-exchange properties of these new materials are being evaluated to establish composition-structure-property correlation that will be further utilized to refine synthetic strategy to optimize porous materials for efficient energy-related applications.

Recent Progress

The current BES project started about 9 months ago. In the following, results obtained in the past 9 months leading to 4 publications are summarized.

1. Anion Stripping as a General Method to Create Cationic Porous Framework with Mobile Anions

In addition to developing new anionic framework materials to promote cationic proton conductivity, we are also interested in developing a synthetic strategy for the generation of cationic porous framework materials with high anionic mobility. Anion-conducting MOFs could be utilized in anion exchange membrane fuel cells. As is well known, direct synthesis of porous materials generally leads to metal-organic frameworks (MOFs) with neutral frameworks. For researchers who desire to synthesize cationic porous framework materials with high anionic mobility, such neutral frameworks are usually considered undesirable and should be avoided as much as possible. We, however, take a different view. Our hypothesis is that if we could develop a synthetic method capable of converting a neutral framework into a cationic one, we would be able to tap into the vast resources (i.e., neutral MOFs) that are available in the MOF field. Here in this work, we demonstrate our first success in converting neutral MOFs into cationic ones with high anionic mobility.

It is the nature's preference to form neutral frameworks by the attachment of anionic species such as F^- or OH^- to the framework metal sites, neutralizing an otherwise cationic scaffolding. How can we undo what the nature has done? Our method is based on the differential affinity between different metal ions with framework anionic species. Specifically, Al^{3+} (in the form of $AlCl_3$) is used to strip fluoride anions away from framework Cr^{3+} sites (because Al^{3+} has a higher affinity for F^- than Cr^{3+}), leading to cationic frameworks with mobile Cl^- anions. The

subsequent anion exchange with OH^- further leads to a porous network with mobile OH^- anions. New materials prepared by anion stripping can undergo ion exchange with anionic organic dyes and also exhibit dramatically improved ionic conductivity compared to the original neutral frameworks. The work has been published in *J. Am. Chem. Soc.* **2014**, *136*, 7579-7582.

2. *Direct Observation of Two Types of Proton Conduction Tunnels Co-existing in A New Porous Indium-Organic Framework*

The development of new fast proton conduction materials is an important step in the fuel cell applications. Metal-organic frameworks are an emerging class of materials that have shown great potential for fast proton conduction. However, currently, only a small number of MOFs have been reported sporadically and further advancement in this important field requires much deeper insight into the proton conduction mechanism and development of versatile synthetic strategy and new conduction pathway.

In this work, we have developed a prototypical synthetic system that has a great potential to enhance the proton conductivity. One key feature of this work is the deliberate targeting of the anionic framework that helps to introduce mobile extra-framework NH_4^+ species that carry high concentration of conducting protons. Another key feature is the introduction of 4,5-imidazoledicarboxylic acid (H_3imdc) into the oxalate system (MOFs based on oxalates are well known for proton conduction), leading to a new anionic indium-organic framework incorporating mixed ligands (oxalic acid and 4,5-imidazoledicarboxylic acid). H_3imdc not only provides proton conduction pathway through formation of extended hydrogen bonding network with other guest or host species, but also contributes an extra proton (compared to typical dicarboxylates such as oxalate) to increase the proton concentration in the tunnel. The exploration of such multifunctional ligand represents a new strategy to develop proton conducting MOFs with enhanced conductivity.

Because the application of proton conduction generally requires high aqueous or moisture stability, we have designed our synthesis in rather harsh hydrothermal conditions to ensure that our new material possesses needed stability for potential applications. Another unique aspect of this work is that in addition to high proton conductivity, our new MOF material possesses two types of proton conducting tunnels simultaneously, which have so far rarely seen among fast proton conductors. The excellent crystallographic data has allowed us to pinpoint the location of protons, which make it feasible for us to propose possible proton conduction pathways. The work has been published in *Chem. Mater.* **2014**, *26*, 2492-2495.

3. *Porous MOFs constructed from New Lithium Ion Clusters*

Being at the center of important technological applications, the synthetic and structural chemistry of lithium ions is of great interest, from battery materials for electric vehicles to porous materials for gas storage and separation applications. Two novel types of lithium clusters, Li_4 tetramer and Li_2 dimer, have been created as the building blocks of MOFs in this study. Such clusters like Li_4 tetramers are unusual and have not been proposed or synthesized before.

The Li₂ paddlewheel dimer is equally unusual, because even though paddlewheel dimer based on divalent metal ions such as Cu²⁺ and Zn²⁺ are well known, it has not been expected to occur for monovalent lithium ions. The assembly of such unprecedented clusters with two types of tricarboxylate ligands leads to two highly open frameworks, one of which exhibits a high CO₂ uptake capacity among Li-based MOFs (Fig. 1). The synthesis of the material is based on a simple and yet quite effective synthetic strategy of using highly negative ligands (tricarboxylic acid) to promote the lithium ions to cluster around into either lithium tetramer or dimer. For example, in this study, the use of the low-

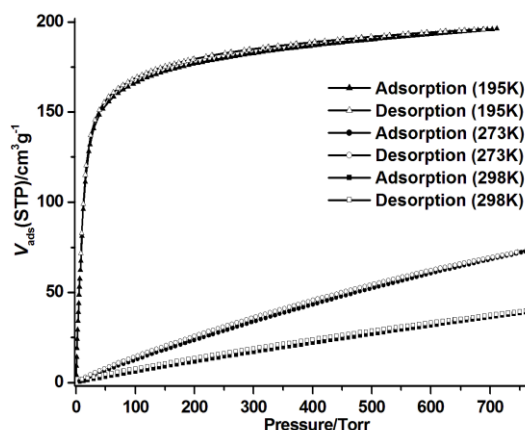


Figure 1. CO₂ sorption isotherms of CPM-46 at different temperatures.

cost BTC ligand (BTC =1,3,5-benzenetricarboxylate) induces a dramatic clustering of four lithium ions into the unprecedented square-planar configuration. This study reveals the interesting and unprecedented synthetic and structural chemistry of lithium ions. The work has been published in *Cryst. Growth Des.* **2014**, *14*, 897-900.

4. Perfect Statistical Symmetrization of a Heterofunctional Ligand Induced by Pseudo-Copper Trimer in an Expanded Matrix of HKUST-1

In this work, a heterofunctional ligand based on pyridyl and carboxyl functionalities was used to create an intriguing assembly with a highly symmetrical porous framework, despite the low symmetry of the ligand. The new material shows a total CO₂ uptake of 55 cm³/g at 1 atm and 273 K (Fig. 2). The structure has the same connectivity as the famous HKUST-1 type structure. The exceptional crystallization process resulted from the intricate cooperative process between two different inorganic units (copper monomer and dimer) that rarely go together and an organic ligand with two geometrically equivalent oxygen and nitrogen sites. The ultimate result is the creation of this new expanded HKUST-1 type material from a

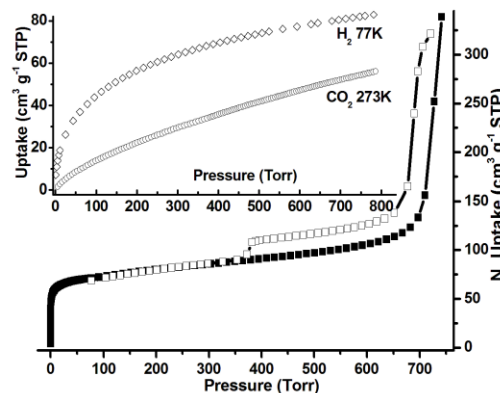


Figure 2. N₂ sorption isotherm at 77 K, (highlighted in blue box) showing the hysteresis generated from the mesoporosity in CPM-101. (inset) H₂ (diamonds), and CO₂ (circles) sorption isotherms. (solid symbols, adsorption; open symbols, desorption)

ligand that is supposed to do something else, at least according to the general MOF design principles that we are accustomed to. This work represents a rare example of perfect symmetrization of the heterofunctional ligand due to the equalization of pyridyl and carboxyl groups. The unusual behavior of the ligand arises out of the need to respond to the occurrence of either copper monomer or dimers in the same spatial region. The work is published in *Cryst. Growth Des.* **2013**, *13*, 5175-5178.

Future Plans

We will continue to pursue our proposed objectives of the project. Specifically, we will seek to design synthetic strategies that permit methodological introduction of crystallographically ordered functional groups onto the porous frameworks materials. We will further refine our synthetic strategies for architectural pore space engineering including pore space partition to create multiple domains of pore space with pore size commensurate with the size of the gas molecules for enhanced solid-gas interactions and to fully characterize thermal and chemical stability and gas (e.g., CH₄, CO₂, N₂, and H₂) sorption properties. Crystal structure analysis is an important part in the development of new materials because it allows us to identify compositional and structural features that correlate with such properties and can reveal previously unseen compositional and structural patterns that may lead to new or improved design strategies and more advanced materials. We will further build up on our recent successes and expand our efforts on the development of porous materials based on early transition metal ions (e.g., Ti and V),¹ by taking advantage of recent advances in synthetic methodology. Such materials have rich structural features and a variety of useful properties.

References

1. “A Novel Vanadium MOF Catalyst and X-ray Multistage Snapshots of Olefin Epoxidation Reaction”, L. Wang, T. Wu, X. Bu, P. Feng, to be submitted for publication.

Publications

1. “Anion Stripping as a General Method to Create Cationic Porous Framework with Mobile Anions” C. Mao, R. A. Kudla, F. Zuo, X. Zhao, L. J. Mueller, X. Bu, P. Feng, *J. Am. Chem. Soc.* **2014**, *136*, 7579-7582.

2. “Direct Observation of Two Types of Proton Conduction Tunnels Coexisting in a New Porous Indium–Organic Framework” X. Zhao, C. Mao, X. Bu, P. Feng, *Chem. Mater.* **2014**, *26*, 2492–2495.

3. “New Lithium Ion Clusters for Construction of Porous MOFs” A. Clough, S. Zheng, X. Zhao, Q. Lin, P. Feng, X. Bu, *Cryst. Growth Des.* **2014**, *14*, 897–900.

4. “Perfect Statistical Symmetrization of a Heterofunctional Ligand Induced by Pseudo-Copper Trimer in an Expanded Matrix of HKUST-1” Q. Lin, X. Bu, P. Feng, *Cryst. Growth Des.* **2013**, *13*, 5175-5178.

Atomically Defined Edge Doping of Graphene Nanoribbons for Mesoscale Electronics

Felix R Fischer

Department of Chemistry University of California Berkeley

Program Scope

The outstanding transformative potential of graphene, an infinite two-dimensional sheet of carbon atoms tightly packed into a honeycomb lattice, has been recognized mostly due to its exceptionally high charge carrier mobility, thermal conductivity, and tensile strength.¹⁻³ These undeniably very desirable properties, however, represent only a very small facet of the true potential of all- sp^2 carbon materials and its promise to revolutionize the field of molecular electronics. Graphene's most unusual characteristics can be observed when the infinite two dimensional sheet is scaled down to nanometer dimensions.^{4,5} The central objective of this research is to develop the technology and the tools required to synthesize and to fine-tune the properties of atomically defined graphene nanoribbons (GNR) with a particular focus on controlling the absolute dimensions (length, width), the symmetry, and the edge-substitution pattern of mesoscale carbon materials. Specific goals of this project are: (1) To develop a complementary set of bottom-up strategies toward atomically defined GNRs from small molecule building blocks, (2) to tune the intrinsic band gap of semiconducting GNRs by controlled edge-doping, (3) to devise a strategy to fabricate segmented GNRs featuring heterojunction architectures, (4) to identify mesoscale structure-performance relationships.

Recent Progress

(1) *Development of complementary bottom-up strategies toward GNRs:* We have developed three new families of molecular building blocks for the fabrication of atomically defined GNRs from small molecule precursors on solid supports and in solution. (a) We expanded the substrate scope for a surface catalyzed bottom-up synthesis of GNRs on Au(111) surfaces. Chemical modification of a common building block gives access to 7-, 13- and 17- armchair GNRs featuring atomically smooth edge-structures varying in width between 0.7 and 2.0 nm. UHV STM imaging confirms the predicted molecular structure while dI/dV spectroscopy gives direct access to the band gap of the resulting GNRs. A newly designed building block based on a pyrene core gave access to a new family of semiconducting GNRs ($3n+2$) that features band gaps between 0.5 and 1 eV. The assembly of these new precursors into

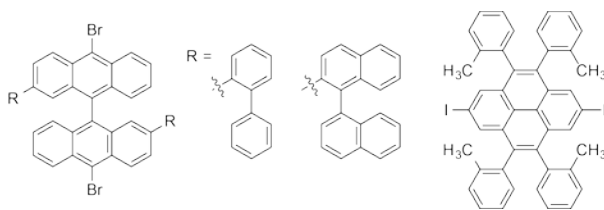


Figure 1 Molecular building blocks for N=7, 13, and 17 AGNRs. Pyrene based building blocks for N=11 AGNRs.

GNRs demonstrates, for the first time, that an sp^3 hybridized carbon atom in the building blocks can readily be rehybridized and seamlessly incorporated into the extended GNRs. This new design strategy significantly expands the accessible substrate scope and enables the synthesis of previously inaccessible GNR symmetries.

(b) We developed a solution-based strategy towards the bottom up synthesis of GNRs. Nickel catalyzed cross-coupling reactions of suitable polyphenylene precursors yields highly soluble substituted polyphenylene precursors that can be converted into GNRs either by a solution-based oxidation strategy or by annealing on a catalytically active surface. The width of the resulting GRNs is defined by the structure of the monomeric building block while adjusting the concentrations of catalyst and monomer during the polymerization can control the length. We observe that even in the presence of competent surfactants solution oxidized GNRs tend to aggregate and form bundles similar to those observed for carbon nanotubes. The formation of isolated GRNs can be observed if the highly solubilized polymer precursor is deposited on a metallic substrate and annealed to give the fully conjugated GNR.

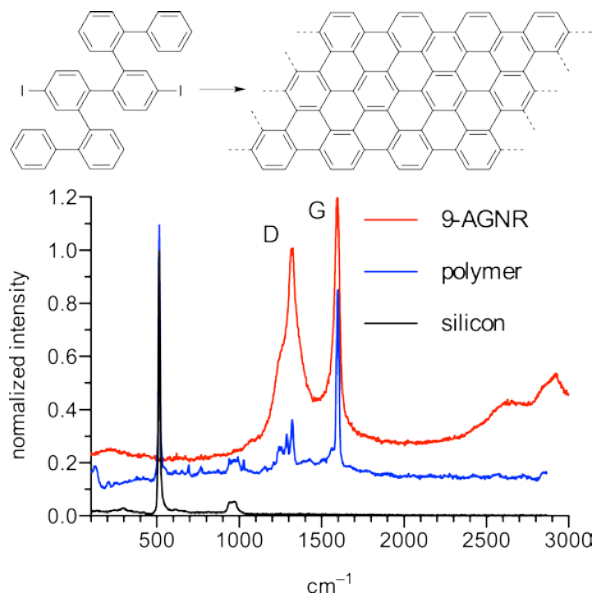


Figure 2 Raman spectra showing the characteristic D and G peak for 9-AGNRs fabricated through a solution-based approach (red). Polymer precursor (blue) and silicon background (black).

(c) We developed a novel solution based polymerization technique relying on the isomerization of small molecule building blocks derived from 1,2-diethynylbenzene. A thermally induced Bergman cyclization of the enediyne structure in the building blocks reversibly generates a 1,4-benzyne intermediate that can undergo radical polymerization to form a polyphenylene based GNR precursor. Analogous processing as described for the solution based processes in (b) yield the fully extended GNR on surfaces. The superior advantage of this strategy is that during the synthesis no transition metal catalyst is required that could deteriorate the electronic structure of the resulting GNRs through metal doping effects.

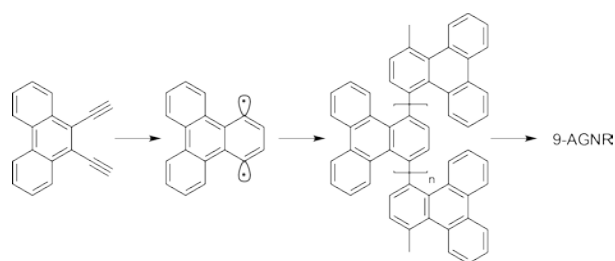


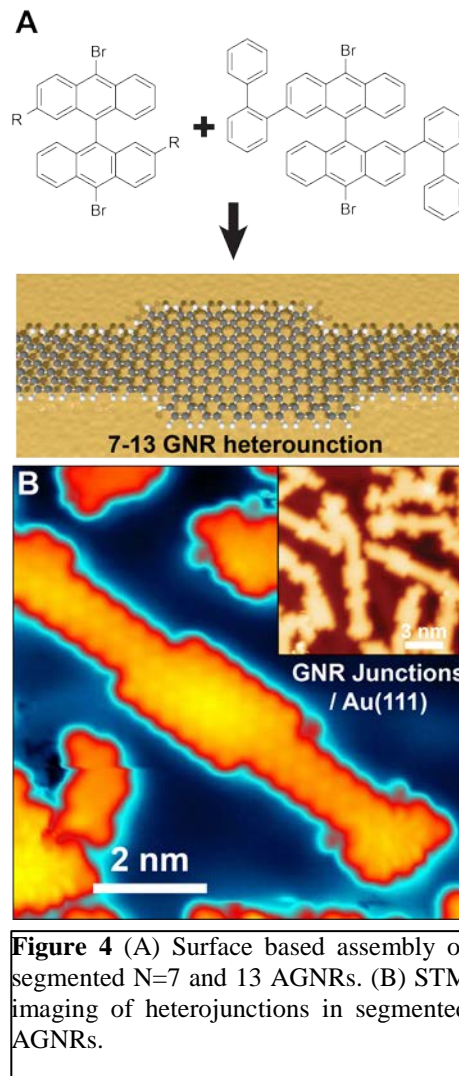
Figure 3 Solution-based synthesis of GNR precursors through a radical polymerization of 1,4-benzyne intermediates.

(2) *Tuning the band gap of semiconducting GNRs:* Based on our initial successes in task (1a) we modified the synthesis of GNR precursor to incorporate electron donating and accepting

functional groups or heteroatoms into the structure of the GNRs. Initial experiments using pyridine and bipyridine substituents indicated that the interaction of the heteroatom with the metal surface prevented the free diffusion of activated building blocks along the surface. The length of the resulting GNRs rarely exceeded 5 nm. To circumvent this initial problem we redesigned the building blocks to incorporate functional groups (fluorene, fluorenone, dibenzofuran, dibenzothiophen) that only interact weakly with the underlying metal surface. Similar design strategies have been applied to monomers used in the solution-based approach detailed in (1b) and are currently under investigation.

Recently we have been able to perform the simultaneous polymerization of two distinctive molecular building blocks on surfaces. The co-deposition of a precursor for 7-AGNRs and 13-AGNRs yields structures featuring a random alternating pattern of wide and narrow GNR segments. Using SPM spectroscopy we were able to resolve the molecular structure at the interphase between the ribbon segments and to determine the electronic band structure across the junction. dI/dV imaging reveals that the electronic band structure of GNRs is largely unchanged from the pristine ribbons and is localized in the respective segment. The interphase between 7-AGNRs and 13-AGNRs represents the first demonstration of the rational synthesis of a Type I heterojunction within an individual ribbon. The schematic band diagram derived from scanning probe spectroscopy is depicted in Figure 5. We will further explore these functional heterojunction architectures as active materials in tunneling transistor architectures.

(3) *Strategies to fabricate segmented GNRs:* Key to the bulk fabrication of functional heterojunctions is the rational synthesis of segmented GNRs. We explored polymer-based strategies to control the assembly of block copolymers as precursors for segmented GNRs. Living ring-opening metathesis provides access to linear poly(phenylene ethynylene) that can be converted into a polyphenylene precursor for armchair graphene nanoribbons using post polymerization benzannulation techniques. This polymeric precursor was either oxidized either in solution or on a substrate to yield the extended GRN. The inherent advantage of this technique is that the living polymerization enables the absolute control over the length and the segmentation of the GNR by controlling the concentration of monomers during the ROAMP.



(4) *Mesoscale structure performance relationships*: Based on the experimental results obtained from dI/dV mapping of pristine GRNs on solid substrates we derived GNR materials featuring a functional Type I heterojunction architecture. The band alignment in armchair GNRs featuring fused segments of varying width ($N=7$ and $N=13$) is very similar to Type I semiconductor junctions. This provides a possible means to fabricate graphene quantum dot devices with sub nm feature sizes and single atom layer thickness. The additional advantage over traditional graphene based quantum dot structures is that the device can readily be contacted by the GNR wires extending on both sides from the heterojunction.

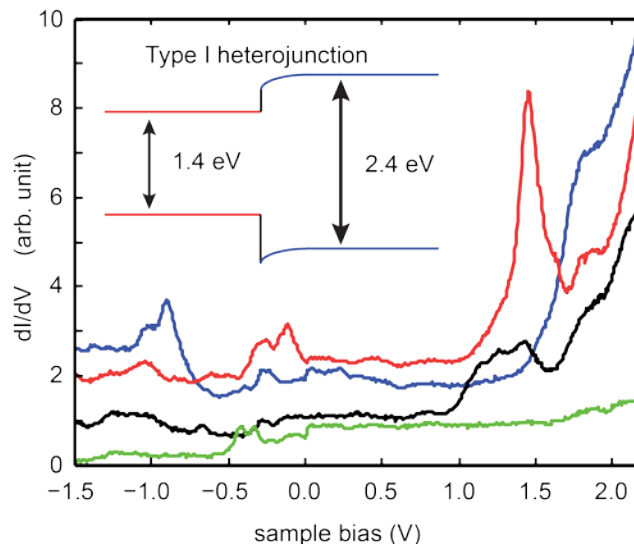


Figure 5 STS of a segmented $N=7$ and 13 AGNR. The band structure resembles a Type I heterojunction.

Future Plans

(1) We will expand our current focus on the design of edge- and width-doped GNRs from small molecule precursors. We will complete the synthesis of a library of building blocks that allow us to tailor the absolute size and the relative position of the band gap in AGNRs. In this effort we will rely both on the self-assembly strategy on surfaces, which enables the detailed study of the electronic structure using SPM, as well as on a solution based synthesis of GNRs that allows a superior control over the length of the ribbons.

(2) We will develop solution-based strategies that enable the controlled fabrication of segmented GNRs featuring alternating doping patterns. For this purpose we will further explore living polymerization strategies that give access to block-copolymer precursors for GNRs.

(3) Based on the successful demonstration of the rational assembly of heterojunctions within individual GNRs we will develop controlled strategies to assemble n-p-n and p-n-p junctions from segmented GNRs.

References

- (1) Novoselov, K.S.; Geim, A.K.; Morozov, S.V.; Jiang, D.; Dubonos, S.V.; Grigorieva, I.V.; Firsov, A.A., *Science* **2004**, *306*, 666.
- (2) Novoselov, K.S.; Geim, A.K.; Morozov, S.V.; Jiang, D.; Katsnelson, M.I.; Grigorieva, I.V.; Dubonos, S.V.; Firsov, A.A., *Nature* **2005**, *438*, 197.
- (3) Geim, A.K.; Novoselov, K.S., *Nat. Materials* **2007**, *6*, 183.
- (4) Tapasztó, L.; Dobrik, G.; Lambin, P.; Biro, L., *Nat. Nanotechnology* **2008**, *3*, 397.
- (5) Man, M.Y.; Ozyilmaz, B.; Zhang, Y.; Kim, P., *Phys. Rev. Lett.* **2007**, *98*, 206805(4).

Chemical Frustration: A Design Principle for the Discovery of New Complex Intermetallic and Alloy Phases (DE-SC0003947)

Daniel C. Fredrickson, Department of Chemistry, University of Wisconsin—Madison

Program Scope

Intermetallic phases comprise a large and diverse family of solid state compounds formed from combinations of metallic elements. They exhibit an array of valuable properties, including superconductivity, thermoelectric effects, hydrogen storage, catalysis, and a variety of magnetic phenomena. However, a limiting factor in developing these phases for materials applications is our inability to control or guide their crystal structures, which can range from simple variants on elemental structures, to complex structures whose unit cells contain thousands of atoms or even defy description within the concept of 3D periodicity (as is the case for incommensurately modulated compounds or quasicrystals). In this project, we are developing a theoretical framework for understanding and predicting the emergence of complexity in these phases: the concept of *chemical frustration*.

An emerging theme both in our research and in the literature is a correlation between the structural complexity in intermetallics and the coexistence of or competition between incompatible bonding or packing modes. For instance, the giant cubic unit cell of NaCd_2 (>1000 atoms/cell)^{1,2} has been connected to an interpenetration of relatively polar and non-polar domains,³ interactions which are normally mutually exclusive. Likewise, the several thousand atom unit cells observed by Steurer and Harbrecht et al. in the Al-Cu-Ta system have been rationalized in terms of an intergrowth of structural regions that adopt geometrical arrangements optimized for lattice periodicity and regions that are based on radially-grown clusters.^{4,5}

The aim of our work here is to test and expand upon these observations by attempting induce such frustration in intermetallic phases through performing synthesis in systems chosen for their bonding incompatibilities, as well as the structural and theoretical characterization of the reaction products. Our strategy is to use ternary systems in which the component binary subsystems exhibit preferences for bonding or packing types that are incompatible (Figure 1). For instance, in the “carbon template” systems, we combine pairs of metallic elements (that combine to form tetrahedral close-packing) with carbon (which in carbides prefers larger octahedral or trigonal prismatic coordination environments). A ternary carbide phase will then be faced with reconciling the preference of the metals for the formation of tetrahedral interstices with the geometrical

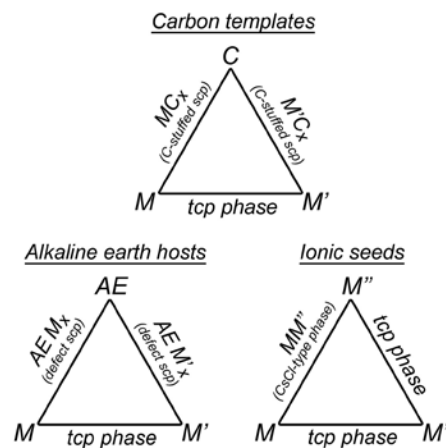


Figure 1. The use of chemical love-triangles in the design of chemically frustrated ternary systems.

requirements of the carbon atoms. One interesting possible outcome of this conflict is illustrated by the crystal structure of $\text{Yb}_{11}\text{Ni}_{60}\text{C}_6$,⁶ in which blocks of a C-stuffed fcc structure connected through fragments of the intermetallic structure YbNi_5 .

In parallel with our experimental endeavors, we are developing theoretical approaches to analyzing frustration between bonding types in intermetallics. Our effort here has focused on tools that analyze the effect of local geometrical arrangements—as will differ between domains of different bonding types—on the electronic structure of the compound. The Method of Moments, as applied to DFT-calibrated Hückel calculations has been our major tool here due to the direct and transparent connection that it provides between local geometrical features and the electronic density of states.

Recent Progress

μ_3 -neutralization as a driving force for the intergrowth of TCP-SCP features. In attempting to apply the Method of Moments to examining frustration in intermetallic phases, we have developed a new moments-based model of acidity that extends Lewis theory to intermetallics: the μ_3 -acidity model. Here the method of moments is used to determine to what degree the electron counts on metal atoms are excess or fall short of their ideal value. In our earlier applications of this idea, we saw that the division of elemental metals into μ_3 -acids and μ_3 -bases elucidates a driving force for the formation of a large number of intermetallic phases between transition metals. Our recent progress has been in showing that some of the most intriguing structural motifs that arise in intermetallics, such as helices and icosahedral clusters (Figure 2), can emerge as a structural response to poorly matched acid and base strengths. For instance, in the crystal structure of $\text{Sc}_{57}\text{Ir}_{13}$,⁷ the μ_3 -acidic Sc greatly out-numbers the μ_3 -basic Ir. To allow the small number of Ir atoms to provide effective neutralization to the majority Sc atoms, the structure adopts an intergrowth of simple close packed (SCP) and tetrahedral close-packing (TCP) arrangements. Ir@Sc₁₂ icosahedra (TCP) allows for strong Sc-Ir interactions, while wrapping these icosahedra with Sc octahedra (SCP) minimizes Sc-Sc interactions. This maximizes the role of the heteroatomic interactions in shaping the density of states distribution of the compound. The result is the Mackay cluster, a key building unit in Mackay-type quasicrystals.

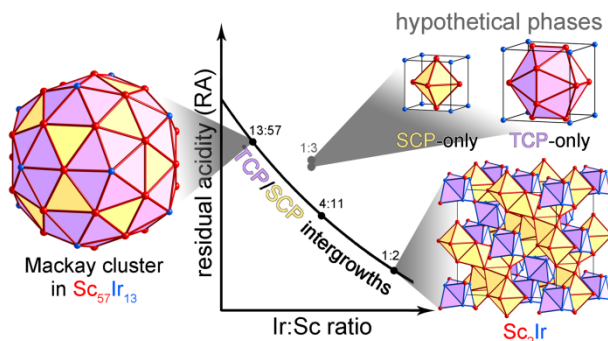


Figure 2. The icosahedral Mackay cluster as a product of the intergrowth of tetrahedral and simple close packing (TCP and SCP) driven by μ_3 -neutralization.

Chemical frustration and the formation of icosahedral Bergman clusters. Our synthesis in the Ca-Cu-Cd system has led to a compound that reveals our clearest manifestation to date of chemical frustration: $\text{Ca}_{10}\text{Cu}_2\text{Cd}_{27}$. This phase exhibits a new packing of the icosahedral clusters that form the basis of Bergman-type quasicrystals, in which Friauf polyhedra share triangular-faces with a central icosahedron (Figure 3). The emergence of a Bergman cluster in a phase composed largely of Ca and Cd was surprising, as the Ca-Cd system itself is known for its Tsai-type quasicrystal and approximants.^{8,9} We eventually realized, with the help of DFT-Chemical Pressure calculations, that its formation in this system is due to chemical frustration induced by the presence of Cu. Nearby in composition is the MgZn_2 -type phase CaCd_2 (for a certain temperature range) based on Friauf polyhedra (like the Bergman cluster). The addition of Cu to this phase has a destabilizing effect because of the size mismatch between Cd and Cu, which leads to a segregation of Ca-Cd and Cu-Cd interactions from each other. The preference of Cu-Cd interactions for icosahedral arrangements then offers nuclei for the Ca-Cd Friauf polyhedra to wrap in Bergman clusters. A core-shell segregation between Ca-Cd and Cu-Cd interactions results, which closely resembles the architecture of a micelle in soft-matter.

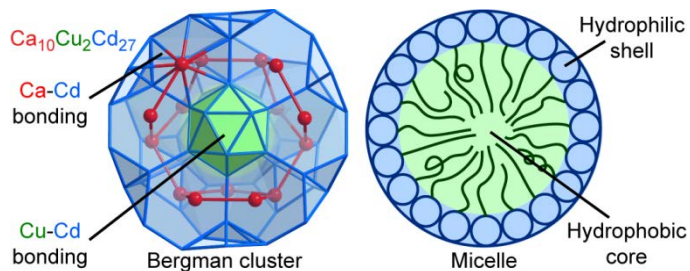


Figure 3. Parallels between the bonding domains of the Bergman clusters of $\text{Ca}_{10}\text{Cu}_2\text{Cd}_{27}$ and the biphasic character of micelles.

Emergent bonding and structural chemistry in carbometalate systems. Our investigations of carbon-templated systems revealed the new carbometalate structures of $\text{Gd}_{13}\text{Fe}_{10}\text{C}_{13}$ and its oxycarbide. These phases are remarkable for their H-shaped C_2FeFeC_2 fragments exhibiting unusually short Fe-Fe contacts of ca. 2.38 Å, as well as their prevalence of short Fe-C distances that are well-below the sum of the covalent radii. Using a combination of ^{57}Fe Mössbauer spectroscopy and our recently developed reversed approximation Molecular Orbital analysis (raMO), we have found that the strong interactions at these contacts can be understood in terms of conjugated π -systems much like those of organic molecules. These results points toward a simple bonding scheme for carbometalates that respects the strong covalency of their interactions.

Future Plans

Our future plans include tightening the integration of our theoretical and experimental approaches to chemical frustration. Following the lead of the $\text{Ca}_{10}\text{Cu}_2\text{Cd}_{27}$ structure, we will use DFT-Chemical Pressure analysis to identify binary phases in which substitution with a third element should lead to a size mismatch that induces a segregation of interactions. We will then perform synthesis in those systems to test these predictions. In addition, we will continue the

development of the μ_3 -acidity approach, with a specific focus of extending its applicability beyond transition metal elements. We also have synthesized and determined the structures of several new compounds of relevance to the concept of chemical frustration. Finalizing the experimental work and theoretical analysis of these phases should provide additional future research directions.

References

- (1) Samson, S. *Nature* **1962**, *195*, 259-262.
- (2) Yang, Q.-B.; Andersson, S.; Stenberg, L. *Acta Crystallogr. B* **1987**, *43*, 14-16.
- (3) Fredrickson, D. C.; Lee, S.; Hoffmann, R. *Angew. Chem. Int. Ed.* **2007**, *46*, 1958-1976.
- (4) Conrad, M.; Harbrecht, B.; Weber, T.; Jung, D. Y.; Steurer, W. *Acta Crystallogr. B* **2009**, *65*, 318-325.
- (5) Weber, T.; Dshemuchadse, J.; Kobas, M.; Conrad, M.; Harbrecht, B.; Steurer, W. *Acta Crystallogr. B* **2009**, *65*, 308-317.
- (6) Moss, M. A.; Jeitschko, W. *J. Alloys Compd.* **1992**, *182*, 157-164.
- (7) Cenxual, K.; Chabot, B.; Parthé, E. *Acta Crystallogr. C* **1985**, *41*, 313-319.
- (8) Gómez, C. P.; Lidin, S. *Angew. Chem. Int. Ed.* **2001**, *40*, 4037-4039.
- (9) Gómez, C. P.; Lidin, S. *Phys. Rev. B* **2003**, *68*, 024203.

Publications

1. Y. Guo; T. E. Stacey; D. C. Fredrickson. *Acid-base chemistry in the formation of Mackay-type icosahedral clusters: μ_3 -acidity analysis of Sc-rich phases of the Sc-Ir system.* *Inorg. Chem.* **2014**, *53*, 5280-5293.
2. V. J. Yannello; B. J. Kilduff; D. C. Fredrickson. *Isolobal analogies in intermetallics: The reversed approximation MO approach and applications to CrGa₄ and Ir₃Ge₇-type phases.* *Inorg. Chem.* **2014**, *53*, 2730-2741.
3. A. B. Hadler; N. A. Harris; D. C. Fredrickson. *New roles for icosahedral clusters in intermetallic phases: Micelle-like segregation of Ca-Cd and Cd-Cu interactions in Ca₁₀Cd₂₇Cu₂.* *J. Am. Chem. Soc.* **2013**, *135*, 17369-17378.
4. D. C. Fredrickson; I. Doverbratt[†]; S. Ponou[†]; S. Lidin[†]. *Bonding schemes for polar intermetallics through molecular orbital models: Ca-supported bonding in Ca₁₀Pt₇Si₃.* *Crystals*, **2013**, *3*, 504-516.
5. T. E. Stacey; D. C. Fredrickson. *Structural acid-base chemistry in the metallic state: How μ_3 -neutralization drives interfaces and helices in Ti₂₁Mn₂₅.* *Inorg. Chem.* **2013**, *52*, 8349-8359.

Towards the Rational Design of Glassy Polymer Materials

Karl F. Freed

James Franck Institute and Department of Chemistry, The University of Chicago

Program Scope

The development of reliable approaches for predicting the thermodynamic properties of polymer systems is crucial for the rational design of polymer materials. These theories should readily translate microscopic information into predictions for macroscopic properties. Although fully atomistic simulations can generate useful microscopic information, they cannot readily provide a unified understanding of the influence of molecular factors on the thermodynamic properties of polymer systems. The lattice cluster theory (LCT) of Freed and coworkers [1,2] represents a new class of coarse grained approaches that retain the essential features (e.g., bond connectivity, cohesive energy, chain stiffness, etc.) of molecular structure and interactions while enjoying analytic tractability and computational simplicity.

The LCT builds on the mathematical simplification conferred by lattice models of polymers to enable predicting new phenomena and explaining existing data. While classic Flory-Huggins (FH) theory explains why long polymer chains in the liquid state generally tend to be immiscible, FH theory completely neglects monomer structure and chain architecture (i.e., cannot distinguish between linear, branched or star polymers or between diblock and random copolymers, etc.). The LCT rectifies this significant deficiency by endowing monomers with explicit structures that preserve bonding patterns, thereby enabling addressing the influence of monomer size, shape, stiffness, and interactions of the constituents on the thermodynamic properties of polymer melts and blends. Not surprisingly, the LCT provides microscopic explanations for a variety of previously enigmatic observations and offers a valuable vehicle for predicting new phenomena [1,2]. The successful applications of the LCT and its extension (the generalized entropy theory (GET)) to describe glass-formation [3,4] open the opportunity to establish useful guidelines for the design of polymer glass-formers.

The structural relaxation time τ governs the long time viscoelastic behavior of materials, and the glass transition temperature T_g is defined empirically by the choice $\tau(T_g) = 100$ s. The slope of $\log(\tau(T))$ at T_g determines the quantity m , the “fragility”, which is a measure of temperature sensitivity of glass-formers. The combination of m and T_g dictate whether a material can be processed by extrusion, casting, ink jet, etc. The temperature variation of $\tau(T)$ is used to define the shift factor that enables devising a unified description of the viscoelastic moduli for many materials. The structural relaxation time is calculated within the GET by incorporating the Adam-Gibbs relation between τ and the configurational entropy of the fluid. An important finding of GET is the identification of the packing efficiency in the melt as the decisive factor governing the magnitude of the fragility of glass-forming polymers. The packing efficiency in turn depends on chain rigidity, cohesive energy, and molecular details, such as the lengths of the backbone and side group. Recent experiments and simulations validate this simple picture of fragility, but they also pose significant questions that motivate our current research..

Recent Progress

P1. The GET has been used to provide molecular understanding of the finding that data for dynamic properties, such as the viscosity, relaxation time, and diffusion coefficient, which formally depend on separately on temperature T and specific volume v , can be described by a unique scaling function of the ratio Tv^γ , where γ is a material dependent constant that reflects the relative importance of pressure effects (e.g., activation barriers) and volume effects (e.g., free volume). The GET predicts that chain rigidity, cohesive energy, and backbone and side group chain lengths all significantly affect the magnitude of γ , and computed trends agree well with experiments. The GET explains the variations of γ with molecular parameters as emerging from a correlation between γ and fragility, thereby establishing the packing efficiency as the universal physical mechanism determining both the fragility and the scaling exponent γ .

P2. Recent experiments by Sokolov (ONL, UT) for a series of vinyl polymers with different side groups provide tests that ultimately validated and refined the GET prediction that fragility correlates with the ratio of the stiffnesses of the backbone and side groups. The experiments also validate the GET prediction that T_g of melts increases with the cohesive energy ϵ or bending energy E_b (a measure of stiffness) and that the fragility parameter increases with E_b but diminishes with ϵ . However, difficulties arise when both ϵ and E_b vary. Thus, we began calculations to explain the puzzling data and thereby extend the predictive powers of the GET.

Experimentalists have raised the question of how to determine the bending energy E_b for further predictions and tests of the theory. Preliminary analysis of the variation of T_g and m with *both* ϵ and E_b for polymers with the chain structure of polypropylene enable us to find analytical fits in the form of $T_g = f(\epsilon, E_b)$ and $m = g(\epsilon, E_b)$ which upon inversion enable determining the parameters ϵ and E_b of the model from experimental data for T_g and m . A manuscript describing this work is currently in preparation. The continuation of this computationally intensive study will consider the dependence on monomer structure, molecular weight, side group length and stiffness, etc., to provide a wider range of predictions in a simply useable form.

P3. A series of experiments by Sokolov focuses on changes of T_g and m with the polarity of the side group, an important chemical question that could not be addressed previously because of the tacit assumption in the LCT that all united atom groups (e.g., CH_n for $n = 1, 2$, or 3) interact with the same monomer averaged interaction energy ϵ , whereas the systems investigated by Sokolov involve very different interaction energies ϵ in the backbone and side group. The extremely lengthy calculations for expression for the LCT free energy with different interaction energies ϵ for the backbone and side group completed, and a first theoretical paper is submitted.

P4. While the projects described above greatly expand our understanding of the relation between monomer structure and interactions and glass formation in polymer melts, most materials are fabricated as mixtures (called blends), but the description of glass formation in polymer blends has been beset by fundamental questions of how to explain the observations in some miscible blends (above the critical temperature T_c) of two distinct structural relaxation times, findings in conflict with the normal picture of miscible fluids as being compositionally uniform on a molecular scale (away from T_c). However, chain connectivity in polymers leads to relatively large composition fluctuations in miscible polymer blends (even far from T_c), and the *minimal* scale of the composition fluctuations is typically on the order of the chain radius of

gyration (nm) rather than the size of atoms (\AA) as in simple non-associating small molecule mixtures. Thus, while miscible mixtures of small molecule fluids normally may be considered as possessing a uniform average composition, miscible polymer blends, associating fluids, and other complex fluids exhibit *mesoscale* composition fluctuations, with sizes ranging between 1 nm and 1 μm , a scale large enough for the materials to be regarded more like molecular composites than molecular dispersions. Attempts at explaining the observation of two structural relaxation times have been based on simple phenomenological models for ideal, non-interacting chain models. These phenomenological models fail to explain the size of the composition fluctuations, i.e., when they are large enough to observe, the temperature dependence of the structural relaxation times, the two different T_g , the blend composition, critical point, and more.

We explore how the scale and intensity of composition fluctuations in binary blends vary with the reduced temperature $\tau_{\text{red}} = (T-T_c)/T$ (where T_c is the critical temperature) and with the asymmetry in the rigidities of the components. Knowledge of these variations is crucial for understanding the dynamics of materials fabricated from polymer blends and for understanding glass-formation in these materials. Our quantitative theory (a synthesis of the generalized entropy theory for glass-formation in polymer materials and the KB theory for concentration fluctuations in binary mixtures) explains the occurrence of two structural relaxation times and two glass transition temperatures for *partially miscible* polymer blends. In particular, the theory predicts that spontaneous concentration fluctuations may lead to the appearance of *two* mesoscopic regions of enriched local concentration (with dimensions exceeding 1 nm but less than a few microns) in macroscopically homogeneous, but *locally inhomogeneous*, one-phase binary polymer blends. When sufficient dynamic contrast exists between the blend components, *two* glass transitions may appear with separate structural relaxation times $\tau_{\text{red},i}$ and glass transition temperatures $T_{g,i}$. The composition fluctuations for mixtures of small molecule (non-associating) fluids normally occur on a molecular scale, so only one T_g is generally present. Size really does matter! Engineering the asymmetry in the monomer structures thus enables controlling and tuning the correlation length, phase stability, and glass transition. Further theoretical and experimental investigations are, however, needed to understand the complex relation between structure and dynamics in polymer blends in order to measure and control glass properties in the design of new blend materials.

Future Plans

F1. As briefly mentioned above, we are in the process of mapping out the multivariate dependence of the glass transition temperature and fragility on molecular properties and have demonstrated that we can fit the results of extensive GET computations to simple useable analytical formulas for the simplest model of chains with the structure of PP and with the two parameters ε and E_b . This work will be expanded to consider the dependence of τ , T_g , and m on monomer structure, molecular weight, length of side group, different E_b for backbone and side group, different ε for backbone and side groups, and selected monomer structures. This data should enable us to construct a web site for determining molecular parameters (e.g., ε and E_b , etc.) from measured T_g , m , and vice versa.

F2. Similar fitting procedures will be pursued to predict the parameters C_1 and C_2 in the WLF equation for the shift factors that are used to combine frequency dependent data, generated

necessarily at several temperatures in narrow frequency ranges for, e.g., the dielectric relaxation, the storage and loss shear moduli, etc., to a single master curve over a vastly wider range of frequencies. This time-temperature superposition principle applies to a many substances and provides dynamical information for experimentally inaccessible ranges of frequency and temperature. Moreover, since the shift factors are determined from the structural relaxation times $\tau(T)$, perhaps, we can investigate systems that violate time-temperature superposition.

F3. The study of the structural relaxation time(s) in binary blends will be extended to study less miscible, phase separating blends in which the lowest T_g of the pure components lies below the critical temperature T_c of the mixture. This situation can be used to fabricate materials with a variety of different microstructures by programming a series of quenches where, for instance, the first quench places the system in the two-phase region, so a subsequent quench drives one of the phases into the glassy state while other phase remains fluid and may further be quenched into the glassy state or into another glass/fluid two phase region, etc. Additional studies will consider glass formation in binary blends of a high polymer with short oligomers. We plan to apply the LCT to describe the molecular basis for the faster β -relaxation process.

References

1. K. W. Foreman and K. F. Freed, *Adv. Chem. Phys.* 103, 335 (1998).
2. K. F. Freed and J. Dudowicz, *Adv. Polym. Sci.* 183, 63 (2005).
3. J. Dudowicz, K. F. Freed, and J. F. Douglas, *Adv. Chem. Phys.* **137**, 125-222 (2008).
4. K. F. Freed, *Acc. Chem. Res.* **44**, 194-203 (2011).

Publications

1. Thermodynamic Scaling of Dynamics in Polymer Melts: Predictions from the Generalized Entropy Theory. W.-S. Xu and K. F. Freed, *J. Chem. Phys.* 138, 234501 (2013).
2. Concentration Fluctuations in Miscible Polymer Blends: Influence of Temperature and Chain Rigidity. J. Dudowicz, K. F. Freed, and J. F. Douglas, *J. Chem. Phys.* 140, 194901 (2014).
3. Two Glass Transitions in Miscible Polymer Blends? J. Dudowicz, J. F. Douglas, *J. Chem. Phys.* (submitted).
4. Perturbative Many-body Expansion for Electrostatic Energy and Field for System of Polarizable Charged Spherical Ions in a Dielectric Medium. K. F. Freed, *J. Chem. Phys.* (submitted).
5. Lattice cluster theory for polymer melts with specific interactions. W.-S. Xu and K. F. Freed, *J. Chem. Phys.* (submitted).

Cathode Catalysis in Hydrogen/Oxygen Fuel Cells: New Catalysts, Mechanism, and Characterization

Andrew A. Gewirth, Paul J.A. Kenis, Ralph G. Nuzzo, and Thomas B. Rauchfuss

Department of Chemistry, Department of Chemical and Biomolecular Engineering, and the Fredrick Seitz Materials Research Laboratory, University of Illinois at Urbana-Champaign, Urbana, IL 61801

Program Scope

In this project, we are engaged in a comprehensive plan of research directed at developing new catalysts and new understandings relevant to the operation of low temperature hydrogen-oxygen fuel cells. The focal point of this work is centered on the Oxygen Reduction Reaction (ORR), the electrochemical process that most fundamentally limits the technological utility of these environmentally benign energy conversion devices.

Utilizing support from this project, we continued our development of new ORR catalysts, based on Cu dimers and multimers. In this area, we developed substantial new insight into design rules required to establish better ORR materials, inspired by the three-Cu active site in laccase which has the highest ORR onset potential of any material known. We also developed a new method of characterization for the ORR on conventional (metal-based) catalysts, where we explore the effect of adsorbates on the change in metal-metal distances. Finally, we developed a new platform to study the rate of proton transfer relevant to proton coupled electron transfer (pcet) reactions, of which the ORR is an exemplar.

Recent Progress

1. *New Catalysts for the Oxygen Reduction Reaction*

Utilizing support from this project, we developed a new class of ORR catalysts, based on Cu dimers and multimers.[1] These new materials exhibit ORR onsets at potentials higher than any other Cu-based material in neutral and basic environments[2] and are inspired by the three-Cu active site in laccase which has the highest ORR onset potential of any material known. We recently reviewed the area of Cu complexes for the ORR.[3]

We showed that $\mu\text{-}\eta^1\text{:}\eta^1$ coordination of Cu using a tris(2-pyridylmethyl)amine (TPA) ligand to O_2 yields the most positive potential onset for the ORR in aqueous acidic solution relative to any Cu-containing complex thus far examined. Derivatives of TPA exhibit even higher onset potentials at the cost of some stability. With these complexes ORR activity is low at low pH values, but becomes much more interesting at higher pH values.

As part of the effort to synthesize new Cu-containing ORR catalysts, we designed

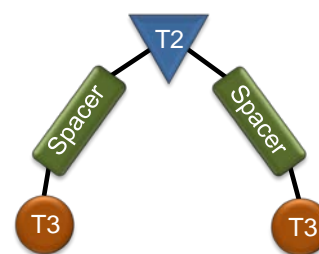


Figure 1. Design plan for a laccase mimic showing T3 and T2 coordination areas.

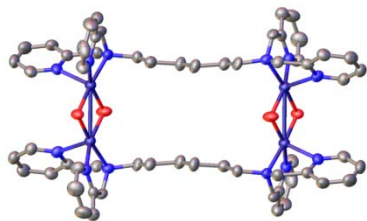


Figure 2: Scheme showing the intramolecular coordination of O_2 between two bis-DPA Cu complexes.

new polypyridyl ligands such as bis[di(2-picolyl)amine] (DPA) derivatives as scaffolds for Cu-based ORR catalysts. The concept is to mimic the three-Cu active site in laccase as closely as possible, as shown in Figure 1. In the enzyme the T3 centers feature three N donors each, while the T2 center features two N donors. In particular, we have prepared and characterized dicopper(II) complexes of 1,6-bis[di(2-picolyl)amino]hexane (L) including $[LCu_2Cl_4]$, which is a precatalyst for the ORR. Reflecting the reactivity of dicopper species oxygen, the dicopper(I) species $[LCu_2(MeCN)_2]^{2+}$ undergoes oxygenation to afford a dimeric (i.e. tetranuclear) cluster in which formal reduction of O_2 affords OH^- ligands bound to Cu(II) centers, as shown in Fig. 2. The intramolecular oxygenation yields ORR behavior is no better than that found with dinuclear Cu complexes previously. A focus of future work then is to prevent intramolecular oxygenation by using bulkier ligands.

2. Characterization of ORR catalysts

During this last grant period, we monitored the Pt electrocatalyst during the ORR through use of an in-situ electrochemical X-ray Absorption Spectroscopy (XAS) cell developed in this program. Our results conclusively demonstrate that the presence of O_2 in the electrochemical environment leads to a marked electronic d-band vacancy increase over a wide potential range between 0.4 and 1.2 V vs. RHE in acid.

One consequence of this d-band vacancy must be a change in the Pt-Pt distance with O_2 exposure. We performed in situ EXAFS measurements with and without O_2 . This measurement showed that changes in Pt-Pt distance with O_2 exposure are only slightly above zero, except possibly at 400 mV.

If the Pt-Pt bond expansion in the presence of O_2 found in the EXAFS does in fact occur, it should be manifested in other measurements, specifically in situ electrochemical stress measurements. Fig. 3A shows electrochemical surface stress-thickness changes occurring on the cathodic sweep with and without the presence of O_2 . The figure shows that while surface stress-thickness curves from Ar and O_2 saturated solutions exhibit similar patterns, the curve from the O_2 -exposed sample is displaced in a more compressive direction over the entire potential window interrogated. Fig. 3B shows the difference between the Ar and O_2 cases more directly, with the O_2 displacement between 0.05 and 0.2 N/m. Interestingly, we can use the Pt-Pt bond distance change determined from EXAFS to calculate a strain in the Pt adlayer. By using Young's modulus, this strain can be recast as a

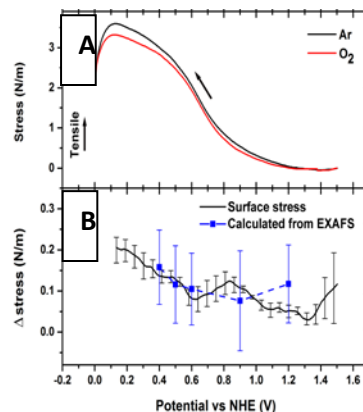


Figure 3. (A) Stress data of Pt/glass of both Ar and O_2 conditions, (B) The black line shows delta stress of Ar minus O_2 and the blue points indicate the expected delta stress based on the Pt-Pt bond strains obtained via EXAFS.

stress. Fig. 3B shows the stress calculated from the EXAFS-derived Pt-Pt bond length changes (blue) overlaid with those from the electrochemical stress measurement. The corroborating surface stress measurements may potentially yield a simpler method to examine metal-metal bond expansion during electrochemical reactivity.

3. Controlling Proton Transfer to an Electrocatalyst for the ORR

PCET reactions are fundamental to many energy conversion processes, in particular, the four-electron four-proton ORR to water is one of the most intensely studied PCET reactions. To examine the effect of changing the rate of proton transfer on ORR catalysis, we designed a Cu ORR catalyst embedded inside a Hybrid Bilayer Membrane (HBM) system.

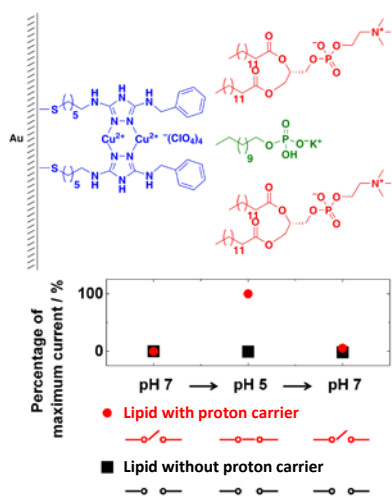


Figure 4. Our HBM is composed of the Cu complex of BTT (blue), the 1,2-dimyristoyl-sn-glycero-3-phosphocholine (DMPC) lipid layer (red), and the alkyl phosphate proton carrier (green). The bottom figure shows the pH-induced pcet switch.

Inspired by biological systems, we incorporate an alkyl phosphate, mono-*N*-dodecyl phosphate (MDP), to facilitate proton transport to the embedded catalyst. At pH 5, MDP predominantly exists with a negative charge. This species can then be protonated to give a neutral molecule, which shuttles protons across the hydrophobic lipid layer of the HBM, giving an increase in ORR current when one equivalent of MDP is incorporated in the lipid layer of the HBM.

The different responses exhibited by the HBM system at different pH values naturally leads to the idea of a ‘pcet switch.’ Figure 4 (bottom) shows the chronocoulometric response of the HBM to changing the pH from pH=7 to pH=5 and then back to pH=7 in O₂ saturated solution. The figure shows that when the lower pH is applied to the HBM system, current associated with the ORR increases. This behavior is consistent with our understanding that the lower pH accesses the neutral form of the alkylphosphonate and allows this proton carrier to penetrate the lipid. When the pH is raised back to pH 7, however, the monovalent and divalent forms of the alkylphosphonate are inhibited from penetrating the lipid layer, and ORR activity ceases for lack of protons. We envision this HBM platform will have broad impact on the field of catalysis and provide valuable mechanistic insights into the ORR.

Future Plans

Future work will build on the present program. We will continue our work synthesizing three-Cu laccase mimics and develop methods to immobilize them on electrode surfaces to insure high activity and stability. We will use our pcet switch platform to perform work directed at understanding the interplay between proton transfer and the rate of the ORR under different conditions. Characterization will emphasize newly advanced electrochemical stress methods,

here conjoined with advanced *in-situ* synchrotron methods that report on electrode dynamics during the ORR.

References

- (1) Thorum, M. S.; Yadav, J.; Gewirth, A. A. *Angew. Chem. Int. Ed.* **2009**, *48*, 165.
- (2) Brushett, F. R.; Thorum, M. S.; Lioutas, N. S.; Naughton, M. S.; Tornow, C.; Jhong, H. R.; Gewirth, A. A.; Kenis, P. J. A. *J. Am. Chem. Soc.* **2010**, *132*, 12185.
- (3) Thorseth, M. A.; Tornow, C. E.; Tse, E. C. M.; Gewirth, A. A. *Coord. Chem. Rev.*, **2013**, *257*, 130-139.

Publications resulting from this work (last 2 years)

1. "In Situ Electrochemical X-ray Absorption Spectroscopy of Oxygen Reduction Electrocatalysis with High Oxygen Flux" Erickson, E. M.; Thorum, M. S.; Vasić, R.; Marinković, N. a. S.; Frenkel, A.; Gewirth, A. A.; Nuzzo, R. G., *J. Am. Chem. Soc.* **2012**, *134*, 197-200.
2. "Analysis of Pt/C electrode performance in a flowing electrolyte alkaline fuel cell" F.R. Brushett, M.S. Naughton, J.W.D. Ng, L. Yin, P.J.A. Kenis, *J. Hydrogen Energy*, **2012**, *37*, 2559-2570.
3. "Quantitative Analysis of Single-Electrode Plots to Understand In-Situ Behavior of Individual Electrodes" Naughton, Matt S. Moradia, Akash A, Kenis, Paul J. A. *Journal Of The Electrochemical Society* **2012**, *159*, B761-69.
4. "Combining Structural and Electrochemical Analysis of Electrodes Using Micro-Computed Tomography and a Microfluidic Fuel Cell" H-R.M. Jhong, F.R. Brushett, L. Yin, D.M. Stevenson, P.J.A. Kenis, *J. Electrochem. Soc.* **2012**, *159* (3), B292-B298.
5. "*In-situ* measurement of ethanol tolerance in an operating fuel cell", M. S. Naughton, C. Tornow, Y. Bonita, H. R. Jhong, F. R. Brushett, A. A. Gewirth, and P. J. A. Kenis, *International Journal Of Hydrogen Energy* **2013**, *38*(21), 8980-91.
6. "Tailoring electrode hydrophobicity to improve anode performance in alkaline media" Naughton, Matt S.; Gu, Geun Ho; Moradia, Akash A.; Kenis, P. J. A. *Journal Of Power Sources* **2013**, *242*, 581-588.
7. "Ligand Effects on the Overpotential for Dioxygen Reduction by tris(2-Pyridylmethyl)amine Derivatives" Matthew A. Thorseth, Christopher S. Letko, Edmund C.M. Tse, Thomas B. Rauchfuss, Andrew A. Gewirth *Inorg. Chem.* **2013**, *52*(2), 628-634.
8. "Effect of pH on the Oxygen Reduction Reaction with a Pyrolyzed Fe Phthalocyanine Catalyst: Role of Azide" Justin L. Oberst, Matthew S. Thorum, Andrew A. Gewirth *J. Phys. Chem.C.* **2012**, *116*, 25257-25261.
9. "Behavior of a Copper Complex of 3,5-Diamino-1,2,4-Triazole and its Derivatives Toward Oxygen Reduction" Claire E. Tornow and Andrew A. Gewirth *Inorganic Chemistry* **2014**, submitted.
10. "Modulating Oxygen Reduction by a Hybrid Bilayer Membrane-embedded Dinuclear Copper Electrocatalyst using a Proton Switch" Barile, C. J.; Tse, E. C. M.; Li, Y.; Sobyra, T. B.; Zimmerman, S. C.; Hosseini, A.; Gewirth, A. A. *Nat. Mater.* **2014**, in press.
11. "In-situ EXAFS observed platinum bond expansion during electrochemical oxygen reduction" Evan M. Erickson, Muhammed E. Oruc, Matthew W. Small, Diya Li, Anatoly I. Frenkel, Andrew A. Gewirth, and Ralph G. Nuzzo, *Anal. Chem.* **2014** submitted.
12. "Multicopper models for the laccase active site: effect of nuclearity on electrocatalytic oxygen reduction" Edmund C.-M. Tse, David Schilter, Thomas B. Rauchfuss and Andrew A. Gewirth, *Inorg. Chem.* **2014** submitted.

Materials and Interfacial Chemistry for Next-Generation Electrical Energy Storage

John B. Goodenough and Arumugam Manthiram, University of Texas at Austin

Program Scope

Our current program explores next-generation rechargeable alkali-metal cell chemistries with conventional and alternative separators that are low cost, safe, and capable of fast discharge/charge with high energy density and long cycle and shelf life, where applicable, in collaboration with Oak Ridge National Laboratory.

Recent Progress

Cell chemistries with conventional separator (Celgard): Lithium-ion batteries are currently assembled in discharged state. Formation of solid-electrolyte interphase (SEI) layer on anode irreversibly robs Li^+ or Na^+ from cathode on initial charge, and fast charge requires lowering the anode electrochemical potential over 0.5 V below the Fermi Energy E_F of metallic Li or Na. An increase in energy density requires increasing the product of mean voltage and capacity. We have (i) investigated surface structure of high-voltage $\text{Li}[\text{Ni}_{0.5}\text{Mn}_{1.5}]\text{O}_4$ spinel with/without doping to determine how to stabilize cycling at 60 °C by particle morphology, (ii) developed alloy anodes for Li-ion and Na-ion batteries that allow a fast charge, and (iii) fabricated electrode morphologies providing ultrafast charge/discharge.

Cell chemistries with semi-permeable oxide/polymer composite separator: We have fabricated low-cost, large-area, semi-permeable oxide/polymer composite membranes that are thin, mechanically robust, and flexible and allow assembly of cells in charged state with an alkali-metal anode. The loading of the polymer with Sb_2O_3 leaves the membrane flexible and blocks dendrites from the anode. We have demonstrated a Na-ion battery operating at 5C rate with a hexacyanide cathode and a Li-ion battery at 1C rate with a LiFePO_4 cathode.

Cell chemistries with solid-oxide separator: With a commercial NASICON-based oxide separator, we have demonstrated the potential for a hybrid Li-air or Na-air battery operating with an organic anolyte, an aqueous catholyte, inexpensive carbon-based (metal-free) catalysts for the oxygen reduction reaction (ORR), and inexpensive oxide catalysts for the oxygen evolution reaction (OER). We have also developed oxide catalysts with bifunctional ORR and OER activities by tuning the electron occupation of the active redox couple through soft-chemistry lithium insertion/extraction reactions.

Future Plans

- Stabilization of high-voltage $\text{Li}[\text{Ni}_{0.5}\text{Mn}_{1.5}]\text{O}_4$ to 60 °C over a long life
- Development of new nanocomposite alloy anodes for fast charge/discharge of both Li-ion and Na-ion batteries
- Optimization of semi-permeable oxide-polymer composite membranes for both Li-ion and Na-ion batteries
- Evaluation of hybrid Li-air and Na-air cells with solid electrolyte membranes
- Demonstration of cells with alternative membranes and flow-through liquid cathodes
- Evaluation of the problems with alkali-metal anodes and their stabilization

Publications

Articles Already in Print

1. J. Song, D. W. Shin, Y. Lu, C. D. Amos, A. Manthiram, and J. B. Goodenough, "Role of Oxygen Vacancies on the Performance of $\text{Li}[\text{Ni}_{0.5-x}\text{Mn}_{1.5+x}]\text{O}_4$ ($x = 0, 0.05, \text{ and } 0.08$) Spinel Cathodes for Lithium-Ion Batteries," *Chemistry of Materials* **24**, 3101-3109 (2012).
2. L. Li, X. Zhao, Y.-Z. Fu, and A. Manthiram, "Polyprotic Acid Catholyte for High Capacity Dual-Electrolyte Li-air Batteries," *Physical Chemistry and Chemical Physics* **14**, 12737-12740 (2012).
3. E.-S. Lee, K.-W. Nam, E. Hu, and A. Manthiram, "Influence of Cation Ordering and Lattice Distortion on the Charge-Discharge Behavior of $\text{LiMn}_{1.5}\text{Ni}_{0.5}\text{O}_4$ Spinel between 5.0 and 2.0 V," *Chemistry of Materials* **24**, 3610-3620 (2012).
4. Y. Li, J.-T. Han, C.-A. Wang, H. Xie, and J. B. Goodenough, "Optimizing Li^+ Conductivity in a Garnet Framework," *Journal of Materials Chemistry* **22**, 15357-15361 (2012).
5. Y. Dong, H. Xie, J. Song, M. Xu, Y. Zhao, and J. B. Goodenough, "The Prepared and Electrochemical Property of Mg Doped LiMnPO_4 Nanoplates as Cathode Materials for Lithium-Ion Batteries," *Journal of the Electrochemical Society* **159**, A995-A998 (2012).
6. H. Xie, Y.-T. Li, J. Han, Y. Song, M. P. Paranthaman, L. Wang, M. Xu, A. Gupta, Z. Bi, C. A. Bridges, M. Nakanishi, A. P. Sokolov, and J. B. Goodenough, " $\text{Li}_6\text{La}_3\text{SnMO}_{12}$ ($\text{M}=\text{Sb}, \text{Nb}, \text{Ta}$), A Family of Lithium Garnets with High Li-Ion Conductivity," *Journal of the Electrochemical Society* **159**, A1148-A1151 (2012).
7. A. Gupta, C. B. Mullins, and J. B. Goodenough, "Electrochemical Probing of $\text{Li}_{1+x}\text{VS}_2$," *Electrochimica Acta* **78**, 430-433 (2012).
8. X. Zhao, Y.-Z. Fu, W. Li, and A. Manthiram, "Hydrocarbon Blend Membranes with Suppressed Chemical Crossover for Redox Flow Batteries," *RSC Advances* **2**, 5554-5556 (2012).
9. B. Reeja-Jayan, K. L. Harrison, K. Yang, C.-L. Wang, A. E. Yilmaz, and A. Manthiram, "Microwave-assisted Low-temperature Growth of Thin Films in Solution," *Scientific Reports* **2**, 1003 (2012).
10. Y. Dong, L. Wang, S. Zhang, Y. Zhao, J. Zhou, H. Xie, and J. B. Goodenough, "Two-Phase Interface in LiMnPO_4 Nanoplates," *Journal of Power Sources* **215**, 116-121 (2012).
11. L. Baggetto, E. Allcorn, A. Manthiram, and G. M. Veith, " Cu_2Sb Thin Films as Anode for Na-ion Batteries," *Electrochemistry Communications* **27**, 168-171 (2012).
12. E.-S. Lee and A. Manthiram, "Influence of Doping on the Cation Ordering and Charge-Discharge Behavior of $\text{LiMn}_{1.5}\text{Ni}_{0.5-x}\text{M}_x\text{O}_4$ ($\text{M} = \text{Cr}, \text{Fe}, \text{Co}, \text{ and } \text{Ga}$) Spinels between 5.0 and 2.0 V," *Journal of Materials Chemistry A* **1**, 3118-3126 (2013).
13. K. L. Harrison, C. Bridges, M. Paranthaman, C. U. Segre, J. Katsoudas, V. A. Maroni, J. C. Idrobo, J. B. Goodenough, and A. Manthiram, "Temperature Dependence of Aliovalent-vanadium Doping in LiFePO_4 Cathodes," *Chemistry of Materials* **25**, 768-781 (2013).
14. G. Liu, K. Park, J. Song, and J. B. Goodenough, "Influence of Thermal History on the Electrochemical Properties of $\text{Li}[\text{Ni}_{0.5}\text{Mn}_{1.5}]\text{O}_4$," *Journal of Power Sources* **243**, 260-266 (2013).
15. M. Xu, L. Wang, J. Song, H. Xie, Y. Lu, and J. B. Goodenough, " $\text{Na}_3\text{V}_2\text{O}_2(\text{PO}_4)_2\text{F}$ /Graphene Sandwich Structure for High-Performance Cathode of a Sodium-Ion Battery," *Physical Chemistry Chemical Physics* **15**, 13032-13037 (2013).

16. L. Li and A. Manthiram, "Dual-electrolyte Lithium-air Batteries: Influence of Catalyst, Temperature, and Solid-electrolyte Conductivity on the Efficiency and Power Density," *Journal of Materials Chemistry A* **1**, 5121-5127 (2013).
17. E.-S. Lee, A. Huq, and A. Manthiram, "Understanding the Effect of Synthesis Temperature on the Structural and Electrochemical Characteristics of Layered-Spinel Composite Cathodes for Lithium-ion Batteries," *Journal of Power Sources* **240**, 193-203 (2013).
18. Y.-S. Su, Y. Fu, B. Guo, S. Dai, and A. Manthiram, "Fast, Reversible Lithium Storage with Sulfur/Long-Chain Polysulfide Redox Couple," *Chemistry - A European Journal* **19**, 8621-8626 (2013).
19. Z. Jiang, B. Pei, and A. Manthiram, "Randomly Stacked Holey Graphene Anodes for Lithium Ion Batteries with Enhanced Electrochemical Performance," *Journal of Materials Chemistry A* **1**, 7775-7781 (2013).
20. J. Pan, Y. Sun, W. Li, J. Knight, and A. Manthiram, "A Green Lead Hydrometallurgical Process Based on a Hydrogen-lead Oxide Fuel Cell," *Nature Communications* **4**, 2178-1 – 2178-6 (2013).
21. I. T. Kim, E. Allcorn, and A. Manthiram, "High-performance $M_xSb-Al_2O_3-C$ ($M = Fe, Ni,$ and Cu) Nanocomposite Alloy Anodes for Sodium-ion Batteries," *Energy Technology* **1**, 319-326 (2013).
22. C. A. Bridges, K. L. Harrison, R. Unocic, J. Idrobo, M. P. Paranthaman, and A. Manthiram, "Defect Chemistry of Phospho-olivine Nanoparticles Synthesized by a Microwave-assisted Solvothermal Process," *Journal of Solid State Chemistry* **205**, 197-204 (2013).
23. F. Cheng, J. Chen, H. Zhou, and A. Manthiram, "Structural and Electrochemical Characterization of $(NH_4)_2HPO_4$ -treated Lithium-rich Layered $Li_{1.2}Ni_{0.2}Mn_{0.6}O_2$ Cathodes for Lithium-ion Batteries," *Journal of the Electrochemical Society* **160**, A1661-A1667 (2013).
24. L. Baggetto, E. Allcorn, R. R. Unocic, A. Manthiram, G. M. Veith, "Mo₃Sb₇ as a Very Fast Anode Material for Lithium-ion and Sodium-ion Batteries," *Journal of Materials Chemistry A* **1**, 11163-11169 (2013).
25. Y.-Z. Fu and A. Manthiram, "Silicon Nanoparticles Supported on Graphitic Carbon Paper as a Hybrid Anode for Li-ion Batteries," *Nano Energy* **2**, 1107-1112 (2013).
26. Y.-Z. Fu, C. Zu, and A. Manthiram, "In Situ-formed Li_2S in Lithiated Graphite Electrodes for Lithium-Sulfur Batteries," *Journal of the American Chemical Society* **135**, 18044-18047 (2013).
27. C. Liao, K. S. Han, L. Baggetto, D. A. Hilleshim, R. Custelcean, E.-S. Lee, B. Guo, Z. Bi, D.-E. Jiang, G. M. Veith, E. W. Hagaman, G. M. Brown, C. A. Bridges, M. P. Paranthaman, A. Manthiram, S. Dai, and X.-G. Sun, "Synthesis and Characterization of Lithium Bis(fluoromalonato)borate for Lithium-Ion Battery Applications," *Advanced Energy Materials* **4**, 1301368: 1-12 (2014).
28. T. Maiyalagan, K. R. Chemelewski, and A. Manthiram, "Role of the Morphology and Surface Planes on the Catalytic Activity of Spinel $LiMn_{1.5}Ni_{0.5}O_4$ for Oxygen Evolution Reaction," *ACS Catalysis* **4**, 421-425 (2014).
29. E. Allcorn and A. Manthiram, "NiSb- Al_2O_3 -C Nanocomposite Anodes with Long Cycle Life for Li-ion Batteries," *Journal of Physical Chemistry C* **118**, 811-822 (2014).
30. F. R. Beck, Y. Q. Cheng, Z. Bi, M. Feyngenson, C. A. Bridges, Z. Moorhead-Rosenberg, A. Manthiram, J. B. Goodenough, M. Paranthaman, and A. Manivannan, "Neutron Diffraction

- and Electrochemical Studies of $\text{Na}_{0.79}\text{CoO}_2$ and $\text{Na}_{0.79}\text{Co}_{0.7}\text{Mn}_{0.3}\text{O}_2$ Cathodes for Sodium-Ion Batteries,” *Journal of the Electrochemical Society* **161**, A1-A8 (2014).
31. L. Li and A. Manthiram, “O- and N-doped Carbon Nanoweb as Metal-Free Catalysts for Hybrid Li-Air Batteries,” *Advanced Energy Materials* **DOI:** 10.1002/aenm.201301795 (2014).
 32. E. Allcorn and A. Manthiram, “ $\text{FeSb}_2\text{-Al}_2\text{O}_3$ Nanocomposite Anodes for Lithium-ion Batteries,” *ACS Applied Materials & Interfaces* **DOI:** 10.1021/am500448f (2014).
 33. I.-T. Kim, J. C. Knight, H. Celio, and A. Manthiram, “Enhanced Electrochemical Performances of Li-rich Layered Oxides by Surface Modification with Reduced Graphene Oxide/ AlPO_4 Hybrid Coating,” *Journal of Materials Chemistry A* **DOI:** 10.1039/C4TA00898G (2014).

Articles in Press

34. T. Maiyalagan, K. A. Jarvis, S. Therese, P. J. Ferreira, and A. Manthiram, “Spinel-type Lithium Cobalt Oxide as a Bifunctional Electrocatalyst for Oxygen Evolution and Oxygen Reduction Reactions,” *Nature Communications* (in press).
35. S.-H. Chung and A. Manthiram, “Bifunctional Separator with a Light-weight Carbon-coating for Dynamically and Statically Stable Lithium-Sulfur Batteries,” *Advanced Functional Materials* (in press).
36. J.-Y. Liao and A. Manthiram, “Mesoporous $\text{TiO}_2\text{-Sn/C}$ Core-shell Nanowire Arrays as High-performance 3D Anodes for Li-ion Batteries,” *Advanced Energy Materials* (in press).
37. X. Yu and A. Manthiram, “Highly Reversible Room-temperature Sulfur/Long-chain Sodium Polysulfide Batteries,” *Journal of Physical Chemistry Letters* (in press).
38. K. L. Harrison, C. A. Bridges, C. U. Segre, C. D. Varnado, Jr., D. Applestone, C. W. Bielawski, M. P. Paranthaman, and A. Manthiram, “Chemical and Electrochemical Lithiation of LiVOPO_4 Cathodes for Lithium-ion Batteries,” *Chemistry of Materials* (in press).
39. V. Augustyn and A. Manthiram, “Characterization of Layered LiMO_2 Oxides for the Oxygen Evolution Reaction in Metal-air Batteries,” *ChemPlusChem* (in press).
40. S.-H. Chung and A. Manthiram, “High-performance Li-S Batteries with an Ultra-lightweight MWCNT-coated Separator,” *Journal of Physical Chemistry Letters* (in press).

Articles Submitted

41. L. Li, S.-H. Cai, S. Dai, and A. Manthiram, “Advanced Hybrid Li-air Batteries with High-performance Mesoporous Nanocatalysts,” *Energy & Environmental Science* (submitted).
42. C. Zu and A. Manthiram, “Stabilized Lithium Surface in a Polysulfide-Rich Environment of Lithium-Sulfur Batteries,” *Angewandte Chemie* (submitted).
43. I.-T. Kim, E. Allcorn, and A. Manthiram, “High-performance FeSb-TiC-C Nanocomposite Anodes for Sodium-ion Batteries,” *Physical Chemistry Chemical Physics* (submitted).
44. X. Yu and A. Manthiram, “Capacity Enhancement and Discharge Mechanisms of Room-temperature Sodium-Sulfur Batteries,” *ChemElectroChem* (submitted).
45. Y. Ansari, B. Guo, J. Song, K. Park, and J. B. Goodenough, “Low-Cost, Dendrite-Blocking Polymer Composite for Lithium and Sodium Batteries,” *Journal of the Electrochemical Society* (submitted).

Cyclometalation Syntheses of Phosphorescent Complexes

Thomas G. Gray, Department of Chemistry, Case Western Reserve University

Program Scope

Current work focuses on new syntheses of cyclometalated organometallics using boron transmetalation protocols. The targeted complexes are triplet-state lumophores that are intended as emitting elements in electroluminescent devices such as OLEDs. At present, cyclometalation syntheses are being optimized for complexes of iridium(III) and group 11 metals. Anionic, cyclometalating ligands are C[^]N and N[^]N chelators, including complexes of the azadiptyromethene ligand set. New luminescent materials are diamagnetic, and are characterized routinely by multinuclear NMR experiments, absorption and emission spectroscopies (including time-resolved emission), and X-ray diffraction crystallography.

Recent Progress

A. Cyclometalated Ir(III) Complexes of Long-Wavelength Chromophores. Iridium(III) is the leader in light-emitting devices based on metal complexes.¹⁻³ The Gray laboratory has disclosed cyclometalation protocols based on boron transmetalation.⁴ These require milder reaction conditions than those now in wide use. Experiments have demonstrated that C[^]N and C[^]O-type chelating ligands are reliably bound to iridium(III). Work under BES auspices extends this protocol to chromophoric N[^]N chelators.

Boron azadiptyromethenes are a fast-growing class of chromophores; absorption maxima range from yellow to near-infrared wavelengths.⁵⁻⁸ The spectral signature of boron azadiptyromethenes is an intense peak generally near 610 nm. The large majority of azadiptyromethenes are BF₂⁺ chelates. The coordination chemistry of *metalla*-azadiptyromethenes is underdeveloped. An exciting prospect is to combine the excited-state tunability of iridium(III) cyclometalates with the outstanding red- and near-IR photoactivity of azadiptyromethene ligands.

Figure 1 shows the crystal structure of a typical complex. The brominated ligand **L_aBr₂** was chosen for the possibility of derivitization through bromine. A control complex of the

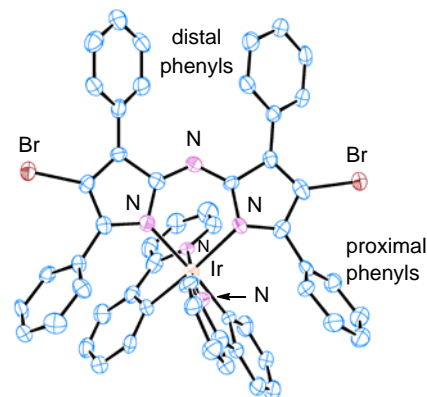


Figure 1. Thermal ellipsoid depiction of a cyclometalated iridium(III) azadiptyromethene complex (50% probability). H atoms are omitted for clarity. A partial atom labeling scheme is indicated; unlabeled atoms are carbon.

nonbrominated ligand confirms that the bromine atoms are spectroscopically silent. Unexpectedly, the new complexes are nonemissive at room-temperature.

Absorption profiles of the new complexes are dominated by a broad, structureless absorption near 590 nm that is characteristic of azadi-pyrromethene ligands. Conflated absorption spectra appear in Figure 2. Absorption features in the range from *ca.* 350–500 nm arise from intraligand transitions involving the C^N ligands and metal-to-ligand charge transfer transitions. The new complexes were also characterized by cyclic voltammetry. In each case, one reversible and one irreversible reduction occurs at potentials that are insensitive to the cyclometalating (C^N) ligand. The first reduction is azadi-pyrromethene-centered; it occurs in the BF_2^+ chelate. This observation demonstrates that the azadi-pyrromethene ligand is the site of one-electron reduction in the new complexes.

B. The First Fluoro Complex of Bis-cyclometalated Iridium(III).

The development of metal *fluorides* has driven much progress in the synthesis of organometallic complexes. Reactions of metal fluoro complexes with silyl reagents bring about new coordination complexes, driven by irreversible Si–F bond formation.

The Gray research group has prepared the first bis-cyclometalated iridium(III) fluoride complexes. The crystal structure of one such complex (**1**) appears as Figure 3. The complex crystallizes with imposed centrosymmetry (*I4m*); the observed Ir–F bond distance is 2.176(2) Å. Other metrics are normal.

Fluoro-bridged iridium(III) dimers luminesce. Such emission is unusual for halide-bridged dimers. The absorption and emission spectra of a representative complex

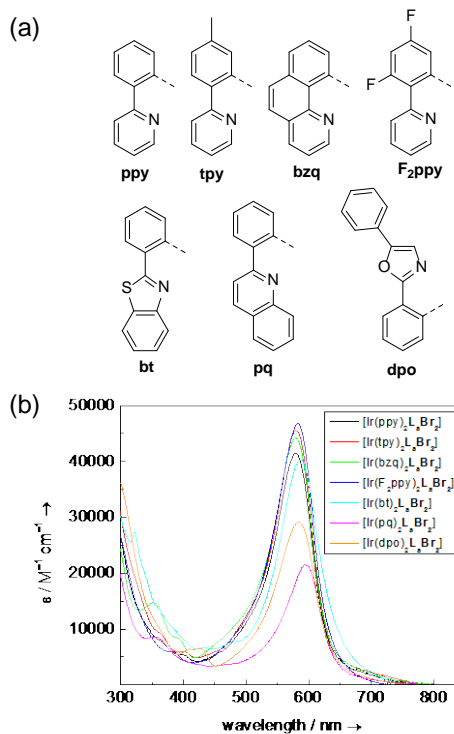


Figure 2. (a) Cyclometalating ligands and abbreviations. (b) Absorption spectra of (azadi-pyrromethene)Ir^{III} complexes in chloroform solution.

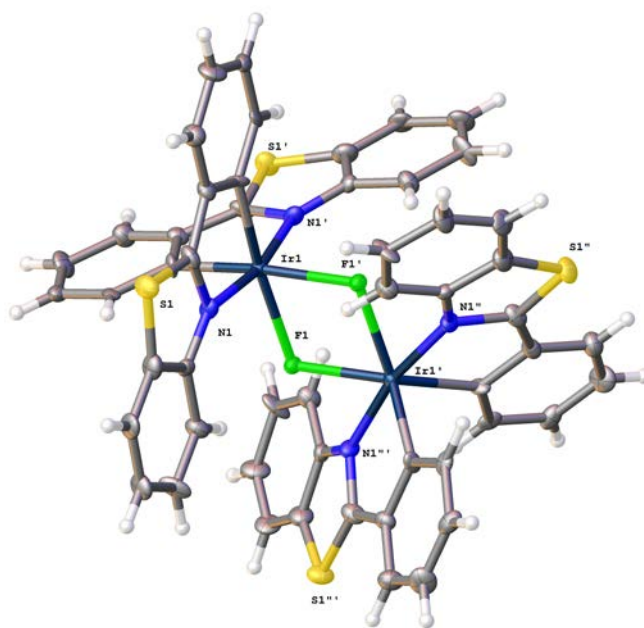


Figure 3. Crystal structure of the iridium(III) dimer $[(\text{bt})_2\text{Ir}(\mu\text{-F})_2]$ (**1**).

(1) appear as Figure 4. Luminescence quenches on exposure to O₂; this combined with a large Stokes shift suggests phosphorescence emission. Vibronic structure is evident in the emission profile, and involvement of the cyclometalating ligands in the excited state is indicated. The emission quantum yield of **1** at 298 K in 2-methyltetrahydrofuran is 0.26, relative to 9,10-diphenylanthracene.

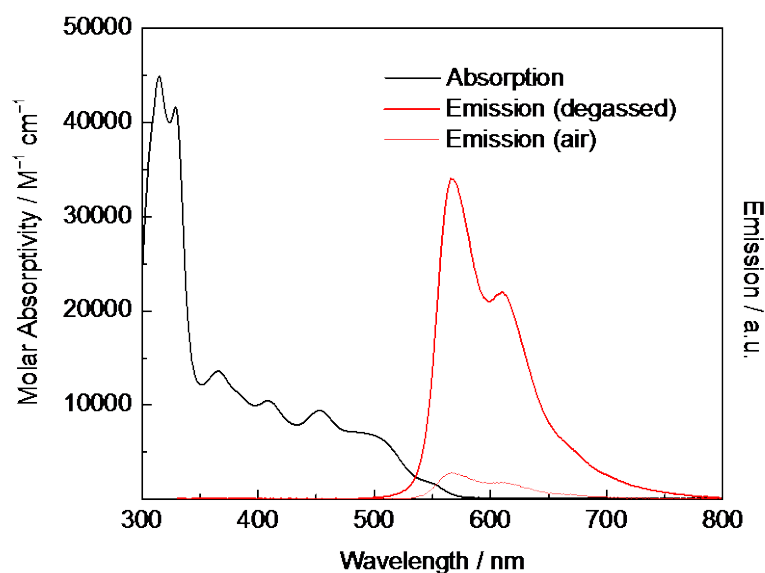


Figure 4. Room-temperature absorption and emission of dimer **1** in 2-methyltetrahydrofuran solution.

Time-dependent density-functional theory

calculations of **1** show multiple low-lying excited states. At least six triplet states are calculated to lie below the first excited singlet state. These triplets are combinations of single-particle transitions between orbitals. That is, states mingle extensively through configuration interaction.

The first *mononuclear, terminal* bis(cyclometalated) iridium(III) fluoride complexes have been achieved and structurally characterized. The reactivity of these terminal fluoro complexes is being investigated.

Cyclometalated complexes of gold(III) are being investigated using the new methods, and early examples are in hand. Results will be reported in due course.

Future Plans

Immediate plans include:

- (1) Continued chemical and photophysical characterization of cyclometalated iridium(III) fluoride complexes. Both terminal and bridged fluorides are luminescent.
- (2) Development of stoichiometric and *catalytic* syntheses of luminescent cyclometalates of gold(III).
- (3) Synthesis of a family of cyclometalated coinage metal complexes that are expected to be triplet-state lumophores.
- (4) Characterization of new luminescent complexes by static and time-resolved emission spectroscopy, including temperature-dependent experiments.

References

- ¹ Zhou, G.; Wong, W.-Y.; Yang, X. “New Design Tactics in OLEDs Using Functionalized 2-Phenylpyridine-Type Cyclometalates of Iridium(III) and Platinum(II),” *Chem. Asian J.* **2011**, *6*, 1706–1727.
- ² Baranoff, E.; Yum, J.-H.; Graetzel, M.; Nazeeruddin, Md. K. “Cyclometalated Iridium Complexes for Conversion of Light into Electricity and Electricity into Light,” *J. Organomet. Chem.* **2009**, *694*, 2661–2670.
- ³ Ulbricht, C.; Beyer, B.; Friebe, C.; Winter, A.; Schubert, U. S. “Recent Developments in the Application of Phosphorescent Iridium(III) Complex Systems,” *Adv. Mater.* **2009**, *21*, 4418–4441.
- ⁴ Maity, A.; Anderson, B. L.; Deligonul, N.; Gray, T. G. “Room-Temperature Synthesis of Cyclometalated Iridium(III) Complexes: Kinetic Isomers and Reactive Functionalities,” *Chem. Sci.* **2013**, *4*, 1175–1181.
- ⁵ Gorman, A.; Killoran, J.; O’Shea, C.; Kenna, T.; Gallagher, W. M.; O’Shea, D. F. “In Vitro Demonstration of the Heavy-Atom Effect for Photodynamic Therapy,” *J. Am. Chem. Soc.* **2004**, *126*, 10619–10631
- ⁶ Loudet, A.; Bandichhor, R.; Burgess, K.; Palma, A.; McDonnell, S. O.; Hall, M. J.; O’Shea, D. F. “*B,O*-Chelated Azadipyrrromethenes as Near-IR Probes,” *Org. Lett.* **2008**, *10*, 4771–4774
- ⁷ Teets, T. S.; Updegraff, J. B.; Esswein, A. J.; Gray, T. G. “Three-Coordinate, Phosphine-Ligated Azadipyrrromethene Complexes of Univalent Group 11 Metals,” *Inorg. Chem.* **2009**, *48*, 8134–8144.
- ⁸ Teets, T. S.; Partyka, D. V.; Esswein, A. J.; Updegraff, J. B. III; Zeller, M.; Hunter, A. D.; Gray, T. G. “Luminescent, Three-Coordinate Azadipyrrromethene Complexes of d^{10} Copper, Silver, and Gold,” *Inorg. Chem.* **2007**, *46*, 6218–6220

Publication

“Cyclometalated Iridium(III) Complexes of Azadipyrrromethene Chromophores,” Deligonul, N.; Browne, A. R. Golen; J. A.; Rheingold, A. L.; Gray, T. G. *Organometallics* **2014**, *33*, 637–643. DOI: 10.1021/om4007032

NMR Studies of Materials for Electrochemical Energy Storage

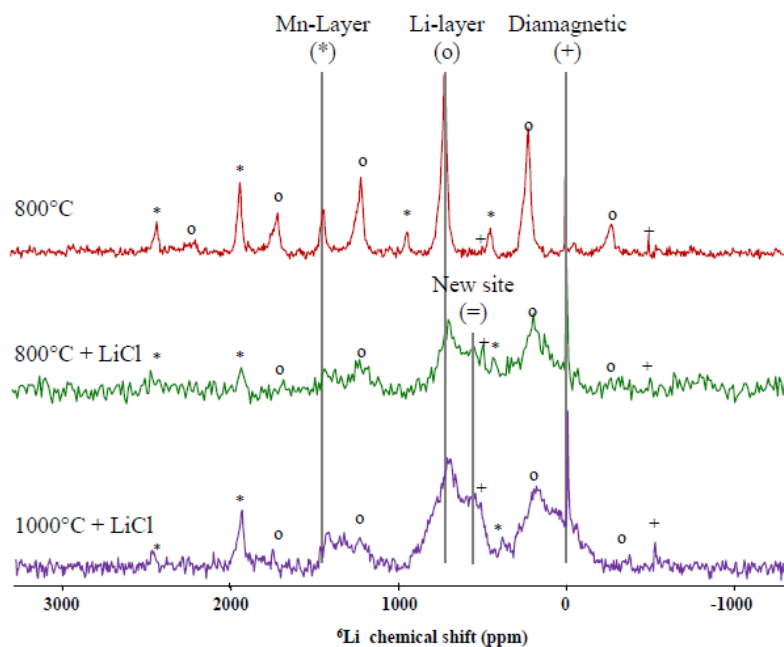
Steve G. Greenbaum, Hunter College of CUNY, New York, NY 10065

Program Scope

Working with several battery materials groups, we apply solid state NMR spectroscopy to elucidate structure and ionic dynamics of novel battery materials. Correlations observed between NMR results and electrochemical performance lead to improved understanding of charge storage and transport mechanisms.

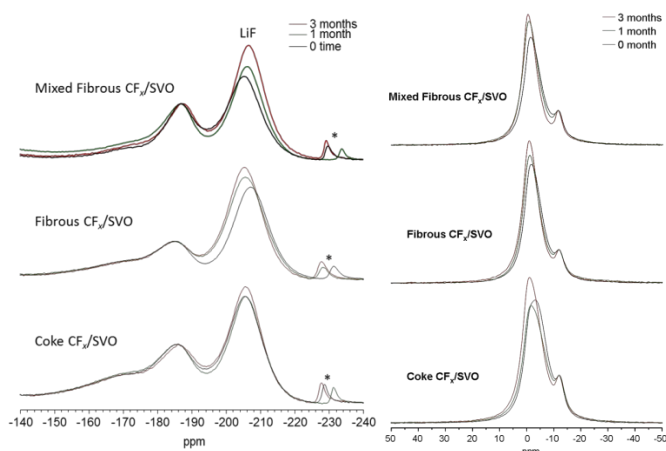
Recent Progress

Three projects are highlighted here, reflecting work done in the 6-12 months and covered in this Review. In collaboration with the University of Puerto Rico and the NASA Jet Propulsion Lab [17] we have studied the effect of a relatively simple LiCl flux treatment in the synthesis of the layered Li cathode material Li_2MnO_3 : $\text{LiMn}_{1/3}\text{Ni}_{1/3}\text{Co}_{1/3}\text{O}_2$ (with 1:1 ratio) prepared by our colleague Will West at JPL. Although the x-ray diffraction results were somewhat inconclusive, solid state $^{6,7}\text{Li}$ NMR measurements showed unambiguously that firing the mixture of the starting compounds in the presence of LiCl flux facilitates interdiffusion of Li^+ ions between the phases and leads to a true solid solution rather than a phase separated nanocomposite. In particular, a new site within the Li layers is observed and correlated with superior reversible capacity.



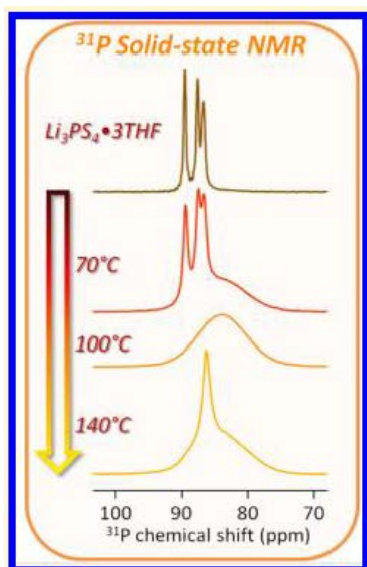
^{6}Li MAS NMR spectra at 23 kHz of the Li_2MnO_3 - $\text{LiMn}_{1/3}\text{Ni}_{1/3}\text{Co}_{1/3}\text{O}_2$ after firing 48 hours at 800°C with no LiCl flux; after firing 48 hours at 800°C with LiCl flux; after firing 6 hours at 1000°C with LiCl flux.

In a collaboration with Medtronic, Inc. (they provided samples but no funding), which has the largest worldwide market share for sales of cardiac pacemakers and implantable defibrillators (ICDs), we tested the hypothesis that the lifetime of these batteries can be extended without sacrificing power capability (which is required for defibrillation) by using a hybrid cathode made with CF_x , which provides the extended energy, and silver vanadate (SVO), which gives high current. The rationale is that during rapid discharge, most of the current will come from the SVO. During the resting phase, the CF_x will actually recharge the SVO through physical contact between particles of the two materials. We have demonstrated this conclusively at the molecular level using multinuclear NMR as shown below.[16]



^{19}F (left) and ^7Li (right) NMR spectra of CF_x/SVO hybrid cathodes following 50% DoD and disassembly after 0, 1, and 3 months. The growth in the LiF component (left) and relative decrease in the Li intercalated in the SVO (smaller spectral feature on right) provides unambiguous proof of the recharge process. Three different kinds of CF_x used in forming the mixtures were investigated.

Finally, in collaboration with Oak Ridge National Lab, we have used multinuclear (^1H , $^6,7\text{Li}$, ^{31}P) NMR, we have tracked the gradual formation of the highly Li^+ conducting β -phase of Li_3PS_4 subjected to thermal treatment of the inorganic-organic precursor.[20] NMR is sensitive to short range structural arrangements in ways that standard XRD is not.



“Journal graphic” of recent publication showing the use of ^{31}P solid state NMR to track the phase evolution of organic solvent assisted preparation of β Li_3PS_4 during heat treatment

Future Plans

If our BES grant is renewed (the grant that funded the work described herein ended February 28, 2014), we will continue our work with ORNL. We have been awarded user access to the ORNL Center for Nanophase Materials Synthesis for our colleagues to prepare materials for our NMR investigations. One project we'd like to begin involves highly conducting composites based on milled mixtures of Li_3PS_4 and LiI . We will also continue collaborating with JPL on analysis of SEI formation on Si-based anodes in contact with next-generation electrolytes and on low temperature transport properties of such electrolytes. Also planned are investigations of Na battery chemistries, both electrodes and electrolytes, in collaboration with LBNL and Tel Aviv University.

References

Please refer to publications

Publications (2-yr, BES funding only)

1. "Advanced Techniques to Elucidate Electrochemical Reactions in Lithium Ion Batteries", with P.J. Sideris, **ENCYCLOPEDIA OF SUSTAINABILITY SCIENCE AND TECHNOLOGY**, Springer, Volume no. 9, pp. 6067—6097 (2012).
2. "Tin-coated graphite electrodes as composite anodes for Li-ion batteries. Effects of tin coatings thickness toward intercalation behavior", with Francesco Nobili, Marilena Mancini, Phil E Stallworth, Fausto Croce, and Roberto Marassi, *Journal of Power Sources*, 198, 243-250 (2012).
3. "Diffusion Coefficients from ^{13}C PGSE-NMR Measurements— Fluorine-Free Ionic Liquids with DCTA^- and DCA^- Anions", with Cristelle Portet, Sufia Khatun, Eric Fox, Patrick Judeinstein, Michel Armand, and Wesley Henderson, *Journal of Physical Chemistry Letters*, 3, 441-444 (2012).
4. " ^7Li and ^{31}P Nuclear Magnetic Resonance Studies of Single Crystal LiMPO_4 ($M = \text{Co}, \text{Fe}$)", with P. Sideris, R. Samuelli, P.E.Stallworth, and D. Vaknin, in *Advances in Inorganic Phosphate Materials*, *Ceramic Transactions*, vol. 233, American Ceramic Society, Wiley, 2012, p.117-123.
5. "Solid State Multinuclear Magnetic Resonance Investigation of Electrolyte Decomposition Products on Lithium Ion Electrodes", with J.H.S.R. DeSilva, V. Udinwe, P.J. Sideris, M. C. Smart, F.C. Krause, C. Hwang, and K. A. Smith, *Electrochemical Society Transactions*, Volume 41, Issue 41, p 207-214 (2012).
6. "Effect of Peptide Nanotube Filler on Structural and Ion-transport Properties of Solid Polymer Electrolytes", with K. Goldstein, D. Golodnitsky, E. Peled, L. Adler-Abramovich, E. Gazit, and S. Khatun, *Solid State Ionics*, 220, 39-46 (2012).
7. "Subsurface Diffusion of Oxide Electrolyte Decomposition Products in Metal Fluoride Nanocomposite Electrodes, with Andrew J. Gmitter, Anna Halajko, Paul J. Sideris, and Glenn G. Amatucci, *Electrochimica Acta*, 88, 735-744 (2013).
8. "A structural, spectroscopic and electrochemical study of a lithium ion conducting $\text{Li}_{10}\text{GeP}_2\text{S}_{12}$ solid electrolyte" , with Jusef Hassoun, Roberta Verrelli, Priscilla Reale, Stefania Panero, Gino Mariotto, and Bruno Scrosati, *Journal of Power Sources*, 229,

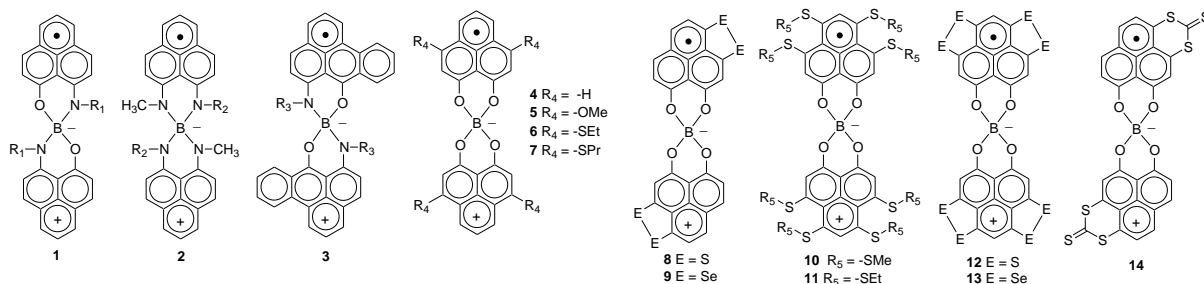
- 117-122 (2013). <http://dx.doi.org/10.1016/j.jpowsour.2012.11.130>.
9. “Examination of Methods to Determine Free-Ion Diffusivity and Number Density from Analysis of Electrode Polarization”, with Yangyang Wang, Che-Nan Sun, Fei Fan, Joshua R. Sangoro, Marc B. Berman, Thomas A. Zawodzinski, and Alexei P. Sokolov, *Physical Review E*, **87**, 042308 (2013).
 10. “Cation-only Conduction in New Polymer/SiO₂ Nano Hybrid Electrolytes”, with Irune Villaluenga, Michel Armand, Xavier Bogle, Izaskun Gil de Muro and Teófilo Rojo, *Journal of Materials Chemistry A*, 2013,**1**, 8348-8352. **DOI:** 10.1039/C3TA11290J
 11. “Recent Progress in NMR Spectroscopy of Polymer Electrolytes for Lithium Batteries”, with Sabina Abbrent, *Current Opinion in Colloid and Interface Science*, **18**, 228–244 (2013).
 12. “Influence of Solvent on Ion Aggregation and Transport in pyr₁₅TFSI Ionic Liquid – Aprotic Solvent Mixtures” with Oleg Borodin, Eric Fox, Wesley A. Henderson, Marc Berman, and Mallory Gobet, *Journal of Physical Chemistry B*, **117**, 10581–10588 (2013) **DOI:** 10.1021/jp406541e
 13. “PEO-NaTFSI polymer electrolyte for sodium-based battery application”, J. Serra Moreno, M. Armand, M.B.Berman, S.G. Greenbaum, B. Scrosati, and S. Panero, *Journal of Power Sources*, Volume 248, 15 February 2014, Pages 695–702
 14. “Single-ion-conducting nanocomposite polymer electrolytes based on PEG400 and anionic nanoparticles: Part 1. Synthesis, structure and properties ”, with F. Bertasi, K. Vezzù, G. A. Giffin, M. Vittadello, V. Di Noto *International Journal of Hydrogen Energy*, **39**, 2872–2883 (2014).
 15. “Single-ion-conducting nanocomposite polymer electrolytes based on PEG400 and anionic nanoparticles: Part 2. Electrical characterization”, with F. Bertasi, K. Vezzù, G. A. Giffin, T. Nosach, P. Sideris, M. Vittadello, V. Di Noto Submitted in: *International Journal of Hydrogen Energy*, **4**, 2884–2895 (2014).
 16. “Charge Transfer in Li/CF_x-Silver Vanadium Oxide Hybrid Cathode Batteries Revealed By Solid State ⁷Li and ¹⁹F Nuclear Magnetic Resonance Spectroscopy” , Paul J. Sideris, Rowena Yew, Ian Nieves, Kevin Chen, Gaurav Jain, Craig L. Schmidt, Steve G. Greenbaum, *Journal of Power Sources*, **Volume 254**, 15 May 2014, Pages 293–297. [doi.org/10.1016/j.jpowsour.2013.12.108](http://dx.doi.org/10.1016/j.jpowsour.2013.12.108)
 17. "Layered-Layered Composite Li₂MnO₃- LiMO₂ (M=Mn, Ni, Co) Synthesis Using LiCl Molten Flux for Cathodes Materials in Li-ion Batteries", with Edwin Ortiz-Quiles, Jessica Soler, Mallory Gobet, Tetiana Nosach, Oscar Resto, Omar Garcia-Ricard, Arturo Hernandez-Maldonado, William West, Carlos Cabrera, *RSC Advances*, **4** 12018 (2014).
 18. “A Ceramic/Polymer Separator for a Rechargeable Alkali-Ion Battery”, with Kyusung Park, Joon Hee Cho, Kadhira Shanmuganathan, Jie Song, Jing Peng, Mallory Gobet, Christopher J. Ellison, and John B. Goodenough, *Journal of Power Sources*, **263**, 52-58 (2014).
 19. “Polymer Electrolytes for Solid State Batteries”, with Sabina Abbrent, in *Handbook of Solid State Batteries*, ed. N.J. Dudney, W.C. West, J. Nanda, World Scientific, in press.
 20. “Structural Characterization and Li dynamics in new Li₃PS₄ ceramic ion conductor by solid-state and pulsed-field gradient NMR”, with Mallory Gobet, Chengdu Liang, and Gayatri Sahu, *Chemistry of Materials*, **DOI:** 10.1021/cm5012058.

Solid State Electronic Structure and Properties of Neutral Carbon-Based Radicals

Robert C. Haddon, University of California, Riverside, CA, 92521

Program Scope

The primary goal of this project is the solid-state characterization of neutral radicals based on (substituted) phenalenyl (PLY) units (**1** – **14**).¹ We have shown that the neutral spirobiphenalenyl carbon-based radicals exhibit unusual conductivity, magnetic and optical properties,² and our current work is focused on the synthesis of suitably modified radicals in order to investigate the effect of electronic structure on the solid state properties of these compounds. The spiro-conjugated boron radical, (**1**, $R_1 = \text{Cyclohexyl}$) showed the highest room temperature conductivity ($\sigma_{RT} = 0.3 \text{ S/cm}$), among the phenalenyl-based neutral radical conductors and it has a high symmetry crystal structure and metal-like temperature-independent Pauli paramagnetism.³ We have crystallized and characterized the first benzophenalenyl (BPLY) based neutral radical conductor (**3**, $R_3 = \text{Benzyl}$), which shows unprecedented solid state properties: radical RVB (resonating valence bond) and σ -dimer CDW (σ -charge density wave) phases coexist over the whole temperature range.⁴



In order to obtain conducting solids, the mode of substitution must be carefully chosen and we have pursued both alkoxy and chalcogenide substitution at the periphery of the PLY unit.^{5, 6} The chalcogenides and sulfur in particular have been popular atoms for incorporation into the peripheries of molecular building blocks for organic conductors because these atoms do not require additional functionality to terminate their valencies and they are associated with strong intermolecular interactions.⁷ Furthermore they have the ability to stabilize multiple oxidation states and to effectively delocalize spin density.

Recent Progress

Chalcogen-substituted Spiro-bisphenalenyl Boron Neutral Radicals

We have successfully incorporated the alkylthio, and dithio- and diseleno-bridging units into 9-hydroxyphenalenones and crystallized some of the associated spiro-biphenalenyl boron neutral radicals.⁸ Alkylthio substitution at the active positions of the phenalenyl units slightly reduces the electrochemical disproportionation potential (ΔE_{2-1}), of the alkylthio-radicals **6** and **7**, but brings about a significant reduction of the ΔE_{2-1} value in the case of disulfide and diselenide functionalization (**8**, **9**). The crystal structures of **6** and **7** indicate that the radicals exist as one dimensional (1-D) π -chains of superimposed

phenalenyl units (Figure 1), and the molecular units pack more efficiently than the oxygen-substituted analogue (**5**). Magnetic susceptibility data shows that in the solid state the radicals remain paramagnetic but there is spin-spin interaction between the molecules along the π -chain direction; the room temperature electrical conductivities of both compounds are found to be $\sigma_{RT} = 1.5 \times 10^{-2}$ S/cm (Figure 1).^{8,9}

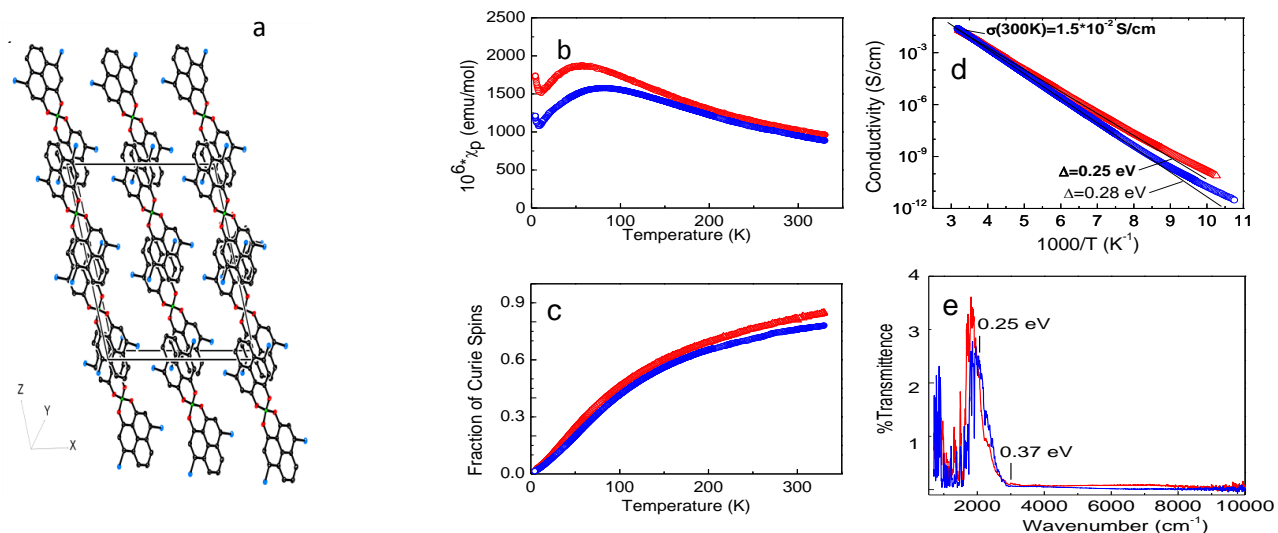


Figure 1. (a) Solid state packing of radical **6**, showing the π -chain overlap between phenalenyl units. Solid state properties of radical **6** (blue) and **7** (red). (b) Magnetic susceptibility as a function of temperature. (c) Fraction of Curie spins. (d) Four probe single crystal conductivity as a function of temperature. (e) Infrared transmission spectra of the radical crystals.

Hexathiophenalenyl Radicals (HTPLY)

We have synthesized two hexathiophenalenylium compounds as stable salts (**15**⁺ and **16**⁺) from the reaction of 3,4,6,7-tetrathio-9-hydroxyphenalenone with Lawesson's reagent, and X-ray crystal structure measurements confirmed the presence of three disulfide linkages (Figure 2).¹⁰

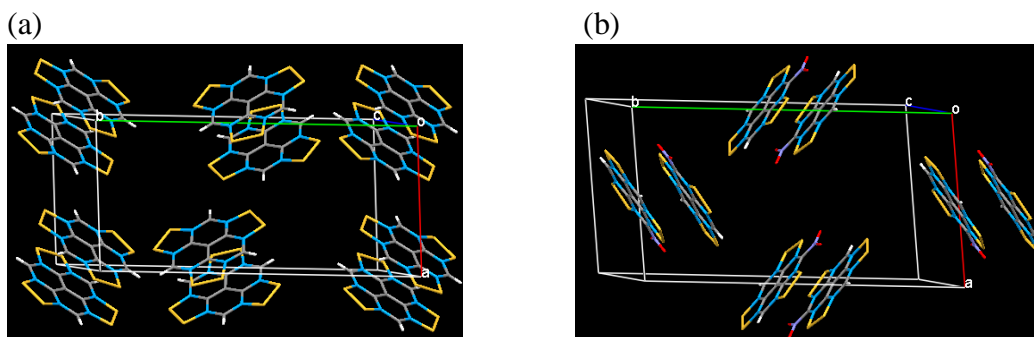


Figure 2. Packing of the cations of (a) **15**⁺ TFAB⁻ and (b) **16**⁺ BPh₄⁻ (Anions and solvent molecules are omitted for clarity).

Future Plans

Annulated Spiro-Biphenalenyl Boron Radicals

In the previous funding period, we crystallized and characterized the first benzannulated phenalenyl (BPLY) neutral radical conductor which shows unprecedented solid state properties: radical RVB (resonating valence bond) and σ -dimer CDW (σ -charge density wave) phases coexist over the whole temperature range.⁴ We targeted these compounds because the greater size of the π -systems in the BPLY units provided an opportunity to increase the bandwidth (W) in structures involving the π -chain stacking motif of highly conducting radicals. Recently, we further develop this theme and synthesized and structurally characterized two spiro-bis-naphthophenalenyl (NPLY) radicals and it seems that the NPLY π -system is even more effective than BPLY in enhancing the bandwidths of the π -superimposed compounds. We pursued the NPLY system in order to increase the number of spin bearing carbon atoms in the core NPLY ring and to allow the registry of all ten spin bearing carbon atoms, thereby increasing the band width compared to the PLY and BPLY based radicals.

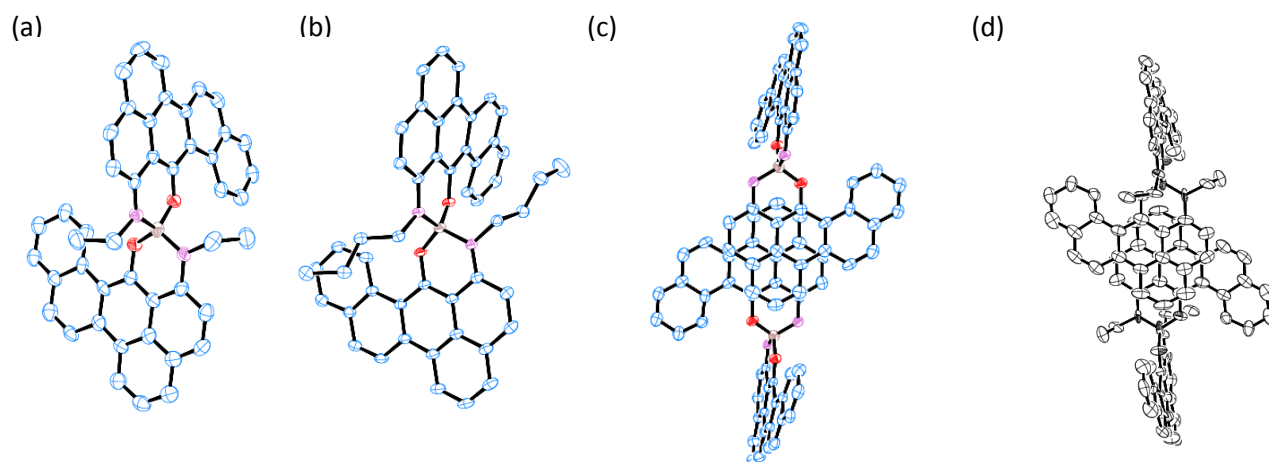


Figure 3. ORTEP drawings of spiro-bis-naphthophenalenyl radicals (a) **17** and (b) **18**. π -Overlaps of the six spin bearing carbon atoms within a dimeric unit of: (c) **17** and, (d) **18**.

Both spiro-bis-naphthophenalenyl radicals (**17** and **18**), show significantly shorter interplanar separations than those observed in the spiro-bis-benzophenalenyl radicals, and this may be attributed to the more efficient overlap in the case of the NPLY compounds in comparison with the BPLY radicals.

Our efforts to prepare structurally well-defined open-shell graphene fragments have focused on the design and synthesis of extended π -electron derivatives of triangular phenalenyl units such as benzophenalenyl (BPLY) and naphthophenalenyl (NPLY). The study of these extended phenalenyl systems could lead to a better understanding of the intriguing electronic and magnetic properties of nanographene and the stability of the spiro-biphenalenyl structures offers a route to large, isolable open shell graphitic substructures that can be studied in the solid state.

Very recent work in our laboratories has shown that it may be possible to vary the electronic band filling in the spirobiphenalenyl radical solids by nontraditional doping chemistry.

References

- (1) Haddon, R. C., Design of Organic Metals and Superconductors *Nature* **1975**, *256*, 394-396.
- (2) Itkis, M. E.; Chi, X.; Cordes, A. W.; Haddon, R. C., Magneto-Opto-Electronic Bistability in a Phenalenyl-Based Neutral Radical *Science* **2002**, *296*, 1443-1445.
- (3) Pal, S. K.; Itkis, M. E.; Tham, F. S.; Reed, R. W.; Oakley, R. T.; Haddon, R. C., Resonating Valence-Bond Ground State in a Phenalenyl-Based Neutral Radical Conductor *Science* **2005**, *309*, 281-284.
- (4) Bag, P.; Itkis, M. E.; Pal, S. K.; Donnadiou, B.; Tham, F. S.; Park, H.; Schleuter, J. A.; Siegrist, T.; Haddon, R. C., Resonating Valence Bond and sigma-Charge Density Wave Phases in a Benzannulated Phenalenyl Radical *J. Am. Chem. Soc.* **2010**, *132*, 2684-2694.
- (5) Beer, L.; Mandal, S. K.; Reed, R. W.; Oakley, R. T.; Tham, F. S.; Donnadiou, B.; Haddon, R. C., The First Electronically Stabilized Phenalenyl Radical: Effect of Substituents on Solution Chemistry and Solid State Structure. *Cryst. Growth & Design* **2007**, *7*, 802-809.
- (6) Beer, L.; Reed, R. W.; Robertson, C. M.; Oakley, R. T.; Tham, F. S.; Haddon, R. C., Tetrathiophenalenyl Radical and its Disulfide-Bridged Dimer *Org. Lett.* **2008**, *10*, 3121-3123.
- (7) Mailman, A.; Winter, S. M.; Yu, X.; Robertson, C. M.; Yong, W.; Tse, J. S.; Secco, R. A.; Liu, Z.; Dube, P. A.; Howard, J. A. K.; Oakley, R. T., Crossing the Insulator-to-Metal Barrier with a Thiazyl Radical Conductor *J. Am. Chem. Soc.* **2012**, *134*, 9886-9889.

Publications

- (8) Sarkar, A.; Pal, S. K.; Itkis, M. E.; Tham, F. S.; Haddon, R. C., Sulfur and Selenium Substituted Spiro-biphenalenyl Boron Neutral Radicals *J. Mater. Chem.* **2012**, *22*, 8245-8256.
- (9) Bag, P.; Pal, S. K.; Itkis, M. E.; Sarkar, A.; Tham, F. S.; Donnadiou, B.; Haddon, R. C., Synthesis of Tetrachalcogenide-Substituted Phenalenyl Derivatives: Preparation and Solid-State Characterization of Bis(3,4,6,7-tetrathioalkyl-phenalenyl)boron Radicals *J. Am. Chem. Soc.* **2013**, *135*, 12936-12939.
- (10) Bag, P.; Tham, F. S.; Donnadiou, B.; Haddon, R. C., Hexathiophenalenylium Cations: Syntheses, Structures, and Redox Chemistry *Org. Lett.* **2013**, *15*, 1198 - 1201.
- (11) Bag, P.; Itkis, M.E.; Pal, S.K.; Bekyarova, E, A.; Donnadiou, B.; Haddon, R.C., Synthesis, structure and solid state properties of benzannulated phenalenyl based neutral radical conductor. *J. Phys. Org. Chem.*, **2012**, *25*, 566 – 573.
- (12) Bag, P.; Itkis, M.E.; Pal, S.K.; Bekyarova, E, A.; Donnadiou, B.; Haddon, R.C., Synthesis, Structure and Solid State Properties of Cyclohexanemethylamine Substituted Phenalenyl Based Molecular Conductor. *Crystals* **2012**, *2*, 446 – 465.

Crystallization-driven assembly of conjugated-polymer-based nanostructures

Ryan C. Hayward, Department of Polymer Science & Engineering, University of Massachusetts Amherst

Program Scope

The goal of this project is to harness solution-state crystallization of conjugated polymers and small molecules to construct well-defined nanoscale building blocks that will facilitate fabrication of optoelectronic devices, especially photovoltaic cells, in scalable and cost-effective ways. We seek to ultimately control the organization, and therefore the electronic properties, of matter on length-scales spanning: (i) the molecular, to achieve highly crystalline semiconducting polymer-based materials capable of efficient charge transport, (ii) the nanoscale, to position electron donating and accepting materials with domain sizes comparable to exciton diffusion lengths (~ 10 nm) to facilitate charge separation, and (iii) the colloidal scale, such that well-defined crystalline nanoscale building blocks can be hierarchically organized into device layers with optimal structures.

Recent Progress

We have recently discovered the formation of ‘shish-kebab’ donor/acceptor nanocrystalline heterostructures through a process of coupled crystal modification [1]. Poly(3-alkyl thiophene) polymers are found to adsorb onto the surfaces of nanocrystals of perylene diimide (PDI) derivatives, thereby slowing the growth of crystals and modifying their shapes from micrometer-scale tape-like structures, to extended nanowires with lateral dimensions below ~ 100 nm. These PDI crystals in turn serve as efficient nucleating agents for growth of polythiophene nanowires, driving growth of the hybrid bicrystalline structures. Work by other groups has indicated that polythiophenes play similar roles during crystallization of pentacene [2] and tetracene [3] derivatives, suggesting the use of conjugated polymers as crystal modifiers may be a rather general strategy in tailoring the crystallization of conjugated small molecules. Subsequently, we have developed an approach relying on polythiophenes as crystal modifiers and ultrasound to facilitate crystallization. As shown in Figure 1,

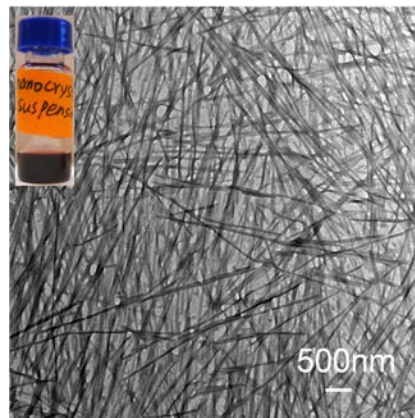


Figure 1. Transmission electron micrograph of PDI nanowires, and (inset) photograph of the nanowire suspension.

this yields suspensions of PDI nanowires with well-controlled widths that show excellent colloidal stability. The widths of these nanowires can be tuned down to ~ 20 nm through variations in polythiophene concentration and molecular weight, and crystallization temperature. Pre-formed ‘seed’ crystals can be extended almost exclusively in the length direction, providing access to high aspect-ratio nanowires and segmented structures.

Future Plans

Ongoing work and future plans include the development of approaches to better control the length and segmentation of nanowires, and to prepare structures containing functional groups that allow for chemical crosslinking, functionalization with opto-electronically active materials, or dispersion in desired solvents. We are also studying the organization of these nanowires into larger-scale superstructures.

References

- [1] L. Bu, E. Pentzer, F.A. Bokel, T. Emrick, R.C. Hayward, "Growth of poly(3-hexyl thiophene)/perylene tetracarboxydiimide donor/acceptor shish-kebab nanostructures by coupled crystal modification", *ACS Nano*, **6**,10924-10929 (2012).
- [2] J. H. Chen, M. Shao, K. Xiao, Z. R. He, D. W. Li, B. S. Lokitz, D. K. Hensley, S. M. Kilbey, J. E. Anthony, J. K. Keum, A. J. Rondinone, W. Y. Lee, S. Y. Hong, Z. A. Bao, “Conjugated Polymer-Mediated Polymorphism of a High Performance, Small-Molecule Organic Semiconductor with Tuned Intermolecular Interactions, Enhanced Long-Range Order, and Charge Transport”, *Chemistry of Materials*, **25**, 4378-4386 (2013).
- [3] T. Suzuki, T. Okamoto, A. Saeki, S. Seki, H. Sato, Y. Matsuo, “Formation of Photoconductive Nanowires of Tetracene Derivative in Composite Thin Film” *ACS Applied Materials & Interfaces*, **5**, 1937-1942 (2013).

Publications

- M. Baghgar, J.A. Labastide, F. Bokel, R.C. Hayward, M.D. Barnes, “Effect of Polymer Chain Folding on the Transition from H- to J-Aggregate Behavior in P3HT Nanofibers”, *The Journal of Physical Chemistry C*, **118**, 2229–2235 (2014). DOI: 10.1021/jp411668g
- E.B. Pentzer, F.A. Bokel, R.C. Hayward, T. Emrick “Nanocomposite "Superhighways" by Solution Assembly of Semiconductor Nanostructures with Ligand-Functionalized Conjugated Polymers”, *Advanced Materials*, **24**, 2254-2258 (2012). DOI: 10.1002/adma.201104788

M. Baghgar, J. Labastide, F. Bokel, I. Dujovne, A. McKenna, A.M. Barnes, E. Pentzer, T. Emrick, R.C. Hayward, M.D. Barnes, ““Probing Inter- and Intrachain Exciton Coupling in Isolated Poly(3-hexylthiophene) Nanofibers: Effect of Solvation and Regioregularity”, *Journal of Physical Chemistry Letters*, **3**, 1674-1679 (2012). DOI: 10.1021/jz3005909

L. Bu, E. Pentzer, F.A. Bokel, T. Emrick, R.C. Hayward, "Growth of poly(3-hexyl thiophene)/perylene tetracarboxydiimide donor/acceptor shish-kebab nanostructures by coupled crystal modification", *ACS Nano*, **6**,10924-10929 (2012). DOI: 10.1021/nn3043836

Optical Spectroscopy and Scanning Tunneling Microscopy Studies of Molecular Adsorbates and Anisotropic Ultrathin Films

John C. Hemminger
Department of Chemistry
University of California, Irvine
Irvine, Ca. 92697

Program Scope

The emphasis of our research is to develop sufficient fundamental understanding to allow the controlled preparation of nano-, and meso-structured surfaces with novel optical properties and chemical reactivity. The research places an emphasis on the synthesis of, sometimes complex, surface structures under conditions that allow for detailed control and understanding of the composition and structure and the subsequent relationship to properties and chemical reactivity. In this research we combine the use of optical probes (Polarization and angle dependent laser reflectivity and Laser Raman Scattering) with modern surface imaging experiments (electron microscopy (SEM, TEM), and variable temperature ultra high vacuum scanning tunneling microscopy (STM)). These experiments are combined with conventional methods of UHV surface science (High Resolution Electron Energy Loss Vibrational Spectroscopy (HREELS), Auger electron spectroscopy (AES), x-ray photoelectron spectroscopy (XPS) and thermal desorption spectroscopy (TDS)). The conventional surface probes provide well-tested methods for the preparation and characterization of substrates. The optical probes used in our experiments provide powerful methods for the characterization of the structure dependent optical properties of novel molecular and nanometer scale, and mesoscale surface structures as well as molecular identification and quantification of adsorbates in monolayers and ultrathin films.

We use a combination of STM and SEM/TEM to study the growth of mesoscopically ordered nanometer sized metal and metal oxide structures on well defined substrates such as highly ordered pyrolytic graphite (HOPG). An example of the metal oxide structures that can be prepared on HOPG substrates is shown in Figure 1. The SEM image in figure 1 shows TiO₂ nanoparticles grown on HOPG by physical vapor deposition. In this instance, the TiO₂ nanoparticles are shown to decorate step edge defects in the HOPG surface.

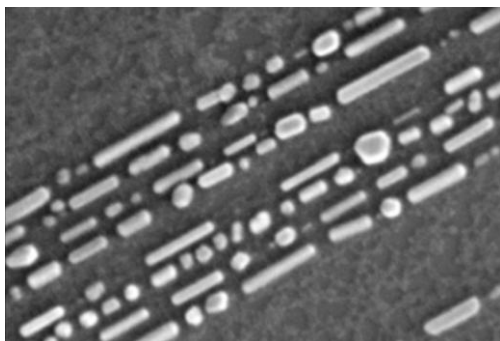


Figure 1. SEM image of TiO₂ nanoparticles that were generated by vapor deposition of Ti on the HOPG while the substrate was held at 550 C, followed by room temperature exposure of the sample to oxygen. The nanoparticles are 10-15 nm wide and occur as either rods or faceted particles.

We continue to develop new methods (e.g. photoelectrochemical deposition) to selectively decorate nanometer scale metal oxide structures, such as those shown in Figure 1, with transition metal nanoparticles, generating Nanoparticles on Nanoscale substrate materials (NpNs). The electronic structure and chemical properties of these new structures are studied and contrasted with those of the more conventional materials that are typically composed of nanoparticles on macroscopic substrate materials. Figure 2 shows an SEM image of NpNs materials. In this case we show an HOPG sample with Ag nanoparticles decorating TiO₂ nanoparticles. The Ag was deposited selectively onto the TiO₂ nanoparticles using photoelectrochemical deposition from a AgNO₃ solution and TiO₂ bandgap radiation. The amount of Ag metal deposition can be followed via the photocurrent in the photoelectrochemical deposition cell.

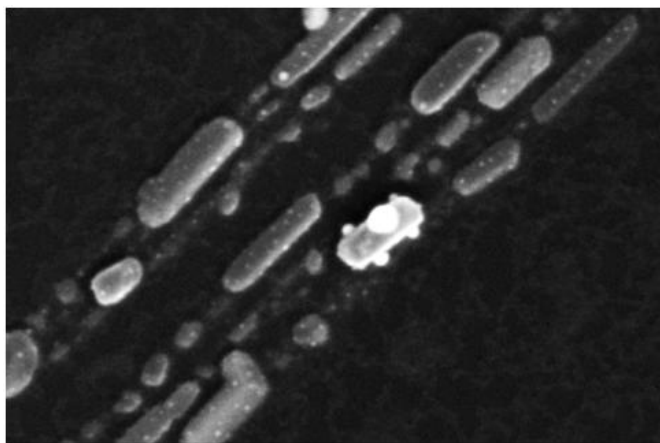


Figure 2. SEM image showing TiO₂ nanoparticles that have been decorated with Ag nanoparticles using the photochemical deposition method described in the text. The TiO₂ particles are ~ 10nm wide. The small Ag nanoparticles are 1—2nm diameter.

Recent Progress

In recent work we have extended the experimental methods to produce a variety of metal oxide nanoparticles for use as highly characterizable oxide supports for transitional metal nanoparticles. In particular, we have demonstrated the ability to produce nanoparticles of Al₂O₃, and Fe₂O₃ using methods similar to those described above for TiO₂. Figure 3 shows an example of Fe₂O₃ nanoparticles on an HOPG substrate. The Fe₂O₃ identity of the particles was determined by XPS and TEM.

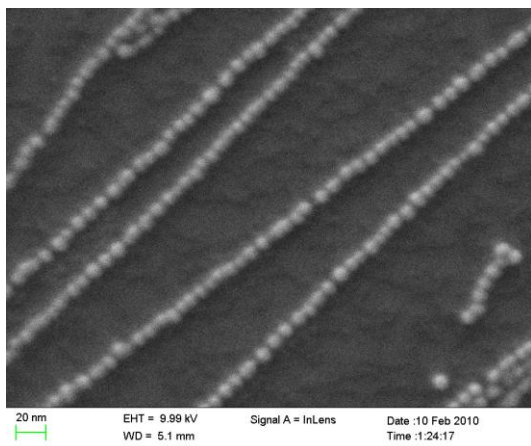


Figure 3. SEM image of iron oxide nanoparticles, with an average size of 6 nm.

Future Plans

The aim of our near term future plans is to build on the experimental and synthetic capabilities that we have developed during the most recent research period. In addition to expanding the types of Nanoparticle/Nanostructured substrate samples to include additional oxides and additional transition metals we plan to utilize our experimental capabilities to carry out studies of the catalytic chemistry properties of the transition metal nanoparticle/metal oxide nanoparticle systems. A major question is whether the samples we have generated by decorating the step defects of HOPG have sufficient active surface area to allow us to directly observe the reactivity of the highly characterized samples. To address this question we will develop methods that will provide a higher density of metal oxide nanoparticles while retaining the simple concept of vapor deposition growth at HOPG defects. In preliminary experiments we have utilized a mild oxygen plasma treatment to generate a high density of atomic scale defects on HOPG. This generates an HOPG surface on which we can grow a high density of metal oxide nanoparticles. Figure 4 shows the results of a preliminary experiment in which we have been able to grow a high density of Fe_2O_3 nanoparticles on a plasma treated HOPG surface.

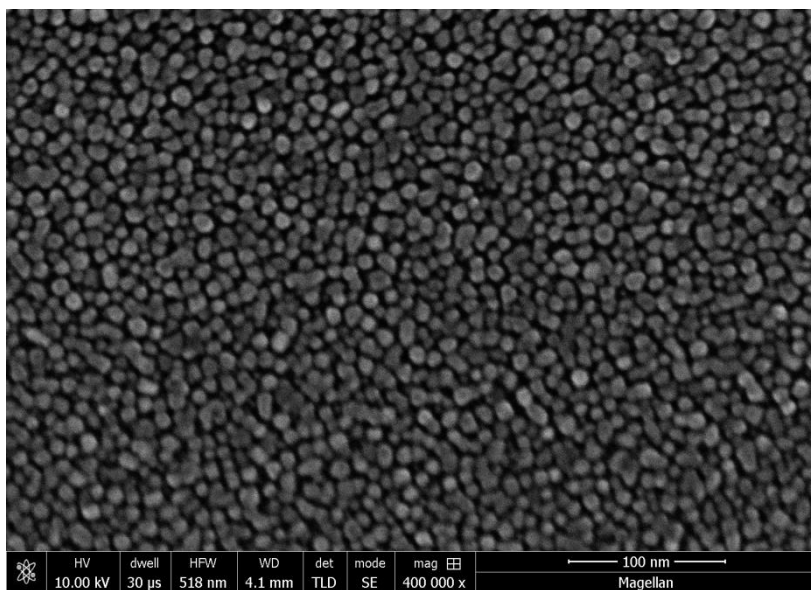


Figure 4. SEM image of Fe_2O_3 nanoparticles deposited on HOPG that was pre-treated by oxygen plasma to generate a high density of surface defects. The 100nm scale bar is shown at the bottom right of the image. The Fe_2O_3 nanoparticles are 20—30nm in diameter. (100nm scale bar is shown at the bottom right of the image).

We have also demonstrated in preliminary experiments that using photoelectrochemical methods we can deposit Pt nanoparticles on the Fe_2O_3 nanoparticles.

The ability to generate NpNs materials with the high densities shown in Figure 4 will allow us to carry out conventional UHV surface studies of adsorption and chemical reactivity using HREELS, XPS, and TPD experimental methods.

Publications

Mesoporous Manganese Oxide Nanowires for High-Capacity, High Rate, Hybrid Electrical Energy Storage.

Wenbo Yan, Talin Ayzvazian, Jungyun Kim, Yu Liu, Keith C. Donovan, Wendong Xing,
Yongyan Yang, John C. Hemminger, and Reginald Penner
ACSNano, 5(10), 8275-8287 (2011). DOI: 10.1021/nn2029583

Project Title: Relationships between the chemistry and physical interaction forces (adhesion, friction & lubrication) between closely apposed surfaces in liquids (DOE Award number: DE-FG02-87ER 45331)

Jacob Israelachvili, Dept Chemical Engineering, Materials Department, and Materials Research Laboratory (MRL), University of California (UCSB), Santa Barbara, CA 93106.

Program Scope

1. Measure and characterize complex dynamic molecular interactions by continuing to apply and develop new experimental techniques [9]

to gain fundamental understandings of the adhesion, friction, lubrication and particularly the initiation of wear (damage) to surfaces of engineering interest, that is, rough or micro-nano structured surfaces, and investigate the dynamics, i.e., the roles of rate and time, on these often non-equilibrium interactions. **2. Correlating chemistry with (physical) interaction forces** by further developing and applying new experimental techniques for measuring the above interactions while *simultaneously* measuring and controlling the voltages and currents between or flowing through the solid-liquid interfaces to establish the (electro)chemical reactions going on at each interface.

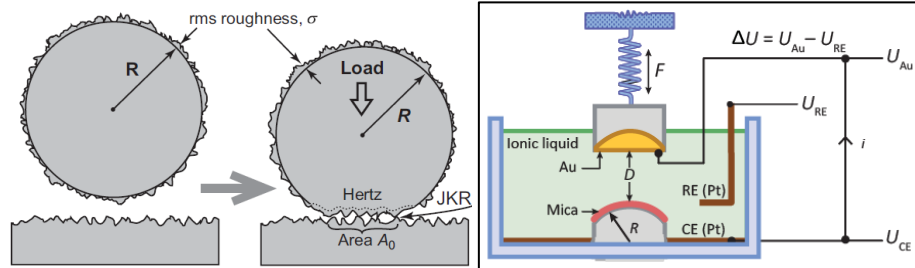


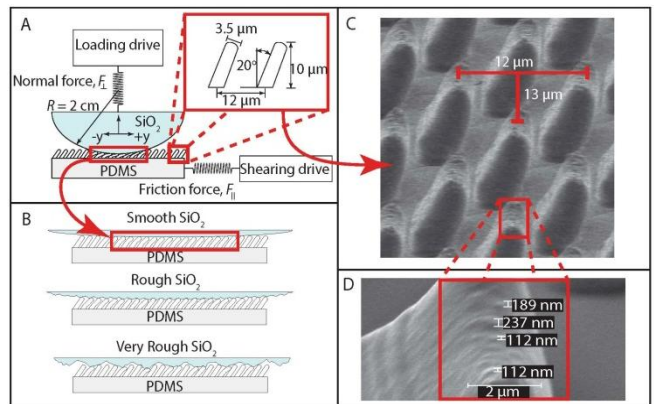
Fig. 1. (A) Adhesion and friction forces between "real" (rough or textured) surfaces as opposed to "ideal" molecularly smooth surfaces are being measured over 7 orders of magnitude of length and time (rate) scales, including **(B)** simultaneous visualization, control and measurement of electro-chemical

Recent Progress

Adhesion and friction of randomly rough and anisotropically patterned or lubricated polymer surfaces: Applying modified JKR theory for adhesion hysteresis and stick-slip sliding [refs 2,3,7,11]

There have been new advancements in obtaining quantitative adhesion and friction models for rough and patterned surfaces that cannot be analyzed in terms of the Hertz and Johnson-Kendall-Roberts (JKR) theories (Fig. 1A). Adhesion and friction tests were performed with fabricated tilted PDMS polymer flaps (Fig. 2 C, D) against smooth and a variety of randomly rough (micro-scale) silica surfaces. Using the SFA technique (Fig. 2A) hysteretic adhesion and anisotropic friction forces were measured on loading and unloading, and when shearing the flaps along or against the tilted direction (Fig. 2B). The effects correlated not only with the rms roughness but more with how the topologies of the two surfaces matched. A modified JKR model was developed in terms of effective stiffness and adhesion energy parameters that appears to quantitatively describe the 'contact mechanics' or 'adhesion mechanics' of the tilted structures against a smooth silica surface. Under certain circumstances stick-slip frictional sliding can occur during peeling as well as during shearing of two structured surfaces, which can initiate surface damage (wear).

Fig. 2. (A) Schematic of the Surface Forces Apparatus (SFA) and piezoelectric bimorph slider setup for measuring normal (adhesion) forces, F_{\perp} , and lateral (friction) forces, F_{\parallel} . **(B)** Schematic of the roughness of the top silica (SiO_2) surface and how the anisotropic PDMS polymer flaps fit into the varying asperities on the silica surfaces (surface interlocking or commensurability). **(C)** Low mag SEM image of the array of tilted flaps. **(D)** Zoom-in on one flap displaying its nano-asperities.



The electrochemical SFA [refs 4, 10], and EC-SFA studies of ionic liquids [ref 8]

We have used the newly developed electrochemical attachment to the SFA (see Figs 3A and 5) to measure electric double-layer forces across a commonly studied ionic liquid confined between a gold electrode and an inert, negatively-charged mica surface [Fig. 3B and ref 8]. This study enabled us to demonstrate that more than 99% of the ions that make up the ionic liquid are “stuck” in a highly correlated neutral state at room temperature, while a small fraction of the ions can be viewed as existing in a charge-separated “free” state. This insight is notable, because only the ions that exist in the “free” state are able to contribute to ion conduction and energy storage in electrochemical devices, such as batteries or capacitors. The major practical outcome of this study was the proposal of new design rules that may enable researchers to develop ionic liquids for specific applications by controllably tuning the populations of ions in the “free” versus “stuck” states.

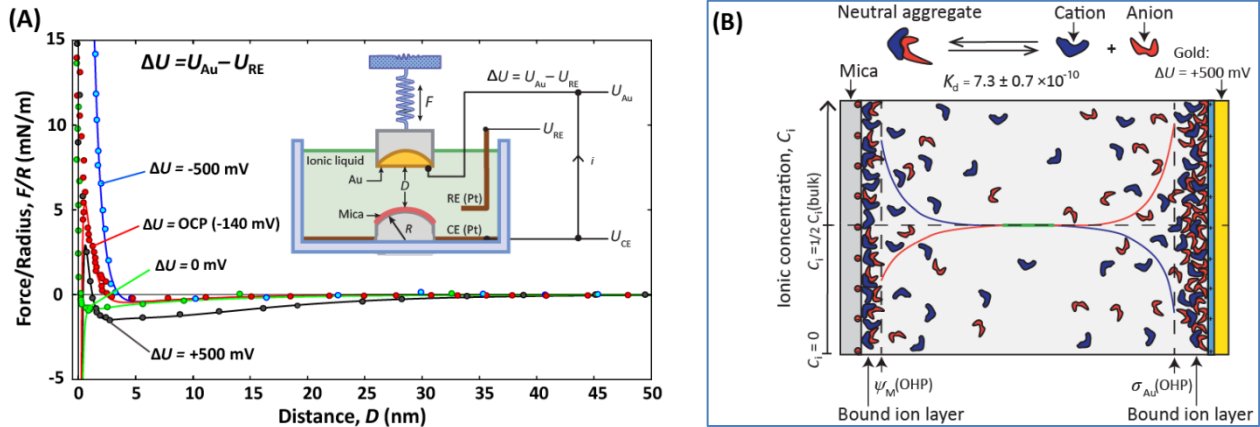


Fig. 3. (A) Diagram of the EC-SFA setup [4, 10, 13] and force-distance profiles measured across an ionic liquid under applied electrochemical potentials [8]. Points correspond to experimental data and solid lines correspond to the theoretical ‘electric double-layer’ forces. (B) Schematic of ionic liquid ions between two charged surfaces at room temperature. Grey shading represents the ionic liquid ions that exist in the neutral state (99% of all ions): blue = positive ions, red = negative ions. The reaction illustrates the balance between neutral (“stuck”) and charge-separated (“free”) states. Only mobile charge-separated species contribute to ionic conduction.

Adhesion and surface interactions of self-healing polymers [ref 12]

We have investigated the surface properties and self-adhesion mechanism of a new class of ‘self-healing’ or ‘self-sealing’ polymers that can fully re-seal via quadruple hydrogen bonding groups after being cut or debonded. These poly(butyl acrylate) (PBA) copolymers contain the functional comonomers 2-ureido-4[1H]-pyrimidinone (UPy), and are referred to as PBA-UPy polymers. Using a SFA coupled with a top-view optical microscope, the resealed adhesion strengths of two kinds of PBA-UPy polymers were measured from ‘JKR plots’ found to depend on the H-bond content, contact time, temperature, and relative humidity (Fig. 4).

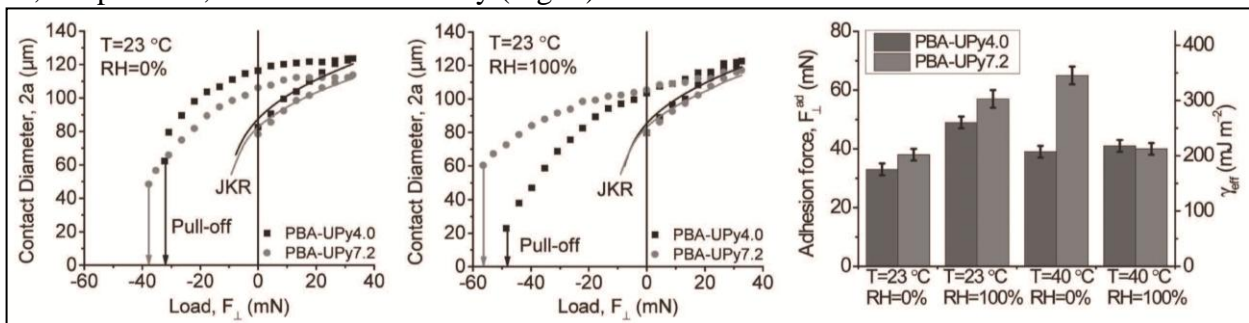


Fig. 4. Left & Middle: ‘JKR plots’ (cf. Fig. 1A) of contact diameter vs. applied load for PBA-UPy polymers in different relative humidities (RH). Right: Summary of measured adhesion forces and effective surface energies of PBA-UPY polymers at different experiment conditions. The full or close-to-full adhesion strengths are regained under all conditions.

Future & Ongoing Plans

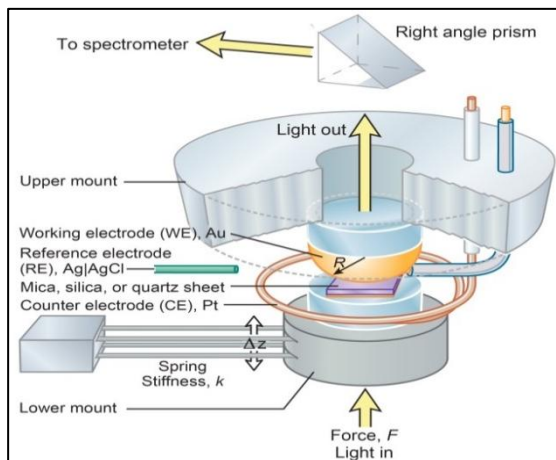
Reversible covalent bonding: Developing novel self-healing and stimuli-responsive materials: The results of Fig. 4 provide new insights into and fundamental understanding of the adhesive mechanisms of multiple hydrogen-bonding polymers containing *reversible intermolecular* crosslinks. We propose to study how resealing of “covalent adaptable network” (known as CAN) interfaces can be further enhanced or initiated by specific stimuli, and the effects of crosslink content, contact time, and environmental conditions on adhesion, friction and wear.

Static and dynamic adhesion, friction & wear: These experiments (described above) should result in quantitative models that could be used to determine design rules and modes of operation for building energy-efficient and wear-resistant materials, surfaces, and articulated robotic devices.

Ionic liquids: We are currently testing a fundamental framework that quantitatively describes the dissociation we measured for ionic liquids. Our model and initial results show that temperature strongly impacts the relative populations of “free” and “stuck” ions, even over relatively small temperature ranges (roughly doubling for a 25°C change in temperature). This would be an important contribution to the existing literature since many electrochemical storage devices, such as batteries, are operated in highly variable temperature environments.

Instrumental developments: We are expanding the scope and capabilities of the SFA technique, particularly the electrochemical attachment (Fig. 5). A multi-modal mini-SFA is currently under development (Fig. 6) that is suitable for placing on top of a microscope stand for combined and

Fig. 5. Recently improved 3-electrode Electrochemical Surface Forces Apparatus (EC-SFA) attachment that has the capabilities of *in-situ* simultaneous, measurement of forces, control of potential differences, currents, and surface electro-chemistries, visualization of dissolution/corrosion [13], while moving the surfaces towards or away from each other, or shearing them laterally. The lower surface can be placed in a small cup if only small volumes of liquid are available. [Adapted from refs 10, 13.]



simultaneous force-distance measurements with optical and spectroscopic (e.g., fluorescence, SPR, IR, x-ray reflectivity/scattering) measurements. These combined approaches are expected to provide further molecular-level insights into the static and dynamic physico-chemical interactions of complex material systems.

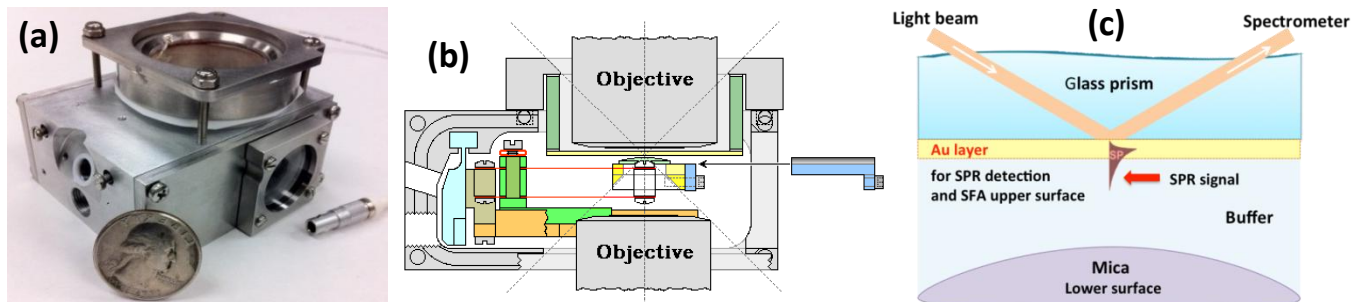


Fig. 6. Proposed multi-modal mini-SFA. (a) Prototype of main chamber. (b) Side view showing access of disks (sample surfaces) and microscope objectives, including wide confocal objectives for both top and inverted imaging, and both grazing incidence and wide-angle x-ray scattering (dashed cone). (c) Sketch of the proposed simultaneous SFA and, for example, SPR-spectroscopy setup.

Other studies in progress: We are continuing with our studies of the interplay of surface forces (adhesion, friction, wear, etc.) with changes in the structure (deformations, dissolution, corrosion [13]) of surfaces, as well as in the (anisotropic) thin films between them. Work on the relationship between dynamic contact angle hysteresis and surface deformations of structured (including monolayer and nanoparticle-coated) surfaces and fluids is also in progress [1, 5, 6, 14].

References / Publications (2 years: mid 2012 – mid 2014)

- 1. Hydrophobic forces, electrostatic steering and acid-base bridging between atomically smooth self-assembled monolayers and end-functionalized PEGolated lipid bilayers.** Markus Valtiner, S. H. Donaldson Jr., M. Gebbie, J. N. Israelachvili. *J. Am. Chem. Soc.* (2012) **134** (3) 1746–1753.
- 2. Measurements of anisotropic (off-axis) friction-induced motion** Kai Kristiansen, Xavier Banquy, Hongbo Zeng, Eric Charrault, Suzanne Giasson, Jacob Israelachvili. *Adv. Matls.* (2012) **24** (38) 5236-5241 PMID: 22815190.
- 3. Friction and adhesion of gecko-inspired PDMS flaps on rough surfaces.** Jing Yu, Sathya Chary, Saurabh Das, John Tamelier, Kimberly Turner and Jacob Israelachvili. *Langmuir* (2012) **28** (31), 11527–11534. PMID: 22779923.
- 4. The electrochemical surface forces apparatus: The effect of surface roughness, electrostatic surface potentials and anodic oxide growth on the interaction forces and friction between dissimilar surfaces in aqueous solutions.** Valtiner, Markus; Banquy, Xavier; Kristiansen, Kai; Greene, George; Israelachvili, Jacob. *Langmuir* (2012) **28** (36) 13080–13093. PMID: 22877582.
- 5. Origin of the Contact Angle Hysteresis of water on Chemisorbed and Physisorbed Self-Assembled Monolayers.** Nataly Belman, Kejia Jin, Yuval Golan, Jacob N. Israelachvili, Noshir S. Pesika. *Langmuir* **2012**, **28** (41), 14609–14617. PMID: 22978680.
- 6. Directed Co-Assembly of Oriented PbS Nanoparticles and Monocrystalline Sheets of Alkylamine Surfactant.** Rabkin, Alexander; Belman, Nataly; Israelachvili, Jacob; Golan, Yuval. *Langmuir* **2012**, **28** (43), 15119–15123. PMID: 23057722.
- 7. Investigation on the molecular shear-induced organization in a molecularly thin film of *n*-hexadecane.** E. Charrault, X. Banquy, K. Kristiansen, J. Israelachvili, S. Giasson. *Tribology Letters* (2013) **50** 421–430.
- 8. Ionic liquids behave as dilute electrolyte solutions.** Matt Gebbie, Markus Valtiner, Xavier Banquy, Eric Fox, Wesley Henderson, Jacob Israelachvili. *PNAS* (2013) **110** (24) 9674-9679.
- 9. A brief history of intermolecular and surface forces in complex fluid systems.** Marina Ruths, Jacob Israelachvili, *Langmuir* (2013) **29** (31) 9605–9619.
- 10. Intersection of Interfacial Forces and Electrochemical Reactions.** J. Israelachvili, K. Kristiansen, M. A. Gebbie, Dong Woog Lee, S. H. Donaldson Jr., Saurabh Das, M. V. Rapp, Xavier Banquy, M. Valtiner, Jing Yu. *J. Phys. Chem. B* (2013) **177** (51) 16369–16387.
- 11. JKR theory for the stick-slip peeling and adhesion hysteresis of gecko mimetic patterned surfaces with a smooth glass surface.** Das, Saurabh; Chary, Sathya; Yu, Jing; Tamelier, John; Turner, Kimberly; Israelachvili, Jacob. *Langmuir* (2013) **29** (48) 15006-15012.
- 12. Adhesion and Surface Interactions of a Self-healing Polymer with Multiple Hydrogen-bonding Groups.** A. Faghihnejad, K. E. Feldman, J. Yu, M. V. Tirrell, J. Israelachvili, C. J. Hawker, E. J. Kramer, H. Zeng. *Adv. Funct. Materials* (2014) **24** (16) 2322-2333.
- 13. Electrochemical control of specific adhesion between amine-functionalized polymers and noble metal electrode interfaces.** S.H. Donaldson Jr., T. Utzig, M.A. Gebbie, S. Raman, B.R. Shrestha, J.N. Israelachvili, M. Valtiner. *Materials and Corrosion* (2014) **65** (4) 362–369.
- 14. A multi-axis confocal rheoscope for studying shear flow of structured fluids.** Neil Lin, Jonathan McCoy, Xiang Cheng, Brian Leahy, Jacob Israelachvili, Itai Cohen. *Review of Scientific Instruments* (2014) **85**, 033905.

Enhanced Mixed Electronic-Ionic Conductors through Cation Ordering

Allan J. Jacobson, University of Houston, Dane Morgan, University of Wisconsin, Clare Grey, Stony Brook University (Cambridge University)

Program Scope

The performance of many energy conversion and storage devices depend on the properties of mixed ionic-electronic conducting (MIEC) materials. Mixed or ambipolar conductors simultaneously transport ions and electrons and provide the critical interface between chemical and electrical energy in devices such as fuel cells, ion transport membranes, and batteries. Enhancements in storage capacity, reversibility, power density and device lifetime all require new materials and a better understanding of the fundamentals of ambipolar conductivity and surface reactivity.

The high temperature properties of the ordered perovskites $AA'B_2O_{5+x}$, where A = rare earth ion, Y and B = Ba, Sr are being studied. The work is motivated by the high oxygen transport and surface exchange rates observed for members of this class of mixed ionic and electronic conductors.

The objectives of the work are to:

1. Understand how the cation and associated anion order lead to high ionic and electronic transport properties and surface reactivity in $AA'B_2O_{5+x}$ perovskites;
2. Develop fundamental understanding of defect chemistry, oxygen diffusion and surface exchange in $AA'B_2O_{5+x}$ perovskites and related defect mixed-metal oxides;
3. Understand the effects of nanostructure and strain on structure and properties;
4. Investigate other promising oxygen storage materials, for example, $YBaMn_2O_6$.

A combined experimental and computational approach, including structural, electrochemical, and transport characterization and modeling is used. The approach attacks the problem simultaneously at global (e.g., neutron diffraction and impedance spectroscopy), local (e.g., nuclear magnetic resonance) and molecular (ab initio thermokinetic modeling) length scales.

Recent Progress:

Experiments: We have measured the surface exchange rate and diffusion coefficient for $Sr_3YCo_4O_{10.5}$ using electrical conductivity relaxation (ECR). The structure of $Sr_3YCo_4O_{10.5}$ consists of layers of tilted CoO_6 octahedra that alternate with oxygen-deficient layers containing the Co atoms in tetrahedra. The oxygen diffusion in this compound has been determined previously by Isotope Exchange Depth Profiling combined with SIMS (IEDP/SIMS),¹ and Molecular Dynamics calculations (MD).² We have investigated oxygen diffusion with ECR in the temperature range 650 – 900 °C by following switches of pO_2 : 2% ↔ 5%, 10% ↔ 20%,

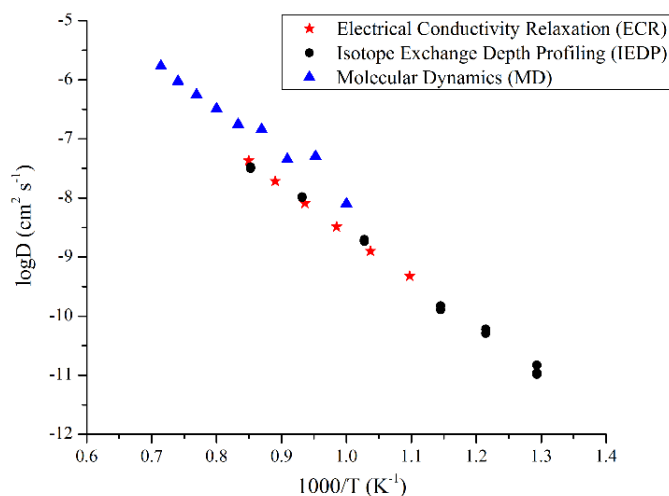


Figure 1: Oxygen ion diffusion in $Sr_3YCo_4O_{10.5}$ obtained by ECR, IEDP/SIMS, and MD.

10% \leftrightarrow 75%. Values of chemical oxygen diffusion and chemical surface exchange were obtained after the fitting of all profiles (relative conductivity vs. time). Activation energies for D_{chem} and k_{chem} are 1.16 ± 0.01 eV and 0.76 ± 0.05 eV, respectively. Values of chemical oxygen diffusion do not depend on the initial and final oxygen partial pressures and depend only on the temperature. To compare the results of oxygen diffusion determined by ECR technique with the results of Isotope Exchange Depth Profiling, the thermodynamic factor, $\frac{1}{2} \ln(pO_2)/\ln(C_O)$, where C_O is the concentration of oxygen atoms in $Sr_3YCo_4O_{10.5}$ was determined by thermogravimetric analysis. The corrected data obtained by ECR is compared with the results from IEDP and MD in Figure 1. Very good agreement is observed between the different methods.

Non stoichiometric oxides which rapidly and reversibly release and take-up oxygen molecules are of interest as oxygen storage materials for use in a variety of hydrocarbon and small molecule oxidation reactions. Recently the double perovskite oxide, $YBaMn_2O_6$, has been shown to store and release a significant amount of oxygen ($\sim 3.85\%$) at moderate temperatures ($350 - 750$ °C). The oxygen uptake and release kinetic behavior have been studied but nothing is known concerning the thermodynamics and reversibility under near equilibrium conditions. We have investigated the non-stoichiometric behavior of $YBaMn_2O_x$ in sealed electrochemical cells using the technique described previously by us for other double perovskites.³ A representative set of data obtained on reduction at 650 °C are shown in Figure 2. As expected from previous X-ray data, the compound shows three well defined phases, two with narrow ranges of non-stoichiometry

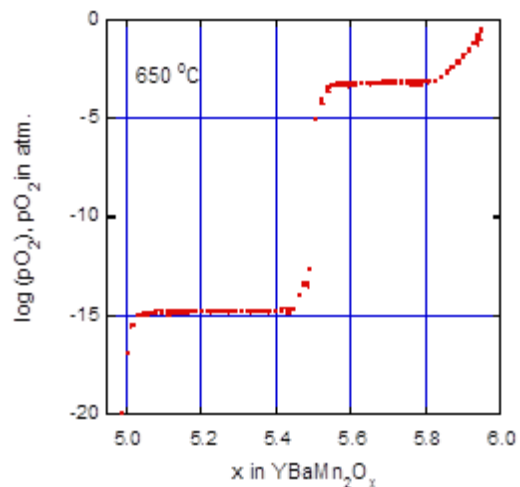


Figure 2: Non-stoichiometry data for $YBaMn_2O_{5+x}$ showing the presence of three distinct phases.

(5.0 and 5.5) and one with a broader range from 5.95 to 5.83 at 650 °C, separated by two phase regions. At higher temperature (850 °C), the reduction reaction is not reversible due to the instability of the compound at high pO_2 and temperature with respect to phase separation to $BaMnO_{3-x}$ and $YMnO_3$. At lower temperature, the kinetics of this phase separation are slow compared to the measurement time and the system behaves reversibly.

NMR studies in this period have focused on a ^{17}O NMR study of La_2NiO_{4+x} , where we have identified the NMR signatures of the three distinct crystallographic sites, compared the results with hyperfine shift (DFT) calculations. NMR studies have been performed to study mobility as a function of temperature.

Modeling: Early work in this grant has focused on being able to predict defect chemistry and basic surface properties of MIECs. We have now extended this work to a greatly enhanced understanding of surface, interface, and catalytic properties of MIECs. For example, Figure 3 shows a single master curve for $LaMnO_3$ defect and impurity segregation energy when normalized by charge of the species, demonstrating the dominant role of charge in governing segregation to polar surfaces in MIECs.⁴ This result offers valuable insights into expected activity of different polar surface for oxygen reduction reactions.

Present work is focused on MIEC bulk, interface and catalytic properties. We have screened for stable bulk compounds of the form $AA'B_2O_{5+x}$ to guide development of future alloyed materials, identifying many stable compounds. We have also performed extensive studies of $(La,Sr)CoO_3$ and $(La,Sr)(Co,Fe)O_3$ (001) surface segregation tendencies, demonstrating the strong Sr segregation and stable AO type termination for both systems. Finally, we have developed the first full molecule scale model for oxygen reduction catalysis on a MIEC and are comparing predicted surface exchange rates to those found in experiments. These modeling approaches are also being extended to low-temperature oxygen reduction reaction catalysts to identify similarities between the low and high-temperature chemistry.

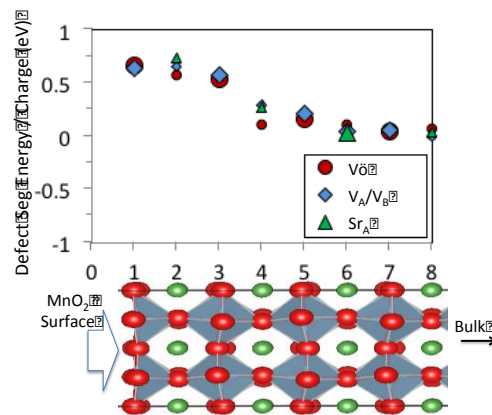


Figure 3: $LaMnO_{3-d}$ defect and impurity segregation energetics near a MnO_2 surface showing a single master curve when scaled by charge. (from ref. 4).

Future Plans

The experimental investigation of the $AA'Co_2O_{5+x}$ compounds including measurements of the transport properties of $LnBaCoFeO_{6-\delta}$ ($Ln = La, Pr, Nd, Sm, Eu$ and Gd) will be completed. Thermodynamic measurements on the oxygen storage materials $LnBaMn_2O_6$ ($Ln = Y, Gd,$ and Pr) will be analyzed. Although the Stony Brook contract has ended we are currently writing up the work on $Ba_2In_2O_5$ and La_2NiO_4 . In the last few months of the award, modeling will focus on completing papers, with a particular focus on completing the first molecular scale model for oxygen reduction on the $(La,Sr)CoO_3$ (001) surface. This model will provide a foundation for rational design of highly oxygen active miecs for SOFC and related applications.

References

- 1 Rupasov, D. P.; Berenov, A. V.; Kilner, J. A.; Istomin, S. Y.; Antipov, E. V. *Solid State Ionics*, **2011**, 197, 18-24.
- 2 Rupasov, D.; Chreanos, A.; Parfitt, D.; Kilner, J. A.; Grimes, R. W.; Istomin, S. Ya.; Antipov, E. V. *Physical Review B*, **2009**, 79, 172102/1-172102/4.
- 3 Yoo, J.; Jacobson, A. J., *Proceedings Electrochemical Society* **2003**, 2002-26(Solid-State Ionic Devices III), 354-363.
- 4 Lee, Y. L.; Morgan, D., *Physical Review B*, **2014**, under review.

Publications 2012-2014

1. Thin-film solid oxide fuel cell (SOFC) materials, A. J. Jacobson, C. Yu, W. Gong, Woodhead Publishing Series in Energy **2012**, 35 (Functional Materials for Sustainable Energy Applications), 478-514.
2. Effects of interlayer thickness on the electrochemical and mechanical properties of bi-layer cathodes for solid oxide fuel cells, Q. Su, D. Yoon, Y. N. Kim., W. Gong, A. Chen, S. Cho, A. Manthiram, A. J. Jacobson., H. Wang, *Journal of Power Sources* **218** (2012) 261-267.

3. Strain Effects on Defect Chemistry in Epitaxial Perovskite Thin Films for Solid Oxide Fuel Cells, M. Gadre, Y.-Lin Lee, N. Swaminathan, D. Morgan, *ECS Transactions*, 2011, 35(1), 2113-2118.
4. Prediction of solid oxide fuel cell cathode activity with first-principles descriptors, Y.-L. Lee, J. Kleis, J. Rossmeisl, Y. Shao-Horn, D. Morgan, *Energy & Environmental Science*, 2011, 4(10), 3966.
5. Ab initio and empirical defect modeling of $\text{LaMnO}_{3\pm\delta}$ for solid oxide fuel cell cathodes, Y. L. Lee, D. Morgan, *Physical Chemistry Chemical Physics* 2012, 14 (1), 290-302.
6. Cation Interdiffusion Model for Enhanced Oxygen Kinetics at Oxide Heterostructure Interfaces, M. J. Gadre, Y.-L. Lee, D. Morgan, *Phys. Chem. Chem. Phys.*, 2012, 14, 2606–2616.
7. Visualizing oxygen anion transport pathways in $\text{NdBaCo}_2\text{O}_{5+d}$ by in situ neutron diffraction, R. A. Cox-Galhotra, A. Huq, Jason P. Hodges, J.-H. Kim, C. Yu, X. Wang, A. J. Jacobson and S. McIntosh, *J. Mater. Chem. A*, 2013, 1 (9), 3091 – 3100.
8. Ab initio -based calculations of A-site migration in $\text{La}_{1-x}\text{Sr}_x\text{MnO}_3$, B. Puchala, Y.-L. Lee and D. Morgan, *ECS Transactions* 50, 97-110 (2012).
9. A-Site Diffusion in $\text{La}_{1-x}\text{Sr}_x\text{MnO}_3$: Ab Initio and Kinetic Monte Carlo Calculations, B. Puchala, Y.-L. Lee and D. Morgan, *Journal of the Electrochemical Society* 160, F877-F882 (2013).
10. Ab initio energetics of charge compensating point defects: A case study on MgO, S.-K. Lin, C.-K. Yeh, B. Puchala, Y.-L. Lee and D. Morgan, *Computational Materials Science* 73, 41-55 (2013).
11. Including Magnetic Contributions in LaMnO_3 Defect Models Y.-L. Lee and D. Morgan, *ECS Trans.* 50 (27), 91-95, (2013).
12. An in-situ neutron diffraction study of the crystal structure of $\text{PrBaCo}_2\text{O}_{5+\delta}$ at high temperature and controlled oxygen partial pressure, R. A. Cox-Galhotra, A. Huq, J. P. Hodges, C. Yu, X. Wang, W. Gong, A. J. Jacobson, S. McIntosh, *Solid State Ionics* 249–250 (2013) 34–40.
13. Joint Experimental and Computational ^{17}O Solid State NMR Study of Brownmillerite $\text{Ba}_2\text{In}_2\text{O}_5$, R. Dervişoğlu, D. S. Middlemiss, F. Blanc, L. A. Holmes, Y.-L. Lee, D. Morgan, C. P. Grey, *Phys. Chem. Chem. Phys.*, 2014, 16 (6), 2597 – 2606.
14. Interlayer Effects on Oxygen Reduction Kinetics in Porous Electrodes of $\text{La}_{0.5}\text{Sr}_{0.5}\text{CoO}_{3-\delta}$ Q. Su, W. Gong, D. Yoon, C. Jacob, Q. Jia, A. Manthiram, A. J. Jacobson, and H. Wang, *J. Electrochem. Soc.*, 161(4) F1-F8 (2014)
15. Anomalous Interface and Surface Strontium Segregation in $(\text{La}_{1-y}\text{Sr}_y)_2\text{CoO}_{4\pm\delta}/\text{La}_{1-x}\text{Sr}_x\text{CoO}_{3-\delta}$ Heterostructured Thin Films, Z. Feng, Y. Yacob, M. J. Gadre, Y.-L. Lee, W. T. Hong, H. Zhou, M. D. Biegalski, H. M. Christen, S. B. Adler, D. Morgan, and Y. Shao-Horn, *Journal of Physical Chemistry Letters* 5, p. 1027–1034 (2014).

Theory and Simulations of Polymer Nanocomposites Linking Molecular Features of the Polymers and Additives to Composite Morphology for Organic Photovoltaic Applications

Arthi Jayaraman, Department of Chemical and Biological Engineering & Materials Science and Engineering Program, University of Colorado at Boulder

i) Program Scope

Organic solar cells consist of an active layer made of an electron donating species (e.g. conjugated polymer) and an electron accepting species (e.g. fullerene derivative). The efficiency of a solar cell is dependent on the morphology of the donor and acceptor materials. For examples, it has been suggested that for high efficiency the morphology must have a) large interfacial area to facilitate charge separation, while being small enough so charge carriers can diffuse to the donor-acceptor interface before their energy is dissipated and b) continuous pathways for charge carriers to reach their respective electrodes, among other features. The donor-acceptor composite morphology is dependent on the chemistry and architecture of the conjugated polymer and its interactions with the additive acceptor material (fullerene derivatives). This Department of Energy (DOE) supported research program in the Jayaraman research group is focused on using theory and simulation techniques to connect molecular features of polymers and nanoscale additives to the blend/composite morphology, thereby guiding synthesis of new materials for organic photovoltaic applications.

In the first research thrust, our studies are aimed at tuning morphology in polymer nanocomposites containing conjugated polymers (donors), fullerene-derivatives (acceptor), and small molecule additives. Our goal is to understand the effects of varying conjugated polymer architecture and chemistry, fullerene derivative chemistry, solvent chemistry, third component additive chemistry and size, and processing conditions (temperature) on order-disorder transition and morphology within the blends. We are achieving this goal through development of appropriate coarse-grained models of thiophene-based conjugated polymer and fullerene derivatives used in bulk heterojunction solar cells, and through use of these models in molecular dynamics simulations on high performance resources (NERSC) supported by Department of Energy.

In the second research thrust our studies are aimed at finding design rules for polymer functionalization on the nanoparticles (that could serve as acceptors or third component additive) and achieving a dispersed morphology in the polymer nanocomposites. One can tailor the inter-particle interactions and precisely control the spatial organization of the nanoscale additives in the polymer matrix by functionalizing nanoparticle surfaces with polymers, and systematically tuning the composition, chemistry, molecular weight and grafting density of the ligands. We have developed an integrated self-consistent approach involving Polymer Reference Interaction Site Model (PRISM) theory and Monte Carlo/molecular dynamics simulations to study polymer grafted nanoparticles in polymer matrix, and understand the effect of polydispersity and flexibility, both in the grafted polymers and matrix polymers, on the potential of mean force between functionalized nanoparticles, and the resulting dispersion/assembly of polymer grafted nanoadditives in polymer nanocomposite.

This Department of Energy supported research in the Jayaraman group serves as an example of the tremendous power of well-developed molecular models and high performance computational methods in “accelerating the pace of materials discovery” [1] by elucidating

valuable molecular level guidelines and mechanisms that govern macroscale morphology, and in turn material properties in various energy- related applications.

ii) Recent Progress

In the first research thrust, most recently we have performed coarse-grained molecular dynamics simulations of thiophene-based conjugated oligomers to elucidate how the oligomer architecture, specifically the orientation and density of alkyl side chains extending from the thiophene backbones, impacts the order-disorder temperatures and the various ordered morphologies that the oligomers form [2] (see Figure 1). We have found that the orientation of side chains along the oligomer backbone plays a significant role in determining the thermodynamically stable morphologies and the phase transition temperatures. Oligomers with side chains oriented on both sides of the backbone form lamellae, while oligomers with side chains oriented on one side of the backbone assemble into hexagonally packed cylinders that can undergo a second, lower temperature transition to lamellae or ribbons depending on side chain – side chain interaction strength. The strength of side chain – side chain interactions, which can be tuned by choosing appropriate solvents, also affects

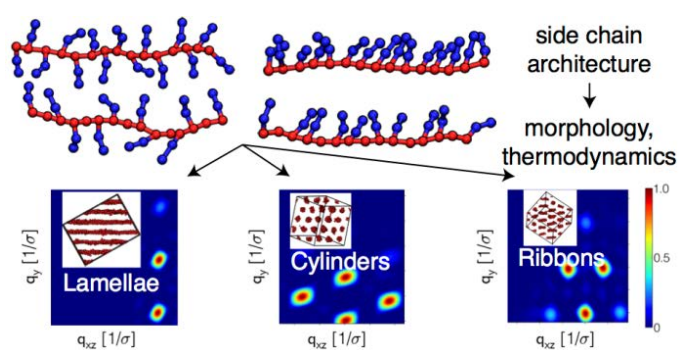


Figure 1: Simulation work linking thiophene-based conjugated oligomer architecture, specifically the orientation and density of alkyl side chains extending from the thiophene backbones to the order-disorder temperatures and ordered morphologies.

the order-disorder temperature, with oligomers with moderately attractive side chains (poor solvents) having higher transition temperatures than those with weakly attractive side chains (slightly poor to theta solvents). The side-chain

entropy drives the formation of cylinders, while potential energy drives the formation of lamellae and ribbons. Lastly, side chain length modulates the spacing between morphological features, such as cylinders and lamellae, and affects the order – disorder temperature differently depending on oligomer architecture.

In the second research thrust, we have shown the effect of polydispersity in molecular weights of the polymer in the matrix and on the grafts that are functionalized on the nanoscale additive. By grafting the nanoparticle surface with polymers that are compatible with the matrix polymer, one can tune the interactions between the polymer grafted nanoparticles in the polymer matrix, and thus tailor the morphology of the composite. We had shown in 2012-2013 [3] that increasing polydispersity in polymers grafted on spherical nanoparticles improves wetting of the grafted layer by the matrix chains and stabilizes particle dispersions even at conditions that cause particle aggregation for monodisperse grafts. These predictions were then confirmed by experiments by Schadler and coworkers [4]. Most recently [5], we have presented a theory-simulation study elucidating the effect of *polydispersity in matrix polymers* on the morphology of polymer nanocomposites with polymer grafted nanoparticles. This study is of importance because limitations during polymer synthesis naturally lead to a broad distribution of polymer molecular weights or polydispersity. In this study we explain how short and long chains in a polydisperse (modeled as bidisperse) matrix wet/dewet the polymer grafted particle and as a result impact particle morphology, and the thermodynamic driving forces for our observations.

We find that matrix bidispersity drives the increased wetting of the monodisperse polymer grafted layer by the short matrix chains and reduced wetting of the grafted layer by the long chains. However, despite the change in the relative wetting of the short and long chains, the matrix length bidispersity does not significantly change the overall wetting of the grafted layer, and as a result does not alter the tendency for dispersion/aggregation of the grafted particles. Linking to our previous publication we find that graft length bidispersity is better than matrix length bidispersity for stabilizing dispersions of polymer grafted nanoparticles in a chemically identical polymer matrix.

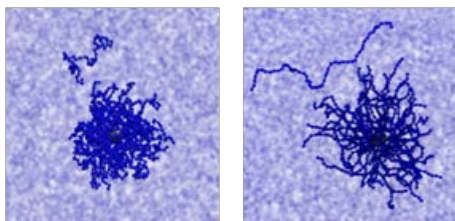


Figure 2: Simulation snapshots showing polymer grafted particle in a chemically identical polymer matrix, and effect of decreasing flexibility (going from left to right) in the graft and matrix polymers, relevant for conjugated polymers, on the dispersion of the grafted particle in the matrix.

While significant past work, both by our group and others, (see review article [6]) in the polymer nanocomposites field have established the design rules for achieving dispersion/aggregation in systems with *flexible* graft and matrix polymers, the *role of semi-flexibility, which is relevant for conjugated oligomers*, has largely been left unexplored. In a recently submitted paper [T. B. Martin, A. Jayaraman, under review, ACS Macroletters] we present a molecular simulation study elucidating the effect of *flexibility in graft and matrix* polymers on the morphology of polymer nanocomposites. Interestingly, we find that decreasing flexibility of the graft and matrix polymers leads to significantly improved wetting of the grafted layer by the

matrix polymers, and as a result improved grafted particle dispersion in the polymer matrix. *We also show quantitatively that this remarkable improvement in wetting and particle dispersion* brought upon by decreasing graft and matrix flexibility is driven largely by a significant increase in mixing entropy of the graft and matrix polymers, and not by reduction in conformational entropy loss of matrix/graft chains, the two thermodynamic driving forces that have been linked to wetting/dewetting behavior. These results are exciting as they suggest that nanoscale acceptors densely grafted with semi-flexible conjugated oligomers will disperse well in conjugated polymers (donor) matrix.

iii) Future Plans

Within research thrust one, our next step includes three component blends. We have begun studies on blends containing thiophene based polymers, fullerene derivatives and a minority component additive, such as diiodooctane (DIO) and chloronaphthalene (CN), to alter blend morphology. We plan to use coarse-grained molecular dynamics simulations of conjugated polymer and fullerene derivative blends with additives of varying length, chemical functionalization, and volume fraction to understand how these additives affect morphology and to elucidate what physical and chemical features of solvent additives are important for tuning morphology. In particular, the questions we wish to answer are: how does the size and chemical compatibility of the additives with the side chains on the polymers.

Within research thrust two, our next step is to study role of specific interactions between the grafted polymers and matrix polymers, to elucidate how to choose polymer pairs that are capable of hydrogen bonding to enthalpically drive dispersion, in addition to the entropically driven dispersion discussed in our recently published and submitted work.

iv) References

1. Materials Genome Initiative www.whitehouse.gov/mgi
2. H. S. Marsh, E. Jankowski, A. Jayaraman, *Macromolecules* 47 (8), 2736–2747 (2014)
3. T. B. Martin, A. Jayaraman, *Macromolecules* 46 (22), pp 9144–9150 (2013); T. B. Martin, A. Jayaraman, *Soft Matter* 9 (29), 6876 – 6889 (2013); A. Jayaraman, *Journal of Polymer Science B: Polymer Physics* 51(7), 524–534 (2013); T. B. Martin, P. Dodd, A. Jayaraman, *Physical Review Letters* 110, 018301 (2013)
4. Y. Li *et al.* *Langmuir*, 29 (4) 1211-1220 (2013)
5. T. B. Martin, A. Jayaraman, *J. Polymer Science B: Polymer Physics* (2014) (in press)
6. V. Ganesan and A. Jayaraman, review article *Soft Matter*, **10**, 13-38 (2014)

v) Publications in the 2 year period 2013-2014 (* indicates corresponding author)

1. T. B. Martin, **A. Jayaraman***, Effect of Matrix Bidispersity on the Morphology of Polymer Grafted Nanoparticle filled Polymer Nanocomposites’ *J. Polymer Science B: Polymer Physics* (2014) (accepted)
2. C. Estridge, **A. Jayaraman***, Assembly of diblock copolymer functionalized spherical nanoparticles as a function of copolymer composition . *J. Chem Phys* (2014) 140 (14) 144905
3. H. S. Marsh[#], E. Jankowski[#], **A. Jayaraman***, Controlling the morphology of model conjugated thiophene oligomers through alkyl side chain length, placement and interactions . *Macromolecules* 47 (8), 2736–2747 (2014) (*This was one of 20 most downloaded articles from Macromolecules in May 2014*)
4. V. Ganesan* and **A. Jayaraman***, Theory and simulation studies of effective interactions, phase behavior and morphology in polymer nanocomposites, Invited peer-reviewed review article to *Soft Matter*, **10**, 13-38 (2014)
5. T. B. Martin, **A. Jayaraman***, Identifying the ideal characteristics of a polydisperse polymer graft length distribution for maximizing dispersion of polymer grafted nanoparticles in a polymer matrix *Macromolecules* 46 (22), pp 9144–9150 (2013)
6. E. Jankowski[#], H. S. Marsh[#], **A. Jayaraman***, Computationally linking molecular features of conjugated polymers and fullerene derivatives to bulk heterojunction morphology *Macromolecules* 2013 ([#] equal contribution) 46 (14) 5775-5785 (2013) (*This was one of 20 most downloaded articles from Macromolecules in July 2013*)
7. T. B. Martin, **A. Jayaraman***, Polydisperse Polymer Grafts for Stabilizing Dispersion of Homopolymer Grafted Nanoparticles in Chemically Identical Homopolymer Matrix. Peer-reviewed article for special issue on ‘*Emerging Investigators in Soft Matter*’ in *Soft Matter* 9 (29), 6876 – 6889 (2013)
8. **A. Jayaraman***, Polymer Grafted Nanoparticles: Effect of Chemical and Physical Heterogeneity in Polymer Functionalization on Particle Assembly and Dispersion, Invited Peer-reviewed Feature Article for special issue *highlighting innovative young polymer researchers* in *Journal of Polymer Science B: Polymer Physics* 51(7), 524–534 (2013) (*This was the fourth most downloaded article in the Journal in February 2013*)
9. T. B. Martin, P. Dodd, **A. Jayaraman***, Polydispersity in polymer grafts for tuning potential of mean force between polymer grafted nanoparticles in a polymer matrix *Physical Review Letters* 110, 018301 (2013)
10. H. S. Marsh, **A. Jayaraman***, Morphological Studies of Blends of Conjugated Polymers and Acceptor Molecules using Langevin Dynamics Simulations ‘ *J. Polymer Science B: Polymer Physics* 51 (1), 64-77 (2013)

Molecular and Nanoscale Engineering of High Efficiency Excitonic Solar Cells

Samson A. Jenekhe, Guozhong Cao and David S. Ginger
University of Washington, Departments of Chemical Engineering, Chemistry, and Materials Science and Engineering, Seattle, WA 98195

Program Scope

By coupling tailored materials design of both organic and inorganic materials closely with device measurements and optical spectroscopy we propose to use new materials to harvest more of the solar spectrum while generating larger cell voltages by uncovering the fundamental factors such as energy level offsets, relative dielectric constants, interfacial chemistry, and morphology that control relative branching ratios between geminate recombination and free carrier generation at a range of model donor/acceptor interfaces. These studies will identify the design rules and fundamental performance limits for new organic and hybrid organic/inorganic photovoltaic materials. We thus propose to: (1) develop new p-type polymers with tailored energy level offsets and different morphologies (e.g. nanowires) to systematically explore the effects of energetics and morphology on recombination loss in polymer/fullerene systems; (2) explore new n-type polymers with a range of energy levels, optical bandgaps and carrier mobilities to enable investigation of effects of energetics and morphology on device performance and recombination loss in polymer/polymer bulk heterojunction (BHJ) solar cells for comparison with fullerene acceptors; (3) design and study new hybrid inorganic quantum dot/polymer combinations for extending the response of solution-processable solar cell materials into the near and mid-IR, while exploring the role of acceptor dielectric constant and surface chemistry; (4) manipulate the surface chemistry and facets of ZnO nanostructures towards studies of effects of dielectric constant and morphology on charge injection rate and surface recombination rate in organic/inorganic hybrid systems; and (5) use test beds of experimental tools to probe and quantify the performance limits and loss mechanisms in BHJ solar cells based on various model donor/acceptor pairs produced in this project.

Recent Progress

1. Charge Photogeneration in Hybrid Polymer/PbS Blends. We used photoinduced absorption (PIA) spectroscopy to study charge generation in films of low band gap PbS quantum dots blended with poly(3-hexylthiophene) (P3HT) as a function of excitation energy. Building on our previous work, we were able to selectively excite the quantum dots (or both quantum dot and polymer components) and probe the resulting long-lived excited states on the polymer by using the relatively narrow-gap P3HT host. We

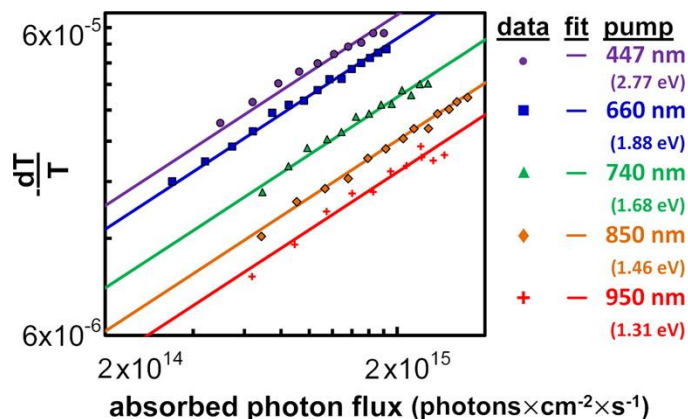


Fig. 1. Intensity dependence of the PIA polaron signal at 1050 nm (1.18 eV) for different pump energies as a function of absorbed photon flux. The straight lines are fits to the data, as explained in the text. The fit equations are as follows: $dT/T_{447} = 5.30 \times 10^{-14}(\Phi)^{0.59}$, $dT/T_{660} = 4.48 \times 10^{-14}(\Phi)^{0.59}$, $dT/T_{740} = 2.94 \times 10^{-14}(\Phi)^{0.59}$, $dT/T_{850} = 2.16 \times 10^{-14}(\Phi)^{0.59}$, and $dT/T_{950} = 1.72 \times 10^{-14}(\Phi)^{0.59}$. For clarity, we display only one data set for each pump excitation wavelength; however, the fits are best fits to the entire set of repeated measurements with each pump LED.

looked for evidence of “hot” (nonthermalized) hole transfer from photoexcited quantum dots to the conjugated polymer by measuring the yield of long-lived charge carriers in polymer/quantum dot hybrid films with varying excitation wavelength. Figure 1 shows the fractional change in probe beam transmission at the polaron peak plotted against absorbed photon flux (incident photon flux corrected by sample absorption). This gives the pump intensity-dependence of the polaron feature for the five excitation wavelengths as a function of the number of photons absorbed by the sample each second. We observe that, per photon absorbed, the yield of photogenerated holes present on the conjugated polymer increases with pump energy, even at wavelengths where only the quantum dots absorb. We attribute this result to the transfer of nonthermalized holes from the photoexcited quantum dots to the polymer host. These results help understand the mechanisms for charge generation in hybrid organic/inorganic photovoltaics.

2. Highly Efficient Polymer/Polymer Bulk Heterojunction Solar Cells. We have fabricated and characterized polymer/polymer (all-polymer) bulk heterojunction (BHJ) solar cells with a 4.8 % power conversion efficiency (PCE)

achieved by using a thiazolothiazole-based donor polymer (PSEHTT) and a newly developed naphthalene diimide copolymer-based acceptor polymer (PNDIS-HD) (**Figure 2a**). Very high short circuit current density of 10.47 mA/cm² and external quantum efficiency (EQE) of 61.3 % were obtained, showing some of the best photovoltaic parameters reported to date for all-polymer solar cells. Enhanced and balanced charge transport was observed in PSEHTT:PNDIS-HD blend films processed from chlorobenzene(CB):1,2-dichlorobenzene(DCB) mixture solvent. We observed phase-separated polymer domain sizes in tens of nanometers by AFM imaging, which could account for the efficient charge dissociation at the polymer/polymer donor/acceptor interface. The photovoltaic performance of similarly fabricated reference PSEHTT:PC₆₁BM solar cells (PCE = 3.3 %, J_{sc} = 8.46 mA/cm², EQE = 53.7 %, **Figure 2c,d**) was found to be inferior to our all-polymer solar cells. Significant light harvesting by the acceptor polymer indicates that both *photoinduced hole transfer* and *photoinduced electron transfer* are important pathways in the charge photogeneration in these highly efficient all-polymer solar cells. Our results suggest that with a suitable choice of donor and acceptor semiconducting polymers and optimized device fabrication strategies, the performance of all-polymer BHJ solar cells can exceed that of the corresponding polymer/fullerene BHJ systems.

3. Effects of ZnO-SrTiO₃ and ZnO-Ta₂O₅ Films as Cathodic Buffer Layers in Inverted Polymer Solar Cells. The influences of chemical composition and dielectric properties of cathodic buffer layers on power conversion efficiency in inverted polymer solar cells have been

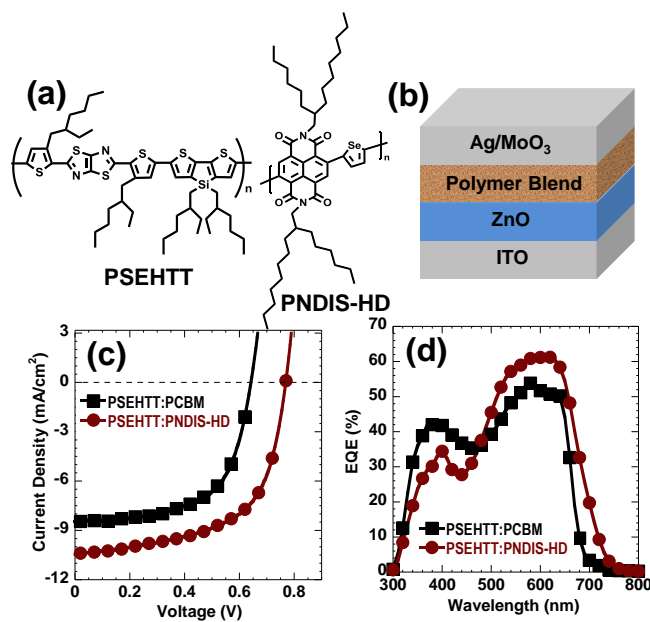


Fig. 2. (a) Molecular structures of donor (PSEHTT) and acceptor (PNDIS-HD) polymers. (b) Schematic of inverted solar cells. (c) J - V curves; and (d) external quantum efficiency (EQE) spectra of PSEHTT:PNDIS-HD and PSEHTT:PCBM solar cells.

studied. Both SrTiO₃-ZnO and ZnO-Ta₂O₅ films with varied composition ratios were fabricated by sol-gel processing and used as the cathodic buffer layer (CBL) in inverted polymer solar cells, showing enhanced power conversion efficiency. The device performance was found to be strongly dependent on the amount of SrTiO₃ in the ZnO CBL. With a small amount of quasiamorphous SrTiO₃ added in the ZnO film, some local ordered structure with aligned TiO₆ octohedra would likely form spontaneous polarization, and induce a self-built electric field on the interface between the BHJ active layer and the CBL, which would prevent hole transport through the CBL and reduce charge recombination and result in enhanced power conversion efficiency. However, a continued increase in the amount of quasiamorphous SrTiO₃ in the ZnO film led to lower electron mobility. In the present study, we found that SrTiO₃:ZnO composition at 10:90 offered the best performance of P3HT/PC₆₁BM devices and the power conversion efficiency increased from 3.58% (pure ZnO) to 4.1%, a 15% enhancement.

Similar to SrTiO₃-ZnO films, we found that the power conversion efficiency was strongly dependent on the amount of Ta₂O₅ in the ZnO CBLs. X-ray photoelectron spectroscopy data suggested that with the presence of Ta in ZnO CBL resulted in Ta-O-Zn bonding. Moreover, some surface grain boundaries might be covered by Ta₂O₅ and resulted in less oxygen adsorbing sites, and also Ta₂O₅, with a high dielectric constant, might provide a self-built electric field on the interface between the BHJ active layer and the CBL to reduce charge recombination. A continued increase in the amount of Ta₂O₅ in ZnO film led to lower electron mobility and low crystallinity of the ZnO CBLs. The power conversion efficiency with P3HT/PC₆₁BM system increases from 3.7% to 4.12%, an 11% enhancement; in the case of PSEHTT/PC₇₁BM system, from 5.29% to 5.61%. The long-term stability of unencapsulated inverted OPVs was periodically measured for 42 days, and all devices retain around 100% of their original power conversion efficiencies as shown in Figure 3.

Future Plans

The present joint project among the three PIs (Jenekhe, Cao, and Ginger) will formally conclude at the end of this fiscal year.

Publications (Selected from 38 total journal papers in the last 2 years)

- (1) Strein, E.; de Quilettes, D. W.; Hsieh, S. T.; Colbert, A. E.; Ginger, D. S. "Hot Hole Transfer Increasing Polaron Yields in Hybrid Conjugated Polymer/PbS Blends," *J. Phys. Chem. Lett.* **2014**, *5*, 208-211
- (2) Nagaoka, H.; Colbert, A. E.; Strein, E.; Janke, E. M.; Salvador, M.; Schlenker, C. W.; Ginger, D. S. "Size-Dependent Charge Transfer Yields in Conjugated Polymer/Quantum Dot Blends," *J. Phys. Chem. C* **2014**, *118*, 5710-5715.

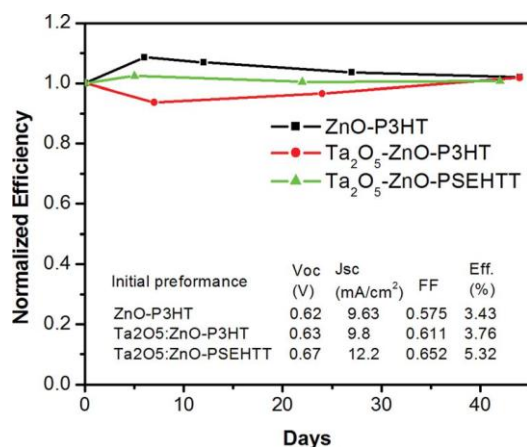


Fig. 3. The long term stability of inverted OPVs with ZnO or Ta₂O₅-ZnO films as the cathodic buffer layer; the devices were stored in ambient environment.

- (3) Murari, N. M.; Crane, M. J.; Earmme, T.; Hwang, Y. -J.; Jenekhe, S. A. "Annealing Temperature Dependence of the Efficiency and Vertical Phase Segregation of Polymer/Polymer Bulk Heterojunction Photovoltaic Cells," *Appl. Phys. Lett.* **2014**, *104*, 223906.
- (4) Lan, J. -L.; Cherng, S.-J.; Yang, Y.-H.; Zhang, Q.; Subramaniyan, S.; Ohuchi, F. S.; Jenekhe, S. A.; Cao, G. "The effects of Ta₂O₅-ZnO films as cathodic buffer layers in inverted polymer solar cells," *J. Mater. Chem. A* **2014**, *2*, 9361-9370.
- (5) Lan, J. -L.; Liang, Z.; Yang, Y. H.; Ohuchi, F. S.; Jenekhe, S. A.; Cao, G. Z. "The Effect of SrTiO₃:ZnO as Cathodic Buffer Layer for Inverted Polymer Solar Cells," *Nano Energy* **2014**, *4*, 140-149.
- (6) I. Gao, R.; Cui, Y.X.; Liu, X.J.; Wang, L.D.; Cao, G.Z., "A ZnO nanorod/nanoparticle hierarchical structure synthesized through a facile in situ method for dye-sensitized solar cells," *J. Mater. Chem. A* **2014**, *2*, 4765-4770.
- (7) Earmme, T.; Hwang, Y. -J.; Murari, N. M.; Subramaniyan, S.; Jenekhe, S. A. "All-Polymer Solar Cells with 3.3% Efficiency Based on Naphthalene Diimide-Selenophene Copolymer Acceptor," *J. Am. Chem. Soc.* **2013**, *135*, 14960-14963.
- (8) Shoaee, S.; Subramaniyan, S.; Xin, H.; Keiderling, C.; Tuladhar, P. S.; Jamieson, F.; Jenekhe, S. A.; Durrant, J. R. "Charge Photogeneration for a Series of Thiazolo-Thiazole Donor Polymers Blended with the Fullerene Electron Acceptors PCBM and ICBA," *Adv. Funct. Mater.* **2013**, *23*, 3286-3298.
- (9) Ren, G.; Schlenker, C. W.; Ahmed, E.; Subramaniyan, S.; Olthof, S.; Kahn, A.; Ginger, D. S.; Jenekhe, S. A. "Photoinduced Hole Transfer Becomes Suppressed with Diminished Driving Force in Polymer-Fullerene Solar Cells While Electron Transfer Remains Active," *Adv. Funct. Mater.* **2013**, *23*, 1238-1249.
- (10) Strein, E.; Colbert, A.; Subramaniyan, S.; Nagaoka, H.; Schlenker, C. W.; Janke, E.; Jenekhe, S. A.; Ginger, D. S. "Charge generation and energy transfer in hybrid polymer/infrared quantum dot solar cells," *Energy Environ. Sci.* **2013**, *6*, 769-775.
- (11) Colbert, A. E.; Janke, E. M.; Hsieh, S. T.; Subramaniyan, S.; Schlenker, C. W.; Jenekhe, S. A.; Ginger, D. S. "Hole Transfer from Low Band Gap Quantum Dots to Conjugated Polymers in Organic/Inorganic Hybrid Photovoltaics," *J. Phys. Chem. Lett.* **2013**, *4*, 280-284.
- (12) Tian, J.J.; Zhang, Q.F.; Uchaker, E.; Zhang, S.G.; Qu, X.H.; Cao, G.Z., "Architecting mesoporous ZnO photoanodes for highly efficient quantum dot sensitized solar cells," *Energy Environ. Sci.* **2013**, *6*, 3542-3547.
- (13) Gao, R.; Tian, J.J.; Liang, Z.Q.; Zhang, Q.F.; Wang, L.D.; Cao, G.Z., "Nanorod-Nanosheet Hierarchically Structured ZnO Crystals on Zinc Foil as Flexible Photoanodes for Dye-sensitized Solar Cells," *Nanoscale* **2013**, *5*, 1894-1901.
- (14) Zhang, Q.F.; Candelaria, S.L.; Uchaker, E.; and Cao, G.Z., "Nanostructured materials for energy conversion and storage," *Chem. Soc. Rev.* **2013**, *42*, 3127-3171.
- (15) I. Tian, J.; Zhang, Q.; Zhang, L.; Gao, R.; Shen, L.; Zhang, S.; Qu, X.; Cao, G.Z., "ZnO/TiO₂ nanocable structured photoelectrodes for CdS/CdSe quantum dot co-sensitized solar cells," *Nanoscale* **2013**, *5*, 936-943.
- (16) Hwang, Y. -J.; Ren, G.; Murari, N. M.; Jenekhe, S. A. "n-Type Naphthalene Diimide-Biselenophene Copolymer for All-Polymer Bulk Heterojunction Solar Cells," *Macromolecules* **2012**, *45*, 9056-9062.
- (17) Ren, G.; Ahmed, E.; Jenekhe, S. A. "Nanowires of Oligothiophene-functionalized Naphthalene Diimides: Self Assembly, Morphology, and All-Nanowire Bulk Heterojunction Solar Cells," *J. Mater. Chem.* **2012**, *22*, 24373-24379.

Fundamental Studies of Charge Transfer in Nanoscale Heterostructures of Earth-Abundant Semiconductors for Solar Energy Conversion

Song Jin, John C. Wright, and Robert J. Hamers

Department of Chemistry, University of Wisconsin-Madison, Madison, Wisconsin 53706

(jin@chem.wisc.edu, wright@chem.wisc.edu, rjhamers@wisc.edu)

Program Scope

We create new earth-abundant semiconductor nanostructures and their heterojunctions with well-defined chemistry and develop new laser spectroscopies and atomic force microscopy integrated with ultrafast spectroscopy that probe charge transport at the quantum mechanical level in nanoscale heterostructures. They provide the fundamental understanding required to enable transformative coherent solar energy nanotechnologies.

Recent Progress

A. Enhanced catalytic properties of layered metal chalcogenide (MX_2) nanostructures.

We have developed the chemical vapor deposition (CVD) synthesis of nanostructures of MoS_2 , WS_2 , MoSe_2 , and WSe_2 , which consist of nanoflakes with 10–15 layer thickness (Fig. 1b, d). More importantly, we have discovered that chemical exfoliation of these MX_2 nanostructures can dramatically increase the availability of active edge sites while simultaneously converting the as-synthesized MX_2 material from its semiconducting 2H polymorph to the metallic 1T polymorph (Fig. 1a), granting dramatically enhanced electrocatalytic activity for hydrogen evolution reaction (HER). The resulting 1T- MoS_2 and 1T- WS_2 nanosheets (Fig. 1c, e) exhibit dramatically enhanced HER electrocatalytic performance as compared to their corresponding 2H polymorphs (Figs. 1f and 1g, respectively). Structural characterization and electrochemical studies confirm that the nanosheets of the metallic MoX_2 polymorph exhibit facile electrode kinetics, low-loss electrical transport, and possess a proliferated density of catalytic active sites. These distinct and previously unexploited features of 1T- MoX_2 make these metallic nanosheets highly competitive earth-abundant HER catalysts. Furthermore, we have also recently coupled

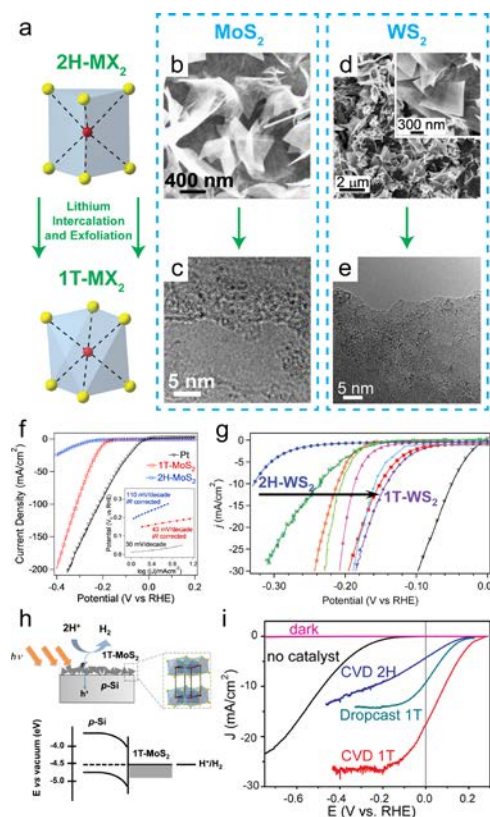


Fig. 1. Chemical exfoliation (a) of MoS_2 (b) and WS_2 (d) nanostructures using a butyl lithium treatment results in the formation of metallic MoS_2 (c) and WS_2 (e) nanosheets that display much enhanced catalytic activity (f, g) for hydrogen evolution reaction (HER). (h) Direct growth of 1T- MoS_2 nanosheets on a p-type Si photocathode enables (i) efficient hydrogen evolution driven by solar energy.

electrocatalytic 1T-MoS₂ to a *p*-type silicon photoelectrode (Fig. 1h) to enable hydrogen evolution driven by solar energy. Due to the excellent HER activity of 1T-MoS₂ and the high-quality catalyst–semiconductor interface enabled by the direct CVD growth of MoS₂ on silicon (followed by chemical exfoliation), a much higher photocurrent density for hydrogen evolution was achieved as compared to 2H-MoS₂ on silicon (Fig. 1i).

B. Growth of novel 2D MX₂ heterostructures via van der Waals epitaxy.

We have also developed a facile CVD growth of vertical heterostructures of two-dimensional (2D) MX₂ materials enabled by van der Waals epitaxy. Few layers of MoS₂, WS₂, and WSe₂ were grown uniformly onto microplates of SnS₂ under mild CVD reaction conditions and the heteroepitaxy between them was unequivocally characterized using TEM by resolving the Moiré patterns. New photoluminescence properties were observed in heterostructures of MoS₂-SnS₂, which can be understood with electronic structure calculations to result from electronic coupling and charge separation between MoS₂ and SnS₂ layers. This work opens up the exploration of novel heterostructures of diverse MX₂ materials for electronic structure engineering of 2D heterostructures and novel applications. The charge transfers across the heterostructures could be important for enabling heterojunctions solar conversion devices.

C. Continued development of QD nanoscale heterostructures.

Building on our success in synthesizing epitaxial heterostructures of quantum dots (QDs) with nanowires (NWs), we have expanded to the epitaxial heterostructures of PbSe QDs on TiO₂ with different morphologies (nanoparticles, nanorods, nanosheets). TEM and scanning TEM (STEM) characterization of such PbSe QD–TiO₂ nanoscale heterostructures showed good QD coverage and uniform size distribution, confirmed these QDs are nucleated and grown directly on TiO₂ surface, and elucidated the heteroepitaxial relationship at the interface. Optical properties of these epitaxial QDs are compared with PbSe QD–TiO₂ NP heterostructures connected with linker molecules. These QD heterostructures are being investigated by coherent multidimensional spectroscopy to provide the fundamental understanding of charge transfer.

D. Multidimensional spectroscopy studies of nanomaterials and heterostructures.

We have used multiresonant coherent multidimensional spectroscopy (CMDS) to probe the dynamics of the electronic states in 2D MX₂ materials. Figure 2 shows four frames of a movie of the 2D spectrum for a few-layer MoS₂ sample on a quartz substrate. The time delay, $T = \tau_{21} = \tau_2 - \tau_1$, can be positive or negative: positive delays measure the coherent dynamics where the first pulse excites a coherent superposition state (a coherence) and the latter pulses (2 and 2') measure the frequencies of the final coherences after T . Negative delays measure the incoherent dynamics where the 2 and 2' pulses create an electronic state population and ν_1 pulse measures the final coherence. The absorption spectra superimposed show the frequencies of the A and B excitons of MoS₂ while the 2D spectra resolve the substructure of states lying beneath the A and B excitons. The frames of the movie show the coherent and incoherent dynamics of the substructure of states within the A and B excitons. The narrow anti-diagonal width represents the excitonic homogeneous width resulting from coherence dephasing and the diagonal width represents the

inhomogeneous width determined by the different environments. The population dynamics that appears at longer negative delay times defines how energy flows between states.

We are also using this methodology to study the electronic states of metal chalcogenide quantum confined core/shell structures and chalcogenide QD-TiO₂ heterojunctions. The chalcogenide quantum confined structures exhibit a range of excitonic dynamics include rapid coherent and incoherent relaxation between substructure states within the quantum confined excitonic line-shape, relaxation between quantum confined excitonic states and localized states, and relaxation to surface defect states. Different sample preparations change the relative importance of each process.

Future Plans

We will continue to develop synthesis of well-controlled MX₂ materials to achieve improved electrocatalytic activity for solar photoelectrochemical energy conversion. We are also developing new chemistry to control the electronic structure and properties of 2D nanosheets. Ligand modifications of the MX₂ edges will be investigated to passivate the edge electronic states and improve the optoelectronic properties and solar performance. These modified 2D materials will be studied with Kelvin force probe microscopy (KFM) and other surface sensitive techniques to elucidate the impacts of edge modifications to their electronic properties.

We have been developing new methods using three color CMDS excitation pulses that create spectrally resolved output frequencies and are insensitive to scattering, and new reflective CMDS geometries that can be used for opaque samples. Current CMDS methods are limited to transmissive samples where scattering does not dominate but many of our samples are not amenable to current CMDS methods. We will use these new CMDS methods and previously developed methods to measure the changes in electronic states, excitonic coupling, and dynamics in heterostructures between different combinations of MX₂ structures, QDs and metal oxides (TiO₂, SnO₂, Fe₂O₃); and the different strategies for linking the materials (epitaxial attachment, linkers). The presence of a heterojunction will change both the quantum states and the dynamics and both changes will be reflected in the multidimensional spectroscopy. We should also be able to see interface states, particularly if we use multiple quantum coherences involving electronic states of both the donor and acceptor. The charge transfer dynamics can also include coherent and incoherent mechanisms and each can be resolved using different CMDS pathways that are either fully or partially coherent. The coherent transfer will introduce a characteristic quantum

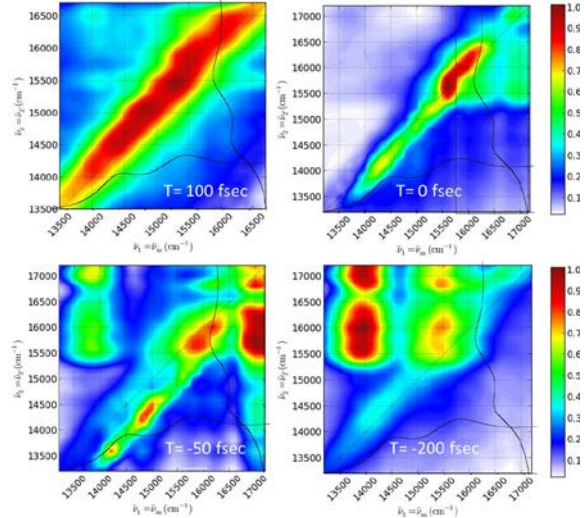


Fig. 2. Example frames of a movie showing the temporal changes of the 2D spectrum of few-layer

beating between the zero quantum coherences involved in the transfer. These processes are also likely to be affected by the surface passivation methods used to modified the nanostructures and again, the changes should become apparent in the CMDS spectra.

Furthermore, we are integrating the surface photovoltage (SPV) method with atomic force microscopy (AFM) and the CMDS system to simultaneously probe the charge separation dynamics in the 2D MX₂ materials and the QD heterostructures we have synthesized on nanometer length scale and the quantum state resolved dynamics.

References (see the next section)

Publications

1. Ding, Q.; Meng, F.; English, C. R.; Caban-Acevedo, M.; Shearer, M. J.; Liang, D.; Daniel, A. S.; Hamers, R. J.; Jin, S.; “Efficient Photoelectrochemical Hydrogen Generation Using Heterostructures of Si and Chemically Exfoliated Metallic MoS₂” *J. Am. Chem. Soc.*, **2014**, *136*, ASAP DOI: 10.1021/ja5025673J.
2. Lukowski, M. A.; Daniels, A. S.; English, C. R.; Meng, F.; Forticaux, A.; Hamers, R. J.; Jin, S.; “Highly Active Hydrogen Evolution Catalysis from Metallic WS₂ Nanosheets” *Energy Environ. Sci.*, **2014**, Accepted Manuscript, DOI: 10.1039/C4EE01329H.
3. Zhang, X.; Meng, F.; Christianson, J. R.; Arroyo-Torres, C.; Lukowski, M. A.; Liang, D.; Schmidt, J. R., D.; Jin, S.; “Vertical Heterostructures of Layered Metal Chalcogenides by van der Waals Epitaxy” *Nano Letters* **2014**, *14*, ASAP. DOI: [dx.doi.org/10.1021/nl501000k](https://doi.org/10.1021/nl501000k).
4. Tan, Y.; Jin, S.; Hamers, R. J.; “Photostability of CdSe Quantum Dots Functionalized with Aromatic Dithiocarbamate Ligands” *ACS Appl. Mater. Interfaces* **2013**, *5*, 12975-12983.
5. Lukowski, M. A.; Daniels, A. S.; Meng, F.; Forticaux, A.; Li, L.; Jin, S.; “Enhanced Hydrogen Evolution Catalysis from Chemically Exfoliated Metallic MoS₂ Nanosheets” *J. Am. Chem. Soc.* **2013**, *135*, 10274- 10277.
6. Faber, M. S.; Park, K.; Cabán-Acevedo, M.; Santra, P. K.; Jin, S.; “Earth-Abundant Cobalt Pyrite (CoS₂) Thin Film on Glass as a Robust, High-Performance Counter Electrode for Quantum Dot-Sensitized Solar Cells” *J. Phys. Chem. Lett.* **2013**, *4*, 1843-1849.
7. Tan, Y.; Jin, S.; Hamers, R. J.; “Influence of Hole-Sequestering Ligands on Photostability of CdSe Quantum Dots” *J. Phys. Chem. C.*, **2013**, *117*, 313-320.
8. Selinsky, R. S.; Ding, Q.; Faber, M. S.; Wright, J. C.; Jin, S.; “Quantum Dot Nanoscale Heterostructures for Solar Energy Conversion” *Chem. Soc. Rev.* **2013**, *42*, 2963-2985. (Invited Feature Review)
9. Franking, R.; Li, L.; Lukowski, M. A.; Meng, F.; Tan, Y.; Hamers, R. J.; Jin, S.; “Facile Post-Growth Doping of Nanostructured Hematite Photoanodes for Enhanced Photoelectrochemical Water Oxidation” *Energy Environ. Sci.* **2013**, *6*, 500-512.
10. Block, S. B.; Yurs, L. A.; Pakoulev, A. V.; Selinsky, R. S.; Jin, S.; Wright, J. C.; “Multiresonant Multidimensional Spectroscopy of Surface-Trapped Excitons in PbSe Quantum Dots” *J. Phys. Chem. Lett.* **2012**, *3*, 2707-2712.
11. Selinsky, R. S.; Shin, S.; Lukowski, M. A.; Jin, S.; “Epitaxial Heterostructures of Lead Selenide Quantum Dots on Hematite Nanowires” *J. Phys. Chem. Lett.* **2012**, *3*, 1649-1656.

SISGR: BI-CONTINUOUS MULTI-COMPONENT NANOCRYSTAL SUPERLATTICES FOR SOLAR ENERGY CONVERSION

Cherie R. Kagan, Christopher B. Murray, James M. Kikkawa, Nader Engheta, University of Pennsylvania, Philadelphia, PA 19104

Program Scope: Our SISGR program studies multi-component superlattices assembled from different combinations of semiconductor or semiconductor and plasmonic nanocrystal (NC) building blocks. We are developing the synthesis and assembly of combinations of NCs that form bicontinuous semiconductor NC sublattices with type-II energy offsets to drive charge separation onto electron and hole transporting sublattices for collection and introduce plasmonic NCs to increase solar absorption and charge separation. Using combinations of structural, optical and electrical measurements and modeling, we probe energy and charge transfer and transport in NC assemblies. We aim to discover the design rules to construct multicomponent NC superlattices that efficiently convert sunlight into electricity.

Recent Progress: We synthesized semiconductor and plasmonic NC samples, tunable in diameter, shape and composition and monodisperse to <5%, to use as building blocks for single and multi-component NC superlattices. We expanded synthetic methods increasing the NC chemistries in our toolbox, as exemplified by our work on copper indium diselenide NCs.^{D1} Using these NC building blocks, we recently demonstrated the fabrication of ordered single component and binary nanocrystal superlattices (BNSLs) from a wide range of NC compositions by dipcoating,^{D2} which is a particularly attractive method for NC assembly and deposition as it provides greater control *via* solvent selection and

substrate withdrawal rates, it allows wafer scale deposition, and it is commonly employed in the construction of NC active areas in solar cells. **Figure 1(a-c)** shows examples of targeted bicontinuous BNSLs in the $MgZn_2$, AB_2 and AB_{13} crystal structures assembled from larger PbSe and smaller PbS NCs achieved by dipcoating. A combination of [**Fig. 1(d-g)**] TEM and [**Fig. 1(h-k)**] grazing incident small-angle x-ray scattering (GISAXS) reveals that dipcoating forms large-area, ordered single component superlattices from NCs of different shape (spheres and cubes) and different composition ($CoFe_3O_4$, Bi, $MnFe_3O_4$, PbSe).

Previously we demonstrated through a combination of ligand exchange with compact chemistries and remote doping at the NC surface introduced *via* thermal evaporation and diffusion that we could realize high electron mobilities of $27 \text{ cm}^2/\text{Vs}$ in CdSe NC thin films.¹ Recently we have (i) extended concepts of remote doping of NC thin films to different dopants, processes and semiconductor NCs, (ii) integrated these materials into electronic and optoelectronic devices, and (iii) continued to uncover the fundamentals of charge transport in NC films.

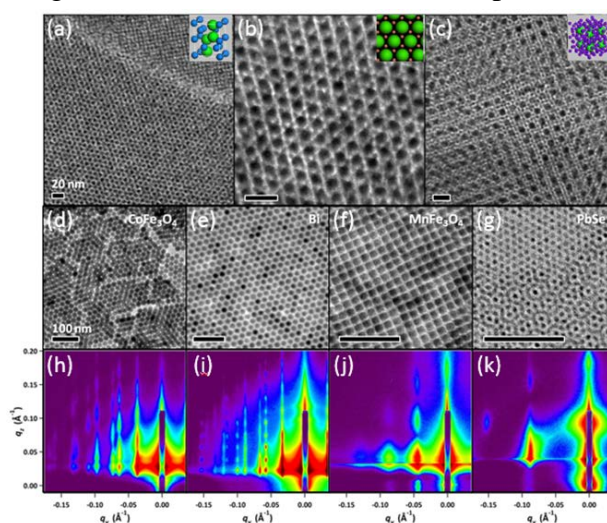


Figure 1 TEM images of dipcoated PbSe and PbS BNSLs assembled in (a) $MgZn_2$, (b) AB_2 and (c) AB_{13} architectures and of dipcoated single component (d) $CoFe_3O_4$, (e) Bi, (f) $MnFe_3O_4$, and (g) PbSe NC superlattices. (h-k) Corresponding GISAXS of single component NC superlattices shown in (d-g).

In particular, we showed that non-stoichiometry in NC semiconductor thin films can be used to greatly control charge carrier type, concentration and mobility. In the first example, we applied the doping method of thermal evaporation and diffusion to the IV-VI NC thin films of PbSe and PbS.^{D3} We n-doped the semiconductor films upon the introduction of excess Pb and p-doped them through the use of excess Se, akin to the effects of non-stoichiometry known in bulk analogs. Controlling the amount of deposited Pb or Se, we showed through a combination of capacitance-voltage and Hall measurements that we can tailor the electron and hole concentrations from 10^{15} - $10^{20}/\text{cm}^3$ to form thin films that are semiconducting and intrinsic, n-type, and p-type to metallic at high, degenerate doping levels, moving the Fermi level across the NC thin film bandgap [Fig. 2(a)]. Using this control over NC thin film stoichiometry, we demonstrated lead chalcogenide NC field-effect transistors (FETs) with characteristics ranging from ambipolar to n-type to p-type. Notably, Pb-doped PbSe NC FETs showed field-effect mobilities of $10 \text{ cm}^2/\text{Vs}$, an order of magnitude higher than previously demonstrated [Fig. 2(b)]. We also showed enhanced power conversion efficiencies in PbSe NC solar cells through Se-doping to increase the junction of Schottky solar cells [Fig. 2(c)]. We subsequently extended the concept of remote doping through stoichiometric control by introducing a simple, solution-based, post-deposition colloidal atomic layer process to introduce excess chalcogen and excess metal through their salts and tailor the carrier statistics and therefore the performance of devices.^{D4, D5}

Building on our high mobility CdSe NC FETs we: 1) demonstrated the first NC integrated circuits and their fabrication and operation on flexible plastics and at low-voltages^{D6} and 2) showed that NC devices may be repaired after air and solvent exposure allowing large-area device fabrication (using conventional cleanroom techniques) and, upon encapsulation, stable operation in air.^{D7} The high mobility, encapsulated CdSe NC FETs allowed us to explore their very low temperature and gate dependent transport and magnetotransport. Low temperature resistance measurements indicate that these NC FETs show a characteristic temperature

dependence of $\rho(T) = \rho_0 \exp\left(\frac{T_0}{T}\right)^{2/3}$ for temperature T. The 2/3 exponent is consistent with a

recent model based on Coulomb gap variable range hopping plus thermal broadening. The measured changes in resistivity with applied gate bias, V_G , communicate an increase in the product of the localization length and dielectric constant (κa) as the Fermi energy is increased, in

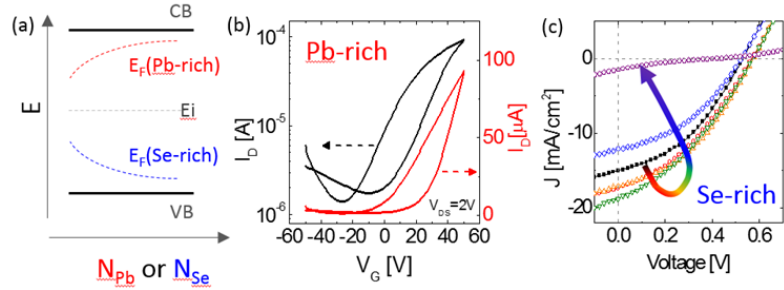


Figure 3 (a) Schematic mapping the Fermi energy of PbE (E=S, Se) NC thin films as a function of the concentration of Pb (red) or Se (blue) atoms added to NC thin films. (b) Transfer characteristics of PbSe NC FETs in the linear regime after 3 Å of deposited Pb. (c) Current-density (J) versus V characteristics of Se-rich Schottky junction solar cells (black) before and after (red) 0.1 Å, (orange) 0.2 Å, (green) 0.4 Å, (blue) 0.8 Å, and (purple) 2 Å of deposited Se.

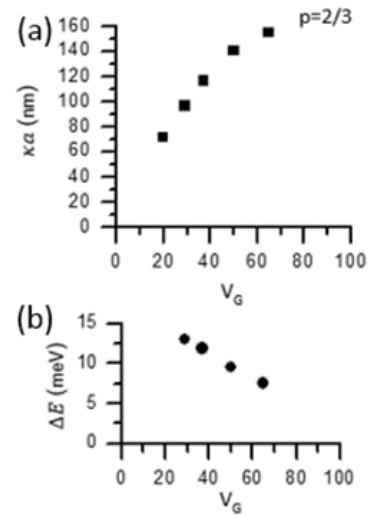


Figure 2 Gate bias (V_G) dependence of (a) localization product (κa) and (b) of the mobility gap (ΔE).

accord with the theory of Anderson [Fig. 3(a)]. Under any reasonable assumptions, the localization length increases significantly beyond the particle diameter as gate bias is applied, consistent with the extended state transport we previously reported.¹ Magnetoresistance (MR) measurements display both positive and negative MR contributions whose magnitudes depend on both V_G and T . For each V_G , we observe a universal lineshape describing negative MR for higher temperatures ($T > 20\text{K}$) that scales as $T^{-4/3}$, consistent with expectations for Zeeman MR with $p=2/3$. Zeeman modulation of the mobility gap (ΔE) is in many ways a magnetic counterpart to the application of a gate bias. In contrast to a gate bias, however, the exact variation in the gap is known from the magnetic field and the electron g -factor. Thus, we can obtain a numerical value for the mobility gap for each value of V_G , shown in Figure 3(b). With increasing gate bias the calculated mobility gap clearly decreases, and the trend of the gate bias dependence indicates that for sufficiently high values of V_G the devices may transition to a metallic state.

Additional work supported by the DOE SISGR grant are our studies on the: 1) optical properties of anisotropic nanorods and dot-in-rod NCs that diversify the shape and properties of NC building blocks for BNSLs,^{D9-11} 2) ligand exchange and electrical properties of plasmonic Au and Ag NC assemblies,^{D12,D13} and 3) structural,^{D14-18} electrical^{D19,D20} and optical^{D21} characterization of NCs and their assemblies.

Future Plans: We will take advantage of the large area assembly of BNSLs to explore BNSLs with increasing diversity in NC size, shape and composition and integrate these in structures to enable electrical and optical measurements of energy and charge transport in ordered versus disordered single, multicomponent assemblies, and with the introduction of plasmonic NCs.

References

¹ “Bandlike Transport in Strongly Coupled and Doped Quantum Dot Solids: A Route to High-Performance Thin-Film Electronics,” J-H Choi, AT Fafarman, SJ Oh, D-K Ko, DK Kim, BT Diroll, S Muramoto, JG Gillen, CB Murray, CR Kagan, *Nano Lett.* **12**, 2631-2638 (2012).

Publications (additionally referenced in abstract above)

^{D1} “Three-Dimensional Self-Assembly of Chalcopyrite Copper Indium Diselenide Nanocrystals into Oriented Films” DC Reifnsyder, X Ye, TR Gordon, C Song, CB Murray, *ACS Nano* **7**, 4307-4315 (2013).

^{D2} “Assembly of Binary Nanocrystal Superlattices and Long Range Ordered Single Component Films *via* Dipcoating,” EA Gauling, BT Diroll, ED Goodwin, CR Kagan, CB Murray, in preparation (2014).

^{D3} “Stoichiometric Control of Lead Chalcogenide Nanocrystal Solids to Enhance Their Electronic and Optoelectronic Device Performance,” SJ Oh, NE Berry, J-H Choi, EA Gauling, T Paik, S-H Hong, CB Murray, CR Kagan, *ACS Nano* **7** 2413-2421 (2013).

^{D4} “Designing High-Performance PbS and PbSe Nanocrystal Electronic Devices through Stepwise, Post-Synthesis, Colloidal Atomic Layer Deposition,” SJ Oh, NE Berry, J-H Choi, EA Gauling, H Lin, T Paik, BT Diroll, S Muramoto, CB Murray, CR Kagan,” *Nano Lett.* **14**, 1559-1566 (2014).

^{D5} “Solution-Based Stoichiometric Control over Charge Transport in Nanocrystalline CdSe Devices,” DK. Kim, AT Fafarman, BT Diroll, SH Chan, TR Gordon, CB Murray, CR Kagan, *ACS Nano* **7**, 8760-8770 (2013).

- ^{D6} “Flexible and low-voltage integrated circuits constructed from high-performance nanocrystal transistors,” DK Kim, Y Lai, BT Diroll, CB Murray, CR Kagan, *Nature Comm.* 2218 (2012).
- ^{D7} “*In Situ* Repair of High-Performance, Flexible Nanocrystal Electronics for Large-Area Fabrication and Operation in Air,” J-H Choi, SJ Oh, Y Lai, DK Kim, T Zhao, AT Fafarman, BT Diroll, CB Murray, CR Kagan,” *ACS Nano* **7**, 8275-8283 (2013).
- ^{D8} “Gate Induced Carrier Delocalization in Nanocrystal Field Effect Transistors,” ME Turk, SJ Oh, J-H Choi, BT Diroll, CB Murray, CR Kagan, JM. Kikkawa, in preparation (2014).
- ^{D9} “Interpreting the Energy-Dependent Anisotropy of Colloidal Nanorods Using Ensemble and Single-Particle Spectroscopy,” BT Diroll, T Dadosh, A Koschitzky, YE Goldman, CB Murray, *J. Phys. Chem C* **117**, 23928-23937 (2013).
- ^{D10} “Tunable Optical Anisotropy of Seeded CdSe/CdS Nanorods,” BT Diroll, A Koschitzky, CB Murray, *J. Phys. Chem. Lett.* **5**, 85-91 (2014).
- ^{D11} “High-Temperature Photoluminescence of CdSe/CdS Core/Shell Nanoheterostructures,” BT Diroll, CB Murray, *ACS Nano ASAP* (2014).
- ^{D12} “Chemically Tailored Dielectric-to-Metal Transition for the Design of Metamaterials from Nanoimprinted Colloidal Nanocrystals,” AT Fafarman, S-H Hong, H Caglayan, X Ye, BT Diroll, T Paik, N Engheta, CB Murray, CR Kagan, *Nano Lett* **13**, 350-357 (2013).
- ^{D13} “Air-Stable, Nanostructured Electronic and Plasmonic Materials from Solution-Processable, Silver Nanocrystal Building Blocks,” AT Fafarman, S-H Hong, SJ Oh, H Caglayan, X Ye, BT Diroll, N Engheta, CB Murray, CR Kagan, *ACS Nano* **8**, 2746-2754 (2014).
- ^{D14} “Enhanced Energy Transfer in Quasi-Quaternary Nanocrystal Superlattices,” M Cargnello, BT Diroll, EA Gaubing, CB Murray, *Advanced Materials*, **26**, 2419-2423 (2014).
- ^{D15} “Engineering Catalytic contacts and Thermal Stability: Gold/Iron Oxide Binary Nanocrystal Superlattices for CO Oxidation,” Y Kang, X Ye, J Chen, L Qi, RE Diaz, V Doan-Nguyen, G Xing, CR Kagan, J Li, RJ Gorte, EA Stach, CB Murray,” *J. Am. Chem. Soc.* **135**, 1499-1505 (2013).
- ^{D16} “Competition of shape and interaction patchiness for self-assembling nanoplates,” X Ye, J Chen, M Engel, JA Millan, W Li, L Qi, G Xing, JE Collins, CR Kagan, J Li, SC Glotzer, CB Murray, *Nature Chemistry*, **5**, 466-473 (2013).
- ^{D17} “Seeded Growth of Monodisperse Gold Nanorods Using Bromide-Free Surfactant Mixtures,” X Ye, Y Gao, J Chen, DC Reifsnnyder, C Zheng, CB Murray, *Nano Lett.* **13**, 2163-2171 (2013).
- ^{D18} “Seeded Growth of Metal-Doped Plasmonic Oxide Heterodimer Nanocrystals and Their Chemical Transformation,” X Ye, DC Reifsnnyder-Hickey, J Fei, BT Diroll, T Paik, J Chen, CB Murray, *J. Am. Chem. Soc.* **136**, 5106-5115 (2014).
- ^{D19} “Bistable Magnetoresistance Switching in Exchange-Coupled CoFe₂O₄-Fe₃O₄ Binary Nanocrystal Superlattices by Self-Assembly and Thermal Annealing,” J Chen, X Ye, SJ Oh, JM Kikkawa, CR Kagan, CB Murray, *ACS Nano* **7**, 1478-1486 (2013).
- ^{D20} “Solution-Processed Phase-Change VO₂ Metamaterials from Colloidal Vanadium Oxide (VO_x) Nanocrystals,” T Paik, S-H. Hong, EA Gaubing, H Caglayan, TR Gordon, N Engheta, CR Kagan, CB Murray, *ACS Nano* **8**, 797-806 (2014).
- ^{D21} “Metal-Enhanced Upconversion Luminescence Tunable through Metal Nanoparticle-Nanophosphor Separation,” M. Saboktakin, X Ye, SJ Oh, S-H Hong, AT Fafarman, UK Chettiar, N Engheta, CB Murray, CR Kagan, *ACS Nano* **6**, 8758-8766 (2012).

Molecularly Designed Localized Static Charging for Energy Efficiency in Organic Electronics

Howard E. Katz, Daniel H. Reich, and Nina Markovic

Program Scope

The program is to create dielectric materials with localized distributions of static charge as a means of controlling properties of adjacent organic semiconductors. Compositional factors controlling local charge densities include incorporated electron donors and acceptors, substituent hydrophobicity, and profiles of internal interfaces. Synthetic approaches include controlled radical polymerization of styrene monomers, crosslinking, donor/acceptor side chain attachment, and block polymer interpenetration. Analytical methods include x-ray and neutron scattering to measure interfacial thicknesses and roughnesses, scanning Kelvin probes to measure surface potentials, and current extraction by linearly increased voltage (CELIV) to measure retained charge quantities and stabilities. The broad fundamental goal is to determine the effects of charge quantities in dielectrics, charge stabilities, and distances of charges from semiconductors on the effectiveness of the charges in controlling on/off states of semiconductors in transistors. A second goal is to isolate these charges in semiconductor layers forming pn junctions.

Recent Progress: Synthesis

Styrene and trifluorostyrene polymers with electron donor and acceptor groups attached were synthesized using controlled radical polymerization followed by substitution or coupling of donor and acceptor derivatives (Figure 1). These polymers, with their dilute distributions of charge trapping sites, are expected to provide stable matrices for localized static charges.

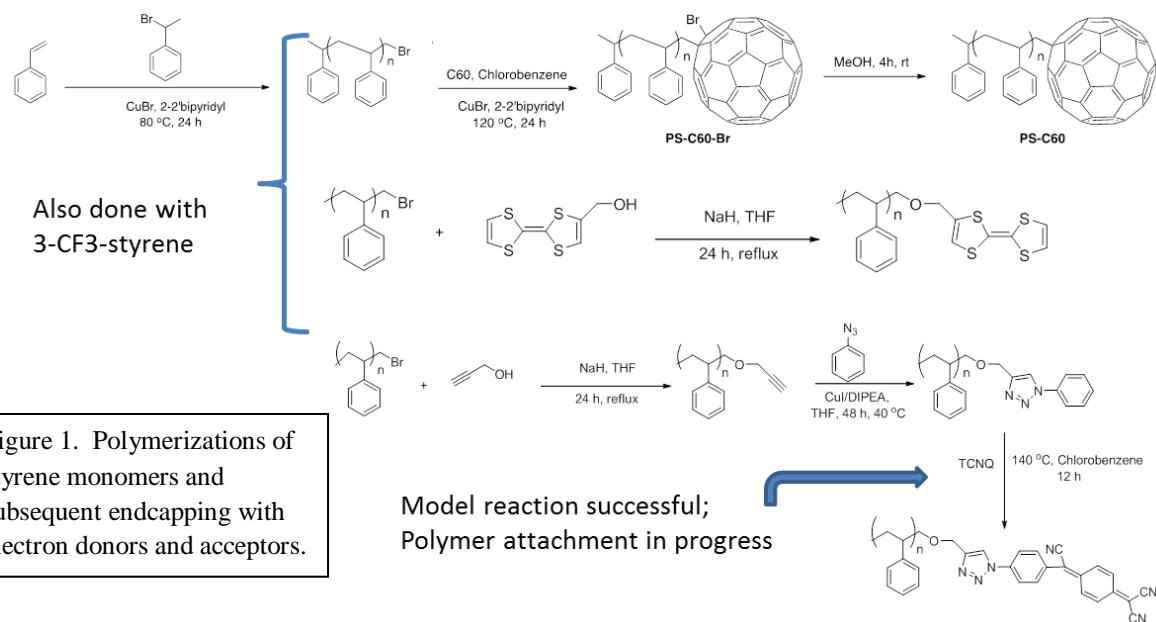


Figure 1. Polymerizations of styrene monomers and subsequent endcapping with electron donors and acceptors.

Interfacial morphology

Vertical multilayer structures are made by consecutive spincoating steps, can serve as gate dielectrics for conventional organic transistors, and are characterized using scattering methods. Desirable attributes of the vertical stacks are the avoidance of intermixing of the layers and surface smoothness. Accomplishing this with polystyrenes was more challenging than expected, but a solution was found using cyclobutenostyrene as a crosslinking comonomer. A 10% incorporation of the monomer in a polystyrene copolymer gave smooth, cured films after annealing to form “xl-PS”. X-ray and neutron reflectivity studies show that both polystyrene and poly(3-trifluoromethylstyrene) can be deposited on top of the xl-PS, yielding clean bilayer structures. Examples of neutron reflectivity data are shown in Figure 2.

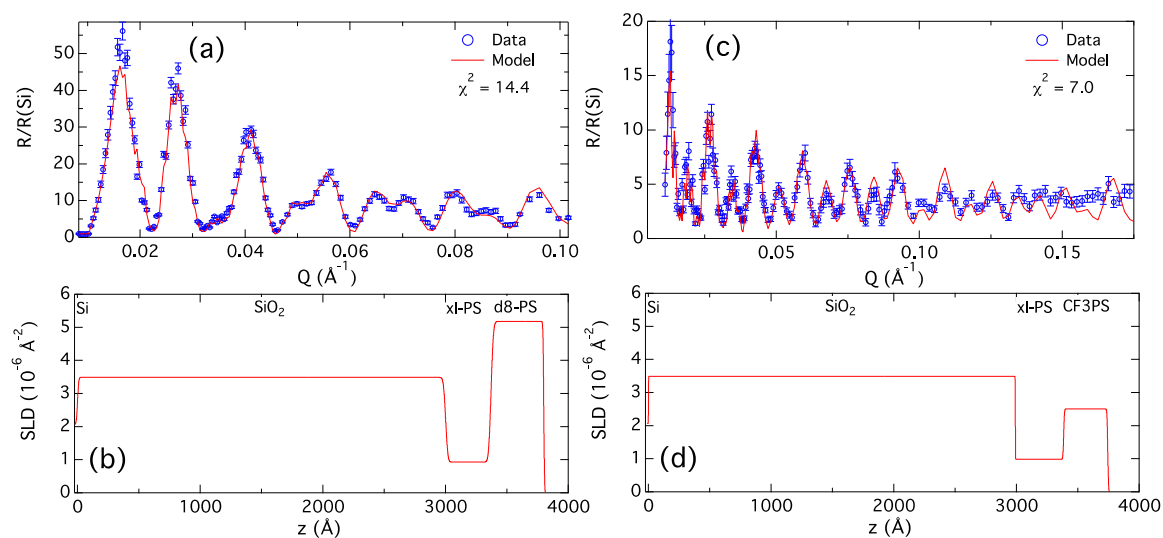


Figure 2. Preliminary neutron reflectivity measurements. (a) Fresnel reflectivity $R/R(\text{Si})$ for an xl-PS/d8-PS bilayer on a thermally oxidized Si wafer. Model curve in (a) corresponds to depth profile shown in (b). (c) Fresnel reflectivity for an xl-PS/CF3PS bilayer. Model curve in (c) corresponds to depth profile shown in (d). Interface roughnesses from fits: xl-PS/d8-PS = 15 Å; xl-PS/CF3PS = 5 Å.

Charge trapping and release in polystyrene dielectrics with pentacene semiconductor

We use “charge extraction by linearly increasing voltage” (CELIV) to observe charging and discharging of semiconductor-dielectric stacks. We compared bilayers of pentacene and either atactic polystyrene or poly(3-trifluoromethylstyrene). DC charging of the stack had a greater effect on the amount of excess charge (above and beyond capacitive charging) extracted in the CELIV experiment with the fluorinated polymer compared to plain polystyrene. This is consistent with our earlier observation that while the fluorinated polymer is inherently more stable to bias stress than unsubstituted polystyrene, a pre-charging step actually destabilizes the fluorinated polymer, presumably by creating new energy levels in which charge can be trapped.

Lateral device characterization

Lateral organic field-effect transistors (OFETs), consisting of a polystyrene (PS) polymer gate material and a pentacene organic semiconductor (OSC), were electrically polarized from bias

stress during operation or in a separate charging step, and investigated with scanning Kelvin probe microscopy (SKPM) and current-voltage determinations. The charge storage inside the polymer was indicated, without any alteration of the OFET, as a surface voltage with SKPM, and correlated to a threshold voltage (V_T) shift in the transistor operation. The SKPM method allows the gate material/OSC interface of the OFET to be visualized and the surface voltage variation between the two gate material interfaces to be mapped. The charge distribution for three samples was derived from the surface voltage maps using Poisson's equation. Charge densities calculated this way agreed with those derived from the V_T shifts and the lateral gate-OSC capacitance. We also compared the behavior of two other polymers with PS: PS accepted the most static charge in its entire volume, poly(3-trifluoromethylstyrene) (F-PS) had the most stability to bias stress, and poly (methyl methacrylate) (PMMA) showed the most leakage current and least consistent response to static charging of the three polymers. *This is the first demonstration that surface voltage on a working OFET gate material can be related to the quantity of static charge responsible for bias stress and nonvolatility in OFETs.* A device photograph, measurement schematic, and representative data are shown in Figure 3. Images (a,c,e) and (b,d,f) correspond to individual samples. The samples are first imaged before electrical testing (a,b). After the transistor electrical measurements, the samples are scanned (c,d). The samples were then charged to -100 V (e) and +100 V (f) for 10 minutes and rescanned.

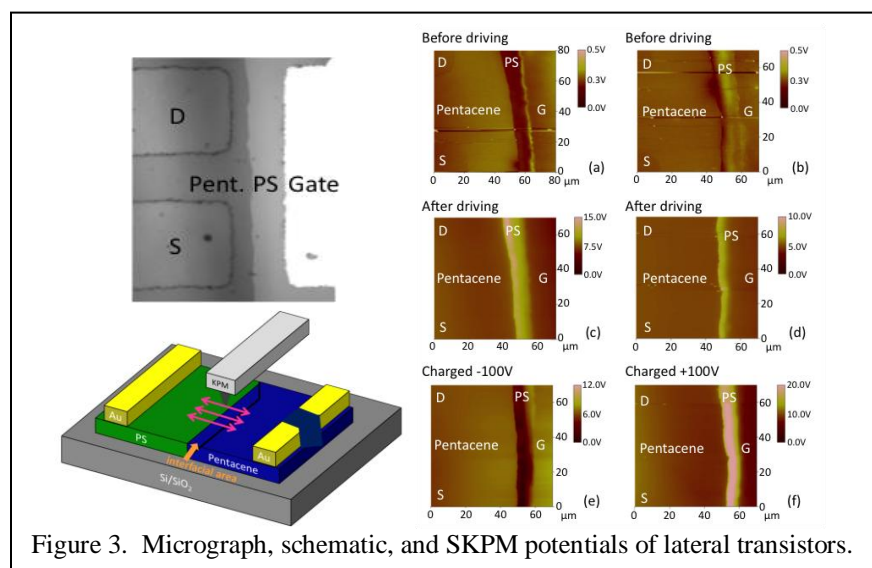


Figure 3. Micrograph, schematic, and SKPM potentials of lateral transistors.

with two and three different dielectrics in series; we have already made and charged such structures from polystyrene and poly (trifluoromethyl styrene). In the longer term, we will build on an initial synthesis of a diblock polymer with a single electroactive molecule protruding some distance away from a semiconducting block, and use this structure to modulate charge distributions at nanometer distances from layers of that semiconductor.

Publications

Dawidczyk, T.; Johns, G.L.; Ozgun, R.; Alley, O.; Andreou, A.G.; Markovic, N.; Katz, H.E. "Kelvin Probe Microscopic Visualization of Charge Storage at Polystyrene Interfaces with Pentacene and Gold" *Applied Physics Letters*, 100, 073305 (2012)

Future Plans

The immediate plans are to extend both the morphology and charge distribution/extraction studies to include materials with attached donors and acceptors as illustrated in the synthesis sections. We will also characterize electronic heterostructures

Poehler, T.O. and Katz, H.E. “Prospects for Polymer-based Thermoelectrics: State of the Art and Theoretical Analysis” *Energy and Environmental Science*, 5, 2110-2115 (2012)

Streifel, B.C.; Peart, P.A; Martinez Hardigree, J.F.; Katz, H.E.; Tovar, J.D.
“Torsional Influences within Disordered Organic Electronic Materials Based upon Non-Benzenoid 1,6-Methano[10]annulene Rings” *Macromolecules*, 45, 7339-7349 (2012)

Ireland, R.M.; Zhang, L.; Gopalan, P.; and Katz, H.E. “Tellurium Thin Films in Hybrid Organic Electronics: Morphology and Mobility” *Adv. Mater.*, 25, 4358-4364 (2013)

Sinha, J. Lee, S.J.; Kong, H.; Swift, T.W.; Katz, H.E. “Tetrathiafulvalene (TTF)-functionalized Thiophene Copolymerized with 3, 3’’-Didodecylquaterthiophene: Synthesis, TTF Trapping Activity, and Response to Trinitrotoluene” *Macromolecules* 46, 708-717 (2013)

Sanders, A.; Dawidczyk, T.J.; Katz, H.E.; Tovar, J.D. “Peptide-based Supramolecular Semiconductor Nanomaterials via Pd-catalyzed Solid-phase “dimerizations” *ACS Macro Letters* 1 1326-1329 (2012)

R.M. Ireland; T.J. Dawidczyk; P. Cottingham; T. McQueen; G. Johns; N. Markovic; L. Zhang; P. Gopalan; H. E. Katz “Effects of Pulsing and Interfacial Potentials on Tellurium-Organic Heterostructured Films” *ACS Applied Materials and Interfaces*, 5, 1604-1611 (2013)

Sinha, J.; Ireland, R.M.; Lee, S.J.; Katz, H.E. “Synergistic Thermoelectric Power Factor Increase in Films Incorporating Tellurium and Thiophene-based Semiconductors” *MRS Comm* 3, 97-100, highlighted article in *MRS e-News* (2013)

Kola, S.; Kim, J.H.; Ireland, R.; Yeh, M-Y.; Smith, K.; Guo, W.; Katz, H.E.
“Pyromellitic Diimide – Ethynylene Based Homopolymer Film as an N-Channel Organic Field-Effect Transistor Semiconductor” *ACS Macro Letters*, 2, 664-669 (2013)

Martinez Hardigree, J.F.; Dawidczyk, T.J.; Ireland, R.M.; Johns. G.L.; Jung, B.-J.; Nyman, M.; Österbacka, R.; Markovic, N.; Katz, H.E. “Reducing Leakage Currents in n-Channel Organic Field-effect Transistors Using Molecular Dipole Monolayers on Nanoscale Oxides” *ACS Applied Mat. Int.* 5, 7025-32 (2013)

Martinez Hardigree, J.F, Katz, H.E. “Through Thick and Thin: Tuning the Threshold Voltage in Organic Field-Effect Transistors” *Accounts of Chemical Research*, 47, 1369-1377 (2014)

Dawidczyk, T.J.; Martinez Hardigree, J.F.; Johns, T.L.; Ozgun, R.; Alley, O.; Andreou, A.G.; Markovic, N.; Katz, H.E. “Visualizing and Quantifying Charge Distributions Correlated to Threshold Voltage Shifts in Lateral Organic Transistors” *ACS Nano*, 8, 2714-2724 (2014)

Mathias Nyman, Oskar Sandberg, Josué F. Martínez Hardigree, Srinivas Kola, Howard E. Katz, and Ronald Österbacka “Voltage dependent displacement current as a tool to measure the vacuum level shift caused by self-assembled monolayers on aluminum oxide” *Applied Physics Letters*, 103, 243502 (2013)

Unconventional clathrates based on transition metal pnictides: a paradigm-shifting approach to materials with enhanced thermoelectric properties

Kirill Kovnir, *Department of Chemistry, University of California, Davis*

Program Scope

This project is devoted to the development of novel thermoelectric materials based on clathrate compounds with framework formed by late transition metal and phosphorus. Thermoelectric (TE) materials convert heat into electric energy and *vice versa*. An effective TE material should be a good electrical conductor and induce a high voltage in response to a temperature gradient, but should be a poor heat conductor. “Phonon glass-electron crystal (PGEC)” concept suggests the use of perfectly crystalline compounds containing loosely bonded atoms inside oversized cages. These materials are expected to have low thermal conductivity and low electrical resistivity. Clathrates is a widely studied class of PGEC compounds containing a three-dimensional framework with large cavities in which guest atoms are situated. We believe that clathrates containing a high concentration of transition metals in the framework will exhibit structural chemistry and transport properties that are different from conventional tetrel-based clathrates.

Recent Progress

Ba₈Au₁₆P₃₀. Ba₈Au₁₆P₃₀ was successfully synthesized from elements using a two-step annealing process at 1073 K. All studied single crystals revealed strong tendencies for twinning which hampers crystal structure determination. Crystal structure of this compound was determined by means of the high resolution synchrotron powder X-ray diffraction (XRD). The determined unit cell corresponds to a $\sqrt{2}a_{\text{subcell}} \times a_{\text{subcell}} \times 2\sqrt{2}a_{\text{subcell}}$ superstructure of the prototype clathrate-I unit cell. In the crystal structure of Ba₈Au₁₆P₃₀, gold and phosphorus atoms form the clathrate-I framework. Ba atoms are situated inside the large cages of the framework. The formation of the superstructure is caused by the ordering of gold and phosphorus atoms within different framework positions. In the framework of Ba₈Au₁₆P₃₀ five crystallographically independent Au-P cages are formed: two pentagonal dodecahedra and three tetrakaidecahedra (Figure 1). According to the Zintl concept each barium atom donates two electrons to the framework becoming Ba²⁺. Each Au and P framework atom requires four electrons for the formation of 2c–2e bonds, *i.e.* 46×4 = 184 electrons per formula unit. Assuming that Au atoms have a closed shell *d*¹⁰ configuration, gold and phosphorus atoms are expected to provide one and five valence electrons, respectively. The total number of electrons per formula unit is 8×2 + 16×1 + 30×5 = 182 electrons, which is two electrons less than what is required by the Zintl counting scheme to be electron balanced. Violation of the Zintl electron balance should result Ba₈Au₁₆P₃₀ having metallic properties with holes as the main charge carriers.

Transmission Electron Microscopy (TEM) was applied to confirm the structural model obtained from powder X-ray diffraction (Figure 2). The diffraction patterns can be completely indexed in the $Pbcn$ space group using the unit cell parameters determined by powder XRD. All HRTEM images exhibit uniform contrast free of any modulation and defects within the single crystallite indicating a perfectly ordered crystal structure for the $Ba_8Au_{16}P_{30}$ clathrate.

The calculated images for different zones, different thicknesses, and defocus volumes are in good agreement with experimental HRTEM images. No features resulting from long range or short range atom or vacancy ordering have been observed. Macroscopic defects in $Ba_8Au_{16}P_{30}$ may be responsible for the difficulties in single crystal XRD data analysis. HRTEM, HAADF and ED studies provide a clear answer to the question of why all single crystal X-ray diffraction experiments failed.

$Ba_8Au_{16}P_{30}$ exhibits quite a number of extended defects such as anti-phase boundaries (APB) and twinning with pseudo three- and four-fold rotational axes. The latter symmetry elements are present in the ideal clathrate-I structure, but are absent in the observed orthorhombic superstructure of $Ba_8Au_{16}P_{30}$.

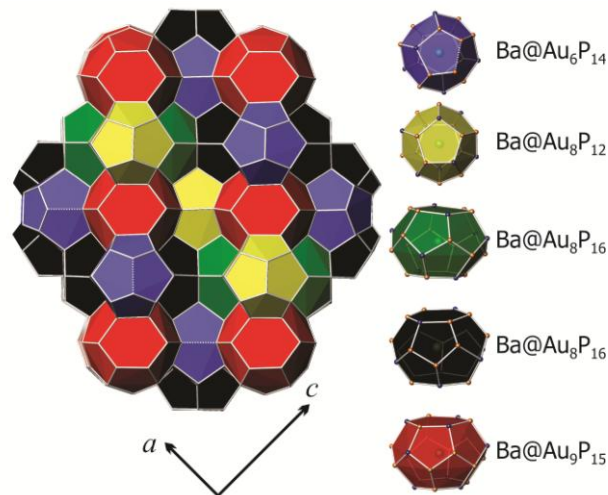


Figure 1. Polyhedral representation of the crystal structure of $Ba_8Au_{16}P_{30}$. Polyhedra color legend is given on the right.

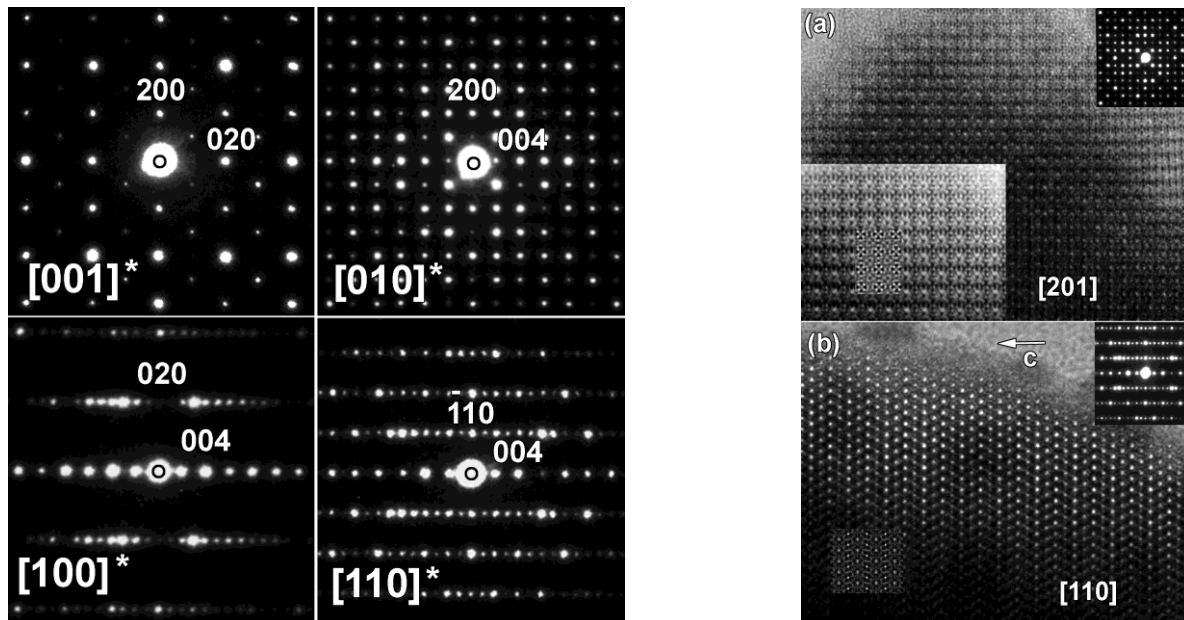


Figure 2. Left: ED patterns along the main zones $[001]^*$, $[010]^*$, $[100]^*$, and $[110]^*$ of $Ba_8Au_{16}P_{30}$. Right: HRTEM images along the most informative zones: (a) $[201]$ and (b) $[110]$, corresponding ED patterns given in the insets.

Thermoelectric properties investigation indicates that holes are the main charge carriers as expected from the Zintl count. Deviation from an electron balance resulted in a metallic-like temperature dependence of resistivity and a relatively small absolute value of the Seebeck coefficient. Despite its metal-like electrical conductivity, $\text{Ba}_8\text{Au}_{16}\text{P}_{30}$ exhibits very low total thermal conductivity of $0.6 \text{ W m}^{-1}\text{K}^{-1}$ (Figure 3).

The charge carrier contribution to the thermal conductivity can be estimated from the Wiedemann–Franz law, $k_{\text{electronic}}$

$= L_0 T / \rho$, where the ideal Lorentz number is calculated as $L_0 = \frac{1}{3}(\pi k_B / e)^2$. The lattice contribution to thermal conductivity was estimated by subtracting the electronic thermal conductivity from the total (Figure 3). Room temperature (300 K) lattice thermal conductivity is unprecedentedly low, $0.18 \text{ W m}^{-1}\text{K}^{-1}$. The complex crystal structure, the presence of the large number of heavy atoms in the unit cell, as well as multiple intergrowth and twinning defects are factors defining extremely low lattice thermal conductivity for $\text{Ba}_8\text{Au}_{16}\text{P}_{30}$.

Future Plans

$\text{Ba}_8\text{Cu}_x\text{Au}_{16-x}\text{P}_{30}$. We investigated the solid solution $\text{Ba}_8\text{Cu}_x\text{Au}_{16-x}\text{P}_{30}$ to determine whether the thermal conductivity can be further reduced by the introduction of structural disorder in the clathrate framework. We determined that this solid solution exists in the whole stoichiometry range from $x = 0$ to $x = 16$ with the unit cell volume linearly decreasing with increasing Cu content. Single crystal X-ray diffraction reveals a non-uniform distribution of Cu and Au atoms among the eight crystallographic positions of the metal atoms. Cu atoms tend to occupy positions with the shortest M-P distances while Au atoms tend to occupy positions with the longest M-P distances. This atomic distribution is expected to further decrease the lattice thermal conductivity. High resolution synchrotron X-ray diffraction analysis indicates that $\text{Ba}_8\text{Cu}_x\text{Au}_{16-x}\text{P}_{30}$ samples are not uniform and actually contain a mixture of several phases with close but not identical Cu content. Uniform single phase samples may only be obtained by melting the sample followed by slow cooling of the melt. We will characterize the thermoelectric properties for both types of samples, single and multi-phase. Comparison of the data will reveal how multiple phase boundaries which are present in non-uniform samples affect the thermal conductivity and thermoelectric properties.

$\text{Ba}_8\text{Zn}_x\text{Cu}_{16-x}\text{P}_{30}$. Besides thermal conductivity, the charge carrier concentration also needs to be optimized to achieve a high thermoelectric figure of merit. We started with the optimization of

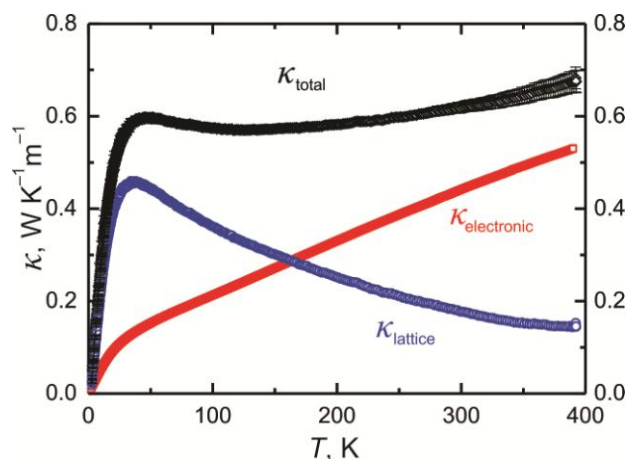


Figure 3. Total (black), electronic (red), and lattice (blue) thermal conductivities of $\text{Ba}_8\text{Au}_{16}\text{P}_{30}$.

the charge carrier concentration in the $\text{Ba}_8\text{Cu}_{16}\text{P}_{30}$ system. In accordance with the Zintl electron count, $\text{Ba}_8\text{Cu}_{16}\text{P}_{30}$ exhibits metallic resistivity with holes as the main charge carriers. To fill the valence band and realize semiconductor-like behavior, it is necessary to dope electrons. This can be achieved by the substitution of Cu with Zn. We investigated the solid solution $\text{Ba}_8\text{Zn}_x\text{Cu}_{16-x}\text{P}_{30}$ with a wide range of Zn content, $0 \leq x \leq 5$. The clathrate phase can be synthesized in the whole investigated range. However, the incorporation of Zn atoms resulted in significant structural re-arrangements in the framework. For materials with $0 \leq x < 2$, the orthorhombic clathrate-I superstructure is preserved. The composition with $x = 2$ can be crystallized in both the orthorhombic superstructure and cubic substructure of clathrate-I. Compositions with $x > 2$ crystallize in the partially ordered rhombohedral variant of the cubic substructure. These results indicate that the incorporation of ~12% Zn atoms is sufficient to distort the ordering of the Cu and P atoms within clathrate framework and stabilize the disordered substructure where each framework atomic position is occupied by three elements, Cu, Zn, and P. Zn and Cu are neighbors in the periodic system and cannot be distinguished by means of X-ray diffraction techniques. To determine the exact distribution of these elements across the clathrate framework we collected high resolution time-of-flight neutron powder diffraction data on representative samples. Analysis of the neutron diffraction data indicates that in the disordered phase, Cu and Zn are uniformly distributed over the framework positions. Currently, we are investigating the thermoelectric properties of these phases.

References

1. Lee, K.; Synnestvedt, S.; Bellard, M.; Kovnir, K. GeP and $(\text{Ge}_{1-x}\text{Sn}_x)(\text{P}_{1-y}\text{Ge}_y)$ ($x = 0.12, y = 0.05$): Synthesis, structure, and properties of two-dimensional layered tetrel phosphides. *J. Solid State Chem.* **2014**, DOI 10.1016/j.jssc.2014.04.021.
 2. Dolyniuk, J.; Kaseman, D.; Sen, S.; Zhao, J.; Osterloh, F.E.; Kovnir, K. *mP*- BaP_3 : A New Phase from an Old Binary System. *Chem. Europ. J.* **2014**, DOI: 10.1002/chem.201305078.
 3. Dolyniuk, J.; Kovnir, K. Zintl Salts $\text{Ba}_2\text{P}_7\text{X}$ ($\text{X} = \text{Cl}, \text{Br}, \text{and I}$): Synthesis, Crystal, and Electronic Structure. *Crystals*, **2013**, *3*, 431-442.
 4. Fulmer, J.; Lebedev, O.I.; Roddatis, V.V.; Kaseman, D.; Sen, S.; Dolyniuk, J.; Lee, K.; Olenov, A.V.; Kovnir, K. Clathrate $\text{Ba}_8\text{Au}_{16}\text{P}_{30}$: The "Gold Standard" for Lattice Thermal Conductivity. *J. Amer. Chem. Soc.* **2013**, *135*, 12313-12323.
- This paper has been highlighted in C&EN:*
Clathrate Expands Thermoelectrics List. *C&EN News* **2013**, *91(30)*, 29.
5. Fulmer, J.; Kaseman, D.; Dolyniuk, J.; Lee, K.; Sen, S.; Kovnir, K. BaAu_2P_4 : Layered Zintl Polyphosphide with Infinite (P^-) Chains. *Inorg. Chem.* **2013**, *52*, 7061-7067.

Biaxiality in Nematic and Smectic Liquid Crystals

Satyendra Kumar, Quan Li, and D. M. Agra-Kooijman, Kent State University
Alejandro Rey, McGill University
M. Srinivasarao, Georgia Institute of Technology

Program Scope

This project strives to advance our fundamental understanding of the phenomena of biaxiality and its molecular origin in the nematic and smectic liquid crystals. New bent-core, calamitic, and hybrid mesogens are designed and synthesized to induce biaxial order. They are investigated to understand the role of molecular architecture, symmetry, and organization in the formation of thermodynamically stable LC phases. Models are developed to provide an atomic-to-micro scale characterization to complement experimental studies of their structure, phase transitions, phase diagrams, defects, electro-mechanics, and viscoelasticity.

Recent Progress

Only some of the major advances in understanding molecular organization and relationship between molecular structure and LC phases made under the project are summarized below.

A. Biaxial smectic phases without layer shrinkage: The biaxial SmC phase with large director tilt but no corresponding layer shrinkage was reported [1] in mesogens with a short siloxane terminal segment. The factor that compensates the SmC layer shrinkage remained a mystery for the past ~ 35 yrs. Our recent measurements [Fig. 1] of the nematic order parameters (OPs) $\langle P_2 \rangle$, $\langle P_4 \rangle$, and $\langle P_6 \rangle$ and the orientational distribution function (ODF) show [2, P5] that the ODF becomes narrower in the SmC phase, thereby increasing the effective molecular length and compensating for the increased tilt. Other unexpected results, such as different degree of order and polar tilt of the hydrocarbon and siloxane parts of the molecule, and a hockey-stick molecular conformation were revealed [P5] for the first time. The results suggest that, for a complete description of these phases one needs two orientational, two tilt, and two smectic order parameters.

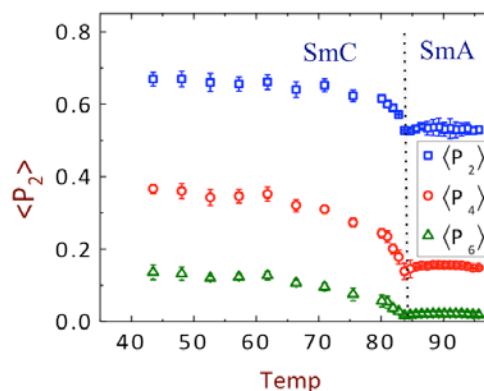


Fig. 1. Temperature dependence of orientational OPs in the SmA and SmC phases.

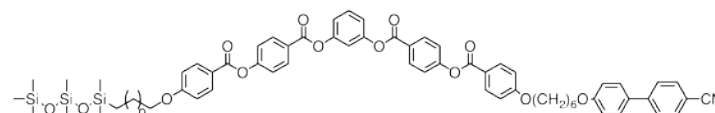


Fig. 2. Hybrid mesogen with siloxane segment forms SmA phase.

Li's group has synthesized over 20 novel bent-core, rod-like, and hybrid trimer mesogens [P18, P19, P26] with and without a siloxane group. A new hybrid trimer [3] with siloxane segment [Fig. 2] forms the de Vries SmA phase. This approach provides a new pathway to the synthesis of families of de Vries smectics, which should help us understand their true nature.

The de Vries materials have never been found to form the N phase. However, based on the molecular tendencies, the N_{tb} phase [4, 5] may prove to be the precursor to the de Vries smectic phases.

B. Twist-bend nematic (N_{tb}): The N_{tb} phase has a unique spiral-like director configuration [4, 5]. It has recently captured the imagination of scientists due to its negative bend elastic constant. We made the first measurements of the nematic OPs as a function of temperature in the nematic phases of the most studied CB7CB system. The results in Fig. 3 show that the three OPs are positive in the higher temperature N phase above $\sim 88^\circ\text{C}$. In the N_{tb} phase, $\langle P_2 \rangle$ and $\langle P_4 \rangle$ decrease, and $\langle P_6 \rangle$ becomes negative leading to a volcano-shaped ODF with the cone angle of approximately 7.5° . This is consistent with theoretical expectations in the N_{tb} and the de Vries Sma phases.

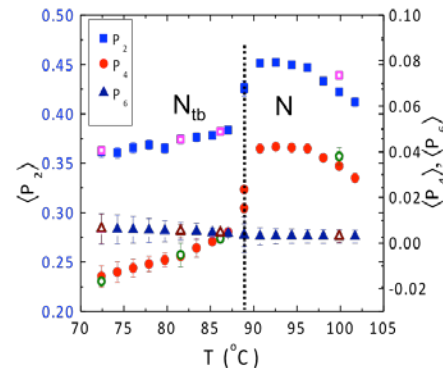


Fig. 3. OPs in the N phases of CB7CB.

A hybrid bent-core trimer mesogen with cyano group at both extremities [Fig. 4] was synthesized to test their role in the formation of the N_{tb} phase. Cyano groups apparently play an important role as this mesogen also exhibits [3] the N_{tb} and N phases.

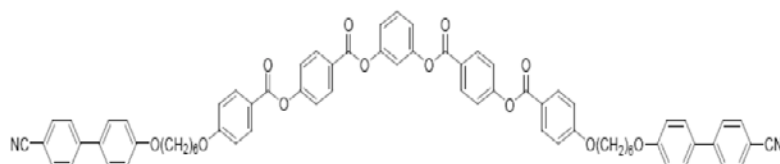


Fig. 4. Hybrid trimer with cyano terminal groups.

C. Measurements of order parameters, visco-elasticity, and defect dynamics: It is important to measure the various order parameter and the dynamics of the nematic and smectic phases discussed above to quantitatively understand them. These properties are traditionally measured with optical and dynamic light scattering (DLS) methods. *Srinivasarao, et al*, are pioneering [6] the use of the *differential dynamic microscopy* (DDM) which has considerable advantages over DLS. DMM enables access to scattering information at very low q (not possible with DLS) and over a wide range of q (dependent on the numerical aperture of the objective) from a single experiment. To test the methodology and fidelity of the technique, experiments were performed on a relatively well known chromonic LC (Sunset Yellow) with 5CB as the reference. There is satisfactory agreement between the DLS data and the DDM data [8].

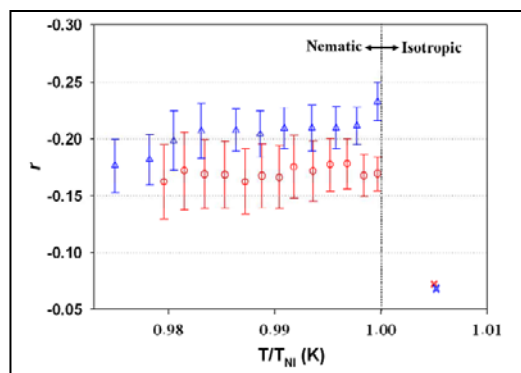


Fig. 5. Variation of “r” through the isotropic nematic phase transition for 5CB and 8CB as calculated from the method of Jones et al. [7]

Rey has used density functional tight binding molecular dynamic simulations to compute the value of differential polarizability ratio “r” in the isotropic and N phases that are in close

agreement, Fig. 5, with the experimentally measured values [7]. *This is the first time for polarized Raman measurements that such an agreement between simulation and experiments has been obtained.* After this initial phase, DDM method will be deployed to investigate the N_{tb} and de Vries SmA and SmC phases.

Future Plans

We will continue the design and synthesis of new series of bent-core dimers and trimers with and without the siloxane and cyano end groups to determine the role of different molecular fragments in the formation of de Vries and biaxial smectic phases as well as the N_{tb} phase. Guided by modeling and the multiscale simulations, quantitative investigations of static and dynamical properties, defects, and the various relevant order parameters will continue with high-resolution x-ray diffraction, Raman, dielectric, and electrooptical measurements. The exciting development of the DMM technique will provide important data to further our understanding of these interesting systems.

References

- [1] A. de Vries and D. L. Fishel, *Mol Cryst Liq Cryst* **16**, 311 (1972).
- [2] H. Yoon, D. M. Agra-Kooijman, K. Ayub, R. P. Lemieux, and S. Kumar, *Phys Rev Lett* **106**, 087801 (2011).
- [3] Y. Wang, H. Bisoyi, D. M. Agra-Kooijman, G. Singh, S. Kumar, & Q. Li, to be submitted.
- [4] D. Chen, J. H. Porada, J. B. Hooper, *et al.*, *Proc Natl Acad Sci USA* **110**, S1 (2013).
- [5] I. Dozov, *EPL* **56**, 247 (2001).
- [6] B.-J. Yoon, M. Smith, J. O. Park, A. Lyon, M. Srinivasarao, to be submitted to *Soft Matter* (2014).
- [7] W.J. Jones, D. K. Thomas, D. W. Thomas, and G. Williams, *J Mol Struct* **708**, 145 (2004).
- [8] K. Nayani, J. O. Park and M. Srinivasarao, to be submitted to *Soft Matter* (2014).

Publications (Titles and DOI #s are given only for the pending manuscripts, to save space.)

- P1. R. Jose, T. J. Patel, T. A. Cather, D. J. Willhelm, J. Grebowicz, H. Han, P. K. Bhowmik, L. Sharpnack, D. M. Agra-Kooijman, and S. Kumar, *Thermotropic mesomorphism in catanionic surfactants synthesized from quaternary ammonium surfactants and sodium dodecylbenzenesulfonate: Effect of chain length and symmetry*, Submitted *J. Colloid and Interface Science* (2014).
- P2. S. Dey, D.M. Agra-Kooijman, W. Ren, O.J. McMullen, A. C. Griffin, and S. Kumar, *Dual relaxation and structural changes under uniaxial strain in a main chain smectic-C elastomer*, Submitted to *Phys. Rev. E* (2014).
- P3. X. Yao, M. Crne, M. S. Park, B.-J. Yoon, J. O. Park and M. Srinivasarao, *Orientational Order of a Lyotropic Chromonic Liquid Crystal with planar alignment by Polarized Raman Spectroscopy*, Submitted to *J. Phys. Chem. (Lett)*, (2014).
- P4. A. Shams, X. Yao, M. Srinivasarao, J. O. Park and A.D. Rey, *Theoretical Predictions of Disclination Loop Growth for Nematic Liquid Crystals under Capillary Confinement*, Submitted to *Phys Rev E* 2014.
- P5. D.M. Agra-Kooijman, G. Sing, A. Lorenz, P.J. Collings, H. Kitzerow, and S. Kumar, *Phys. Rev* **E89**, xxxx (2014); DOI: 10.1103/PhysRevE.00.002500.

- P6. D. M. Agra-Kooijman, H.-Y Yoon, S. Dey, and S. Kumar, *Phys. Rev.* **E89**, 032506 (2014).
- P7. Y. A. Getmanenko, N. Shakya, C. Pokherel, S.-W. Kang, S. Kumar, S. D. Bunge, B D. Ellman, and R. J. Twieg, *J. Mat. Chem. C* **2**, 2600-2611 (2014).
- P8. H. K. Bisoyi and Q. Li, Chap. in *Kirk-Othmer Encyclopedia*, John Wiley & Sons (2014).
- P9. H. K. Bisoyi and Q. Li, Chap. 7 in *Nanoscience with Liquid Crystals: From Self-Organized Nanostructures to Applications*, Q. Li, Editor, Springer (2014).
- P10. Y. A. Getmanenko, S.-W. Kang, N. Shakya, C. Pokherel, S. D. Bunge, S. Kumar, B D. Ellman, and R. J. Twieg, *J. Mat. Chem. C* **2**, 256-274 (2014).
- P11. D.M. Agra-Kooijman and S. Kumar, Chap. 10, *Handbook of Liquid Crystals Vol 1*, editors: Collings, Gleeson, and Goodby, Wiley-VCH Verlag GmbH & Co. KGaA, Weinheim, Germany (2014).
- P12. A. D. Rey and E. E. Herrera-Valencia, *Phil. Trans. Royal Soc. A, Mathematical, Physical and Engineering Sciences*, RSTA-2013-0369, in press (2014).
- P13. A. Shams, X. Yao, M. Srinivasarao, J. O. Park and A.D. Rey, *Soft Matt.* **10**, 3245 (2014).
- P14. A. D. Rey and E. E. Herrera-Valencia, *Soft Matt.*, **10**, 1611-1620 (2014).
- P15. E. E. Herrera-Valencia and A. D. Rey, *ChemPhysChem* **15**, 1405–1412 (2014).
- P16. A. Lorenz, D. M. Agra-Kooijman, N. Zimmermann, H.-S. Kitzerow, D. R. Evans, and S. Kumar, *Phys. Rev.* **E 88**, 062502 (2013).
- P17. R. Jose. T. J. Patel. P. K. Bhowmik, T. A. Cather, R. R. Davilla, J. Grebowicz, S. Han, D. M. Agra-Kooijman, and S. Kumar, *J. Colloid & Interf. Sci.* **411**, 61-68 (2013).
- P18. R. Sun, C. Xue, X. Ma, M. Gao, H. Tian and Q. Li, *J Am Chem Soc* **135**, 5990 (2013).
- P19. H. Bisoyi and Q. Li, *Stimuli Responsive Alignment Control of Semiconducting Discotic Liquid Crystalline Nanostructures*, Chap. 3 in *Intelligent Stimuli Responsive Materials: From Well-defined Nanostructures to Applications*, Q. Li, Ed., John Wiley & Sons, New Jersey, 2013.
- P20. J. He, D. M. Agra-Kooijman, G. Singh, C. Wang, C. Dugger, L. Zang, J. Zeng, L. Zang, S. Kumar, and C. S. Hartley, *J. Mater. Chem. C* **1**, 5833–5836 (2013).
- P21. A.D. Rey, P. Servio and E. E. Herrera-Valencia, *Physical Review E* **87**, 022505 1-12, 2013.
- P22. S. Dey, D.M. Agra-Kooijman, W. Ren, P.J. McMullan, A. C. Griffin, and S. Kumar, *Crystals* **3**, 363-390, (2013).
- P23. A. Lorenz, N. Zimmermann, S. Kumar, S.R. Evans, G. Cook, M. F. Martinez, and H. S. Kitzerow, *Applied Optics* **52**, E1-E5 (2013). Invited article.
- P24. A. Lorenz, N. Zimmerman, S. Kumar, D. R. Evans, G. Cook, M. F. Martinez, and H. S. Kitzerow, *J. Phys. Chem. B* **117**, 937–941 (2013).
- P25. A. Lorenz, N. Zimmerman, S. Kumar, D. R. Evans, G. Cook, and H. S. Kitzerow, *Phys. Rev.* **E 86**, 051704, (2012).
- P26. Y. Wang, H.-G. Yoon, H. K. Bisoyi, S. Kumar and Q. Li, *J. Materials Chemistry* **22**, 20363 (2012).
- P27. B.R. Acharya and S. Kumar, pp 427-448, Chapter 13 in *Liquid Crystals Beyond Displays*, Editor Q. Li, Wiley and Sons (2012).
- P28. A. Shams, X. Yao, J. O. Park, M. Srinivasarao and A.D. Rey, *Soft Mat.* **843**, 11135 (2012).

Project Title: Materials Science of Electrodes and Interfaces for High-Performance Organic Photovoltaics

PI: Tobin J. Marks (Chemistry, Materials Science Depts.), Co-PIs: Robert P.H. Chang (Materials Science Dept.), Arthur J. Freeman (Physics Dept.), Thomas O. Mason (Materials Science Dept.), Kenneth R. Poeppelmeier (Chemistry Dept.), Northwestern University, Evanston, IL 60208

Program Scope

This program is an integrated basic research effort by an experienced, highly collaborative five-PI interdisciplinary team with expertise in solid-state materials chemistry, organic materials and interfaces, quantum theory, solar cell fabrication and characterization, microstructure fabrication, and low temperature materials processing. The team addresses in unconventional ways, critical electrode-interfacial issues underlying organic photovoltaic (OPV) performance parameters—controlling band offsets between transparent electrodes and organics, addressing current loss/leakage problems at interfaces, and implementing new techniques in low temperature and large area cell fabrication to minimize cost. The research goals of this effort are: 1) Theory-guided design and subsequent synthesis of advanced TCOs with high conductivity and transparency but without (or minimizing) the use of indium. 2) Development of a theory-based understanding of the ideal interface between oxide electrodes/interfacial layers and OPV active layers composed of molecules and polymers. 3) Exploration and development of new processing techniques and cell architectures for next-generation large-area flexible OPVs. The goal is to develop for the photovoltaic community the fundamental scientific understanding needed to design, fabricate, prototype, and ultimately test high-efficiency OPV cells incorporating these new concepts.

Recent Progress

Advanced TCOs, GITO. The ternary T-phase ($\text{Ga}_{3-x}\text{In}_{5+x}\text{Sn}_2\text{O}_{16}$, where $0.3 \leq x \leq 1.6$) in the $\text{Ga}_2\text{O}_3\text{-In}_2\text{O}_3\text{-SnO}_2$ (GITO) system is under study in a Poeppelmeier, Mason, Freeman collaboration. Though only moderate conductivity was reported in T-phase GITO at the time of its discovery at Northwestern, recent developments indicate that the conductivity can be optimized by manipulating composition and processing conditions--values approaching 2000 S/cm have been achieved. LDA calculations by Freeman and conductivity + thermopower measurements by Mason indicate that the carrier mobility and Fermi level are essentially invariant with composition and processing conditions. By a combination of first-principles theory and experiment, this is attributed to two offsetting factors--the decrease in fundamental band gap and increase in carrier density (and Burstein-Moss shift) at higher In contents. The bixbyite ($\text{Ga,Sn-doped In}_2\text{O}_3$) phase in the GITO system was also studied. A two-variable regression analysis of the bixbyite lattice parameter was used to determine the phase boundaries of the bixbyite phase in the GITO system and its equilibria with tin oxide, β -gallia, and T-phase GITO (**Fig. 1**).

Transition from crystalline to amorphous InO--Chang in collaboration with Mason and Qin Ma of the Argonne Nat. Lab. APS, has been studying the pure indium oxide which is a progenitor of many TCO systems, including ZITO and GITO. Pure indium oxide (IO) has an advantage over doped systems as it removes the ambiguity and convolution introduced by dopants in analyzing experimental results particularly in the interpretation on EXAFS data. Chang has focused on the study of IO films during the past year. Data gathered from these studies has helped other team members in studies of complex oxides. IO films (typically 350 nm

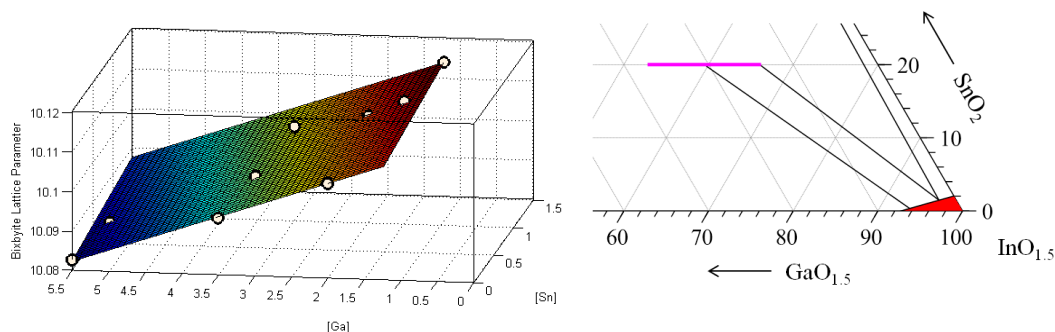


Figure 1. (left) Three-dimensional representation of the two-variable linear regression of the bixbyite lattice parameter (in Å) with substitution of In by Ga and Sn ($R^2_{\text{adj}} = 0.9952$). [Ga] and [Sn] are plotted in atomic percent. (right) Select phases in the In_2O_3 corner of the GITO phase diagram at 1250 °C, showing the refined bixbyite (red) phase boundaries and its equilibria with T-phase (pink) and SnO_2 .

thick) were grown on fused silica substrates in an initial study using IO as a representative bixbyite materials system. As expected, carrier mobility decreases from $\sim 70 \text{ cm}^2/\text{V}\cdot\text{s}$ to $\sim 20 \text{ cm}^2/\text{V}\cdot\text{s}$ as the growth temperature is decreased from 600°C to 100°C. Commensurate with decreased mobility is the degradation in the crystal structure as evidenced by X-ray diffraction. As the temperature falls, a reduction of grain size from $\sim 220 \text{ nm}$ to $\sim 100 \text{ nm}$ is observed with an increase in lattice constant from $\sim 10.05 \text{ \AA}$ to $\sim 10.3 \text{ \AA}$. Only minor changes in the local structure as probed by EXAFS are observed. In the first-shell the In-O coordination number ($N_{\text{In-O}} \sim 6$), In-O bond distance ($R_{\text{In-O}} \sim 2.17 \text{ \AA}$), second shell In-In coordination number ($N_{\text{In-In}} \sim 6$), and In-In bond distance ($R_{\text{In-In}} \sim 3.36 \text{ \AA}$) change little. There is, however, a noticeable increase in the statistical spreads of the In-O and In-In bond distances ($\sigma^2_{\text{In-O}}$ and $\sigma^2_{\text{In-In}}$) from 0.007 \AA^2 to 0.008 \AA^2 and 0.004 \AA^2 to 0.008 \AA^2 respectively. This indicates greater disorder in the regular structure. When the deposition temperature is further decreased (100°C to 25°C), the mobility does not decrease, but increases from $\sim 20 \text{ cm}^2/\text{V}\cdot\text{s}$ to $\sim 50 \text{ cm}^2/\text{V}\cdot\text{s}$, despite the fact that the X-ray diffraction peaks progressively lose intensity and broaden; the grain size continues to decrease to $\sim 50 \text{ nm}$ and the lattice constant increases to $\sim 10.35 \text{ \AA}$. Here $N_{\text{In-O}}$ decreases from ~ 6 to ~ 5.3 , $R_{\text{In-O}}$ decreases from 2.17 \AA to $\sim 2.14 \text{ \AA}$, $\sigma^2_{\text{In-O}}$ remains at $\sim 0.008 \text{ \AA}^2$, $N_{\text{In-In}}$ decreases from ~ 6 to ~ 3.8 , $R_{\text{In-In}}$ remains at $\sim 3.36 \text{ \AA}$ and $\sigma^2_{\text{In-In}}$ increases from $\sim 0.008 \text{ \AA}^2$ to $\sim 0.013 \text{ \AA}^2$. As the fully amorphous region is entered (0°C), no major changes in $N_{\text{In-O}}$, $R_{\text{In-O}}$, $\sigma^2_{\text{In-O}}$, $R_{\text{In-In}}$ or $\sigma^2_{\text{In-In}}$ are observed; $N_{\text{In-In}}$ continues to decrease to ~ 2 . The mobility remains high ($\sim 50 \text{ cm}^2/\text{V}\cdot\text{s}$) suggesting only minor changes in structure versus the slightly crystalline film grown at 25°C. As the deposition temperature is decreased further, the mobility again decreases to $\sim 20 \text{ cm}^2/\text{V}\cdot\text{s}$ at -100°C. Although no changes in the EXAFS parameters are noted, x-ray reflectivity measurements on 65 nm thick IO films indicate the film density decreases as the deposition temperature is lowered beyond the point where amorphous films are first produced.

Flexible Solar Cells with Amorphous ZITO Electrodes---Chang and Marks fabricated the first a-ZITO films on AryLite plastic foils; they have low sheet resistance, high optical transparency, and mechanical flexibility for use in OPV electrodes. These a-ZITO films afford comparable optical and electrical parameters to commercial polycrystalline ITO/glass, and bulk-heterojunction (BHJ) OPVs were fabricated with two representative donor polymers, P3HT and PTB7. Compared to ITO-based devices, the a-ZITO/glass and a-ZITO/AryLite devices exhibit similar performance metrics, yielding flexible OPVs with *PCEs* of 3.63% using P3HT, and a record high flexibility *PCE* = 6.42% using PTB7. Bending measurements on both a-ZITO/AryLite substrates and completed OPVs indicate that the a-ZITO/AryLite substrates retain

low sheet resistance $<30 \Omega/\square$, and the flexible P3HT:PC₆₁BM and PTB7:PC₇₁BMPSC devices retain up to ~90% and ~85%, respectively, of the original PCEs after flexing/relaxing at bending radii of ~5 mm for 10 times. This demonstrates that a-ZITO electrodes can replace the widely utilized polycrystalline ITO, but can add mechanical flexibility characteristics essential for next-generation ultraflexible, roll-to-roll manufacturable OPVs. **Fig. 2** shows properties of the a-ZITO electrodes and OPVs.

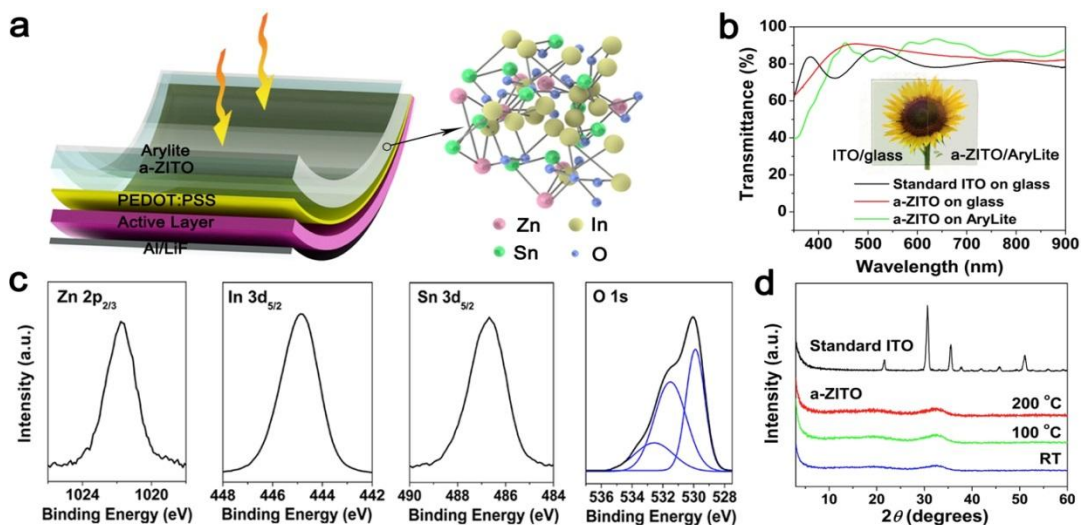


Figure 2. Flexible device architecture, optical transparency, XPS and GIXRD characteristics of a-ZITO films. (a) AryLite/a-ZITO/PEDOT:PSS/Active Layer/LiF/Al device architecture. (b) Comparison of optical transmittance of standard ITO on glass, a-ZiTO/glass, and a-ZITO/AryLite substrates. (c) XPS of spectra of an a-ZITO/AryLite film showing Zn 2p_{2/3}, In 3d_{5/2}, Sn 3d_{5/2}, and O1s peaks. The O1s peak is de-convoluted showing three principal features at 530.0, 531.7, and 532.6 eV. (d) GIXRD scan of a-ZITO/AryLite film measured at room temperature, after annealing at 100 °C, and after annealing at 200 °C, compared to a standard polycrystalline ITO film.

Tunable Electrode Interfacial Layers. With the goal of investigating and enhancing anode performance in BHJ OPV cells, the glass/ITO anodes have been modified with a series of silane-tethered bis(fluoroaryl)amines to form self-assembled interfacial layers (IFLs). The modified ITO anodes were characterized by contact angle measurements, X-ray reflectivity, ultraviolet photoelectron spectroscopy, X-ray photoelectron spectroscopy, grazing incidence X-ray diffraction, atomic force microscopy, and cyclic voltammetry. These techniques reveal the presence of hydrophobic amorphous monolayers of 6.68 to 9.76 Å thickness, and correspondingly modified anode work functions ranging from 4.66 to 5.27 eV. Two series of glass/ITO/IFL/active layer/LiF/Al BHJ OPVs were fabricated with the active layer = P3HT:PC₆₁BM or PTB7:PC₇₁BM. Photovoltaic analysis under AM 1.5G conditions reveals significant performance enhancements versus unmodified glass/ITO and glass/PEDOT:PSS anodes. Strong positive correlations between the electrochemically-derived heterogeneous electron transport rate constants (k_s) and the device open circuit voltage (V_{oc}), short circuit current (J_{sc}), hence OPV power conversion efficiency (PCE), are observed for these modified anodes. Furthermore, the strong functional dependence of the device response on k_s increases as greater densities of charge carriers are generated in the BHJ OPV active layer, which is attributable to enhanced anode carrier extraction in the case of high- k_s interfacial layers.

Publications

1. Buchholz, D. B.; Proffitt, D. E.; Wisser, M. D.; Mason, T. O.; Chang, R. P. H., Electrical and band-gap properties of amorphous zinc–indium–tin oxide thin films. *Prog. Nat. Sci.* **2012**, *22* (1), 1-6.
2. Hoel, C. A.; Buchholz, D. B.; Chang, R. P. H.; Poepelmeier, K. R., Pulsed-laser deposition of heteroepitaxial corundum-type ZITO: cor-In-2 (-) (2x) $Zn_xSn_xO_3$. *Thin Solid Films* **2012**, *520*, 2938-2942.
3. Hopper, E. M.; Sauvage, F.; Chandiran, A. K.; Grätzel, M.; Poepelmeier, K. R.; Mason, T. O., Electrical Properties of Nb-, Ga-, and Y-Substituted Nanocrystalline Anatase TiO_2 Prepared by Hydrothermal Synthesis. *J. Am. Ceram. Soc.* **2012**, *95*, 3192-3196.
4. Lee, B.; Buchholz, D. B.; Chang, R. P. H., An all carbon counter electrode for dye sensitized solar cells. *Energy Environ. Sci.* **2012**, *5*, 6941-6952.
5. Hopper, E.M.; Peng, H.; Hawks, S. A.; Freeman, A. J.; Mason, T. O., Defect mechanisms in the $In_2O_3(ZnO)_k$ system ($k = 3, 5, 7, 9$). *J. Appl. Phys.* **2012**, *112*, 093712.
6. Yoon, S. M.; Lou, S. J.; Loser, S.; Smith, J.; Chen, L. X.; Facchetti, A.; Marks, T., Fluorinated Copper Phthalocyanine Nanowires for Enhancing Interfacial Electron Transport in Organic Solar Cells. *Nano Lett.* **2012**, *12*, 6315-6321.
7. Buchholz, D. B.; Zeng, L.; Bedzyk, M. J.; Chang, R. P. H., Differences between amorphous indium oxide thin films. *Prog. Nat. Sci.* **2013**, *23*, 475-480.
8. Hopper, E. M.; Zhu, Q.; Gassmann, J.; Klein, A.; Mason, T. O., Surface electronic properties of polycrystalline bulk and thin film $In_2O_3(ZnO)_k$ compounds. *Appl. Surf. Sci.* **2013**, *264* (0), 811-815.
9. Song, C. K.; White, A. C.; Zeng, L.; Leever, B. J.; Clark, M. D.; Emery, J. D.; Lou, S. J.; Timalina, A.; Chen, L. X.; Bedzyk, M. J.; Marks, T. J., Systematic Investigation of Organic Photovoltaic Cell Charge Injection/Performance Modulation by Dipolar Organosilane Interfacial Layers. *ACS Applied Materials & Interfaces* **2013**, *5*, 9224-9240.
10. Dolgonos, A.; Lam, K.; Poepelmeier, K. R.; Freeman, A. J.; Mason, T. O., Electronic and optical properties of $Ga_{3-x}In_{5+x}Sn_2O_{16}$: An experimental and theoretical study. *J. Appl. Phys.* **2014**, *115*, 013703.
11. Loser, S.; Valle, B.; Luck, K. A.; Song, C. K.; Ogien, G.; Hersam, M. C.; Singer, K. D.; Marks, T. J., High-Efficiency Inverted Polymer Photovoltaics via Spectrally Tuned Absorption Enhancement. *Adv. Energy Mater.* **2014**, in press, DOI: 10.1002/aenm.201301938.
12. Zhou, N.; Buchholz, D. B.; Zhu, G.; Yu, X.; Lin, H.; Facchetti, A.; Marks, T. J.; Chang, R. P. H., Ultraflexible Polymer Solar Cells Using Amorphous Zinc–Indium–Tin Oxide Transparent Electrodes. *Adv. Mater.* **2014**, *26*, 1098-1104.
13. Dolgonos, A.; Wells, S. A.; Poepelmeier, K. R.; Mason, T. O., Phase Stability and Optoelectronic Properties of the Bixbyite Phase in the Gallium-Indium-Tin-Oxide System, *J. Am. Ceram. Soc.*, **2014**, submitted for publication.
14. Song, C.K.; Luck, K.A.; Zhou, N.; Zeng, L.; Manley, E.; Heitzer, H.M.; Goldman, S.; Hersam, M.C.; Chang, R.P.H.; Bedzyk, M.J.; Chen, L.X.; Ratner, M.A.; Marks, T.J.; “Supersaturated” Self-Assembled Charge-Blocking Layers for Organic Solar Cells, *Am. Chem. Soc.*, **2014**, submitted for publication
15. Kim, M.-G.; Zhou, N. Loser, S.C.; Yoshida H.; Smith J. Guo, X.; Song, C. K.; Jin, H; Yoon S. M.; Freeman, A. J.; Chang, R. P. H.; Facchetti, A.; Marks, T.J. Amorphous Oxide Interfacial Layers in Inverted Organic Solar Cells. Energy Level Tuning to Match Organic Active Layer Components, **2014**, submitted for publication.

Leveraging Kinetic Control in the Assembly and Sorption Properties of Nanostructured Porous Materials

Principal Investigator: Adam J. Matzger

Co-Investigator: Antek G. Wong-Foy

Department of Chemistry and the Macromolecular Science and Engineering Program

University of Michigan, Ann Arbor, MI 48109-1055

Program Scope

The overarching theme of the program is to develop, understand, and deploy new methods for sorbent synthesis. The development of new high performance sorbents is critical for a variety of established (separations, purification) and emerging (hydrogen storage, carbon capture) technologies. Coordination polymers offer tremendous promise for such applications and complement greatly established materials such as zeolites and carbons. The specific goal of this program is to develop an understanding of how kinetic control elements can be leveraged to improve MCP synthesis. A major issue is control over phase selection by manipulating the kinetic pathways leading to phase formation thereby affording access to advanced sorbents from simple feedstocks. In a second aspect of the work we are developing an approach to interface crystalline MCPs with soft materials, such as polymers, by leveraging some of our developments in the area of mixed linker MCPs.

Recent Progress

MCP phase direction by timed addition of non-coordinating organic linker

The formation of the MCPs by existing synthetic methods relies on secondary building unit (SBU) assembling with one or more organic linkers. The SBU assembles dynamically whereas the linker, with the exception of conformational changes, is static. However, if the ligand structure can change, then competition among assembly of different ligand structures as well as different SBUs has the potential to lead to a rich structural landscape. To test this notion, we chose a system based on the prototype benzene tribenzoic acid (H₃-BTB) linker (used for MOF-177¹ synthesis) where the H₃-BTB linker is modified with a non-coordinating second mode of reactivity – an amine functionality. We envisioned that formation of different MCP phases can be achieved by the timed addition of an organic ligand that can only react with non-coordinating amine functionality on the linker. Thus the incubation time of the two components (linker and organic ligand) may control the overall MCP structure. To examine this concept a dialdehyde (terephthalaldehyde) was added after various delay times into the reaction mixture containing a Zn(II) metal salt and the amine modified H₃-BTB linker. Different addition times yield 2 morphologically different phases (Figure 1): yellow colored needle-shaped phase I at early delay times and block-shaped phase II at the later stages of addition. An X-ray diffraction study revealed that phase I consists of octahedral Zn₄O(O₂CR)₆ SBUs linked together by two amine modified BTB linkers condensed with a single terephthalaldehyde residue *via* imine linkages (Figure 2) and phase II is amine functionalized MOF-177. Similarly, orange colored

needle shaped crystals were observed by employing anthracene-9,10-dialdehyde which is isostructural with phase I.

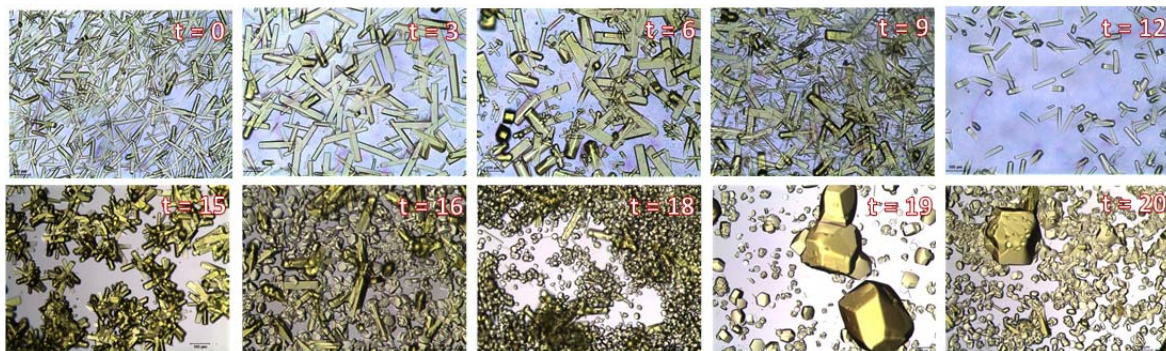


Figure 1. Optical micrographs of phase I and phase II at different delay times (t in hours), of terephthalaldehyde addition. Total reaction time was 30 hours.

From these images we can see that diimine formation, a step in formation of some covalent organic frameworks (COFs), outcompetes the coordination chemistry, under these conditions. These MCPs are permanently porous and exhibit Type I N_2 gas sorption isotherms for the guest free materials. The experimental surface areas of phase I, phase II and the phase derived from anthracene-9,10-dialdehyde are 2820, 4631 and 2520 m^2/g respectively.

An array of commercially available or readily accessible poly (di, tri, tetra)-aldehydes and amine functionalized linkers suggest that the above approach may be generalizable.

Controlled phase selection by linker mixing to thwart interpenetration.

Open space in MCPs is the key to their sorptive properties but also limits aspects of their performance. If pores are too large they can offer only a weak attractive potential for gases, and residual void space after sorption leads to poor volumetric sorption capacity. For example, we have recently discovered that IRMOF-8, a cubic MCP derived from commercially available components, can be obtained with extremely high surface area using a combination of room temperature synthesis and a flowing supercritical CO_2 activation.² Examining residual porosity by positron annihilation lifetime spectroscopy reveals that for IRMOF-8, the pore filling during methane adsorption stops after monolayer coverage.³ We hypothesized that the uptake of IRMOF-8 would improve if additional sorptive sites were introduced to occupy the wasted pore space. To test this notion, functional groups were appended to naphthalene-2,6-dicarboxylate

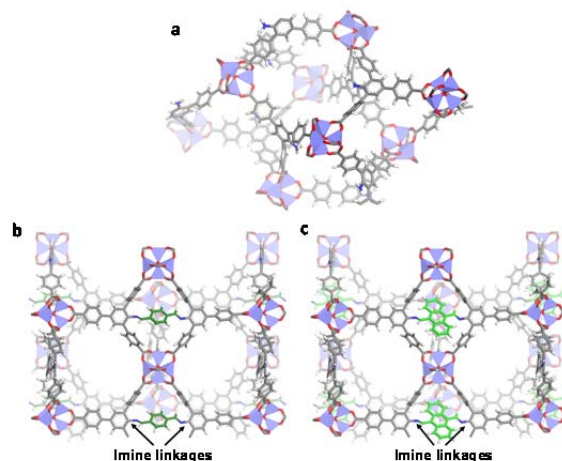


Figure 2. Structures of MCPs from X-ray diffraction: a) block shaped phase II b) yellow needle-shaped phase I and c) orange needle shaped phase from anthracene-9,10-dialdehyde.

(NDC) to produce *t*BuNDC and PhNDC (fig. 3). It was hypothesized that the *t*butylethynyl or phenylethynyl functional groups would occupy the central part of the pore and serve as additional adsorptive surfaces. Moreover, the presence of these functional groups was hypothesized to prevent network interpenetration; this was indeed borne out and now non-interpenetrated IRMOF-8 derivatives can be prepared rapidly at high temperature and at relatively high concentrations (Figure 3).

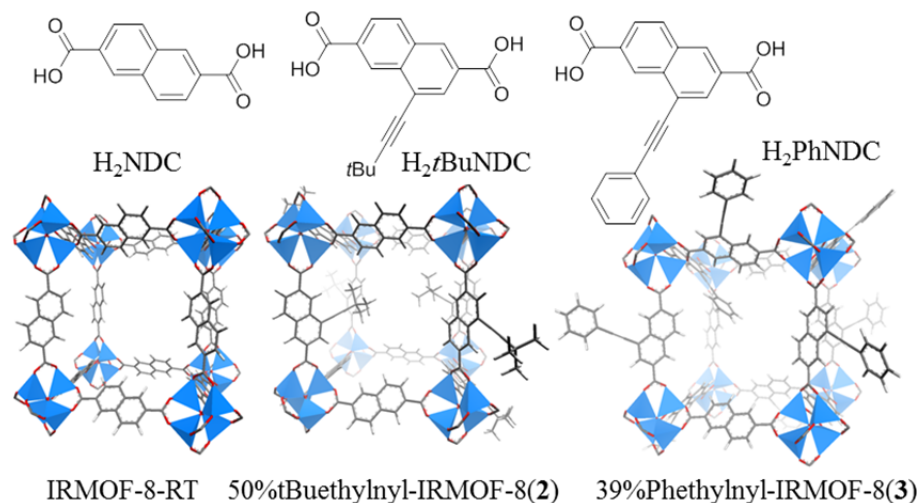


Figure 3. (a) Chemical structures of linkers: H₂NDC, H₂*t*BuNDC, and H₂PhNDC (b) Models of IRMOF-8-RT, 50% *t*Buethynyl-IRMOF-8 (2): composed of a mixture of NDC and *t*BuNDC linkers in a 1:1 ratio, and 39% Phethynyl-IRMOF-8 (3): composed of a mixture of 61% NDC and 39% PhNDC linkers

Indeed, the series of *t*Buethynyl-IRMOF-8 and Phethynyl-IRMOF-8 were prepared by solvothermal reactions at 85 °C using mixtures of different ratio of NDC and functionalized linkers. All of the MCPs in the series possess high surface area (>3200 m²/g), suggested that non-interpenetrated MCPs have been archived using this method. Among those MCPs prepared, 100% *t*Buethynyl-IRMOF-8 (1), 50% *t*Buethynyl-IRMOF-8 (2), and 39% Phethynyl-IRMOF-8 (3) were chosen to study methane adsorption due to their high BET surface (3346-4095 m²/g) areas and high concentrations of the mixed linkers.

At room temperature, IRMOF-8-RT has a methane uptake of 114 cc/cc at 58 bar. Complete substitution of NDC by *t*BuNDC results in the significant change of the methane isotherm. As compared to IRMOF-8-RT, **1** can adsorb more methane at low pressures and reached saturation sooner. Despite the fact that **1** can adsorb more methane at lower pressure compared to IRMOF-8-RT, its methane uptake capacity was not significantly enhanced, especially at high pressure. At 60 bar, RT **1** has the excess volumetric uptake of 121 cc/cc, only 6% higher than the uptake of IRMOF-8 under similar conditions. The materials **2** and **3**, on the other hand, showed significant improvement in excess volumetric uptake as compared with IRMOF-8-RT. The material **2** has an uptake capacity of 108 cc/cc at 35 bar, which is 25% higher than the amount adsorbed by IRMOF-8-RT under similar conditions. At 60 bar, **2** can achieve an uptake of 133 cc/cc, 16% higher than the uptake of IRMOF-8-RT. Finally, **3** has considerably higher methane uptake compared with IRMOF-8-RT. In particular, methane capacities of 107

cc/cc (24% improvement) and 134 cc/cc (17% improvement) were obtained at 35 bar and 60 bar, respectively. These studies validate the use of judicious pore filling to enhance guest uptake.

Future Plans

In year 2 of the program attention is turning to the problem of using temporal control over addition of linkers in systems where multiple metal-linker coordination modes are locally identical (for example metal-carboxylate) but new topologies can be realized though pushing non-default coordination modes of three or more building blocks. Our work on interfacing organic polymers with coordination polymers are also starting to yield fruit and it is anticipated that diffusional control of guest molecule access to the porous coordination polymer core will be demonstrated this year. The highest priority areas for development are demonstrating substantially defect-free coating methodology and kinetically controlled selection of competitive sorbates by polymer-mediated diffusion.

References

1. Chae, H. K.; Siberio-Perez, D. Y.; Kim, J.; Go, Y.; Eddaoudi, M.; Matzger, A. J.; O'Keeffe, M.; Yaghi, O. M. A route to high surface area, porosity and inclusion of large molecules in crystals. *Nature* **2004**, *427*, 523-527.
2. Feldblyum, J. I.; Wong-Foy, A. G.; Matzger, A. J. "Non-Interpenetrated IRMOF-8: Synthesis, Activation, and Gas Sorption," *Chem. Commun.* **2012**, *48*, 9828-9830.
3. Feldblyum, J.I.; Dutta, D.; Wong-Foy, A.G.; Dailly, A.; Imirzian, J.; Gidley, D. W.; Matzger, A. J., "Interpenetration, Porosity, and High-Pressure Gas Adsorption in $Zn_4O(2,6\text{-naphthalene dicarboxylate})_3$ " *Langmuir*, **2013**, *29*, 8146-8153.

Publications

- Dutta, A.; Wong-Foy, A. G.; Matzger, A. J., "Coordination Copolymerization of Three Carboxylate Linkers into a Pillared Layer Framework" *Chem. Sci.* **2014**, *Submitted*.
- Guo, P.; Wong-Foy, A. G.; Matzger, A. J., "Microporous Coordination Polymers as Efficient Sorbents for Air Dehumidification" *Langmuir*, **2014**, *30*, 1921-1925.
- Feldblyum, J.I.; Dutta, D.; Wong-Foy, A.G.; Dailly, A.; Imirzian, J.; Gidley, D. W.; Matzger, A. J., "Interpenetration, Porosity, and High-Pressure Gas Adsorption in $Zn_4O(2,6\text{-naphthalene dicarboxylate})_3$ " *Langmuir*, **2013**, *29*, 8146-8153.
- Dutta, D.; Feldblyum, J.I.; Gidley, D.W.; Imirzian, J.; Liu, M.; Matzger, A.J.; Vallery, R.S.; Wong-Foy, A.G., "Evidence of Positronium Bloch States in Porous Crystals of Zn_4O -Coordination Polymers" *Phys. Rev. Lett.* **2013**, *110*, 197403.
- Liu, B.J.; Wong-Foy, A.G.; Matzger, A.J., "Rapid and enhanced activation of microporous coordination polymers by flowing supercritical CO_2 " *Chem. Commun.* **2013**, *49*, 1419-1421.

Charge Recombination, Transport Dynamics, and Interfacial Effects in Organic Solar Cells

Alan J. Heeger, Guillermo C. Bazan, Thuc-Quyen Nguyen, Fred Wudl, University of California, Santa Barbara (UCSB)

Program Scope

The objective of this program is to take advantage of new device strategies, function-specific materials, and interfacial phenomena to improve the performance (open circuit voltage, short circuit current, fill-factor (FF) and power conversion efficiency) of polymer-based photovoltaic devices fabricated by processing all layers from solution. Fundamental understanding of charge generation, transport, and recombination dynamics in thin film bulk heterojunction (BHJ) polymer:fullerene blends and in solar cells made from such BHJ blends will be studied using transient photoconductivity and impedance spectroscopy. Conjugated polyelectrolyte and oligoelectrolyte interlayers are used to improve open-circuit voltage and fill factor in BHJ solar cells with an emphasis on establishing a deeper understanding of the working mechanism. Sensitive probes and experimental methods that enable detailed characterization of the interfaces, the local molecular organization and the charge generation at the nanoscale provide details of the structure/property relationships across multiple length scales.

Recent Progress

Our recent research efforts have focused on the understanding of interfacial properties with different approaches and experimental methodologies. In order to tackle charge extraction in OPVs, we established a versatile strategy to modify organic/metal interfaces by incorporating CPEs,¹⁻⁵ metal oxides,⁶⁻⁹ or by solvent treatments.^{10,11} Figure 1 illustrates device structures of OPVs upon various active layer/electrode interface modifications using CPEs, solvent treatment, Barium or Calcium, and ZnO or MoOx. PEDOT:PSS has been used as a conductive hole injection/extraction layer atop ITO substrates for both OLEDs and OPVs, respectively. However, the acidic and hygroscopic nature of PEDOT:PSS tends to induce chemical instability between the active layer and electrodes. For example, PEDOT:PSS has been shown to interact with some organic semiconductors especially those containing basic functional groups or atoms; therefore, reducing both device performance and device lifetime. Recently, we discovered that a thin layer (< 10 nm) of self-doped CPEs developed for thermoelectric application can be used effectively as hole extraction to replace PEDOT:PSS in BHJ solar cells (Figure 1, top panel, middle). The HOMO of this CPE is 4.9 eV similar the work function of the PEDOT:PSS.

We attain equal or better PCE for conjugated polymer and small molecule based on 7,7'-(4,4-bis(2-ethylhexyl)-4H-silolo[3,2-b:4,5-b']dithiophene-2,6-diy)bis(6-fluoro-4-(5'-hexyl-[2,2'-

yl)benzo[*c*][1,2,5]thiadiazole), (*p*-DTS(FBTTh₂)₂), blended with [6,6]-phenyl C₇₁ butyric acid methyl ester (PC₇₁BM) BHJ devices when compared to devices using the commercial PEDOT:PSS.¹² For these small molecule devices, incorporation of the CPE-

K interlayer leads to reduced bulk resistivity and series resistance R_s as well. R_s decreases from 2.2 $\Omega \text{ cm}^2$ to 1.7 $\Omega \text{ cm}^2$ when replacing PEDOT:PSS hole transporting layer (HTL) with **CPE-K** HTL resulting in a better FF, beneficial for the device performance (Figure 2).

The properties of CPE thin films were characterized by different methods including atomic force microscopy (AFM) and conducting-AFM (c-AFM). C-AFM was employed to study the local charge transport in the vertical direction in PEDOT:PSS HTL and **CPE-K** HTL. Current images of PEDOT:PSS and **CPE-K** thin films measured at +50 mV are comparatively shown in Figure

3a and 3b. For c-AFM, the current was measured by applying a positive bias to the ITO substrates while keeping the Au tip grounded. Due to the deep work function of Au (5.1 eV) and ITO (4.9 eV), the current is mainly carried by holes and electron injection is effectively blocked. The magnitude of current in c-AFM then indicates the local hole conductivity of the HTLs. It has been found that the vertical electrical conductivity in spin-cast PEDOT:PSS thin films is up to 3 orders lower than that along the parallel direction, due to the lamellar structure of PEDOT and the insulating PSS. The anisotropy in electrical conductivity is preferentially reduced in **CPE-K**, which is

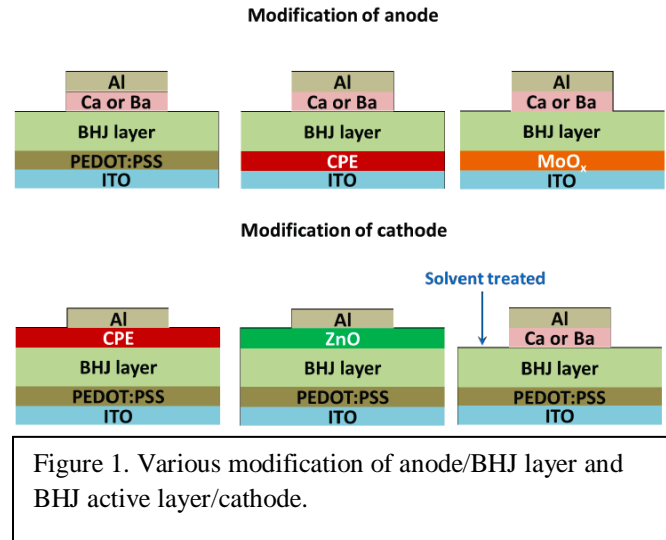


Figure 1. Various modification of anode/BHJ layer and BHJ active layer/cathode.

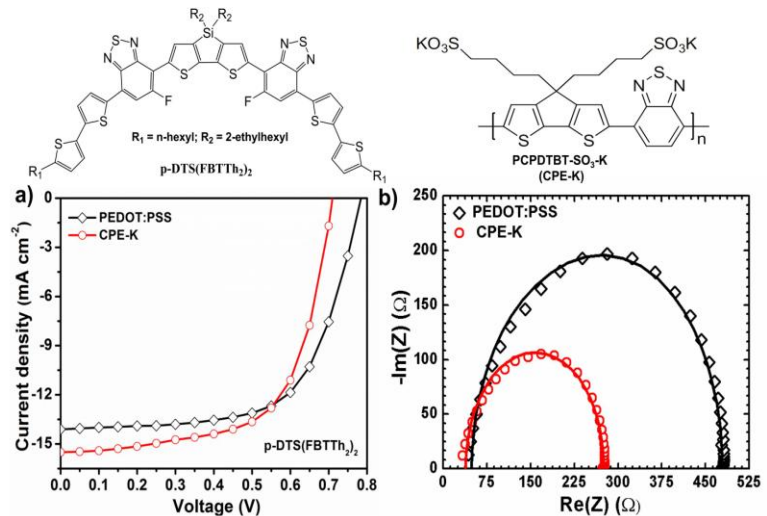


Figure 2. Chemical structures of the molecular donor and the self-doped CPE CPE-K interfacial agent. (a) J-V curves of solar cells comprising of active layers of p-DTS(FBTTh₂)₂ incorporating PEDOT:PSS or CPE-K HTLs. (b) Impedance spectra (Nyquist plots) of p-DTS(FBTTh₂)₂:PC₇₁BM using PEDOT:PSS and CPE-K as the hole transport layer.

attributed to the self-doping occurring in the polymer backbone. The **CPE-K** is much more conductive than PEDOT:PSS (Figure 3b). The higher and more uniform hole conduction in **CPE-K** help improve the hole extraction and consequently the J_{sc} in the solar cell when using the **CPE-K** as HTLs.

The advantages of the highly conductive CPE over PEDOT:PSS are more obvious for devices based on a donor material with electron-rich units such as pyridyl[2,1,3]thiadiazole (PT). The feature of being neutral helps prevent protonation of the active layer due to the present PT group. Because of the self-doping mechanism, the electron conduction in **CPE-K** is not only high ($\sigma=1.5\times 10^{-3}$ S/cm at 300K) but homogenous. Such electrical property is beneficial for the minimization of voltage losses in the actual device.

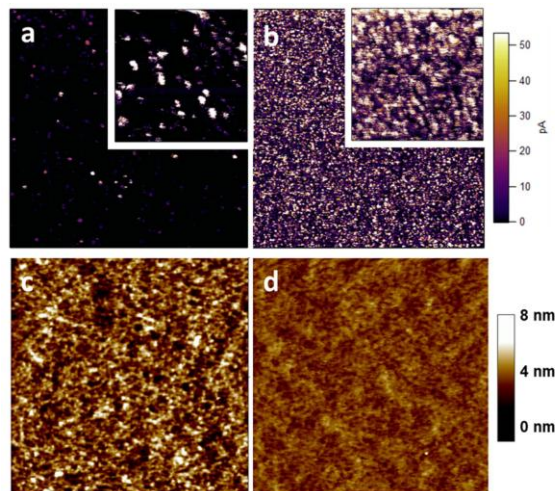


Figure 3. Current images (size: $1\ \mu\text{m} \times 1\ \mu\text{m}$) of PEDOT:PSS (a) and CPE-K (b) HTLs on ITO. Insets show current images in small area scan ($0.25\ \mu\text{m} \times 0.25\ \mu\text{m}$) at +1 V for PEDOT:PSS and at +50 mV for CPE-K.

Future Plans

This technological breakthrough provides the motivation to conduct a systematic study of the internal and surface properties of these novel materials and their impact in different type of metal contacts and optoelectronic devices. We plan to examine interlayer properties as a function of different processing conditions and chemical structure by using scanning microscopy techniques that yield information on structural features, surface potential and nanoscale conductivity.

References

- 1) Seo, J. H., Namdas, E. B., Gutacker, A., Heeger, A. J. & Bazan, G. C. *Adv. Funct. Mater.* **21**, 3667–3672 (2011).
- 2) Seo, J. H., Gutacker, A., Sun, Y., Wu, H., Huang, F., Cao, Y., Scherf, U., Heeger, A. J. & Bazan, G. C. *J. Am. Chem. Soc.* **133**, 8416–8419 (2011).
- 3) Seo, J. H., Yang, R., Brzezinski, J. Z., Walker, B., Bazan, G. C. & Nguyen, T.-Q. *Adv. Mater.* **21**, 1006 (2009).
- 4) Seo, J. H., Gutacker, A., Walker, B., Cho, S., Garcia, A., Yang, R., Nguyen, T.-Q., Heeger, A. J. & Bazan, G. C. *J. Am. Chem. Soc.* **131**, 18220 (2009).
- 5) Henson, Z. B., Zhang, Y., Nguyen, T.-Q., Seo, J. H. & Bazan, G. C. *J. Am. Chem. Soc.* **135**, 4163 (2013).
- 6) Kyaw, A. K. K., Wang, D. H., Gupta, V., Zhang, J., Chand, S., Bazan, G. C. & Heeger, A. J. Efficient Solution-Processed Small-Molecule Solar Cells with Inverted Structure. *Adv. Mater.*

25, 2397 (2013).

7) Jasieniak, J. J., Seifert, J., Jo, J., Mates, T. & Heeger, A. J. *Adv. Funct. Mater.* **22**, 2594 (2012).

8) Kyaw, A. K. K., Wang, D. H., Gupta, V., Leong, W. L., Ke, L., Bazan, G. C. & Heeger, A. J. *Acs Nano* **7**, 4569 (2013).

9) Kyaw, A. K. K., Wang, D. H., Wynands, D., Zhang, J., Nguyen, T.-Q., Bazan, G. C. & Heeger, A. J. *Nano Lett.* **13**, 3796 (2013).

10) Zhou, H., Zhang, Y., Seifert, J., Collins, S. D., Luo, C., Bazan, G. C., Nguyen, T.-Q. & Heeger, A. J. High-Efficiency Polymer Solar Cells Enhanced by Solvent Treatment. *Adv. Mater.* **25**, 1646 (2013).

11) X. Liu, W. Wen & Bazan, G. C. *Adv. Mater.* **24**, 4505 (2012).

12) Zhou, H., Zhang, Y., Mai, C.-K., Collins, S. D., Nguyen, T.-Q., Bazan, G. C. & Heeger, A. J. *Adv. Mater.* **26**, 780 (2014).

Publications

1. Jason Seifert, Yanming Sun, and Alan J. Heeger, "Transient Photocurrent Response of Small-Molecule Bulk Heterojunction Solar Cells", *Adv. Mater.* **2014**, online. DOI: 10.1002/adma.201305160
2. C. Zhong, F. Huang, Y. Cao, D. Moses, and Alan J. Heeger, "Role of Localized States on Carrier Transport in Bulk Heterojunction Materials Comprised of Organic Small Molecule Donors", *Adv. Mater.* **2014**, online. DOI: 10.1002/adma.201304791.
3. L.T. Dou, Y. H. Zheng, X. Q. Shen, G. Wu, K. Fields, W. C. Hsu, H. P. Zhou, Y. Yang, and F. Wudl, "Single-Crystal Linear Polymers Through Visible Light-Triggered Topochemical Quantitative Polymerization", *Science* **2014**, *343*, 272.
4. Y. H. Zheng, and F. Wudl, "Organic spin transporting materials: present and future", *J. Mater. Chem. A* **2014**, *2*, 48.
5. C. K. Mai, H. Q. Zhou, Y. Zhang, Z. B. Henson, T.-Q. Nguyen, A. J. Heeger, and G. C. Bazan, "Facile Doping of Anionic Narrow-Band-Gap Conjugated Polyelectrolytes During Dialysis", *Angew. Chem. Int. Ed.* **2013**, *52*, 12874.
6. J. H. Liu, Y. M. Sun, P. Moonsin, M. Kuik, C. M. Proctor, J. S. Lin, B. B. Hsu, V. Promarak, A. J. Heeger, and T.-Q. Nguyen, "Tri-Diketopyrrolopyrrole Molecular Donor Materials for High-Performance Solution-Processed Bulk Heterojunction Solar Cells", *Adv. Mater.* **2013**, *25*, 5898.
7. V. Gupta, A. K. K. Kyaw, D. H. Wang, S. Chand, G. C. Bazan, and A. J. Heeger, "Barium: An Efficient Cathode Layer for Bulk-Heterojunction Solar Cells" *Sci. Rep.* **2013**, *3*, 1965.
8. A. K. K. Kyaw, D. H. Wang, V. Gupta, W. L. Leong, L. Ke, G. C. Bazan, and A. J. Heeger, "Intensity Dependence of Current-Voltage Characteristics and Recombination in High-Efficiency Solution-Processed Small-Molecule Solar Cells", *ACS Nano* **2013**, *7*, 4569.
9. L. G. Kaake, Y. M. Sun, G. C. Bazan, and A. J. Heeger, "Fullerene concentration dependent bimolecular recombination in organic photovoltaic films", *Appl. Phys. Lett.* **2013**, *102*, 133302.
10. H. Q. Zhou, Y. Zhang, J. Seifert, S. D. Collins, C. Luo, G. C. Bazan, T.-Q. Nguyen, and A. J. Heeger, "High-Efficiency Polymer Solar Cells Enhanced by Solvent Treatment", *Adv. Mater.* **2013**, *25*, 1646.

Programming Function in Soft Matter

University of Illinois at Urbana-Champaign

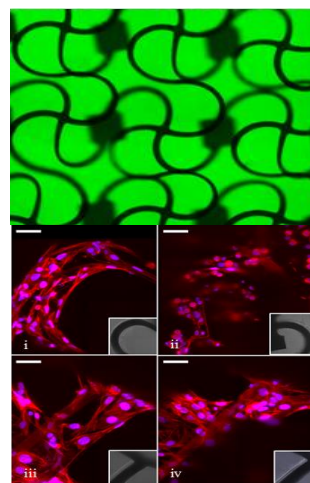
PI and Collaborating Contributors: Ralph G. Nuzzo, John A. Rogers, Jeffrey S. Moore, and K. Jimmy Hsia

Program Scope

The efforts of the current program of work seek to define the mesoscopic design principles that can provide unprecedented forms of functional behavior in soft materials systems—work highlighting explorations of programmable forms of chemomechanical actuation and transduction, as might benefit new methods sensing, detection, and mechanical energy harvesting.

Recent Progress

Recent progress made in collaborative work exploring functional soft materials and new approaches to the fabrication of soft devices have provided insights into the needs for new materials and forms of integration that will be needed to realize high capability modes of performance—ones embedding elements of structure and modes of operation that mimic complex functional behaviors exhibited by biological systems. In this work, the design rules and forms of materials integration involve numerous interesting but generally difficult to realize attributes. These include: the ability to accommodate living systems—cells or microorganisms—as well as highly functional/chemically complex materials; to sustain or manipulate fluid flows; enable dynamic molecular patterning that is elicited both temporally and spatially; embed complex multiscale, non-planar/curvilinear and 3D structural forms; and provide capacities for enabling useful forms of mechanics—flexure, folding, and actuation as examples of issues explored in our work. Our work highlights opportunities for materials integration and device fabrication that exploit emerging capabilities for printing and transfer assembly—methods allowing the construction complex 3D device architectures encompassing nanocomposite materials structures that exhibit “programmable” temporal behaviors. Of particular concern in this work are the needs for new fundamental understandings of the mesoscopic design principles that most beneficially support useful and programmable forms of function in soft devices. Specific examples of recent work that addresses these goals include systems that embed modes of both autonomous and programmable chemomechanical actuation—devices that integrate new classes of soft functional



Curvilinear 3D single-crystalline Si electronics integrating a confluent sheath of fibroblast cells.

composites (e.g. catalytically-coupled actuator materials, biomimetic gels, living cells, etc.) with 3D electronics for sustaining/programming their response.

In an exemplary system illustrating these ideas, we explored a composite 3D architecture in which embedded electronics in poly-N-isopropylacrylamide gel provided an ability to program deformations in non-uniform geometries by the use of highly deformable, embedded electronics with open, serpentine mesh layouts. The work illustrated generalizable design principles for the electronics that provide simple, programmable patterns of localized Joule heating, to control non-uniform swelling and deswelling of the hydrogel. The results demonstrated fully reversible control over diverse 3D shapes in ways that would be difficult to achieve using other approaches and control schemes that can be quantitatively modeled.

Future Plans

In the work conducted going forward we will develop new forms of soft devices, chemomechanical actuators being one class of special interest, that enable a realization of dynamics that, for a soft materials system, are without precedent. For actuators this will entail the development of mesoscopic design principles that can elicit strain dynamics that mimic and ultimately match inspirations afforded by biology (e.g. muscle). This effort will emphasize approaches that can provide optimal mesoscopic organizations of materials structure that most efficiently transduce chemical and thermal energy into useful forms of chemomechanical work. It will highlight efforts in synthesis joined to new forms of fabrication to provide benchmark systems against which theoretical and computational models can be tested. Of particular interest in this work will be the development of actuators that can convert an energy input—photons and electrochemical sources as exemplars—into chemically driven forms of materials dynamics.

Publications

(1) “Electronically Programmable, Reversible Shape Change in Two- and Three-Dimensional Hydrogel Structures,” Yu, C.; Duan, Z.; Yuan, P.; Li, Y.; Su, Y.; Zhang, X.; Pan, Y.; Dai, L. L.; Nuzzo, R. G.; Huang, Y.; Jiang, H.; Rogers, J. A. *Advanced Materials* 2013, 25, 1541-1546 DOI: 10.1002/adma.201204180.

(2) “UV Patternable Thin Film Chemistry for Shape and Functionally Versatile Self-Oscillating Gels,” Yuan, P.; Kuksenok, O.; Gross, D. E.; Balazs, A. C.; Moore, J. S.; Nuzzo, R. G. *Soft Matter* 2013, 9, 1231-1243 DOI: 10.1039/c2sm27100a.

(3) “Synthesis, Assembly and Applications of Semiconductor Nanomembranes,” Rogers, J. A.; Lagally, M. G.; Nuzzo, R. G. *Nature* 2011, 477, 45-53 DOI: 10.1038/nature10381.

(4) “Transfer Printing Techniques for Materials Assembly and Micro/Nanodevice Fabrication,” Carlson, A. W.; Bowen, A. M.; Hong, Y.; Nuzzo, R. G.; Rogers, J. A. *Advanced Materials* 2012, 24, 5284-5318 DOI: 10.1002/adma.201201386.

(5) "Functional Protein Microarrays by Electrohydrodynamic Jet Printing," Shigeta, K.; He, Y.; Sutanto, E.; Kang, S.; Le, A.-P.; Nuzzo, R. G.; Alleyne, A. G.; Ferreira, P. M.; Lu, Y.; Rogers, J. A. *Analyt. Chem.* 2012. 84, 10012-10018 DOI: 10.1021/ac302463p.

Fundamental ion-association and acid-base behavior of aqueous species: Unprecedented perspective from anomalous solubility

May Nyman, Oregon State University

Program Scope

This is a new program; with ~6 months of activity. Ion-association in water is a fundamental process that controls self-assembly and dissolution of aqueous nanomaterials from the incipient state, in both natural and laboratory settings. The overarching goal of this program is to develop fundamental understanding of the complex interrelationship between ion-association, solubility trends, acid-base behavior of oxo, hydroxyl and aqua ligands, and electron transfer. In the early stages of this program, we are utilizing the Group V/VI polyoxometalates (POMs) as model systems for studies, as they are discrete anions that are water soluble, host the full range of aqua ligands, and can be tailored with a range of size and charge density, redox activity, and counterions. Most of our studies are/will be solution-based and include SAX and SWAX (Small-angle X-ray Scattering and Small and Wide angle X-ray Scattering; utilizing both an in-house instrument and Synchrotron facilities), HEXS (synchrotron-based high-energy X-ray scattering), electrochemistry, multi-nuclear and multi-dimensional NMR techniques, conductivity and potentiometry, and Raman spectroscopy. We are also beginning computational and thermochemical components via collaborations.

Recent Progress

Contrasting-ion association and self-assembly behavior of Group V/VI POMs. $[\text{M}_6\text{O}_{19}]^{8-}$ (M=Nb,Ta; also known as the Lindqvist ion, see **figure 1**) is the simplest Group V/VI POM geometry, consisting of a superoctahedron of six mutually edge-sharing MO_6 octahedra. They can be made of salts of any alkali and also tetramethylammonium hydroxide (TMA) and exhibit a reverse solubility trend compared to what we expect: that is, the Cs-salt with maximum ion-association is most soluble, whereas the Li-salt with less ion-association is least soluble. **Figure 2** shows the different types of liquid-phase ion-association as described by Marcus and Hefter.¹ Thus the Group V Lindqvist-ion is ideal for study in order to understand solubility trends and ion-association and specifically address the effect of the *f*-orbital shell that both renders the Nb and Ta POMs absolutely isostructural, yet with vastly different aqueous self-assembly behavior. Prior we have studied² the ion-association behavior of the Nb-analogue, and currently we are studying the Ta-analogue. Their respective aqueous states differ in ways we did not expect; yet the contrasting behavior can be utilized to rationalize differences in the self-assembly of Nb-POMs and Ta-POMs, as well as related materials formed from water. **Figure 3** shows the pair-distance distribution function (PDDF) of Small-Angle X-ray Scattering (SAXS) curves of $[\text{Ta}_6\text{O}_{19}]^{8-}$ solutions along with representative PDDFs for $[\text{Nb}_6\text{O}_{19}]^{8-}$ solutions; and distinct differences are apparent.

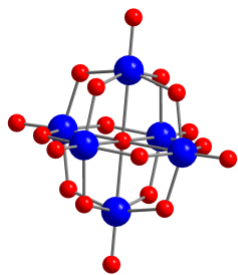


Figure 1. (above) Illustration of $[M_6O_{19}]^{8-}$ ($M=Nb,Ta$) Lindqvist ion. Blue spheres are M; red spheres are O.

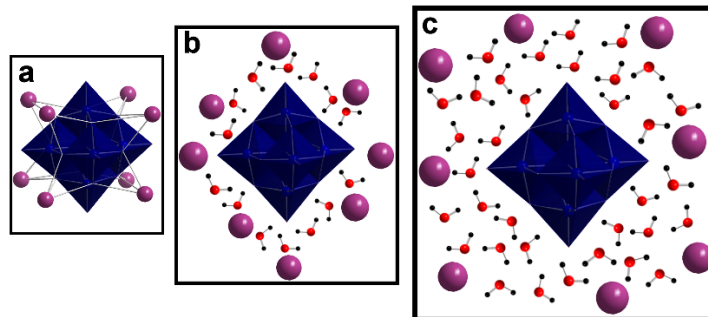


Figure 2. (above) Illustrating different types of ion-pairing between the Lindqvist ion (blue polyhedra) and alkali (purple spheres). Contact ion-pairing (a), solvent shared (b) and solvent-separated (c).

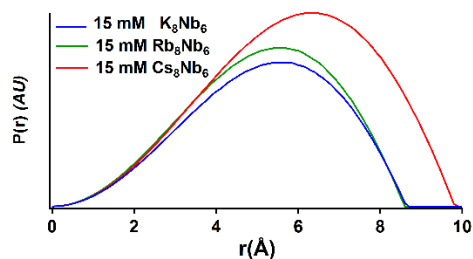


Figure 3 (left). Representative PDDF curves for aqueous solutions of K^+ , Rb^+ and Cs^+ salts of $[Nb_6O_{19}]^{8-}$; showing the classic core-shell profile, due to contact ion-pairing behavior of these cation-anion pairs.

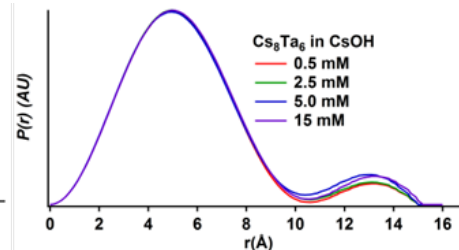
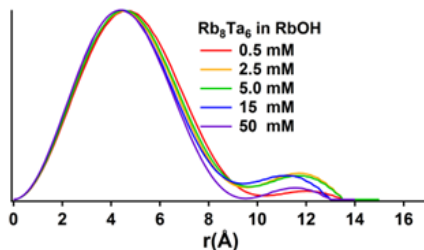
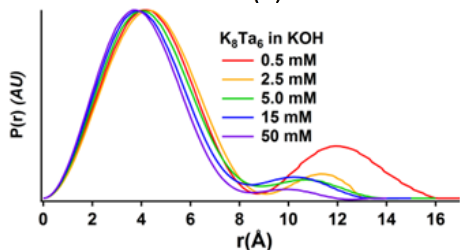


Figure 4 (below). PDDF of K^+ , Rb^+ and Cs^+ salts of $[Ta_6O_{19}]^{8-}$ with varying concentration, showing the dimerization (K^+ only), solvent-separated ion-pairing and solvent-shared ion-pairing of these cation-anion pairs.

While $[Nb_6O_{19}]^{8-}$ solutions show distinct contact ion-pairing between the anionic cluster and counteranion, $[Ta_6O_{19}]^{8-}$ solutions show solvent-separated or solvent-shared ion-association, and even dimerization of the cluster via mutual H-bonding for the lowest concentration of K^+ . The contrasting solution states between Nb and Ta analogues will be discussed with respect to differing solubility and acid-base behavior, as well as self-assembly in water.

The mixed Group V/VI Lindqvist ions $[M_{6-x}W_xO_{19}]^{(8-x)-}$ ($M=Nb,Ta$) affords the opportunity to investigate ion-association and self-assembly processes as a function of counterion in a stepwise manner, as a function of charge-density (charge ranging from 8- to 2-). While synthetic methods have been developed for the Nb-analogues, we are currently developing synthetic methods for Ta-analogues and ion-exchange strategies so solution behavior of all the analogues can be investigated in identical conditions. Ion-association is already playing a significant role in this synthetic study. If the synthesis targeting $[Ta_3W_3O_{19}]^{5-}$ is carried out using Cs-salts of starting materials, the pure *fac*- $[Ta_3W_3O_{19}]^{5-}$ isomer is obtained. On the other hand, if K-salts are utilized, we obtained compositional and isomeric mixtures. Controlling isomeric and compositional purity is very important to be able to produce pure materials for both fundamental and applied science. While the 3:3 W:Ta composition was obtained using synthetic techniques adapted from the analogous niobate chemistry; the 5:1 W:Ta produced different phases entirely; $[TaW_9O_{32}]^{5-}$ and $[Ta_2W_8O_{32}]^{6-}$, shown in **figure 5**. This cluster of a more open and higher

charge-density structure with 4 corner-sharing octahedra in addition to the edge-sharing octahedra, with the TaO₆ octahedra occupying the corner-sharing positions. It is well-known that substituting Nb for W in polyoxoanions decreases the redox activity significantly. This has not been explored for Ta-analogues, due to lack of synthetic strategies for pure and stable compounds. We are interested in both the counterion effect and any possible relativistic effects that differentiate niobate chemistry from tantalate chemistry. Preliminary electrochemical studies of [W₉TaO₃₂]⁵⁻ show a distinct effect of the counterion, see figure below. In Na⁺ electrolyte, there is one redox wave; whereas there are two in the Cs⁺ solution. In comparison to prior^{3,4} electrochemical studies of [W₁₀O₃₂]⁴⁻: this compound also exhibits two redox events, but the reduction potential is much more negative with substitution of a single Ta-atom. Prior computational studies⁵ on [W₁₀O₃₂]⁴⁻ predict the electrons are localized in the ‘belt’ region of the cluster, where the single Ta-cation resides. Since Ta⁵⁺ is far less reducible than W⁶⁺, it will be of interest to perform computational studies to determine if the location of the added electron(s) change by the substitution of Ta for W (see future plans).

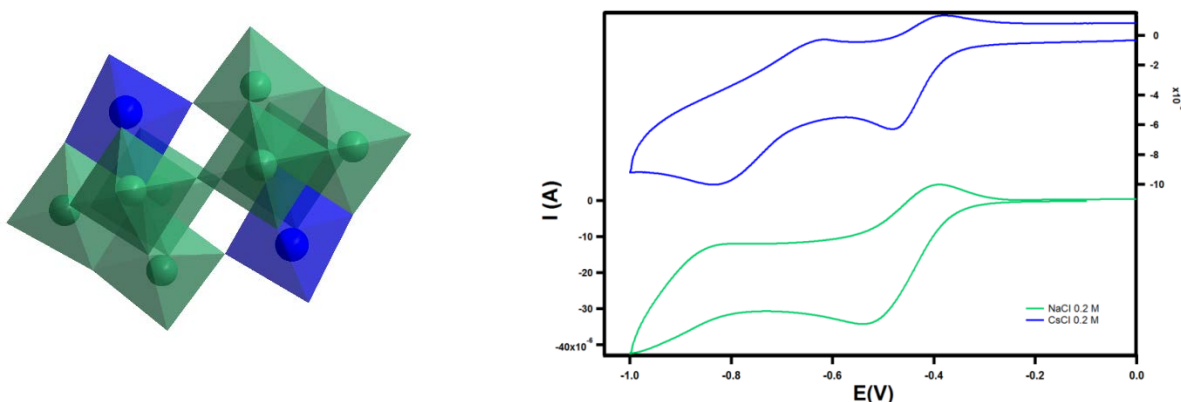


Figure 5. Left: structure of [W₈Ta₂O₃₂]⁶⁻ (blue polyhedral are TaO₆ and green polyhedral are WO₆. Right: cyclic voltammograms of a solution of [W₉TaO₃₂]⁵⁻ in NaCl (green) and CsCl (blue).

Polymerization of clusters into chains, influence of solution conditions. Besides ion-association, another phenomenon that appears to be controlled by charge-density of metal-oxo clusters is its acid-base behavior. In a prior study,⁶ we observed that through proton association, controlled by pH and countercation association, ‘capped’ dodecaniobate Keggin [NbO(GeNb₁₂O₄₀)]¹³⁻ ions link together into chains, via hydrolysis and condensation of the cap oxo-ligands. (see **figure 6**) In the prior studies, the caps were niobyl. We are currently studying the polymerization reaction of a similar cluster with vanadyl caps instead of niobyl caps, [(VO)₂[PNb₁₂O₄₀]]⁹⁻. The theme of this study is to relate the charge-density and chemistry of the ‘cap’ to the polymerization reaction. In the prior study, the niobyl capped clusters protonate when dissolved in water, as observed by the rise in pH. With the Rb-counterion, chain-polymerization is observed. With the Cs-counterion, polymerization is minimal, probably due to a greater degree of ion-association. In a more alkaline solution, the polymerization reaction is inhibited. On the other hand in the current study, the vanadyl-capped clusters do not protonate upon dissolution in water, as evidenced by the neutral self-buffering pH. Likewise, they do not undergo any polymerization. Since these clusters are stable down to ~pH-4, we can acidify the solution; and acidification does indeed induce extensive polymerization. This is evident by the SAXS data in **figure 6**.

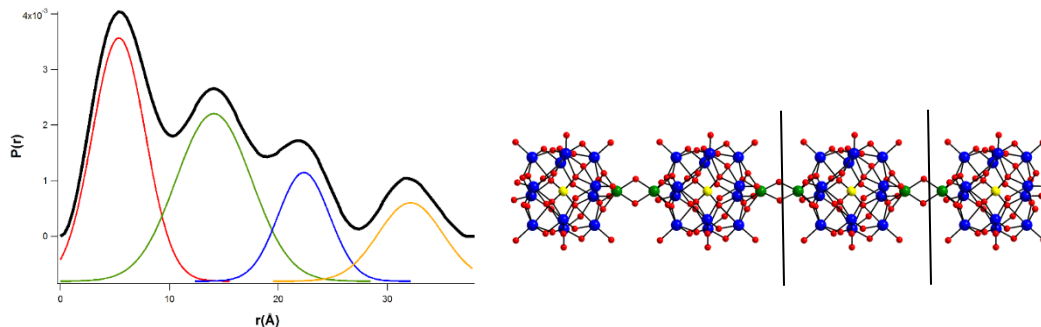


Figure 6. (left) PDDF plot of $[(VO)_2[P Nb_{12}O_{40}]^{9-}]$ at pH-4 that is fitted with four Gaussian curves, each representative in diameter and shape of a single capped Keggin ion. (right): schematic illustration of four polymerized Keggin ions. Between the vertical black lines is a single monomeric, bicapped Keggin ion.

Future Plans Future plans are many; some immediate plans include the following:

- Focused efforts on the Cs-salt of $[Nb_6O_{19}]^{8-}$ including SWAXS and ^{133}Cs NMR studies in aqueous solutions, mixed solvents and in confined inverse micelles to distinguish solution condition effects as well as seek unprecedented phenomena in confined spaces.
- On a series of isostructural clusters with variable charge density based on mixed metal compositions, we will develop synthesis and ion-exchange methods so that direct comparisons can be made in electrochemical response and ion-association.
- We will begin a thermochemical study to delineate the effect of ion association on solubility behavior for our series of compounds. Graduate student Dylan Sures will carry out these studies at U.C. Davis in the lab of Dr. Alex Navrotsky. (will initiate Fall 2014).
- We will submit proposals for SAXS and HEXS beamtime at APS for the Fall/Winter cycle: SAXS for chemical systems that are challenging for our in-house instrument and HEXS to observe atom-atom distances directly in solution and between clusters and counterions.
- We will initiate computational studies in collaboration with Dr. Pere Miro (Jacobs University, Bremen, DE), beginning with elucidating electrochemical behavior of the W-Ta system.

References

- (1) Marcus, Y.; Hefter, G. *Chem Rev* **2006**, *106*, 4585.
- (2) Antonio, M. R.; Nyman, M.; Anderson, T. M. *Angew Chem Int Edit* **2009**, *48*, 6136.
- (3) Gracia, J.; Poblet, J. M.; Fernandez, J. A.; Autschbach, J.; Kazansky, L. P. *Eur J Inorg Chem* **2006**, 1149.
- (4) Chemseddine, A.; Sanchez, C.; Livage, J.; Launay, J. P.; Fournier, M. *Inorg Chem* **1984**, *23*, 2609.
- (5) Vila-Nadal, L.; Sarasa, J. P.; Rodriguez-Forteza, A.; Igual, J.; Kazansky, L. P.; Poblet, J. M. *Chem-Asian J* **2010**, *5*, 97.
- (6) Hou, Y.; Zakharov, L. N.; Nyman, M. *J Am Chem Soc* **2013**, *135*, 16651.

Publications: Two currently being drafted

- **Contrasting Ion-Association Behaviour Between Ta and Nb Polyoxometalates** L. B. Fullmer, P. I. Molina, Mark R. Antonio and M. Nyman: targeted for June 2014 submission to *Chemical Communications*.
- **Charge-density and acid-base influence on synthetic strategies for niobotungstate and tantalotungstate POMs** P. I. Molina, D. Sures, L.N. Zakharov and M. Nyman: targeted for August 2014 submission to *Inorganic Chemistry*

The Dynamic Stoichiometry of Metal Chalcogenide Nanocrystals

Jonathan S. Owen, Columbia University, Department of Chemistry, New York, NY 10025

Program Scope

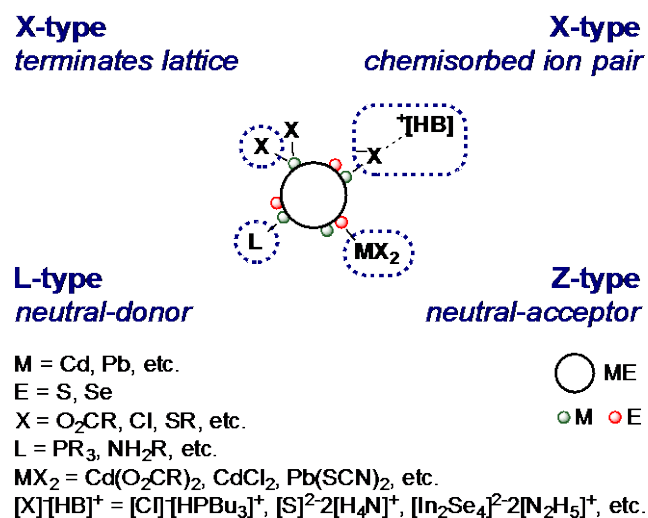
The goal of this project is to understand and control the interplay between nanocrystal stoichiometry, surface ligand binding and exchange, and the optoelectronic properties of semiconductor nanocrystals in solution and in thin solid films. We are pursuing three research directions with this goal in mind: 1) We aim to characterize nanocrystal nonstoichiometry and its influence on the number of L-type and X-type binding sites, the thermodynamics of ligand binding, and the kinetics and mechanisms of ligand exchange. 2) We aim to develop a quantitative understanding of the relationship between surface ligand passivation and photoluminescence quantum yield. 3) We aim to develop methods to replace the organic ligands on the nanocrystal with halide ligands and controllably deposit these nanocrystals into thin films. Electrical measurements on these films will make it possible to evaluate the effect of the nonstoichiometric ligand layer on surface passivation and internanocrystal electronic coupling.

Recent Progress

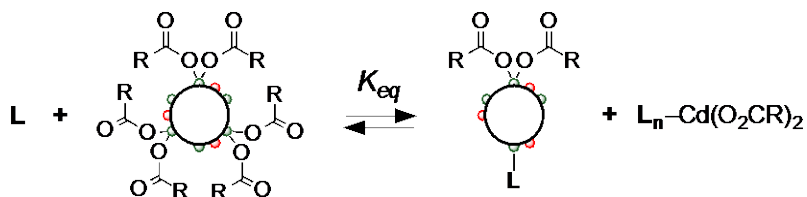
Characterizing and manipulating nanocrystal surfaces is a forefront challenge in nanochemistry and the subject of this grant. We aim to understand the important influence of nanocrystal stoichiometry on nanocrystal coordination chemistry. This approach has led to a more sophisticated ligand coordination model that distinguishes between ligand types using the well-known covalent bond classification method developed by M.L.H Green (Figure 1). Using this model, we aim to describe a coordination chemistry of nanocrystal surfaces, including the reactivity of surface bound ligands and their influence on electronic structure.

Among the novel findings from this study, we have discovered that metal ions found in excess on nanocrystals rapidly and reversibly desorb at room temperature. As a result nanocrystal stoichiometry depends on the concentration and composition of the reaction medium. This is a new dimension in nanocrystal passivation with significant implications for exciton recombination and the design of novel passivating surface structures. We have begun to investigate the influence of stoichiometry on exciton recombination as well as the energy of surface trap states. Two sections below describe what we have learned regarding the reversible binding of surface ligands and how this behavior influences optoelectronic properties, such as photoluminescence.

Figure 1. Nanocrystal ligand classes as described by the covalent bond classification method.^a



Scheme 1. Reversible displacement of $\text{Cd}(\text{O}_2\text{CR})_2$ with neutral donors.^a



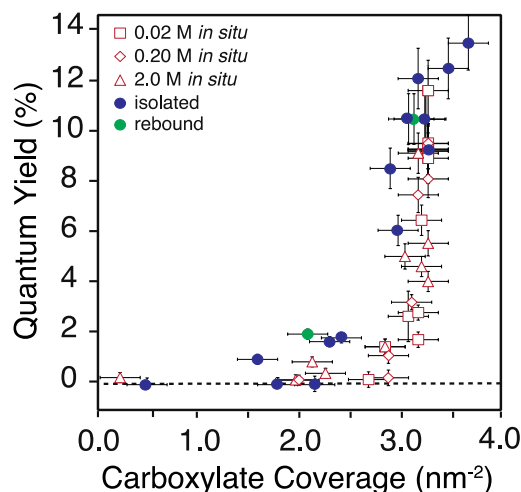
^a Red = surface Se, green = surface Cd, white = a stoichiometric CdSe crystal. L = neutral two electron donor, e.g. amines, phosphines, and other Lewis bases

We discovered that surface cadmium carboxylate complexes reversibly desorb from surfaces at room temperature via a process that is promoted by the binding of L-type ligands to the nanocrystal as well as the solution cadmium complex (Scheme 1). By carefully tuning the displacement equilibrium we isolated nanocrystals with a range of stoichiometries. These samples made it possible to assess the influence of cadmium carboxylate surface coverage on the photoluminescence quantum yield (Figure 2). A very steep dependence was observed that is currently under more careful investigation. Importantly the observed quantum yield could be obtained upon rebinding cadmium carboxylate to the nanocrystals or upon removing cadmium carboxylate from as-synthesized materials. These results help demonstrate that the observed quantum yield is a consequence of the nanocrystals metal-enriched surface structure rather than the method of preparation. Thus, the lability of surface metal carboxylate complexes has significant consequences for nanocrystal electronic structure.

The dependence of photoluminescence quantum yield on ligand coverage shown in Figure 2 is the first quantitative study of its kind. The steep dependence clarifies several important mysteries and raises many interesting questions. Foremost, the assumption that ligand coverage is proportional to the photoluminescence quantum yield is incorrect, undermining previous studies where quantum yield was used to measure ligand binding affinity. More importantly, the photoluminescence quantum yield is very sensitive to coverage near saturation. Combined with the facile displacement reactivity we have observed, it is clear that slight modifications of the solution conditions might only slightly change the formula but will dramatically influence exciton recombination. This conclusion helps explain the large number of conflicting and irreproducible studies of photoluminescence quantum yield. It also clearly demonstrates the importance of careful synthetic and analytical chemistry; nanocrystal scientists must gain precise control over stoichiometry in order to draw general conclusions regarding nanocrystal optoelectronic properties.

In collaboration with Matt Sfeir at Lawrence Berkeley National Laboratory

Figure 2. Dependence of photoluminescence quantum yield on carboxylate coverage. Empty red shapes taken from *in situ* measurements. Filled circles correspond to samples where the coverage was measured after isolation following displacement (blue) or rebinding (green) of $\text{Cd}(\text{O}_2\text{CR})_2$.



we have investigated the charge trapping dynamics in cadmium selenide nanocrystals as a function of cadmium carboxylate coverage (Figure 3). By comparing time resolved photoluminescence and transient absorption data, we demonstrate that decreasing the cadmium coverage increases the rate of hole trapping. Moreover, the trapped hole leads to a long-lived “dark” nanocrystal that undergoes rapid nonradiative recombination upon photoexcitation. A comprehensive kinetic model that accounts for the fraction of “dark” nanocrystals can explain the dependence of the photoluminescence quantum yield on the coverage shown in Figure 2.

Tri-*n*-alkylphosphine bound nanocrystals synthesized in year 1-2 of this project make it possible to directly monitor L-type ligand binding and exchange with ^{31}P NMR spectroscopy. Previous studies of ligand binding to cadmium selenide surfaces have assumed that the fluorescence quantum yield is proportional to ligand coverage, and can be used to estimate binding constants. However, as described above, we have demonstrated this assumption is unreliable, which helps to explain why these studies led to irreproducible and conflicting results. Using ^{31}P NMR spectroscopy we have directly measured relative ligand binding affinities *in situ*: $\text{H}_2\text{NR} \gg \text{PBu}_3 > \text{imidazole} > \text{pyridine} > \text{HNR}_2 > \text{O}=\text{PR}_3 > (\text{SR}_2, \text{OR}_2, \text{CN-R}, \text{NC-R}, \text{NR}_3)$ (Figure 4). These data clearly demonstrate that steric factors play an important role in the binding affinity, while Lewis basicity and hard-soft principles are less important, a novel principle that has little precedent in nanocrystal science. Previous attempts to measure these exchange reactions directly with NMR spectroscopy have not been possible because ligand exchange at cadmium centers is typically much faster than the time resolution of the NMR experiment. As a result, these

Figure 3. Time correlated single photon counting of nanocrystals luminescence and band edge transient absorption bleach recovery versus carboxylate coverage.

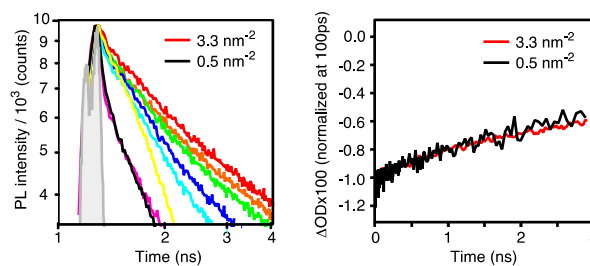
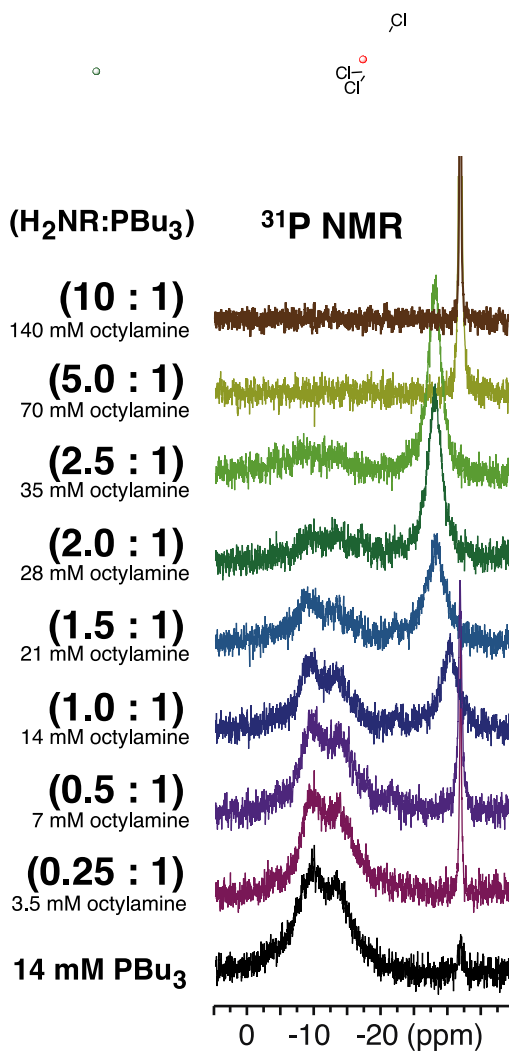


Figure 4. ^{31}P NMR monitoring of Bu_3P displacement with *n*-octylamine.



measurements are the first direct determination of relative ligand affinities for nanocrystal surfaces.

We have discovered that surface bound metal ions are labile and rapidly equilibrate with the solution to reach an equilibrium coverage that depends on concentration. Careful measurements of nanocrystal stoichiometry have shown that photoluminescence quantum yields depend sensitively on the coverage of cadmium carboxylate. Binding of cadmium carboxylate passivates surface selenium atoms and guards against hole trapping. In addition, we have investigated the competitive binding of L-type ligands and determined factors that control the relative affinity for the nanocrystals surface. Steric factors sensitively influence the binding affinities, with the least sterically encumbered ligands having the greatest affinities.

Future Plans

Period three will explore the role of the metal-ligand layer in three ways: 1) We have identified conditions to prepare stoichiometric nanocrystals solely supported by L-type ligands. These materials are being used to investigate the binding of foreign metal ions using NMR spectroscopy. 2) We will use lessons from these studies to prepare thin nanocrystals films, whose transport is influenced by the surface bound metal-ion layers. 3) We will extend these findings to other metal chalcogenide nanocrystals, particularly lead chalcogenides that are under investigation in our labs.

Publications

- (1) “Ligand Exchange and the Stoichiometry of Metal-Chalcogenide Nanocrystals: Spectroscopic Observation of Facile Metal-Carboxylate Binding and Displacement.” Anderson, N. C.; Hendricks, M. P.; Choi, J. J.; Owen, J. S.; *J. Am. Chem. Soc.*, **2013**, *135*, 18536-18548.
- (2) “Soluble Chloride-Terminated Cadmium Selenide Nanocrystals: Ligand Exchange Monitored by ^1H and ^{31}P NMR spectroscopy” Anderson, N.C.; Owen, J.S.; *Chem. Mater.*, **2013**, *25*, 69-76.

Activation of Hydrogen under Ambient Conditions by Main Group Molecules

Philip P. Power
Department of Chemistry
University of California
Davis, California 95616

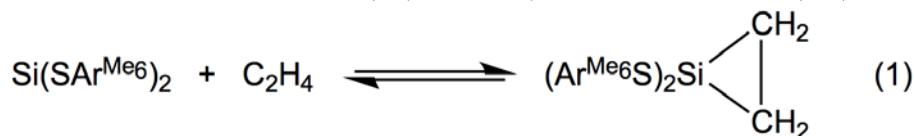
Program Scope

The main objective of the work is to understand the reaction pathways of main group compounds, whose structures are related to those of their element surfaces, with important small molecules such as hydrogen, ammonia, ethylene, carbon monoxide, or isocyanides. This knowledge will help to develop catalysts based upon abundant, inexpensive elements such as aluminum or silicon. The common feature of the main group compounds we study is that they have electron-rich and electron-poor sites with geometries that resemble those at surfaces.^{1,2}

In the current program we have, over the past year, investigated the reactions of silicon, germanium, tin, and gallium compounds whose strained geometries resemble the geometries of exposed atoms on the surfaces of these elements. The small molecule reactions studied involved ethylenes, isocyanides, and elemental phosphorus (P₄).

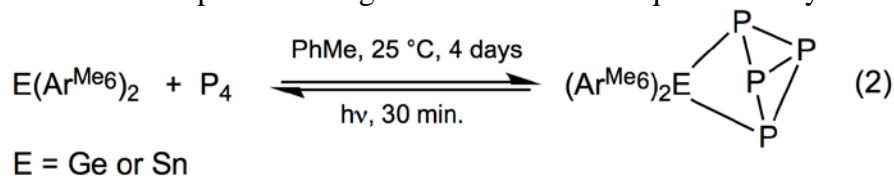
Recent Progress

The major theme of our recent work has been the reactions of small molecules, particularly hydrogen and olefins, with unsaturated group 13 and 14 species. In order for such reactions to be applicable in catalysis, they should be reversible, or nearly reversible, under ambient conditions. An example is provided by the reversible coordination of ethylene to silicon.³ The recently synthesized silylenes :Si(SAr^{Me6})₂ and :Si(SAr^{Pri4})₂ (Ar^{Me6} = C₆H₃-2,6(C₆H₂-2,4,6-Me₃)₂); Ar^{Pri4} = C₆H₃-2,6(C₆H₃-2,6-Prⁱ)₂), which feature a non-bonded lone pair (i.e. a donor) and an empty 3p-orbital (acceptor site) have been shown to reversibly bind ethylene under ambient conditions (according to eq. 1), for which the $\Delta H_{\text{assn.}} = -83.61(84) \text{ kJ mol}^{-1}$, and $\Delta G_{\text{assn.}} = -24.9(2.5) \text{ kJ mol}^{-1}$.



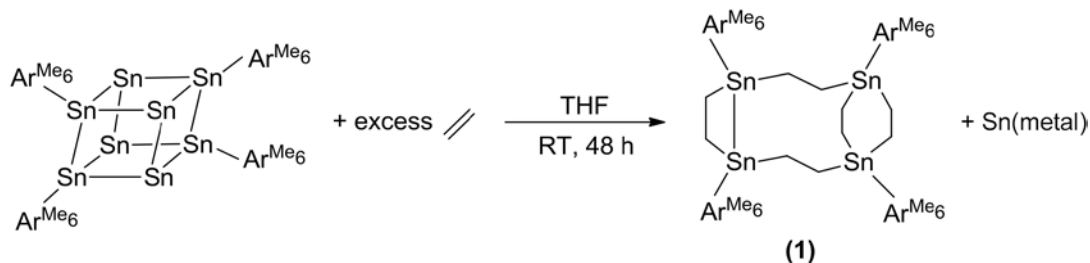
This was the first demonstration of reversible olefin binding by a coordinatively unsaturated silicon center. Calculations in collaboration with the group of Tuononen showed that the binding was dependent on the HOMO-LUMO gap at silicon.

Reversibility was also observed in the reaction between the related heavier group 14 metalylenes Ge(Ar^{Me6})₂ and Sn(Ar^{Me6})₂, which react directly with white phosphorus (P₄) at room temperature to insert into one of the PP bonds (eq. 2).⁴ Photolysis at room temperature reverses the process to regenerate the reactants quantitatively.

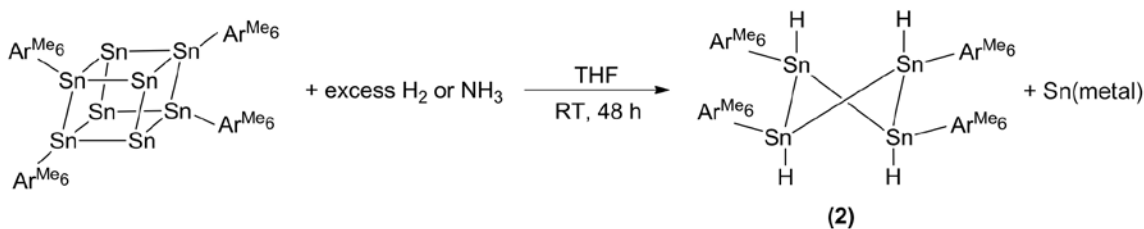


It was shown that this process can be repeated 10 times, during which time *ca.* 70% of the phosphorus complex can still be detected in the ^{31}P NMR spectrum.

We are also investigating the reactions of main group clusters with small molecules. For example, the reaction of the eight metal cluster $\text{Sn}_8(\text{Ar}^{\text{Me}_6})_4$ with ethylene, shown in Scheme 1, shows that this cluster incorporates five equivalents of ethylene, and four equivalents of tin metal are eliminated.⁶



Scheme 1: Reaction of $\text{Sn}_8(\text{Ar}^{\text{Me}_6})_4$ with ethylene.



Scheme 2: Reaction of $\text{Sn}_8(\text{Ar}^{\text{Me}_6})_4$ with dihydrogen or ammonia.

The reaction of the cluster with hydrogen or ammonia leads to the cyclic tetrastannane, as shown in Scheme 2. The reactions in Schemes 1 and 2 are the first instances in which a stable main group cluster has been shown to react with ethylene or H_2 under ambient conditions.

Future Plans

The next investigation of the reactions of main group clusters will concern the known indium cluster $\text{In}_8(\text{Ar}^{\text{Me}_6})_4$,⁷ which we have already characterized and which has a stoichiometric relationship with the tin cluster described above. We are also investigating the synthesis of the silicon and aluminum clusters related to these via the reduction of terphenyl aryl-substituted silicon or aluminum halide starting materials, as well as the exploration of their reaction chemistry. We intend to focus also on the synthesis of the first stable dialuminenes, which are compounds of the general formula RAIAlR . Only one example ($\text{Ar}^{\text{Pr}^i}_4\text{AlAlAr}^{\text{Pr}^i}_4$) has been previously obtained as a reactive intermediate in solution, and it has very high reactivity.⁸ For example, the Al-Al bond undergoes a [2+4] cycloaddition to the aromatic ring of solvent toluene. We plan to isolate and fully characterize such a species by using different, more lipophilic types of terphenyl aryl substituent, which should permit increased solubility in alkane solvents and the avoidance of aromatic solvents with which such species readily react. The reactions of heterometallic molecules that have bonds between group 13 and 14 element, e.g. Si-Al, Ge-Al, etc. with small molecules will also be examined.

References

1. Buriak, J. M. Organometallic Chemistry on Silicon and Germanium Surfaces. *Chem. Rev.* **2002**, *102*, 1271-1308.
2. Shong, B.; Wong, K. T.; Bent, S. F. Strong Carbon-Surface Dative Bond Formation by *tert*-Butyl Isocyanide on the Ge(100)-2x1 Surface. *J. Am. Chem. Soc.* **2014**, *136*, 5848-5851.
3. Lips, F.; Fettinger, J. C.; Mansikkamäki, A.; Tuononen, H. M.; Power, P. P. Reversible Complexation of Ethylene by a Silylene. *J. Am. Chem. Soc.* **2014**, *106*, 634-637.
4. Dube, J. W.; Graham, C. M. E.; MacDonald, C. L. B.; Brown, Z. D.; Power, P. P. Ragogna, P. J. Reversible Photo-Induced Activation of White Phosphorus by Low Coordinate Main Group Compounds. *Chem. Eur. J.* **2014**, *20*, 6739-6744.
5. Eichler, B. E.; Power, P. P. Synthesis and Characterization of [Sn₈(2,6-Mes₂C₆H₃)₄] (Mes = C₆H₂-2,4,6-Me₃): A Main Group Cluster with a Unique Structure. *Angew. Chem. Int. Ed.* **2001**, *40*, 796-797.
6. Vasko, P.; Tuononen, H. M.; Power, P. P. Unpublished results.
7. Eichler, B. E.; Hardman, N. J.; Power, P. P. In₈(C₆H₃-2,6-Mes₂)₄ (Mes=C₆H₂-2,4,6-Me₃): A Metal-Rich Main-Group Cluster with a Distorted Cubane Structure. *Angew. Chem. Int. Ed.* **2000**, *39*, 383-385.
8. Wright, R. J.; Phillips, A. D.; Power, P. P. The [2 + 4] Diels–Alder Cycloaddition Product of a Probable Dialuminene, Ar'AlAlAr' (Ar' = C₆H₃-2,6-Dipp₂; Dipp = C₆H₃-2,6-Prⁱ₂), with Toluene. *J. Am. Chem. Soc.* **2003**, *125*, 10784-10785.

2-Year List of Publications Supported by BES

1. Brown, Z. D.; Vasko, P.; Fettinger, J. C.; Tuononen, H. M.; Power, P. P. A Germanium Isocyanide Complex Featuring (n → π*) Back-Bonding and Its Conversion to a Hydride/Cyanide Product via C-H Bond Activation Under Mild Conditions. *Journal of the American Chemical Society.* **2012**, *134*, 4045-4048. DOI: 10.1021/ja211874u.
2. Caputo, C.; Guo, J.-D.; Nagase, S.; Fettinger, J. C.; Power, P. P. Reversible and Irreversible Higher-Order Cycloaddition Reactions of Polyolefins with a Multiple Bonded Higher-Order Group 13 Alkene Analogue: Contrasting Behavior of a System with π-π, π-π*, and π-n₊ Frontier Molecular Orbitals. *Journal of the American Chemical Society.* **2012**, *134*, 7155-7164. DOI: 10.1021/ja301247h.
3. Brown, Z. D.; Guo, J.-D.; Nagase, S.; Power, P. P. Experimental and Computational Study of Auxiliary Molecular Effects in the Addition of Hydrazines to a Low-Valent Germanium Complex. *Organometallics.* **2012**, *31*, 3768-3772. DOI: 10.1021/om300271c.
4. Summerscales, O. T.; Caputo, C. A.; Knapp, C. E.; Fettinger, J. C.; Power, P. P. The Role of Group 13 Element Hydrides in the Activation of C-H Bonds in Cyclic Olefins. *Journal of the American Chemical Society.* **2012**, *134*, 14595-14603. DOI: 10.1021/ja305853d.

5. Brown, Z. D.; Erickson, J. D.; Fettinger, J. C.; Power, P. P. Facile, High Yield Functionalization of Germanium and Tin by Oxidative Insertion of Tetrelenes into the E-H Bonds of Inorganic Acids (E = C, N, O, F): Arene Elimination versus Oxidative Addition and Formation of a Germanium Cation–Water Complex. *Organometallics*. **2013**, *32*, 617-627. DOI: 10.1021/om301121x.
6. Caputo, C. A.; Koivistoinen, J.; Moilanen, J.; Boynton, J. N.; Tuononen, H. M.; Power, P. P. Counterintuitive Mechanisms of the Addition of Hydrogen and Simple Olefins to Heavy Group 13 Alkene Analogues. *Journal of the American Chemical Society*. **2013**, *135*, 1952-1960. DOI: 10.1021/ja3116789.
7. Brown, Z. D.; Vasko, P.; Erickson, J. D.; Tuononen, H. M.; Power P. P. Mechanistic Study of Methylisocyanide Coupling and C-H Activation Mediated by a Low-Valent Main Group Molecule. *Journal of the American Chemical Society*. **2013**, *135*, 6257-6261. DOI: 10.1021/ja4003553.
8. Caputo, C. A.; Power, P. P. Heavier Main Group Dimetallene Reactivity: Effects of Frontier Orbital Symmetry. *Organometallics*. **2013**, *32*, 2278-2286. DOI: 10.1021/om4000049.
9. Brown Z. D.; Power; P. P. The Mechanisms of Reactions of Open-Shell, Heavier Group 14 Derivatives with Small Molecules: $n \rightarrow \pi^*$ Back-Bonding in Isocyanide Complexes, C-H Activation Under Ambient Conditions, CO-Coupling, and Ancillary Molecular Interactions. *Inorganic Chemistry*. **2013**, *52*, 6248-6259. DOI: 10.1021/ic4007058.
10. Mansikkamäki, A.; Power, P. P.; Tuononen, H. M. Computational Analysis of ($n \rightarrow \pi^*$) Back-Bonding in Metallylene-Isocyanide Complexes R_2MCNR' (M = Si, Ge, Sn; R = *t*Bu, Ph; R' = Me, *t*Bu, Ph). *Organometallics*. **2013**, *32*, 6690-6700. DOI: 10.1021/om400558e.
11. Melton, C. E.; Dube, J. W.; Ragogna, P. J.; Fettinger, J. C.; Power, P. P. Synthesis and Characterization of Primary Aluminum Parent Amides and Phosphides. *Organometallics*. **2014**, *33*, 329-337. DOI: 10.1021/om4010675.
12. Lips, F.; Fettinger, J. C; Mansikkamaki, A.; Tuononen, H. M.; Power, P. P. Reversible Complexation of Ethylene by a Silylene. *Journal of the American Chemical Society*. **2014**, *136*, 634-637. DOI: 10.1021/ja411951y.
13. Dube, J. W.; Brown, Z. D.; Caputo, C. A; Power, P. P.; Ragogna, P. J. Activation of Gaseous PH_3 with Low Coordinate Diaryltetrylene Compounds. *Chemical Communications*. **2014**, 1944-1936. DOI: 10.1039/C3CC48933G.
14. Dube, J. W.; Graham, C. M. E.; Macdonald, C. L. B.; Brown, Z. D.; Power, P. P.; Ragogna, P. J. Reversible Photo-Induced Activation of White Phosphorus by Low Coordinate Main Group Compounds. *Chemistry - A European Journal*. **2014**, *20*, 6739-6744. DOI: 10.1002/chem.201402031.

Molecular Processes Underlying the Structure and Assembly of Thin Films and Nanoparticles at Complex interfaces

PI: Geraldine L. Richmond, University of Oregon

Program Scope

Fluid interfaces are a platform for a variety of important processes that include oil recovery and water remediation, engineering new materials from the self-assembly of molecular components, interface catalyzed reactions, ion transfer, nanoparticle synthesis and assembly, as well as biological processes that occur at the interface between a fluid cell membrane and water. These processes often depend on the adsorption and assembly of large, ionizable molecules or particles to the interface between a nonpolar fluid and water. Although much has been learned in recent years about the molecular factors that drive adsorption and assembly at solid surfaces, the knowledge and predictability of how complex adsorbate systems such as polymers, polyelectrolytes, PE-surfactant mixtures and organically modified nanoparticles adsorb and assemble at a liquid/liquid interface is in its infancy. The focus of our DOE sponsored research is on understanding the molecular factors that contribute to the assembly of macromolecules and nanoparticles at the liquid-liquid interface using a combination of nonlinear surface spectroscopy, interfacial tension measurements and molecular dynamics simulations.

An exciting new direction of part of our DOE sponsored research involves the study of the formation of peptoid nanosheets at the liquid-liquid interface. Peptoid nanosheets are a novel class of two dimension nanomaterials that form from the assembly of peptoid polymers.¹ The Zuckermann group at the Molecular Foundry has discovered that the air-water interface catalyzes the formation of nanosheets.² Specifically, the mechanism for nanosheet synthesis first involves the assembly of a peptoid monolayer at the interface, with subsequent compression leading to monolayer collapse and formation of stable bilayer structures. Recently, we have been working with the Zuckermann group in showing that ordered nanosheet formation can occur via the oil-water interface, and that this interface provides a unique platform for synthesis that has the potential to increase nanosheet functionality and stability.³

In order to increase the complexity and functionality of these novel nanomaterials, as well as to better explain the mechanism of formation, it is essential to understand the molecular level details of the key peptoid monolayer intermediate that either contribute to or inhibit nanosheet formation. A depiction of the monolayer is shown in Figure 1. In particular, it is important to understand the structural requirements of peptoids at the interface (such as degree of backbone and side chain ordering, intermolecular interactions, and packing density) required to make nanosheets.

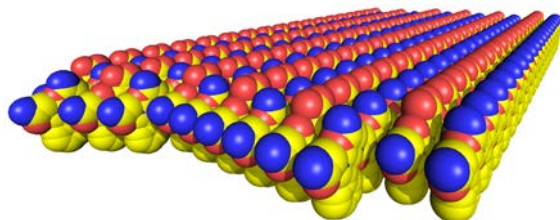


Figure 1. Cartoon of a peptoid monolayer.

One way of examining this adsorption and structural ordering is to use vibrational sum frequency (VSF) spectroscopy. This is a well-established surface selective technique that produces vibrational spectra of oriented interfacial molecules,⁴ and in particular carboxylic acid

containing polymers.⁵⁻⁹ This technique provides fundamental information related to bond strengths, interactions between chemical species, and orientations of molecules specifically at the interface. Based on these characteristics, VSF spectroscopy is an ideal technique to probe the atomistic details of peptoid monolayers at the oil-water interface. We therefore have utilized this technique, along with complementary interfacial tension studies, to study monolayers of a variety of sequence specific peptoids at the oil-water interface, in which the ability or inability of the peptoid to form nanosheets is known. By understanding the role of each molecular moiety of the peptoid in interfacial assembly and subsequent nanosheet formation, peptoid polymers can be better designed to more effectively assemble into nanosheets for a variety of interesting applications that include molecular sensors,¹⁰ artificial membranes, and catalysts.

Recent Progress

We have recently been exploring two peptoids in order to answer some outstanding questions about the role of electrostatic interactions in either peptoid monolayer assembly and subsequent nanosheet assembly using VSF and surface tension measurements. The chemical structures of these two peptoids are depicted in Figure 2.

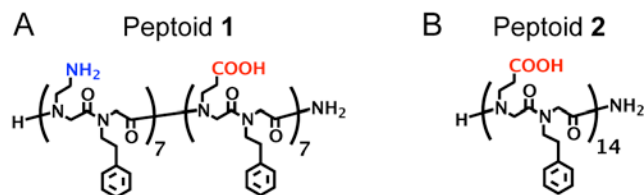


Figure 2. Chemical structures of peptoids used in previous VSF spectroscopic study.

At pH 8, where the carboxylic acid and amine groups are both charged, Peptoid 1 has been shown by the Zuckerman group to be able to form nanosheets, while Peptoid 2 is not. In that original work it was speculated that the difference in behavior of these two peptoids is an electrostatic interaction between the oppositely charged moieties on Peptoid 1 that is absent in Peptoid 2.^{2,3} Our VSF spectroscopic results confirm that this is the case, that a favorable electrostatic interaction does exist between the negatively charged carboxylate groups and the positively charged amine groups, and that the spectral signature can be found in the VSF spectrum as shown in Figure 3.

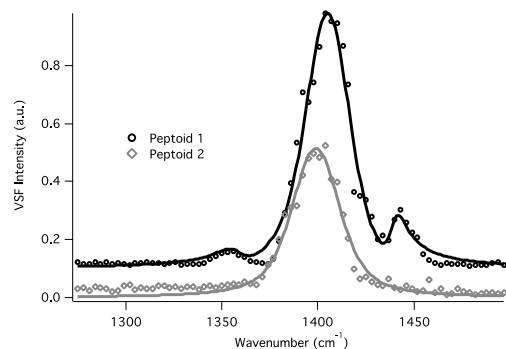


Figure 3. VSF spectra of the carboxylate stretching region for 20 μM Peptoid 1 (black circles) and Peptoid 2 (gray diamonds) at pH 8. The solid lines are fits to the data. The data are offset for clarity.

For Peptoid 1, three peaks are seen in spectrum in Figure 3 and appear near 1350 cm^{-1} , 1405 cm^{-1} , and 1440 cm^{-1} . The two lower frequency peaks are assigned to carboxylate groups with differing degrees hydrogen bonding from solvating water molecules, while the high

frequency peak is assigned to carboxylate groups that are electrostatically interacting with the positively charged amine groups. This electrostatic interaction peak near 1440 cm^{-1} does not appear in the spectrum of Peptoid 2. Here, only one peak appears near 1400 cm^{-1} that is assigned to hydrated carboxylate groups. The electrostatic interactions between positively charged amine and negatively charged carboxylate groups are key in the ability for Peptoid 1 to form a highly packed monolayer at the oil-water interface (surface pressure = 36 mN/m), which contributes to the ability of the monolayer to collapse and form nanosheets. Charge-charge repulsions in monolayers of Peptoid 2 hinder ordered interfacial assembly (surface pressure = 24 mN/m), which contributes to the inability of this peptoid to form nanosheets.

Future Plans

Since electrostatics are so influential, we propose to study the role of pH and metal cations (Ca^{2+} , Mg^{2+} , Mn^{2+} , and Cu^{2+}) in the ability of carboxylic acid containing peptoids, such as Peptoid 2, to form nanosheets via the oil-water interface. The Zuckermann group has recently shown that nanosheets form from such peptoids at lower pH values and also in the presence of certain metal ions. VSF spectroscopic measurements will be used to determine how the molecular level details of the monolayer at the oil-water interface relate to the ability of the peptoid to form nanosheets. For the pH studies, we will probe the carboxylate and carbonyl regions to observe any changes in hydrogen bonding between the protonated carboxylic acid groups that may contribute to nanosheet formation. For the metal ion studies, we will specifically look for electrostatic interactions between the carboxylate group and the metal ions by probing the carboxylate stretching mode near 1400 cm^{-1} . Observing the specific peak frequency will allow us to determine whether the interactions between the metal ions and the carboxylate groups are purely electrostatic in nature, or if the carboxylate groups are able to chelate the metal ions.

We will also explore the role of the bulkiness hydrophobic moieties by studying peptoids that contain different ethyl phenyl groups, as shown in Figure 4. By probing the CH moieties of the adsorbed peptoid backbone, side chains, and aromatic groups, we will be able to obtain information related to the packing ability of these peptoids at the oil-water interface and how this degree of packing relates to the ability to form nanosheets.

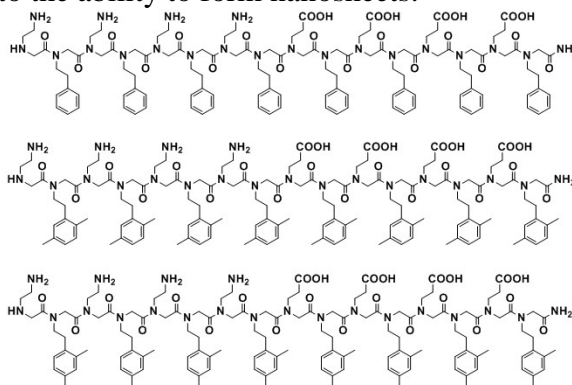


Figure 4. Chemical structures of peptoids in which the bulkiness of the phenyl group is varied.

We are interested in whether the bulkiness of the aromatic rings would inhibit peptoid packing at the oil-water interface that would in turn affect the degree of electrostatic interactions. In this way these future studies will allow a deeper understanding of how to construct nanosheets of increasing material complexity and functionality.

References

1. Nam, K. T. et al. *Nat. Mater.* **2010**, *9*, 454-460.
2. Sanii, B. et al. *J. Am. Chem. Soc.* **2011**, *133*, 20808-20815.
3. Robertson, E. J.; Olivier, G. K.; Quan, M.; Proulx, C.; Zuckermann, R. N.; Richmond, G. L., *submitted*.
4. Richmond, G. L. *Chem. Rev.* **2002**, *102*, 2693-2724.
5. Beaman, D. K.; Robertson, E. J.; Richmond, G. L. *Langmuir* **2011**, *27*, 2104-2106.
6. Beaman, D. K.; Robertson, E. J.; Richmond, G. L. *Proc. Natl. Acad. Sci. U. S. A.* **2012**, *109*, 3226-3231.
7. Beaman, D. K.; Robertson, E. J.; Richmond, G. L. *Langmuir* **2012**, *28*, 14245-14253.
8. Robertson, E. J.; Richmond, G. L. *Langmuir* **2013**, *29*, 10980-10989.
9. Robertson, E. J.; Carpenter, A. P.; Olson, C. M.; Ciszewski, R. Richmond, G. L. *J. Phys. Chem C* **2014**, *submitted*.
10. Olivier, G. K.; Cho, A.; Sanii, B.; Connolly, M. D.; Tran, H.; Zuckermann, R. N. *ACS Nano* **2013**, *7*, 9276-9286.

Publications

1. "Assembly and Molecular Order of Two-Dimensional Peptoid Nanosheets through the Oil-Water Interface", Robertson, E. J.; Olivier, G. K.; Quan, M.; Proulx, C.; Zuckermann, R. N.; Richmond, G. L., *PNAS*, *submitted*.
2. "Metal Ion Induced Adsorption and Ordering of Charged Macromolecules at the Aqueous/Hydrophobic Liquid Interface", Robertson, E. J.; Carpenter, A. P.; Olson, C. M.; Ciszewski, R. Richmond, G. L.. *J. Phys. Chem C* **2014**, *submitted*.
3. "Chunks of Charge: Effects at Play in the Assembly of Macromolecules at Fluid Surfaces", Robertson, E. J.; Richmond, G. L.. *Langmuir* **2013**, *29*, 10980-10989.
4. "The Water/Hydrophobic Interface: Neutral and Charged Solute Adsorption at Fluorocarbon and Hydrocarbon SAMs", A.J. Hopkins and G.L. Richmond, *Appl. Spec.*, *67* (261-273) 2013.
5. "Metal Ions: Driving the Orderly Assembly of Polyelectrolytes at Hydrophobic Surfaces", D. K. Beaman, E. J. Robertson and G.L. Richmond, *Langmuir*, *28* (14245-53) 2012.

Project Title: Programming Function via Soft Materials

Principle Investigators: Paul V. Braun, Randy Ewoldt, Steve Granick, K. Jimmy Hsia, Xiuling Li, Jeffrey S. Moore, Ralph G. Nuzzo, John A. Rogers (Cluster Leader), Kenneth S. Schweizer – All at University of Illinois, Urbana/Champaign

Program Scope: Our collaborative program focuses on developing, understanding, and applying in energy-relevant contexts new classes of responsive materials with functionalities that derive from and/or exploit structural dynamics from the nanometer to mesoscopic to continuum scale. The approach involves dynamically reconfigurable 3-dimensional organization of building blocks into architectures that facilitate ion and electron transport and the harvesting of mechanical energy, with potential for broad utility in advanced energy applications. Work on materials synthesis and processing, characterization, theory and modeling occurs in two synergistic thrusts:

1. Reconfigurable and Dynamic Assemblies – are realized using a diverse suite of responsive colloids and nanoparticles of various shapes, sizes, softness, and chemistry created via chemical synthesis, cluster assembly and mechanical instabilities.
2. Responsive 3D Mesoscale Networks – exploit residual and mismatch stress to “mechanically synthesize” deterministic functional networks of diverse chemistries and geometries including fractal motifs. These networks can be used in isolation or in combination with colloidal assemblies for mechanical energy transduction.

Recent Progress: Below we highlight several of this year’s research accomplishments in these two areas, each of which would not have been possible without collaborations within our cluster team.

1. Reconfigurable and Dynamic Assemblies – The emphasis is on synthesis and assembly of anisotropic, ‘active’ colloids, including dynamic processes guided not only through colloidal interactions but via local fields and networks, in four areas.

(i) Theory of assembly in Janus colloids and colloids interacting with networks – Motivated by the experiments of **Granick, Schweizer** formulated a new predictive statistical mechanical theory for the crystalline phase behavior of monolayers of amphiphilic spherical Janus colloids. The phase diagrams are a rich function of Janus balance, temperature and pressure. Calculations are in qualitative agreement with the experiments of **Granick**. In our integrated experiment-theory effort (**Ewoldt, Braun, Schweizer**) to fabricate hybrid colloid-gel composites that can reversibly switch from insulating to conductive, we developed a microscopic theory of the thermodynamics, structure and electrical conductivity of large mesh rigid rod networks and spherical colloids. The new interconnected colloidal structures provide remarkably high, switch-like conductivity even at very low absolute particle volume fractions.

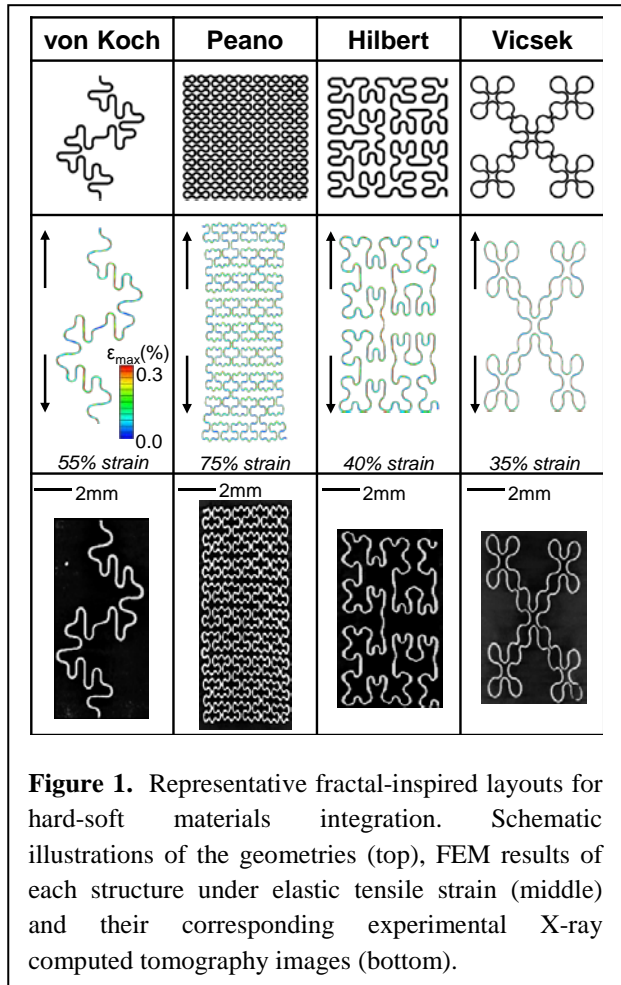
(ii) Active colloids – Snap-action colloids are structures that can be triggered to switch between two or more stable (or metastable) shapes. Unlike conventional responsive colloidal particles, which change shape slowly by swelling or contracting, in a snapping system, an energetic barrier between the stable or metastable shapes results in rapid transformations. In collaboration with **Hsia**, **Schweizer** and **Braun** established a new synthetic route to fabricate snap-action colloids that are structurally and functionally anisotropic, with selective responses toward specific stimuli. Snapping of particles between two distinct shapes occurs with changes in pH or exchange of solvent, consistent with computational modeling of **Hsia**.

(iii) Chemically synthesized network gels – **Moore** and **Braun** studied reversible-deactivation fibril assembly as a mechanism for controlling supramolecular polymerization of one-dimensional filaments to form structurally well-defined assemblies with narrow polydispersity. Taking amyloid peptide as the model system of fibrillar self-assembly, we designed multivalent polymer-peptide conjugates (mPPCs) as modulators that redirect self-assembly into formation of discrete nanostructures. AFM studies show that mPPCs have the ability to reverse the fibrillation process by converting long, unbranched fibrils into nanostructures with lateral dimensions around 100 nm. These results demonstrate that the design of mPPCs is an effective strategy to noncovalently control supramolecular polymerization.

(iv) Fundamental studies of rheology in complex networks and dynamic colloidal suspensions – **Ewoldt**, **Schweizer** and **Braun** pursued theoretical and experimental rheological studies of hybrid polymer-colloid systems relevant to the materials systems described above. In particular, polymer networks with large (>1 micron) persistence length allow for length-scale separation between the colloidal particles and the network mesh size. We obtained preliminary rheological measurements with model networks of collagen (type-I) and fibrin. **Ewoldt** derived universal predictions for *asymptotically-nonlinear* viscoelastic signatures in the terminal regime of long timescales and experimentally confirmed these predictions with novel measurements.

2. Responsive 3D Mesoscale Networks – New methods in guided materials assembly provide routes to 3D mesoscale networks that form as a result of compressive stresses. Geometric layouts in fractal inspired motifs provide new paradigms for deterministic composites in both 3D and 2D configurations. Incorporating piezoelectric materials into such systems create new opportunities in actuators and harvesters, both of relevance to energy.

(i) Fractal concepts in deterministic 2D composites – **Rogers, Hsia** and **Nuzzo** developed fractal geometries for configuring hard materials with thin filamentary designs into soft matrices. This scheme allows co-integration of multiple high-performance material platforms with high spatial resolution and engineering control, in ways that also allow proper electrical contacts, both internal and external to the system. Results indicate that concepts in fractal geometry, which are known to determine behaviors in traditional 3D, non-deterministic composites, can be valuable in this new context. The choices of topologies span a rich range, capable of tailoring to specific electronic applications through integration and interdigitation of multiple structures. Fig. 1 presents some examples, from lines to loops and branch-like meshes. **Rogers** and **Hsia** demonstrated the essential underlying aspects in materials and mechanical science and engineering, in the context of Peano, Greek cross, Vicsek and other fractal constructs for space-filling structures of electronic materials, including monocrystalline silicon.



(ii) Piezoelectric nanomaterials for mechanical energy harvesting – **Rogers, Hsia** and **Nuzzo** identified growth and fabrication strategies for high performance, thin film piezoelectric structures capable of mechanical-to-electrical energy conversion at high efficiencies. Comprehensive experiments, computational results, and findings in multilayer configurations revealed the key behaviors and their relation to intrinsic properties of the constituent materials.

(iii) Soft actuators – **Rogers, Hsia** and **Nuzzo** investigated new classes of composite soft materials devices that can effect and exploit forms of electromechanical and chemomechanical actuation, using the concepts described previously. In a first example, a flexible wire mesh is integrated in a gel matrix with a topology that allows programmatic and fully reversible 3D transformations of shape in response to patterns of electrical current flow.

(iv) 2D and 3D mesoscale networks as scaffolds for soft materials and cells – **Li, Rogers** and **Hsia** demonstrated strain-induced self-rolled-up membranes as a platform for three-dimensional (3D) hierarchical tubular architectures. Strained SiN_x membranes served as electrically insulating and optically transparent mechanical supports to yield 3D forms involving

carbon nanotube arrays, graphene sheets, and passive electronic components. By using similar platforms, **Li** and **Granick** showed that colloids can pack into monolayers between the microtube sidewalls during the membrane rolling process in saline solution. Microtube-colloid interactions result in microtubes that have non-symmetric axial geometry and varying tubular shapes.

Future Plans:

1. Reconfigurable and Dynamic Assemblies – In the coming year, we will (i) generalize and apply theory constructs to experimental systems (ii) demonstrate the scope and generality of mPPCs, including stimuli-degradable versions as a prototypical template to design other multivalent modulators that control fibrillar assemblies of supramolecular gels or proteins and (iii) continue our development of complex colloid structures and study of their rheological properties.

2. Responsive 3D Mesoscale Networks – Building upon the above successes, in the coming year we plan to further develop and exploit deterministic strategies for the design, assembly, and integration of multiscale functional 2D and 3D structures, with active functionality of relevance to use and harvesting of energy.

References: None.

Selected Publications (full list in the annual report)

1. P. Yuan, O. Kuksenok, D.E. Gross, A.C. Balazs, J.S. Moore and R.G. Nuzzo, “UV Patternable Thin Film Chemistry for Shape and Functionally Versatile Self-Oscillating Gels,” *Soft Matter* **9**, 1231 (2013).
2. S. Xu, Y. Zhang, L. Jia, K.E. Mathewson, K.-I. Jang, J. Kim, H. Fu, X. Huang, P. Chava, R. Wang, S. Bhole, L. Wang, Y.J. Na, Y. Guan, M. Flavin, Z. Han, Y. Huang, J.A. Rogers, “Soft Microfluidic Assemblies of Sensors, Circuits, and Radios for the Skin,” *Science* **344**, 70 (2014).
3. J.A. Fan, W.-H. Yeo, Y. Su, Y. Hattori, W. Lee, S.-Y. Jung, Y. Zhang, Z. Liu, H. Cheng, L. Falgout, M. Bajema, T. Coleman, D. Gregoire, R.J. Larsen, Y. Huang and J.A. Rogers, “Fractal Design Concepts for Stretchable Electronics,” *Nature Communications* **5**, 3266 (2014).
4. C. Dagdeviren, B.D. Yang, Y. Su, P.L. Tran, P. Joe, E. Anderson, J. Xia, V. Doraiswamy, B. Dehdashti, X. Feng, B. Lu, R. Poston, Z. Khalpey, R. Ghaffari, Y. Huang, M.J. Slepian and J.A. Rogers, “Conformal Piezoelectric Energy Harvesting and Storage From Motions of the Heart, Lung, and Diaphragm,” *Proceedings of the National Academy of Sciences USA* **111**(5), 1927 (2014).

Interfacial Behavior of Polymers: Using Interfaces to Manipulate Polymers

Thomas P. Russell, University of Massachusetts, Amherst, MA 01003

DE-FG02-96ER45612 Program Scope

By controlling interfacial interactions and/or by manipulating the entropy of chains or aggregates of chains at interfaces through topological constraints, by varying the packing entropy of microdomains at interfaces, or by use of external triggers to spatially manipulate interfacial interactions, a quantitative understanding of and control over directed self-assembly processes can be achieved that, in turn, will open new routes to functional mesoscale assemblies where the 2-D and 3-D spatial arrangements of elements can be controlled or manipulated over multiple length scales. Our studies extend the DSA of BCPs to their limits by using polymers with unusual topologies (tailoring entropy) and by use of the chemical complexation to enhance interactions (tailoring enthalpy). Studies on solvent annealing, lateral ordering and externally triggered control over lateral ordering aim to understand and control pathways to macroscopic arrays of BCP microdomains that are kinetically trapped in states that are far removed, overcoming relaxation processes that would destroy the sought-after structure and functionality.

DE-FG02-96ER45612 Recent Progress

When a neutral solvent is introduced to a BCP, the period of the BCP will decrease and the lateral dimension, *e.g.* length of cylinder, will increase. However, in thin films, the BCP is laterally confined to the area of the substrate, resulting in an incommensurability with the decreasing period of the BCP during swelling. When the BCP film is swollen, the total volume of the film increases and, due to the lateral confinement, the film thickness increases, since the occupied surface area on the substrate remains fixed. The swelling ratio, R , is the thickness of the swollen film divided by the original thickness. For microdomains oriented normal to the surface, this thickness change can be accommodated by the translational diffusion of the BCP chains along the interface between the microdomains. When the microdomains are oriented parallel to the substrate, there is an incommensurability between the swollen film thickness and the period of the swollen BCP microdomains. Consequently, there must be a re-distribution of BCP chains in the film, the generation of more microdomains, and the appearance of a surface topography. Upon solvent removal, the mobility of the BCP chains in a microphase separated environment and the reformation of microdomains are critical in defining the final morphology of the dried film. These points have been ignored up to this point.

BCP films were placed in a custom-designed solvent vapor-annealing chamber to carry out real-time *in situ* GISAXS at $23 \pm 0.5^\circ\text{C}$ as solvent vapor was added or removed. Two gas streams, a pure N_2 gas and a THF-rich N_2 , were mixed before flowing into the annealing chamber, so that the vapor pressure could be controlled. The fraction of solvent vapor in the experimental cell, *i.e.* the partial pressure and vapor pressure of THF, could be varied by adjusting the relative flow rates of the pure and THF-rich N_2 . This design also enabled the removal of solvent vapor inside the chamber by closing the THF-saturated vapor

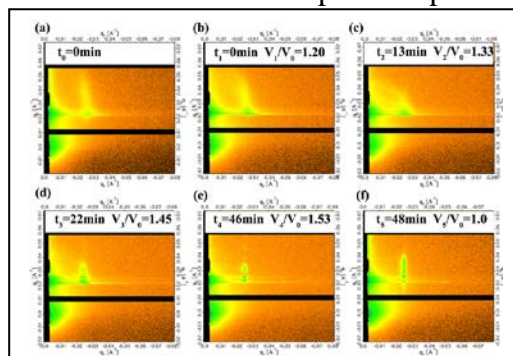


Figure 1. GISAXS scattering patterns of a swollen BCP film at different times. The indicated volume ratio corresponds to the swelling ratio as determined from the increase of film thickness during annealing.

inlet and purging the chamber with pure N₂. The rate of solvent removal from the chamber was controlled by varying the flow-rate of pure N₂ into the chamber.

A series of GISAXS profiles obtained for PS-*b*-P2VP as a function of time during swelling with THF is shown in Figure 1. The scattering profile of the as-spun PS-*b*-P2VP thin film (t_0) shows a well-defined, but diffuse reflection, at a Bragg spacing of 23.2 nm, much less than the equilibrium period of this BCP. Initially the film swells, decreasing T_g (to ~18°C) but the scattering profiles did not change significantly. After 8 min (t_1), the reflection shifts to smaller q_y , larger spacing in-plane, with the bowing of the reflection in q_z being still evident. With increasing annealing time (t_2), the reflection broadens further, with a ring of scattering developing, indicating a further re-organization and disordering of the BCP. However, as the swelling of the BCP film continues (t_3), the GISAXS reflection continues to shift to smaller q_y , corresponding to a larger in-plane spacing, intensifies, and sharpens considerably. With further swelling (t_4), the reflection maintains its overall shape, but shifts slightly to larger q_y . The solvent was rapidly removed, the scattering pattern stretched in the q_z direction, due to the reduced film thickness. The domain spacing and the FWHM increased slightly, indicating the introduction of some disorder during the solvent removal process.

The Bragg spacing corresponding to the peak position, the FWHM and the film thickness are plotted in Figure 2. From these data, an apparent induction period is observed up to t_1 , followed by a sharp increase in the spacing with little change to the FWHM up to t_2 , then a further increase of the spacing with a sharpening of the reflection (t_3), and then a slight decrease in the Bragg spacing, along with a further narrowing of the reflection (t_4). Plotted in a log-log manner, it is very evident that the decrease in the period with increasing solvent concentration (from t_3 to t_4) follows a power law behavior with an exponent of 0.64 (~2/3). This exponent is much larger than that reported previously by Hashimoto and coworkers [1] and Lodge and coworkers [2], where the period of the lamellar microdomain morphology varied with the volume fraction of BCP as $\phi_{BCP}^{1/3}$. Two additional solvent removal rates were examined. All the data are coincident during swelling. When the solvent is very rapidly removed, the T_g of the film increases above room temperature almost instantly, kinetically trapping the morphology. However, the period increases slightly and the FWHM increases, indicating that the BCP has undergone some re-organization and there is some disordering of the BCP microdomains. By controlling the rate of solvent removal, the domain spacing increases up to a point where no further increase in the period was observed. The increase in the period results from an increase in the effective χ , which causes the BCP chains to stretch at the interface. Throughout the solvent removal process, the period and FWHM increase indicating a reorganization of the BCP microdomains as the solvent is removed.

From these results and others not shown, we can conclude that the microdomain re-organization and ordering are kinetically trapped when $\phi_{BCP} > 0.83$. For polymer concentrations $0.80 > \phi_{BCP} > 0.65$, the domain spacing changed to the equilibrium size within minutes. THF, a neutral solvent for PS-*b*-P2VP, screens the unfavorable interactions between the PS and P2VP segments, allowing the BCP chains to relax at the interface, gives rise to a decrease in the period

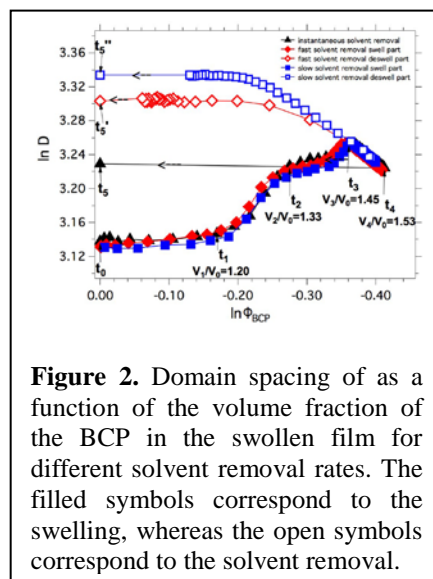


Figure 2. Domain spacing of as a function of the volume fraction of the BCP in the swollen film for different solvent removal rates. The filled symbols correspond to the swelling, whereas the open symbols correspond to the solvent removal.

with increasing solvent concentration. For BCP concentrations of $0.80 > \phi_{BCP} > 0.65$, $D \sim (\phi_{BCP})^{2/3}$. Both, the swelling ratio and the solvent removal rate not only affect the domain spacing of block copolymers but also dictate the extent of lateral ordering of the BCP microdomains. Larger grain sizes were observed at higher swelling ratio. To preserve the maximal lateral ordering of the microdomains in the swollen status, the fastest solvent removal rate is required to freeze in the ordered microdomain structure of the swollen BCP film.

DE-FG02-96ER45612 Future Plans

We will continue studies on the solvent annealing studies on block copolymer thin films. These studies include grazing incidence x-ray and neutron scattering studies on block copolymers on surfaces with well-defined topographies, specifically on reconstructed faceted sapphire surfaces and surfaces prepared by nano-imprint and e-beam lithography. Studies are being performed on the swelling of the block copolymers using neutral and preferential solvents, to quantify the ordering process and develop metrics to quantitatively characterize lateral order. We will initiate studies on mikto-arm terpolymers, three polymer chains covalently joined at one end, so as to enhance the lateral ordering using the configurational constraints of the three different chains at the interface to promote perfect lateral order, a challenge that has never been met.

References

1. M. Shibayama, T. Hashimoto, H. Hasegawa, H. Kawai, *Macromolecules* **1983**, *16*, 1427–1433.
2. T. P. Lodge, K. J. Hanley, B. Pudil, V. Alahapperuma, *Macromolecules* **2003**, *36*, 816–822.

DE-FG02-96ER45612 Publications

1. X. Wei, W. Gu, W. Chen, X. Shen, F. Liu, J.W. Strzalka, Z. Jiang, and T.P. Russell, “Disorder-to-Order Transitions Induced by Alkyne/Azide Click Chemistry in Diblock Copolymer Thin Films,” *Soft Matter*, **8**(19), 5273-5282. (2012).
2. X. Gu, P. Dorsey, and T.P. Russell, “High Density and Large Area Arrays of Silicone Oxide Pillars with Tunable Domain Size for Mask Etch Applications,” *Advanced Materials* **24**(40) 5505-5511 (2012).
3. S.W. Hong, D.L. Voronov, D.H. Lee, A. Hexemer, H.A. Padmore, T. Xu and T.P. Russell, “Controlled Orientation of Block Copolymers on Defect-free Faceted Surfaces,” *Adv. Mat.* **24**(31), 4278-4283 (2012).
4. S. Choi, E. Kim, H. Ahn, S. Naidu, Y. Lee, D.Y. Ryu, C.J. Hawker, and T.P. Russell, “Lamellar Microdomain Orientation and Phase Transition of Polystyrene-*b*-poly(methyl methacrylate) Films by Controlled Interfacial Interactions,” *Soft Matter*, **8**(12), 3463-3469, 2012.
5. X. Gu, Z. Liu, I. Gunkel, S.T. Chourou, S.W. Hong, D.L. Olynick, and T.P. Russell, “High Aspect Ratio Sub-15 nm Silicon Trenches From Block Copolymer Templates,” *Adv. Mat.*, **24**(42), 5688–5694 (2012).
6. W. Zhao, T.P. Russell, and G.M. Grason, “Orientational Interactions in Block Copolymer Melts: Self-Consistent Field Theory,” *J. Chem. Phys.* **137**(10), 104911 (2012).
7. S.W. Hong, J. Huh, X. Gu, D.H. Lee, W.H. Jo, S. Park, T. Xu, and T.P. Russell, “Unidirectionally Aligned Line Patterns Driven by Entropic Effects on Faceted Surfaces,” *PNAS*, **109**(5), 1402-1406 (2012).
8. W. Gu, S.W. Hong and T.P. Russell, "Orienting Block Copolymer Microdomain with Block Copolymer Brushes," *ACS Nano* **6**(11), 10250 – 10257 (2012).
9. A. Serghei, W. Zhao, D. Miranda, and T.P. Russell, “Curie Transitions for Attograms of Ferroelectric Polymers,” *Nano Letters*, **13**(2), 577-580, DOI:10.1021/nl304103y

- (January 14, 2013).
10. W. Gu, J. Huh, S.W. Hong, B. Sveinbjornsson, C.Park, R. Grubbs and T.P. Russell, "Self-Assembly of Symmetric Brush Diblock Copolymers," *ACS Nano*, **7**(3), 2551–2558, DOI: 10.1021/nn305867d (2013).
 11. X. Wei, W. Gu, L. Li, X. Shen, J.-K. Kim and T.P. Russell, "Synthesis and Morphology Investigations of a Novel Alkyne-Functionalized Diblock Copolymer," *J. Polym Sci., Part B: Polymer Physics* **51**(1), 78-85, DOI: 10.1002/polb.23183 (January 1, 2013).
 12. A. Serghei, W. Zhao, D. Miranda, and T.P. Russell, "Curie Transitions for Attograms of Ferroelectric Polymers," *Nano Letters*, **13**(2), 577-580, DOI:10.1021/nl304103y (2013).
 13. W. Zhao, T.P. Russell and G. Grason, "Chirality in Block Copolymer Melts: Mesoscopic Helicity from Intersegment Twist," *Phys. Rev. Lett.*, **110**, 058301 (2013).
 14. W. Zhao, D. Chen, G.M, Grason and T.P. Russell, "Formation of H* Phase in Chiral Block Copolymers: Effects of Solvents and Solution Cast Conditions," *Macromolecules*, **46**(2), 455-462, DOI: 10.1021/ma301928x, (January 22, 2013).
 15. W. Zhao, F. Liu, X. Wei, D. Chen, G.M. Grason, and T.P. Russell, "Formation of H* Phase in Chiral Block Copolymers: Morphology Evolution as Revealed by Time-Resolved X-ray Scattering," *Macromolecules*, **46**(2), 474-483, DOI:10.1021/ma302139m, (January 22, 2013).
 16. W. Gu, J. Xu, J-K Kim, S.W. Hong, X. Wei, X. Yang, K.Y. Lee, D.S. Kuo, S. Xiao, "Solvent Assisted Directed Self-Assembly of Spherical Microdomain Block Copolymers to High Areal Density Arrays," *Advanced Materials*, DOI: 10.1002/adma.201300899 (July 19, 2013).
 17. J. Xu, T.P. Russell and A. Checco, "Lattice Deformation and Domain Distortion in the Self-Assembly of Block Copolymer Thin Films on Chemical Patterns," *Small* **9**(5) 779-784, DOI: 10.1002/sml.201201950 (March 11, 2013).
 18. X. Wei, W. Gu, X. Shen, J. Strzalka, Z. Jiang and T.P. Russell, "Deviations from Bulk Morphologies in Thin Films of Block Copolymer/Additive Binary Blends," *Chin. J. Polym. Sci.*, DOI: 10.1007/s10118-013-1320-x (September, 2013).
 19. W. Gu, H. Zhao, Q. Wei, E.B. Coughlin, P. Theato and T.P. Russell, "Line Patterns from Cylinder-Forming Photocleavable Block Copolymers," *Adv. Mat.*, **25**(34) 4690-4695, 10.1002/adma.201301556, (September 14, 2013).
 20. X. Gu, I. Gunkel and T.P. Russell, "Block Copolymer Lithography: A "Bottom-Up" Approach to High-Density Pattern Transfer," *Phil. Trans. A*, **371**(2000), DOI: 10.1098/rsta.2012.0306, (September 2, 2013).
 21. S.W. Hong, W. Gu, J. Huh, Y. Xia, B. Sveinbjornsson, G. Jeong, R.H. Grubbs and T.P. Russell, "On the Self-assembly of Brush Block Copolymers in Thin Films," *ACS Nano* **7**(11), 9684-9692, (November 2013).
 22. Z. Sun, T. Feng and T.P. Russell, "Assembly of Graphene Oxide at Water/Oil Interfaces: Tessellated Nanotiles," *Langmuir*, **29**(44), 13407-13413, (November 2013).
 23. X. Gu, I. Gunkel, A. Hexemer, W. Gu and T.P. Russell, "Block Copolymer Thin Films During Solvent Vapor Annealing: Effect of Solvent Removal Rate," *Advanced Materials*, DOI: 10.1002/adma.2013302562.
 24. X. Gu, I. Gunkel, A. Hexemer, W. Gu, and T.P. Russell, "An In Situ Grazing Incidence X-Ray Scattering Block Copolymer Thin Films During Solvent Vapor Annealing," *Advanced Materials*, **26**(2), 273-281, DOI: 10.1002/adma.201302562, (January 2014).

Dielectric Ceramics in Nanosheet Form

Tina T. Salguero, Assistant Professor
Department of Chemistry
University of Georgia
Athens, GA 30602

Program Scope

Nanosheets are characterized as being freestanding nanomaterials from one to several monolayers thick and up to tens of micrometers in lateral dimensions. The nanosheet morphology has several unique features that put it at the frontier of materials development, foremost the fact that nanosheets can combine remarkable, quantum effect-derived properties with large surface areas and the advantages of solution-based manipulation methods.

To date, well-defined nanosheets have been derived from lamellar materials via exfoliation processes; examples include selected perovskites, various transition metal oxides and chalcogenides, hexagonal boron nitride, and graphene. We are interested in materials for energy applications that go beyond these examples, specifically ternary oxide ceramics. The important initial challenge is that there is no bulk precursor that can simply be exfoliated to provide nanosheets of these materials. However, when this preparative hurdle is surmounted, these nanosheets will provide an opportunity to better understand the properties of complex oxide ceramics at a size regime down to one monolayer, as well as allow us to study the roles of surface functionalization and interface interactions. Our approach in this area of two-dimensional ceramic nanomaterials encompasses synthesis, characterization, and deposition methods.

Recent Progress

Aim (1): To develop innovative methodologies for preparing dielectric ceramics in nanosheet form. The first step is to prepare dielectric ceramics as nanosheets, a non-natural form of these materials. This synthetic challenge requires novel strategies and techniques encompassing solid-state inorganic chemistry as well as solution-based modification and processing. Our innovation is to apply template-based and topotactic chemical transformations to pre-existing nanosheet starting materials. We have focused so far on two classes of ternary oxide materials that have well-characterized ferroelectric properties: the titanate-based perovskites ATiO_3 ($A = \text{Ba}, \text{Sr}, \text{Pb}$) and the bismuth-based Aurivillius materials Bi_2MO_6 ($M = \text{Mo}, \text{W}$).

Our synthetic studies to produce ATiO_3 nanosheets have focused on the topotactic conversion of titania- or titanate-containing nanosheet precursors. For example, we have developed direct $\text{TiO}_2(\text{B})$ nanosheet to BaTiO_3 nanosheet conversion chemistry that uses $\text{Ba}(\text{OH})_2 \cdot 8\text{H}_2\text{O}$ as both the source of “BaO” and as a solvent that permits reaction temperatures $< 200^\circ\text{C}$ (Figure 1). A large part of this effort has involved an in-depth study of the mechanism of BaTiO_3 nanosheet formation. In brief, the topotactic transformation is highly dependent upon the structure and stoichiometry of the precursor (titanate type and structure, level of demetallation, protonation, degree of exfoliation, surfactant stabilization, metal pretreatment). A matrix of 25+ starting materials has been examined, including hydrothermal, solvothermal, and

melt reaction conditions. This work suggests that the success of $\text{TiO}_2(\text{B})$ nanosheet to BaTiO_3 nanosheet conversion depends upon three main factors: (a) the open structure of $\text{TiO}_2(\text{B})$ that leads to high reactivity, (b) the use of a mild reaction temperature to preserve the nanosheet morphology, and (c) the low solubility of titania nanosheets in $\text{Ba}(\text{OH})_2 \cdot 8\text{H}_2\text{O}$, which limits dissolution-precipitation mechanisms that lead to nanoparticles.

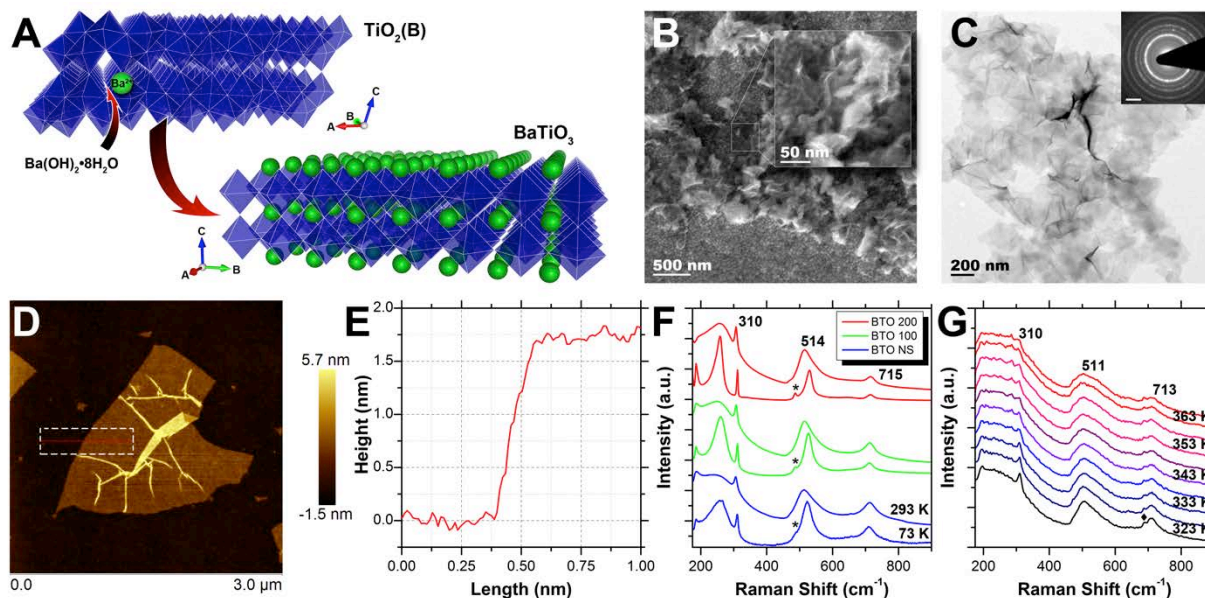


Figure 1. Synthesis and selected characterization of BaTiO_3 nanosheets: (A) Reaction scheme that illustrates the conversion of $\text{TiO}_2(\text{B})$ nanosheets into BaTiO_3 nanosheets. (B) SEM image of crumpled nanosheets with HRSEM inset. (C) TEM image of nanosheets with SAED pattern (inset) that can be indexed to BaTiO_3 . (D) Topographic AFM image of a single BaTiO_3 nanosheet with a corresponding step height measurement (E) showing an average thickness of ~ 1.7 nm. (F) Raman spectra of BaTiO_3 nanosheet (BTO NS) and nanoparticle (BTO 100 and BTO 200) samples collected at 293 and 77 K. (G) Raman spectra of BaTiO_3 nanosheets from 323 to 368 K.

In the Bi_2WO_6 system, we developed a double nanosheet template route to preparing high-quality Bi_2WO_6 nanosheets. As illustrated in Figure 2, the most successful approach involves the reaction of two nanosheet materials under hydrothermal conditions: surfactant-free cesium tungstate $\text{Cs}_4\text{W}_{11}\text{O}_{36}^{2-}$ nanosheets and bismuth oxide-based $[\text{Bi}_6\text{O}_6](\text{OH})_3(\text{NO}_3)_3$ nanosheets that are generated *in situ* from $\text{Bi}(\text{NO}_3)_3$. Monitoring these reactions by powder X-ray diffraction and electron microscopy techniques confirmed the proposed mechanism. The Bi_2WO_6 nanosheet product exhibits well-defined edges and thicknesses of 10-15 nm.

Aim (2) To characterize the fundamental properties of dielectric ceramic nanosheets. Our innovation is to use the unique combination of morphology and surface functionalization of monolayer-thick ceramic nanosheets to tune their properties. Both BaTiO_3 and Bi_2WO_6 nanosheets prove to exhibit surprising and interesting properties. In the case of BaTiO_3 nanosheets, structure analysis by Raman spectroscopy and synchrotron X-ray diffraction reveal that the material is tetragonal at room temperature (Figure 1), which is a key prerequisite for

ferroelectric properties. Recent piezoresponse force microscopy (PFM) measurements with collaborators (Prof. Matt Dawber, SUNY Stony Brook, Physics) have shows that BaTiO₃ nanosheets show a clear piezoresponse at room temperature.

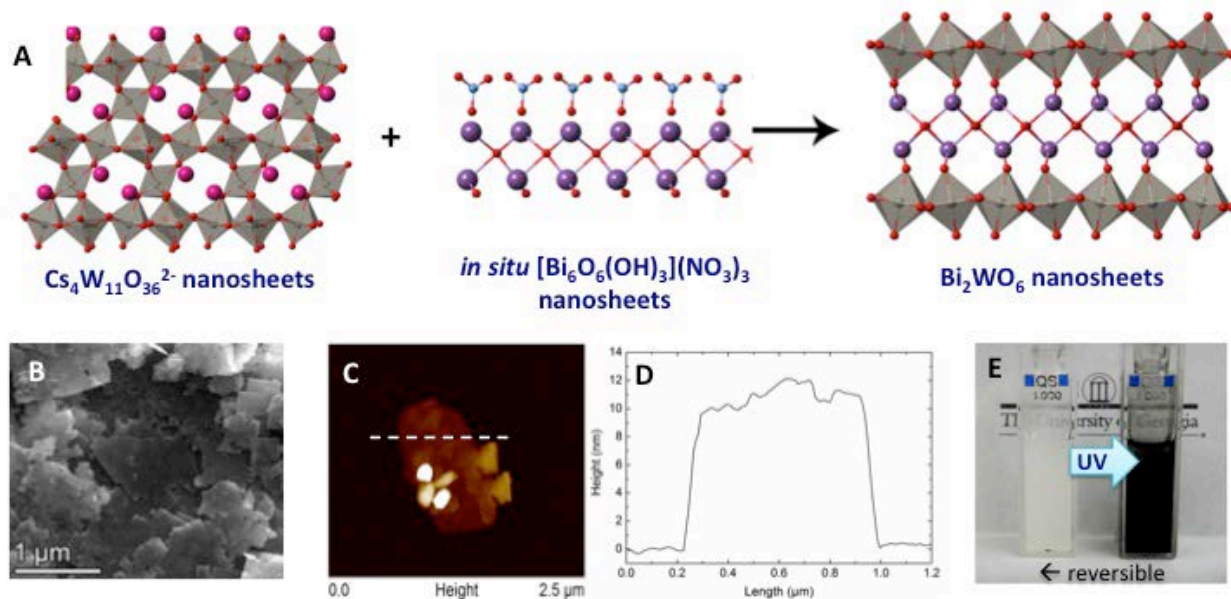


Figure 2. Synthesis and selected characterization of Bi₂WO₆ nanosheets: (A) Reaction scheme that illustrates the conversion of Cs₄W₁₁O₃₆²⁻ and [Bi₆O₆](OH)₃(NO₃)₃ nanosheets into Bi₂WO₆ nanosheets. (B) SEM image of isolated Bi₂WO₆ nanosheet product. (C) Topographic AFM image of a Bi₂WO₆ nanosheet with a corresponding step height measurement (D) showing an average thickness of ~11 nm. (E) Photograph showing the color change between a Bi₂WO₆ nanosheet dispersion (white sample at left) and a UV-irradiated sample (black at right). The chromism is reversible upon isolating and heating the solids.

We characterized the band gap of Bi₂WO₆ nanosheets compared to other nanomorphologies and bulk material, an important factor in its well-known photocatalytic properties. We also discovered that this material is reversibly chromic with respect to both UV irradiation (Figure 2) and lithium intercalation.

Future Plans

Aim (1): We plan to further expand synthetic efforts to include ruthenate-based ternary oxides as well as apply template-based methods to preparing Bi₂MoO₆ nanosheets.

Aim (2): The next focus of characterization efforts is on the variable temperature behavior of ternary oxide nanosheets, particularly Raman spectroscopy, optical band gap measurements, synchrotron diffraction, and PFM.

Aim (3): To process dielectric ceramic nanosheets via solution-based techniques. We plan to utilize inkjet printing of ternary oxide nanosheet inks; because nanosheets typically exhibit liquid crystal properties, the solid components will be well-ordered when the ink dries,

which leads to high-quality (near crystalline) materials. In addition, we plan to use dielectric ceramic nanosheets in the assembly of layered, hybrid, and composite macroscale materials. Such well-ordered materials can contain tailored interfaces between dissimilar materials, controlled layer thicknesses, gradients, varied nanosheet dimensionality (flat vs. crumpled), and so on. In addition, solution-based approaches enable the preparation of macroscale samples on large and/or flexible substrates at ambient conditions.

Publications

Timothy R. Pope, Melissa N. Lassig, Gregory Neher, Richard D. Weimar III, and Tina T. Salguero, "Chromism of Bi_2WO_6 in Single Crystal and Nanosheet Forms" Highlighted in the "2014 Emerging Investigators" issue: *J. Mater. Chem. C*, **2014**, 2, 3223-3230.

Christopher A. Barrett, Sara J. Callori, Matthew Dawber, and Tina T. Salguero, "Freestanding Nanosheets of Barium Titanate" submitted.

Computation-Guided Synthetic Strategies for Nanocomposite Electrode Structures Designed to Probe Critical Size Effects on Charge Storage and Transport

Andreas Stein, Donald G. Truhlar, William H. Smyrl

Program Scope

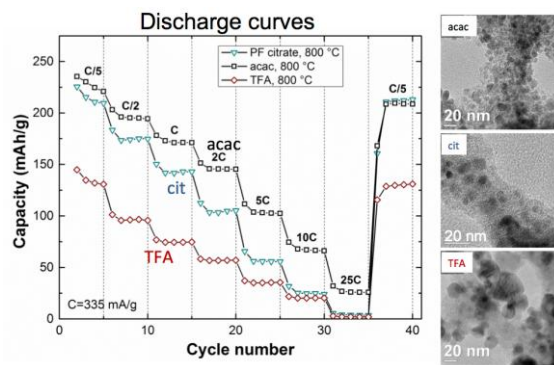
Templating methods are developed for synthesizing nanostructured composite electrodes, in which a redox active phase with limited intrinsic charge carrier conductivity but other attractive properties for charge storage (e.g., high specific capacities, specific target potentials, low cost, safety, etc.) interpenetrates a porous host as a secondary conductive phase. The secondary phase enhances electrical conductivity, maintains electrolyte access, and provides structural, functional, and mechanical stabilization. The nanocomposite structure of conductive and active phases ensures that nm-sized dimensions are precisely controlled to keep diffusion paths short and to maximize the interface between all phases. Such constructs provide new opportunities for employing charge storage materials with desirable properties, but which previously were not considered usable due to low electronic conductivities, slow ion diffusion kinetics, large volume changes during charge storage and release, and/or poor reversibility. The choice of materials and material dimensions is guided by theory and computational modeling involving density functional theory.

Recent Progress

Control over particle size and placement of electroactive phases in multicomponent nanocomposite electrodes. Enhanced utilization of ion intercalation electrode materials and improved charge and discharge rates are possible by reducing particle size to the nanometer regime. Close contact of these particles with an electronically conductive phase, such as carbon, facilitates electron transport through the extended composite electrode phase, so that even poorly conducting materials can achieve reasonable charge capacities. However, if the conductive phase fully embeds the active material, access of ions may be impeded. Therefore, in the design of composite electrodes, both size and distribution of electroactive and conductive phases must be controlled. One such structured nanocomposite system of interest is the TiO₂/carbon system. TiO₂ has been investigated as an alternative electrode material to carbon anodes in rechargeable lithium ion batteries. It offers a distinct safety advantage when compared to commercial graphite anodes, since Li⁺ intercalation into TiO₂ occurs at a higher voltage than for graphite. We developed a facile, robust synthesis of nanostructured TiO₂/carbon composites using a combination of colloidal crystal templating and surfactant templating with a single precursor solution for the titania and carbon components. This synthesis produced three-dimensionally ordered macroporous (3DOM) TiO₂/C composites with mesoporous walls (3DOM/m). Control

over the size and location of the TiO_2 crystallites in the composite was achieved by changing the chelating agent in the titania precursor, which controls interactions between precursors and the poly(methyl methacrylate) (PMMA) based colloidal crystal template. We studied titania complexes with three different chelating agents that allowed systematic variation of precursor polarity and carbon content, namely trifluoroacetic acid (*TFA*), acetylacetonate (*acac*), and citric acid (*cit*) (in order of increasing polarity). The titania precursor was mixed with a phenol-formaldehyde (PF) resol as the major carbon precursor. With *TFA* as chelating agent, the nonpolar precursor associated mainly with the PMMA template surface, so that TiO_2 particles grew at the interface with the polymeric colloidal crystal template (Figure 1). In contrast, with *acac* as chelating agent, titania particles were uniformly distributed throughout the resol-derived carbon phase. The polarity of the titanium-*acac* complex is similar to that of the ethanolic resol component, leading to the uniform component distribution. With polar *cit* as the chelating agent, a similar uniform distribution of titania was obtained throughout the composite structure. Thus, by controlling interactions between precursor components and template, we can precisely place components of nanocomposites through self-organization.

The choice of titania location throughout a polymeric precursor for carbon also affects the resulting titania particle sizes and, in turn, the electrochemical properties of the composites. Particle sizes of titania embedded in carbon were smaller than those of titania at the carbon surface, because surrounding polymer/carbon mitigated grain growth during the carbonization process. In composites prepared with *cit* as the chelating agent, titania particles were surrounded by a larger fraction of carbon because *cit* acted as a secondary source of carbon, partially impeding Li^+ access, as borne out in electrochemical studies. Adjustment of the pyrolysis temperature has allowed us to strike a balance between the size of the TiO_2 crystallites and the degree of carbonization. Using these pathways to optimize performance, the primarily macroporous TiO_2/C composites can attain good capacities at moderate rates (171 mAh/g at a rate of 1C). The performance of the TiO_2/C composites is better than that of many ordered mesoporous TiO_2 materials. Additionally, the carbon in these composites can function as a secondary template for high surface area, macroporous TiO_2 with disordered mesoporous voids.



Combining the advantages of a nanocrystalline framework and significant open porosity, the macroporous TiO_2 offers good rate performance and delivers a stable capacity (>170 mAh/g at a rate of C/2) over 100 cycles.

Figure 1. TEM of 3DOM/m *TFA*- TiO_2/C , *acac*- TiO_2/C , and *cit*- TiO_2/C materials and their delithiation behavior at various discharge rates. The temperature in the legend refers to the pyrolysis temperature of the composite materials.

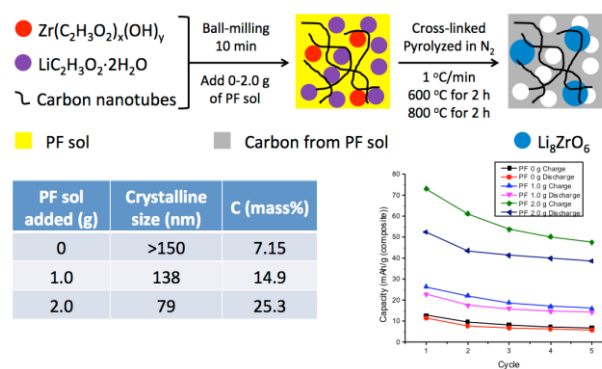
Cathode materials for lithium ion batteries that can deliver more than one Li/formula unit. To probe the limits of poorly conducting materials as potential novel charge storage

materials, we investigated Li_8ZrO_6 /carbon composites as potential cathode materials for Li^+ storage. Li_8ZrO_6 has a layered structure suitable for intercalation and a high molar Li:mass ratio (8 Li:242.8 g = 1 Li/30.3 g, compared to 1 Li:157.8 g in LiFePO_4 and 1 Li:97.9 g in LiCoO_2). Although a single-crystal structure of Li_8ZrO_6 has not yet been determined, it is believed to be isostructural with Li_8SnO_6 , having layers containing octahedral ZrO_6 units and Li ions, sandwiching a double layer of Li ions. We confirmed this structure by Rietveld refinement of powder X-ray diffraction data and by geometry optimization using Kohn–Sham density functional theory with the PBE, N12, and M06-L exchange-correlation functionals. If a large fraction of Li ions in Li_8ZrO_6 could be reversibly removed, this material would be interesting for cathodes in rechargeable lithium ion batteries (LIBs). Every extractable Li ion from a Li_8ZrO_6 unit provides a specific capacity of 110.5 mAh/g. If two or more Li ions are electrochemically active, an improvement in the capacity over commercialized materials can be expected.

Theoretical studies of the electrode materials in LIBs provide crucial information on structural changes and charge transport during the lithiation and delithiation processes. We used M06-L and N12 exchange-correlation functionals to predict the voltage of Li_8ZrO_6 and lithium diffusion barriers in LIBs. To simulate the charging and discharging processes, we generated lithiated and delithiated Li_xZrO_6 structures from the Li_8ZrO_6 structure. Using the CM5 charge model we found a large charge variation on oxygen during charging and discharging. It is easier to remove the Li atoms in the tetrahedral voids than to remove those in the octahedral voids. We found that the Li_7ZrO_6 and Li_6ZrO_6 materials can still keep the layered structure of Li_8ZrO_6 , and the volume of the unit cell does not change much (less than 5%), while in Li_5ZrO_6 configurations, either the layered structure is not kept or the volume of the unit cell decreases by more than 10%. The M06-L functional predicts a voltage of 4.0 eV vs. Li/Li^+ for the extraction of the first Li atom. We found that it is easier to remove the second and third Li atoms than the first one. The delithiation structure can be metastable and may release O_2 ; the delithiation of Li_8ZrO_6 in LIB may follow a nonthermodynamic path – that is, it may be kinetically controlled. When three lithium atoms are extracted from Li_8ZrO_6 , the layered structure is greatly distorted, so the delithiation no longer appears topotactic. Li diffusion in Li_8ZrO_6 crystals most likely happens in a 2D zigzag path between the Li tetrahedral layers. The (001) surface is the most stable one, and its voltage is ~ 0.1 eV higher than that of bulk. Diffusion into the oxide has a barrier comparable to diffusion between O_h and T sites in bulk.

It has been noted that Li_8ZrO_6 “is difficult to synthesize as a single phase because of its high content of volatile lithium components.” We optimized a published synthesis of Li_8ZrO_6 to reliably obtain pure-phase products in the form of bulk powders, and we tested the electrochemical properties of these materials. The charge and discharge curves of cells containing Li_8ZrO_6 /carbon/PVDF composite cathodes and lithium foil anodes showed large polarization because of the low conductivity of Li_8ZrO_6 , which was measured to be $8 \times 10^{-10} \text{ S cm}^{-1}$ at room temperature by impedance spectroscopy.

To decrease the large polarization of the electrode, we are developing various methods of reducing dimensions of the Li_8ZrO_6 particles, including mechanical grinding, delamination by sonication, templating with colloidal crystals, and in-situ confinement in polymeric carbon precursors. Each of these methods provides access to Li_8ZrO_6 particles with different sizes and aspect ratios, either as a single phase or embedded in a carbon matrix. So far, the smallest crystallite sizes obtained are in the 70–80 nm range, using colloidal crystal templating and in-situ confinement. These parameters are then correlated to electrochemical behavior. Figure 2 shows an example of the effect of precursor composition on grain size of Li_8ZrO_6 and the concomitant effect on capacity for Li^+ . Although the capacity is still below its theoretical value, an increase in



capacity with decreasing crystallite size is clearly seen, and these data support the viability of using Li_8ZrO_6 -type structures as electrode materials for LIBs.

Figure 2. Schematic procedure for the synthesis of Li_8ZrO_6 prepared through in-situ confinement in PF carbon. The table shows the dependence of Li_8ZrO_6 crystallite size and carbon content on the amount of PF added. Corresponding charge and discharge curves are also shown.

Future Plans

During the next year, we will continue to develop and improve syntheses that provide greater control over dimensions and aspect ratios of nanostructured Li_8ZrO_6 and related composites with conductive phases, and examine structural changes during electrochemical lithiation and delithiation by in-situ XRD. We will also examine dopants to increase the conductivity of Li_8ZrO_6 . Similar synthetic and computational approaches will be applied to other intercalation materials that potentially deliver more than one cation per formula unit.

Publications

Vu, A.; Stein, A. “Lithium iron phosphate spheres as cathode materials for high power lithium ion batteries”, *J. Power Sources* **2014**, *245*, 48–58.
[dx.doi.org/10.1016/j.jpowsour.2013.06.116](https://doi.org/10.1016/j.jpowsour.2013.06.116)

Petkovich, N. D.; Rudisill, S. G.; Wilson, B. E.; Mukherjee, A.; Stein, A.; “Control of TiO_2 Grain Size and Positioning in Three-Dimensionally Ordered Macroporous TiO_2/C Composite Anodes for Lithium-Ion Batteries”, *Inorg. Chem.* **2014**, *53*, 1100–1112.
[dx.doi.org/10.1021/ic402648f](https://doi.org/10.1021/ic402648f)

Wilson, B. E.; Smyrl, W. H.; Stein, A.; “Design of a Low-Cost Electrochemical Cell for In-Situ XRD Analysis of Electrode Materials”, *J. Electrochem. Soc.* **2014**, *161*, A700–A703.
[dx.doi.org/10.1149/2.034405jes](https://doi.org/10.1149/2.034405jes)

“Electrochemically Smart Bimetallic Materials Featuring Group 11 Metals: In-situ Conductive Network Generation and Its Impact on Cell Capacity”

PI: SUNY Distinguished Professor Esther S. Takeuchi^{a,b}
co-PIs: SUNY Distinguished Teaching Professor Kenneth J. Takeuchi^a
Research Associate Professor Amy C. Marschlok^a
Affiliations: ^a Stony Brook University; ^b Brookhaven National Laboratory

Program Scope. This project will provide mechanistic insight and fundamentally advance the three key performance metrics for energy storage: energy density, power delivery, and reversibility. These goals will be realized through development and study of a new class of bimetallic and trimetallic materials: $MwM'xOz$, $MwM'xOPyOz$, and $MwM'xPyOz$.

Recent Progress. In the practical deployment of energy storage devices, there is a gap between the theoretical energy content and the realizable energy delivered. Recent experiments conducted under this program strive to gain mechanistic insight regarding the discharge process in bimetallic cathode materials, taking advantage of the unique resources at Brookhaven National Laboratory. Specifically, we shed light on the pathways of electron conduction and ion migration in active batteries by the use of a) in situ EDXRD permitting tomography-like measurements, and b) ex situ XAS providing oxidation state information.

a) In-situ Energy Dispersive X-ray Diffraction (EDXRD). Silver vanadium diphosphate, $Ag_2VP_2O_8$, is an inherently non-conducting material with the unique capability of forming its own conductive pathways *in-situ*. The study of $Ag_2VP_2O_8$ as a model system provides insights into the electrochemical reduction process for inherently poorly conducting phosphate and diphosphate based cathode materials. The Ag^0 metal product formed upon discharge of $Li/Ag_2VP_2O_8$ is a strong x-ray scatterer, and as such its presence can be detected in small amounts. EDXRD presents a special opportunity to achieve spatial resolution of the electrochemical reduction process within the electrode of a functioning electrochemical cell, providing the opportunity for tomographic-like data analysis.

In this study, *in-situ* EDXRD measurements are conducted on intact lithium/silver vanadium diphosphate cells, $Li/Ag_2VP_2O_8$, at various depths of discharge selected to deliberately probe the early stage reduction where the large change in resistance has been noted.[1] The use of EDXRD enables spatial visualization of Ag^0 formation, including relative estimation of concentration as a function of position, **Figure 1**.

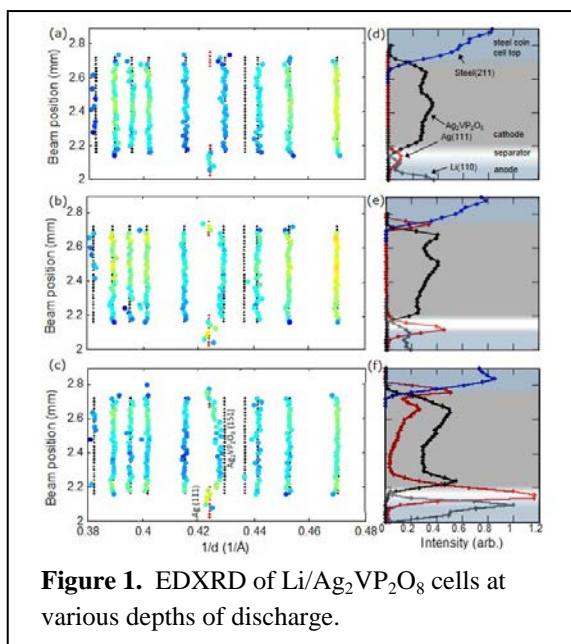


Figure 1. EDXRD of $Li/Ag_2VP_2O_8$ cells at various depths of discharge.

As with other silver bimetallic phosphorous oxide compounds, a large decrease in impedance in discharged cells as compared to the not-discharged cell coincides with the development of Ag^0 nanoparticles. The data presented suggest two possible mechanisms contributing to the decrease in impedance: formation of a percolation network that decreases conductivity throughout the entire cathode, and a decrease in the charge-transfer layer resistance by creating a conducting layer around the particles of active material increasing the electronically accessible surface area of the cathode. Once a particle begins to discharge, the formation of Ag^0 would make it easier to continue discharging in that local region. Thus, more surface area of the insulating $\text{Ag}_2\text{VP}_2\text{O}_8$ active material particles could be accessed as a result of rapid charge transfer through the highly conducting silver nanowires. The EDXRD results indicate that a majority of the Ag^0 formation occurs at the can and anode interfaces of the cathode, only moving throughout the cathode with higher levels of discharge.[1]

Ex-situ X-ray Absorption Spectroscopy (XAS). Nanostructured materials possess important properties which can affect the electrochemistry of Li-ion batteries. For example, reducing crystallite dimension decreases the path length for the transport of ions and electrons, which has been linked to higher achieved capacity of electrode materials in particular under high rate discharge. We completed a study on the relationship of size and electrochemical performance of magnetite. Rietveld refinement and x-ray absorption spectroscopy (XAS) investigation of nanosized Fe_3O_4 as a function of crystallite size (7-26 nm) was completed. Rietveld refinement established that the Fe_3O_4 samples were phase pure, while the extended x-ray absorption fine structure (EXAFS) and x-ray absorption near edge structure (XANES) provided insight into the local geometries and electronic structure of the iron centers, including oxidation state assignment. From our current and recent studies, we suggest that the surface of the Fe_3O_4 crystallites is rich in Fe^{3+} , thus as the Fe_3O_4 crystallite size decreases, the electrochemical capacity increases, due to a net enrichment of Fe_3O_4 in Fe^{3+} . [2]

Our unique synthesis of magnetite nanoparticles, a low-temperature coprecipitation method, allowed the systematic variation of crystallite size with reactant concentration, in the absence of a constraining medium. Electrochemical cells based on $\text{Li}/\text{Fe}_3\text{O}_4$ show a linear increase in capacity with decreasing crystallite size. The effects of crystallite size on electrochemical performance were evaluated by comparing the discharge capacity for various crystallite sizes at specific voltages. Notably, the capacities to all four voltage limits displayed > 2 fold capacity increases between the smaller (9 nm) and larger (26 nm) crystallite size parent Fe_3O_4 materials, with the most significant improvement at 1.2 V, where the 9 nm sample achieved a 280% increase in delivered capacity over the commercial material.[3]

To investigate the structural differences during electrochemical discharge of Fe_3O_4 , we characterized partially discharged electrodes. Analysis of X-ray diffraction patterns of discharged electrodes focused on two peaks attributable to the tetrahedral (311, 36°) and octahedral (400, 43°) environments. At 0.7 electron equivalents, there are no significant, structural differences among the commercial (26.2 nm), 10.6 nm, and 9.2 nm samples. For all crystallite sizes, the powder XRD patterns can still be indexed to the inverse cubic spinel Fe_3O_4 phase. At 2.8 electron equivalents, the XRD patterns indicate that the iron ions have begun to vacate the tetrahedral sites and occupy octahedral sites. Once the magnetite-based electrodes have been discharged to 4 electron equivalents, the average structure of all three samples (26.2, 10.6, and 9.2 nm) is consistent with the rock-salt phase. At 8 electron equivalents, evidence of a rock-salt phase persists, but with reduced crystallinity, particularly for the 10.6 and 9.2 nm

samples. In general, the commercial (26.2 nm) sample retains the most crystalline profile through electrochemical reduction, while the coprecipitation prepared (9.2, 10.6 nm) samples show similar crystallographic transitions, but with reduced crystallinity.

Notably, while multiple changes in curvature were evident in the voltage profiles, comparison of the XRD patterns indicated only one phase transition from inverse cubic spinel to rock-salt structure. Thus, extended x-ray absorption fine structure (EXAFS) was used as a local probe to investigate the fine structural changes as a function of electrochemical reduction. Evidence of phase transitions in the EXAFS data were observed in both the first and second coordination shells consistent with the following sequence:

1. conversion from inverse cubic spinel (Fe_3O_4) to rock-salt-like (Li_yFeO_2) phase,
2. conversion from rock-salt-like (Li_yFeO_2) phase to $\text{Li}_2\text{O} + \text{Fe}^0$

The transition from the inverse cubic spinel to a rock-salt like phase occurs between 2.8 and 4 electron equivalents. The second phase transition is marked by the appearance of a shoulder peak in the magnitude of the Fourier transformed EXAFS signal near 2.3 Å, between the first and second coordination shells of the rock-salt-like Li_xFeO_2 phase. Conclusive support of the formation of metallic Fe^0 is lacking in the powder X-ray diffraction patterns, however, EXAFS provides information complementary to x-ray diffraction results. The formation of metallic Fe^0 in the EXAFS region,

Figure 2 is most apparent in the coprecipitation prepared Fe_3O_4 samples with crystallite sizes ≤ 10.9 nm and is also reflected by the XANES plots. Prior reports have proposed formation of metallic iron upon electrochemical reduction of Fe_3O_4 . This work provides the *first experimental evidence* indicative of Fe^0 nanoparticle formation.[3] Notably, while the metallic Fe^0 particles are not detectable by x-ray diffraction, x-ray absorption spectroscopy provides a complimentary method as a probe suitable for Fe^0 detection.

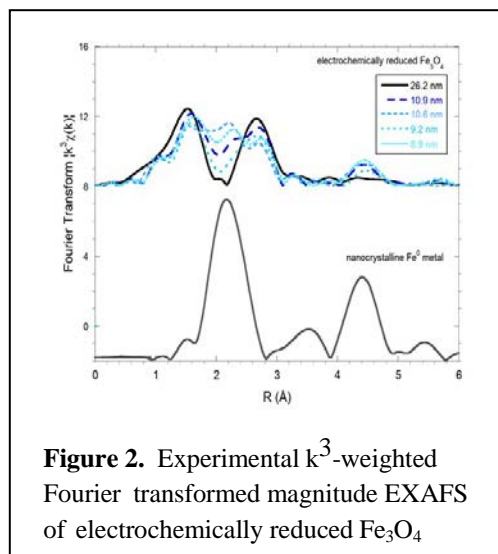


Figure 2. Experimental k^3 -weighted Fourier transformed magnitude EXAFS of electrochemically reduced Fe_3O_4

Future Plans. We will continue our focus on fundamental understanding of the reduction/oxidation behavior of the Mn, V, and Fe based materials. We will probe the relationship of synthetic size control and electrochemistry. We will leverage both in-situ and ex-situ methods to further the understanding of the redox processes.

References. References [1 – 3] used in text above match those in the Publications list below.

Publications.

1. K.C. Kirshenbaum, D.C. Bock, Z. Zhong, A.C. Marschilok, K.J. Takeuchi, E.S. Takeuchi, “In situ profiling of lithium/ $\text{Ag}_2\text{VP}_2\text{O}_8$ primary batteries using energy dispersive X-ray diffraction,” *Phys. Chem. Chem. Phys.*, **2014**, *16*(19), 9138-47.
2. M.C. Menard, A.C. Marschilok, K.J. Takeuchi, E.S. Takeuchi, “Variation in the iron oxidation states of magnetite nanocrystals as a function of crystallite size: the impact on electrochemical capacity.” *Electrochimica Acta*, **2013**, *94*, 320-6.

3. M.C. Menard, K.J. Takeuchi, A.C. Marschilok, E.S. Takeuchi, "Electrochemical discharge of nanocrystalline magnetite: structure analysis using X-ray diffraction and X-ray absorption spectroscopy," *Phys. Chem. Chem. Phys.*, **2013**, *15*(42), 18539-48.
4. K.J. Takeuchi, S.Z. Yau, A. Subramanian, A.C. Marschilok, E.S. Takeuchi, "The electrochemistry of silver hollandite nanorods: Enhancement of electrochemical battery performance via dimensional and compositional control," *J. Electrochem. Soc.*, **2013**, *160*(5), A3090-4.
5. E.S. Takeuchi, C.-Y. Lee, P.-J. Cheng, M.C. Menard, A.C. Marschilok, K.J. Takeuchi "Silver Vanadium Diphosphate $\text{Ag}_2\text{VP}_2\text{O}_8$: Electrochemistry and Characterization of Reduced Material providing Mechanistic Insights." *J. Solid State Chem.* **2013**, *200*, 232-40.
6. Y.J. Kim, K.J. Takeuchi, A.C. Marschilok, E.S. Takeuchi, " $\text{Ag}_{3.2}\text{P}_{1.5}\text{O}_{7.8}$: a high voltage silver vanadium phosphate cathode material," *J. Electrochem. Soc.*, **2013**, *160*(11), A2207-11.
7. E.S. Takeuchi, A.C. Marschilok, K.J. Takeuchi, A. Ignatov, Z. Zhong, M. Croft, "Energy dispersive x-ray diffraction of lithium-silver vanadium phosphorous oxide cells: In-situ cathode depth profiling of an electrochemical reduction-displacement reaction" *Energy Environ. Sci.*, **2013**, *6*(5), 1465-70.
8. D.C. Bock, A.C. Marschilok, K.J. Takeuchi, E.S. Takeuchi, "A Kinetics and Equilibrium Study of Vanadium Dissolution from Vanadium Oxides and Phosphates in Battery Electrolytes: Possible Impacts on ICD Battery Performance." *J. Power Sources*, **2013**, *231*, 219-25.
9. A.C. Marschilok, C.P. Schaffer, K.J. Takeuchi, E.S. Takeuchi. "Carbon nanotube-metal oxide composite electrodes for secondary lithium based batteries." *J. Composite Mater.*, **2013**, *47*(1), 41-49.
10. K.J. Takeuchi, S.Z. Yau, M.C. Menard, A.C. Marschilok, E.S. Takeuchi, "Synthetic control of composition and crystallite size of silver hollandite: impact on electrochemistry." *ACS Appl. Mater. Interfaces*, **2012**, *4*, 5547-54.
11. E.S. Takeuchi, A.C. Marschilok, K.J. Takeuchi, "Secondary Battery Science: At the Confluence of Electrochemistry and Materials Engineering." *Electrochemistry*, **2012**, *80*(10), 700-5. (Invited highlight)
12. K.E. Farley, A.C. Marschilok, E.S. Takeuchi, K.J. Takeuchi, "Synthesis and electrochemistry of silver ferrite." *Electrochem. S. S. Lett.* **2012**, *15*(2), A23-A27.

Transition Metal Oxides Spinel Nanomaterials for Supercapacitor Reactions

Xiaowei Teng, Department of Chemical Engineering, University of New Hampshire

Program Scope

Electrochemical capacitors, also called supercapacitors, are a class of energy storage devices that fill the gap between high-energy-density batteries and high-power-density electrostatic capacitors. This project is to investigate the transition metal oxides (TMOs) for use as electrode materials for electrochemical capacitors. Through the novel material syntheses, structural and functional characterizations, and synchrotron-/neutron-based in situ measurements, the overall objectives of the proposed research are to (i) identify the effects of size, crystalline structure and chemical composition on energy storage capabilities of TMOs, and (ii) provide fundamental understanding of charge storage mechanism of these TMOs electrodes that can store more energy while maintaining a stable electrode/electrolyte interface.

Recent Progress

The major accomplishment of FY 2014 is the synthesis and characterization of vanadium pentoxide (V_2O_5) 1D nanostructures (nanofibers) as effective electrode materials for K-ion storage in aqueous phase electrochemical capacitor reactions. Designing nanostructured TMOs with unusual dimensions, i.e. 1D nanotubes/fibers or 2D nanolayers, have attracted attention as potential anodic materials for energy storage devices. These 1D or 2D TMO nanostructures usually have open, mesoporous and robust structures that favor efficient transport of alkaline cations and fast charge-transfer kinetics. Among these TMOs, V_2O_5 has been widely studied over the past decade due to its low cost, low toxicity and wide valence states from V^{2+} to V^{5+} . To obtain V_2O_5 nanostructures with different dimensions, many methods are used, including hydrothermal, electro-deposition, and template-assisted growth. However, a simple and low-cost method that can provide V_2O_5 with large quantities for practical applications is currently lacking. In FY 2014, we have developed simple two-step methods to synthesize 1D and 2D V_2O_5 nanostructures as electrode materials for K-ion storage via aqueous phase electrochemical capacitor reactions.

Figure 1a shows XRD (wavelength: 0.3196 \AA) pattern of the 1D V_2O_5 nanofibers (VNFs), attributed to the (00l) set of diffraction (blue label), showing high degree ordering of lamellar structures; and the conventional (hkl) set of reflection (black label). The XRD reflection is in good agreement with a layered, potassium-intercalated V_2O_5 ($K_{0.49}V_2O_5$, JCPDS 81045) as Figure 1b shows, except that the peak at $2\theta = 2.46^\circ$ is indexed as the (002) plane of non-layered $K_xV_2O_5$ (JCPDS 27718). The strongest diffraction peak at $2\theta = 1.98^\circ$ is indexed to the (001)

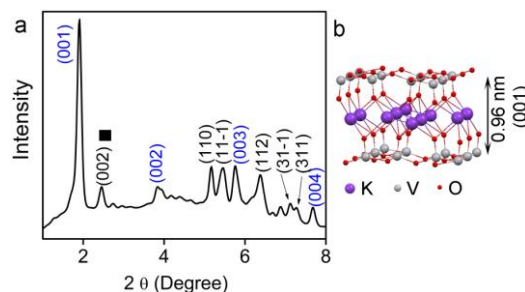


Figure 1. (a) XRD pattern and (b) atomic structure of VNFs.

basal reflection with a corresponding d_{001} of 0.96 nm.

Energy dispersive X-ray spectroscopy (EDS) shows that the final product contained 13.6% K and 83.7% V, giving a chemical

formula of $K_{0.33}V_2O_5$. Figure 2a and b show the TEM images of a typical VNF, conducted at the Center for Functional Nanomaterials at Brookhaven National Laboratory (BNL). An averaged repeating distance of 0.71 nm is obtained between layers in the direction parallel to long axis of the VNF (growth direction). Figure 2c shows the selected-area electron diffraction (SAED) pattern from the same VNF shown in Figure 2b. The fringe distances are calculated from SAED to be 0.67 nm and 0.32 nm, matching well with the distances calculated from TEM. The interplanar distance ($d_{001} = 0.71$ nm) obtained from HRTEM is considerably smaller than that calculated from XRD (0.96 nm), which can be explained by the removal of structured water between VNF layers during TEM analysis.

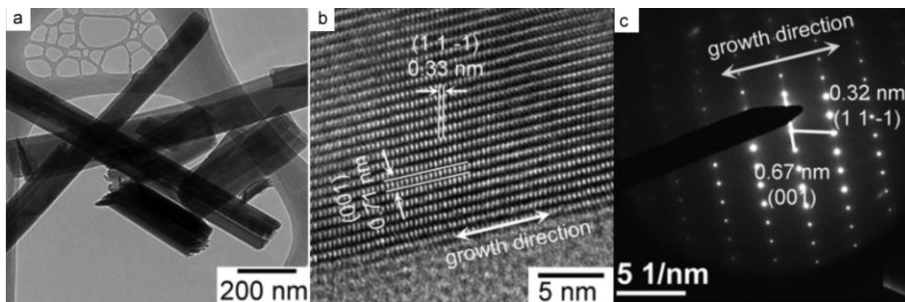


Figure 2. TEM images of VNFs. (c) SAED of VNF shown in (b).

Figure 3a shows the cyclic voltammograms (CVs) of the mixture of VNFs and conductive polymer (poly ethylenedioxythiophene) (PEDOT). The calculated gravimetric capacitance (C_{MS}) is strongly dependent on the scan rate as shown in Figure 3b. At a scan rate of 5 mV/s, the C_{MS} reached the maximum

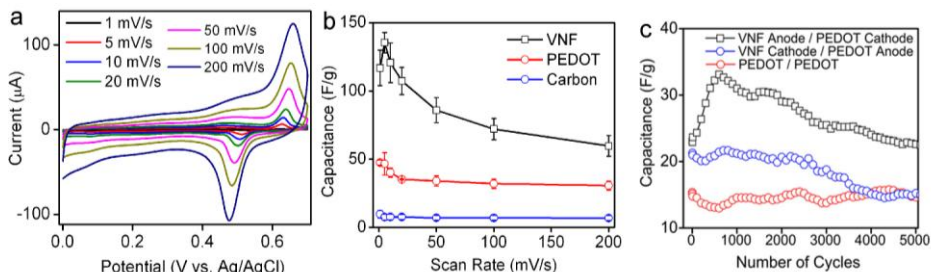


Figure 3. (a, b) half-cell analyses: (a) CVs of VNF/PEDOT as loading of 5 μg and 1.25 μg , respectively); (b) C_{MS} of VNF, PEDOT and active carbon vs. scan rates. And (c) C_{MS} vs. cycle number for button-cells.

value of 136 F/g (based on the mass of VNF only). In general, the electrical conductivity of a bulk V_2O_5 is low ($10^{-5} \sim 10^{-3} / \Omega\text{cm}$), so the addition of highly conductive PEDOT into VNFs improves rate capability, although the C_{MS} value of VNFs/PEDOT electrode is associated strongly with the VNF as shown in Figure 3b. The long-term cyclability of VNFs was investigated in two-electrode button-cells subjected to 5,000-cycle of galvanostatic charge/discharge analyses with a charge/discharge current density of 2 A/g. Figure 3d plots the C_{MS} values as a function of cycle number, in which the anodically loaded VNF electrode shows a 98% capacitive retention rate over 5,000 cycles. Figure 3d also shows that the VNFs don't

perform well: only 71% capacitive retention is achieved. Although PEDOT symmetric cell shows a high retention rate of 94%, its capacitance is low after 5,000 cycles.

Figure 4a shows a series of time-resolved XRD (wavelength = 0.3196 Å) patterns of VNFs using an electrochemical cell in 2 M KCl aqueous solution. The experiments were conducted at X7B at National Synchrotron Light Source at BNL. XRD patterns were obtained during anodic (black curves) and cathodic scans (blue curves) within the potential window between 0 V and 0.9 V using a CV program at a scan rate of 1 mV/s. The changes of (001) diffraction during the CV cycling are shown in Figure 4b.

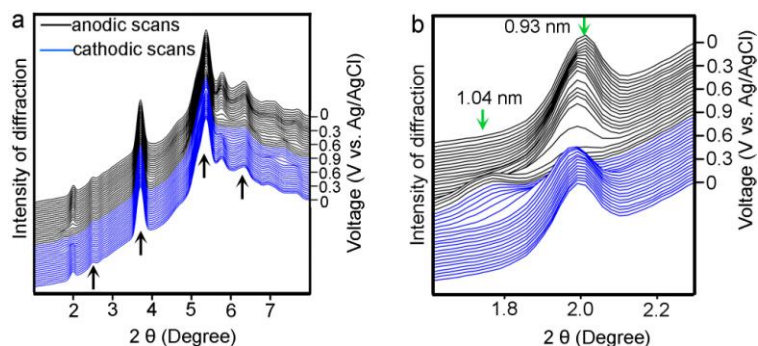


Figure 4. (a) In situ XRD of VNFs at potentials from 0 to 0.9 V. The diffraction peaks from graphite oxide were marked by arrows. (b) The evolution of the (001) planes.

During the anodic scan, the expansion of d_{001} values from 0.93 ($2\theta = 1.98^\circ$) nm to 1.04 nm ($2\theta = 1.76^\circ$), corresponding to 12% expansion, is observed. Consequently, contraction of d_{001} values from 1.04 nm to 0.95 nm is observed during the cathodic scan. The expansion and contraction of d_{001} match very well with the electrochemical extraction and insertion of K^+ ions into VNF lattice. During the anodic scans, VNF oxidation is accompanied with the removal of K^+ from interplanar layers of VNFs. Depletion of K^+ weakens the electrostatic interaction between K^+ and negatively charged $[VO_6]$ octahedral units within the VNF layers, increasing the interplanar distance (d_{001}) and facilitating the insertion of water into the interplanar gap. Conversely, during the cathodic scans, VNFs are reduced, accompanying with insertion of K^+ into layers. The strengthened electrostatic interaction between $[VO_6]$ layers and K^+ decreases the interplanar distance, and are accompanied with the removal of the water molecule between layers.

The other accomplishments of FY 2014 include synthesis and characterization of vanadium pentoxide (V_2O_5) 2D layered nanostructures (Figure 5). The electrochemical tests show that V_2O_5 nanolayers (with layer to layer distance over 1.0 nm) have a very good capacitive behavior at high scan rates CV measurements (100 mV/sec to 1000 mV/sec), in sharp contrast to 1D VNFs reported here, and other conventional TMOs.

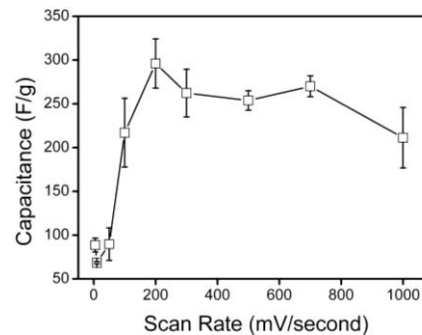


Figure 5. (a) Capacitance as a function of scan rates from 2D V_2O_5 nanolayers, obtained from CV measurements.

The accomplishments in FY 2014 also include the syntheses and electrochemical analysis of MnO_2 , Mn_3O_4 and Co-doped Mn_3O_4 spinel nanoparticles using three-electrode half-cell. Data show that the gravimetric capacitances of these materials are in the order of $MnO_2 < Mn_3O_4 < Co-Mn_3O_4$.

Future Plans

- 1) Electrochemical analyses in half-cell and button-cell of Ni- and Co-doped Mn_3O_4 spinel nanoparticles to determine the effect of Ni and Co doping on capacitance and cycle life.
- 2) Neutron scattering measurements and analyses of pure Mn_3O_4 spinel, Co-doped Mn_3O_4 spinel, and 1D/2D V_2O_5 at beam line X1B (NOMAD) at Spallation Neutron Source at the Oak Ridge National Laboratory via user proposal.
- 3) Understand the effect of the layer structure of V_2O_5 on the charge-storage capacity, especially during the fast charge-discharge processes.

Publications

- 1) Yeager, M. P.; Du, W. X.; Bishop, B.; Sullivan, M.; Xu, W.; Su, D.; Senanayake, S. D.; Hanson, J.; Teng, X. W., *Storage of Potassium Ions in Layered Vanadium Pentoxide Nanofiber Electrodes for Aqueous Pseudocapacitors*, **ChemSusChem** 2013, 6, 2231-2235
- 2) (Book Chapter) Teng, X.W., Charles, D. S., Shan, X.Q., Wu, Y. T., “*In Situ Studies of Charge-Storage Mechanism of Manganese Oxide Nanomaterials for Electrochemical Capacitors*”, Page 1-32. In book “*Supercapacitors: Electrochemical Properties, Applications and Technologies*”, Nova, 2014, ISBN: 978-1-63321-019-6 (In press)

Mesoscale photophysical properties of anisotropic hybrid nanostructure assemblies

Vladimir V. Tsukruk, Mostafa El-Sayed

School of Materials Science and Engineering and School of Chemistry and Biochemistry, Georgia Institute of Technology, Atlanta, Georgia, 30332, USA

Program Scope

We focus on the assembling of hybrid nanomaterials from a variety of noble metal nanoparticles (nanocubes, nanoframes) with well-controlled dimensions, shapes, and stability as well as their functionalization with different polymer shells in order to control their interparticle interactions and surface tethering properties and understand their photophysical properties. The directed assembly of these functionalized nanoparticles into organized meso-structures with controlled interparticle distances, surface distributions, and ordering is achieved by a variety of bottom-up and top-down techniques. These methods include Langmuir-Blodgett (LB), layer-by-layer (LbL) assembly, template-assisted assembly, and electron beam lithography (EBL). Well-controlled organization, combined with the specific light-matter interactions of nanoparticles and their assemblies, offers a unique opportunity to create hierarchical structures and materials with inherently anisotropic optical, and transport properties. A comprehensive, multi-length scale characterization of these hybrid assemblies is combined with the simulation of local plasmonic and coupling phenomena related to the shape and composition of core-shell hybrids and their local organization in order to understand their plasmonic, coupling, and other light interactions effects in organized nanostructures.

Recent Progress

Recently, we have made significant progress towards understanding factors, which can potentially improve the performance of sensing platforms based on plasmonic nanostructures displaying surface-enhanced Raman scattering (SERS), and localized surface plasmon resonance (LSPR) phenomena. We have shown that silver nanocube (AgNC) aggregates on different solid substrates can lead to substantial improvement of the refractive index sensitivity (RIS), which defines the chemical sensing ability. An extraordinary experimental RIS of about 770 nm per refractive index unit was found for aggregates inside cylindrical pores, which is more than an order of magnitude higher than that observed earlier and calculated for nanocubes on planar solid substrates. (Figure 1). The experimentally observed plasmon mode excitations for an individual

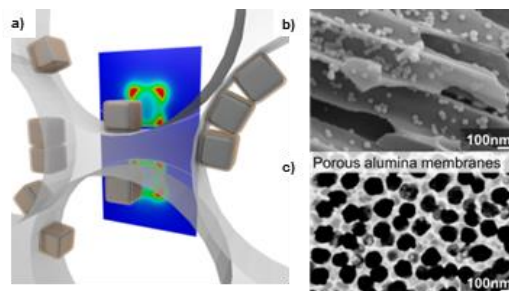


Figure 1. a) Inter-pore SPR coupling of adjacent nanocube aggregates located across the ultrathin pore walls. b), c) SEM images of a PAM with deposited AgNC.

nanocube and for complex multiple cube aggregates were evaluated with the assistance of finite-difference time-domain (FDTD) simulations. The results are compared with RIS measurements from a flat glass surface, a flat alumina surface, and a concave alumina substrate in relation to sensitive 3D SERS substrates. Numerical simulations suggested that the dramatically enhanced sensitivity of nanocubes in cylindrical alumina pores can largely be attributed to inter-pore coupling of nanocube aggregates closely across the ultrathin pore walls.

The broadband absorption of light in the visible regime was also investigated during the course of this project. Typically, the absorption of plasmonic nanostructures and their assemblies is limited by the narrow spectral bands that arise from wavelength specific resonances. To achieve a high broadband absorption, it is possible to combine multiple plasmonic resonances from different nanostructure elements in a fashion that ultimately enhances the total light absorption. Therefore, we engineered metal-

dielectric-metal nanostructures with broadband absorbing properties in the visible spectral range by combining the plasmonic resonances of different noble metal nanostructures via a hybrid top-down-bottom-up approach. Silver nanocubes and gold nano-gratings were coupled to each other using a dielectric polymer spacer with controllable thickness, resulting in a large multiplicative

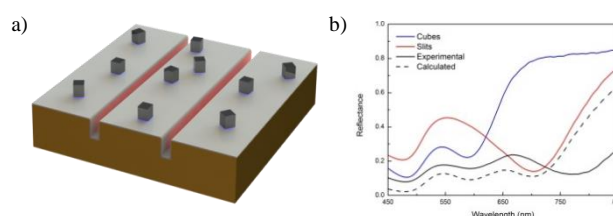


Figure 2. a) Silver nanocubes separated from an underlying gold nano-grating by a polymer spacer can be used in designing structures with broadband light absorption properties. b) Reflectance spectra of nanocubes, gratings, and the overall assembly.

enhancement of absorption properties across a broad spectral range (Figure 2a). Narrow, long nanogrooves in a gold film were first fabricated using EBL, after which a polymer spacer layer with a controllable thickness ranging from 4 to 12 nm was assembled by spin-assisted LbL assembly. Finally, silver nanocubes with different surface coverage from 12% to 22% were deposited. The individual plasmon resonances of these different nanostructures are located at significantly different optical frequencies and were tuned in this study to allow a significant increase of light absorbance to an average value of 84% across the broad wavelength range of 450-850 nm (Figure 2b).

Next, we discovered that optical scattering sites with a complex combination of local surface plasmon resonances and top-down electromagnetic hotspots could be created by considering 3D confined plasmonic resonances compared to traditional 2D ones. To this end, hollow rectangular gold nanostructures prepared by electron beam lithography (EBL) with gold caps show a significant red shift in their main scattering peak as compared to the solid structures (Figure 3a). FDTD modeling shows that the plasmonic response of these structures is dominated by higher order plasmonic modes and that the strength of these modes is shown to

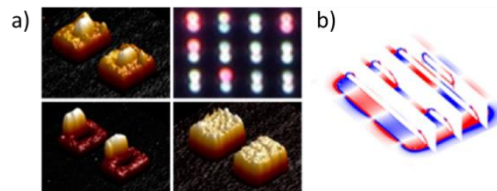


Figure 3. a) AFM images and hyperspectral imaging of the arrayed EBL nanostructures. b) FDTD modeling of charge distributions for the EBL nanostructures.

vary according to whether a cap is present (Figure 3b). The higher order dipolar mode caused by the capped nanostructure results in a manifold increase in the intensity of the electric field compared to the quadrupolar mode of a solid rectangle. In addition, the stacking scheme presents a new route for modifying the optical response of plasmonic nanostructures through top-down coupling, which yield plasmon resonance modes not observed in common 2D nanostructures.

We envisaged a plasmon-active hybrid nanomaterial design with electrochemical tunability of the local surface plasmon resonances. The plasmonic-active nanostructures are composed of silver nanocube aggregates embedded into an electrochromic polymer coating on an indium tin oxide electrode, with the nanocube aggregation controlled by the surface pressure during LB deposition (Figure 4). These polymer-nanocube hybrid nanomaterials demonstrated unique tunable plasmonic behavior under an applied electrochemical potential. A significant reversible experimental peak shift of 22 nm at an electric potential of 200 mV has been achieved in these measurements. FDTD simulations show that, under the full oxidation potential, a maximal spectral shift of ca. 80 nm can be potentially achieved which corresponds to a RI sensitivity of 178 nm per refractive index unit. Furthermore, FDTD modeling suggests that the electrochemically-controlled tunability of plasmonic peaks is caused by reversible changes in the refractive index of the electrochromic polymer coating caused by oxidation or reduction reactions under an applied external electrical field.

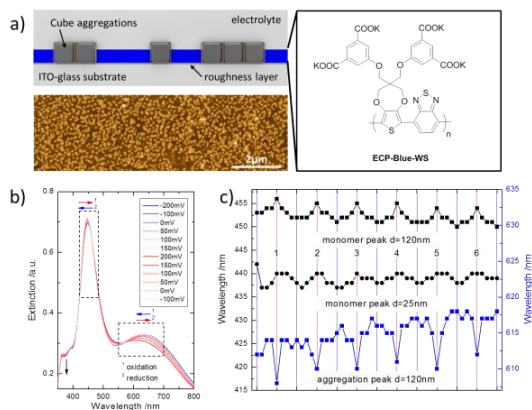


Figure 4. a) Experimental setup and AFM images of silver nanocube aggregations on ITO-glass substrate coated with the ECP-Blue-WS polymer; b, c). Reversible plasmonic shifts of nanocubes under variable electrical field.

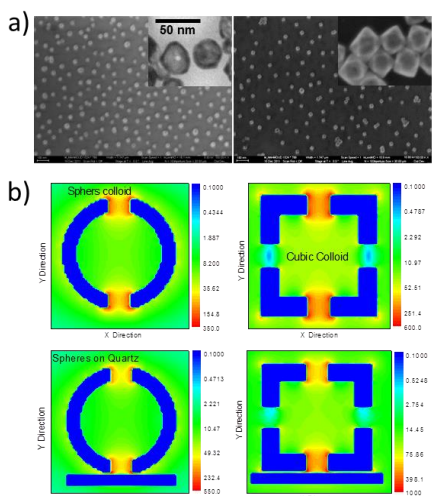


Figure 5. a) SEM images of AuHS and AuHC monolayers. b) Plasmon field distribution contours from DDA simulations.

Finally, gold hollow nanospheres (AuHSs) and gold hollow nanocubes (AuHCs) were synthesized by the galvanic replacement technique using silver nano templates. (Figure 5a). Colloidal AuHSs were found to have a higher sensitivity factor than that of AuHCs. As the separation gap between AuHCs nanoparticles decreases, their localized surface plasmon resonance red shifts more than AuHSs when assembled into LB monolayer. Furthermore, the SERS of thiophenol has higher intensity when measured on AuHCs than on AuHSs. Although the sensitivity factor of the studied AuHSs is higher than that of AuNCs, the quality of AuHSs as a LSPR sensor decreased more than that of AuNCs after placing on a substrate. As was shown by the discrete dipole approximation (DDA) calculations the coupling between the plasmon fields of the AuHCs pair is

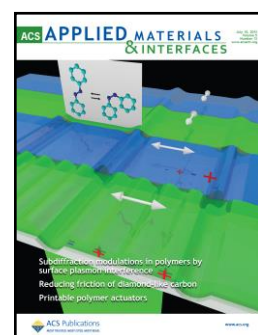
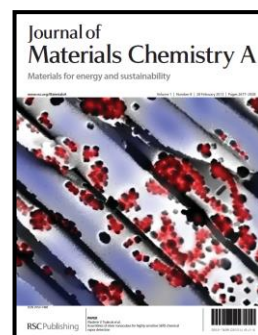
stronger than that between AuHSs pair (Figure 5b). Furthermore, the DDA calculation showed that the substrate does not change the plasmon field far from the surface of the substrate.

Future Plans

We will focus on the investigation of reversible shifting of noble metal nanostructure plasmonic resonances under an applied external electrical field using coatings from electrochromic polymers with variable absorbance wavelengths. Furthermore, tunable plasmonic assemblies based on silver nanocubes with different dimensions and various photochromic hybrid POSS-Dye conjugates will be investigated. Further research is planned on assemblies of plasmonic nanoparticles with different shapes and sizes, prepared by colloidal chemical techniques, into 2D organized arrays of different fractal morphologies. Finally, we will seek the understanding of the optical properties of these 2D arrays for their potential utilization for enhancing the light absorption efficiency.

Selected related project publications (2013-2014)

- König, T. A.F.; Ledin, P.A.; Kerszulis, J.; Mahmoud, M. A.; El-Sayed, M. A.; Reynolds, J. R.; Tsukruk, V. V. Electrically Tunable Plasmonic Behavior of Nanocube-Polymer Nanomaterials Induced by a Redox Active Electrochromic Polymer. *ACS Nano* **2014**, Accepted.
- König, T.; Kodyath, R.; Combs, Z. A.; Mahmoud, M. A.; El-Sayed, M. A.; Tsukruk, V. V. Silver Nanocube Aggregates in Cylindrical Pores for Higher Refractive Index Plasmonic Sensing. *Particles*. **2014**, *31*, 274-283.
- Malak, S. T.; König, T.; Near, R.; Combs, Z. A.; El-Sayed, M. A.; Tsukruk, V. V. Stacked Gold Nanorectangles with Higher Order Plasmonic Modes and Top-Down Plasmonic Coupling. *J. Phys. Chem. C* **2014**, *118*, 5453-5462.
- Geryak, R.; Tsukruk, V. V. Reconfigurable and actuating structures from soft materials. *Soft Matter* **2014**, *10*, 1246-1263.
- Kodyath, R.; Malak, S. T.; Combs, Z. A.; König, T.; Mahmoud, M. A.; El-Sayed, M. A.; Tsukruk, V. V. Assemblies of silver nanocubes for highly sensitive SERS chemical vapor detection. *J. Mater. Chem. A* **2013**, *1*, 2777.
- Mahmoud, M. A.; El-Sayed, M. A. Substrate Effect on the Plasmonic Sensing Ability of Hollow Nanoparticles of Different Shapes. *J. Phys. Chem. B* **2013**, *117*, 4468-4477.
- Combs, Z. A.; Malak, S. T.; König, T.; Mahmoud, M. A.; Chavez, J. L.; El-Sayed, M. A.; Kelley-Loughnane, N.; Tsukruk, V. V. Aptamer-Assisted Assembly of Gold Nanoframe Dimers. *Particles*. **2013**, *30*, 1071-1078.
- Lisunova, M.; Dorokhin, A.; Holland, N.; Shevchenko, V. V.; Tsukruk, V. V. Assembly of the anisotropic microcapsules in aqueous dispersions. *Soft Matter* **2013**, *9*, 3651-3660.
- König, T.; Tsukruk, V. V.; Santer, S. Controlled Topography Change of Subdiffraction Structures Based on Photosensitive Polymer Films Induced by Surface Plasmon Polaritons *ACS Appl. Mater. Interfaces* **2013**, *5*, 6009-6016.



Novel ‘singlet fission’ in low-bandgap polymers for enhancing the efficiency of organic photovoltaic solar cells

Z. Valy Vardeny

Department of Physics & Astronomy, University of Utah, Salt Lake City, Utah 84112

Program Scope

The thermodynamic limit of organic photovoltaic (OPV) solar cell is $\sim 25\%$ for single-junction cells [1]. So far the world record certified power conversion efficiency (PCE) of OPV solar cells is 10.6%, for a solar cell based on low bandgap (LBG) polymers [2]. Despite aggressive efforts in the past two years, only minor progress in PCE of organic solar cells has been made, and thus game-changing fundamental understanding is critically needed for the next breakthrough in PCE enhancement. This may be achieved by finding new energy transfer pathways that circumvent the loss mechanisms known to exist in organic donor (D)-acceptor (A) bulk heterojunction (BHJ) blends. Consequently, our goal in the present DOE project is to seek, understand and provide new energy transfer processes in polymeric and molecular D-A OPV devices, through a concerted research effort using ultrafast and cw spectroscopy that include transient magnetic field effect, device fabrication and electrical characterization; and advanced computation via collaboration. Based on the deeper understanding gained by our research progress, new materials and processes will be developed to reduce losses in the basic processes of charge photogeneration, transport, and collection in OPV cells that will boost the device PCE.

Recent Progress

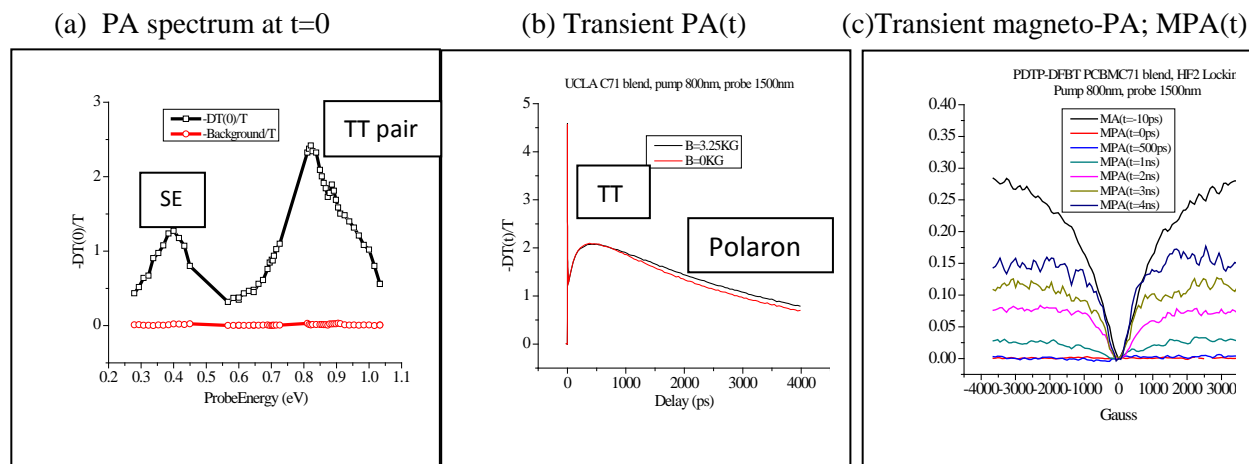


Figure 1: Picosecond transient photoinduced absorption (PA) spectroscopy in the mid-IR spectral range of: (a) pristine low bandgap polymer, PDTP-DFBT very diluted in polystyrene (0.1% weight); and (b) PDTP-DFBT/PC₇₁BM optimum blend (1;2) measured at 1500 nm probe wavelength, where the transient decay of the TT band and build-up of the polaron band are revealed. The PA bands for singlet excitons (SE), TT pairs and polarons are assigned. (c) The transient magnetic field response, MPA(t) of the polaron band at 1500 nm at different delay times after the pump pulse excitation, up to 4 ns. The transient MPA shows that the spin degree of freedom is involved in the carrier photogeneration process in this blend, indicating that the primary excitations in the LBG polymer are TT pairs in addition to SE that otherwise would not show an MPA response. [Unpublished results, for illustration only].

Our approach to fulfill this goal has involved understanding why charge photogeneration at the polymer-fullerene interface with the state-of-the-art LBG polymers is significantly higher than with traditional donor materials [2]. Our recent experimental research indicates that there exist in LBG polymers *unusual charge photogeneration channels* with yield above that of the normal charge photogeneration channel of singlet exciton (SE) dissociation; which involve either a triplet exciton that results from singlet fission (SF) [3,4], or a spin-singlet state that is a quantum entangled triplet-triplet (TT) state [5] (see Fig. 1a). These unpublished conclusions were reached from novel preliminary ultrafast spectroscopy measurements under the influence of an external magnetic field that were completed in our laboratories on pristine and blends based on LBG (Fig. 1c), which show *the ultrafast photogeneration of a novel intrachain TT state that undergoes SF and ionizes at the D-A interface to polaron-pairs* (Fig.1b). Also preliminary sophisticated calculations (in collaboration with Mazumdar at UoA [6]) of ground state and excited state absorptions within correlated-electron models of π -conjugated polymers justify our conclusions. These calculations show that intrachain TT pairs may be readily photogenerated in LBG polymers upon photon absorption, as a result of their intrachain D-A backbone structure.

Future Plans

We have identified key questions that need be understood for utilizing the new energy flow channels related to the TT pair state that we have discovered in LBG polymers; in order to ultimately increase the photocurrent, photo-voltage, and fill-factor of OPV devices. These are:

- What is the nature of the new photogenerated TT state in LBG polymers?
- How fast it is generated? Are coherent processes important in its generation process?
- Can we control the branching ratio, r between the photogenerated singlet exciton and TT pair by chemical modification?
- What is the mechanism of the TT pair ionization at the D-A interface (Fig.1)?
- Can we control the D-A blend to obtain more than 100% internal quantum efficiency due to the singlet fission of the TT pair into two triplets, followed by subsequent triplet ionization?
- Can the TT pair ionization be controlled by spin- $\frac{1}{2}$ radical additives?

To answer these questions we have devised the following research plan:

We have in our possession excellent LBG polymers that were supplied to us by various sources including: *PDTP-DFBT* polymer (UCLA [2]) in which preliminary results have shown that the primary excitations here are SE *and* TT pairs (Fig. 1); *PTB7* polymer (Un. of Chicago); and Si-containing co-polymer (Milano). Our plan is to study these polymers and D-A blends as follow.

- (i) We will use PA spectroscopy with 30 fs time resolution for studying the branching ratio, r between the photogeneration of SE and TT state in pristine LBG polymers. This time resolution will also be sufficient to study the presence of coherences in the excited states that govern r .
- (ii) We will use the transient magneto-PA (MPA) response for identifying the unique ultrafast processes related with the photogenerated SE and TT species, such as SF and T-T fusion.
- (iii) The same two techniques will be applied to BHJ blends of the LBG polymers and fullerene acceptors. Our preliminary results indicate that the TT pair species are involved in the charge

photogeneration process (Fig. 1(b)), and this process is *spin dependent* (Fig. 1(c)). We will thus focus our investigation on the dissociation process of the TT and SE species. The main research focus would be to calibrate the branching ratio between the following two processes: (a) $TT \rightarrow PP+PP$ (where PP is a polaron pair excitation across the D-A interface); and (b) $TT \rightarrow PP+T$. We note that process (a) has the capability to **double the photocurrent in the device [4]**. (iv) We will add spin $\frac{1}{2}$ radicals to the D-A blends based on LBG polymers to change the dynamics of SE, TT, and PP species [7]. Our preliminary results show that the spin $\frac{1}{2}$ radical *galvinoxyl* indeed changes the TT dissociation dynamics. However for the success of this process the radical SOMO energy should be in resonance with the PP species (or the TT species). (v) We also plan to measure ultrafast energy flow in bilayers of small molecule/fullerene in order to simulate the photosynthesis process in Nature. The molecule of choice is from the class of the acene derivatives that are known to show strong SF. The question we would like to resolve; *is the photogeneration of TT pair species generic in many photosynthesis reactions?*

References

1. N. C. Giebink *et al.*, “The Thermodynamic Efficiency Limit of Excitonic Solar Cells”, *Phys. Rev. B* 83, 195326 (2011).
2. J. B. You *et al.*, “A polymer tandem solar cell with 10.6% power conversion efficiency”, *Nature Commun.* 4, 1446-1449 (2013).
3. A. Rao *et al.*, “Exciton Fission and Charge Generation via Triplet Excitons in Pentacene/C60 Bilayers, *Journal of the American Chemical Society* 132, 12698-12703 (2010).
4. D. N. Congreve *et al.*, “External Quantum Efficiency Above 100% in a Singlet-Exciton-Fission-Based Organic Photovoltaic Cell”. *Science* 340, 334-337 (2013)
5. P. M. Zimmerman, Z. Zhang, and C. B. Musgrave. Singlet Fission in Pentacene through Multi-exciton Quantum States. *Nature Chemistry*, 2, 648–652 (2010).
6. K. Aryanpour *et al.*, "Evidence for Excimer Photoexcitations in Ordered π -conjugated Polymer Films", *Phys. Rev. B* 83, 155124 (2011).
7. Y. Zhang *et al.*, “Spin-enhanced Organic Bulk Heterojunction Photovoltaic Solar Cells”. *Nature Commun.* 3, 1043-1046 (2012).

Publications

1. “Spectroscopy of Organic Random Lasers near Threshold”, R. C. Polson and Z. V. Vardeny, *Synth. Metals* 162, 276 (2012).
2. “Random Lasing Highlighted by π -Conjugated Polymer Films“, R. C. Polson and Z. V. Vardeny, invited chapter in a book on “Optical Properties of Photonic Structures; Interplay between Order and Disorder“, edited by Mikhail Limonov and Richard De La Rue, Taylor & Francis Press, pp 379-393, June 2012.
3. “Two-step Charge Photogeneration Process in Polymer/Fullerene Blends for Organic Photovoltaic Applications”, S. Singh, B. Pandit, S. Li, D. Laird and Z. V. Vardeny, *Phys. Rev. B* 85, 205206 (2012).
4. “Study of Photoexcitations in Poly(3-hexylthiophene) for Photovoltaic Applications”, G. Hukic, T. Basel, S. Singh, S. Li, D. Laird and Z. V. Vardeny, *Appl. Phys. Lett.* 100, 213903 (2012).
5. “Ultrafast Intrachain Exciton Dynamics in π -Conjugated Polymers”, C.-X. Sheng and Z. V. Vardeny, chapter 10 in the *Handbook of organic materials for optical and optoelectronic*

devices: properties and applications, Editor: Oksana Ostroverkhova, Woodhead Publishing Ltd. pp. 297-318 (2013).

6. “Spin-Enhanced Organic Bulk Heterojunction Photovoltaic Solar Cells”, Ye Zhang, Tek P. Basel, Xiaomei Yang, Debra J. Mascaro, Feng Liu and Z. Valy Vardeny, *Nature Communications*, **3**, 1043 (2012).

7. “Ultrafast Transient Spectroscopy of Nano-domains of Polymer/fullerene Blend for Organic Photovoltaic Applications”, Sanjeev Singh, Bill Pandit, Golda Hukic-Markosian, Tek P. Basel, Z. Valy Vardeny, S. Li and D. Laird, *Jour. of Applied Physics* **112**, 123505 (2012).

8. “Photoexcitation Dynamics in Polythiophene/fullerene Blends for Photovoltaic Applications”, C.-X. Sheng, B. Pandit, T. P. Basel, and Z. V. Vardeny, *Organic Electronics* **13**, 1031 (2012).

9. “Ultrafast Transient Spectroscopy of Nano-domains of Donor-Acceptor Blends for Organic Photovoltaic Applications”, S. Singh and Z. Valy Vardeny, *Materials* **6**, 897-910 (2013).

10. “Phosphorescence Superradiance in a Pt-containing π -Conjugated Polymers”, B. Khachtryan, Tho D. Nguyen, Z. Valy Vardeny and E. Ehrenfreund, *Phys. Rev. B* **86**, 195203 (2012).

11. “Magnetic Field Effects in C₆₀-based Films and Devices”, Bhoj R. Gautam, Tho D. Nguyen, Eitan Ehrenfreund, and Z. Valy Vardeny, *Jour of Appl. Phys.* **113**, 143102 (2013).

12. “Spin Diffusion in Fullerene-based Devices; Morphology Effect”, Tho D. Nguyen, Fujian Wang, Xiao-Guang Li, Eitan Ehrenfreund, Z. Valy Vardeny, *Phys. Rev. B.* **87**, 075205 (2013).

13. “Organic Spin-Valves; from Unipolar to Bipolar Devices”, E. Ehrenfreund and Z. V. Vardeny, *Phys. Chem. Chem. Phys.* **15**, 7967-7975 (2013).

14. “Ultrafast Intersystem-Crossing in Platinum Containing π -Conjugated Polymers with Tunable Spin-Orbit Coupling”, C.-X. Sheng, S. Singh, A. Gambetta, T. Drori, M. Tong, S. Tretiak, and Z. V. Vardeny, *Scientific Reports* **3**, 2653 (2013).

15. “Ultrafast Transient Spectroscopy of RR-P3HT/PCBM Blends for Photovoltaic Solar Cells evaluation”, B. Pandit, B. R. Gautam, T. P. Basel, and Z. V. Vardeny, *Organic Electronics* **15**, 1149-1154 (2014).

16. “Infrared Optical Probing of Photoexcitations in π -Conjugated Polymer/Fullerene Blends for OPV Applications”, C.-X. Sheng, U. Huynh and Z. V. Vardeny, in *Ultrafast Dynamics in Molecules, Nanostructures and Interfaces*, edited by G.G. Gurzadyan, Series in Optics and Photonics-Vol.8, World Scientific, ISBN 978-981-4556-91-0, pp. 79-93 (2014).

17. “Polymers with Large Spin-Orbit Coupling”, Z.V. Vardeny, invited article submitted for the Encyclopedia of Polymeric Nanomaterials, editor K. Muller, submitted to Springer April 2014.

18. “The development of organic spin-valves from unipolar to bipolar operation”, T.D. Nguyen, E. Ehrenfreund and Z. V. Vardeny, submitted to MRS bulletin, Jan. 2014 (invited paper).

19. “Magneto-photocurrent in hybrid perovskite photovoltaic cells”, C. Zhang, D. Su¹, C-X. Sheng, K. Mielczarek, A. Zakhidov, and Z. V. Vardeny, submitted to Phys. Rev. Appl. May 2014.

Important Comment

Our group has initiated research investigations of *hybrid organic/inorganic perovskites* using the same experimental techniques as in the original proposal to the DOE. Since these materials are *hybrid organic/inorganic* and are ‘hot research subject matter’ these days, we thought that a limited effort in this field is in order. We have thus performed both transient and cw spectroscopies of MAPbI₃ (including laser action), and also used our expertise in magneto-photocurrent of OPV to study perovskite PV cells (see ref. 19 above). Please let me know if you would like me to present this work as oral or poster at the July meeting.

Linking Metal Ions via Inorganic Click (iClick) Reactions

Adam S. Veige, University of Florida, Department of Chemistry

Program Scope: 1) Expand the scope of iClick synthesis beyond Au^I/Au^I reactions.
2) Elucidate a Cu^I-catalyzed iClick reaction.
3) Synthesize/characterize tri-/tetra-metallics as models for metallopolymers.

Inorganic click (iClick) is the cycloaddition reaction between a metal-azide and a metal-acetylide providing metal ions linked by a triazolite bridge (Figure 1). This program is a one-year project to determine the scope of the iClick reaction, including a Cu^I-catalyzed version and extension to tri- and tetra-metallic complexes that will serve as models for metallopolymer materials. This program delineates experiments that will afford a detailed understanding of the electronic and steric effects of the monomer units that govern this reaction. The goal is to firmly grasp both the advantages and limitations of this new technology to facilitate, beyond this one year program, the controlled synthesis of one- and two-dimensional metallopolymers and metal-containing networks.

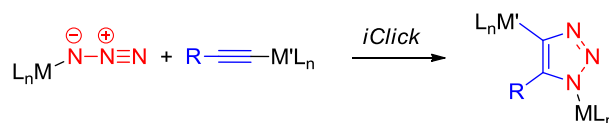


Figure 1. General iClick reaction

Recent Progress: 1) Expand the scope of iClick synthesis beyond Au^I/Au^I reactions.

A primary goal of the project is to expand the iClick reaction beyond the limits of a Au^I/Au^I only reaction, i.e. where $M = M' = Au^I$ in Figure 1. Anticipating a need to manipulate the electronic structure of materials derived from iClick reactions, we explored the compatibility of the iClick reaction between Au^I and other transition metals, namely, iridium, rhodium and ruthenium. Recent progress confirms that other metal ions will participate in iClick reactions. We have successfully extended the iClick reaction to include Rh^I, Ir^I, and Ru^{II}. Treating the square planar azido complexes **1-M** ($M = Rh^I$, and Ir^I) with $Ph_3PAu^I-C\equiv CPh-NO_2$ (**2-NO₂**) forms the iClick heterobimetallic complexes **3-M**. Moreover, treating the cyclopentadienyl azido ruthenium complex **4** with $Ph_3PAu^I-C\equiv CPh-R$ (**2-R**; $R = NMe_2$, OMe) results in the triazolite bridged Au^I-Ru^{II} complexes **5-R** according to Figure 2.

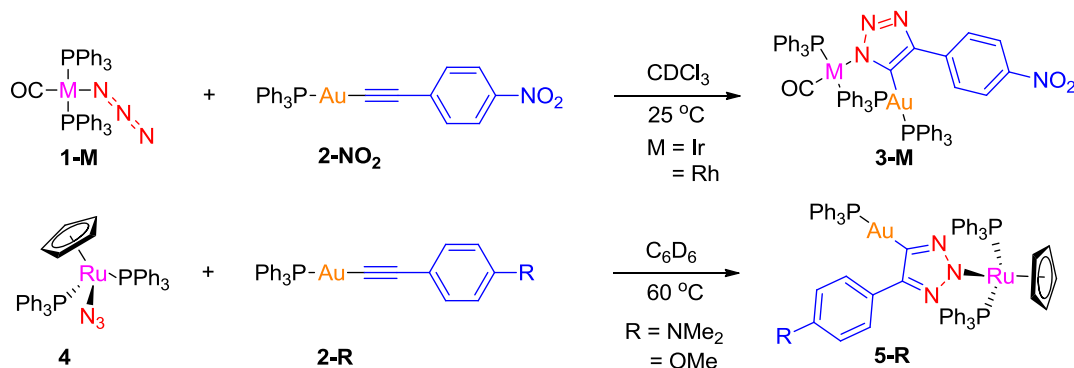


Figure 2. Extension of the iClick reaction to include Au^I/M heterobimetallic synthesis (M = Rh^I, Ir^I, and Ru^{II}).

Recent Progress: 2) Elucidate a Cu^I-catalyzed iClick reaction.

The second goal of the project is to probe different Cu(I) sources and reaction conditions to elucidate Cu(I) catalyzed iClick reactions. Results garnered from objective 1 indicate one limitation with the direct iClick reaction is that at least one of the metal partners has to be Au^I. We have yet to successfully perform an iClick reaction without one of the metal ions being Au^I. One remedy for this problem is to employ terminal acetylides and execute a prototypical “organic” copper(I) catalyzed azide-alkyne cycloaddition (CuAAC) according to Figure 3. Using this route, any metal ion is plausible because the mechanism involves only the alkyne fragment.

The first challenge for this project is to synthesize different metal complexes bearing a *terminal* acetylide. Previously, we presented a Cu(I) catalyzed metal-acetylide-organic azide cycloaddition reaction between (PEt₃)₂Pt(C≡CH)₂ and benzyl azide (Figure 4). However, under the same conditions, treating (PEt₃)₂Pt(C≡CH)₂ with PEt₃AuN₃ gave several unidentifiable products which might be the result of azide-alkyne ionic ligand exchange between the platinum gold species. Even at 60 °C, there was no reaction observed between (PEt₃)₂Pt(C≡CH)₂ and (PEt₃)₂Pt(N₃)₂ while employing copper(I) acetate as the catalyst.

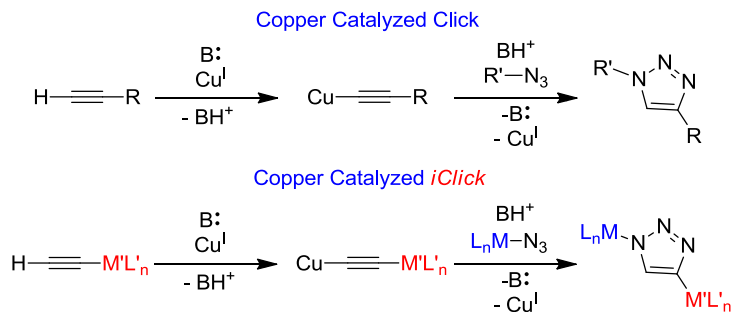


Figure 3. Proposed Cu^I catalyzed iClick reaction and the analogous typical copper catalyzed Click.

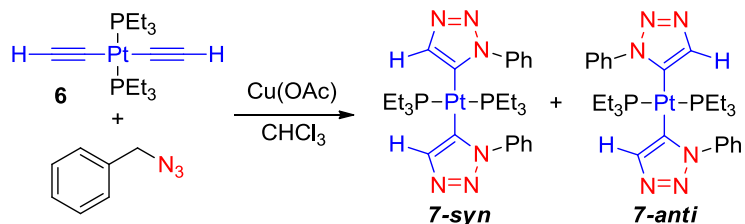


Figure 4. Cu^I-catalyzed cycloaddition result.

Recent Progress: 3) Synthesize/characterize tri-/tetra-metallics as models for metallopolymers.

The ultimate goal of this program is to elucidate the fundamental principles that govern the iClick reaction to enable the synthesis of new metallopolymers. **We have achieved this objective and have prepared metallopolymers employing the iClick reaction!!!**

A) iClick synthesis of gold(I) coordination polymers via the reaction of gold(I) azide and gold(I)isocyanide.

The examples of iClick shown above all employ a metal-acetylide. The iClick reaction can also employ a metal bearing an isocyanide ligand. Upon reaction of **8-^tBu** with $\text{PR}_3-\text{Au}-\text{N}_3$ (**9-R**, R=Ph, Et) in CDCl_3 , a white, fibrous material precipitates and the ³¹P-NMR spectrum of the reaction mixture reveals consumption of the starting material, with the concomitant appearance

of a new resonance attributable to PR_3AuCl . The insoluble white material is proposed to be the Au^{I} coordination polymer **10-^tBu**, depicted in Figure 5. Metallopolymer **10-^tBu** consists of Au^{I} centers bridged by 4-*tert*-butyl-1,2,3,4-tetrazole units, through connectivity at the anionic C-5 position of one tetrazole, and the neutral N-1 position of another tetrazole.

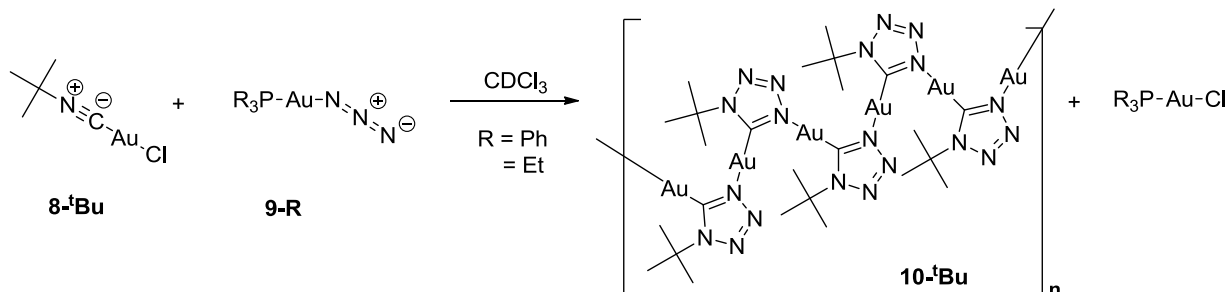


Figure 5. iClick reaction between Au^{I} -azide (**9-R**, R = Ph, Et) and Au-isocyanide (**8-^tBu**), yielding **10-^tBu**.

Due to limited solubility of **10-^tBu** in organic solvents, attempts to increase the solubility of the product material were sought. A small library of additional gold-isocyanide species was synthesized. The results are positive. The reaction of $\text{Bn-N}\equiv\text{CAuCl}$ with $\text{PPh}_3\text{-Au-N}_3$ in CDCl_3 results in a *soluble* Au^{I} metallopolymer, which permits the solution phase characterization and is the subject of Future Plans below.

B) iClick synthesis of a oligomers with main chain tetragold clusters.

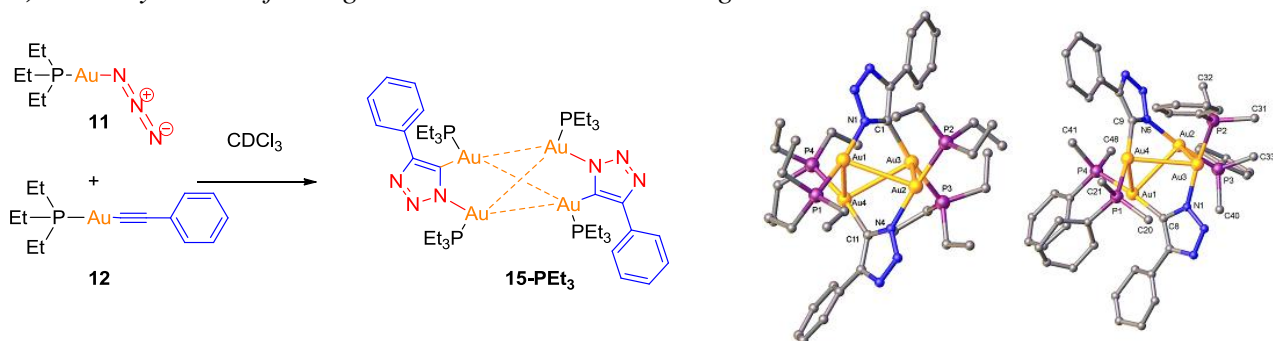


Figure 6. iClick synthesis of the tetragold clusters **13-PR₃** ($\text{PR}_3 = \text{PEt}_3, \text{PMe}_2\text{Ph}$).

We discovered that when small ancillary PR_3 ligands are employed in the $\text{Au}^{\text{I}}/\text{Au}^{\text{I}}$ iClick reaction, instead of forming bimetallic Au_2^{I} complexes (as in Figure 1), the tetragold complex **13-PR₃** forms (Figure 6). These results prompted us to attempt to synthesize oligomeric species with tetragold nodes along the backbone according to the Figure 7. By employing the digold acetylide complex **14** we successfully linked multiple tetragold clusters. Unfortunately, single crystals of the oligomeric species eluded isolation. However, using diffusion coefficients from DOSY NMR, we conclusively established that compounds **15-PR₃** are at least oligomeric. These materials are unprecedented. **The implementation of an iClick reaction into the synthesis of a metallopolymer marks the second successful achievement of objective 3!!!**

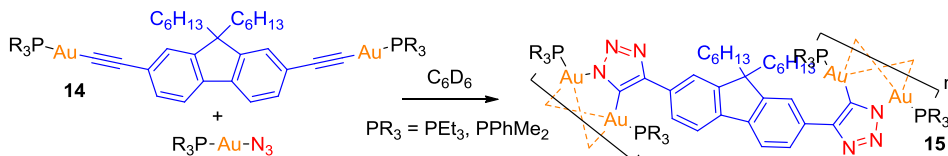


Figure 7. iClick synthesis of the organometallic oligomers **15-PR₃** (PR₃ = PEt₃, and

Future Plans: 1) *Expand the scope of iClick synthesis beyond Au^I/Au^I reactions.*

Many failed attempts to extend the iClick reaction beyond Au^I/Au^I, though disappointing, are actually part of the objectives of this program. The objective is to elucidate the fundamental aspects of this reaction. It appears that Au^I ions (or at least group 11) must be one of the partners in the reaction. We will finish the series of reactions outlined in the recent progress and complete that objective. No further attempts to thermally iClick non-Au^I complexes will be attempted. Instead, we will focus on objective 2, which fundamentally does not require Au^I.

2) *Elucidate a Cu^I-catalyzed iClick reaction.*

We plan to probe more organometallic copper(I) complexes to catalyze the iClick reaction. Phosphine supported Cu(I) complexes such as (PPh₃)₂Cu(NO₃), (PPh₃)₂Cu(OTf), (PPh₃)₂Cu(OOC₃H₇) and (PEt₃)₂Cu(OOCH₃) will be one of the series investigated. Another possibility are the Cu(I) *N*-heterocyclic carbene complexes which have been utilized in CuAAC and exhibit excellent catalytic properties. Figure 8 includes some of the Cu-NHC complexes to be employed to conclude this study.

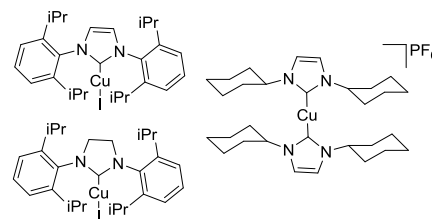


Figure 8. Cu(I) NHC complexes

3) *Synthesize and characterize tri- and tetra-metallic complexes as models for metallopolymers.*

We will expand the library of the organic linkers for synthesizing different gold metallo-oligomers/polymers. Organic linkers with different functional groups and steric hindrances will influence the structures of the gold metallo-oligomers/polymers. In order to study the influence, different multi-ethynyl functionalized compounds will be applied as linkers for synthesis of various gold metallo-oligomers/polymers. Figure 9 includes some of these organic linkers. Another important goal is to isolate and determine a solid state structure of an oligomer/polymer complex. We will also continue the full characterization of the materials we have already synthesized. Also, theoretical calculation will be applied to simulate the structures of the current synthesized metallo-oligomer complexes.

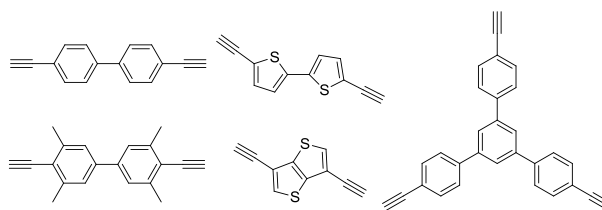


Figure 9. Potential terminal diynes and triynes linkers.

Publications: This project was initiated in August 2013. Manuscripts describing the recent progress results outlined above are *in preparation*.

Donor-Acceptor π -Extended Porphyrins for Solar Energy Conversion

Hong Wang, Associate Professor, Department of Chemistry, Miami University

Lei Kerr, Professor, Department of Chemical and Paper Engineering, Miami University

Program Scope

Porphyrins have been of intense research interests for decades owing to their interesting electronic and photophysical properties. π -Extended porphyrins, in which aromatic rings(s) are fused to the porphyrin periphery, have displayed broadened and red-shifted absorptions along with other unusual electronic and photophysical properties due to their extended π -conjugation. As such, π -extended porphyrins constitute especially attractive organic materials with potential applications in various areas ranging from biomedicine to organic electronics.¹⁻³ In contrast to their un-extended counterparts, *pi*-extended porphyrins have only been scarcely studied, because π -extended porphyrins, in particular functionalized π -extended porphyrins are very difficult to access due to the limit availability of the synthetic methods. In order to make breakthroughs in this area, new methods must be developed. The Wang group has developed a couple of concise and versatile methods, thus opening the door to access a large number of functionalized extended porphyrins.⁴⁻⁶

Dye-sensitized solar-cells (DSSCs) have emerged as one of the most promising photovoltaic technologies in solar energy conversion.⁷⁻⁹ Despite of the advances in the last two decades, organic dyes having better overlap with the solar spectrum and high thermostability are still in high demands. π -Extended porphyrins appear to be ideal candidates to satisfy these criteria as sensitizer for DSSCs. The goal of this DOE supported project is to synthesize and characterize novel functionalized π -extended porphyrins, and study the electronic and photophysical properties of these organic materials. The evaluation of their potentials as sensitizer for dye-sensitized solar cells will also be performed.

Recent Progress

Two novel classes of donor-acceptor π -extended porphyrins have been prepared in the Wang's laboratory. To our knowledge, the porphyrins presented here represent the first examples of *pull-pull* π -extended porphyrins. The *push-pull* functional groups installed at the extended porphyrin periphery are expected to facilitate intramolecular and intermolecular electron transfer. Red-shifted and broadened absorptions are also expected due to the *push-pull* groups along with the π -extension. The design and synthesis of these organic materials take advantage of the chemistry of bromoporphyrins¹⁰⁻¹¹ and a palladium (0) catalyzed cascade reaction developed in the Wang group.⁴⁻⁶ The electronic and optical properties of these π -extended porphyrins were measured using UV-Vis spectroscopy, life-time and steady state fluorescence spectroscopy, and cyclic voltammetry. DFT calculations were also performed for these porphyrins.

Fig. 1 illustrates the structure, absorption and emission spectra of the symmetrical *push-pull* dibenzoporphyrins. Two trends were observed for these porphyrins: first, upon gradual extension of the π -extension, gradual red shifting and broadening were observed for both the absorption and emission bands; second, increasing the *push-pull* strength of the functional groups, red shifting was observed for both the absorption and emission bands. DFT calculation and CV data match well with the observed spectra. However, no significant difference for the lifetime of the excited states of these porphyrins was detected using lifetime fluorescence spectroscopy (all are in picosecond range).

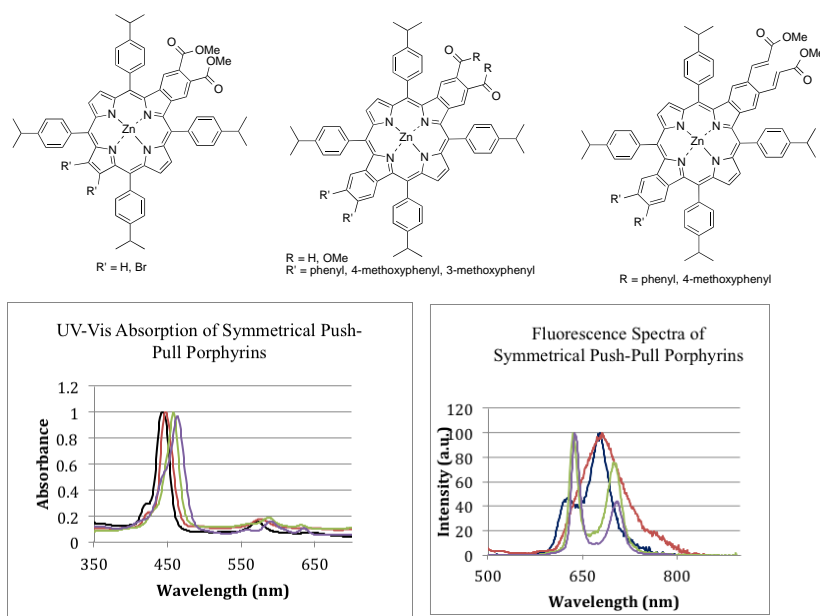


Fig. 1 Symmetrical *push-pull* dibenzoporphyrins, their absorption and emission spectra.

Fig. 2 shows the structure, absorption, emission and MCD spectra of the unsymmetrical *push-pull* monobenzoporphyrins. These unsymmetrical porphyrins also displayed similar trends observed for the symmetrical dibenzoporphyrins. Of particular note, an unusual flipping in the MCD spectra and an unusual emission band were observed for one unsymmetrical porphyrin bearing a strong electron-withdrawing group. The lifetimes of the excited state of these unsymmetrical porphyrins (in nanosecond range) are longer than the above symmetrical dibenzoporphyrins.

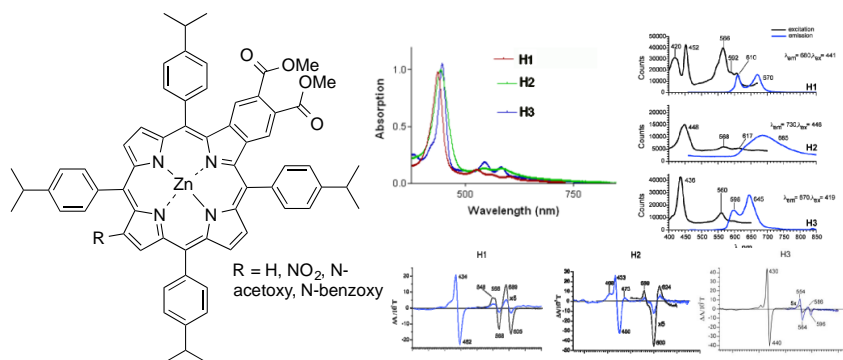


Fig. 2 Unsymmetrical *push-pull* monobenzoporphyrins, their absorption, emission and MCD spectra.

Future Plan

1. Develop synthetic methods to complete the synthesis and characterization of unsymmetrical and symmetrical donor-acceptor porphyrins with further π -extended systems proposed in the proposal; conduct the study of the electronic properties of these compounds using UV-Vis spectroscopy, time-resolved and steady state fluorescence spectroscopy, cyclic voltammetry and DFT calculations; establish structure-property relationships of these compounds.
2. Optimize the cell fabrication process for porphyrin dyes; evaluate the solar to electricity efficiencies of DSSCs based on these porphyrins; establish structure-property-efficiency relationships of these porphyrins.

Reference

1. V. Cheprakov, M. A. Filatov, *J. Porphyrin Phthalocyanines* 2009, **13**, 291-303.
2. S. Banala, T. Ruhl, K. Wurst, B. Krautler, *Angew. Chem. Int. Ed.* 2009, **48**, 599-603.
3. S. Banala, R. G. Huber, T. Muller, M. Fechtel, K. R. Liedl, B. Krautler, *Chem. Commun.* 2012, **48**, 4359-4361.
4. R. Deshpande, L. Jiang, G. Schmidt, J. Rakovan, X. P. Wang, K. Wheeler, H. Wang, *Org. Lett* 2009, **11**, 4251-4253
5. L. Jiang, R. A. Zaenglein, J. T. Engle, C. Mittal, C. S. Hartley, C. J. Ziegler, H. Wang, *Chem. Commun.* 2012, **48**, 6927-6929
6. L. Jiang, J. T. Engle, L. Sirk, C. S. Hartley, C. J. Ziegler, H. Wang, *Org. Lett.*, 2011, **13**, 3020-3023.
7. M. Akita, S. Hiroto, H. Shinokubo, *Angew. Chem. Int. Ed.* 2012, **51**, 2894-2897.
8. N. Armaroli, V. Balzani, V. *Angew. Chem. Int. Ed.* 2007, **46**, 52-66.
9. N. Robertson, *Angew. Chem. Int. Ed.* 2008, **47**, 1012-1014.
10. M. J. Crossley, P. L. Burn, S. S. Chew, F. B. Cuttance, I. A. Newsom, I. A. J. Chem. Soc. Chem. Commun, 1992, 1564-1566.
11. L. Jaquinod, R. G. Khoury, K. M. Shea, K. M. Smith, *Tetrahedron*, 1999, **55**, 13151-13158.

Publication

1. Lin Jiang, James T. Engle, Ross A. Zaenglein, Alex Matus, Christopher J. Ziegler, Hong Wang and Martin J. Stillman, "Largely π -Conjugated Multichromophoric Systems: Pentacene-Fused Diporphyrins", submitted to *organic letters*.

Extracting hot carriers from photoexcited semiconductor nanocrystals

Xiaoyang Zhu, Columbia University

Program Scope

This research program addresses a fundamental question related to the use of nano-materials in solar energy -- namely, whether semiconductor nanocrystals (NCs), also called quantum dots (QDs), can help surpass the efficiency limits in conventional solar cells. As is known as the so-called “Shockley-Queisser” limit, the maximum theoretical efficiency of a single-junction solar cell is ~**31%**. This is because absorption of photons with energies above the semiconductor bandgap generates “hot” charge carriers that quickly “cool” to the band edges before they can be utilized to do work. If instead, all of the energy of the hot carriers could be captured, solar-to-electric power conversion efficiencies could be increased, theoretically, to as high as **66%**. Two proposals have been put forward: one increases photocurrent by converting the hot carrier energy to multiple electron-hole pairs; and the other increases photovoltage by capturing the hot carriers. In both scenarios, it is essential to understand charge carriers or excitons significantly above the bandgap.

The PI is addressing two questions: How does quantum confinement affect hot carrier/exciton dynamics? How to harvest hot carriers from quantum confined materials, including quantum dots? The first question is of general significance to solar energy harvesting. The sun is a white light source and photoexcitation in a semiconductor material under solar irradiation should involve mostly excitation above the bandgap. Thus understanding hot carriers and excitons in semiconductor materials, including quantum-confined materials, is a necessary step in laying a mechanistic foundation for the application of these materials in solar energy conversion. The second question is specifically related to the potential implementation of the hot carrier solar cell idea. The key to the success of the hot carrier solar cell concept lies not only in the efficient harvesting of hot carriers before phonon relaxation, but also in the possibility of hot carrier – hot carrier scattering and quasi equilibration in the electronic degrees of freedom with realistic concentration of solar radiation.

Recent Progress

The PI has made two major advances in understanding hot carrier relaxation in the model system in PbSe QDs (Nano Lett. 2012, 2013). How hot electrons relax in semiconductor quantum dots is of critical importance to many potential applications, such as solar energy conversion, light emission, and photon detection. A quantitative answer to this question has not

been possible due in part to limitations of current experimental techniques in probing hot electron populations. The PI has successfully applied femtosecond time-resolved two-photon photoemission spectroscopy for a complete mapping in time- and energy-domains of hot electron relaxation and multi-exciton generation (MEG) dynamics in PbSe quantum dots functionalized with 1,2-ethanedithiols. This experiment led to the discovery of a linear scaling law between the hot electron relaxation rate and its energy above the conduction band minimum. There was no evidence of MEG from intra-band hot electron relaxation for excitation photon energy as high as three times the bandgap ($3E_g$). Rather, MEG occurs in this system only from inter-band hot electron transitions at sufficiently high photon energies ($\sim 4E_g$). More insight into the behavior of hot carriers in PbSe QDs comes from transient absorption experiments. The best-understood property of semiconductor quantum dots (QDs) is the size-dependent optical transition energies due to the quantization of charge carriers near the band edges. In contrast, much less is known about the nature of hot electron-hole pairs resulting from optical excitation significantly above the bandgap. Here, the PI and students have discovered a transient Stark effect imposed by a hot electron-hole pair on optical transitions in PbSe QDs. The hot electron-hole pair does not behave as an exciton, but more bulk-like as independent carriers, resulting in a transient and varying dipole moment which breaks the symmetry of the QD. As a result, we observe redistribution of optical transition strength to dipole forbidden transitions and the broadening of dipole-allowed transitions during the picosecond lifetime of the hot carriers. The magnitude of symmetry breaking scales with the amount of excess energy of the hot carriers, diminishes as the hot carriers cool down, and disappears as the hot electron-hole pair becomes an exciton. Such a transient Stark effect should be of general significance to the understanding of QD photophysics above the bandgap.

More recently, the PI and students has made a breakthrough discovery (manuscript in preparation) on a new class of solar harvesting materials, organic–inorganic lead halide-based perovskites, particularly $\text{CH}_3\text{NH}_3\text{PbI}_3$, which has been shown to give spectacular power-conversion efficiency close to 20%. The PI and students have carried out a systematic study on exciton and carrier dynamics in these materials, including a quantitative comparison of dynamics in the three dimensional $\text{CH}_3\text{NH}_3\text{PbI}_3$ and the two dimensional quantum confined $(\text{BuNH}_3\text{I})_2(\text{CH}_3\text{NH}_3\text{I})_{n-1}(\text{PbI}_2)_n$, where $n = 1, 2, \text{ or } 3$ represents the thickness of the quantum well, i.e., the lead iodide core, Fig. 2. One of the most important questions concerns the nature of excitonic and/or charge carrier traps in these materials. Using femtosecond laser spectroscopies

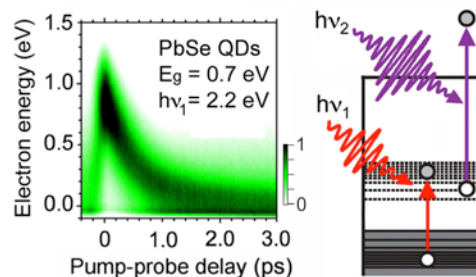


Figure 1. Pseudo-color representation of time-resolved two photon photoemission (TR-2PPE) spectrum of a PbSe quantum dot thin film (0.7 eV band gap) with excitation photon energy $h\nu_1 = 2.20$ eV and probe photon energy $h\nu_2 = 4.28$ eV. The electron energy is referenced to the bottom of the conduction band. The right shows schematically the principle of TR-2PPE.

and photoemission spectroscopies, the PI and students have discovered that band gap trap states in both 2D and 3D perovskite materials are of charge transfer (CT) exciton characteristics, mostly likely stabilized by polarization in nuclear coordinates (i.e., self-trapped CT excitons). These charge transfer excitons possess weak oscillatory strength for direct optical excitation, but can be more efficiently formed from the relaxation of hot exciton states. Minimizing these bandgap CT excitons and charge traps represents a viable approach to further increase the power conversion efficiency of solar cells made from these remarkable materials.

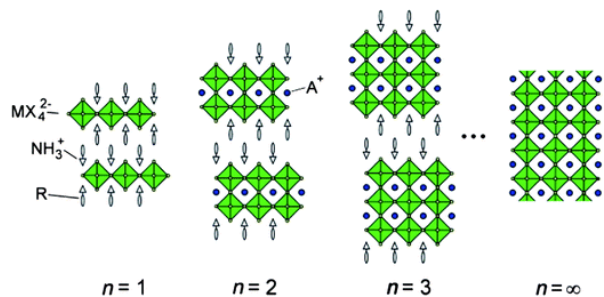


Figure 2. Schematic illustration of 2D quantum confined ($n = 1, 2, 3$) and 3D organic-inorganic lead iodide perovskites. For the 2D materials, n is the thickness of the inorganic lead iodide quantum well.

Future Plans

The PI and students will focus on the photophysics, particularly hot carrier and hot exciton physics, in quantum confined 2D perovskites and other 2D semiconductors (e.g., MoS₂) and the possibility of achieving sufficient hot carrier scattering/equilibration in these materials.

Publications

L. Miaja-Avila, J. Tritsch, A. Wolcott, W.-L. Chan, C. A. Nelson, X.-Y. Zhu, "Direct mapping of hot electron relaxation and multiexciton generation dynamics in PbSe quantum dots," *Nano Lett.* **2012**, *12*, 1588-1591.

C. A. Nelson, X.-Y. Zhu, "Reversible electronic traps in PbS quantum dot solids induced by an order-disorder phase transition in capping molecules," *J. Am. Chem. Soc.* **2012**, *134*, 7792-7795.

K. J. Williams, C. A. Nelson, X. Yan, L. Li, X.-Y. Zhu, "Photo-induced hot electron transfer from graphene quantum dots to TiO₂," *ACS Nano* **2013**, *7*, 1388-1394.

M. Tuan Trinh, M. Y. Sfeir, J. J. Choi, J. S. Owen, X.-Y. Zhu, "A hot electron-hole pair breaks the symmetry of a semiconductor quantum dot," *Nano Lett.* **2013**, *13*, 6091-6097.

C. A. Nelson, N. R. Monahan, X.-Y. Zhu, "Exceeding the Shockley-Queisser Limit in Solar Energy Conversion," *Energy & Environmental Science* **2013**, *6*, 3508-3519.

Yu Zhong, Bharat Kumar, Seokjoon Oh, M. Tuan Trinh, Ying Wu, Katherine Elbert, Panpan Li, X.-Y. Zhu, Shengxiong Xiao, Fay Ng, Michael L. Steigerwald, Colin Nuckoll, "Helical Ribbons for Molecular Electronics," *J. Am. Chem. Soc.* **2014**, *136*. <http://dx.doi.org/10.1021/ja503533y>

Spectroscopy of Charge Carriers and Traps in Field-Doped Single Crystal Organic Semiconductors

Xiaoyang Zhu, Columbia University
C. Daniel Frisbie, University of Minnesota

Program Scope

The proposed research aims to achieve quantitative, molecular level understanding of charge carriers and traps in field-doped crystalline organic semiconductors via in situ linear and nonlinear optical spectroscopy, in conjunction with transport measurements and molecular/crystal engineering. Organic semiconductors are emerging as viable materials for low-cost electronics and optoelectronics, such as organic photovoltaics (OPV), organic field effect transistors (OFETs), and organic light emitting diodes (OLEDs).¹⁻⁶ Despite extensive studies spanning many decades,^{7,8} a clear understanding of the nature of charge carriers in organic semiconductors is still lacking. It is generally appreciated that polaron formation and charge carrier trapping are two hallmarks associated with electrical transport in organic semiconductors; the former results from the low dielectric constants and weak intermolecular electronic overlap while the latter can be attributed to the prevalence of structural disorder. These properties have led to the common observation of low charge carrier mobilities, e.g., in the range of 10^{-5} - 10^{-3} cm^2/Vs , particularly at low carrier

concentrations.⁹ However, there is also growing evidence that charge carrier mobility approaching those of inorganic semiconductors and metals can exist in some crystalline organic semiconductors, such as pentacene, tetracene and rubrene. A particularly striking example is single crystal rubrene (Figure 1), in which hole mobilities well above $10 \text{ cm}^2/\text{Vs}$ have been observed in OFETs operating at room temperature.^{10,11} Temperature dependent transport¹² and spectroscopic measurements¹³ both revealed evidence of free carriers in rubrene. Outstanding questions are: *what are the structural features and physical properties that make rubrene so unique? How do we establish fundamental design principles for the development of other organic semiconductors of high mobility?* These questions are critically important but not comprehensive, as the nature of charge carriers is known to evolve as the carrier concentration increases, due to the presence of intrinsic disorder in organic semiconductors. Thus, a complementary question is: *how does the nature of charge transport change as a function of carrier concentration?*

To answer these questions, the PIs extend their successful collaboration that combines transport measurements with in situ spectroscopy (Fig. 1); the new focuses are on single crystal organic semiconductor field effect devices gated with ionic liquid or ion gel for high charge

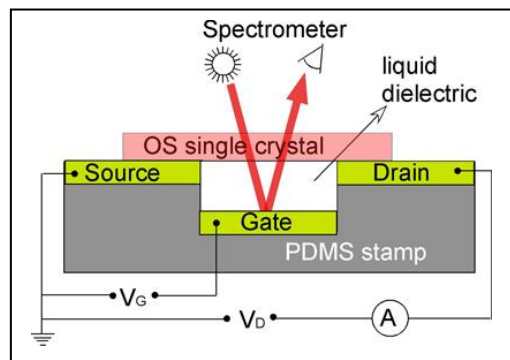


Figure 1. In situ optical absorption spectroscopy of an OFET structure with ionic liquid dielectric.

carrier doping densities.¹⁴ The OFET structure provides control of surface charge concentration and the determination of carrier transport characteristics (e.g. mobility), while optical spectroscopy provides physical insight into the nature of charge carriers, as polarons and free carriers possess distinct optical signatures and also provide direct measurements of the energetics of charge carriers with respect to HOMO & LUMO bands.^{15,16} The establishment of synergistic collaboration between transport and spectroscopy of the two laboratories over the past funding period and the successful development of a set of powerful experimental tools and model systems have now set the stage for the two PIs to tackle the most fundamental and most important problems in organic semiconductor research. A long-term outcome will be rationally designed materials and interfaces for high performance OFETs and for the exploration of new physical phenomena in organic semiconductors.

Recent Progress

We have carried out transport measurements on ionic liquid (electrolyte) gating of two benchmark organic semiconductors, poly(3-hexylthiophene) and rubrene. The goal of these experiments is to use the giant capacitance of ionic liquids to induce large carrier densities in the organic semiconductors and to explore transport in the high carrier density regime. We find that in the case of P3HT, the mobility becomes high enough at the 3D highest charge densities, near 10^{21} cm^{-3} , that the Hall effect can be reproducibly observed. Furthermore, it is clear from extensive resistivity measurements versus temperature that a metallic state in P3HT is approached, though it is not realized likely due to gating induced disorder. In the case of rubrene single crystals, carrier mobilities as large as $4 \text{ cm}^2/\text{V}\cdot\text{s}$ are achieved at 2D hole densities of 0.15 charges/rubrene, $\sim 3 \times 10^{13} \text{ cm}^{-2}$. These large mobilities lead to an easily detected Hall signal that verifies the charge density estimated from capacitance-voltage measurements. Furthermore, at optimum carrier densities, the near-onset of metallic behavior is clearly observed for rubrene.

Concurrent with transport experiments, we carried out spectroscopic measurements to quantify the density of doping upon the formation of the rubrene/ionic liquid (ion gel) interface. Based on charge modulation FTIR spectroscopy, we discovered that there is an intrinsic doping of the rubrene capacitor with an ionic gel dielectric of $\sim 1.5 \times 10^{13} \text{ cm}^{-2}$ holes (manuscript in preparation). Such an intrinsic density of doped holes can be removed with a positive gate bias of $V_G = 0.8 \text{ V}$. These intrinsically doped holes are believed to result from the stabilization of hole carriers at the interface by counter ions (anions) in the ionic gel, a process similar to the trap healing mechanism discovered recently by Podzorov and coworkers.¹⁷ For negative gate bias up to $V_G = -1.0 \text{ V}$, we find additional hole doping up to $\sim 3 \times 10^{13} \text{ cm}^{-2}$, in agreement with transport measurements. These findings suggest a new mechanism for gate doping of organic semiconductors with ionic liquid or ion gel dielectrics.

Future Plans

During the next funding period, the PIs will continue mechanistic studies on the nature of charge carriers at organic semiconductor/ionic liquid or ion gel interfaces. We will focus on single crystal rubrene and will also carry out a comparative study of the P3HT/ionic liquid or ion gel interfaces. Recent progress in our laboratories provided evidence for Hall effect and Mott

insulator to metal transition in these system, despite the fact that charge carriers may be strongly bound at the immediate interface. It is likely that additional charge carriers injected at $V_G < 0$ are free carrier like, not subjected to the localized Coulomb potential at the interface. We will closely correlate spectroscopy with transport to find out the nature of gate-doped charge carriers responsible for the Hall effect and for the observed Mott transition at these interfaces.

References

- 1 Dimitrakopoulos, C. D.; Malenfant, P. R. L. Organic thin film transistors for large area electronics. *Adv. Mater.* **2002**, *14*, 99.
- 2 Forrest, S. R. The path to ubiquitous and low-cost organic electronic appliances on plastic. *Nature* **2004**, *428*, 911–918.
- 3 Brabec, C. J. Organic photovoltaics: technology and market. *Solar Energy Materials and Solar Cells* **2004**, *83*, 273-292.
- 4 Coakley, K. M.; McGehee, M. D. Conjugated Polymer Photovoltaic Cells. *Chemistry of Materials* **2004**, *16*, 4533-4542.
- 5 Hung, L. S.; Chen, C. H. Recent progress of molecular organic electroluminescent materials and devices. *Materials Science and Engineering: R: Reports* **2002**, *39*, 143–222.
- 6 Forrest, S. R. The road to high efficiency organic light emitting devices. *Organic Electronics* **2003**, *4*, 45–48.
- 7 Silinsh, E. A.; Capek, V. *Organic molecular crystals: interaction, localization, and transport phenomena* (1994, AIP Press, Woodbury, NY).
- 8 Pope, M. & Swenberg, C. E. *Electronic Processes in Organic Crystals and Polymers, 2nd edition* (1999, Oxford University Press, Oxford).
- 9 Coropceanu, V.; Cornil, J.; da Silva Filho, D. A.; Olivier, Y.; Silbey, R.; Brédas, J.-L. Charge Transport in Organic Semiconductors. *Chem. Rev.* **2007**, *107*, 926-952.
- 10 Menard, E.; Podzorov, V.; Hur, S. H.; Gaur, A.; Gershenson, M. E.; Rogers, J. A. High-performance n-and p-type single-crystal organic transistors with free-space gate dielectrics. *Advanced Materials* **2004**, *16*, 2097–2101.
- 11 Podzorov, V.; Menard, E.; Borissov, A.; Kiryukhin, V.; Rogers, J.; Gershenson, M. Intrinsic Charge Transport on the Surface of Organic Semiconductors. *Phys. Rev. Lett.* **2004**, *93*, 086602.
- 12 Podzorov, V.; Menard, E.; Rogers, J.; Gershenson, M. Hall Effect in the Accumulation Layers on the Surface of Organic Semiconductors. *Phys. Rev. Lett.* **2005**, *95*, 226601.
- 13 Li, Z. Q.; Podzorov, V.; Sai, N.; Martin, M. C.; Gershenson, M. E.; Di Ventra, M.; Basov, D. N. Light Quasiparticles Dominate Electronic Transport in Molecular Crystal Field-Effect Transistors. *Phys. Rev. Lett.* **2007**, *99*, 016403.
- 14 Xia, Y.; Cho, J. H.; Lee, J.; Ruden, P. P.; Frisbie, C. D. Comparison of the Mobility-Carrier Density Relation in Polymer and Single-Crystal Organic Transistors Employing Vacuum and Liquid Gate Dielectrics. *Adv. Mater.* **2009**, *21*, 2174-2179.
- 15 Cornil, J.; Beljonne, D.; Bredas, J. L. Nature of optical transitions inconjugated

-
- oligomers. I. Theoretical characterization of neutral and doped oligo(phenylenevinylene)s. *J. Chem. Phys.* **1995**, *103*, 834-841.
- 16 Horowitz, G.; Yassar, A.; von Bardeleben, H. J. ESR and optical spectroscopy evidence for a chain-length dependence of the charged states of thiophene oligomers. Extrapolation to polythiophene. *Synth. Met.* **1994**, *62*, 245-252.
- 17 Lee, B.; Chen, Y.; Fu, D.; Yi, H. T.; Czelen, K.; Najafov, H.; Podzorov, V. "Trap healing and ultralow-noise Hall effect at the surface of organic semiconductors", *Nature Mater.* **2013**, *12*, 1125-1129.

Publications

Wang, S; Ha, MJ; Manno, M; Frisbie, CD; Leighton, C. "Hopping transport and the Hall effect near the insulator-metal transition in electrochemically gated poly(3-hexylthiophene) transistors." *Nature Communications*, **2012**, *3*, 1210. DOI: 10.1038/ncomms2213

Morris, J. D.; Atallah, T. L.; Park, H.; Ooi, Z.; Dodabalapur, A.; Zhu, X.-Y. "Quantifying space charge accumulation in organic bulk heterojunctions by nonlinear optical microscopy," *Organic Electronics* **2013**, *14*, 3014-3018.

Morris, J. D.; Atallah, T. L.; Lombardo, C. J.; Dodabalapur, A.; Zhu, X.-Y. "Mapping electric field distributions in biased organic bulk heterojunctions under illumination by nonlinear optical microscopy," *Appl. Phys. Lett.* **2013**, *102*, 033301.

Xie, W.; Wang, S.; Zhang, X.; Leighton, C.; Frisbie, C. D. "High Conductance 2D Transport around the Hall Mobility Peak in Electrolyte-Gated Rubrene Crystals", *Phys. Rev. Lett.*, submitted, **2014**.

A Synthetic Strategy to Prepare New Complex Uranium- and Thorium-Containing Oxides: Predictive Solid State Synthesis of New Composition using Radius Ratio Rules and Materials Discovery based on Crystal Growth from High Temperature Solutions

Hans-Conrad zur Loye
Department of Chemistry and Biochemistry
University of South Carolina

Program Scope

Our research program focuses on expanding the boundaries of uranium(IV) and uranium(VI) oxide chemistry via three approaches: 1) the targeted synthesis of complex oxides with compositions and structures predicted by radius ratio rules, 2) the crystal growth of new complex uranium oxides from high temperature solutions as an effective method for materials discovery, and 3) the mild hydrothermal crystal growth method to obtain large high quality crystals of uranium (IV) containing fluorides via an in-situ reduction step. In all cases, we perform the structural characterization of these crystals and characterize the physical properties of the new materials synthesized.

Recent Progress

During the first year we succeeded in obtaining single crystals of new uranium containing oxides and fluorides, the former involving U(VI) and the latter involving U(IV). Furthermore, we initiated work on the $A_2MnU_3O_{11}$ ($A = K, Rb$) and $Cs_2Mn_3U_6O_{22}$ family of oxides, the $Na_4MU_6F_{30}$ ($M = Mg, Mn, Fe, Co, Ni, Cu, Zn$) family of fluorides, the $U_3F_{12}(H_2O)$ system, and the planned exploration of new U(IV) and U(VI) oxides. In the second year we focused on a successful area of crystal growth that yielded new ternary U(IV) containing fluorides via our mild hydrothermal route and a new series of U(VI) containing oxy-chlorides via high temperature solution growth. We also begun to explore the uranium silicate phase space that yielded very promising results so far.

The specific approaches we have taken for the synthesis and characterization of new uranium containing systems are based on whether we targeted U(VI) or U(IV) containing products. The growth of U(VI) containing systems requires a different approach from the growth of U(IV) containing materials. First, stabilizing the 6+ oxidation state in an open flux system is relatively easy and little precautions have to be taken to conserve the oxidation state of the starting materials. To prepare U(IV) containing materials, however, greater care must be taken to avoid oxidizing the uranium to the 6+ oxidation state. To avoid oxidation issues we can also pursue in-situ reduction steps, assuring that we maintain reducing conditions throughout the crystal growth process. Finally, solid state reactions to prepare larger quantities of products are carried out in sealed fused silica tubes, thereby assuring that the composition of the final product is based on the quantities of the starting materials.

Fluxes, such as halides (KCl, for example) can be used for both U(VI) and U(IV) containing systems. In the latter case, air must be excluded from the reagents during crystal growth and the creation of U(IV) containing precursors is an important factor in the crystal growth of U(IV) containing systems. We have continued to use the in-situ reduction under mild hydrothermal conditions that we developed during the first year and were successful in obtaining new U(IV) containing fluorides. We have also used halide fluxes to obtain U(VI) containing

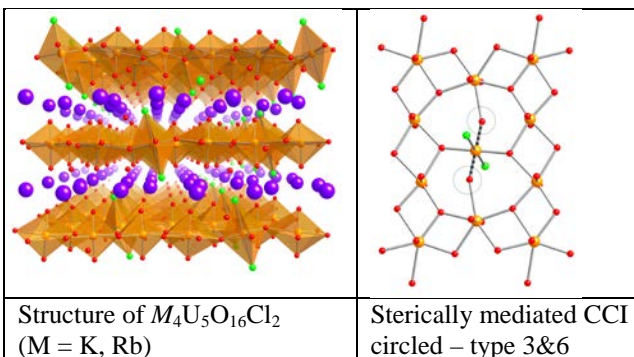
oxychlorides, where the evaporation of the flux to “push” the reaction towards the desired products represented an essential step in the synthesis.

In this abstract, I want to provide a summary of our successful preparation of new U(IV) and U(VI) containing systems. We have discovered a significant number of new compositions in new as well as known structure types. The samples discussed here are all fully structurally characterized and their physical characterization is in various degrees of completeness.

I. U(VI) containing oxychlorides

The complex U(VI) containing oxychlorides, $K_4U_5O_{16}Cl_2$, $Rb_4U_5O_{16}Cl_2$, $Cs_5U_7O_{22}Cl_3$, $RbUO_3Cl$, and $CsUO_3Cl$, were all grown from molten chloride fluxes and structurally characterized by single crystal X-ray diffraction. All of the materials are monoclinic. The first three crystallize in the space group $P2_1/n$ and exhibit a 2D layered structure with a novel layer topology, consisting of UO_6 , UO_7 , and UO_4Cl_2 polyhedra and cation-cation interactions (CCIs) within the plane of the uranyl sheet. The latter two crystallize in the space group $P2_1/m$ and exhibit 1D zipper-like chains of UO_5Cl_2 polyhedra.

We observed cation-cation interactions in some of these oxychlorides that were sterically mediated by the orientation of the uranyl polyhedra. The chloride atoms are located above and below the plane of the uranium, forcing the uranyl oxygens to lie in-plane and create CCIs. To better describe the CCIs we observed in $M_4U_5O_{16}Cl_2$ ($M = K, Rb$) and $Cs_5U_7O_{22}Cl_3$, we derived the general scheme for all types of CCIs (shown below) that can be used for any uranium containing system. In the appendix of the inorganic chemistry paper where we reported these results we also included a generalized scheme that applies to actinides.



II. Ternary Fluorides

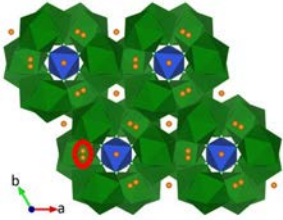
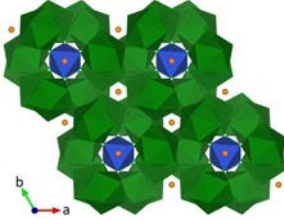
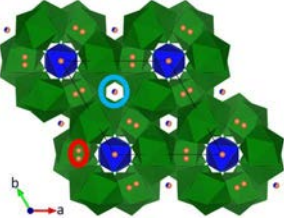
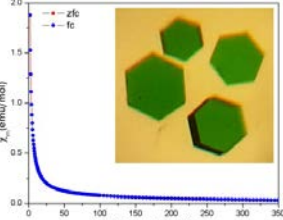
Single crystals of several ternary alkali uranium fluorides, $LiUF_5$, KU_2F_9 , $K_7U_6F_{31}$, $RbUF_5$, RbU_2F_9 and RbU_3F_{13} , have been obtained in a mild hydrothermal process using $UO_2(CH_3CO_2)_2(H_2O)_2$ as the uranium source. Their crystal structures were determined by single crystal X-ray diffraction. The uranium in the starting reagent was successfully reduced from U^{6+} to U^{4+} in a dilute hydrofluoric acid environment, aided by the presence of a copper salt. All materials

exhibit highly complex crystal structures that range from two-dimensional to three-dimensional. The U^{4+} cations are found in high (UF_8 and UF_9) coordination environments. The magnetic susceptibility measurements yielded effective magnetic moments of $3.01 - 3.83 \mu_B$ for the U^{4+} cations. The temperature dependent magnetic susceptibility measurements confirmed that the U^{4+} cation exhibits a nonmagnetic singlet ground state at low temperature. No long-range magnetic order was observed for any of the above compositions down to 2 K. Optical and thermal behavior of the fluorides were also investigated.

III. Quaternary Fluorides

In the first year we reported the synthesis of a new family of U(IV)-containing quaternary fluorides, $Na_4MU_6F_{30}$ ($M = Mn^{2+}, Co^{2+}, Ni^{2+}, Cu^{2+},$ and Zn^{2+}) via a mild hydrothermal technique utilizing an *in situ* U(VI) to U(IV) reduction step. These isostructural fluorides crystallize in a new structure type in the trigonal space group $P\bar{3}c1$ and exhibit a complex three-dimensional

crystal structure consisting of corner- and edge-shared UF_9 and MF_6 polyhedra. The main building block, a $U_6F_{30}^{6-}$ group, is arranged to create two distinct hexagonal channels, inside which MF_6 octahedra and Na^+ cations are located.

			
Na(3) disordered: $Na_4MU_6F_{30}$ family	No disordered sites: $Na_3MU_6F_{30}$ family	$Na_3\&Na_1/M^{2+}$ disordered: $Na_{3-x}M_{1+y}U_6F_{30}$ family	Crystals and magnetic susceptibility of $Na_4MnU_6F_{30}$

We continue to explore this structural family, in particular since we noticed that iron was present as Fe^{3+} rather than as the expected Fe^{2+} . To charge balance this higher oxidation state, one sodium cation that occupied a split position in the $Na_4MU_6F_{30}$ structure, was gone, creating the $Na_3MU_6F_{30}$ family. We managed to synthesize additional members by focusing on traditional +3 cations, such as Ga^{3+} , Al^{3+} , and more unusual +3 cations, such as V^{3+} and Cr^{3+} . Finally, we observed that by varying the synthesis conditions we were able to create variable cation content on the A site, for example in $(Na_{1.33}Mg_{0.43})MgU_6F_{30}$, and variable A and M site occupancies, for example in $Na_{2.5}Mn_{1.75}U_6F_{30}$. We are currently investigating other $Na_xM_yU_6F_{30}$ compositions by controlling the disorder on the different sites and investigating the magnetic properties. Interestingly, while the magnetic properties of the compounds follow single ion behavior, the divalent transition metal cations impact on the spin gap arising from triplet to singlet transition of the U(IV) cation, suggesting potential f-d magnetic interactions for new compositions.

Future Plans

U(VI) containing oxychlorides: We have developed a successful methodology of preparing oxychlorides and are planning to expand this to a) additional oxychlorides systems and b) oxyfluoride and oxybromide systems. We expect most of these structures to exhibit CCIs that we will investigate. A final goal will be to expand this chemistry to U(IV) systems.

Ternary Fluorides: We have successfully synthesized a large number of ternary fluorides. A lot of research into fluorides was done in the 60s and 70s, however, often the structures were not determined due to lack of instrumentation and crystals and in many cases the physical properties were not extensively investigated. With our new mild hydrothermal approach we should be able to systematically expand this work and create crystals of both compositionally known but not structurally characterized systems as well as of completely new systems.

Quaternary Fluorides: We have extensively explored one structural family of quaternary fluorides containing metals in the 2+ and 3+ oxidation state. In addition to completing our investigation into this family, we will attempt to synthesize other quaternary fluoride systems.

Silicates: This is an exciting new area that can potentially be very fruitful with respect to synthesizing new complex uranium containing oxide systems – both U(VI) and U(IV) containing structures. We have just begun our research in this area and are planning to continue to investigate this area of uranium silicate chemistry.

Oxides: $A_2MnU_3O_{11}$ ($A = K, Rb$) and $Cs_2Mn_3U_6O_{22}$. We are planning to extend the number of compositions to include the sodium and lithium analog. In addition, we believe that it will be possible to substitute other +2 or +3 cations for Mn^{2+} into this structure – such as Co^{2+} , Ni^{2+} , Zn^{2+} , Mg^{2+} etc. Furthermore, in order to carry out a thorough characterization of the physical properties, including the magnetic properties, we are exploring the solid-state synthesis of these oxides in order to have multi gram quantities on hand. This is a general goal as it would enable us to perform neutron diffraction measurements on these systems, in particular structures that exhibit long range magnetic order.

PUBLICATIONS:

1. Read, C. M., Bugaris, D. E., zur Loye, H.-C., “Single Crystal Growth and Structural Characterization of Four Complex Uranium Oxides: $CaUO_4$, $\beta-Ca_3UO_6$, $K_4CaU_3O_{12}$, and $K_4SrU_3O_{12}$ ”, *Solid State Sciences*, **2013**, *17*, 40-45.
2. Yeon, J., Smith, M. C., Sefat, A. S., zur Loye, H.-C., “Crystal Growth, Structural Characterization, and Magnetic Properties of New Uranium(IV) Containing Mixed Metal Oxalates, $Na_2U_2M(C_2O_4)_6(H_2O)_4$ ($M = Mn^{2+}$, Fe^{2+} , Co^{2+} , and Zn^{2+})”, *Inorg. Chem.*, **2013**, *52*, 2199-2207.
3. Yeon, J., Sefat, A. S., Tran, T. T., Halasyamani, P. S., zur Loye, H.-C., “Crystal Growth, Structure, Polarization and Magnetic Properties of Cesium Vanadate, $Cs_2V_3O_8$: A Structure-Property Study”, *Inorg. Chem.*, **2013**, *52*, 6179-6186.
4. Read, C. M., Smith, M. D., zur Loye, H.-C., “Synthesis and Crystal Structure of a New Complex Uranium Oxide, $Na_{4.5}Nd_{5}UO_6$ ”, *J. Chem. Cryst.*, **2013**, *43*, 484-487.
5. Yeon, J., Smith, M. D., Sefat, A. S., Tran, T. T., Halasyamani, P. S., zur Loye, H.-C., “ $U_3F_{12}(H_2O)$, a Non-Centrosymmetric Uranium (IV) Fluoride Prepared via a Convenient In-situ Route that Creates U^{4+} under Mild Hydrothermal Conditions”, *Inorg. Chem.*, **2013**, *52*, 8303–8305.
6. Yeon, J., Smith, M. D., Tapp, J., Möller, A., zur Loye, H.-C., “Application of a Mild Hydrothermal Approach Containing an In Situ Reduction Step to the Growth of Single Crystals of the Quaternary U(IV)-containing Fluorides $Na_4MU_6F_{30}$ ($M = Mn^{2+}$, Co^{2+} , Ni^{2+} , Cu^{2+} , and Zn^{2+}) Crystal Growth, Structures, and Magnetic Properties”, *J. Am. Chem. Soc.*, **2014**, *136*, 3955–3963. DOI:10.1021/ja412725r.
7. Read, C. M., Yeon, J., Smith, M. D., zur Loye, H.-C., “Crystal Growth, Structural Characterization, and Optical Properties of Uranium(VI) Containing Oxychlorides, $A_4U_5O_{16}Cl_2$ ($A = K, Rb$), $Cs_5U_7O_{22}Cl_3$, and AUO_3Cl ($A = Rb, Cs$)”, *Cryst. Eng. Comm.*, **2014**, accepted, DOI: 10.1039/c4ce00281d.
8. Yeon, J., Smith, M. D., Tapp, J., Möller, A., zur Loye, H.-C., “Mild Hydrothermal Crystal Growth, Structure, and Magnetic Properties of Ternary U(IV) Containing Fluorides; $LiUF_5$, KU_2F_9 , $K_7U_6F_{31}$, $RbUF_5$, RbU_2F_9 , and RbF_3F_{13} ”, *Inorg. Chem.* **2014**, accepted.

INVITED TALKS

The Materials Project: Accelerated and Large-Scale Materials Research through Computation and Data Mining

Gerbrand Ceder, Department of Materials Science and Engineering, Massachusetts Institute of Technology.

Kristin Persson, Lawrence Berkeley National Laboratory, Berkeley, CA

Novel materials design has become a critical capability to address several urgent societal problems, including clean energy. The Materials Project (www.materialsproject.com), has as its objective to leverage fundamental insights and novel method development by using high-throughput first principles computations on an unparalleled scale to provide basic materials property data on all known and many potential new inorganic compounds, thereby facilitating the search for new materials. The use of experimental data is integral to the Materials Project as it is used to both benchmark and leverage computational into areas where it is less accurate.

I will show successful examples of using high-throughput computations to discover, optimize, and understand new cathode materials and solid state conductors for safe Li-ion batteries.

Finally, I will show examples of how computations can be used to address the remaining challenge of directed materials synthesis.

CEMD, Neutron instruments for Chemistry

AJ (Timmy) Ramirez-Cuesta
Chemical and Engineering Materials Division, Oak Ridge National Laboratory,
Oak Ridge, Tennessee 37831-6475, United States

ramirezcueaj@ornl.gov

The CEMD (Chemical and Engineering Materials Division) at Oak Ridge National Laboratory has a suite of instruments that are particularly suited to study material sciences. The instrumentation, located at the SNS and HIFR includes: diffraction, stress measurements, small angle neutron scattering, magnetism, spectroscopy etc.

In this talk I will just briefly present the capabilities of the CEMD and will present in more details inelastic neutron scattering (INS) and some examples of its applications in chemistry.

INS is a technique that is ideally suited to study hydrogen-containing materials due to the high cross section of hydrogen¹; it is also the case that INS spectra are straightforward to model². Neutrons are also highly penetrating particles, so the use of complex sample environment is usually not an issue.

The VISION spectrometer located at the Spallation Neutron Source (SNS) Oak Ridge National Laboratory in Tennessee, USA, is the world's only high throughput, high resolution broadband INS spectrometer, with access to energy transfer range from -3 meV to 1000 meV a resolution $\Delta\omega/\omega \sim 1.5\%$ above 2 meV, the resolution at the elastic line is 150 μeV FWHM.

One of the main barriers to the use of INS was long time required for data collection and large samples. Thanks to the optimization in the design, the use of the most advanced neutron optics available at the present moment and the brightest spallation neutron source in the world. VISION has already measured INS spectra, of publication quality in 200 sec or less³, this is a major breakthrough for the application of INS to chemistry and catalysis.

At the moment we are in the process of procuring a newly designed sample changer that will allow the exploitation of the high throughput capability and we will establish a mail-in program during fall 2014.

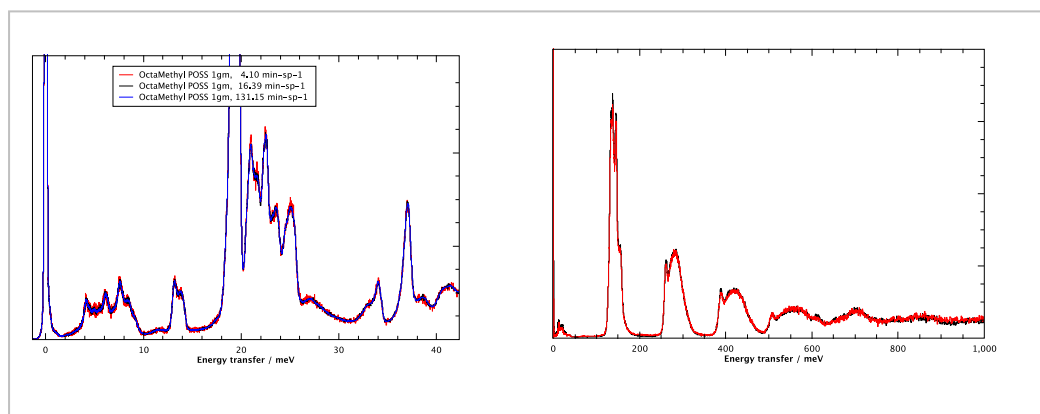


Figure 1. Left panel: the INS of Octamethyl-POSS Nanoparticles collected 4 mins (black) 16 mins blue 120 mins (blue). Right panel: The INS of ZrH_2 .

References

¹ PCH Mitchell, SF Parker, AJ Ramirez-Cuesta and J Tomkinson "Vibrational Spectroscopy with Neutrons" World Scientific, London, (2005).

² A J Ramirez-Cuesta, Comp Phys Commun **157** 226-238 (2004).

³ Jalarvo, N., Gourdon, O., Ehlers, G., Tyagi, M., Kumar, S. K., Dobbs, K. D., Crawford, M. K. (2014). Structure and Dynamics of Octamethyl-POSS Nanoparticles. *The Journal of Physical Chemistry C*, 118(10), 5579–5592. doi:10.1021/jp412228r

Poster Sessions

**Materials Chemistry
Principal Investigators' Meeting 2014**

Poster Session 1

Monday, July 14, 4:00–6:00 pm

Session 1a. Predictive Materials Discovery

1. Theory and Simulations of Polymer Nanocomposites Linking Molecular Features of the Polymers and Additives to Composite Morphology for Organic Photovoltaic Applications
Arthi Jayaraman, University of Colorado at Boulder 179

Session 1b. Inorganic Conductors, Semiconductors, and Superconductors

2. New Superconducting Materials
Robert Cava, Princeton University..... 103
3. Two-Dimensional Chalcogenide Nanomaterials
Yi Cui, SLAC National Accelerator Laboratory 3
4. Molecular Magnets Based on a Modular Approach: Investigation of Coupling, Anisotropy, and Electronic Factors on Bistability
Kim R. Dunbar, Texas A&M University 120
5. Enhanced Mixed Electronic-Ionic Conductors through Cation Ordering
Allan J. Jacobson, University of Houston..... 175
6. Enhanced Mixed Electronic-Ionic Conductors through Cation Ordering
Dane Morgan, University of Wisconsin..... 175
7. Rational Synthesis of Superconductors
Mercouri Kanatzidis, Argonne National Laboratory/ Northwestern University..... 32
8. Fundamental Studies of Charge Transfer in Nanoscale Heterostructures of Earth-Abundant Semiconductors for Solar Energy Conversion
Song Jin, University of Wisconsin–Madison 187
9. Materials Science of Electrodes and Interfaces for High-Performance Organic Photovoltaics
Tobin J. Marks, Northwestern University 207

10. Dielectric Ceramics in Nanosheet Form <i>Tina T. Salguero, University of Georgia</i>	246
11. Crystal Growth, Structure, Phase Relationships, and Magnetic Properties of Transition Metal Substituted $Mn_{1-x}Bi$ Compounds <i>Srinivasa Thimmaiah, Ames Laboratory and Iowa State University</i>	68
12. Physical Chemistry of Inorganic Nanostructures <i>Peidong Yang, Lawrence Berkeley National Laboratory</i>	80
13. A Synthetic Strategy to Prepare New Complex Uranium- and Thorium-Containing Oxides: Predictive Solid State Synthesis of New Composition using Radius Ratio Rules and Materials Discovery based on Crystal Growth from High Temperature Solutions <i>Hans-Conrad zur Loye, University of South Carolina</i>	285

Session 1c. Organic and Polymer Assemblies and Networks

14. Biaxiality in Nematic and Smectic Liquid Crystals <i>Satyendra Kumar, Kent State University</i>	203
15. Hydroxide Conductors for Energy Conversion Devices <i>Bryan Pivovar, National Renewable Energy Laboratory</i>	52
16. Polymer-Based Multicomponent Materials <i>Tomonori Saito, Oak Ridge National Laboratory</i>	56
17. Linking Metal Ions via Inorganic Click (iClick) Reaction <i>Adam S. Veige, University of Florida</i>	270
18. Toward Hierarchically Structured Functional Nanocomposites <i>Ting Xu, Lawrence Berkeley National Lab/ University of California–Berkeley</i>	72
19. Understand Organic/Inorganic Interface Toward Electroactive Nanocomposites <i>Ting Xu, Lawrence Berkeley National Lab/ University of California–Berkeley</i>	76

Session 1d. Metal and Covalent Organic Frameworks

20. Tuning Sorption Properties of Metal–Organic Frameworks via Postsynthetic Covalent Modification <i>Seth Cohen, University of California–San Diego</i>	107
21. Metal and Covalent Organic Frameworks <i>Mircea Dincă, Massachusetts Institute of Technology</i>	111

22. Small Gas Storage and Selective Carbon Dioxide Capture by Nanoporous Organic Polymers <i>Hani El-Kaderi, Virginia Commonwealth University</i>	124
23. Pore Space Engineering and Functionalization in Porous Metal-Organic Framework Materials <i>Pingyun Feng, University of California–Riverside</i>	128
24. Leveraging Kinetic Control in the Assembly and Sorption Properties of Nanostructured Porous Materials <i>Adam J. Matzger, University of Michigan</i>	211

The following poster from Session 2e will be on display Monday afternoon instead of Tuesday afternoon:

25. Rational Design and Nanoscale Integration of Multi-heterostructure Photocatalysts <i>Xiangfeng Duan, University of California–Los Angeles</i>	116
--	-----

The following poster from Session 2c will be on display Monday afternoon instead of Tuesday afternoon:

26. Bi-continuous Multi-component Nanocrystal Superlattices for Solar Energy Conversion <i>Cherie Kagan, University of Pennsylvania</i>	191
--	-----

Poster Session 2

Tuesday, July 15, 4:00–6:00 pm

Session 2a. Materials Characterization

1. Control of Interface- and Mesoscopic Structure in High Performance Organic Solar Cells: Towards a Predictive Device Paradigm
Harald Ade, North Carolina State University.....87
2. Chemical Frustration: A Design Principle for the Discovery of New Complex Intermetallic and Alloy Phases
Daniel C. Fredrickson, University of Wisconsin–Madison..... 136
3. Optical Spectroscopy and Scanning Tunneling Microscopy Studies of Molecular Adsorbates and Anisotropic Ultrathin Films
John C. Hemminger, University of California–Irvine 167
4. Relationships between the Chemistry and Physical Interaction Forces (Adhesion, Friction, and Lubrication) between Closely Apposed Surfaces in Liquids
Jacob Israelachvili, University of California–Santa Barbara 171
5. ^{125}Te NMR and Thermoelectric Properties of Complex Tellurides: The Role of Materials Chemistry
E. M. Levin, Ames Laboratory36
6. Nuclear Magnetic Resonance
Alexander Pines, Lawrence Berkeley National Laboratory..... 48
7. Molecular Processes Underlying the Structure and Assembly of Thin Films and Nanoparticles at Complex Interfaces
Geraldine L. Richmond, University of Oregon 234
8. Structure and Dynamics of Solid-Liquid Interfaces
Miquel Salmeron, Lawrence Berkeley National Lab/Univ. of California, Berkeley 60
9. Directed Energy Interactions with Surfaces
Michael Savina, Argonne National Laboratory 64

Session 2b. Organic and Polymer Assemblies and Networks: *Electronics and Photonics*

10. Fundamental Charge Transfer Processes in Stable Free-Radical Organic Polymer Systems
Thomas Gennett, National Renewable Energy Laboratory 20
11. Cyclometalation Syntheses of Phosphorescent Complexes
Thomas G. Gray, Case Western Reserve University..... 152
12. Molecularly Designed Localized Static Charging for Energy Efficiency in Organic Electronics
Howard E. Katz, Johns Hopkins University..... 195
13. Donor-Acceptor π -Extended Porphyrins for Solar Energy Conversion
Hong Wang, Miami University of Ohio 274
14. Extracting Hot Carriers from Photoexcited Semiconductor Nanocrystals
Xiaoyang Zhu, Columbia University..... 278
15. Spectroscopy of Charge Carriers and Traps in Field-Doped Single Crystal Organic Semiconductors
Xiaoyang Zhu, Columbia University..... 281

Session 2c. Nanostructures and Low-Dimensional Structures

16. “Giant” Nanocrystal Quantum Dots: Controlling Charge Recombination Processes for High-Efficiency Solid-State Lighting
Jennifer A. Hollingsworth, Los Alamos National Laboratory 28
17. Bi-continuous Multi-component Nanocrystal Superlattices for Solar Energy Conversion
Cherie Kagan, University of Pennsylvania 191
18. Mesoscale Photophysical Properties of Anisotropic Hybrid Nanostructure Assemblies
Vladimir V. Tsukruk, Georgia Institute of Technology..... 262

Session 2d. Electrochemical Interfaces and Energy Storage

19. Mitigating Breakdown in High Energy Density Perovskite Polymer Nanocomposite Capacitors
Richard L. Brutchey, University of Southern California..... 99

20. Linking Ion Solvation and Lithium Battery Electrolyte Properties <i>Wesley Henderson, Pacific Northwest National Laboratory</i>	24
21. Materials and Interfacial Chemistry for Next-Generation Electrical Energy Storage <i>Arumugam Manthiram, University of Texas at Austin</i>	148
22. Energy and Fuels from Multifunctional Electrochemical Interfaces <i>Nenad Markovic, Argonne National Laboratory</i>	40
23. Activation of Hydrogen under Ambient Conditions by Main Group Molecules <i>Philip P. Power, University of California–Davis</i>	230
24. Electrochemically Smart Bimetallic Materials Featuring Group 11 Metals: In Situ Conductive Network Generation and Its Impact on Cell Capacity <i>Esther S. Takeuchi, Stony Brook University / Brookhaven National Laboratory</i>	254

Session 2e. Energy Generation and Conversion

25. Rational Design and Nanoscale Integration of Multi-heterostructure Photocatalysts <i>Xiangfeng Duan, University of California–Los Angeles</i>	116
(This poster will be presented Monday afternoon rather than Tuesday afternoon.)	
26. Cathode Catalysis in Hydrogen/Oxygen Fuel Cells: New Catalysts, Mechanism, and Characterization <i>Andrew A. Gewirth, University of Illinois at Urbana-Champaign</i>	144
27. Programming Function in Soft Matter <i>Ralph G. Nuzzo, University of Illinois at Urbana-Champaign</i>	219
28. Programming Function via Soft Materials <i>John Rogers, University of Illinois at Urbana-Champaign</i>	238

*Author Index
and
List of Participants*

Ade, Harald	87	Hamers, Robert J.	187
Agra-Kooijman, D. M.....	203	Hayward, Ryan C.....	164
Alivisatos, Paul.....	72, 76, 80	Heeger, Alan J.	215
Baldo, M. A.....	91	Hemminger, John C.	167
Bates, Frank	56	Henderson, Wesley	24
Bazan, Guillermo C.	215	Hollingsworth, Jennifer A.	28
Bobev, Svilen	95	Hsia, K. Jimmy	219, 238
Bocharova, Vera.....	56	Htoon, Han	28
Braun, Paul V.	238	Hwang, Harold	3
Bridges, C. A.....	11	Israelachvili, Jacob	171
Brutchey, Richard L.	99	Jacobson, Allan J.	175
Cao, Guozhong.....	183	Jayaraman, Arthi.....	179
Cava, Robert J.	103	Jenekhe, Samson A.	183
Ceder, Gerbrand	291	Jin, Song.....	187
Chang, Robert P. H.....	207	Kagan, Cherie R.	191
Cohen, Seth M.....	107	Kanatzidis, Mercouri G.....	32
Cui, Yi.....	3	Katz, Howard E.	195
Cuk, Tanja.....	76	Kenis, Paul J. A.	144
Curtiss, Larry A.	7	Kerr, Lei.....	274
Dadmun, Mark	56	Kikkawa, James M.....	191
Dai, S.	11	Kisliuk, Alex	56
de Pablo, Juan J.	15	Kovnir, Kirill.....	199
Dincă, Mircea	111	Kumar, Satyendra	203
Duan, Xiangfeng	116	Leone, Stephen	80
Dunbar, Kim R.	120	Levin, E. M.....	36
El-Kaderi, Hani M.	124	Li, Quan	203
El-Sayed, Mostafa	262	Li, Xiuling	238
Engheta, Nader	191	Lin, Qisheng	68
Engtrakul, Chaiwat	52	Liu, Yi.....	72, 76
Ewoldt, Randy.....	238	Long, Hai.....	52
Feng, Pingyun	128	Macomber, Clay	52
Fischer, Felix R.	132	Manthiram, Arumugam.....	11, 148
Fréchet, Jean.....	72	Markovic, Nenad M.	40
Fredrickson, Daniel C.....	136	Markovic, Nina.....	195
Freed, Karl F.	140	Marks, Tobin, J.....	207
Freeman, Arthur J.....	207	Marschilok, Amy C.....	254
Frisbie, C. Daniel.....	281	Mason, Thomas O.....	207
Gennett, Thomas	20	Matzger, Adam J.....	211
Gewirth, Andrew A.	144	Mays, Jimmy	56
Ginger, David S.....	183	Melosh, Nick	44
Goodenough, John B.	11, 148	Miller, Gordon J.	68
Granick, Steve	238	Moore, Jeffrey S.	219, 238
Gray, Thomas G.	152	Morgan, Dane	175
Greenbaum, Steve G.....	156	Murray, Christopher B.	191
Grey, Clare	175	Nealey, Paul F.	15
Haddon, Robert C.....	160	Nguyen, Thuc-Quyen.....	215

Nuzzo, Ralph G.	144, 219, 238
Nyman, May.....	222
Owen, Jonathan S.	226
Paranthaman, M. P.	11
Pellin, Michael J.	7, 64
Persson, Kristin	291
Pines, Alexander.....	48
Pivovar, Bryan.....	52
Poepelmeier, Kenneth R.	207
Power, Philip P.	230
Ramirez-Cuesta, AJ (Timmy)	292
Rauchfuss, Thomas B.	144
Reich, Daniel H.	195
Rey, Alejandro	203
Richmond, Geraldine L.....	234
Rogers, John A.	219, 238
Russell, Thomas P.	242
Saito, Tomonori.....	56
Salguero, Tina T.	246
Salmeron, Miquel B.....	60, 72, 76
Savina, Michael.....	64
Scheiner, Peter.....	44
Schmidt-Rohr, K.	36
Schweizer, Kenneth S.	56, 238
Shen, Z. X.	44
Smyrl, William H.	250
Sokolov, Alexei.....	56
Somorjai, Gabor	60
Srinivasarao, M.	203
Stamenkovic, Vojislav	40
Stein, Andreas	250
Sturgeon, Matthew	52
Sumpter, Bobby.....	56
Sun, X. G.....	11
Takeuchi, Esther S.....	254
Takeuchi, Kenneth J.	254
Teng, Xiaowei.....	258
Thimmaiah, Srinivasa	68
Tirrell, M.	15
Truhlar, Donald G.	250
Tsukruk, Vladimir V.....	262
Urban, Volker.....	56
Vajda, Stefan	7
Van Voorhis, T.....	91
Vardeny, Z. Valy	266
Veige, Adam S.	270
Veith, G. M.....	11
Wang, Hong.....	274
Wang, Lin-Wang	76
Wong-Foy, Antek G.	211
Wright, John C.....	187
Wudl, Fred.....	215
Xu, Ting	72, 76
Yang, Peidong	60, 80
Zapol, Peter	7
Zhu, Xiaoyang	278, 281
Zinovev, Alexander	64
zur Loye, Hans-Conrad	285

Participant List

Harald Ade
North Carolina State University
harald_ade@ncsu.edu

Svilen Bobev
University of Delaware
bobev@udel.edu

Paul Braun
University of Illinois
pbraun@illinois.edu

Richard Brutchey
University of Southern California
brutchey@usc.edu

Robert Cava
Princeton University
rcava@princeton.edu

Gerbrand Ceder
Massachusetts Institute of Technology
gceder@mit.edu

Robert Chang
Northwestern University
rphchang@gmail.com

Seth Cohen
University of California – San Diego
scohen@ucsd.edu

Teresa Crockett
U.S. Department of Energy
teresa.crockett@science.doe.gov

YI Cui
Stanford University/SLAC
yicui@stanford.edu

Larry Curtiss
Argonne National Laboratory
curtiss@anl.gov

Sheng Dai
Oak Ridge National Laboratory
dais@ornl.gov

Juan de Pablo
Argonne National Laboratory/University of
Chicago
depablo@uchicago.edu

Mircea Dincă
Massachusetts Institute of Technology
mdinca@mit.edu

Xiangfeng Duan
University of California – Los Angeles
xduan@chem.ucla.edu

Kim Dunbar
Texas A&M University
dunbar@chem.tamu.edu

Hani El-Kaderi
Virginia Commonwealth University
h elkaderi@vcu.edu

Pingyun Feng
University of California – Riverside
pingyun.feng@ucr.edu

Felix Fischer
University of California – Berkeley
ffischer@berkeley.edu

Daniel Fredrickson
University of Wisconsin – Madison
danny@chem.wisc.edu

Karl Freed
University of Chicago
freed@uchicago.edu

Daniel Frisbie
University of Minnesota
frisbie@umn.edu

Thomas Gennett
National Renewable Energy Laboratory
thomas.gennett@nrel.gov

Bonnie Gersten
U.S. Department of Energy
Bonnie.Gersten@science.doe.gov

Andrew Gewirth
University of Illinois
agewirth@illinois.edu

John Goodenough
University of Texas – Austin
jgoodenough@mail.utexas.edu

Thomas Gray
Case Western Reserve University
tgray@case.edu

Steve Greenbaum
Hunter College of CUNY
steve.greenbaum@hunter.cuny.edu

Robert Haddon
University of California – Riverside
haddon@ucr.edu

Ryan Hayward
University of Massachusetts – Amherst
rhayward@mail.pse.umass.edu

John Hemminger
University of California – Irvine
jchemmin@uci.edu

Wesley Henderson
Pacific Northwest National Laboratory
Wesley.Henderson@pnnl.gov

Craig Henderson
U.S. Department of Energy
craig.henderson@science.doe.gov

Jennifer Hollingsworth
Los Alamos National Laboratory
jenn@lanl.gov

Han Htoon
Los Alamos National Laboratory
htoon@lanl.gov

Jacob Israelachvili
University of California – Santa Barbara
jacob@engineering.ucsb.edu

Allan Jacobson
University of Houston
ajjacob@uh.edu

Arthi Jayaraman
University of Colorado – Boulder
arthi.jayaraman@colorado.edu

Samson Jenekhe
University of Washington
jenekhe@u.washington.edu

Song Jin
University of Wisconsin – Madison
jin@chem.wisc.edu

Rebecca Jones-Albertus
U.S. Department of Energy
Pauline.Perando@ee.doe.gov

Cherie Kagan
University of Pennsylvania
kagan@seas.upenn.edu

Mercouri Kanatzidis
Northwestern University
m-kanatzidis@northwestern.edu

Howard Katz
Johns Hopkins University
hekatz@jhu.edu

Jonathan King
Lawrence Berkeley National Laboratory
jpking@lbl.gov

Aravinda Kini
U.S. Department of Energy
a.kini@science.doe.gov

Kirill Kovnir
University of California - Davis
kkovnir@ucdavis.edu

Satyendra Kumar
Kent State University
skumar@kent.edu

Evgenii Levin
Ames Lab/Iowa State University
levin@iastate.edu

Xiuling Li
University of Illinois – Urbana-Champaign
xiuling@illinois.edu

Quan Li
Liquid Crystal Institute -KSU
qli1@kent.edu

Arumugam Manthiram
University of Texas - Austin
manth@austin.utexas.edu

Nenad Markovic
Argonne National Laboratory
nmmarkovic@anl.gov

Michael Markowitz
U.S. Department of Energy
mike.markowitz@science.doe.gov

Tobin Marks
Northwestern University
t-marks@northwestern.edu

Adam Matzger
University of Michigan
matzger@umich.edu

Nick Melosh
SLAC/Stanford University
nmelosh@stanford.edu

Thuc-Quyen Nguyen
University of California – Santa Barbara
quyen@chem.ucsb.edu

Ralph Nuzzo
University of Illinois – Urbana-Champaign
r-nuzzo@illinois.edu

May Nyman
Oregon State University
may.nyman@oregonstate.edu

Jonathan Owen
Columbia University
jso2115@columbia.edu

Mariappan Paranthaman
Oak Ridge National Laboratory
paranthamanm@ornl.gov

Bryan Pivovar
National Renewable Energy Laboratory
bryan.pivovar@nrel.gov

Timothy Pope
University of Georgia
timpope@uga.edu

Philip Power
University of California
pppower@ucdavis.edu

AJ (Timmy) Ramirez-Cuesta
Oak Ridge National Laboratory
ramirezcueaj@ornl.gov

Daniel Reich
Johns Hopkins University
reich@jhu.edu

Alejandro Rey
McGill University
alejandro.rey@mcgill.ca

Geraldine Richmond
University of Oregon
richmond@uoregon.edu

John Rogers
University of Illinois – Urbana-Champaign
jrogers@illinois.edu

Tomonori Saito
Oak Ridge National Laboratory
saitot@ornl.gov

Miquel Salmeron
Lawrence Berkeley National Laboratory
mbsalmeron@lbl.gov

Michael Savina
Argonne National Laboratory
msavina@anl.gov

Michael Sennett
U.S. Department of Energy
michael.sennett@science.doe.gov

Vojislav Stamenkovic
Argonne National Laboratory
vrstamenkovic@anl.gov

Andreas Stein
University of Minnesota
a-stein@umn.edu

Bobby Sumpter
Oak Ridge National Laboratory
sumpterbg@ornl.gov

Esther Takeuchi
Stony Brook University
esther.takeuchi@stonybrook.edu

Xiaowei Teng
University of New Hampshire
xw.teng@unh.edu

Srinivasa Thimmaiah
Ames Laboratory
srini@ameslab.gov

Matthew Tirrell
Argonne National Laboratory/Institute for
Molecular Engineering/University of
Chicago
mtirrell@uchicago.edu

Vladimir Tsukruk
Georgia Institute of Technology
vladimir@mse.gatech.edu

Zeev Valentine Vardeny
University of Utah
val@physics.utah.edu

Adam Veige
University of Florida
veige@chem.ufl.edu

Hong Wang
Miami University
wangh3@miamioh.edu

Philip Wilk
U.S. Department of Energy
philip.wilk@science.doe.gov

Lane Wilson
U.S. Department of Energy
lane.wilson@science.doe.gov

Ting Xu
Lawrence Berkeley National Lab/University
of California – Berkeley
Tingxu@berkeley.edu

Peidong Yang
Lawrence Berkeley National Lab/University
of California – Berkeley
p_yang@berkeley.edu

Xiaoyang Zhu
Columbia University
xyzhu@columbia.edu

Hans-Conrad zur Loye
University of South Carolina
zurloye@mailbox.sc.edu